

Lecture Notes in Civil Engineering

Cavit Atalar
Feyza Çinicioğlu *Editors*

5th International Conference on New Developments in Soil Mechanics and Geotechnical Engineering

Proceedings of ZM 2022

 Springer

Lecture Notes in Civil Engineering

Volume 305

Series Editors

Marco di Prisco, Politecnico di Milano, Milano, Italy

Sheng-Hong Chen, School of Water Resources and Hydropower Engineering,
Wuhan University, Wuhan, China

Ioannis Vayas, Institute of Steel Structures, National Technical University of
Athens, Athens, Greece

Sanjay Kumar Shukla, School of Engineering, Edith Cowan University, Joondalup,
WA, Australia

Anuj Sharma, Iowa State University, Ames, IA, USA

Nagesh Kumar, Department of Civil Engineering, Indian Institute of Science
Bangalore, Bengaluru, Karnataka, India

Chien Ming Wang, School of Civil Engineering, The University of Queensland,
Brisbane, QLD, Australia

Lecture Notes in Civil Engineering (LNCE) publishes the latest developments in Civil Engineering—quickly, informally and in top quality. Though original research reported in proceedings and post-proceedings represents the core of LNCE, edited volumes of exceptionally high quality and interest may also be considered for publication. Volumes published in LNCE embrace all aspects and subfields of, as well as new challenges in, Civil Engineering. Topics in the series include:

- Construction and Structural Mechanics
- Building Materials
- Concrete, Steel and Timber Structures
- Geotechnical Engineering
- Earthquake Engineering
- Coastal Engineering
- Ocean and Offshore Engineering; Ships and Floating Structures
- Hydraulics, Hydrology and Water Resources Engineering
- Environmental Engineering and Sustainability
- Structural Health and Monitoring
- Surveying and Geographical Information Systems
- Indoor Environments
- Transportation and Traffic
- Risk Analysis
- Safety and Security

To submit a proposal or request further information, please contact the appropriate Springer Editor:

- Pierpaolo Riva at pierpaolo.riva@springer.com (Europe and Americas);
- Swati Meherishi at swati.meherishi@springer.com (Asia—except China, Australia, and New Zealand);
- Wayne Hu at wayne.hu@springer.com (China).

All books in the series now indexed by Scopus and EI Compendex database!

Cavit Atalar · Feyza Çinicioğlu
Editors

5th International Conference on New Developments in Soil Mechanics and Geotechnical Engineering

Proceedings of ZM 2022

 Springer

Editors

Cavit Atalar
Earthquake and Research
and Evaluation Center
Near East University
Nicosia, North Cyprus, Turkey

Feyza Çinicioğlu
Department of Civil Engineering
Özyeğin University
Çekmeköy, İstanbul, Turkey

ISSN 2366-2557

ISSN 2366-2565 (electronic)

Lecture Notes in Civil Engineering

ISBN 978-3-031-20171-4

ISBN 978-3-031-20172-1 (eBook)

<https://doi.org/10.1007/978-3-031-20172-1>

© The Editor(s) (if applicable) and The Author(s), under exclusive license to Springer Nature Switzerland AG 2023

This work is subject to copyright. All rights are solely and exclusively licensed by the Publisher, whether the whole or part of the material is concerned, specifically the rights of translation, reprinting, reuse of illustrations, recitation, broadcasting, reproduction on microfilms or in any other physical way, and transmission or information storage and retrieval, electronic adaptation, computer software, or by similar or dissimilar methodology now known or hereafter developed.

The use of general descriptive names, registered names, trademarks, service marks, etc. in this publication does not imply, even in the absence of a specific statement, that such names are exempt from the relevant protective laws and regulations and therefore free for general use.

The publisher, the authors, and the editors are safe to assume that the advice and information in this book are believed to be true and accurate at the date of publication. Neither the publisher nor the authors or the editors give a warranty, expressed or implied, with respect to the material contained herein or for any errors or omissions that may have been made. The publisher remains neutral with regard to jurisdictional claims in published maps and institutional affiliations.

This Springer imprint is published by the registered company Springer Nature Switzerland AG
The registered company address is: Gewerbestrasse 11, 6330 Cham, Switzerland

Committees

Conference Honorary Chair

Suat İ. Günsel Conference Honorary Chair, Founding President of Near East University, North Cyprus

Conference Chair

İrfan S. Günsel Chairman of the Board of Trustees of Near East University, North Cyprus

Organising Committee Honorary Chair

Ergün Toğrol Honorary President of Turkish Society of Soil Mechanics and Geotechnical Engineering, Turkey

Organising Committee Chairs

Feyza Çinicioğlu Immediate Past President of Turkish Society of Soil Mechanics and Geotechnical Engineering, Turkey, Özyeğin University, Turkey

Cavit Atalar President of Earthquake and Soil Research and Evaluation Center, Near East University, North Cyprus

Organising Committee Members

Rasin Düzceer	President of Turkish Society of Soil Mechanics and Geotechnical Engineering, Turkey, Kasktaş, A.Ş. Turkey
Ahmet Sağlamer	Past President of Turkish Society of Soil Mechanics and Geotechnical Engineering, Turkey
Mehmet Berilgen	Yıldız Technical University, Turkey
İlknur Bozbey	İstanbul University—Cerrahpaşa, Turkey
Kemal Önder Çetin	Middle East Technical University, Turkey
Özer Çinicioğlu	General Secretary of Turkish Society of Soil Mechanics and Geotechnical Engineering, Turkey
Braja M. Das	California State University Sacramento, USA
Turan Durgunoğlu	Boğaziçi University, Turkey
Alp Gökalp	Kasktaş, A.Ş. Turkey
Erol Güler	Boğaziçi University, Turkey
Nejan Huvaj	Middle East Technical University, Turkey
Banu İkizler	Karadeniz Technical University, Turkey
Havvanur Kiliç	Yıldız Technical University, Turkey
Müge İnanir	Geogrup, Turkey
Recep İyisan	İstanbul Technical University, Turkey
Kutay Özyaydin	Yıldız Technical University, Turkey
Eun C. Shin	Immediate Past Vice-President of the Issmge for Asia, Korea
Ivan Vanicek	Past Vice-President of the Issmge for Europe, Czech Republic
Thomas Zimmie	Rensselaer Polytechnic Institute, USA

International Advisory Board

Atila Ansal	Özyeğin University, Turkey
Sivakumar Babu	President, Indian Geotechnical Society, India
Fatma Baligh	Past Vice-President of the Issmge for Africa, Egypt
Ayşe Pekrioğlu Balkis	Cyprus Internatiol University, North Cyprus
Huriye Bilsel	Cyprus Internatiol University, North Cyprus
Mounir Bouassida	Past Vice-President of the Issmge for Africa, Tunisia
Luljeta Bozo	President, Albanian Geotechnical Society, Albania
Heinz Brandl	Vienna University of Technology, Austria
Jean-Louis Briaud	Immediate Past President of the Issmge, USA
Moonkyung Chung	President, Korean Geotechnical Society, Korea
Ayşe Edinçliler	President Turkish Geosynthetics Society, Turkey
Tuncer Edil	University of Wisconsin-Madison, USA
Pedro Ferreira	University College London, United Kingdom
Jana Frankovska	Chairwoman, Czech and Slovak Committee for Smge, Slovakia

Antonio Gens	Past Vice-President of the Issmge for Europe, Spain
Thomas L. Holzer	USGS, Menlo Park, USA
Mahdi O. Karkush	President Iraqi Scientific Society for Soil Mechanics and Foundation Engineering, Iraq
Nilay Keskin	Süleyman Demirel University, Turkey
Suzanne Lacasse	Norwegian Geotechnical Institute, Norway
Lyesse Laloui	Vice-President of the Issmge for Europe, Switzerland
Mustafa Laman	Liverpool University, UK
Madhira Madhav	Past Vice-President of the Issmge for Asia, India
Murat Mollamahmutoglu	Gazi University, Turkey
Mario Manassero	Immediate Past Vice-President of the Issmge for Europe, Italy
Maher Omar	Sharjah University, UAE
Akın Önalp	Okan University, Turkey
Gürkan Özden	Dokuz Eylül University, Turkey
Jovan Papic	President, Macedonian Association for Geotechnics, North Macedonia
Chittaranjan Patra	Department of Civil Engineering, National Institute of Technology, India
Kok Kwang Phoon	Provost, Singapore University of Technology and Design, Singapore
Zalihe Nalbantoglu Sezai	Eastern Mediterranean University, North Cyprus
Siva Sivakugan	James Cook University, Australia
Aykut Şenol	İstanbul Technical University, Turkey
Alejo O. Sfriso	Immediate Past Vice-President of the Issmge for South America, Arjantina
Khaled Sobhan	Florida Atlantic University, USA
Bariş Trak	Past Technical Director Council of Europe Development Bank, France
Selçuk Toprak	Gebze University, Turkey
Mojca Ravnikar Turk	President Slovenian Geotechnical Society, Slovenia
Erol Tutumluer	University of Illinois, USA
Mehmet Tümay	Louisiana State University, USA
Eriş Uygur	Eastern Mediterranean University, North Cyprus
Gülgün Yilmaz	Anadolu University, Turkey
Chungsik Yoo	President International Geosynthetics Society, Korea
Yeliz Yükselen-Aksoy	Dokuz Eylül University, Turkey
Şahin Zaimoğlu	Atatürk University, Turkey
Askar Zhusupbekov	Past Vice-President of the Issmge for Asia, Kazakhstan

Preface

The Fifth International Conference on New Developments in Soil Mechanics and Geotechnical Engineering (5. ICNDSMGE—ZM 2022) organized jointly by the Turkish Society of Soil Mechanics and Geotechnical Engineering and Near East University was held online due to COVID-19 pandemic from June 30 to July 2, 2022. The conference is the fifth of the conference series started in 2003. This conference like the four previous conferences initially was organized to be held face to face at Near East University, Nicosia, North Cyprus on September 3 to 5, 2020. It had, however, needed to be postponed in the view of the continuing spread of the coronavirus (COVID-19). All conferences were participated by eminent ISSMGE members including five Presidents, Immediate Past Presidents, and Vice Presidents, renowned keynote speakers and colleagues from all over the world. We would like to extend our deep appreciation to the attendees of the 5th conference for showing the same interest and involvement.

The topics of the conference are Soil Properties and Characterization; Shallow and Deep Foundations; Environmental Preservation, Water and Energy; Modelling; Emerging Subjects in Geotechnical Engineering; Stability of Slopes and Landslides; Excavations, support systems, earth-retaining structures and underground systems; Earthquake Geotechnical Engineering and Associated Problems; and Special Subjects in Geotechnical Engineering and Soil Improvement.

These proceedings would not have been possible but for the dedication, commitment, and expertise of each of the papers' authors. All papers submitted to the conference were carefully reviewed by the members of the International Advisory Board. The proceeding contains four of the keynote papers presented at the conference.

We would like to thank the members of the Organizing Committee, the members of the International Advisory Board, Keynote Speakers, Session Chairs, and the authors of the papers included in these proceedings. We also offer our heartfelt gratitude to Springer Publishers that assembled the proceedings.

We are very grateful to the Founding President of Near East University Dr. Suat İ. Günsel and Chairman of the Board of Trustees of Near East University Prof. Dr. İrfan Suat Günsel for their support and assistance.

North Cyprus, Turkey
İstanbul, Turkey

Cavit Atalar
Feyza Çiniciođlu

Contents

Keynote Lectures

Bearing Capacity of Shallow Strip Foundation on Granular Soil Under Eccentric, Inclined and Eccentrically Inclined Loading—A Review	3
B. M. Das, C. R. Patra, R. N. Behera, K. Sobhan, and C. Atalar	
Static and Dynamic Behavior of Shallow Foundation Reinforced by Honey Cell Modular Block	37
Eun Chul Shin, Chul Hee Lee, and Jeong Ku Kang	
The “Site Recognition Challenge” in Data-Driven Site Characterization	49
Kok-Kwang Phoon and Jianye Ching	
New Tool for the Measurement of Soils’ Shear Strength	63
Mounir Bouassida and Dalel Azaiez	
Soil Properties and Characterization Final	
Apparatus Design and Measuring of Apparent Swelling Pressure of Compacted Bentonite	79
Hailong Wang, Takumi Shirakawabe, and Daichi Ito	
Volume Change Behavior of Natural Sands with the Addition of Mica Particles	89
Furkan Egemen Kahya and Tugba Eskisar	
Estimation of Compression Index of Lightly Overconsolidated Soils from In-Situ Time-Settlement Plots	97
T. Lenin, M. R. Madhav, and V. Padmavathi	
Granular Soil Relationship Between Angle of Internal Friction and Uniformity Coefficient	105
Mindaugas Zakarka and Šarūnas Skuodis	

Mechanical Strength Tests of Building Blocks of the Historical British Government Building in Famagusta, North Cyprus 113
 Salih Saner and Hasan Okaygun

Using Compression and Swelling Indices to Characterize Expansive Soils 121
 Sergio Andrew Manigniavy, Yosra Bouassida, Dalel Azaiez, and Mounir Bouassida

Probabilistic Interpretation of CPTu-DMT Data for Soil Profiling 129
 Stefano Collico, Marcos Arroyo, and Amadeu Deu

Clay Soil Stabilization Using Xanthan Gum and Sodium Alginate as Biopolymers 139
 Ayberk Temurayak and Tugba Eskisar

Estimation of OCR and Compression Index by Different Methods 145
 Zeeshan Firdous, V. Padmavathi, and M. R. Madhav

Shallow and Deep Foundations

Limit Load Exemplary Analyses of Foundations Accidentally Placed on Sand Underlain by Peat Using Their Various Parameters 157
 Łukasz Kaczmarek, Maria Grodzka-Łukaszewska, and Grzegorz Sinicyn

Interaction of Laterally Loaded Free Head Barrette Pile in Elastic Soils 165
 Yasar Taner and Gurkan Ozden

Environmental Preservation, Water, and Energy

Influence of Thermal Cycles on the Volume Change of Ulexite Added Sand-Bentonite Mixtures 175
 Sukran Gizem Alpaydin and Yeliz Yukselen-Aksoy

Assessment of Climate Impact and Costs Comparing Two Railway Embankment Fill Methods 181
 Ida Samuelsson, Johan Spross, and Stefan Larsson

Modelling

Field Trial to Rapidly Classify Soil Using Computer Vision with Electric Resistivity and Soil Strength 193
 Y. J. Eugene Aw, Soon-Hoe Chew, Yeow-Chong Tan, Pei-Ling Goh, Cheng-Soon Teo, Danette S. E. Tan, and Mei-Lin Leong

Influence of Excess Pore Pressure Development on Inertial Pile Response 203
 Hande Yumuk and Gurkan Ozden

Numerical Study of Uplift Induced Levee Failure for the Design of a Centrifuge Test 213
 Veronica Girardi, Elena Dodaro, Roberta Ventini, Marianna Pirone, Carmine Gerardo Gragnano, Daniela Giretti, Francesco Zarattini, and Fabio Gabrieli

Emerging Subjects in Geotechnical Engineering

Prediction of Load Capacities of Closed-Ended Piles Using Boosting Machine Learning Methods 225
 S. Karakaş, M. B. C. Ülker, and G. Taşkın

Shear Strength Behavior of Perlite Added Sand-Bentonite Mixtures Under Room Temperature and Thermal Cycles 235
 Esra Güneri and Yeliz Yukselen-Aksoy

Role of BIM for Different Phases of Geotechnical Investigation of the Transport Infrastructure 243
 Ivan Vaníček and Martin Vaníček

Use of Neural Networks to Predict Correlations Between CPT and PMT Tests for Clay and Marl Soils 255
 Mohamed Khiatine and Ramdane Bahar

Stability of Slopes and Landslides

Numerical Analysis of Slope Instability Due to Water Pipe Leakage 267
 K. H. Park and G. Ramnauth

GIS Susceptibility Maps for Shallow Landslides: A Case Study in Shawinigan, Quebec, Canada 275
 Michael Barbosu and James Gray

Determination of Critical Height of Unsupported Vertical Cuts Using Experimental and Numerical Methods 285
 Z. Nil Kutlu, Gregory Brennan, and Won Taek Oh

Slope Stability Analysis of Open-Pit Mines Using Statistical Methods 293
 Petra Olah and Péter Gorog

Investigation of Ground Stability of the Surroundings of the “Statue of Peace and Freedom”, Alsancak-North Cyprus 303
 Salih Saner

Dynamic Response Analysis of Highway Embankments 311
 Yasin S. Toksoy and Ayşe Edinçliler

Motion Analysis of Ground Failure Considering Rainfall and Ground Water Migration in Sandy Slopes	321
Yan Liu, Hemanta Hazarika, Divyesh Rohit, Sahibbi Ali, Yasuhide Fukumoto, Masanori Murai, Nguyen Thi Hoai Linh, and Yurika Taguchi	
Excavations, Support Systems, Earth-Retaining Structures and Underground Systems	
Experimental Investigation and Visualization of Failure Surfaces in Pipe-Soil Interaction Problems Using PIV Technique	333
Selçuk Bildik, Peter Rogenbuke, Gizil Tak, Baran Tulan, and Özer Çinicioğlu	
Earthquake Geotechnical Engineering and Associated Problems	
P-Y Curves for Piles in Sand Based on the SPT Test–Parametric Study and Practical Recommendations	343
Abdesselem Laouedj and Ali Bouafia	
Behaviour of Embedded Beam Formulations Under Dynamic Loading	353
Andreas-Nizar Granitzer and Franz Tschuchnigg	
Estimation of Ground Motion at One of the Damaged Building Sites Following the October 30, 2020, Samos Earthquake	363
Doga Altunevlek and Gurkan Ozden	
Analysis of the Pile Foundation Calculation Results Given the Action of an Earthquake and Soaking of the Loess Base	373
Nyamdorj Setev and Dashjamts Dalai	
Proposal of a Model Setup for Verification of the Origin of High Frequency Motion in Soil	383
Piotr Kowalczyk	
A Comparison Study Between 1D and 2D Site Response Analyses Based on Observed Earthquake Acceleration Records	393
Shima Shamekhi, Atilla Ansal, and Aslı Kurtuluş	
Subsurface Study of Flowslide Liquefaction in Petobo, Palu, Indonesia	403
Togani Cahyadi Upomo, Muhsung Chang, Rini Kusumawardani, Galih Ady Prayitno, Ren-Chung Huang, and Muhammad Hamzah Fansuri	
Deformation of Earthquake Resistant Gravel-Tire Chips Mixture as Drains	413
Yutao Hu and Hemanta Hazarika	

Special Subjects in Geotechnical Engineering

Evaluation of Relationships Between Strength Properties of Rock Samples and Drilling Rate Index	423
--------------------------------------------------------------------------------------------------------------	-----

Efe Aslan, Hakan Köpüklü, and H. Turan Durgunoğlu

Unsaturated Geomechanical and Physicochemical Characterisation of Soils Used for Adobe Blocks	433
------------------------------------------------------------------------------------------------------------	-----

Jose Concha-Riedel and Susana Lopez-Querol

Soil Improvement

The Evaluation of Stone Column and Jet Grouting Soil Improvement by Conducting a Comprehensive Experimental Program	443
----------------------------------------------------------------------------------------------------------------------------------	-----

Arshiya Abadkon and Erol Güler

Feasibility Study of Transforming Excavated Clayey Soil into ‘Sand-Like’ Material	453
------------------------------------------------------------------------------------------------	-----

Juan-Wei Koh, Sathyamoorthy Subramanian, Soon-Hoe Chew, Yeow-Chong Tan, Cheng-Soon Teo, Meng-Yang Charmaine Koh, Hui-Bin Grace Foo, Ting-Hong Hadley Cheung, Tamilselvan Thangayah, and Czha-Yheaw Tan

Estimation of Modular Ratio and Modulus of Deformation of Granular Piles from in Situ Compression Tests Under Direct Loading	463
-------------------------------------------------------------------------------------------------------------------------------------------	-----

M. Najamuddin, M. R. Madhav, and V. Padmavathi

Resilient Modulus as a Technical Parameter for Evaluating the Cement-Stabilized Soil	473
---------------------------------------------------------------------------------------------------	-----

Patryk Dobrzycki, Katarzyna Zabielska-Adamska, and Mariola Wasil

Effect of Freeze–Thaw Cycles on the Strength of a Nanosilica and Lime Treated Clay	483
-------------------------------------------------------------------------------------------------	-----

İsmail Taş and Tugba Eskisar

Improvement of Shear Strength of Fine-Grained Soils by Waste Glass	493
---------------------------------------------------------------------------------	-----

Victor Ojotisa and Ayse P. Balkis

Keynote Lectures

Bearing Capacity of Shallow Strip Foundation on Granular Soil Under Eccentric, Inclined and Eccentrically Inclined Loading—A Review



B. M. Das, C. R. Patra, R. N. Behera, K. Sobhan, and C. Atalar

Abstract Bearing capacity of shallow foundations is one of the most important areas of study in geotechnical engineering. Since the founding work of Karl Terzaghi in 1943, results of several theoretical and experimental investigations have been published. Most of these studies relate to the case where the foundation is subjected to centric vertical load. In the present paper, an attempt has been made to summarize the important developments related to the estimation of the ultimate bearing capacity of shallow foundations on granular soil subjected to eccentric vertical loading, inclined centric loading, and eccentrically inclined loading. Reduction factors to estimate the ultimate bearing capacity of foundations under eccentric, inclined, and eccentrically inclined loading from that subjected to vertical centric loading have been discussed.

Keywords Eccentric vertical loading · Eccentrically inclined loading · Granular soil · Inclined loading · Reduction factor · Shallow foundation · Ultimate bearing capacity

1 Introduction

In 1943, Karl Terzaghi published the landmark theory for estimation of the ultimate bearing capacity of a shallow foundation subjected to vertical centric loading in a $c-\phi$ soil. Since that time numerous studies, both theoretical and experimental, have been published on this topic. These studies included some modifications to Terzaghi's

B. M. Das
California State University, Sacramento, USA

C. R. Patra · R. N. Behera
National Institute of Technology, Rourkela, India

K. Sobhan (✉)
Florida Atlantic University, Boca Raton, USA
e-mail: ksobhan@fau.edu

C. Atalar
Near East University, Nicosia, North Cyprus, Turkey

theory as well as extension of it for cases where the foundation is subjected to eccentric, inclined and eccentrically inclined loading. In this paper, an attempt has been made to summarize the results of some of those studies for the case of a shallow strip foundation supported by a granular soil ($\phi \neq 0, c = 0$).

2 Ultimate Bearing Capacity of Strip Foundation—Centric Loading

The failure surface in soil for a shallow strip foundation as assumed by Terzaghi [24] is shown in Fig. 1. According to this theory, a foundation is considered shallow if its depth D_f is equal to or less than the width B . The soil located above the bottom of the foundation is replaced by an equivalent surcharge q ($q = \gamma D_f$, where γ = unit weight of the soil). Also the angle $bac = abc$ in the triangular elastic zone located below the foundation is equal to the soil friction angle ϕ . The ultimate bearing capacity q_u is thus given by,

$$q_u = cN_c + qN_q + \frac{1}{2}\gamma BN_\gamma \quad (1)$$

where, c = cohesion of soil and N_c, N_q and N_γ = bearing capacity factors that are functions of the soil friction angle. The bearing capacity factors were determined by the method of superposition. For granular soil, $c = 0$, thus

$$q_u = qN_q + \frac{1}{2}\gamma BN_\gamma \quad (2)$$

The next major study in the area of ultimate bearing capacity estimation was that developed by Meyerhof [13]. At ultimate load, the failure surface in soil under a

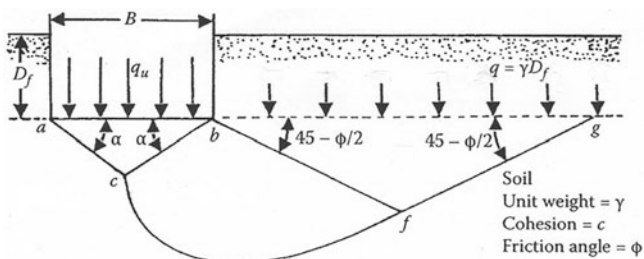


Fig. 1 Failure surface in soil at ultimate load for a rough rigid strip foundation as assumed by Terzaghi [24]

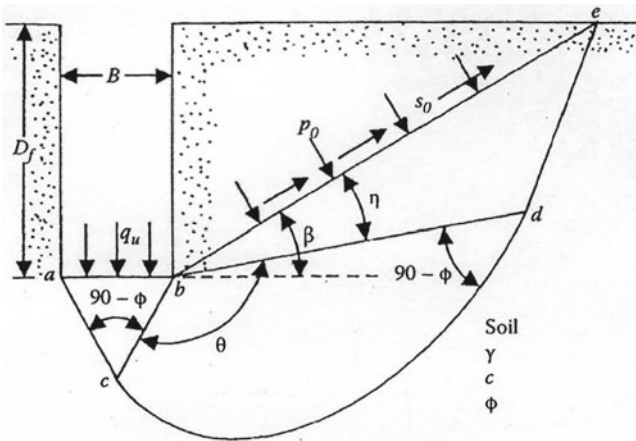


Fig. 2 Failure surface in soil under a rough rigid strip foundation—Meyerhof solution (1951)

rough strip foundation as assumed by Meyerhof is shown in Fig. 2. According to this study,

$$q_u = cN_c + p_oN_q + \frac{1}{2}\gamma BN_\gamma \quad (3)$$

It is important to note the following:

1. p_o is the normal stress on the equivalent free surface be in soil. Also,

$$s_o = m(c + p_o \tan \phi) \quad (4)$$

where, m = degree of mobilization of shear stress ($0 \leq m \leq 1$)

2. The angle $bac = abc$ in the triangular elastic zone is equal to $45 + \phi/2$ (in contrast to ϕ as assumed by Terzaghi and shown in Fig. 1).
3. The bearing capacity factors N_c , N_q and N_γ are functions of ϕ , m and β (where β = angle the equivalent free surface be makes with the horizontal (Fig. 2).

For granular soil, Eq. (3) becomes ($c = 0$),

$$q_u = p_oN_q + \frac{1}{2}\gamma BN_\gamma \quad (5)$$

Figures 3 and 4 show the variations of N_q and N_γ as developed by Meyerhof [13].

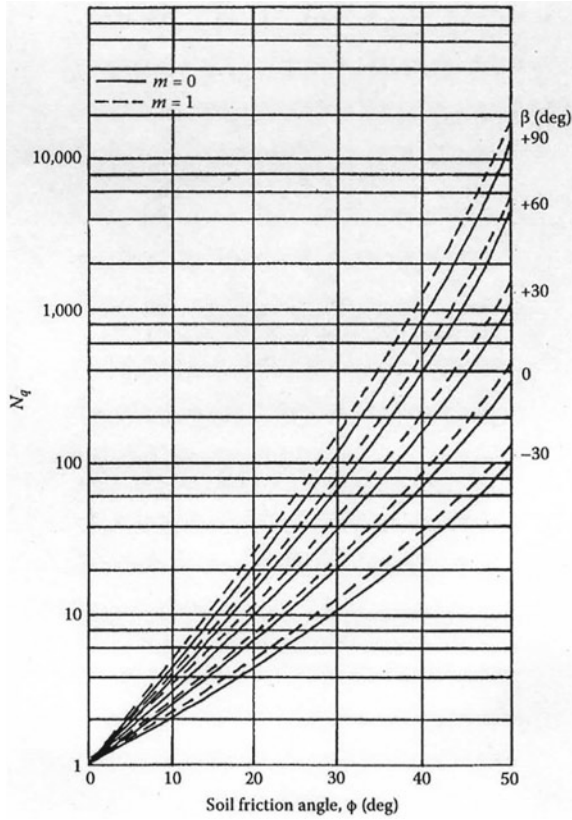


Fig. 3 Variation of Meyerhof's bearing capacity factor N_q with β , ϕ and m

Figure 5 shows a special case of the failure surface shown in Fig. 2, which is a case for a surface foundation with a distributed load $q = \gamma D_f$ at the level of the bottom of the foundation (same as assumed by Terzaghi shown in Fig. 1). For this case, $\theta = \pi/2$; $m = 0$; $\beta = 0$; $\eta = 45 - \phi/2$; $p_o = q = \gamma D_f$.

Hence, Eq. (5) becomes

$$q_u = qN_q + \frac{1}{2}\gamma BN_\gamma \quad (6)$$

where,

$$N_q = e^{\pi \tan \phi} \left(\frac{1 + \sin \phi}{1 - \sin \phi} \right) \quad (7)$$

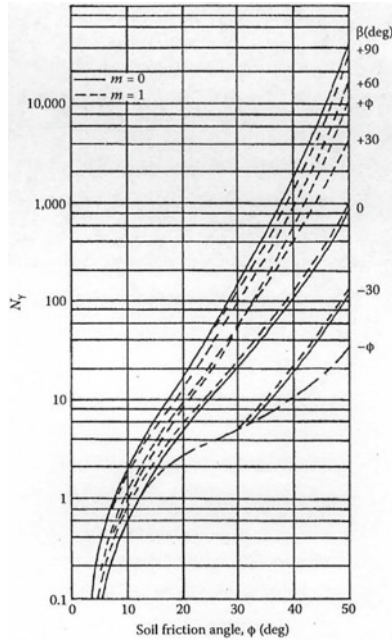


Fig. 4 Variation of Meyerhof's bearing capacity factor N_γ with β , ϕ and m

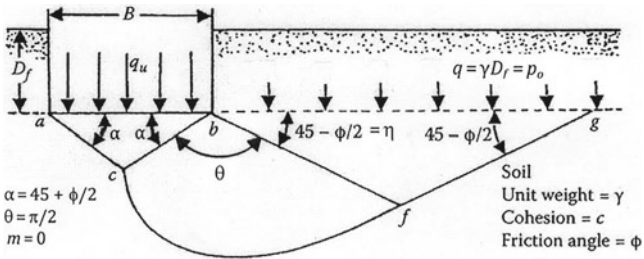


Fig. 5 Special case of Meyerhof's [13] solution

Meyerhof [15] suggested that

$$N_\gamma \approx (N_q - 1) \tan(1.4\phi) \tag{8}$$

Several theoretical studies on bearing capacity evaluation followed Meyerhof's work. For granular soil, the bearing capacity equation for shallow strip foundation

Table 1 N_γ relationships

Investigator	Relationship
Hansen [6]	$N_\gamma = 1.5(N_q - 1) \tan \phi$
Vesic [25]	$N_\gamma = 2(N_q - 1) \tan \phi$
Biarez et al. [2]	$N_\gamma = 1.8(N_q - 1) \tan \phi$
Booker [3]	$N_\gamma = 0.1045e^{9.6\phi}$ (ϕ is in radians)
Kumar [10]	$N_\gamma = e^{(0.66+5.1 \tan \phi)} \tan \phi$
Hjiaj et al. [7]	$N_\gamma = e^{(1/6)(\pi+3\pi^2 \tan \phi)} \times (\tan \phi)^{2\pi/5}$
Martin [12]	$N_\gamma = (N_q - 1) \tan(1.32\phi)$

and the relationship for N_q remained respectively the same as in Eqs. (6) and (7). The relationship for bearing capacity factor N_γ varied depending on the assumptions of study. Some of the relationships found in the literature are given in Table 1.

In order to account for the approximation of replacing the soil located above the bottom of the foundation by a distributed load per unit area $q = \gamma D_f$, depth factors may be incorporated into Eq. (6). Or,

$$q_u = q N_q d_q + \frac{1}{2} \gamma B N_\gamma d_\gamma \quad (9)$$

where, d_q and d_γ = depth factors. The depth factor generally used by geotechnical engineers are those recommended by Hansen [6] and Meyerhof [15]. They are given below:

- Meyerhof [15]

$$d_q = d_\gamma = 1 + 0.1 \left(\frac{D_f}{B} \right) \tan \left(45 + \frac{\phi}{2} \right) \quad (\phi \geq 10^\circ) \quad (10)$$

- Hansen [6]

$$d_q = 1 + 2 \tan \phi (1 - \sin \phi)^2 \left(\frac{D_f}{B} \right) \left(\frac{D_f}{B} \leq 1 \right) \quad (11)$$

$$d_\gamma = 1. \quad (12)$$

3 Foundation on Granular Soil Subjected to Vertical Eccentric Loading

3.1 Meyerhof's Solution

Meyerhof [14] proposed that, for a strip foundation on granular soil subjected to a vertical eccentric loading, the ultimate load per unit length q_u can be obtained as,

$$Q_u = q'_u B' \tag{13}$$

where,

$$B' = B - 2e = \text{effective width (Fig. 6)} \tag{14}$$

e = load eccentricity

$$q'_u = q N_q d_q + \frac{1}{2} \gamma B' N_\gamma d_\gamma \tag{15}$$

Note that Eq. (15) is the same as Eq. (9) where B is replaced by B' . Also the term B in depth factors (Eqs. 10 and 11) should be replaced by B' . This is generally referred to as the effective area method (Fig. 6).

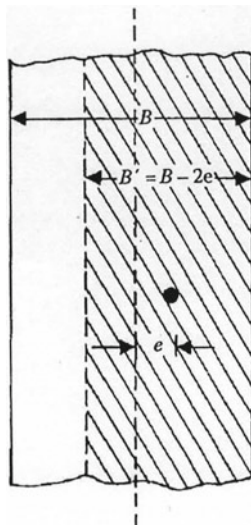


Fig. 6 Definition of effective width B' for a strip foundation

It is important to recognize that q'_u is the hypothetical ultimate load per unit area on a strip foundation having a width of $B' = B - 2e$. Hence the average ultimate load per unit area $q_{u(e)}$ for the strip foundation of width B is

$$q_{u(e)} = \left(\frac{B - 2e}{B} \right) q'_u. \quad (16)$$

3.2 Analysis of Prakash and Saran [21]

Prakash and Saran [21] provided a comprehensive mathematical formulation to estimate the ultimate bearing capacity of a strip foundation under eccentric loading on a $c-\phi$ soil.

Figure 7 shows the failure surface in soil assumed by Prakash and Saran [21]. Q_u is the ultimate load per unit length of the foundation of width B with an eccentricity e . In Fig. 7, zone I is an elastic zone with wedge angles ψ_1 and ψ_2 . Zones II and III are similar to those assumed by Terzaghi (that is, Zone 2 is a radial shear zone and zone III is a Rankine passive zone). The bearing capacity expression can be developed by considering the equilibrium of the elastic wedge abc located below the foundation (Fig. 7b). In Fig. 7b, the contact width of the foundation with the soil is equal to Bx_1 . The assumed variation of x_1 with e/B is shown in Fig. 7c. Neglecting the self-weight of the wedge,

$$Q_u = P_p \cos(\psi_1 - \phi) + P_m \cos(\psi_2 - \phi_m) + C_a \sin \psi_1 + C'_a \sin \psi_2 \quad (17)$$

where, P_p, P_m = passive forces per unit length of the wedge along the wedge faces bc and ac respectively; ϕ = soil friction angle; ϕ_m = mobilized soil friction angle ($\leq \phi$); C_a = adhesive force along wedge face $bc = (cBx_1 \sin \psi_2)/[\sin(\psi_1 + \psi_2)]$; C'_a = adhesive force along wedge face $ac = (mcBx_1 \sin \psi_1)/[\sin(\psi_1 + \psi_2)]$; m = mobilization factor (≤ 1); c = unit cohesion

Equation (17) can be expressed in the form:

$$q_{u(e)} = \frac{Q_u}{(B \times 1)} = \frac{1}{2} \gamma B N_{\gamma(e)} + \gamma D_f N_{q(e)} + c N_{c(e)} \quad (18)$$

where, $N_{\gamma(e)}, N_{q(e)}$ and $N_{c(e)}$ = bearing capacity factors for an eccentrically loaded continuous foundation; $q_{u(e)}$ = average ultimate load per unit area.

In granular soil, $c = 0$. Hence,

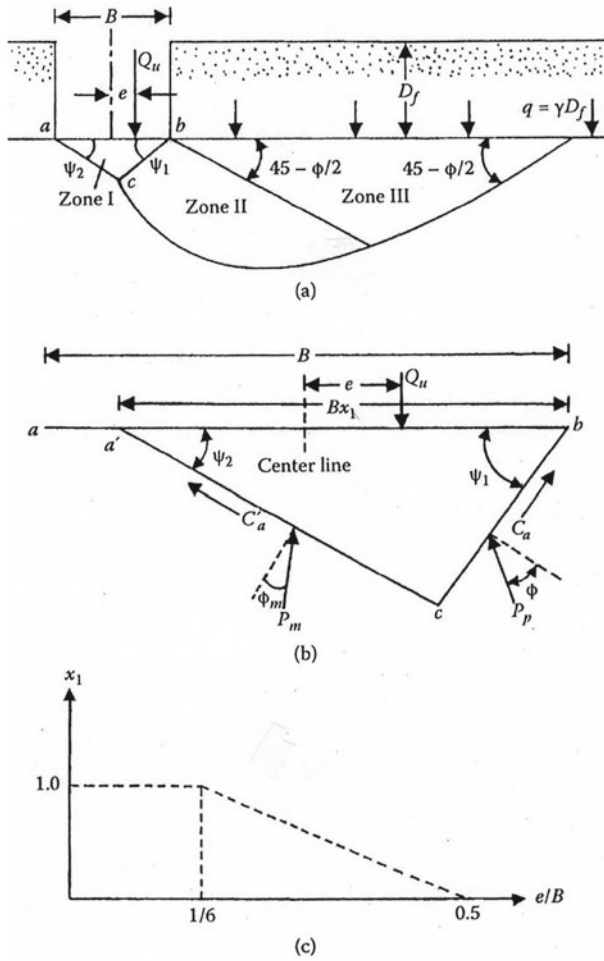


Fig. 7 Derivation of the bearing capacity theory of Prakash and Saran [21] for eccentrically loaded rough strip foundation

$$q_{u(e)} = \gamma D_f N_{q(e)} + \frac{1}{2} \gamma B N_{\gamma(e)} \tag{19}$$

The variations of $N_{q(e)}$ and $N_{\gamma(e)}$ with e/B and ϕ are shown in Figs. 8 and 9. It is important to note that Eq. (18) does not have the depth factors, which makes it conservative, to some extent in the estimation of ultimate load Q_u per unit length.

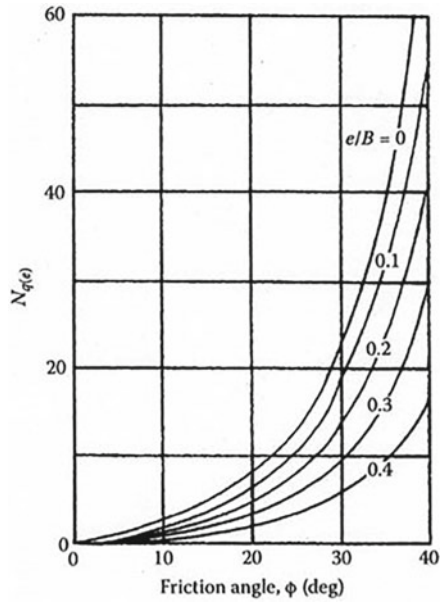


Fig. 8 Prakash and Saran's bearing capacity factor $N_{\gamma(e)}$

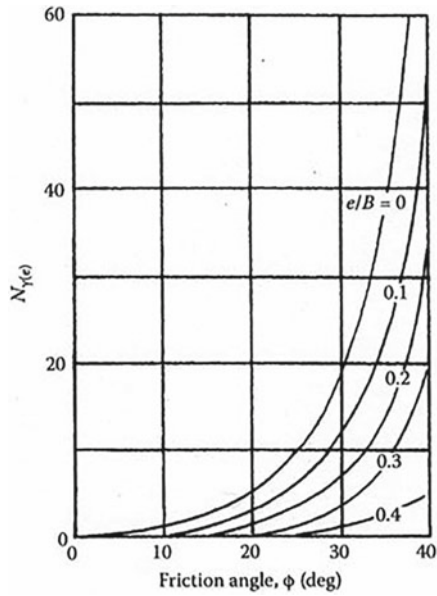


Fig. 9 Prakash and Saran's bearing capacity factor $N_{q(e)}$

3.3 Reduction Factor Method

Purkayastha and Char [22] carried out stability analyses of eccentrically loaded strip foundation supported by sand ($c = 0$) using the method of slices proposed by Janbu [8]. Based on that analysis, it was proposed that

$$R_k = 1 - \frac{q_{u(e)}}{q_u} \tag{20}$$

where R_k = reduction factor; q_u = ultimate bearing capacity of a strip foundation with eccentricity $e = 0$.

The magnitude of R_k can be expressed as

$$R_k = a \left(\frac{e}{B} \right)^k \tag{21}$$

where a and k are functions of the embedment ratio D_f/B (Table 2).

For D_f/B between zero and 1.0, the average values of a and k are about 1.81 and 0.8 respectively. Hence, combining Eqs. (20) and (21),

$$q_{u(e)} = q_u(1 - R_k) = q_u \left[1 - a \left(\frac{e}{B} \right)^k \right] \tag{22}$$

where,

$$q_u = \gamma D_f d_q + \frac{1}{2} \gamma B N_\gamma d_\gamma \tag{23}$$

(Note: $c = 0$ for granular soil)

Figure 10 shows a comparison of R_k for surface foundations ($D_f/B = 0$) as obtained from (a) Eq. (21) and Table 2; (b) some experimental observations; and (c) Meyerhof’s effective area theory. Referring to Fig. 10, the reduction factor R_k based on Meyerhof’s theory for $D_f/B = 0$, can be obtained as,

Table 2 Variations of a and k (Eq. 21)

D_f/B	a	k
0.00	1.862	0.73
0.25	1.811	0.785
0.50	1.754	0.80
1.00	1.820	0.888

$$\begin{aligned}
 R_k &= 1 - \frac{q_{u(e)}}{q_u} = 1 - \left(\frac{q'_u}{q_u}\right) \left(\frac{B - 2e}{B}\right) \\
 &= 1 - \left[\frac{0.5\gamma(B - 2e)N_\gamma}{0.5\gamma BN_\gamma}\right] \left(\frac{B - 2e}{B}\right) \\
 &= 1 - \left(\frac{B - 2e}{B}\right)^2 = 1 - \left(1 - \frac{2e}{B}\right)^2 \tag{24}
 \end{aligned}$$

Patra et al. [17] conducted several laboratory model tests in dense and medium sand with D_f/B varying from zero to 1 and e/B varying from zero to 0.15. Based on those test results it was suggested that, at a given D_f/B ,

$$q_{u(e)} \approx q_u \left(1 - \frac{2e}{B}\right). \tag{25}$$

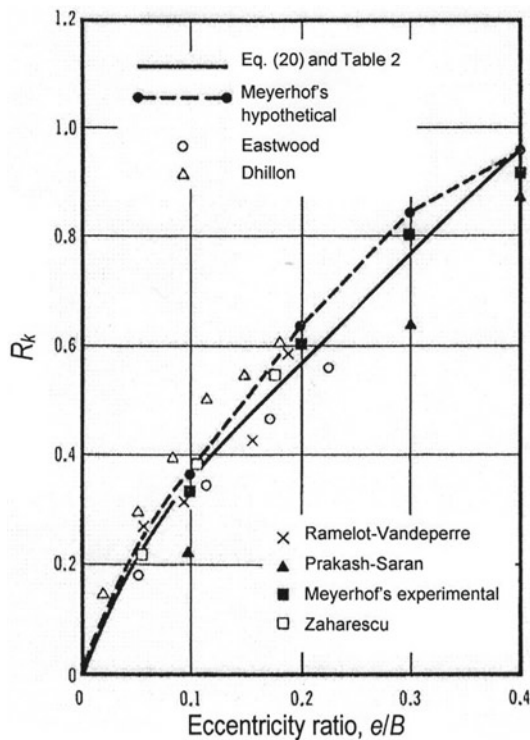


Fig. 10 Comparison of R_k for $D_f/B = 0$ [adapted after Purakyastha and Char 22]

4 Load-Settlement Relationship for Eccentrically Loaded Foundation

Patra et al. [19] provided a procedure to estimate the average settlement (i.e. settlement along the center line of the foundation) of an eccentrically loaded strip foundation. According to this procedure,

$$\frac{s_u}{B} \approx \frac{s'_u}{B} \left[1 + 0.6 \left(\frac{D_f}{B} \right) \right] \left[1 - 2.15 \left(\frac{e}{B} \right) \right] \quad (26)$$

where, s_u = average settlement along the center line of the foundation at a given D_f/B , and s'_u = settlement of the foundation at $D_f/B = 0$ and $e/B = 0$

The magnitude of s'_u/B can be approximated from the work of [4] which is shown in Fig. 11. The figure shows a plot of $\gamma B/p_a$ (p_a = atmospheric pressure ≈ 100 kN/m²) versus s'_u/B (for a circular foundation) for relative density D_r of sand varying from 20 to 90%. Patra et al. [19] approximated these plots by the following relationship

$$\frac{s'_u}{B} (\%) = 30e^{-0.9D_r} + 1.67 \ln \left(\frac{\gamma B}{p_a} \right) - 1$$

$$\left(\text{for } \frac{\gamma B}{p_a} \leq 0.025 \right) \quad (27)$$

where, D_r is expressed as a fraction.

Figure 11 also shows the plots of s'_u/B (%) versus $\gamma B/p_a$ for various values of D_r (%) based on Eq. (27). For $\gamma B/p_a > 0.025$, Eq. (27) may be approximated as,

$$\frac{s'_u}{B} (\%) = 30e^{-0.9D_r} - 7.16 \quad (28)$$

Based on experimental load-settlement curves, Patra et al. [19] proposed that,

$$\beta = \frac{\alpha}{1.461 - 0.461\alpha} \quad (29)$$

where, at a given D_f/B and e/B ,

$$\alpha = \frac{q(e)}{q_{u(e)}} \quad (30)$$

and

$$\beta = \frac{\frac{s}{B}}{\frac{s_u}{B}} \quad (31)$$

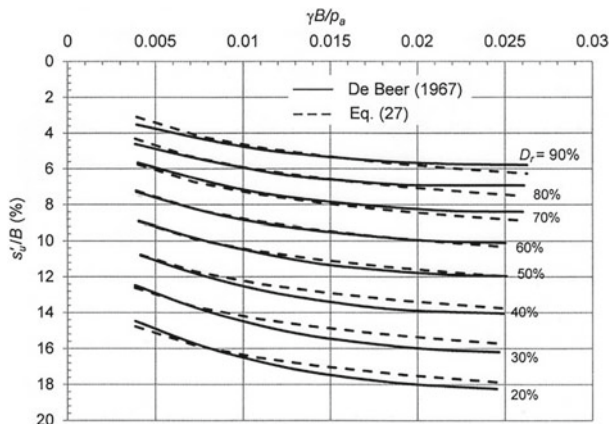


Fig. 11 Plot of s'_u/B versus $\gamma B/p_a$ —comparison of [4] and Eq. (27)

$q_{(e)}$ = average allowable load per unit area of the foundation = $q_{u(e)}/F_s$; F_s = factor of safety; s/B = settlement ratio corresponding to the allowable load per unit area $q_{(e)}$. The magnitudes of s_u/B and $q_{u(e)}$ can be estimated from Eqs. (26) and (25) respectively. It is important to point out that Eq. (29) should be used as a preliminary estimation only.

5 Strip Foundation Subjected to Inclined Load

5.1 Meyerhof's Solution

Meyerhof [14] extended his theory for ultimate bearing capacity under vertical loading to the case with inclined load. Figure 12 shows the plastic zones in the soil under a rough strip foundation with a small, inclined load. The inclined load makes an angle α with the vertical. It needs to be pointed out that Fig. 12 is an extension of Fig. 2. In Fig. 12, abc is an elastic zone, bcd is a radial shear zone and bde is a mixed shear zone. The normal and shear stresses on plane be are p_o and s_o respectively. The solution for the ultimate bearing capacity in granular soil was expressed by Meyerhof [14] as,

$$q_{u(i)-v} = q_{u(i)} \cos \alpha = p_o N_q + \frac{1}{2} \gamma B N_\gamma \tag{32}$$

where, N_q, N_γ = bearing capacity factors for inclined loading condition; γ = unit weight of soil; $q_{u(i)}$ = average ultimate inclined load per unit area of the foundation; $q_{u(i)-v}$ = vertical component of $q_{u(i)}$.

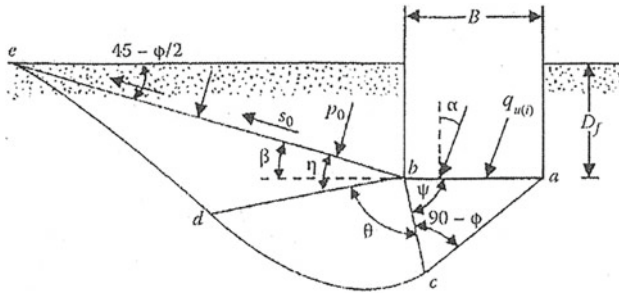


Fig. 12 Plastic zones in soil near a foundation with an inclined load—Meyerhof [14] analysis

The bearing factors can be expressed as,

$$N_q = \frac{1 + \sin \phi \sin(2\psi - \phi)}{1 - \sin \phi \sin(2\eta + \phi)} e^{2\theta \tan \phi} \tag{33}$$

and

$$N_\gamma = \frac{2P_{p\gamma(\min)}}{\gamma B^2} \left[\frac{\sin^2 \psi}{\cos(\psi - \phi)} + \cos(\psi - \phi) \right] - \frac{\sin \psi \cos(\psi - \phi)}{\cos \phi} \tag{34}$$

where $P_{p\gamma(\min)}$ = minimum passive force per unit length of the foundation acting on face bc (Fig. 12) and acts an angle ϕ with the normal drawn to bc .

The relationship given by Eq. (32) can also be expressed as

$$q_{u(i)-v} = q_{u(i)} \cos \alpha = \frac{1}{2} \gamma B N_{\gamma q} \tag{35}$$

Figure 13 shows the variation of bearing capacity factor $N_{\gamma q}$ with α for $D_f/B = 0$ and 1.

In 1963, Meyerhof proposed that Eq. (32) could be expressed in a similar form as Eq. (9). Or, for granular soils,

$$q_{u(i)-v} = q_{u(i)} \cos \alpha = q N_q d_q i_q + \frac{1}{2} \gamma B N_\gamma d_\gamma i_\gamma \tag{36}$$

where d_q, d_γ = depth factors (see Eqs. 10–12); i_q, i_γ = inclination factors.

Meyerhof [15] provided the following inclination factor relationships,

$$i_q = \left(1 - \frac{\alpha^\circ}{90^\circ} \right)^2 \tag{37}$$

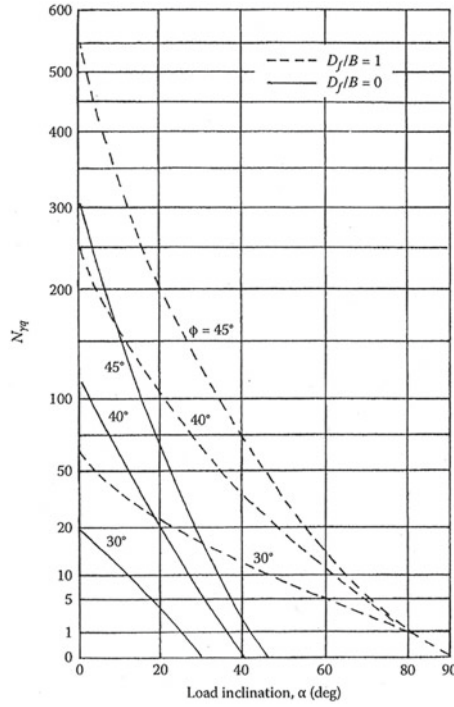


Fig. 13 Meyerhof's bearing capacity factor $N_{\gamma q}$ for cohesionless soil (Eq. 35)

$$i_{\gamma} = \left(1 - \frac{\alpha^{\circ}}{\phi^{\circ}}\right)^2. \tag{38}$$

5.2 Theoretical Solution of Dubrova

Dubrova [5] developed a theoretical solution for the ultimate bearing capacity of a strip foundation with a centric inclined load and expressed it in the following form (for granular soil),

$$q_{u(i)-v} = q_{u(i)} \cos \alpha = [2qN_q^* + B \gamma N_{\gamma}^*] \cos \alpha \tag{39}$$

where, N_q^*, N_{γ}^* = bearing capacity factors; $q = \gamma D_f$.

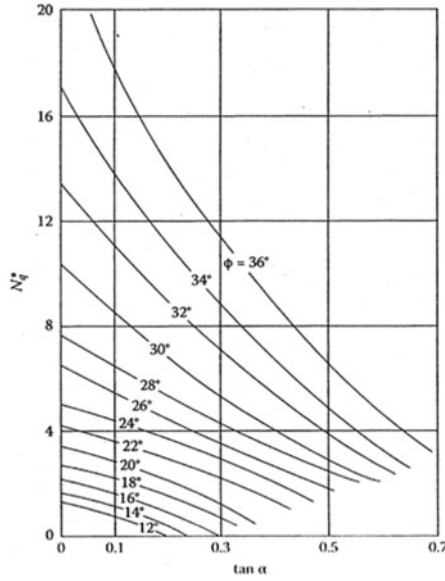


Fig. 14 Variation of N_q^*

The variations of N_q^* and N_γ^* are given in Figs. 14 and 15. For given values of α , ϕ , D_f/B , and B , the magnitudes of $q_{u(i)-v}$ obtained from Eq. (39) will be somewhat conservative compared to those obtained from Eq. (36).

5.3 Empirical Correlations

Based on the results of several field tests, Muhs and Weiss [16] concluded that,

$$\frac{q_{u(i)-v}}{q_u} = \frac{q_{u(i)} \cos \alpha}{q_u} = (1 - \tan \alpha)^2 \tag{40}$$

where, q_u = ultimate bearing capacity with centric vertical loading at similar values of D_f/B . Based on several model tests, Patra et al. [17] suggested that, for any given D_f/B ,

$$\frac{q_{u(i)}}{q_u} = \left(1 - \frac{\alpha}{\phi}\right)^{2-D_f/B} \tag{41a}$$

or

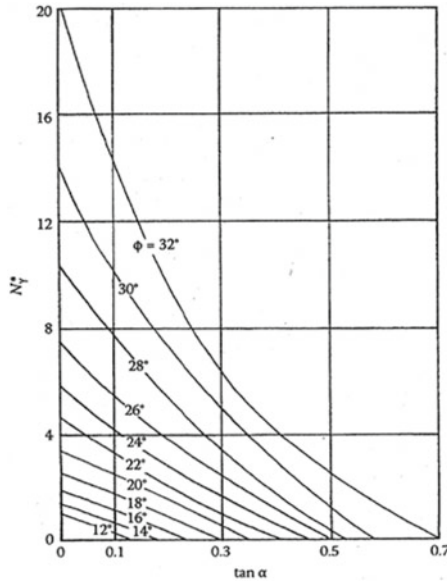


Fig. 15 Variation of N_{γ}^*

$$\frac{q_{u(i)-v}}{q_u} = \cos \alpha \left(1 - \frac{\alpha}{\phi} \right)^{2-D_f/B} \tag{41b}$$

Based on the experience of the authors, Eqs. (41a) and (41b) provide a closer agreement with Eq. (36) provided q_u is estimated using Eqs. (7)–(10).

6 Strip Foundation Subjected to Eccentrically Inclined Load

Figure 16 shows two different modes of application of an eccentrically inclined load on a shallow strip foundation on granular soil. The ultimate eccentrically inclined load per unit length of the foundation is $Q_{u(ei)}$. In Fig. 16a, the line of load application of the foundation is inclined toward the center line of the foundation and was referred to as partially compensated by Perloff and Baron [20]. It is also possible for the line of load application on the foundation to be inclined away from the center line of the foundation as shown in Fig. 16b. Perloff and Baron [20] called this type of load as reinforced case. Practically all of the studies reported so far in the literature related

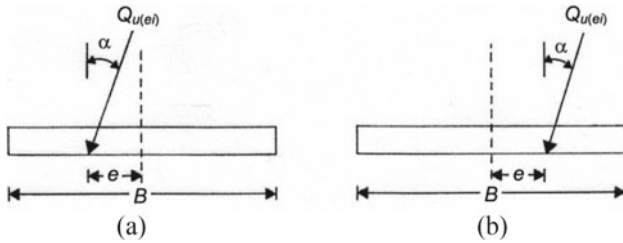


Fig. 16 Eccentrically inclined load on shallow foundation: **a** partially compensated; **b** reinforced

to the partially compensated type of load. Bearing capacity estimation for partially compensated and reinforced cases is separately discussed in the following sections.

7 Eccentrically Inclined Loading—Partially Compensated Case

7.1 Effective Area Method [15]

Based on Meyerhof’s [15] study, the vertical component of the ultimate bearing capacity [$q'_{u(ei)-v}$] on the effective area (i.e. width $B' = B - 2e$) of a strip foundation can be expressed as,

$$q'_{u(ei)-v} = qN_qd_qi_q + \frac{1}{2}\gamma B'N_\gamma d_\gamma i_\gamma \tag{42}$$

where, d_q, d_γ = depth factors (see Eqs. 10–12); i_q, i_γ = inclination factors (see Eqs. (37) and (38)); and $B' = B - 2e$.

Thus, the vertical component of the average ultimate bearing capacity per unit area of the foundation of width B can be given as,

$$\begin{aligned} q_{u(ei)-v} &= q_{u(ei)} \cos \alpha = \frac{Q_{u(ei)} \cos \alpha}{B} \\ &= \left(\frac{B - 2e}{B} \right) \left[qN_qd_qi_q + \frac{1}{2}\gamma(B - 2e)N_\gamma d_\gamma i_\gamma \right]. \end{aligned} \tag{43}$$

7.2 Theoretical Analysis of Saran and Agarwal [23]

Saran and Agarwal [23] performed a theoretical analysis for the average ultimate bearing capacity of a strip foundation $q_{u(ei)}$ subjected to eccentrically inclined load using limit equilibrium method. Based on this analysis, the vertical component of $q_{u(ei)-v}$ can be expressed as,

$$\begin{aligned} q_{u(ei)-v} &= \frac{Q_{u(ei)} \cos \alpha}{B} \\ &= \left[q N_{q(ei)} + \frac{1}{2} \gamma B N_{\gamma(ei)} \right] \cos \alpha \end{aligned} \quad (44)$$

where, $N_{q(ei)}$ and $N_{\gamma(ei)}$ = bearing capacity factors. [Note: With $\alpha = 0$, $N_{q(ei)}$ and $N_{\gamma(ei)}$ are respectively equal to $N_{q(e)}$ and $N_{\gamma(e)}$ as developed by Prakash and Saran [21] and are shown in Figs. 8 and 9.]

The variations of $N_{q(ei)}$ and $N_{\gamma(ei)}$ with soil friction angle ϕ and eccentricity ratio e/B for $\alpha = 0^\circ, 10^\circ, 20^\circ$ and 30° are given in Figs. 17 and 18, respectively. Equation (44) does not provide any recommendations for depth factors d_q and d_γ . It is also difficult to interpolate values of the bearing capacity factors for α other than $0^\circ, 10^\circ, 20^\circ$ and 30° .

7.3 Numerical Analysis by Louikidis et al. [11]

The vertical component of the limit load V_L per unit length of surface strip foundation ($D_f/B = 0$) resting on purely frictional soil and subjected to an eccentrically inclined load was calculated using finite element analysis by Louikidis et al. [11]. According to the research,

$$q_u (D_f/B=0, e/B, \alpha/\phi) = \frac{V_L}{B \cos \alpha} = \frac{\frac{1}{2} \gamma B^2 N_\gamma f_{ie}}{B \cos \alpha} = \frac{1}{2} \gamma B N_\gamma \left(\frac{f_{ie}}{\cos \alpha} \right) \quad (45)$$

where f_{ie} = combined inclination-eccentricity factor, given by

$$f_{ie} = \left[1 - \sqrt{3.7 \left(\frac{e}{B} \right)^2 + 2.1 (\tan \alpha)^2 + 1.5 \left(\frac{e}{B} \right) \tan \alpha} \right]^2. \quad (46)$$

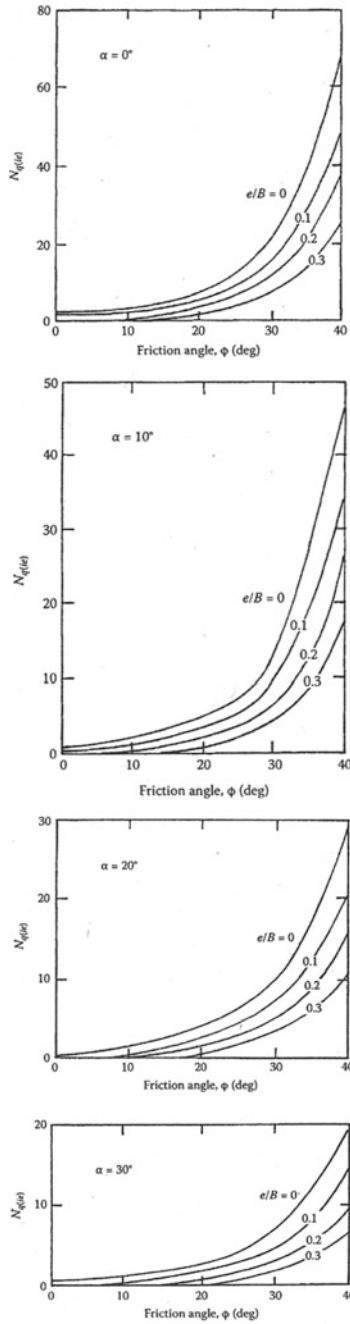


Fig. 17 Variation of $N_{q(ei)}$

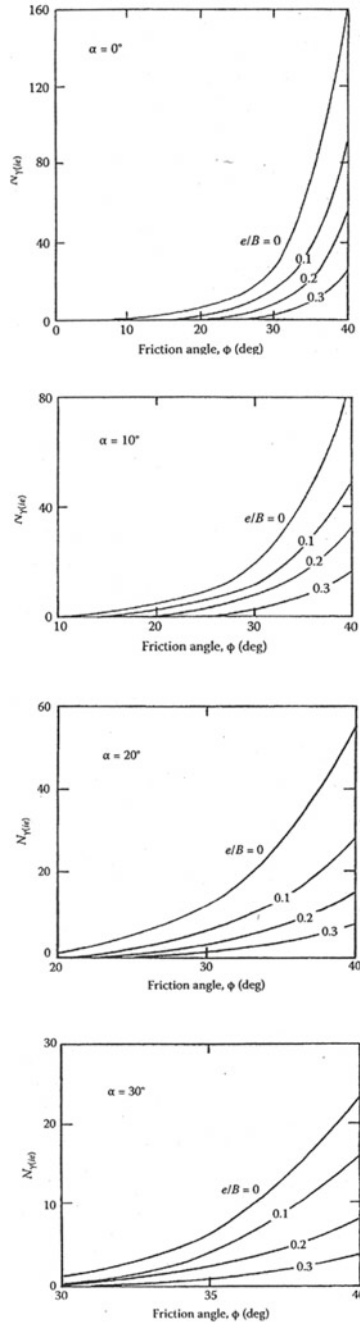


Fig. 18 Variation of $N_{\gamma(er)}$

7.4 Empirical Correlations

Patra et al. [17] reported results of about 120 laboratory test results for the ultimate bearing capacity of a strip foundation on dense and medium sand subjected to eccentrically inclined loading. Based on these test results it was proposed that, for a given D_f/B ,

$$RF_P = \frac{q_{u(ei)}}{q_u} = \frac{Q_{u(ei)}}{Bq_u} \approx \left[1 - 2\left(\frac{e}{B}\right) \right] \left(1 - \frac{\alpha}{\phi} \right)^{2-(D_f/B)} \quad (47)$$

where RF_P = reduction factor; q_u = ultimate bearing capacity for a given D_f/B [same as for $q_{u(ei)}$] and $\alpha = 0$.

Based on Meyerhof's study, from Eqs. (43) and (9), the reduction factor RF_M can be expressed as,

$$RF_M = \frac{q_{u(ei)}}{q_u} = \frac{\frac{(B-2e)}{B \cos \alpha} [q N_q d_q i_q + \frac{1}{2} \gamma (B - 2e) N_\gamma d_\gamma i_\gamma]}{q N_q d_q + \frac{1}{2} \gamma (B - 2e) N_\gamma d_\gamma} \quad (48)$$

(for a given D_f/B)

Substituting Eqs. (7), (8) and (10) for N_q , N_γ , d_q and d_γ , respectively, into Eq. (46), the reduction factor RF_M can be calculated. Table 3 shows a comparison of the reduction factors obtained from laboratory model tests by Patra et al. [17], RF_P (Eq. 47), and RF_M (Eq. 48). The comparison shows that Eqs. (47) and (48) reasonably predict the reduction factors with a maximum deviation of about ± 10 –15%. It needs to be pointed out that, at larger load eccentricity and larger load inclination, Eq. (48) yields a higher value as compared to Eq. (47) for surface foundation condition. Figure 19 shows the plots of the experimental reduction factors versus RF_P and RF_M . Also, Fig. 20 shows a plot of RF_P versus RF_M , according to which,

$$RF_P \approx RF_M + 0.03 \quad (R^2 = 0.95) \quad (49)$$

7.5 Numerical Analysis of Krabbenhoft et al. [9]

Krabbenhoft et al. [9] published lower-bound calculations based on finite element analysis to assess the bearing capacity of a strip foundation subjected to a positive load inclination on cohesionless soil, as shown in Fig. 16a (i.e., partially compensated). As a function of the friction angle, load eccentricity, load inclination, and surcharge, the bearing capacity was presented graphically. Smaller eccentricity ratios (e/B) result in

Table 3 Reduction factor comparison—experimental results of Patra et al. [17]; RF_P (Eq. 47); and RF_M (Eq. 48) (Note $B = 100$ mm for laboratory tests)

Sand type	$\frac{D_f}{B}$	α (deg)	$\frac{e}{B}$	Experimental $q_{u(ei)}$ (kN/m ²) [17]	RF_P	RF_M	Experimental $RF = \frac{q_{u(ei)}}{q_u}$
Dense $\gamma = 14.36$ kN/m ³ $D_r = 69\%$ $\phi = 40.8^\circ$	0	0	0	166.77	1.000	1.000	1.000
	0	0	0.05	133.42	0.900	0.810	0.800
	0	0	0.1	109.87	0.800	0.640	0.659
	0	0	0.15	86.33	0.700	0.490	0.518
	0	5	0	128.51	0.770	0.773	0.771
	0	5	0.05	103.01	0.693	0.626	0.618
	0	5	0.1	86.33	0.616	0.495	0.518
	0	5	0.15	65.73	0.539	0.379	0.394
	0	10	0	96.14	0.570	0.579	0.576
	0	10	0.05	76.52	0.513	0.469	0.459
	0	10	0.1	62.78	0.456	0.370	0.376
	0	10	0.15	51.99	0.399	0.284	0.312
	0	15	0	66.71	0.400	0.414	0.400
	0	15	0.05	53.96	0.360	0.335	0.324
	0	15	0.1	44.15	0.320	0.265	0.265
	0	15	0.15	35.12	0.280	0.203	0.211
	0	20	0	43.16	0.260	0.277	0.259
	0	20	0.05	34.83	0.234	0.224	0.209
	0	20	0.1	29.43	0.208	0.177	0.176
	0	20	0.15	23.54	0.182	0.136	0.141
	0.5	0	0	264.87	1.000	1.000	1.000
	0.5	0	0.05	226.61	0.900	0.855	0.856
	0.5	0	0.1	195.22	0.800	0.721	0.737
	0.5	0	0.15	164.81	0.700	0.597	0.622
	0.5	5	0	223.67	0.822	0.821	0.844
	0.5	5	0.05	193.26	0.740	0.705	0.730
	0.5	5	0.1	165.79	0.658	0.597	0.626
	0.5	5	0.15	140.28	0.575	0.497	0.530
	0.5	10	0	186.39	0.656	0.667	0.704
	0.5	10	0.05	160.88	0.590	0.575	0.607
0.5	10	0.1	137.34	0.525	0.489	0.519	
0.5	10	0.15	116.74	0.459	0.410	0.441	
0.5	15	0	151.07	0.503	0.535	0.570	

(continued)

Table 3 (continued)

Sand type	$\frac{D_f}{B}$	α (deg)	$\frac{e}{B}$	Experimental $q_{u(ei)}$ (kN/m ²) [17]	RF_P	RF_M	Experimental $RF = \frac{q_{u(ei)}}{q_u}$
	0.5	15	0.05	129.49	0.453	0.464	0.489
	0.5	15	0.1	111.83	0.402	0.397	0.422
	0.5	15	0.15	94.18	0.352	0.335	0.356
	0.5	20	0	115.76	0.364	0.422	0.437
	0.5	20	0.05	98.1	0.328	0.369	0.370
	0.5	20	0.1	85.35	0.291	0.318	0.322
	0.5	20	0.15	72.59	0.255	0.271	0.274
	1	0	0	353.16	1.000	1.000	1.000
	1	0	0.05	313.92	0.900	0.878	0.889
	1	0	0.1	278.6	0.800	0.763	0.789
	1	0	0.15	245.25	0.700	0.656	0.694
	1	5	0	313.92	0.877	0.842	0.889
	1	5	0.05	277.62	0.790	0.742	0.786
	1	5	0.1	241.33	0.702	0.648	0.683
	1	5	0.15	215.82	0.614	0.559	0.611
	1	10	0	264.87	0.755	0.705	0.750
	1	10	0.05	239.36	0.679	0.625	0.678
	1	10	0.1	212.88	0.604	0.548	0.603
	1	10	0.15	188.35	0.528	0.475	0.533
	1	15	0	225.63	0.632	0.587	0.639
	1	15	0.05	206.01	0.569	0.522	0.583
	1	15	0.1	179.52	0.506	0.461	0.508
	1	15	0.15	155.98	0.443	0.402	0.442
	1	20	0	183.45	0.510	0.485	0.519
	1	20	0.05	166.77	0.459	0.434	0.472
	1	20	0.1	143.23	0.408	0.385	0.406
	1	20	0.15	126.55	0.357	0.338	0.358
Medium dense $\gamma = 13.97$ kN/m ³ ; $D_r = 51\%$ $\phi = 37.5^\circ$	0	0	0	101.04	1.000	1.000	1.000
	0	0	0.05	84.37	0.900	0.810	0.835
	0	0	0.1	68.67	0.800	0.640	0.680
	0	0	0.15	54.94	0.700	0.490	0.544
	0	5	0	79.46	0.751	0.754	0.786
	0	5	0.05	63.77	0.676	0.611	0.631
	0	5	0.1	52.97	0.601	0.483	0.524
	0	5	0.15	42.18	0.526	0.369	0.417

(continued)

Table 3 (continued)

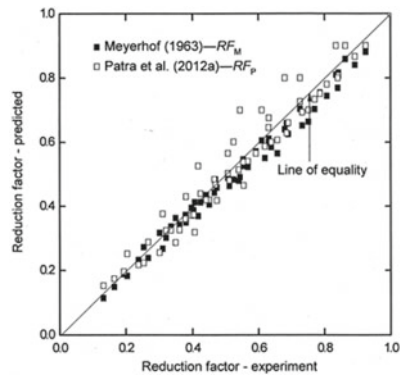
Sand type	$\frac{D_f}{B}$	α (deg)	$\frac{e}{B}$	Experimental $q_{u(ei)}$ (kN/m ²) [17]	RF_P	RF_M	Experimental $RF = \frac{q_{u(ei)}}{q_u}$
	0	10	0	55.92	0.538	0.546	0.553
	0	10	0.05	47.09	0.484	0.442	0.466
	0	10	0.1	38.46	0.430	0.349	0.381
	0	10	0.15	31.39	0.376	0.268	0.311
	0	15	0	38.26	0.360	0.373	0.379
	0	15	0.05	32.37	0.324	0.302	0.320
	0	15	0.1	26.98	0.288	0.239	0.267
	0	15	0.15	20.60	0.252	0.183	0.204
	0	20	0	24.03	0.218	0.232	0.238
	0	20	0.05	19.62	0.196	0.188	0.194
	0	20	0.1	16.68	0.174	0.148	0.165
	0	20	0.15	13.34	0.152	0.114	0.132
	0.5	0	0	143.23	1.000	1.000	1.000
	0.5	0	0.05	123.61	0.900	0.858	0.863
	0.5	0	0.1	103.99	0.800	0.727	0.726
	0.5	0	0.15	87.31	0.700	0.605	0.610
	0.5	5	0	120.66	0.807	0.816	0.842
	0.5	5	0.05	103.99	0.726	0.704	0.726
	0.5	5	0.1	90.25	0.645	0.599	0.630
	0.5	5	0.15	72.59	0.565	0.501	0.507
	0.5	10	0	98.10	0.628	0.659	0.685
	0.5	10	0.05	84.86	0.565	0.571	0.592
	0.5	10	0.1	72.59	0.502	0.489	0.507
	0.5	10	0.15	60.82	0.440	0.412	0.425
	0.5	15	0	79.46	0.465	0.525	0.555
	0.5	15	0.05	67.89	0.418	0.458	0.474
	0.5	15	0.1	56.90	0.372	0.395	0.397
	0.5	15	0.15	48.07	0.325	0.336	0.336
	0.5	20	0	58.27	0.319	0.413	0.407
	0.5	20	0.05	50.03	0.287	0.363	0.349
	0.5	20	0.1	43.16	0.255	0.316	0.301
	0.5	20	0.15	36.30	0.223	0.272	0.253
	1	0	0	208.95	1.000	1.000	1.000
	1	0	0.05	193.26	0.900	0.881	0.925
	1	0	0.1	175.60	0.800	0.769	0.840

(continued)

Table 3 (continued)

Sand type	$\frac{D_f}{B}$	α (deg)	$\frac{e}{B}$	Experimental $q_{u(ei)}$ (kN/m ²) [17]	RF_P	RF_M	Experimental $RF = \frac{q_{u(ei)}}{q_u}$
	1	0	0.15	156.96	0.700	0.663	0.751
	1	5	0	186.39	0.867	0.840	0.892
	1	5	0.05	168.73	0.780	0.743	0.808
	1	5	0.1	153.04	0.693	0.652	0.732
	1	5	0.15	137.34	0.607	0.564	0.657
	1	10	0	160.88	0.733	0.702	0.770
	1	10	0.05	144.21	0.660	0.625	0.690
	1	10	0.1	129.49	0.587	0.550	0.620
	1	10	0.15	112.82	0.513	0.479	0.54
	1	15	0	133.42	0.600	0.584	0.639
	1	15	0.05	118.7	0.540	0.522	0.568
	1	15	0.1	106.93	0.480	0.463	0.512
	1	15	0.15	94.18	0.420	0.406	0.451
	1	20	0	98.10	0.467	0.483	0.469
	1	20	0.05	92.21	0.420	0.435	0.441
	1	20	0.1	84.37	0.373	0.388	0.404
	1	20	0.15	75.54	0.327	0.342	0.362

Fig. 19 Plot of RF_M and RF_P versus experimental reduction factor from Patra et al. [17]



a smaller drop in bearing capacity, while e/B in the range of 0.25–0.35 results in a large reduction in bearing capacity. For larger e/B ratios and, in particular, higher friction angles, the load inclination (α) has an inverse effect on bearing capacity. When compared to centric vertical foundations, the bearing capacity of inclinedly loaded strip foundations increases with eccentricity ratios (e/B) >0.35–0.40 and embedment depth (D_f/B) >0.25.

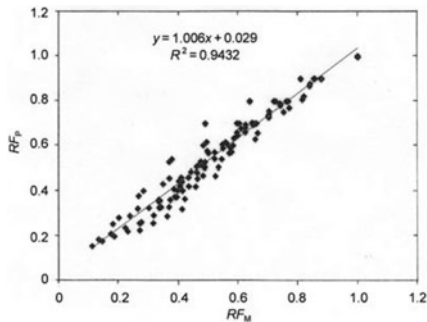


Fig. 20 Plot of RF_P versus RF_M (from Table 3)

8 Eccentrically Inclined Loading—Reinforced Case

8.1 Numerical Analysis by Loukidis et al. [11]

Loukidis et al. [11] used finite element analysis to calculate the collapse load of a rigid strip foundation placed on purely frictional soil subjected to eccentric and inclined loading as depicted in Fig. 16b, called the loading combination “negative.” In order to account for the “negative” loading combination, f_{ie} , Eq. (46) was changed to

$$f'_{ie} = \left[1 - \sqrt{3.7 \left(\frac{e}{B} \right)^2 + 2.1 (\tan \alpha)^2 - 1.5 \left(\frac{e}{B} \right) \tan \alpha} \right]^2. \quad (50)$$

8.2 Empirical Correlations

The only experimental study available at the present time for the reinforced type of eccentrically inclined loading (Fig. 16b) is that of Patra et al. [18]. Based on about 72 laboratory model tests, Patra et al. provided the following empirical relationship for ultimate bearing capacity (at a given D_f/B) and $e/B > 0$,

$$\frac{q_{u(ei)}}{q_u} = \frac{Q_{u(ei)}}{Bq_u} = \left[1 - 2 \left(\frac{e}{B} \right) \right] \left(1 - \frac{\alpha}{\phi} \right)^{1.5 - 0.7(D_f/B)} \quad (51)$$

The definition of notations in the preceding equation is the same as in Eq. (47). Comparison of Eqs. (47) and (51) shows that, for similar D_f/B and e/B , $q_{u(ei)}$ for

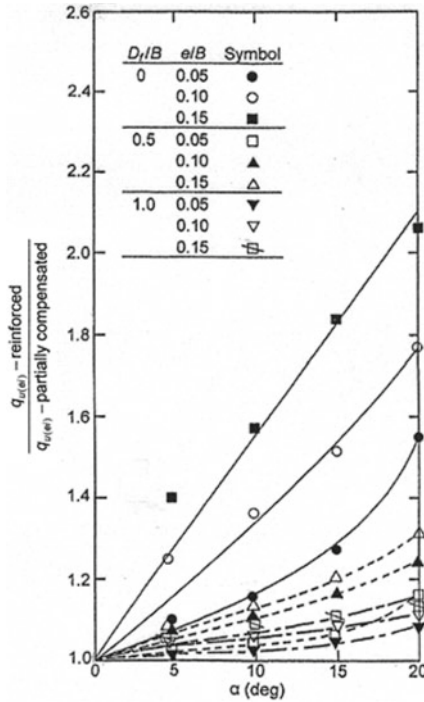


Fig. 21 Plot of $q_{u(ei)}$ -reinforced/ $q_{u(ei)}$ -partially compensated with α (dense sand; $D_r = 69\%$; $\phi = 40.8^\circ$) (after Patra et al. [18])

reinforced case is slightly higher than that for partially compensated case as demonstrated in Figs. 21 and 22 for dense and medium dense sand. The study also showed that, for similar D_f/B and α , the magnitude of the ratio of average settlement at ultimate load is

$$\frac{s_u - \text{reinforced}}{s_u - \text{partially compensated}} \approx \begin{cases} 1 & \text{at } \alpha = 5^\circ \\ \text{to} \\ 1.4 & \text{at } \alpha = 20^\circ \end{cases} \quad (52)$$

This is shown in Figs. 23 and 24.

8.3 Numerical Analysis of Krabbenhoft et al. [9]

Lower-bound calculations using FEM were also performed by Krabbenhoft et al. [9] to estimate the bearing capacity of a strip foundation subjected to reinforced

Fig. 22 Plot of $q_{u(ei)}$ -reinforced/ $q_{u(ei)}$ -partially compensated with α (medium dense sand; $D_r = 51\%$; $\phi = 37.5^\circ$) (after Patra et al. [18])

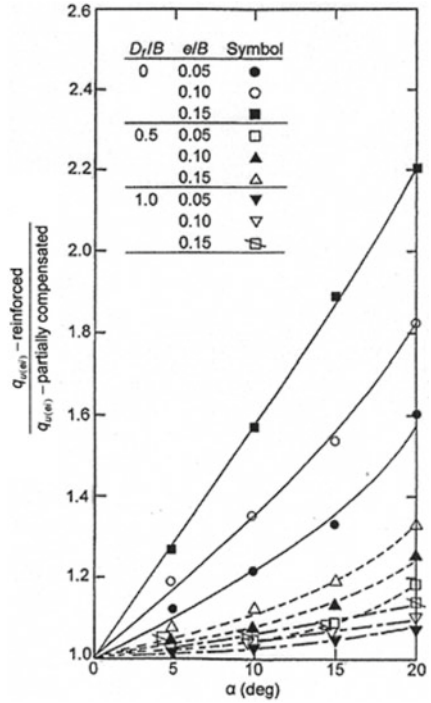


Fig. 23 Plot of s_u -reinforced/ s_u -partially compensated with α (dense sand; $D_r = 69\%$; $\phi = 40.8^\circ$) [18]

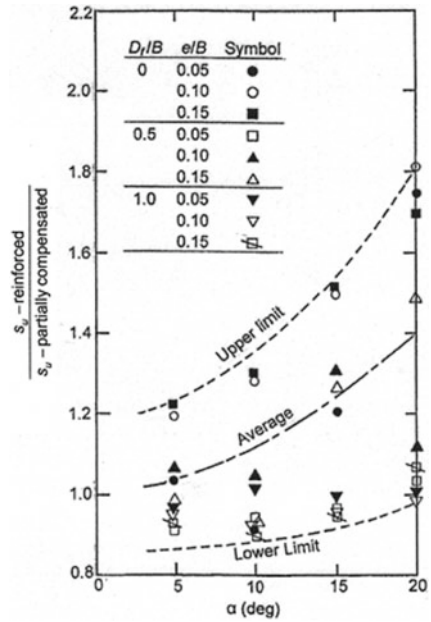
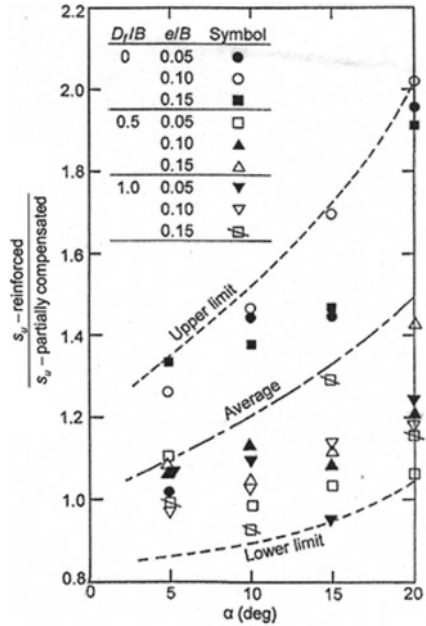


Fig. 24 Plot of $s_{u-reinforced}/s_{u-partially compensated}$ compensated with α (medium dense sand; $D_r = 51\%$; $\phi = 37.5^\circ$) [18]



case type of loading (termed as negative load inclinations). The bearing capacity of negative load inclinations decreases significantly for higher eccentricity ratios (e/B) than positive load inclinations, according to this research.

9 Eccentrically Inclined Loading—Combined Case

Behera et al. [1] developed an empirical non-dimensional reduction factor for a strip foundation supported by sand and subjected to eccentrically inclined load using 192 laboratory model test results from Patra et al. [17, 18] for both types of loading, i.e. line of load application inclined towards the centre line of the foundation (*partially compensated* case) and away from the centre line of the foundation (*reinforced* case). The reduction factor, RF , is given by

$$\begin{aligned}
 RF &= \frac{Q_u(D_f/B, e/B, \alpha/\phi, LA)}{Q_u(D_f/B, e/B=0, \alpha/\phi=0, LA=0)} \\
 &= \left[1 - 1.7 \left(\frac{e}{B} \right)^{0.85} \right] \left(1 - \frac{\alpha}{\phi} \right)^{\left(1.65 - 0.85 \frac{D_f}{B} \right)} e^{\left(0.2 \left(\frac{D_f}{B} \right)^2 - 0.3 \left(\frac{D_f}{B} \right) + 0.14 \right) (LA)} \quad (53)
 \end{aligned}$$

where $q_{u(D_f/B, e/B, \alpha/\phi, LA)}$ = average ultimate inclined load per unit area with eccentricity ratio e/B , inclination ratio α/ϕ , and load arrangement factor LA at an embedment ratio D_f/B ; and $q_{u(D_f/B, e/B=0, \alpha/\phi=0, LA=0)}$ = ultimate bearing capacity with centric vertical loading ($e/B = 0$, $\alpha/\phi = 0$ and $LA = 0$) at an embedment ratio D_f/B . The load arrangement (LA) was assumed as

$LA = -1$ (partially compensated condition as shown in Fig. 16a).

$LA = 0$ (centric, centric inclined and eccentric vertical loading condition)

$LA = 1$ (reinforced condition as shown in Fig. 16b)

The developed reduction factor (Eq. 53) was compared to those similar earlier theories based on Meyerhof [15], Saran and Agarwal [23], Loukidis et al. [11], and Patra et al. [17, 18] and found reasonably good.

10 Conclusions

A review of the developments in the area of ultimate bearing capacity of shallow strip foundations supported by granular soil and subjected to vertical eccentric loading, centric inclined loading, and eccentrically inclined loading has been presented. Based on the review, it appears that Meyerhof's bearing capacity theory incorporating the depth and inclination factors, and the effective area concept is still the best approach.

For foundations subjected to vertical eccentric load, Eq. (25) as proposed by Patra et al. [17] provided a reasonably good estimate of the ultimate bearing capacity. A novel procedure has been presented by Patra et al. [19] for estimating the average settlement of a foundation under an allowable eccentric (vertical) load. However, this estimated settlement should be considered as a first approximation only.

The empirical reduction factor (Eq. 47) proposed by Patra et al. n[17] for estimating the bearing capacity of foundations subjected to eccentrically inclined load from the ultimate bearing capacity of centrally loaded (vertical load) foundations compares reasonably well with Meyerhof's theory (Eq. 48).

The empirical reduction factor (Eq. 53) proposed by Behera et al. [1] for estimating the bearing capacity of foundations subjected to eccentrically inclined load (either *partially compensated* or *reinforced* case) from the ultimate bearing capacity of centrally loaded (vertical load) foundations compares reasonably well with other similar existing theories.

References

1. Behera RN, Patra CR, Das BM, Sivakugan N (2018) Ultimate bearing capacity of shallow strip foundation under eccentrically inclined load—a critical assessment. *Int J Geotech Eng* 15(7):897–905
2. Biarez J, Burel M, Wack B (1961) Contribution á l'étude de la force portante des fondations. In: Proceedings, 5th international conference on soil mechanics and foundation engineering, Paris, vol 1, pp 603–609

3. Booker JR (1969) Application of theories of plasticity for cohesive frictional soils. PhD thesis, University of Sydney, Australia
4. DeBeer EE (1967) Proefondervindelijke bijdrage tot de studie van het gransdraagvermogen van zand onder funderingen op staal, Bepaling von der vormfactor s_b . Annales des Travaux Publics de Belgique 6:481
5. Dubrova GA (1973) Interaction of soils and structures. Rechnoy Transport, Moscow
6. Hansen JB (1970) A revised and extended formula for bearing capacity. Bulletin No. 28, Danish Geo-technical Institute, Copenhagen
7. Hjiiaj M, Lyamin AV, Sloan SW (2005) Numerical limit analysis solutions for the bearing capacity factor N_γ . Int J Solids Struct 42(5–6):1681–1804
8. Janbu N (1957) Earth pressures and bearing capacity calculations by generalized procedure of slices. In: Proceedings, IV international conference on soil mechanics and foundation engineering, London, vol 2, pp 207–211
9. Krabbenhoft S, Damkilde L, Krabbenhoft K (2014) Bearing capacity of strip foundations in cohesionless soil subject to eccentric and inclined loads. Int J Geomech 14(3). [https://doi.org/10.1061/\(ASCE\)GM.1943-5622.0000332](https://doi.org/10.1061/(ASCE)GM.1943-5622.0000332)
10. Kumar J (2003) N_γ for rough strip footing using the method of characteristics. Can Geotech J 40(3):669–674
11. Loukidis D, Chakraborty T, Salgado R (2008) Bearing capacity of strip foundations on purely frictional soil under eccentric and inclined loads. Can Geotech J 45(6):768–787
12. Martin CM (2005) Exact bearing capacity calculations using the method of characteristics. In: Proceedings, 11th international conference of the international association for computer methods and advances in geomechanics, Turin, Italy, vol 4, pp 441–450
13. Meyerhof GG (1951) The ultimate bearing capacity of foundations. Geotechnique 2(4):301–332
14. Meyerhof GG (1953) The bearing capacity of foundations under eccentric and inclined loads. In: Proceedings, 3rd international conference on soil mechanics and foundation engineering, Zurich, vol 1, pp 440–445
15. Meyerhof GG (1963) Some recent research on the bearing capacity of foundations. Can Geotech J 1(1):16–26
16. Muhs H, Weiss K (1973) Inclined load tests on shallow strip footing. In: Proceedings, 8th international conference on soil mechanics and foundation engineering, Moscow, vol 1, no 3, pp 173–176
17. Patra CR, Behera RN, Sivakugan N, Das BM (2012) Ultimate bearing capacity of shallow strip foundation under eccentrically inclined load: part I. Int J Geotech Eng 6(2):342–352
18. Patra CR, Behera RN, Sivakugan N, Das BM (2012) Ultimate bearing capacity of shallow strip foundation under eccentrically inclined load: part II. Int J Geotech Eng 6(4):507–514
19. Patra CR, Behera RN, Sivakugan N, Das BM (2013) Estimation of average settlement of shallow strip foundation on granular soil under eccentric load. Int J Geotech Eng 7(2):218–222
20. Perloff WH, Barron W (1976) Soil mechanics: principles and applications. Ronald Press, New York
21. Prakash S, Saran S (1971) Bearing capacity of eccentrically loaded footings. J Soil Mech Found Divis, ASCE 97(1):95–117
22. Purkayastha RD, Char RAN (1977) Stability analysis for eccentrically loaded footings. J Geotech Eng Divis, ASCE 103(6):647–651
23. Saran S, Agarwal RK (1991) Bearing capacity of eccentrically oblique loaded foundation. J Geotech Eng, ASCE 117(11):1669–1690
24. Terzaghi K (1941) Theoretical soil mechanics. Wiley, New York
25. Vesic AS (1973) Analysis of ultimate loads of shallow foundations. J Soil Mech Found Divis, ASCE 99(1):45–73



Dr. Braja Das is Dean Emeritus of the College of Engineering and Computer Science at California State University, Sacramento. He received his B.Sc. degree with honors in Physics and B.Sc. degree in Civil Engineering from Utkal University, India; his M.S. in Civil Engineering from the University of Iowa, Iowa City; and his Ph.D. in Geotechnical Engineering from the University of Wisconsin at Madison. He is the author/co-author of 16 textbooks and reference books and more than 300 papers. His primary areas of research include shallow foundations, earth anchors, and geosynthetics.

Dr. Das is a Fellow and Life Member of the American Society of Civil Engineers; a Life Member of the American Society for Engineering Education; an Emeritus Member of the Stabilization of Geomaterials and Recycled Materials Committee of the Transportation Research Board, National Research Council (Washington DC). He served as the Co-Editor of the Journal of Geotechnical and Geological Engineering (Springer) from 2000 to 2006. From 2007 through 2019, he was the Editor-in-Chief of the International Journal of Geotechnical Engineering (Taylor & Francis, U.K.). When he stepped down as Editor-in-Chief, he was named as the Founding Editor of the journal. Dr. Das has received numerous awards for teaching excellence, including the AMOCO Foundation Award, the AT&T Award for Teaching Excellence from the American Society for Engineering Education, the Ralph Teetor Award from the Society of Automotive Engineers, and the Distinguished Achievement Award for Teaching Excellence from the University of Texas at El Paso.

Static and Dynamic Behavior of Shallow Foundation Reinforced by Honey Cell Modular Block



Eun Chul Shin , Chul Hee Lee, and Jeong Ku Kang

Abstract The construction of residential building and industrial complex in the soft ground is rather difficult to meet the requirement by the design code in terms of settlement as well as bearing capacity. There are a number of methods to improve the soft ground for shallow foundation with utilizing geosynthetics and chemical stabilizer as well as mechanical compaction. This paper presents the soft ground reinforcement method for shallow foundation by utilizing concrete hollow modular block ($250 \times 250 \times 150$ mm). The space of hollow in the modular block is $150 \times 150 \times 150$ mm. The theoretical formula for estimation of bearing capacity is developed with the modification of Based on the laboratory model tests results, the best combination of soil reinforcement method is proposed for practical use in the field.

Keywords Hollow modular block · Honey comb structure · Ground reinforcement · Shallow foundation · Shaking table test

1 Introduction

Shallow foundation is more efficient than deep foundation when it applies to low weight of construction and improved ground that soft ground replaced by dense ground. The hollow modular block which forms an artificial layered ground can be effectively used for reinforcement of shallow foundation in soft ground. It is foundation reinforcement method that reduces the amount of settlement and increases the bearing capacity. Meyerhof and Hanna [7] proposed the theory of shallow foundation bearing capacity for the layered ground, and Lawton [5] proposed the theoretical

E. C. Shin (✉)

Incheon National University, Korea Consultant Co., Ltd, Incheon 21984, Korea

e-mail: ecshin@inu.ac.kr

C. H. Lee

Korea Institute of Civil Engineering and Building Technology, Goyang-Si 10223, Korea

J. K. Kang

Incheon National University, Incheon 22012, Korea

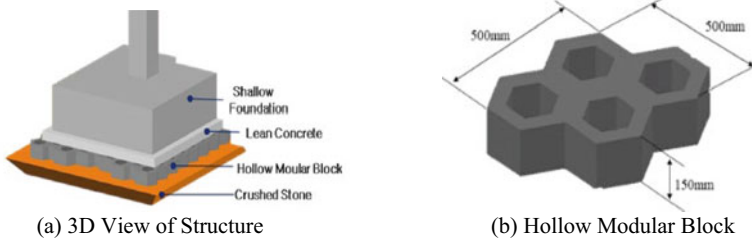


Fig. 1 Design of shallow foundation using hollow modular block

equation of bearing capacity of the layered ground considering the ground improvement and reinforcement effect [5, 7]. Hollow modular block is shaped like a hexagonal honeycomb structure as shown in Fig. 1. The honeycomb structure is generally known as the most economical and earthquake-proof structure and it is widely used as a stable structure that balances the power. Although the effects of hollow modular blocks have been partially verified by empirical construction and previous studies to increase the bearing capacity and reduce settlements, the mechanism of the hollow modular block method is still not fully understood.

A geocell made of a three-dimensional geotextile form may be exemplified as an example similar to the shape of the hollow block. Although the geocell and hollow block shape are similar, the material of the geocell is membrane and the hollow block is made of concrete. In addition, the geocell has a thickness of about 1–2 mm, while the hollow block has a thickness of 50 mm and made of concrete. The mechanism of the geocell can be partially applied nevertheless differences.

Bathurst and Karpurapu [1] evaluated the shear strength of geocell filled with sand and crushed stone. As a result, it was evaluated that the ground reinforcement mechanism of the geocell suppresses the lateral movement of the soil particles filled inside the geocell and increases the shear strength by increasing the restraint stress [1]. Through a model test, Mhaiskar and Mandal [6] analyzed the bearing capacity and settlement amount according to the reinforced or non-reinforced of geocell construction in the sandy ground above the soft layer [6]. Dash et al. (2003) conducted a study on the effect of increasing the strength of the geocell reinforcement in the soft ground through a model test [3]. Yoon et al. [11] conducted research that was a model loading test based on the ratio (H/W) of the geocell, the relative density, the strength of the material, and different thicknesses [11].

As a result of the study, the geocell system showed a tendency that the ultimate bearing capacity of the geocell increases as the ratio of width to height (H/W) increases when the cover soil thickness is the same. Shin et al. [10] reported the reinforcement efficiency of bearing capacity of geocell shape and filling materials through the large-scale model test [8, 10]. In the reinforced ground, the maximum earth pressure decreases by 50–60% in comparison to unreinforced ground.

2 Methodology

Experiment work was performed using laboratory model test by the means of the plate bearing test method. The results of sandy ground, hollow block installation/uninstallation and crushed rock ground were analyzed.

The ultimate bearing capacity reinforcement rate, BCR_u represent the rate of hollow block replacement ground about reinforced/unreinforced ground. The following Eq. (1) is used to estimate the reinforcement efficiency about reinforcement ground with comparison to the unreinforced sandy ground.

$$BCR_u = q_{u(R)}/q_u \quad (1)$$

where, $q_{u(R)}$ represents the ultimate bearing capacity of the hollow block replacement ground, and q_u represents the ultimate bearing capacity of unreinforced ground. The confining pressure build-up in vertical and lateral directions in the hollow modular block upon loading pressure is expressed as Eq. (2). The shear strength, τ between sand and inner concrete inside hollow modular block is expressed in Eq. (3) with considering the measured horizontal stress, $\Delta\sigma_h$.

$$\rho A = \sigma_c A_c + \sigma_{s,0.9} A_s + \tau A_n \quad (2)$$

$$\tau = c' + (1/2\sigma_c)\tan\delta = c' + \sigma_h \tan\delta \quad (3)$$

where, ρ is loading pressure, A is plate area, σ_c is vertical earth pressure of hollow, A_c is area of hollow, $\sigma_{s,0.9}$ is vertical earth pressure of concrete, A_s is area of concrete, τ is shear strength, A_n is side area of hollow, δ is angle of shear resistance between sand and concrete.

The shaking table test was performed using three types of seismic waves such as Ofunato, Hachinohe, and artificial seismic waves [4]. As seismic load occurs, the stability of each seismic waves was analyzed by measuring the acceleration amplification and measuring the horizontal displacement of the upper structure against the seismic load. The reinforcing effect was analyzed with considering of model test conditions under static loading. The lateral displacement of super-structure was measured with the reinforcement of foundation soil by using the shaking table test.

3 Laboratory Model Tests

3.1 Static Behavior of Reinforcement with Hollow Modular Block

The laboratory model tests were conducted to investigate the behavior of static and dynamic loadings. For static load condition, the plate load test was performed for the ground reinforced by a single hollow modular block. For the static load test, the ground was compacted in the soil box which was assembled by steel plate with sand, crushed rock, and sand-concrete material as SP and GP [2]. Soil property tests were performed for sand and crushed rock, and the results are described in Table 1.

The size of model box was 1,000 mm width, 1,200 mm height. Figure 2 shows the top and side view of cylindrical model box and hollow block with hexagonal steel plate of which the equivalent diameter was 250 mm.

The bearing capacity tests were conducted by the Korean Industrial Standard. The applied load was terminated when the test load was at least three times of allowable load or the cumulative settlement exceeded 10% of the diameter of the loading plate. The conditions of the bearing capacity test are sandy ground (A), sandy ground with hollow concrete block (A-1), sandy ground with crushed stone (B), and crushed stone with hollow concrete block (B-1). The crushed stone replacement depth was 150 mm and the height of the hollow block was set at a ratio of 1:1. The replacement width was set to 400 mm that is wider than the plate. The relative density was 85% which is the normal level. Relative degree of compaction (R) is 95.9%. The hexagonal plate was used, and it is the same shape with hollow block. Figure 3 shows the test conditions.

Step-loadings were applied from initial loading pressure 92.4 kN/m² to final loading pressure 738.5 kN/m² as tabulated in Table 2. The measured vertical and

Table 1 Property test results of sand and crushed rock

Types of soil	Specific gravity (G_s)	OMC (w_{omc} , %)	γ_{dmax} (kN/m ³)	c' (kPa)	Φ (°)	USCS
Sand	2.65	9.4	16.9	4.92	33.44	SP
Crushed rock	2.31	15.2	20.7	20.79	43.56	GP
Sand-Concrete	—	—	—	15.92	26.34	—

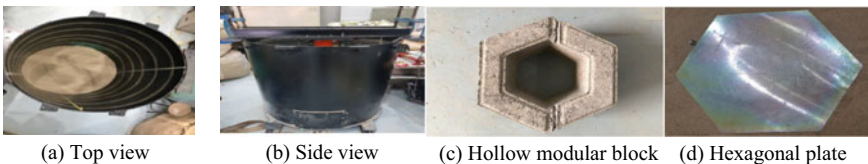


Fig. 2 View of cylindrical model box and hollow block

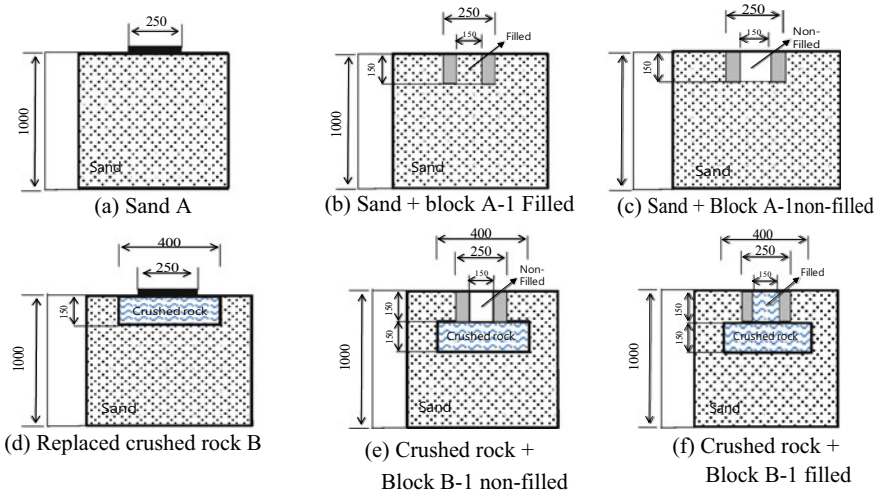


Fig. 3 Schematic diagram of bearing capacity test conditions (unit: mm)

horizontal earth pressures were obtained only for sandy ground because the contact area between load cell and crushed rock is significantly small.

The density of filling material inside of hollow modular block increases upon loading on the surface of hollow modular block, and hence internal confining pressure is increased. Therefore, the shear strength between filling material in hollow block and modular block wall is also increased.

Table 2 Measured vertical and lateral pressure with filled hollow modular block (unit: kN/m²)

Loading pressure, ρ	Vertical earth pressure, $\Delta\sigma_c$	Horizontal earth pressure, $\Delta\sigma_h$	Shear strength $\tau = \sigma_h \tan\delta$	Vertical earth pressure $\Delta\sigma_s$	Vertical earth pressure $\Delta\sigma_{s,0.9}$
92.4	48.3	34.2	16.9	9.9	77.4
184.7	87.7	60.0	29.7	19.0	169.6
277.1	129.4	85.5	42.3	32.7	242.4
369.4	171.0	109.8	54.4	54.5	320.4
461.8	209.0	131.1	64.9	62.8	463.3
554.1	250.4	153.6	76.0	73.3	531.6
646.5	289.8	174	86.1	86.5	623.9
738.5	336.7	196.8	97.4	99.7	716.1

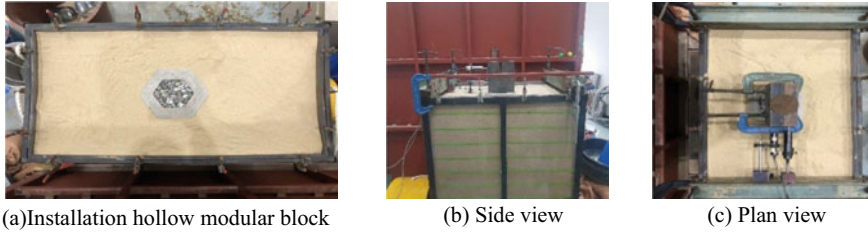


Fig. 4 Shaking test with instrumentation in the model box

3.2 Dynamic Behavior of Reinforcement with Hollow Modular Block

Depending on the relative density of foundation soil, 45% of loose ground, 65% of ordinary ground, and 85% of dense ground were formed. The ground reinforced with hollow modular block condition was set up by filling crushed stone to the interior of hollow modular block. The behavior of upper structure was not only checked by accelerations that 0.154 and 0.22 g were inputted in machine but also the maximum acceleration was measured. When the short and long period waves were applied, horizontal displacement, δ_h/h was measured and analyzed based on measurement results and relative density. According to KS design standard, the limit horizontal displacement, δ/h is specified as 0.015 when an earthquake occurs. The height of the model structure was set up 300 mm. Therefore, the result of horizontal displacement was expected 4.5 mm. LVDT and accelerometer were installed as shown in Fig. 4 b, c. The accelerometer measures acceleration based on one-axis vibration, and it can measure up to 20 m/s^2 , and the error range is about $\pm 1\%$.

4 Result and Analysis

The P-S curve of the plate bearing test in sand or crushed rock replacement ground has been linearly increased up to certain load and after then sudden settlement is occurred. The load distribution ratio on concrete part of hollow modular block is increasing from 53 to 62% initially, which is similar to the tendency to gradually increase as the load increases in the A-1-F load-settlement graph of Fig. 5.

The results of test for bearing capacity on the hollow modular block reinforced loose sandy ground are tabulated in Table 3. The experimental condition of A-1 case does not have a basal reinforcement layer by crushed rock, while the test condition of B-1 case has a basal reinforced layer. The test condition A-1-N case gives the punching shear failure. However, the test condition B-1-N does not show punching shear failure by the hollow modular block due to the additional crushed rock layer under the concrete block. The B-1-F gives the highest allowable bearing capacity

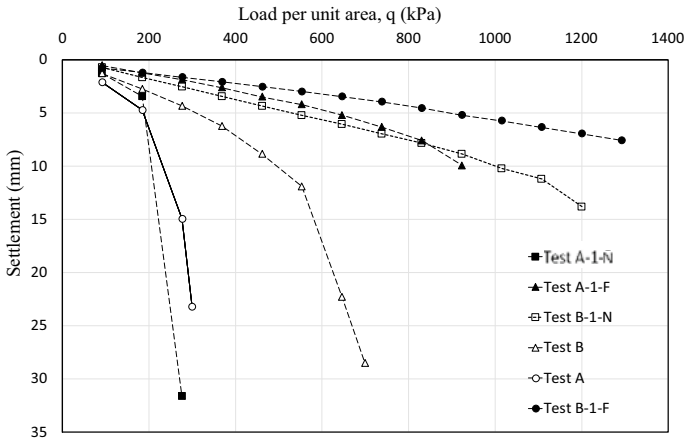


Fig. 5 Results of bearing capacity test

among experimental conditions. B-1-F and B-1-N bearing capacity test results of give the different ultimate and allowable bearing capacities at the time of final loading. However, the magnitude settlement for test B-1-N generated 2 times more than that of B-1-F case.

Based on the experimental bearing capacity test, the bearing capacity increases by the combination force induced by the hollow modular block and filled crushed rock, as well as basal reinforcement layer. The estimated vertical and horizontal confined force inside hollow part using results of Table 3 and Eqs. (2) and (3) are tabulated in Table 4. The load distribution ratio is analyzed with the earth pressure measured by the load, and about 16% of the load is found to be shared by the vertical confined force due to the confined force generated inside the hollow part. The horizontal confined force inside hollow part tends to decrease with increasing load, and shares about 18% of the load at 40kN.

Table 3 Comparison of effective reinforcement ratio for hollow modular block

Test no	Yield load (kPa)	Bearing capacity		Effective of reinforcement ratio BCR_u	
		Ultimate (kPa)	Allow (kPa)	A (Sand)	B (Crushed rock)
A (Sand)	253	300	100	1.0	—
A-1	A-1-N	185	92	0.92	0.40
	A-1-F	730	308	3.08	1.32
B (Crushed rock)	530	700	233	2.33	1.0
B-1	B-1-N	1,080	400	4.0	1.71
	B-1-F	—	431	4.31	1.85

Table 4 Results of calculating load sharing behavior of hollow modular block (unit: kN)

Load $Q = \rho A$	Vertical confined force inside hollow part, $\sigma_c A_c$	Horizontal confined force inside hollow part, τA_n	Load of concrete part $\sigma_{s,0.9} A_s$	Total load of hollow block by measurement
5	0.94 (18.82%)	1.31 (26.15%)	2.68 (53.56%)	4.93 (98.52%)
10	1.71 (19.09%)	2.30 (22.99%)	5.87 (58.71%)	9.88 (98.79%)
15	2.52 (16.81%)	3.27 (21.82%)	8.39 (55.93%)	14.19 (94.57%)
20	3.33 (16.66%)	4.21 (21.05%)	11.09 (55.46%)	18.63 (93.17%)
25	4.07 (16.29%)	5.02 (20.09%)	16.04 (64.15%)	25.13 (100.53%)
30	4.88 (16.27%)	5.88 (19.61%)	18.4 (61.34%)	29.16 (97.22%)
35	5.65 (16.14%)	6.66 (19.04%)	21.6 (61.70%)	33.91 (96.88%)
40	6.56 (16.41%)	7.54 (18.86%)	24.79 (62.00%)	38.89 (97.27%)

The value of the horizontal displacement limit for the total height (h) of a structure was determined under the circumstances not given, but usually within $h/300$. Canada Code proposed a horizontal displacement limit of steel-frame factory buildings below $h/500$, while Germany limited them below $h/400$. The interlayer displacement can be calculated as the difference between the top of the given layer and the lateral displacement of the center of the lower mass on the Korea standard. The displacement of structure caused by earthquakes was limited to less than $0.015 h$ of seismic grade I. The height of the structure was set to 300 mm by applying the upper-floor ratio (1/100), and the resulting horizontal displacement was limited to within 4.5 mm. The results of the shaking model test analyzed the maximum displacement of three seismic waves according to relative density as shown in Table 5. It was established within 3 mm of relative displacement between top-floor and bottom floor, and can be evaluated as stable in the Korea building structure design standard (KDS 41 20 00).

As a result of measuring the displacement of seismic waves, the horizontal displacement under the application of an artificial seismic waves was the highest. However, the limit horizontal displacement occurred within 4.5 mm, so it was determined to be stable according to the Korea structural design standard [9].

5 Conclusion

The laboratory model tests were conducted for static and dynamic loads to evaluate the behavior characteristics of hollow modular block reinforced shallow foundation. Based on the static and dynamic test results the following conclusions are drawn.

1. The hollow modular block reinforced shallow foundation in soft ground is cost effective and easy to construct in the limited area with less vibration and noise-free technique.

Table 5 Evaluation of maximum horizontal displacement based on relative density (unit: mm)

Division	0.154 g		0.22 g		Limit of δ_h
	Top	Bottom	Top	Bottom	
D_r	Ofunato wave				4.5
45%	0.265	0.13	0.595	0.185	
65%	0.21	0.205	0.435	0.24	
85%	0.08	0.03	0.305	0.035	
D_r	Hachinohe wave				4.5
45%	0.42	0.38	1.52	0.94	
65%	0.485	0.385	0.495	0.405	
85%	0.21	0.055	0.265	0.065	
D_r	Artificial seismic wave				4.5
45%	3.38	2.0	3.87	2.535	
65%	2.055	0.975	2.93	1.905	
85%	1.425	0.655	1.98	1.86	

- Experimental bearing capacity test results indicated that the bearing capacity ratio increases 4.31 for sand and 1.85 for crushed rock by the combination force induced by the hollow modular block and filled materials as well as basal reinforcement layer.
- The confined force generated inside the hollow modular block was analyzed using the values derived from the instrument (earth pressure sensor), and the reduction effect of vertical earth pressure by the confined force was found to be about 40%.
- The hollow modular block reinforced shallow foundation is effective against dynamic horizontal loading. The horizontal displacement was decreased with relative density increases, all the measured values are fallen below the KDS limit of 4.5 mm.

References

- Bathurst RJ, Karpurapu R (1993) Large-scale triaxial compression testing of geocell-reinforced granular soils. *Geotech Test J* 16(3):296–303
- Das BM (2017) *Shallow foundations*. CRC Press
- Dash SK, Sireesh S, Sitharam TG (2003) Model studies on circular footing supported on geocell reinforced sand underlain by soft clay. *Geotext Geomembr* 21(4):197–219
- Kagawa T (1978) On the similitude in model vibration tests of earth structures. *Proc Jap Soc Civ Eng* 275:69–77
- Lawton EC (2001) Section 6 of in practical foundation engineering handbook. R.W. Brown, McGraw-Hill, USA
- Mhaiskar SY, Mandal JN (1992) Soft clay subgrade stabilization using geocells, grouting, soil improvement and geosynthetics. *Geotechnical special publication* 30:1092–1103

7. Meyerhof GG, Hanna AM (1978) Ultimate bearing capacity of foundations on layered soils under inclined load. *Can Geotech J* 15(4):565–572
8. Meymand PJ (1988) Shaking table scale model tests of nonlinear soil-pile-superstructure interaction in soft clay. PhD thesis, UC Berkeley
9. Ministry of Land, Infrastructure and Transport (2017) Seismic design standard on slopes, KDS 11 90 00, Korean Design Standard
10. Shin EC, Kang HH, Park JJ (2016) Reinforcement efficiency of bearing capacity with geocell shape and filling materials. *KSCE J Civ Eng* 21(5):1648–1656
11. Yoon YM, Kim PS, Chun SH (2003) Reinforcing effects using model geocell in sand. *J Korean Geo-Environ Soc* 4(3):51–59



Dr. E.C. Shin is currently a Professor of Emeritus at the Incheon National University and a Chairman of Korea Consultant Co., Ltd. in the Republic of Korea. He was born in March 1, 1955 and graduated from Chungbuk National University in Korea. He obtained his M.S. degree from the University of Colorado at Boulder, USA in 1987 and a Ph.D degree in Engineering Science from the Department of Civil and Environmental Engineering, Southern Illinois University at Carbondale, USA in May, 1994 under the supervision of Prof. Braja M. Das. He taught 28 years about geotechnical engineering at the Incheon National University, Korea. Now he an Emeritus Prof. there at the same university.

Prof. EC Shin was the Vice President of International Society for Soil Mechanic and Geotechnical Engineering for Asia (2017-2022). Prof. E.C. Shin was twice awarded the Outstanding Research Professor title from the Incheon National University in the years of 1997 and 2010. Total 52 Ph.D students and 156 M.S students ware graduated under his supervision during his teaching career at the Incheon National University.

He also serves an adjunct professor in the Ph.D program of the Geotechnical Institute at the L.N. Gumilyov Eurasian National University, Nur-Sultan, Kazakhstan, where he has been teaching since 2006. In the past 27 years, he has been a devoted member of the geotechnical activities in Korean Geotechnical Society (The Vice President) and hosted 3 International Conferences, May 2006-Sustainable Development, May 2014-Disaster Prevention and Reduction, May 2016-Cold Region Development in Incheon, Korea. He contributed to the success of many activities took place under the umbrella of ISSMGE, most notably in the technical committees of mega city, soil reinforcement, historical monument, and environmental geotechnics.

He also participated in several geotechnical and geosynthetic touring lectures organized by the ISSMGE and the International Geosynthetic Society in many international locations including Tacna in Peru, Bangkok in Thailand, Hanoi, Hochiminh cities in Vietnam, Japan, China, Greece, Kolkata, Mumbai, Chennai, Cochin, Goa in India, Nur-Sultan city and Almaty in Kazakhstan, Oulu in Finland, Taipei in Taiwan, Singapore, Indonesia, Mexico, Nepal and Yuzhno-Sakhalinsk, Saint Petersburg, Moscow in Russia as a keynote speaker.

He has published 5 books on the geotechnical, geo-environmental, and civil engineering related subjects as well as more than 120 journal papers and 170 conference papers. The Ministry of Education and Science, Ministry of Transportation, Kazakhstan recently presented him an Achievement Medals of 2016 in appreciation of Prof. Shin's dedication to Geotechnical engineering education, and technology transfer contributions. He also received the 2008 Achievement Award presented by the International Geosynthetics Society. He was a Director of Creative Educational Program for Future City Design which is supported by the Ministry of Education in Korea (Total 9 million USD). The extensive overseas volunteer works were carried out with student delegation in Mongolia for planting trees in desert area, and in Nepal for reconstruction of earthquake damaged water supply pipe line.

He received Gersevanov medal from Russian Geotechnical Society in 2021 and awarded Honorary Doctorates Degree from St. Petersburg State University of Architecture and Civil Engineering in 2021.

The “Site Recognition Challenge” in Data-Driven Site Characterization



Kok-Kwang Phoon  and Jianye Ching 

Abstract One distinctive feature of geotechnical engineering is site uniqueness or site-specificity. However, there is no data-driven method to quantify site uniqueness. The corollary is that it is not possible to identify “similar” sites from big indirect data (BIG) automatically and no method to combine sparse site-specific data with big indirect data to produce a quasi-site-specific model that is less biased compared to a generic model and less imprecise compared to a site-specific model. This “site recognition” challenge is difficult because site-specific data is MUSIC-X (Multi-variate, Uncertain and Unique, Sparse, Incomplete, and potentially Corrupted with “X” denoting the spatial/temporal variability). This paper presents the application of 4 methods (hybridization, hierarchical Bayesian model, record similarity method, site similarity method) to construct a quasi-site-specific transformation model between the undrained shear strength and normalized cone tip resistance. The similarity methods are “explainable”, because a list of “similar” sites can be generated explicitly for inspection.

Keywords Site recognition · Big indirect data · MUSIC-X · Hybridization · Hierarchical Bayesian model · Record similarity method · Site similarity method

1 Introduction

Site characterization is a cornerstone of geotechnical and rock engineering. “Data-driven site characterization” (DDSC) refers to any site characterization methodology that relies solely on measured data, both site-specific data collected for the current project and existing data of any type collected from past stages of the same project or past projects at the same site, neighboring sites, or beyond. DDSC is one key

K.-K. Phoon (✉)
Singapore University of Technology and Design, Singapore, Singapore
e-mail: kkphoon@sutd.edu.sg

J. Ching
National Taiwan University, Taipei, Taiwan

application under an emerging field called data-centric geotechnics [20]. Phoon et al. [18] highlighted three challenges in DDSC: (1) ugly data, (2) site recognition, and (3) stratification. The purpose of this paper is to explain the site recognition challenge and to present recent research outcomes.

2 Site Recognition Challenge

The challenge is to quantify “site uniqueness”, directly or indirectly, so that sparse site-specific data can be supplemented by big indirect data (BID) to produce a *quasi-site-specific* model. This idea is not new as geotechnical and rock engineers have been relying on data from similar sites to inform their understanding of a current site. One example is the development of a correlation to estimate a design parameter from a field test parameter, say to estimate the undrained shear strength from the cone tip resistance. A more generic name is a transformation model [14]. In practice, site effects are broadly appreciated based on geology, soil mechanics, and experiences at similar sites, rather than characterized *quantitatively* through a detailed multivariate analysis of the site data. For the undrained shear strength versus cone tip resistance transformation model, the cone factor is expected to be similar at similar sites.

The typical caveat included in design guides would include a general statement such as “caution must always be exercised when using broad, generalized correlations of index parameters or in-situ test results with soil properties. The source, extent, limitations of each correlation should be examined carefully before use to ensure that extrapolation is not being done beyond the original boundary conditions. ‘Local’ calibrations, where available, are to be preferred over the broad, generalized correlations” [11]. Notwithstanding this sensible caveat, the engineer is typically left with no recourse but to use these generalized correlations/transformation models in the absence of “local” versions and lack of knowledge of the “source, extent, limitations”. A local or site-specific transformation model is commonly unavailable, because there is insufficient data to construct a model of sufficient precision to be useful for decision making (estimate design parameter).

The development of a purely data-driven approach that can construct a quasi-site-specific model from site-specific data and similar sites in BID remains an outstanding and difficult challenge, because real site data is “ugly”. Phoon et al. [16] presented a useful mnemonic, MUSIC-X (Multivariate, Uncertain and Unique, Sparse, Incomplete, and potentially Corrupted with “X” denoting the spatial/temporal variability) to highlight seven common “ugly” attributes in real site data. Phoon et al. [18] extended MUSIC-X to MUSIC-3X to cover 3D spatial variability that is more typically exhibited in a real site. “M” and “X” are two distinct types of correlations commonly termed as “cross correlations” and “auto correlations”, respectively.

3 Big Indirect Data (BIG)

Phoon et al. [16] referred to big data as *indirect* to emphasize the point that big data exists in geotechnical engineering, but it is not directly relevant to one specific project at one specific site. Generic soil property databases [5, 15] and load test databases [17, 22] are examples of Big Indirect Data (BIG). These databases have been made available by ISSMGE TC304 for research: <http://140.112.12.21/issmge/tc304.htm?#6>. A clay property BIG consists of multivariate data from many sites. Table 1 shows a typical example of multivariate data at a single site. It is “Sparse” as it has 9 records, and it is “Incomplete” as it has empty cells highlighted in grey. The data from many clay sites can be combined into a BIG. One example is CLAY/10/7490 [2]. It contains 7490 records from 251 studies carried out in 30 countries, clearly much larger than Table 1. Each record contains 10 clay properties:

1. Y_1 = liquid limit (LL)
2. Y_2 = plasticity index (PI)
3. Y_3 = liquidity index (LI)
4. Y_4 = normalized vertical effective stress (σ'_v/P_a)
5. Y_5 = sensitivity (S_t)
6. Y_6 = pore pressure ratio (B_q)
7. Y_7 = normalized preconsolidation stress (σ'_p/P_a)
8. Y_8 = undrained strength ratio (s_u/σ'_v)
9. Y_9 = normalized cone tip resistance [$(q_t - \sigma_v)/\sigma'_v$]
10. Y_{10} = effective cone tip resistance [$(q_t - u_2)/\sigma'_v$]

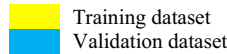
If a record is full, i.e. there are no missing values (or missing test results), this record is complete. A BIG is defined as complete only if every record is complete. Such a complete BIG is rare in geotechnical engineering. It is not unusual for an entire column to be empty as shown in Table 2 (rock mass properties). The percentage of BIG completeness is defined as (number of filled values)/[(number of properties) \times (number of rows)]. The percentage completeness for CLAY/10/7490 is 34%. For a BIG containing rock mass properties, ROCKMass/9/5876, the percentage completeness is 29%. A list of soil/rock property BIGs and percentage completeness is given in Ching et al. [7].

Classical frequentist methods cannot be applied to the MUSIC-X data in Table 1, because it is sparse, incomplete, and there are spatial correlations between records measured at different depths. BIG is not sparse, but it remains incomplete and it is not homogeneous due to inter-site variability (“U” or “Unique” attribute). For example, it is tempting to model the data at each site using a multivariate probability density function (PDF) and to quantify site uniqueness using a statistical distance between two site PDFs. A variety of statistical distances such as the Kullback–Leibler divergence, Bhattacharyya distance, and Mahalanobis distance are available, but they do not apply to MUSIC-X or MUSIC-3X data. There is no frequentist method to construct a site PDF from MUSIC-X data in the first place. It is rarely appreciated that the conventional approach to calculate a correlation coefficient from a bivariate

Table 1 Site data for a Taipei site [13]

No.	Depth (m)	s_u (kN/m ²)	$s_u(\text{mob})$ (kN/m ²)	Test results							
				LL	PI	LI	σ'_{v}/P_a	σ'_p/P_a	$s_u(\text{mob})/\sigma'_v$	q_{t1}	
1	12.8	UU	55.2	46.9	30.1	9.1	1.20	1.26	1.71	0.37	5.17
2	14.8	VST	50.7	52.9	32.8	12.8	1.43	1.43		0.36	4.22
3	16.1	UU	61.9	51.7	36.4	14.5	1.24	1.54		0.33	4.12
4	17.8	UU	54.2	42.8	41.9	18.9	0.90	1.68	1.79	0.25	4.03
5	18.3	VST	59.5	59.3				1.72		0.34	5.27
6	20.2	UU	73.1	60.5	38.1	17.3	0.70	1.88		0.32	4.53
7	22.7	VST	63.3	64.4	37.0	16.0	0.58	2.08		0.31	4.76
8	24.0	UU	82.2	67.5	38.0	16.2	0.75	2.19	2.19	0.30	5.12
9	26.6	UU	98.1	82.1	34.8	13.8	0.80	2.41		0.34	5.32

Note LL = liquid limit; PI = plasticity index; LI = liquidity index; σ'_v = vertical effective stress; σ'_p = preconsolidation stress; P_a = atmospheric pressure = 101.3 kPa; s_u = undrained shear strength; $s_u(\text{mob})$ = the in-situ undrained shear strength mobilized in embankment and slope failures [12]; $q_{t1} = (q_t - \sigma_v)/\sigma'_v$, where q_t = (corrected) cone tip resistance and σ'_v = vertical total stress



dataset cannot be extended to an incomplete multivariate dataset. A necessary positive definite property of the correlation matrix cannot be guaranteed [3]. The only practical approach available thus far is Bayesian, because of the additional support from prior distributions [4].

4 Quasi-Site-Specific Transformation Model

This section presents recent research progress in addressing the site recognition challenge. The objective is to improve the generic transformation model shown in Fig. 1 so that it is less biased and more precise for a specific site (Table 1). This generic model is widely used in practice [11]. Figure 1a, b show the data points in CLAY/10/7490 without and with site differentiation, respectively. It is clear from Fig. 1b that site effects are not easy to distinguish visually, because the marker for each site do not form distinct non-overlapping clusters. Using the BID in Fig. 1 and five site-specific records at row 1, 3, 5, 7, 9 in Table 1 (training dataset), a quasi-site-specific model can be developed using different methods to predict the median and 95% confidence interval (CI) for the undrained strength ratio at row 2, 4, 6, 8 in Table 1 (validation dataset). These 95% CI can be compared with the measured undrained strength ratios, which are available but assumed to be unknown at the model training/calibration stage. For illustration, only the bivariate subset [q_{t1} , (s_u/σ'_v)] is used in this study. The methods presented below are not restricted to

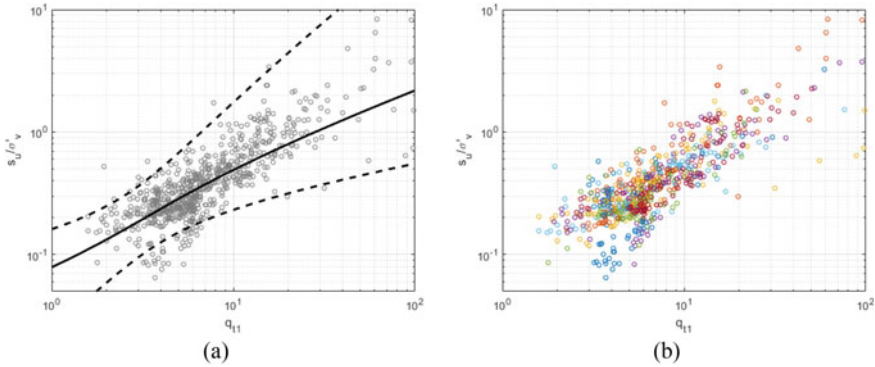


Fig. 1 Generic transformation model for undrained strength ratio (s_u/σ'_v) versus normalized cone tip resistance $q_{t1} = [(q_t - \sigma_v)/\sigma'_v]$ based on CLAY/10/7490: **a** no site differentiation and **b** sites differentiated by distinct markers

bivariate datasets. However, they are restricted by a common assumption that all soil properties that are typically non-normal in marginal distributions can be transformed to standard normal random variables and these variables constitute a multivariate normal vector [3].

Five methods are discussed below: (1) probabilistic multiple regression, (2) hybridization, (3) hierarchical Bayesian model, (4) record similarity method, and (5) site similarity method. The first method is generic. The rest are quasi-site-specific. The last two methods are ‘‘explainable’’ in the sense that an engineer can inspect the ‘‘similar’’ sites supporting the construction of the quasi-site-specific (s_u/σ'_v) versus q_{t1} model.

4.1 Probabilistic Multiple Regression

The probabilistic multiple regression (PMR) was first proposed by Ching and Phoon [1] for an actual multivariate soil property database CLAY/5/345. The basic idea is to first convert the physical $(Y_8, Y_9) = [q_{t1}, (s_u/\sigma'_v)]$ database into a standard normal (X_8, X_9) database and then construct the bivariate normal probability density function (PDF) of (X_8, X_9) based on this standard normal database. For PMR, the training dataset (row 1, 3, 5, 7, 9 in Table 1) is simply added to Figs. 1a and 2a new regression model is calculated (Fig. 2a). However, Fig. 2a is almost the same as Fig. 1a, because the effect of adding five records (red markers) to BID [716 records from 72 sites in CLAY/10/7490 contain both $q_{t1}, (s_u/\sigma'_v)$] is negligible. Prediction is carried out by reading the values of the 95% CI from Fig. 2a at the four different values of Y_9 in the validation dataset (Fig. 2b). It can be seen that the actual measured values (yellow markers) fall within the predicted 95% CI. On the average, one expects 1 measured value out of 20 values to fall outside a 95% CI. PMR is the standard approach widely

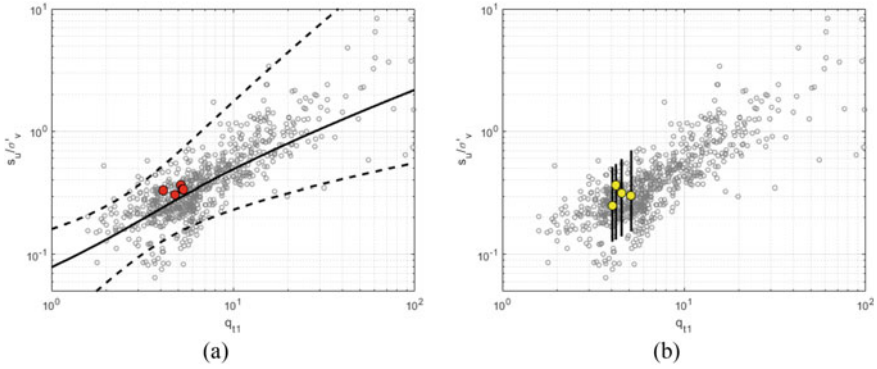


Fig. 2 Generic model using probabilistic multiple regression: **a** “training” (direct combination of site-specific and generic data) and **b** validation. Taipei training dataset in red circular marker. Taipei validation dataset in yellow circular marker

adopted in practice, typically in a bivariate form Kulhawy and Mayne [11]. It produces a generic model, not a quasi-site-specific model. The authors are not aware of any method that can modify PMR for site effects, short of an engineer manually selecting “similar” sites before applying PMR. Figure 2 presents a baseline for comparison with the quasi-site-specific models discussed below.

4.2 Hybridization

The hybridization method (HYB) was proposed by Ching and Phoon [4]. The basic idea is to first construct the generic PDF model in a standard normal (X_8, X_9) space as done in PMR. A site-specific PDF model is next constructed based on the site-specific training dataset using Bayesian machine learning (also in standard normal space). As noted above, there is no classical frequentist approach that can do this for the type of data shown in Table 1 or Table 2. The “trained” quasi-site-specific model is a hybrid PDF that is proportional to the product of the generic PDF and site-specific PDF. There is no theoretical basis for this “product” hybridization step. The hybrid PDF so produced by Taipei data (Table 1) and the generic data (CLAY/10/7490) is shown in Fig. 3a. To assess the ability of hybridization to extrapolate beyond the narrow range of $4.03 < q_{t1} < 5.32$ in Table 1, additional values covering a much wider range of $1 < q_{t1} < 100$ are added. However, the corresponding values of (s_u/σ'_v) are missing, since they are not measured and more fundamentally, the full range may not be exhibited by Taipei clay. This is termed as an “extrapolated” training dataset in this study. For this Taipei example, hybridization does not appear to extrapolate well if one takes the position that the generic transformation model (Fig. 1a) should be used outside the range of Table 1. It is clear that the median and 95% CI from hybridization differ significantly from the corresponding generic solutions presented in the background.

However, hybridization works better than PMR within the range of $4.03 < q_{t1} < 5.32$ as shown by the narrower 95% CI in Fig. 3b.

Table 2 Site data for the İzmir subway site, Turkey (10 out of 32 records shown for illustration) [10]

No.	RQD	RMR*	Q	GSI	E_m (GPa)	E_{em} (GPa)	E_{dm} (GPa)	E_i (GPa)	σ_{ci} (MPa)
1	5	25.5			0.11			4.2	26.0
2	18	35			0.238			7.0	39.5
3	32	41.5			0.83			10.8	72.0
4	35	41			0.564			9.0	62.0
5	37.4	41			0.72			10.7	65.2
6	24	36			0.46			10.0	50.0
7	40	39			0.51			8.0	61.0
8	18	35			0.47			8.5	48.5
9	34	35			0.39			7.5	51.2
10	42.5	44.5			1.17			12.3	86.4

Note RQD = rock quality designation; RMR = rock mass rating; Q = Q-system; GSI = geological strength index; E_m = deformation modulus of rock mass; E_{em} = elasticity modulus of rock mass; E_{dm} = dynamic modulus of rock mass; E_i = Young’s modulus of intact rock; σ_{ci} = uniaxial compressive strength of intact rock

* Average of the lower and upper bounds of RMRs reported in Kincal and Koca [10]

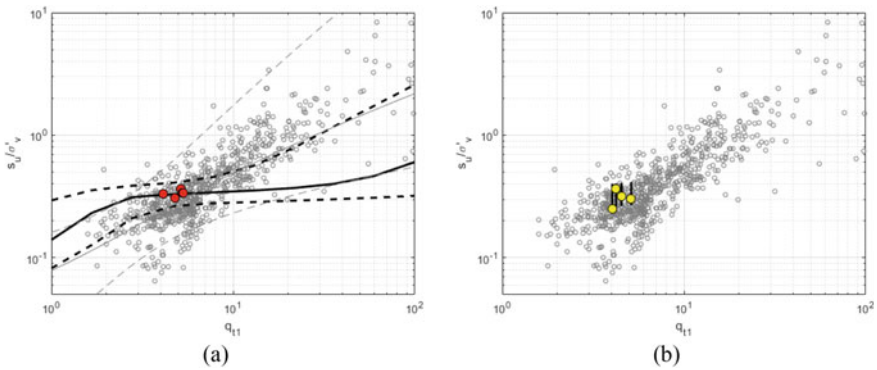


Fig. 3 Quasi-site-specific model using the hybridization method: **a** ‘‘training’’ (product of site-specific and generic PDF) and **b** validation. Taipei training dataset in red circular marker. Taipei validation dataset in yellow circular marker

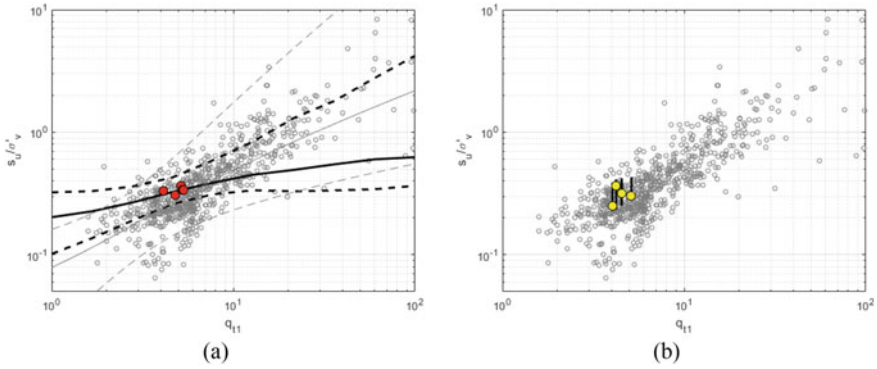


Fig. 4 Quasi-site-specific model using the HBM: **a** training (compute Taipei site PDF based on HBM hyper-parameters calibrated from CLAY/10/7490) and **b** validation. Taipei training dataset in red circular marker. Taipei validation dataset in yellow circular marker

4.3 Hierarchical Bayesian Model

The records for each site can be grouped by a distinct marker as shown in Fig. 1b. The scatter within one group is called intra-site variability. The scatter between groups is called inter-site variability. If CLAY/10/7490 is structured in this way, a natural approach to construct the quasi-site-specific transformation is the hierarchical Bayesian model (HBM) [9]. However, there are two practical problems in applying HBM to site data. First, it can be computationally tedious. Second, HBM has not been applied to MUSIC-X or MUSIC-3X data. Ching et al. [8] proposed an *analytical* HBM for MUSIC data (assuming no spatial variability) based on conjugate priors that is computationally efficient. In comparison to hybridization, HBM has a sound theoretical basis. Although the underlying data structure in CLAY/10/7490 may not follow HBM, particularly an analytical one based on conjugate priors, it is arguably a reasonable first step to study site uniqueness under an established theoretical framework. The quasi-site-specific transformation model based on the extrapolated Taipei training dataset is shown in Fig. 4a. The behaviour of the quasi-site-specific model beyond the range of $4.03 < q_{t1} < 5.32$ seems to be more reasonable than that shown in Fig. 3a. However, the 95% CI for the validation dataset is similar to that shown in Fig. 3b.

4.4 Record Similarity Method

Phoon and Zhang [19] opined that decision making is the responsibility of an engineer (not the operation) and this is ideally carried out if the engineer can understand the inference produced by the operation (“explainable” inference). The key limitation of hybridization and HBM is that they are not “explainable” in the sense that

“similar” sites are not identified and the engineer is thus deprived of an opportunity to inspect the list of “similar” sites against his/her experience and knowledge of regional geology (“reality check”). An engineer cannot engage meaningfully in the decision loop without understanding how an inference is arrived at. This is the well-known “black box” problem in machine learning.

Ching and Phoon [6] proposed the first approach to address this “explainable site recognition” challenge. The basic idea is to construct a site-specific PDF using Bayesian machine learning as presented in Ching and Phoon [4]. The degree of “similarity” of a record in CLAY/10/7490 to the Taipei training dataset is proportional to the value of PDF corresponding to the record. The constant of proportionality changes according to the incompleteness of the record. Based on this adjustment, the similarity of two records with different missing variables (different incompleteness structure) can be compared. A record with “similarity” >1 means it is more “similar” to the Taipei training dataset compared to an average record in CLAY/10/7490. These records are highlighted by a triangular marker in Fig. 5. In contrast to HBM, “similar” records are made known to the engineer for inspection. For example, an engineer can compare the Taipei data (training and validation) with records with “similarity” >1 in the Casagrande plasticity chart (Fig. 6a). The “similar” records do not cluster around the Taipei data in the Casagrande plasticity chart. This does not imply that the record similarity method is incorrect, because “similarity” in this example is measured by (Y_8, Y_9) . The Casagrande plasticity chart measures “similarity” in (PI, LL) or (Y_1, Y_2) . Using classical face recognition problem as an analogue, this means similarity between eyes and nose does not imply similarity between ears and mouth. The results in Fig. 6 seem to hint that similarity should be measured by more than two properties. However, it is also known that all sites become distinct if too many properties are included. The research question on whether an optimum number and/or optimum list of properties exist for explainable site recognition analysis has not been answered.

Finally, a quasi-site-specific transformation model is constructed by performing a weighted regression with the Taipei training dataset and all records in CLAY/10/7490 as shown in Fig. 5a. The weights for the Taipei training dataset are equal to 1. The weight for record in CLAY/10/7490 is close to 1 if it is similar to the Taipei training dataset and close to 0 if it is dissimilar. In this way, it is not necessary to prescribe an arbitrary threshold to divide between “similar” and “dissimilar” sites. The difference between Fig. 5a and Fig. 2a is the use of weights in regression. Figure 2a is based on regression with a weight of 1 for all records regardless of similarity.

The extrapolated quasi-site-specific transformation model appears to be less reasonable than that produced by hybridization (Fig. 3a) and HBM (Fig. 4a). However, in the absence of extrapolation, the 95% CIs for the validation dataset shown in Fig. 3b (hybridization), Fig. 4b (HBM), and Fig. 5b (record similarity) look similar.

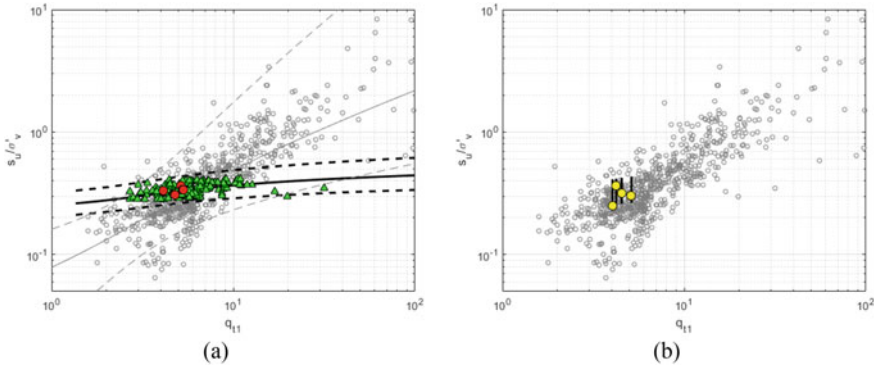


Fig. 5 Quasi-site-specific model using the record similarity method: **a** training (weighted regression with Taipei data carrying a weight of 1 and each record in CLAY/10/7490 carrying a weight proportional to its record “similarity”) and **b** validation. Record similarity index >1 shown in green triangular markers. Taipei training dataset in red circular marker. Taipei validation dataset in yellow circular marker

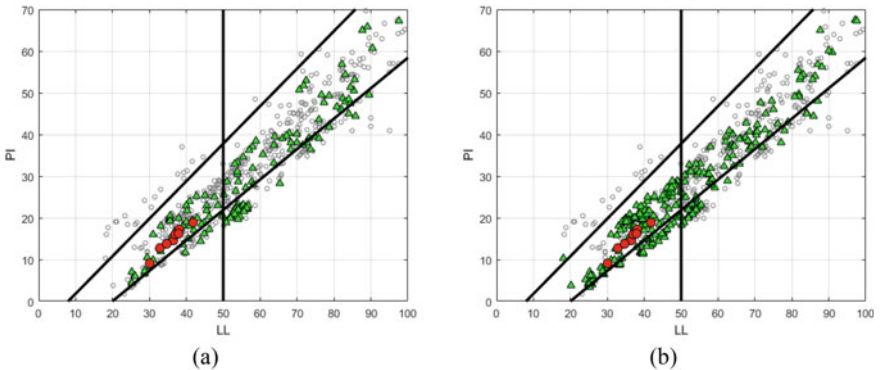


Fig. 6 Comparison between Taipei site (red circular marker) and “similar” sites (green triangular marker) in CLAY/10/7490 using the Casagrande plasticity chart: **a** record similarity index >1 and **b** site similarity index >0.1

4.5 Site Similarity Method

The record similarity method [6] can only compare one record in CLAY/10/7490 with the records in the Taipei site. In other words, it can consider site grouping at the target site (Taipei) but it cannot consider site grouping in CLAY/10/7490. Sharma et al. [21] proposed a site similarity method based on HBM to address this limitation. The site similarity measure is essentially the joint density of the Taipei data based on the PDF of one comparison site in CLAY/10/7490. The PDF is evaluated approximately using HBM. This measure is normalized so that it is unity when the Taipei data is compared with its own PDF (self-similarity). This site similarity measure elegantly reduces to the classical Kullback–Leibler divergence for complete multivariate data.

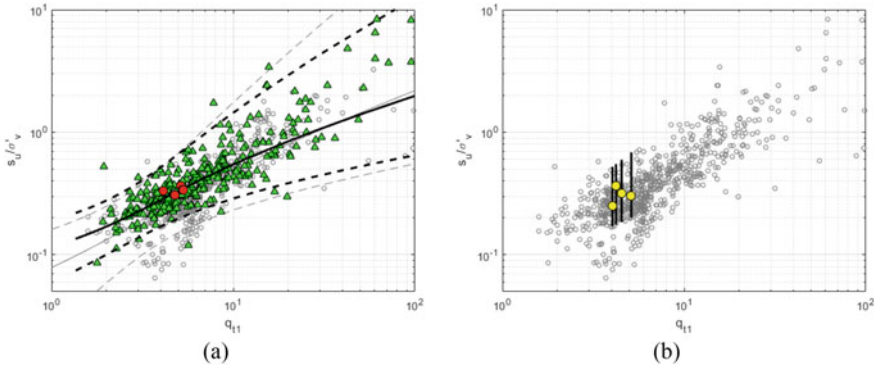


Fig. 7 Quasi-site-specific model using the site similarity method: **a** training and **b** validation. Site similarity index >0.1 shown in green triangular markers. Taipei training dataset in red circular marker. Taipei validation dataset in yellow circular marker

Figure 7a shows the quasi-site-specific model and sites with similarity >0.1 (triangular markers). The quasi-site-specific model is obtained by weighted regression with weights given by the site similarity method (<1). The site similarity method seems to behave reasonably well beyond the range of $4.03 < q_{t11} < 5.32$. However, the 95% CI for the validation dataset is larger than those produced by hybridization, HBM, and record similarity method (Fig. 7b). It is smaller than the one produced by PMR though (Fig. 2b). As shown in Fig. 6b, the ‘‘similar’’ records do not cluster around the Taipei data in the Casagrande plasticity chart as well. The preliminary conclusion is that two soil properties may not be sufficient to establish a robust site similarity measure.

5 Conclusions

In the absence of site-specific data, an engineer is compelled to rely on a generic transformation model to estimate a design parameter, such as the correlation between the undrained shear strength and the normalized cone tip resistance. There is rarely sufficient data to establish a site-specific or local correlation. The engineer understands that a generic transformation model is biased when applied to a specific site. He/she relies on engineering judgment to correct this bias approximately. However, there is no judgment possible to correct the generic transformation uncertainty which is too large for a specific site. Alternately, an engineer may combine site data with data from other similar sites to construct a quasi-site-specific model based on experience and knowledge of geology. No data-driven method is available to construct such a model. This is called the ‘‘site recognition’’ challenge in the data-driven site characterization (DDSC) research agenda. It is a difficult challenge primarily because the attributes of actual site data are MUSIC-3X.

This paper presents four methods to construct a quasi-site-specific model to estimate the undrained shear strength from the normalized cone tip resistance: (1) hybridization, (2) hierarchical Bayesian model, (3) record similarity method, and (4) site similarity method. The last two methods are “explainable” in the sense that the list of “similar” records or sites supporting the quasi-site-specific model is made known to the engineer. In this way, the engineer can delete records/sites deemed unreasonable, thus fostering a meaningful engagement in the decision making (estimation of the undrained shear strength). The effect of extrapolating the quasi-site-specific model beyond the range of the training dataset is also studied.

More research is needed to: (1) ascertain the number and/or type of soil properties needed to identify “similar” sites more robustly in the sense of producing more clustered results in existing soil classification charts (e.g., Casagrande plasticity chart) and (2) understand the bias and precision of making inferences beyond the range of the training dataset.

Acknowledgements The authors thanked Ms Yuanqin Tao for her editorial assistance.

References

1. Ching J, Phoon KK (2012) Modeling parameters of structured clays as a multivariate normal distribution. *Can Geotech J* 49(5):522–545
2. Ching J, Phoon KK (2014) Transformations and correlations among some clay parameters – the global database. *Can Geotech J* 51(6):663–685
3. Ching J, Phoon KK (2015) Constructing multivariate distributions for soil parameters. Chapter 1, *Risk and Reliability in Geotechnical Engineering*, CRC Press, Boca Raton, pp 3–76
4. Ching J, Phoon KK (2019) Constructing site-specific multivariate probabilistic distribution model by Bayesian machine learning. *ASCE J Eng Mech* 145(1):04018126
5. Ching J, Li DQ, Phoon KK (2016) Statistical characterization of multivariate geotechnical data. Chapter 4, *Reliability of geotechnical structures in ISO2394*, CRC Press/Balkema, London, pp 89–126
6. Ching J, Phoon KK (2020) Measuring similarity between site-specific data and records from other sites. *ASCE-ASME J Risk Uncertain Eng Syst Part A: Civ Eng* 6(2):04020011
7. Ching JY, Phoon KK, Ho YH, Weng MC (2021) Quasi-site-specific prediction for deformation modulus of rock mass. *Can Geotech J* 58(7):936–951
8. Ching J, Wu S, Phoon KK (2021) Constructing quasi-site-specific multivariate probability distribution using hierarchical Bayesian model. *J Eng Mech ASCE* 147(10):04021069
9. Gelman A, Hill J (2006) *Data analysis using regression and multilevel/hierarchical models*. Cambridge University Press, Cambridge, England
10. Kincal C, Koca MY (2019) Correlations of in situ modulus of deformation with elastic modulus of intact core specimens and RMR values of andesitic rocks: a case study of the İzmir subway line. *Bull Eng Geol Env* 78:5281–5299
11. Kulhawy FH, Mayne PW (1990) *Manual on estimating soil properties for foundation design*. Report EL-6800, Electric Power Research Institute, Palo Alto, California
12. Mesri G, Huvaj N (2007) Shear strength mobilized in undrained failure of soft clay and silt deposits. In: DeGroot DJ et al (eds) *Advances in measurement and modeling of soil behavior (GSP 173)*. ASCE, pp 1–22

13. Ou CY, Liao JT (1987) Geotechnical engineering research report. GT96008, National Taiwan University of Science and Technology, Taipei
14. Phoon KK, Kulhawy FH (1999) Characterization of geotechnical variability. *Can Geotech J* 36(4):612–624
15. Phoon KK, Prakoso WA, Wang Y, Ching J (2016) Uncertainty representation of geotechnical design parameters, Chapter 3. Reliability of geotechnical structures in ISO2394. CRC Press/Balkema, London, pp 49–87
16. Phoon KK, Ching J, Wang Y (2019) Managing risk in geotechnical engineering—from data to digitalization. In: 7th International symposium on geotechnical safety and risk, Taipei, Taiwan, pp 13–34
17. Phoon KK, Tang C (2019) Characterization of geotechnical model uncertainty. *Georisk Assess Manag Risk Eng Syst Geohazards* 13(2):101–130
18. Phoon KK, Ching J, Shuku T (2022) Challenges in data-driven site characterization. *Georisk Assess Manag Risk Eng Syst Geohazards* 16(1):114–126
19. Phoon KK, Zhang W (2023) Future of machine learning in geotechnics. *Georisk Assess Manag Risk Eng Syst Geohazards*. <https://doi.org/10.1080/17499518.2022.2087884>
20. Phoon KK, Ching J, Cao Z (2022) Unpacking data-centric geotechnics. *Underground space* 7(6):967–989
21. Sharma A, Ching J, Phoon KK (2022) A hierarchical Bayesian similarity measure for geotechnical site retrieval. *J Eng Mech ASCE* 148(10):04022062
22. Tang C, Phoon KK (2021) Model uncertainties in foundation design. CRC Press, Boca Raton



Kok-Kwang Phoon is Cheng Tsang Man Chair Professor and Provost, Singapore University of Technology and Design (SUTD). He obtained his BEng and MEng from the National University of Singapore (NUS) and his PhD from Cornell University. Prior to joining SUTD, Prof Phoon was Senior Vice-Provost (Academic Affairs) and Interim Director of the Lloyd’s Register Foundation Institute for Public Understanding of Risk at NUS. He is a Professional Engineer in Singapore, an ASEAN Chartered Professional Engineer, and past President of the Geotechnical Society of Singapore. He is currently serving as the Deputy Chief Scientific Advisor (DCSA) of the National Research Foundation Singapore. He was elected as a Fellow of the Academy of Engineering Singapore in 2012.

Prof Phoon is particularly interested in developing statistical and other data-driven methods to support decision making in geotechnical engineering. He has edited 3 books and authored 1 book: *Model Uncertainties in Foundation Design* (CRC Press, 2021). He was bestowed the ASCE Norman Medal twice in 2005 and 2020 and the Humboldt Research Award in 2017, among many others. He is the founding editor of *Georisk* (Taylor & Francis) and presently serving on the editorial board for premium journals such as *Structural Safety* and *Probabilistic Engineering Mechanics*. He has delivered the inaugural S.L. Lee Lecture in Singapore, 11th J.E. Jennings Memorial Lecture in South Africa, 10th Sun Jun Lecture in China, 4th Wilson Tang Lecture in the Netherlands, 10th Lumb Lecture in Hong Kong, 4th Suzanne Lacasse Lecture in Taiwan, and 2nd Alfredo Ang Lecture in China.

New Tool for the Measurement of Soils' Shear Strength



Mounir Bouassida and Dalel Azaiez

Abstract Disturbance encountered when testing soft soils both in laboratory and in-situ conditions makes the determination of undrained shear strength, S_u , very challenging. This paper introduces a new tool called “Cylindrical Shear Tool” (CST) to measure the undrained shear strength, S_u , of soft soils. Description of this tool is given and the related shear test procedure is detailed. The proposed tool offers the advantage to avoid the disturbance of soft soils prior to the measurement of shear strength. From recorded measurements, and based on considerations of the existing shear tests, a specific method of determination of S_u is proposed. Recorded results by the CST on a reconstituted Tunis soft clay revealed in fair agreement with those obtained from direct shear tests and from a triaxial test. Using the CST a series of tests was also performed from which the friction angle of the interface between the CST and a compacted sand is determined. First, characterization of the chosen quarry sand comprised identification tests, Proctor tests and the direct shear test (DST). Then follows the preparation of sand samples compacted, in Proctor molds, at the optimum modified and normal Proctor water contents. Those remolded sand specimens were subject to the CST tests for which the failure shear strength is captured. Then the method of determination of the sand specimens' friction angle is detailed.

Keywords Cohesion · Testing · Disturbance · Cylindrical tool · Friction angle · Undrained cohesion

1 Introduction

The determination of soil shear strength relies on producing failure within the soil when subjected to a given loading path. Then, after the measurement of the ultimate load, follows the identification of the soil strength parameters using a specific method

M. Bouassida (✉) · D. Azaiez
Université de Tunis El Manar, École Nationale d'Ingénieurs de Tunis, Ingénierie Géotechnique,
BP 37 Le Belvédère, LR14ES03 Tunis, Tunisia
e-mail: mounir.bouassida@enit.utm.tn

© The Author(s), under exclusive license to Springer Nature Switzerland AG 2023
C. Atalar and F. Çinicioğlu (eds.), *5th International Conference on New Developments in Soil Mechanics and Geotechnical Engineering*, Lecture Notes in Civil Engineering 305, https://doi.org/10.1007/978-3-031-20172-1_4

that depends on the used test procedure. Testing methods to produce a soil failure mostly comprises laboratory tests and in-situ tests.

For laboratory tests, all performed under a prescribed loading rate, one can impose the surface failure as for the direct shear test. In turn, the surface failure is unknown and sometimes non-visible as observed when conducting classical triaxial tests. Instead, for in-situ tests other failure scenarios are considered. For the cone penetration test (CPT) a localized static failure results from the penetration of the tip of cone apparatus into the soil, then the tip resistance is measured. Using well-established correlations, one can deduce the deformation and strength parameters: the Young modulus, friction angle, and the undrained cohesion from the measured tip resistance, etc. For the pressuremeter test, a lateral expansion under a monotonic applied pressure induces a shear deformation up to failure of the surrounding soil [2]. From the measured limit net pressure and pressuremeter modulus, using a specific method, one can proceed for the design of foundations.

In a different way, the vane test, performed both in laboratory and in-situ conditions, is restricted to the measurement of a unique strength parameter that is the undrained cohesion of soft soils. This set of soil investigation methods also includes the dynamic penetration tests, in particular the Standard Penetration Test (SPT) and the dynamic cone device during which a number of blow counts corresponding to a prescribed penetration depth, permits to derive specific strength parameters based on well-established correlations. In case of sands, one can determine the friction angle using the well-know Terzaghi and Peck correlation, Das [8]. In a quite different manner, from the dynamic cone penetration, from the recorded soil resistance, an estimate of the admissible bearing capacity of a shallow foundation is obtained [7].

From the above flashback related to soil testing methods, e.g. tools, for determining in particular shear strength characteristics, there is no limitation, in terms of test procedure, to produce the soil failure, and also to choose the suitable method for determining strength parameters. However, one can outline an important detail that is soil disturbance that can happen into the soil, or not, for the performed testing procedure. Based on this, one can proceed for a classification concerning the preparation for the shear strength measurement. In this regard, one can notice for the vane test that, prior to the commencement of the loading (applied torque), the vane penetrates into the specimen (in laboratory) or the in-situ ground, then, there is a disturbance which may affect the test results [1]. As for the pressuremeter test, the boring of the soil significantly disturbs the vertical edge of the created hole where the measurements cell is mounted to start the lateral expansion. In addition, after discussing the estimation of the undrained cohesion of soft soils, [9] reported the overestimation the S_u value from the recorded limit net pressure during the pressumeter test.

In a different way, concerning the static cone penetration test (CPT) and the standard penetration test (SPT), the measurement of soil shear strength occurs at the bottom of a created hole, and precisely, after an initial penetration of the apparatus where no measurement is taken. As such, one can endorse the fact that soil disturbance will not affect the measurement of soil resistance beyond the initial penetration. Further, especially for the CPT and SPT, note that from the measured resistance, there is a need to use recommended correlations that essentially depend on the soil type

to derive the foreseen strength soil parameters. Therefore, results from the existing is-situ tests do not provide a direct measurement of the basic failure parameters i.e. cohesion and friction angle. Figure 1 schematizes the differences between four in-situ tests, as described in the above, to show where the soil disturbance affects, or rather not, the measurement of soil failure parameters.

Worth mentioning to date there is a lack for determining a reliable undrained cohesion for soft soils. In fact, dependent less of the existing testing tool the disturbance of soft soil is inevitable. Hence, there is a real need to seek for a tool avoiding the soft soil disturbance to assure a reliable S_u determination.

The present work, first, suggests the new Cylindrical Shear Tool for the measurement of soil shear strength recently introduced and patented [4]. This tool enables a direct determination of the undrained cohesion of soft soils without the occurrence of disturbance. Second, this paper presents, a step further, to detail how the use of the cylindrical shear tool (CST), enables the determination of the friction angle of cohesion less soils. The main outcome of the CST relies on the direct and reliable determination of cohesion and/or friction angle without being affected by the soil disturbance.

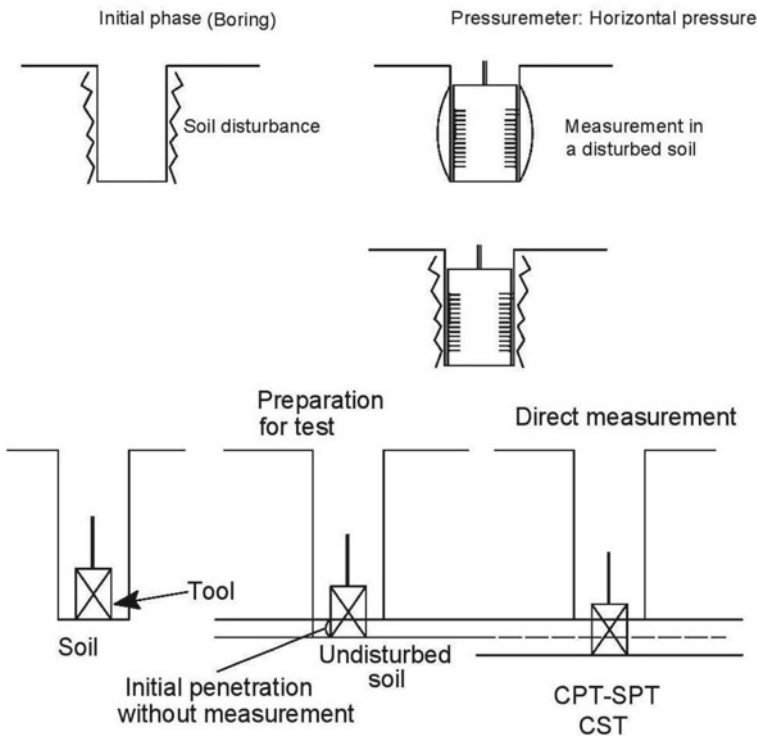


Fig. 1 Schematized preparation for in-situ tests illustrating the occurrence of soil disturbance

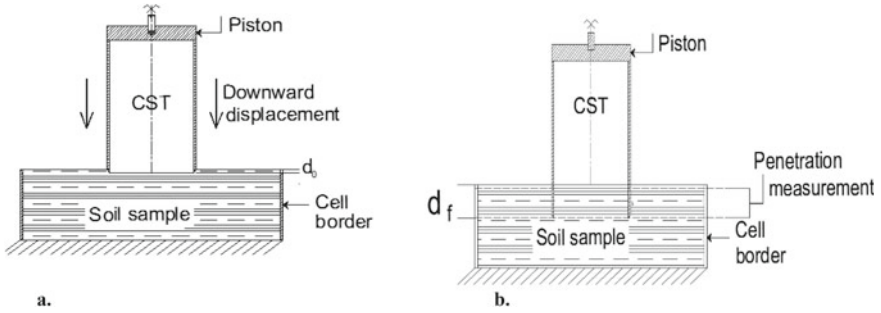


Fig. 2 a. Initial penetration of the cylindrical tool into the test soil prior to the measurement; b. Penetration of the cylindrical tool into the test soil during the measurement of the soil resistance

For each soil type's this paper details the method of determination of its shear strength parameter from the recorded load displacement curves. The validation of the CST test results is discussed after comparison with results obtained by the current testing methods.

2 The Cylindrical Shear Tool (CST)

2.1 Tool Design

The proposed tool is a thin hollow cylindrical tube with a sharpened tip over a short distance $d_0 = 5$ mm. Such a shape facilitates the penetration of the CST into the soft soil, at a prescribed vertical displacement rate, over the distance d_0 (Fig. 2a and b).

The recently published CST test procedure enables the measurement of the soil resistance developed along the circumferential shaft of the penetrated hollow cylinder over the recorded penetration d in the range d_0 to d_f . Therefore, the CST enables a direct measurement of the soil resistance over the imposed soil-tool interface.

Bouassida and Azaiez [3] provided a detailed presentation of the components of the CST for which two sizes, small and big, served for the determination, as a first investigation, of the undrained cohesion of a remolded Tunisian soft clay.

Figure 3 illustrates the two sizes of the manufactured CST for the determination of the soil shear strength parameters.

2.2 Testing Procedure

As experienced during the first investigation [3], the CST test and measurement-assessing transducers are mounted to the loading frame of the triaxial apparatus. The

Fig. 3 Proposed cylindrical shear tool designed in two different sizes



CST fixed in the current position of the conventional loading frame of the triaxial test, penetrates the sample at a uniform vertical displacement rate applied by the moving base platen fixed to the motor drive of the triaxial apparatus.

An s-type load cell, of 2 kN capacity, records the induced vertical force P balancing the soil resistance when the CST penetrates the soil sample.

Besides, using a displacement transducer “4”, VJT0271 of 25 mm travel distance, one records the displacement of the CST when pushed upward to the sample.

Prior to the commencement of the test, one checks, on the motor drive the prescribed displacement rate satisfying either the undrained shear condition or the drained one.

A GDS lab software controls all data acquisition. After checking the GDS lab connection, the first stage of the CST test starts by the penetration of the sharpened tip of the CST into the sample. Then, the re-initialization of all transducers reading to zero to start the second phase corresponding to the CST test that is the shearing of the tested sample. Such a procedure appeals to derive along the soil-tool interface, either the cohesion, in case of soft soils, or the frictional angle governing the contact between the CST and a granular soil.

2.3 Determination of Soil Shear Strength Parameters

Main experimental output from the CST test is the recorded load-penetration curve. After the first investigation, for determining the undrained cohesion of soft soils, Bouassida and Azaiez [3] reasoning's considered the similarity between the direct shear test (DST), and the CST test by concluding the need to mark a limitation of the CST penetration to capture the ultimate vertical force P_{ult} .

As such, one can determine, comprehensively, the soil shear strength parameters. In fact, earlier, Bouassida, [6] explained that the mobilized soil shear strength does not always correspond to the peak of stress–strain (or force–displacement) curve

recorded from any shear test. Worth noted that the limitation of the penetration, d , of the CST into the soft soil also applies for the soil-CST contact area.

3 Determination of Soft Soils' Undrained Cohesion: An Update

Figure 4 shows the variation of the axial force versus the CST penetration as recorded during several tests carried out on reconstituted Tunis soft clay samples.

For each load-penetration curve, the starred point corresponds to the value of the ultimate load determined after the method proposed by Bouassida and Azaiez, [3]. Using the recorded ultimate load, P_{ult} , and the corresponding penetration d_{ult} , illustrated by Fig. 4, one determines the undrained cohesion, S_u , of the tested samples from Eq. (1)

$$S_u = \frac{P_{ult}}{\pi(D_{int} + D_{out})d_{ult}} \tag{1}$$

D_{in} and D_{out} denote the inner diameter and the outer diameter of the CST.

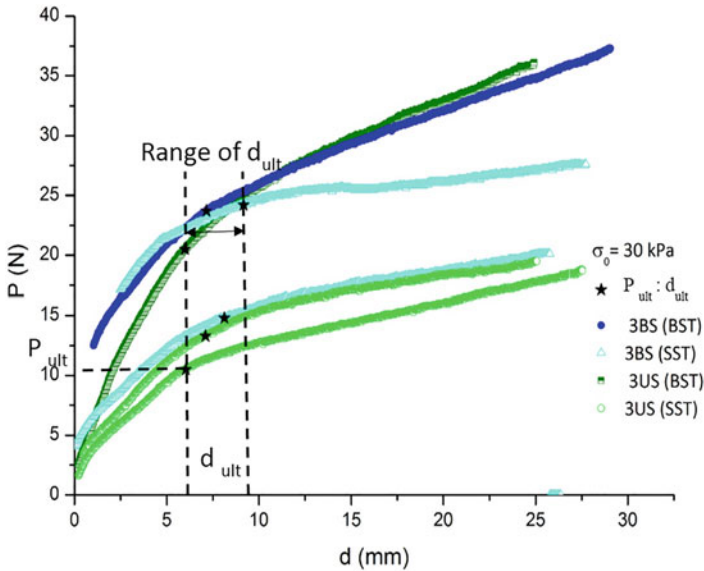


Fig. 4 Variation of the axial force versus the CST penetration in reconstituted Tunis soft clay samples under 30 kPa consolidation stress

Assessment of obtained S_u values from the CST tests showed a fair agreement with values determined for the direct shear test (DST) and a classical triaxial test [3].

4 Determination of Cohesion Less Soils' Friction Angle: First Investigation

The experimental program comprised two steps. First step considered the characterization of a selected quarry sand, including a grain size distribution, Proctor tests and the direct shear test. Second step focused on performing shear tests using the recently patented CST for the determination of the friction angle, by assuming zero cohesion for the tested sand.

4.1 Characterization of the Granular Soil

Bulk sample retrieved from a fill sand, of current use in concrete production, was subject to a sieve analysis with a mesh opening less or equal to 2 mm. Dry sieve analysis was performed after preparing one kilogram of the selected sand. Figure 5 shows, after the particles size distribution, that dimensions corresponding to 60% finer (D_{60}), 30% finer (D_{30}) and 10% finer (D_{10}) approximately take the values 0.55 mm, 0.3 mm and 0.15 mm, respectively. Those data allowed obtaining the coefficient of uniformity: $C_u = \frac{D_{60}}{D_{10}} = \frac{0.55}{0.15} = 3.67$ and the coefficient of gradation $C_c = \frac{D_{30}^2}{D_{10}D_{60}} = \frac{0.3^2}{0.15 \times 0.55} = 1.09$. After the USCS, the tested sand is classified well graded sand.

The characterization of the tested sand using the pycnometer test, led to the specific gravity value in the range: $2.608 < G_s < 2.615$; $G_s = 2.643$.

From the direct shear test carried out on a specimen of the fill sand, the shear strength is characterized by a friction angle $\varphi = 28.9^\circ$ and negligible cohesion. Those characteristics are typical of a loose sand.

Further, after the preparation of compacted samples of the tested sand in standard Proctor moulds the modified and normal Proctor procedures were carried out. Figure 6 shows the two Proctor curves as recorded from the modified Proctor and normal Proctor tests. The recorded modified Proctor parameters are: optimum water content $\omega_{op} = 8.64\%$ and a maximum dry unit weight: $\gamma_d(max) = 18.47\text{kN/m}^3$. Whilst, from the normal Proctor test, the maximum dry unit weight is $\gamma_d(max) = 17.99\text{kN/m}^3$ and the corresponding optimum water content is: $\omega_{op} = 10.38\%$. Table 1 summarizes the recorded data from the performed Proctor tests and the calculated void ratios using the identification test results. From those data, the influence of an intense energy of compaction leads to a decrease in the void ratio and an increased maximum dry density.

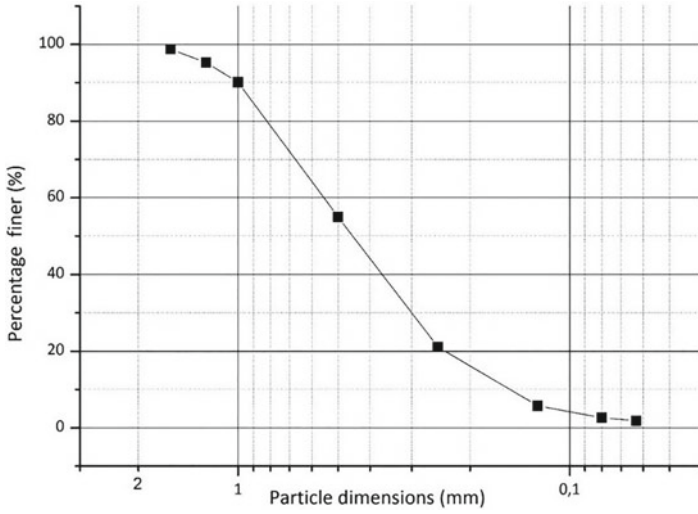


Fig. 5 Grain size distribution of tested sand

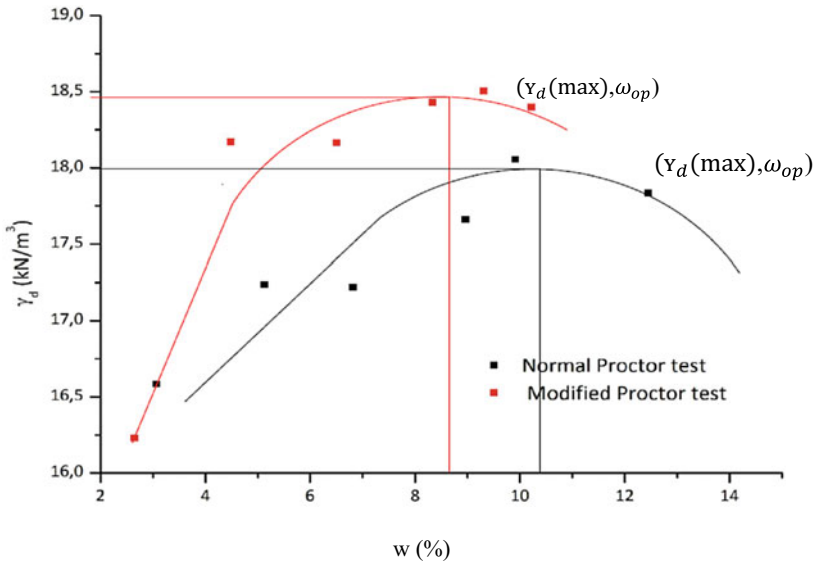


Fig. 6 Proctor test curves of the tested compacted sand

Table 1 Proctor tests results of the compacted sand

Parameters	Modified Proctor test	Normal Proctor test
Optimum water content (%)	8.64	10.38
Max γ_d (kN/m ³)	18.47	17.99
Calculated void ratio	0.552	0.622

4.2 Determination of the Friction Angle of Cohesion Less Soil from the DST and CST Results

Preparation of the sand samples to be subject to the DST and CST test consisted of the compaction of sand specimens in the CBR mold to assure controlled parameters corresponding to the referenced normal Proctor and modified Proctor compactions at related optimum water contents. Opposite extremities sides of the CBR mold specimens served for performing the direct shear tests on the compacted sand specimens.

Those specimens were, then, subject to three CST tests for which the characterization of shear strength parameters were obtained. Then, the method of determination of the friction angles of sand specimens is detailed.

Figure 7 presents the intrinsic curves from recorded results of the DST performed on compacted sand specimens for the normal and the modified Proctor tests.

Table 3 summarizes the obtained shear strength showing a substantial increase of the compacted soil specimen's failure characteristics compared to the friction angle of the dry loose sand (Table 2). The sand compaction significantly enhanced the friction angle, with respect to the performed compaction energy. In addition, the compaction also induced a non-negligible cohesion.

Figure 8 shows the variation of the axial force P versus the CST penetration into the tested compacted sand sample. Noted that during the CST penetration there are fluctuations of the recorded values by the force sensor as illustrated by the dotted band (cloud points). Equation (2) predicts the average of recorded force P (in Newton), during the second CST test performed on the modified Proctor compacted sand sample, as a function of the CST penetration d (in mm), with a linear regression coefficient $R^2 = 0.76$.

$$P = 2.43387d_{ult} \quad (2)$$

By assuming the tested sand as a cohesionless material, the determination of the friction angle resulting from the CST penetration is owed to the developed shear strength along the interface soil-CST. The mobilized shear strength at depth "z" is given by Eq. (3):

$$\tau_f = \sigma_h \tan \delta_f = K_P (\gamma z) \tan \delta_f \quad (3)$$

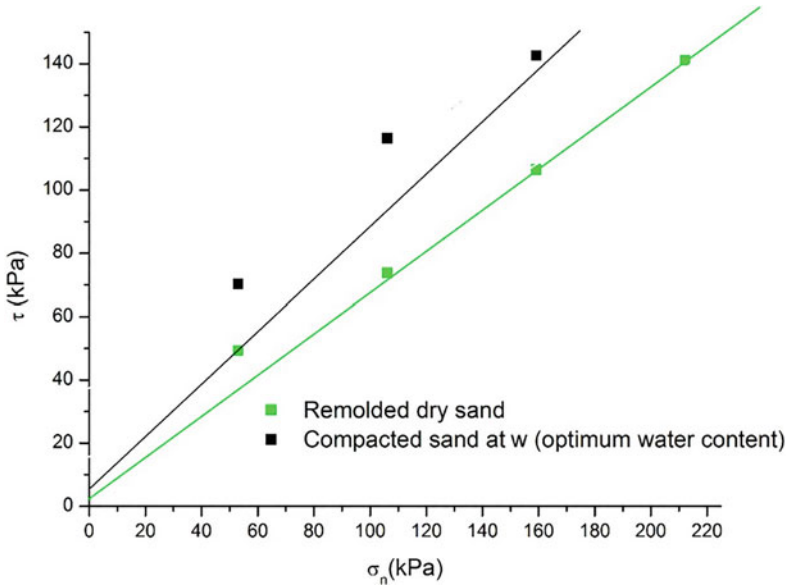


Fig. 7 Intrinsic curves from direct shear tests on the compacted dry sand and specimens at optimum Proctor water content

Table 2 Result of the direct shear test carried out on quarry sand

σ_h (kPa)	τ (kPa)	Horizontal displacement (mm)	Friction angle φ
233	127.2	5.03	28.6°

Table 3 Results of direct shear tests carried out on compacted sand specimens

	C (kPa)	φ (°)
Compacted sand	5.6	39.8
Remolded dry sand	2.6	33.0

σ_h denotes the horizontal stress applied to the CST shaft area.

K_P denotes the passive pressure coefficient which essentially depends of the friction angle of the tested sand (and the roughness of the CST-soil interface).

δ_f denotes the friction angle of the interface between the CST shaft and the tested sand.

Over the increment of the CST penetration dz : $d_0 < dz < d_f$, the vertical force balances the mobilized shear strength, corresponding to the soil failure, over the elementary area, dA_{sh} ; of the CST shaft given by Eq. (4)

$$dA_{sh} = \pi (D_{int} + D_{out})dz \tag{4}$$

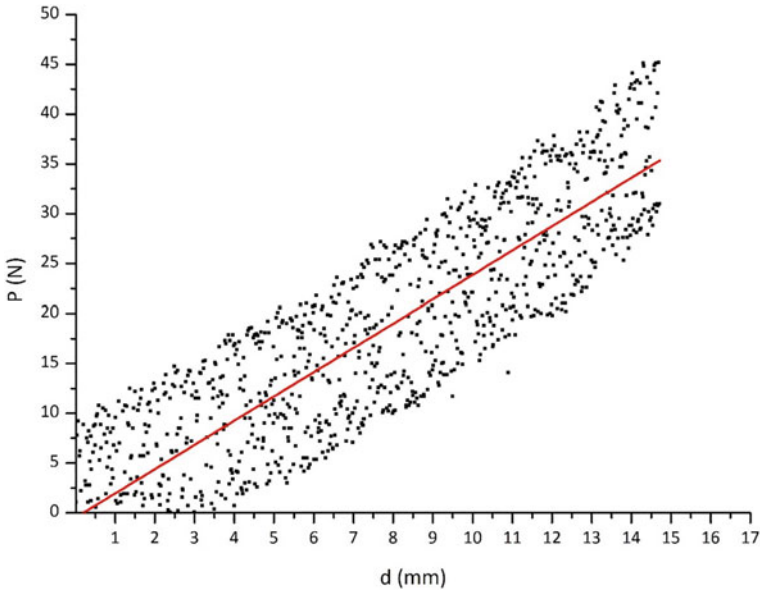


Fig. 8 Recorded axial force P versus the penetration of the CST into the compacted sand sample at the optimum modified Proctor

Using Eqs. (3) and (4), the integration of the shear strength over the total shaft area of the CST leads to the resultant ultimate axial force given by Eq. (5)

$$P_{ult} = \int_{d_0}^{d_f} K_P(\gamma z) \tan \delta_f \pi (D_{int} + D_{out}) dz \quad (5)$$

Integrating Eq. (5), one obtains the ultimate vertical force expressed by Eq. (6)

$$P_{ult} = \frac{1}{2} \gamma (d_f^2 - d_0^2) K_P \tan \delta_f \pi (D_{int} + D_{ext}) \quad (6)$$

As a first basic assumption, in this work, the passive pressure coefficient is given by the well-known formula of Rankine's theory, i.e.

$$K_P = (1 + \sin \varphi) / (1 - \sin \varphi) \quad (7)$$

The effective measurement of the axial load starts after the initial penetration d_0 , and the value of the ultimate axial force, P_{ult} , corresponds to a given value d_{ult} in the range: $d_0 < d_{ult} < d_f$; hence, the friction angle of the interface between the CST and the cohesion less soil is determined from Eq. (8):

$$\tan\delta_f = \frac{2P_{ult}}{\gamma d_{ult}^2 K_p \pi (D_{int} + D_{ext})} \quad (8)$$

The friction angle of the CST-soil interface, δ_f , is proportional to the one of the tested sand, φ as:

$$\delta_f = \alpha\varphi \quad (9)$$

From the literature, in case of a positive frictional soil resistance, as for driven piles, it is common, that coefficient “ α ” introduced by Eq. (9) is the range:

$$0.5 \leq \alpha \leq 0.67 \quad (10)$$

Solution of Eq. (8), in terms of the friction angle of the assumed cohesion less soil, φ , cannot be obtained by performing direct resolution methods. There is a need to perform an iterative procedure for solving such an implicit equation. Plausible solutions should be targeted in the interval $\varphi = 25\text{--}40^\circ$. This investigation is in progress to deliver the suitable determination of the friction angle of purely frictional material from the result obtained by the CST.

5 Conclusions

This paper presented the cylindrical shear tool for testing soils to determine shear strength characteristics. Main benefit of the tool is to avoid the soil disturbance prior to the measurement of shear strength resistance. First investigation considered the determination of the undrained cohesion of purely cohesive soils for which a specific method of determination has been introduced. Thanks to existing direct shear test and a triaxial test results the estimated cohesion using the CST reveals satisfactory [5]. However, more investigation are yet needed for the validation of the proposed method of S_u determination.

Second investigation focused the determination of the friction angle of assumed purely frictional sand. After characterization of a chosen quarry sand including Proctor tests and direct shear test, the influence of compaction has been evidenced by comparing the cohesion and friction angle recorded for compacted sand specimens using the normal and modified Proctor procedures.

After carried out shear tests using the CST, the method of determination of the friction angle of tested sand specimens (assumed of negligible cohesion) is formulated. This investigation is yet in progress to propose a suitable determination of the friction angle of cohesion less soils.

It is also viewed that performing the CST test makes possible the determination of the overall shear resistance of cohesive frictional soils. This third possibility applies for the compacted sand specimens at two different compaction energies.

References

1. Bouassida M, Azaiez D (2019) On the determination of undrained shear strength from vane test. Sustainable civil infrastructures, pp 50–68. <https://doi.org/10.1007/978-3-319-96241N>
2. Baguelin F, Jézéquel JF, Shields DH (1978) The pressuremeter and foundation engineering
3. Bouassida M, Azaiez D (2021) An efficient tool to determine S_u of soft soils. In: Proceeding 3rd Asian conference on physical modelling in geotechnics (Asiafuge-2021), vol 1. Online conference, Singapore, pp 242–251
4. Bouassida M, Azaiez D, Bouassida W (2022) Cylindrical shear Tool. W/O 2022/146238. Priority data /TN2021/050010, 29/12/2020 TN. Simpro Tunisia
5. Bouassida M, Azaiez D (2022) An efficient tool to determine S_u of soft soils. In: Proceeding of the 20th international conference on soil mechanics and geotechnical engineering, Sydney, 1–5May 2022
6. Bouassida M (2006) Modeling the behavior of soft clays and new contributions for soil improvement solutions. Keynote Lecture. In: Proceedings of the 2nd international conference on problematic soils. December 3–5, 6. Petaming Jaya, Salengor, Malaysia. Bujang, Pinto & Jefferson (eds.), pp 1–12
7. Costet J, Sanglerat G (1981) Cours pratique de mécanique des sols, tome 2: calcul des ouvrages, 3ème édition. Dunod, Paris, France
8. Das MB (2022) Principles of principles of geotechnical engineering. 8th edn. ISBN-13: 978–0495411307
9. Frikha W, Ben Salem Z, Bouassida M (2013) Estimation of Tunis soft soil undrained shear strength from pressuremeter data. In: Proceeding of the international symposium ISP6, Paris



Dr. Mounir Bouassida is a professor of civil engineering at the National Engineering School of Tunis (ENIT) of the University of Tunis El Manar where he earned his B.S., M.S., Ph.D., and doctorate of sciences diplomas, all in civil engineering. He co-supervised 23 Ph.D. and 32 Masters of Science graduates. His research focused on soil improvement techniques and the behavior of soft clays. Dr. Bouassida is the (co)author of more than 100 papers in refereed international journals; 180 conference papers including 27 keynote lectures and several book chapters. Further he co-authored three books and three patents as well as book series conferences.

He is Associate Editor of Innovative Infrastructure Innovative Solutions and Ground Improvement (ICE) journals, Geotechnical-Geological journal, International Journal of Geosynthetics and Ground Engineering and the GE section of the Frontiers and Built Environment journal.

As a 2006 Fulbright scholar, Dr Bouassida elaborated a novel methodology for the design of foundations on reinforced soil by columns. He is a co-developer of the software Columns 1.01 used for the design of column-reinforced foundations. He was awarded the 2006 S. Prakash Prize for Excellence in the practice of geotechnical engineering.

In 2008, Dr Bouassida launched a Tunisian consulting office in geotechnical engineering, SIMPRO. As such, he contributed for the design of more than hundred projects.

Prof. Bouassida held the office of the vice president of ISSMGE for Africa (2005–2009) and then and appointed

member of the ISSMGE board (2017-2022). He benefited from grants as a visiting-invited professor in several institutions in the USA, Canada, Europe, Australia and Asia. In 2018, he became a Director of the International Press-In Association.

Since 2019, the launch of the You Tube channel « Mounir Bouassida” gained lot of interest from than 1430 subscribers. Fifty nine uploaded videos, in English and French, to this channel cover themes focusing on soil mechanics, modelling and the study of the behavior of geotechnical engineering structures.

Soil Properties and Characterization Final

Apparatus Design and Measuring of Apparent Swelling Pressure of Compacted Bentonite



Hailong Wang, Takumi Shirakawabe, and Daichi Ito

Abstract Apparent swelling pressure of compacted bentonite (p_s) is a basic parameter for structure design for the geological disposal projects of high-level radioactive waste (HLW). The equilibrium apparent swelling pressure (p_{eq}) observed by wetting compacted bentonite have been reported extensively in past studies, however, p_{eq} variation, i.e. difference between p_{eq} measurements under similar conditions, may significantly large equilibrium swelling pressure. This variation was sometimes attributed to swelling deformation of specimens during testing, however, few studies discussed this issue in detail. In this study, a swelling pressure apparatus was newly developed with aim of obtaining good repeatable p_{eq} measurements. Efforts are made on apparatus design to achieve simple configuration, low cost and low system compliance. A series of tests were conducted to find a proper way of obtaining p_{eq} with less variation for identical specimens. It was found that slight deformation of might not be the fundamental reason for p_{eq} variation, however, slight deformation may introduce difficulties of dry density measurement, which may result in apparent p_{eq} variation. With the new apparatus, good repeatability of p_s measured on identical specimens was obtained. The apparatus may provide an inexpensive tool for further understanding the behaviours of compacted bentonite.

Keywords Apparent swelling pressure · Compacted bentonite · Apparatus · Geological disposal · High-level radioactive waste

1 Introduction

As a candidate material for geological disposal of high-level radioactive waste, highly compacted bentonite has been studied extensively for its swelling properties. One

H. Wang (✉) · D. Ito
Waseda University, Tokyo, Japan
e-mail: whlxy2002@aoni.waseda.jp

T. Shirakawabe
Obayashi Corporation, Tokyo, Japan

of the important swelling properties is the pressure produced by wetting compacted bentonite under a fully confined state. Herein, this pressure and its final equilibrium state were designated apparent swelling pressure p_s and apparent equilibrium swelling pressure p_{eq} , respectively following [13]. There are generally four methods to measure p_{eq} [6, 9], while two of them: constant volume and zero-swell methods were employed extensively for compacted bentonites. In the former method, vertical swelling deformation of compacted bentonite is limited to a narrow range by adjustment of vertical loading during wetting until no further adjustment is necessary. And p_{eq} is equal to vertical load finally applied. The latter method restricts swelling deformation using rigid walls. Equilibrated pressure measured using a load cell or a pressure transducer connected to the rigid wall is regarded as p_{eq} . A literature survey was conducted on p_{eq} measured by these two methods to find measurement variation of p_{eq} . Some representative results are presented in Fig. 1, in which testing conditions, such as testing temperature, specimen wetting liquids, initial water condition, testing apparatus for each dataset are technically the same. Figure 1a shows case of Ca-type bentonites and Fig. 1b is that for Kunigel V1 (hereafter, K_V1), a Na-type bentonite candidate for Japanese geological disposal project. It can be seen from Fig. 1 that p_{eq} variation under the same specimen dry density (ρ_d) for each dataset might be several hundred kilopascals or several megapascals in some cases, although it might also be negligible in other cases. This variation seems also to be larger for higher ρ_d . Villar and Lloret [10] attributed p_{eq} variation to high sensitivity of p_{eq} to certain specimen deformation during tests. Tanaka and Watanabe [8] stated that insufficient stiffness of tested apparatuses would be a source for slight deformation of specimens and result in p_{eq} variation. However, it was not clear how slight deformation could cause p_{eq} variation fundamentally and why p_{eq} variation would occur for specimens with technically the same testing conditions. In this paper, design details of a new apparatus for swell pressure measurement are presented and experiments on identical specimens attempting to obtain p_{eq} values with less variation were conducted. Based on the experimental results, it is implied that slight deformation may not necessarily cause p_{eq} variation.

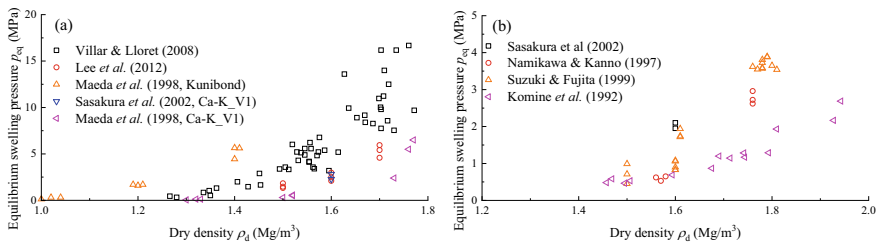


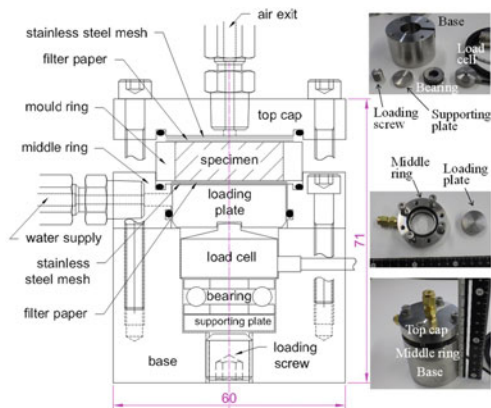
Fig. 1 Typical equilibrium apparent swelling pressure measurements: **a** Ca-type bentonites, and **b** Kunigel V1 (Na-type bentonite)

2 Apparatus Design

Figure 2 presents the apparatus recently developed in this study. A specimen with dimensions of 10 mm in height (H) and 28 mm in diameter (ϕ) is confined radially in a mould ring. The specimen is sandwiched between the top cap and the loading plate to restrain vertical deformation. There is a load cell, a bearing, a supporting plate and a loading screw, respectively beneath the loading plate, so that the loading plate can be raised vertically by rotating the loading screw without introducing torque. Water is designed to be supplied from the opening at the middle ring, where a cylindrical, 0.3-mm-wide gap exists between the loading plate and middle ring, from which water flows into the specimen through a stainless steel mesh and a filter paper. Air escapes from the air exit opening at the top cap. This apparatus measures the averaged p_s of the specimen, though the authors also developed other types to measure local p_s [13, 14].

To restrict specimen deformation, it is natural to apply a confining stress to the mould ring by rotating the bottom loading screw before supplying water. However, it was found that this confining stress drops due to compressibility of filter paper. Two tests with configurations shown in Fig. 3a were conducted, where a load was applied to an empty mould ring in case 1 and a filter paper was added to the mould ring bottom in case 2. Results were plotted to Fig. 3a, where load cell measurements were converted to a stress (σ_{vt}) respecting to the specimen area. Also, given the initial value of σ_{vt} , σ_{vt0} is the initial applied confining stress. It is shown that σ_{vt} decreases significantly larger in case 2 comparing to case 1 and after supplying water in case 2 σ_{vt} drops again. Reduction of σ_{vt} is expected to be mainly induced by deformation creep of the filter paper and change of filter paper compressibility after being wetted. More tests were conducted with the configuration of case 2 under different σ_{vt0} . The results, as shown in Fig. 3b, indicate that the stress drop might vanish only when σ_{vt0} is sufficiently small: 0.05 MPa or less. If initiation of specimen swelling could be artificially controlled, measurement of a bentonite specimen schematically

Fig. 2 Apparent swelling pressure apparatus



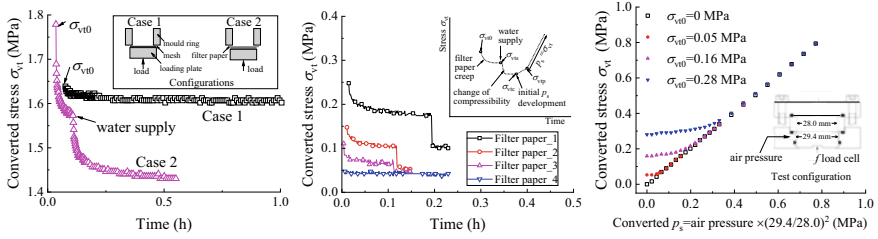


Fig. 3 **a** Three testing configurations with similar σ_{vt0} , **b** For configuration case 3 under different σ_{vt0} , and **c** σ_{vt} development by variation of p_s and σ_{vt0}

illustrated in insert of Fig. 3b can be expected. Measurements first stabilize at a stress σ_{vts} before water supply and again approach to a constant stress σ_{vtc} after water supply. If specimen swelling was initiated from σ_{vtc} , the measurement would increase slowly until it exceeds a stress σ_{vtp} , from which the measurements reflect really behaviours of p_s .

Since measurement could not be observed clearly between σ_{vtc} and σ_{vtp} for a bentonite specimen because swelling will be triggered at the moment of water supply, a test was design with the configuration in the insert of Fig. 3c. In the test, air pressure applied to the inner space of the mould ring was increased stepwise to simulate development of p_s under different σ_{vt0} . Because filter paper was not used in these tests so that approximately $\sigma_{vt0} = \sigma_{vts} = \sigma_{vtc}$. Air pressure is simply converted to p_s based on the mould ring and loading plate diameters, as shown in the X-axis legend in Fig. 3c. It is apparent that the relation between σ_{vt} and p_s almost follows a 1:1 line for the case of $\sigma_{vt0} = 0$ MPa. For other cases, σ_{vt} increment is smaller than that of p_s till converging to the 1:1 line. It can be roughly estimated that $\sigma_{vts} = \sim 1.6 \sigma_{vtc}$ from Fig. 3b and $\sigma_{vtp} = \sim 1.5 \sigma_{vtc}$ from Fig. 3c so that approximately $\sigma_{vtp} = \sigma_{vts}$. This result suggests that σ_{vt0} should not be too large to observe p_s behaviours. In the following contents, σ_{vt} are approximately regarded as p_s when $\sigma_{vt} > \sigma_{vts}$.

3 Test Program

A series of tests was conducted on K_V1 with the new apparatus. Specific gravity of K_V1 is 2.80, water content in laboratory environment (23 °C, 50% relative humidity) is about 7%. The montmorillonite content is about 53% measured by Methylene blue absorption test [15]. Other details on K_V1 are given in Wang et al. [12]. Table 1 shows test conditions. Two experimenters, denoted respectively as WH and ST in the test names, were involved in the experimental works. All specimens were statically compacted to target dry densities using a jack. In this study, the term “identical specimens” is used for specimens with the same target dry density (ρ_d) and initial water contents (w_i), which were also prepared on the same day. Note that ρ_d in Table 1 was calculated by assuming that volume of specimens was the

same as the inter space of the mould ring, where compression of filter papers was not considered. “Pre-sp” expresses whether a pre-reserved space was set or not. The reason of keeping pre-reserved space is discussed in the next section, while to make such a space 5 following steps were done: (1) Trim two surfaces of a specimen after specimen compaction. (2) Install the specimen in the apparatus. Put filter paper at the top end of the specimen (surface 1 in Fig. 4a). Then tighten the top cap screws. (3) Release top cap screws and trim the bottom surface of the specimen (surface 2 in Fig. 4a). (4) Turn the specimen over. Put a normal filter paper beneath surface 1 and a pre-compressed filter paper upon surface 2. Tighten the top cap (Fig. 4b). (5) Apply σ_{vt0} , wait for stress stabilization. Supply water for p_s measurement.

The thickness of the filter paper can be pre-compressed to about 0.13–0.14 mm in the manner shown in Fig. 4c by tightening the top cap screws. In step (2), the edge area of a normal filter paper might normally be compressed to about 0.1 mm

Table 1 Summary of testing specimen conditions

w_i %	ρ_{dt} Mg/m ³	Test name	ρ_d Mg/m ³	w_f %	σ_{vt0} MPa	Pre-sp
7.44	1.6	WH_1	1.54	28.7	1.65	No
		WH_2	1.55	28.5	1.67	
7.94	1.6	WH_3	1.53	29.6	0.22	Yes
		WH_4	1.51	29.8	0.06	
		WH_5	1.53	28.7	0.06	
6.77	1.6	ST_1	1.57	28.1	1.63	No
		ST_2	1.58	26.2	1.12	
		ST_3	1.58	28.3	0.6	
		ST_4	1.58	26.7	0.27	
		ST_5	1.58	28.8	0.11	
6.47	1.6	ST_6	1.56	28.4	1.11	Yes
		ST_7	1.57	28.4	0.54	
		ST_8	1.57	28.4	0.27	
		ST_9	1.58	28.5	0.15	
6.73	1.6	ST_10	1.53	29.4	0.24	
		ST_11	1.53	29.2	0.23	
		ST_12	1.54	29.1	0.24	
	1.66	ST_13	1.6	27	0.3	
	1.68	ST_14	1.65	25.4	0.25	
	1.7	ST_15	1.71	22.9	0.24	
		ST_16	1.72	22.6	0.25	

Notes w_i and w_f : initial and final water contents, respectively. ρ_{dt} and ρ_d : target dry density and dry density after trimming. Pre-sp: whether a pre-reserved space between bottom specimen surface and bottom filter paper was set or not

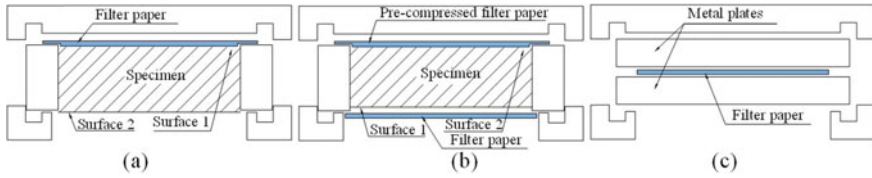


Fig. 4 Depiction of the proposed specimen setup procedure: **a** initial installation of a specimen, **b** installation of a specimen before water supply, and **c** preparation of pre-compressed filter paper

in thickness. In step (4), the edge area of a pre-compressed filter paper might be compressed further to about 0.08–0.09 mm. Consequently, a pre-reserved space of about 50 μm can be made with the above steps.

4 Test Results and Discussions

For two identical specimens (WH_1 and WH_2), 2 h was set for σ_{vt} stabilization after applying σ_{vt0} but before supplying water. As shown in Fig. 5a, very good overall agreement was obtained. After supplying water, σ_{vt} first immediately drops to certain level as shown in the inset, and increases to a peak, reduce to a valley, and increase again to an equilibrium state. These behaviours are consistent with those of p_s commonly observed for compacted bentonite (e.g. Pusch 1980) except the first drops. The σ_{vt} reduction from the peak to the valley at about 50 h is expected to be induced by soil skeleton collapse during wetting (e.g. Wang et al. [13]). The σ_{vt} drop at the beginning is expected to be induced by change of filter paper compressibility as explained in Fig. 3. Five additional tests were conducted using identical specimens (ST_1-ST_5) by differing σ_{vt0} . Results, as shown in Fig. 5b, indicate that the stress drop diminishes and vanishes as σ_{vt0} decreases. In addition, the equilibrium σ_{vt} increases with increased somehow σ_{vt0} when σ_{vt0} exceeds ~ 0.25 MPa. Another four identical specimens (ST_6-ST_9) were further prepared with a pre-reserved space. Test results obtained from the four specimens under different σ_{vt0} are shown in Fig. 5c, which reveals very good overall agreement. Final parts of results in Fig. 5b (ST_1-ST_5) were also plotted to Fig. 5c, which indicates that though the variation of equilibrium σ_{vt} of ST_1-ST_5 is larger, their equilibrium σ_{vt} is consistent with those of ST_6-ST_9 except ST_1 with σ_{vt0} of 1.63 MPa. Results in Fig. 5 imply that: without a pre-reserved space, initially applied σ_{vt0} may also stress the specimens and induces monotonic increase of equilibrium σ_{vt} with σ_{vt0} and this stress may be introduced by compression of bottom filter paper edge; and small deformation during tests may not be a fundamental reason for p_{eq} variation since with the pre-reserved space, specimen deformation of ST_6-ST_9 should be larger than that of ST_1-ST_5, but their equilibrium σ_{vt} values are consistent. For the effect of σ_{vt0} , finding a much thinner or less compressible filter paper would be another solution instead of making a pre-reserved space (e.g. membrane filter with thickness of ~ 0.1 mm in Wang et al.

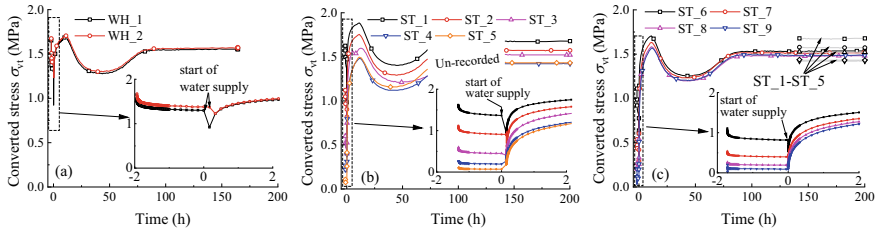


Fig. 5 Time history of ps on identical specimens **a** with similar σ_{vt0} , **b** with different σ_{vt0} , and **c** with different σ_{vt0} , but a pre-reserved space was made

[11]). For p_{eq} variation shown in past studies (i.e. Fig. 1), if the small deformation was not the fundamental reason, difference of measured ρ_d and true ρ_d would be a possible reason causing apparent p_{eq} variation and undetectable slight deformation would be a source for this difference.

Tests were conducted on identical specimens by two experimenters (WH_3-WH_5 and ST_10-ST_12), in which σ_{vt0} was kept small (i.e. 0.06 MPa for WH_4 and WH_5, and 0.22–0.30 MPa for the rest). As shown in Fig. 6, overall agreement of p_s is very good for specimens except WH_5 with higher p_{eq} of about 0.1 MPa. And for WH_5, some abnormal behaviours also observed at the beginning (inset figure). Nevertheless, it may be said p_{eq} with very small variation can be achieved with the new apparatus and pre-reserved space specimen. Some specimens were also prepared with target dry density (ρ_{dt}) ranging from 1.60 to 1.70 Mg/m³ for specimen ST_10-ST_16 to see effect of dry density. Figure 6b shows p_s time histories of these tests, in which ρ_d is labelled. Effect of dry density on p_s , i.e. higher dry density results in higher p_{eq} , can be clearly observed in the tested range.

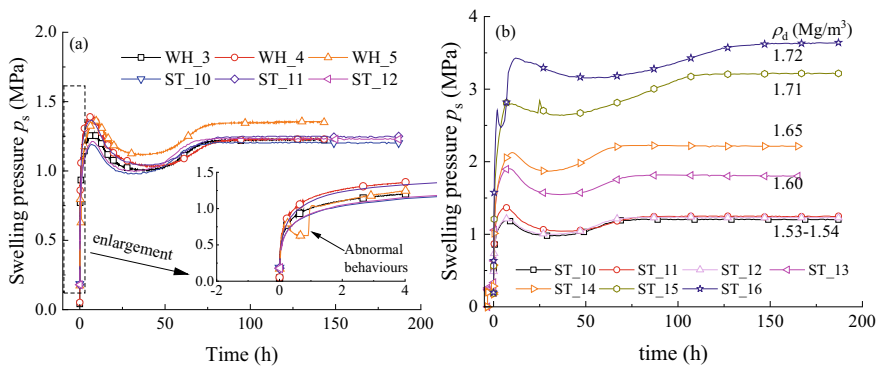


Fig. 6 Time history of **a** p_s for identical specimens prepared by two experimenters, and **b** p_s for specimens with different ρ_d

5 Conclusion

This study developed a new swelling pressure apparatus for compacted bentonite specimens with features of simple design, low cost and system compliance. As a key issue in this study, a series of tests were conducted to confirm the test procedures of obtaining p_{eq} values with less variation for identical specimens. It was found that higher confining stress results in a higher p_{eq} , which implies that the confining stress might be partially applied to specimens due to filter paper compression. With this observation, identical specimens were prepared with pre-reserved spaces at the bottom surface, by which p_{eq} values with very small variation were obtained. For specimen specimens without pre-reserved space, though p_{eq} values were somehow affected by the confining stress, the average value is consistent with p_{eq} of specimen with pre-reserved space. These observations indicate that slight deformation (e.g. induced by pre-reserved space or system compliance) during tests might not necessarily introduce p_{eq} variation by using the apparatus proposed. If this statement can be applied to past studies, p_{eq} variation observed in past studies may not certainly and fundamentally induced by slight deformation, however, slight deformation might introduce difficulties of measuring true dry density of a specimen which would be one reason resulting in p_{eq} variation.

Acknowledgements This work was performed as a part of the activities of the Research Institute of Sustainable Future Society, Waseda Research Institute for Science and Engineering, Waseda University, and supported by Kajima Foundation, Taisei Foundation. The authors express their deep gratitude to all those described above.

References

1. Komine H, Ogata N, Nishi K (1992) Mechanical properties of buffer materials for repositories of high-level nuclear waste (part 1): experimental study on swelling characteristics of compacted bentonite. CRIEPI Research Report, U32039 (in Japanese)
2. Lee J, Lim J, Kang I, Kwon S (2012) Swelling pressures of compacted Ca-bentonite. *Eng Geol* 129–130:20–26
3. Maeda M, Tanai K, Ito M, Mihara M, Tanaka M (1998) Mechanical properties of the Ca exchanged and Ca bentonite: swelling pressure, hydraulic conductivity, compressive strength and elastic modulus. Technical Report, Japan Nuclear Cycle Development Institute, PNC-TN8410 98-021 (in Japanese)
4. Namikawa T, Kanno T (1997) Consolidation property of buffer material. Technical Report, Japan Nuclear Cycle Development Institute, PNC-TN8410 97-051 (in Japanese)
5. Sasakura T, Kuroyanagi M, Okamoto M (2002) Studies on mechanical behavior of bentonite for development of the constitutive model. Technical Report, Japan Nuclear Cycle Development Institute, JNC TJ8400 2002-025 (in Japanese)
6. Sridharan A, Rao A, Sivapullaiah P (1986) Swelling pressure of clays. *Geotech Test J* 9(1):24–33
7. Suzuki H, Fujita T (1999) Swelling characteristics of buffer material. Technical Report, Japan Nuclear Cycle Development Institute, JNC TN8400 99-38 (in Japanese)

8. Tanaka Y, Watanabe Y (2019) Modelling the effects of test conditions on the measured swelling pressure of compacted bentonite. *Soils Found* 59:136–150
9. Tang CS, Tang AM, Cui YJ, Delage P, Schroeder C, De Laure E (2011) Investigating the swelling pressure of compacted crushed-Callovo-Oxfordian claystone. *Phys Chem Earth* 36:1857–1866
10. Villar MV, Lloret A (2008) Influence of dry density and water content on the swelling of a compacted bentonite. *Appl Clay Sci* 39(1–2):38–49
11. Wang H, Koseki J, Nishimura T, Miyashita Y (2017) Membrane filter properties and application of the filter to undrained cyclic triaxial test of unsaturated materials. *Can Geotech J* 54(8):1196–1202
12. Wang H, Shirakawabe T, Komine H, Ito D, Gotoh T, Ichikawa Y, Chen Q (2020) Movement of water in compacted bentonite and its relation with swelling pressure. *Can Geotech J*. 57(6): 921–932. <https://doi.org/10.1139/cgj-2019-0219>
13. Wang H, Komine H, Gotoh T (2022a) A swelling pressure cell for X-ray diffraction test. *Géotechnique* 72(8):675–686. <https://doi.org/10.1680/jgeot.20.00005>
14. Wang H, Ruan K, Harasaki S, Komine H (2022b) Effects of specimen thickness on apparent swelling pressure evolution of compacted bentonite. *Soils Found* 62(1):101099. <https://doi.org/10.1016/j.sandf.2021.101099>
15. Wang H, Ito D, Shirakawabe T, Ruan K, Komine H (2022c) On swelling behaviors of a bentonite under different water contents. *Geotechnique*, online first, <https://doi.org/10.1680/jgeot.21.00312>.

Volume Change Behavior of Natural Sands with the Addition of Mica Particles



Furkan Egemen Kahya  and Tugba Eskisar 

Abstract The volume change behavior of sands is affected by the grain size, shape, mineralogical origin, initial void ratio, effective stress level, and the existence of pore water inside the soil medium. The presence of mica minerals changes the inter-particle force chain and causes the re-arrangement of sand particles under varying stress conditions. The intergranular void ratio concept is a useful approach to evaluate the grain size range that is in control of the soil behavior. Two different natural sand samples were mixed with varying mica contents to perform oedometer tests. The volume change behavior was evaluated with the intergranular void ratio concept. The triaxial test results were used to support the findings of the oedometer test results. The test results indicated that the volume change behavior depending on the mica content differed with the effective stress level and the mineralogical origin of the sand. There was a certain range of mica content, a transition zone, that changed the soil behavior. The behavior was controlled by the fine particles when the soil contained approximately 20% or more mica.

Keywords Sand · Oedometer test · Triaxial test · Intergranular void ratio concept · Volume change behavior

1 Introduction

The volume change behavior of fine-grained soils under varying stress conditions is a time-dependent phenomenon. However, the volume change of sandy soils occurs immediately and it is affected by the grain size and shape, permeability, effective stress condition, initial void ratio, and mineralogical differences in the soil medium. Many natural sands contain different sizes, shapes and they possess different origins. Particularly, the mineralogical origin determines the grain shape due to the cleavage plane. Gilboy [1] conducted a series of tests on sand-mica mixtures and indicated that the volume change behavior of sands is affected by the presence of platy-like particles,

F. E. Kahya · T. Eskisar (✉)

Faculty of Engineering, Civil Engineering Department, Ege University, Bornova/İzmir, Turkey
e-mail: tugba.eskisar@ege.edu.tr

© The Author(s), under exclusive license to Springer Nature Switzerland AG 2023
C. Atalar and F. Çinicioğlu (eds.), *5th International Conference on New Developments in Soil Mechanics and Geotechnical Engineering*, Lecture Notes in Civil Engineering 305, https://doi.org/10.1007/978-3-031-20172-1_6

e.g. mica. Datta et al. [2] reported that calcareous sands formed from the remains of marine organisms had platy-like shape grains, the inter-particle voids of this soil made it vulnerable to crushing. Harris et al. [3] indicated that the platy morphology of mica particles made them behave much differently under stress compared to more equidimensional grains of quartz, feldspar, etc. They also showed that the relative effect of mica content on the soil strength, bearing capacity, and compressibility were most obvious at lower percentages of mica and declined about a range of 10 and 15%. Meshida [4] investigated a highway failure in Nigeria and reported that the flaky structures of micaceous soils resulted in inadequate field compaction. The platy-like grains increased the inter-granular voids in the granular environment [2]. Golightly [5] pointed out that, calcareous sands which contain platy-like, marine animal skeletal remains had high void ratio and inter-particle porosity. Colliat-Dangus et al. [6] indicated that the calcareous sands had very high compressibility due to the inter-particle porosity and the brittleness of their grains.

It is very important to understand inter-granular or inter-particle relations to understand the volume change behavior of sands. When the sand grains experience a loading they transfer loads to each other from inter-granular contact points, at the same time, this creates a fictive force chain in the granular media. Hence, the volume change behavior is controlled by inter-granular relations. The volume change behavior of natural sands is affected by the amount of fines. The intergranular void ratio concept is a useful approach to estimate whether the behavior of sand is controlled by the fine particles or granular particles of the soil matrix.

Thevanayagam [7] investigated silty sands known as sensitive sands based on the inter-granular void ratio concept and showed that when the fines content was greater than about 30%, the behavior of silty sand or sandy silts were similar to that of silts. Salgado et al. [8] pointed out that, sands with 5–20% silt content showed more compressibility than the clean sands. Monkul and Özden [9] made an attempt to understand the effect of intergranular void ratio through one-dimensional compression tests. Reconstituted sand and kaolinite mixtures indicated a transition fines content, below which the compressional behavior was mainly controlled by the coarser grain matrix, and above which was governed by the finer grain matrix. Çabalar [10] mentioned that the mica content leading to the transition zone of the sand-mica mixtures increased with increasing effective stress. The triaxial test results indicated a close relationship between the transition fines content and the mechanical properties of the soil.

This study aimed to determine the one-dimensional volume change behavior and the relationship between the fines content and the mechanical properties of two different natural sands of İzmir, Turkey. The oedometer tests were conducted with varying mica contents (i.e. 0–50% of mica by the dry weight of the soil) to evaluate the effect of mica content on the granular medium and the inter-particle relations. The triaxial tests were conducted to confirm the findings of the oedometer test results.

2 Materials and Methods

Natural sand specimens were taken from Kemalpaşa (Nazarköy) and Yamanlar in İzmir, Turkey. Kemalpaşa sand is a part of Quaternary alluvium deposits of Kemalpaşa Basin. Tepe and Sözbilir [11] stated that the lithostratigraphic units in and around Kemalpaşa Basin are in an age range from Paleozoic to Quaternary [11]. Sözbilir et al. [12] investigated the rock units of area in two different groups as pre-basin-fill and basin-fill respectively. The pre-basin-fill contains metamorphic rocks of Menderes Massif, Bornova Flysch Zone rocks, and two unconformity-bounded Miocene aged units: the Kemalpaşa Group and the Kızılcıca Formation. The basin-fill units are the Görece - Sütçüler Formation and alluvium [11, 12]. Yamanlar sand is a part of Quaternary alluvium deposits of Miocene aged Yuntdağı andesitic rocks and lavas [13].

The soil classifications were made based on the Unified Soil Classification System (USCS) following ASTM D2487 [14]. Nazarköy and Yamanlar sands were classified as poor graded sands (SP). Mica particles of this study were in the range of silty sand and classified as SM. The particle size distribution curves were plotted according to ASTM D6913 [15] (Fig. 1). The specific gravity of Nazarköy and Yamanlar samples were obtained according to ASTM D854 [16] and calculated as 2.60 and 2.44 g/cm³, respectively. Also, the maximum void ratio (e_{max}) of Nazarköy and Tire samples were determined as 1.03 and 1.23, respectively. Within the scope of the experimental study, the grain sizes of natural sand samples were limited between No:10 (2 mm) to No:40 (0.425 mm) sieves. Six different mixtures were prepared with mica contents of 5, 10, 15, 20, 30, 40, 50% to perform oedometer test. Different mixtures which contained 0, 10, 30, and 50% mica were prepared to perform the triaxial tests.

Oedometer tests were conducted following ASTM D2435/D2435M [17]. The sand–mica mixtures were placed in the oedometer ring apparatus layer by layer in a fully saturated condition; apart from that, the top of each layer was flattened with a smooth tamping technique. The incremental loadings were applied in nine stages as 12.5 kPa, 25.0 kPa, 49.9 kPa, 99.9 kPa, 199.8 kPa, 399.6 kPa, 799.1 kPa, 1598.2 kPa, and 3196.5 kPa, respectively. The next loading stage was applied one hour after the end of the primary consolidation settlement of the previous stage as noted in the B method of ASTM D2435 [17]. Eight sets of consolidated undrained triaxial tests were conducted based on ASTM D4767-11 [18]. Four different sand–mica mixtures: 0, 10, 30, and 50% were prepared in congruence with the oedometer test results. The specimens were 50 mm in diameter and 100 mm in height. All samples were placed in five layers and each layer was tamped down using a rod to maintain a relative density of 55–65%. The specimens were saturated until the B-value was greater than 0.95. The effective cell pressures for the consolidation stage were 50, 100 and 200 kPa, respectively.

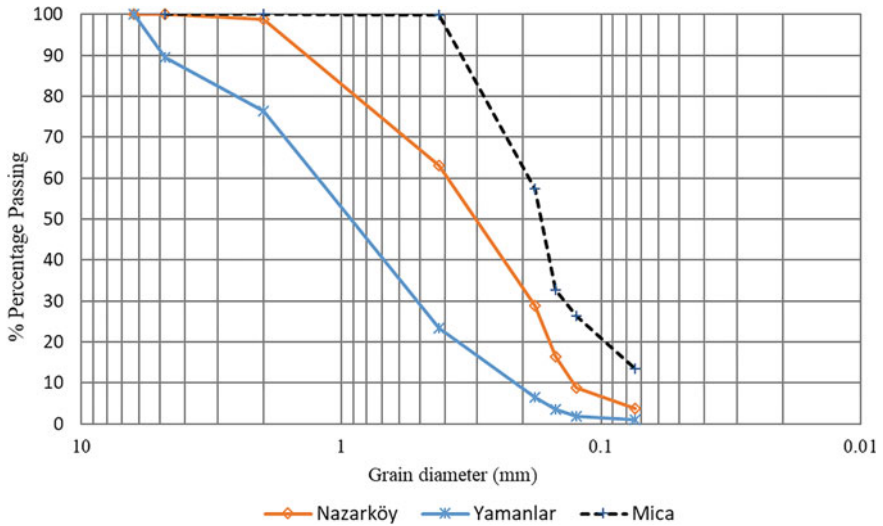


Fig. 1 Particle size distribution of Nazarköy and Yamanlar sands and mica

3 Results and Discussion

3.1 Oedometer Tests

The volume change behavior of natural sand samples was affected by the platy mica particles. The platy-like shape of mica particles routed the sand grains and led to changes in the rearrangement of the granular medium. The intergranular void ratio concept was used to evaluate the effects of mica particles on natural sands. For this purpose, the equation proposed by Thevanyangam was preferred (Eq. 1).

$$e_{(s)} = (e + FC/100)/(1 - FC/100) \quad (1)$$

In Eq. (1), e_s refers to intergranular void ratio, and FC refers to fines content. The one-dimensional volume change behavior of the samples has been plotted in terms of intergranular void ratio (e_s) and the effective oedometer stress ($\log \sigma$) (Figs. 2 and 3). According to the intergranular void ratio concept, when e_s approximates or equals to the e_{max} , this point denotes the transition zone. The transition zone is accepted as the zone, where the volume change behavior transfers from the granular part of the soil to the fine part of the soil [7–10, 20]. The granular materials transfer loads to each other from contact points. Hence, a fictive force chain occurs in the granular media. Also, the volume change behavior of granular materials is controlled by the intergranular friction forces and tensile strength of the particles. When the fines content increases in the granular medium, fine particles tend to place between the voids and on the contact points of grains. Thus, the intergranular force chains are

broken and the rearrangement mechanism known as sliding and rolling takes action; therefore, the volume change behavior of the sands are converged to the transition zone.

Figure 2a shows that Nazarköy samples converged to the e_{max} line approximately at 10–15% mica contents. Beyond 15% mica content, the volume change curves passed over the e_{max} line. On the other side, Yamanlar samples converged to the e_{max} line approximately at 15–20% mica content (Fig. 2b). The behavioral differences between these two different natural sand samples were attributed to the differences of their geological and mineralogical origins, the unit weight, and the gradation. The natural unit weights of Nazarköy and Yamanlar samples were 2.60 and 2.44 g/cm³, respectively. The median grain sizes of samples were 0.3 and 0.92, respectively.

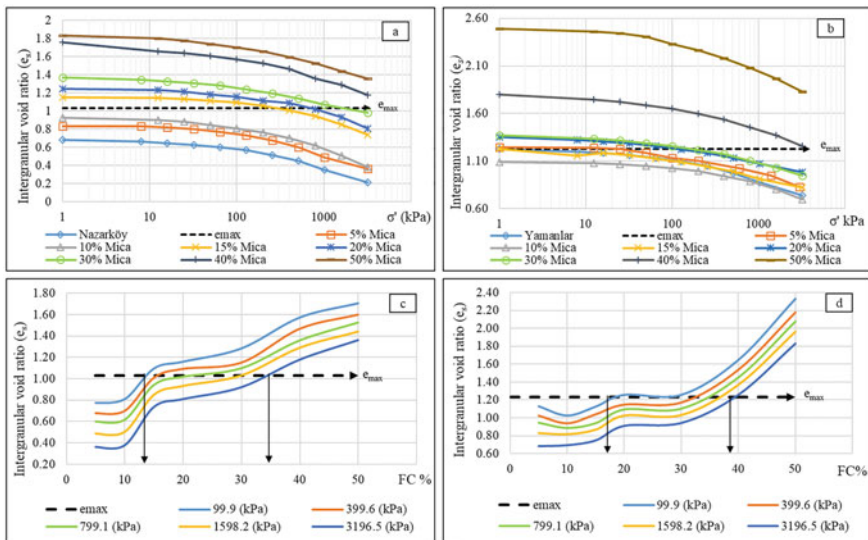


Fig. 2 e_s — $\log(\sigma)$ curves: **a** Nazarköy sand, **b** Yamanlar sand; Relation between e_s —FC as a function of effective stress: **c** Nazarköy sand, **d** Yamanlar sand

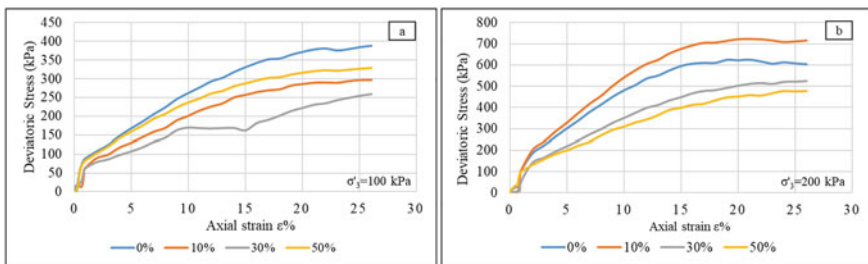


Fig. 3 Deviatoric stress (σ_d)—axial strain (ϵ) curves: **a** Nazarköy sand under 100 kPa stress, **b** Yamanlar sand under 200 kPa stress

Nakata et al. [19] emphasized that the stresses at the yield point and the compression index reduced with increasing median particle size. From this point of view compression indices (C_c) of Nazarköy and Yamanlar samples were found as 0.333 and 0.216, respectively. Besides, specific gravity (G_s) and median grain size (D_{50}) could be attributed as important variables.

The transition zone was evident in terms of the fines content (FC) where e_s curves converged to the e_{max} of the mother soil as denoted by the e_{max} line in Fig. 2a–d. Monkul and Özden [9] highlighted that there was a transition at certain fines content depending on the applied stress. From this point of view, the e_s -FC curves which were plotted as a function of applied stress also declared the transition. Therefore, the intersection of e_s -FC curves and the e_{max} line defined the transition. Figure 2c shows the intersection of the e_{max} line of Nazarköy sand with e_s -FC curves of 99.9 and 3196.5 kPa at 12.5 to 35% FC, respectively. Figure 2d shows the intersection of the e_{max} line of Yamanlar sand with e_s -FC curves of 99.9 and 3196.5 kPa at 17.5 to 39% FC, respectively. The transition values which were obtained from Fig. 2a and b showed approximate values. The transition fines content increased with the applied effective stress in Fig. 2c and d confirming the findings of the previous studies [9, 10, 20].

3.2 Triaxial Tests

The volume changes in sands are not only important in terms of settlements, but also important in terms of shear stress distribution. Moreover, the volume changes influence the strength and the deformation properties. Deviatoric stress (σ_d)–axial strain ($\epsilon\%$) curves were used with the oedometer tests results to evaluate the effects of mica particles on shear strength. Figure 3a and b show σ_d – $\epsilon\%$ curves of Nazarköy and Yamanlar sands with varying the mica contents.

Belkhatir et al. [21] indicated that the undrained shear strength can be correlated to the fines content, intergranular void ratio and hydraulic conductivity. Further, they found that undrained shear strength decreased linearly with the increase of fines content. Similar to the findings of Belkhatir et al. [21], the shear strength of Nazarköy sand reduced with increasing mica content. The shear strength reduction was at its maximum at 30% mica content (Fig. 3a). At 50% mica content, the shear strength increased again. This time, the mica content completely controlled the volume change behavior of the soil. The strength of Yamanlar sand increased at 10% mica content in contrast to Nazarköy sand in Fig. 3b. The initial value of the intergranular void ratio of Yamanlar sand with 10% mica was lower than the natural Yamanlar sand as the mica particles filled the voids of the granular medium passively creating a better packing of the soil particles. In addition to this, the shear strength of Yamanlar sand reduced between 10 and 50% mica contents. This reduction also shows the effects of increasing mica content on shear strength in Fig. 3b.

The internal friction angle (Φ°) and cohesion (c) values of samples were calculated with Mohr–Coulomb criterion (Table 1). Table 1 shows that the internal friction

Table 1 c and Φ values of samples

FC%	Nazarköy				Yamanlar			
	0%	10%	30%	50%	0%	10%	30%	50%
c (kPa)	0	0	0	8	15	20	5	7
Φ (°)	25	25.4	23	18.6	25	33	23	15

angle (Φ°) of Nazarköy samples reduced with the increasing mica content. Also at 50% mica content there was a cohesion of 8 kPa. This cohesion was considered as apparent cohesion due to the capillarity in the specimens. The internal friction angle (Φ°) of Yamanlar sand increased at 10%. From Fig. 2b, the initial intergranular void ratio (e_s) value at 10% mica content was found lower than Yamanlar sand. Hence, this increment might be another explanation for the lower initial intergranular void ratio (e_s) value. However, in the range of 10–50% mica content, the internal friction reduced with the increasing mica content.

4 Conclusions

In this paper, a series of oedometer and triaxial tests were conducted on two different natural sands with mica particles to investigate the effects of mica content on the granular medium. The volume change behavior was evaluated based on the oedometer test data in terms of the intergranular void ratio concept. Also, the triaxial test results were used to support oedometer test findings and used to investigate the effects of mica content on the shear strength. The e_s curves of Nazarköy sand and Yamanlar sand converged to the e_{max} line approximately at the threshold zone of 12.5 and 17.5% mica contents, respectively. The e_s -FC curves showed that the transition zone of Nazarköy sand varied in the range of 12.5–35% of mica content and the transition zone of Yamanlar sand varied in the range of 17.5–39% of mica content. The e_s -FC curves clearly showed that the transition zone increased with the increasing applied stress confirming the works of [9, 10, 20]. The shear strength of Nazarköy sand decreased with increasing applied stress in triaxial tests. The shear strength of Yamanlar sand increased at 10% mica content as the initial void ratio of 10% mica content was lower than the natural Yamanlar sand. The shear strength of both Nazarköy and Yamanlar sands generally decreased with the increasing fines content similar to the findings of [21, 22]. Nazarköy and Yamanlar sands showed certain differences in terms of the volume change behavior and the shear strength due to the median grain size, specific gravity, and geological origin of the sands. The effects of grain mineralogy and microstructural properties would be the next step of this study to determine the behavior of mica added sands.

References

1. Gilboy G (1928) The compressibility of sand-mica mixtures. *Proc ASCE* 54:555–568
2. Datta M, Gulhati SK, Rao GV (1980) Crushing of calcareous sands during drained shear. *Soc Pet Eng AIME J* 20:77–85
3. Harris W, Parker J, Zelazny L (1984) Effects of mica content on engineering properties of sand1. *Soil Sci Soc Am J - SSSAJ* 48
4. Meshida EA (2006) Highway failure over talc-tremolite schist terrain: A case study of the Ife to Ilesha highway, South-Western Nigeria. *Bull Eng Geol Environ* 65:457–461
5. Golightly CR (1989) Engineering properties of carbonate sands. Bradford University
6. Colliat-Dangus JL, Desrues J, Foray P (1988) Triaxial testing of granular soil under elevated cell pressure. *Adv Triaxial Test Soil Rock*, 290–310
7. Thevanayagam S (1998) Effects of fines and confining stress on undrained shear strength of silty sands. *J Geotech Geoenvironmental Eng* 124:479–491
8. Salgado R, Bandini P, Karim A (2000) Shear strength and stiffness of silty sand. *J Geotech Geoenvironmental Eng* 126:451–462
9. Monkul M, Ozden G (2005) Effect of intergranular void ratio on one-dimensional compression behavior
10. Cabalar AF (2010) Applications of the oedometer, triaxial and resonant column tests to the study of micaceous sands. *Eng Geol*. <https://doi.org/10.1016/j.enggeo.2010.01.004>
11. Tepe Ç, Sözbilir H (2017) Tectonic geomorphology of the Kemalpaşa basin and surrounding horsts, southwestern part of the Gediz Graben. *Western Anatolia Geodin Acta* 29:70–90
12. Sözbilir H, Sari B, Uzel B, Sümer Ö, Akkiraz S (2011) Tectonic implications of transtensional supradetachment basin development in an extension-parallel transfer zone: The Kocayay Basin, western Anatolia. *Turkey Basin Res.* 23:423–448
13. Akay E, Erdogan B (2004) Evolution of Neogene calc-alkaline to alkaline volcanism in the Aliaga-Foça region (Western Anatolia, Turkey). *J Asian Earth Sci* 24:367–387
14. ASTM D2487(2011) Standard practice for classification of soils for engineering purposes (Unified Soil Classification System)-D2487, ASTM Int. West Conshohocken, PA, USA ,p 12
15. ASTM D6913 (2009) standard test methods for particle-size distribution (gradation) of soils using sieve analysis. ASTM International, vol 4. West Conshohocken, PA, pp 1–35
16. ASTM D854 (2014) standard test methods for specific gravity of soil solids by water pycnometer, ASTM International. West Conshohocken, PA, USA
17. ASTM (2020) D2435/D2435M-11, Test methods for one-dimensional consolidation properties of soils using incremental Isoading, pp 1–14 ASTM Int. West Conshohocken, PA, USA
18. ASTM D4767-11 (2021), Standard test method for consolidated undrained triaxial compression test for cohesive soils, ASTM Int. West Conshohocken, PA, USA pp 1–14
19. Nakata Y, Kato Y, Hyodo M, Hyde AFL, Murata H (2001) One-dimensional compression behaviour of uniformly graded sand related to single particle crushing strength. *Soils Found* 41:39–51
20. Cabalar AF, Hasan A (2013) Compressional behaviour of various size/shape sand-clay mixtures with different pore fluids. *Eng Geol* 164:36–49
21. Belkhatir M, Schanz T, Arab A (2013) Effect of fines content and void ratio on the saturated hydraulic conductivity and undrained shear strength of sand-silt mixture. *Environ. Earth Sci* 70(6): 2469–2479
22. Hsiao DH, Phan VTA, Hsieh YT, Kuo HY (2015) Engineering behavior and correlated parameters from obtained results of sand-silt mixtures. *Soil Dyn Earthq Eng* 77:137–151

Estimation of Compression Index of Lightly Overconsolidated Soils from In-Situ Time-Settlement Plots



T. Lenin, M. R. Madhav, and V. Padmavathi

Abstract Compression index is an important parameter in the determination of settlement response of soft soils under preloading with PVDs. Compression index typically estimated using oedometer tests on samples with the assumption that the result represents the entire deposit in the field. Most of the soils in in-situ condition are lightly overconsolidated, with Over Consolidation Ratio (OCR) ranging from 1.0 to 2.0 due to glaciation, ground water level fluctuation, aging, isostatic uplift, cyclic loading, creep, erosion, cementation, etc. The effect of overconsolidation ratio on the estimation of compression index is analyzed in this study. The in-situ time-settlement plots at different depths for sites, Suvarnabhumi International Airport [2] and Mukasa Express Way [4], are analysed to estimate compression index of in-situ ground, which truly represents the deposit's overall behavior unlike the values obtained from 'so called' extremely small undisturbed samples tested in the laboratory. The variation of compression index with depth of the deposit are also presented for different OCR values considered.

Keywords Compression Index · Time-Settlement plots · Lightly overconsolidated soil · Over Consolidation Ratio

1 Introduction

Many soils are lightly overconsolidated due to cementation, glaciation, isostatic uplift, creep, excavations, erosions, ground water level fluctuations etc. Bjerrum [3] demonstrated that delayed consolidation and aging leads to lightly overconsolidated state. Consolidation parameters estimated from the 'so called' undisturbed samples laboratory tests may not be reliable nor applicable to the entire soil in the field.

T. Lenin (✉)

Department of Civil Engineering, JNTUH College of Engineering, Hyderabad, India

e-mail: leninthati@gmail.com

M. R. Madhav · V. Padmavathi

JNTUH College of Engineering, Hyderabad, India

Madhav et al. [6] developed a method to estimate compression index and coefficient of consolidation radial and vertical flows of soft clays assuming the deposit as normally consolidated by back analysis of in-situ time-settlement plots. In the present study, time-settlement plots obtained from the field are re-analyzed to estimate the compression index, C_c , by back analysis assuming the deposit as lightly overconsolidated. By using Asaoka [1] method the final primary consolidation settlements are estimated.

2 Methodology

2.1 Estimation of Compression Index

A uniform soft soil layer of thickness, H , initial void ratio, e_0 , subjected to a surcharge of $\Delta \sigma'$ at the surface is shown in Fig. 1. Primary consolidation settlements, (S) for normally and overconsolidated conditions are estimated at the center of the layer using Eqs. (1) and (2) respectively [5]. These equations are strictly valid for thin deposits only.

Settlement of normally consolidated soil:

$$S = \frac{C_c * H}{1 + e_0} * \log \left[\frac{\sigma'_0 + \Delta \sigma'}{\sigma'_0} \right] \tag{1}$$

Settlement of overconsolidated soil:

$$S = \frac{C_c * H}{1 + e_0} * \log \left[\frac{\sigma'_0 + \Delta \sigma'}{\sigma'_c} \right] + \frac{C_s * H}{1 + e_0} * \log(\text{OCR}) \tag{2}$$

where C_c —compression index, σ'_0 —effective overburden pressure at the center of the layer ($H/2$ depth), σ'_c – maximum past pressure C_s —swell index and $\text{OCR} = \sigma'_c / \sigma'_0$.

Fig. 1 Soft soil

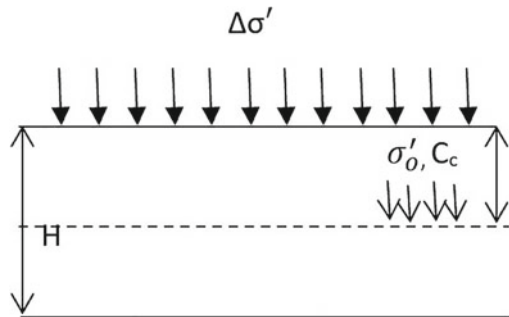
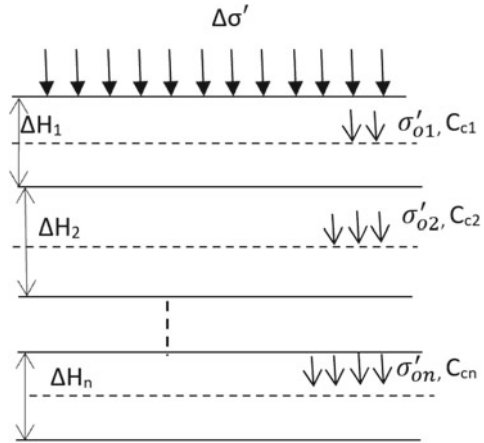


Fig. 2 Compressible layer divided into sub-layers



In the present study Eqs. (1) and (2) are modified with thin sublayers, $i = 1$ to n of thickness ΔH_1 to ΔH_n as shown in Fig. 2.

For normally consolidated soil:

$$\Delta S_i = \frac{C_{ci} \times \Delta H}{1 + e_o} * \log \frac{\sigma'_{oi} + \Delta \sigma'_i}{\sigma'_{oi}} \tag{3}$$

For overconsolidated soils:

$$\Delta S_i = \frac{C_{si} \times \Delta H}{1 + e_o} * \log(OCR) + \frac{C_{ci} \times \Delta H}{1 + e_o} * \log \frac{\sigma'_{oi} + \Delta \sigma'_i}{\sigma'_{ci}} \tag{4}$$

where ΔS_i —settlement, ΔH_i —thickness, σ'_{oi} -effective overburden pressure of soil at the middle of the sub-layer, OCR-overconsolidation ratio, C_{ci} —compression index, C_{si} —swell index of i th sub-layer.

Rearranging the terms in Eqs. (3) and (4), compression index, C_{ci} , of each sub-layer is estimated as

For normally consolidated soil:

$$C_{ci} = \frac{\Delta S_i * (1 + e_o)}{\Delta H \log \left(\frac{\sigma'_{oi} + \Delta \sigma'_i}{\sigma'_{oi}} \right)} \tag{5}$$

For overconsolidated soils and at a certain OCR value:

$$C_{ci} = \frac{\Delta S_i * (1 + e_o)}{\Delta H \left[\frac{c_s}{c_c} * \log \left(\frac{\sigma'_{ci}}{\sigma'_{oi}} \right) + \log \left(\frac{\sigma'_{oi} + \Delta \sigma'_i}{\sigma'_{ci}} \right) \right]} \tag{6}$$

3 Results and Discussion

3.1 Case Study 1 (Suvarnabhumi International Airport)

The case study on construction of Suvarnabhumi International Airport (SBIA), Bangkok, Balasubramaniam et al. [2] is considered for the estimation of in-situ compression indices. Geotechnical parameters such as water content, specific gravity and total unit weight are taken from the case study (Fig. 3). The profile encountered at this site is weathered crust from 0 to 1.8 m depth from the ground surface, followed by very soft clay from 1.8 to 8 m, soft clay from 8 to 11 m depth, soft to medium clay from 11 to 15 m depth and stiff clay from 15 to 20 m depth. The water table is at the ground level. The void ratio and the submerged unit weight estimated from the data are shown in Table 1.

Preloading and vertical drains were used to accelerate the consolidation process in the site. The in-situ time-settlements obtained from instrumentation installed at the site is shown in Fig. 4. The final settlements at surface and at depths of 2, 8 and 12 m are also estimated using Asaoka plots and given in Table 1. The compression indices

Fig. 3 Soil profile of bangkok plain [2]

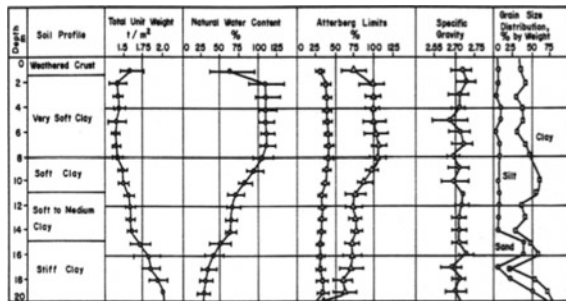


Table 1 Properties of each sublayer

Depth (m)	ΔH (m)	e	S (m)	ΔS (m)	z (m)	γ'	σ'_0 (kPa)	$\Delta\sigma'$ (kPa)	C_c
0			1.65						
	2	2.48		0.25	1.0	4.90	4.9	84	0.3457
2			1.40						
	6	3.00		0.8	5.0	4.20	22.5	84	0.7891
8			0.60						
	4	2.15		0.41	10.0	5.30	45.8	84	0.7131
12			0.19						
	3	1.65		0.19	13.5	6.30	66.0	84	0.4714
15			0						

of the sublayers are estimated considering the strata to be normally consolidated (Eq. (5)) and listed in Table 1.

The compression index for each sublayer is then estimated considering the soil to be lightly overconsolidated with OCR varying from 1.25 to 2.0 (Eq. (6)) and for $C_s/C_c = 0.1$. Variations of C_c with depth for different OCRs is depicted in Fig. 5. Compression index of top layer (0–2.0 m) is relatively small ($C_c = 0.346$) possibly due to desiccation (alternate heating and cooling and wetting and drying). The compression index, for NC soil (OCR = 1.0), decreases from 0.79 at 5 m depth to 0.47 at 13.5 m depth. The compression index increases with the increase in OCR as the settlement kept constant for all OCR values in the analysis. The percentage increase in compression index is 27% as OCR increases from 1.0 to 2.0 for sub layer 0–2 m. Similarly for sublayer 12–15 m the increases in compression index is 315%.

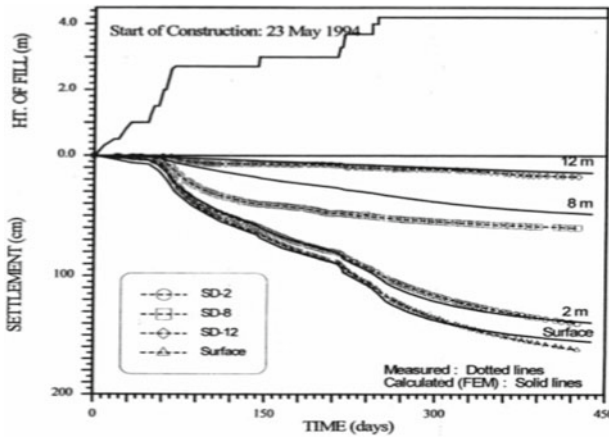
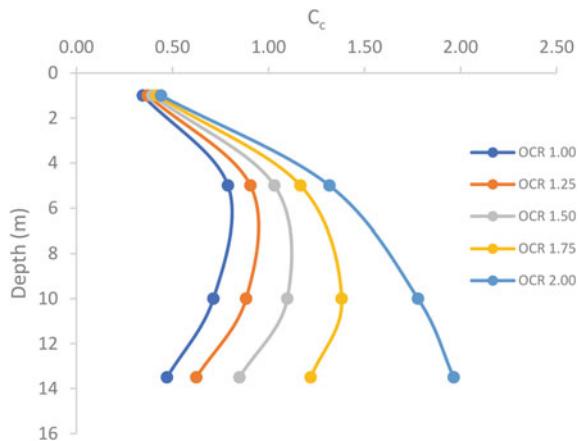


Fig. 4 Time versus settlements at different depths [2]

Fig. 5 Variation of C_c with OCR and depth at SBIA test site



3.2 Case Study 2 (Mukasa Express Way)

Chai et al. [4] studied the Maizuru-Wakasa expressway in the Mukasa area, Fukui Prefecture, Japan, which has a thick soft organic deposit with natural water content ranging from 100 to 250%. Vacuum consolidation with embankment construction (preload) was adopted for this project. The estimated maximum embankment load is 348 kPa. The details of soil profile, variation of vacuum pressure and embankment load with depth are illustrated in Fig. 6. Settlements measured under embankment centreline at different depths in response to the applied pressures are shown in Fig. 7.

The soil properties are taken from the case study (Table 2). Compression index of each sublayer is estimated considering the deposit to be normally consolidated (Eq. (5)) and presented in Table 3.

The compression index for each sublayer is also estimated considering the soil to be lightly overconsolidated with OCR varying from 1.25 to 2.0 and with $C_s/C_c = 0.1$ (Eq. (6)). Variations of C_c with depth for different OCRs are presented in Fig. 8. Compression index of top layer (0–3.8 m) is relatively high ($C_c = 1.46$), possibly

Fig. 6 Estimated vacuum pressure and preload on the ground [4]

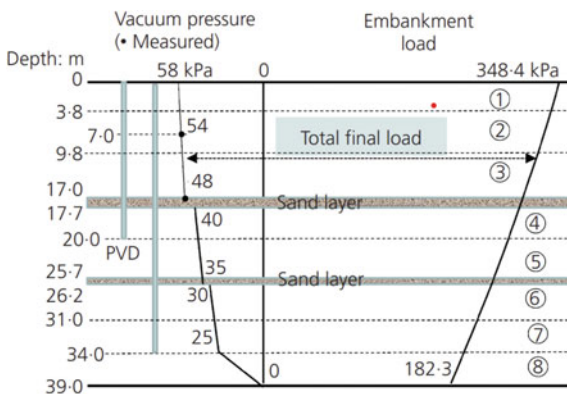


Fig. 7 Time versus settlements at different depths [4]

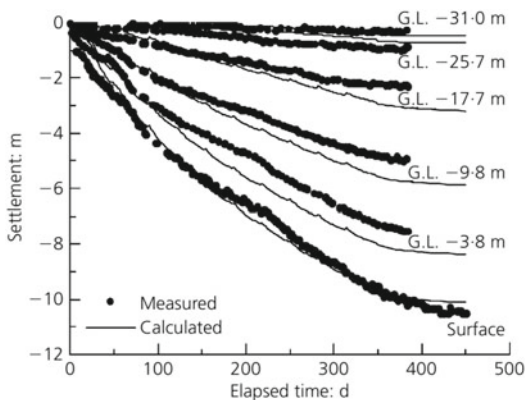


Table 2 Soil properties [4]

Soil layer	Thickness: m	Unit weight: kN/m ³	Void ratio e_0
Clay-1	3.8	13.8	3
Peat-1	6.0	14.1	2.38
Peat-2	7.2	13.4	3
Sand-1	0.7	16.3	1.5
Peat-3	8.0	14.1	2.38
Sand-2	0.5	16.3	1.5
Clay-2	4.8	16.3	1.5
Peat-4	8.0	11.9	5.85

Table 3 Compression index of sub layers

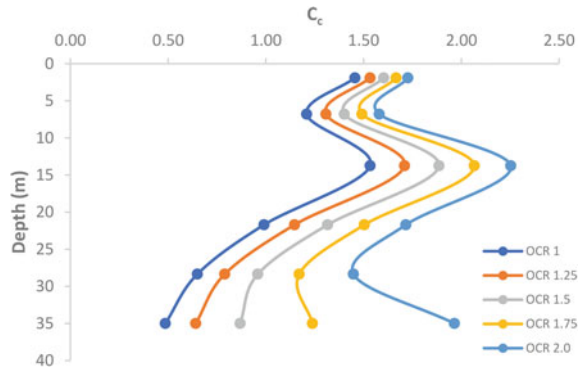
Depth (m)	ΔH (m)	e	S (m)	ΔS (m)	z (m)	γ'	σ'_0 (kPa)	$\Delta\sigma'$ (kPa)	C_c
0			10.00						
	3.8	3.00		2.38	1.90	3.99	7.6	396.9	1.456
3.8			7.61						
	6.0	2.38		2.47	6.80	4.29	28.0	369.5	1.209
9.8			5.14						
	7.9	2.94		2.61	13.75	3.85	56.1	340.1	1.534
17.7			2.53						
	8.00	2.38		1.50	21.70	4.29	88.5	298.5	0.991
25.7			1.03						
	5.3	1.50		0.68	28.35	6.49	122.8	258.0	0.650
31.0			0.35						
	8.0	3.00		0.35	35.00	2.09	148.4	191.6	0.486
39.0			0						

due to presence of recent fill material. Compression index increases with increase in OCR. The percentage increase in compression index is 46% for OCR increasing from 1.0 to 2.0 at a depth of 13.75 m.

4 Conclusions

Most natural deposits get lightly overconsolidated over time because of creep or secondary compression. Bjerrum [3] termed this phenomenon as pseudo-preconsolidation. The in-situ compression index is therefore estimated by back-analysis of time-settlement plots available at various depths considering the ground

Fig. 8 Variation of C_c with OCR and depth at Mukasa express way



to be lightly over-consolidated for OCR values ranging between 1.0 and 2.0 and with $C_s/C_c = 0.1$. Compression index increases with increase in OCR. Settlements estimated considering the deposit to be LOC would be relatively less than those based assuming the deposit to be normally consolidated.

Acknowledgements The contributions of V. Venkata Charan, G. Srikar, former graduate students at JNTU, are gratefully acknowledged.

References

1. Asaoka A (1978) Observational procedure of settlement prediction. *J Soils Found Eng* 18(4):87–101
2. Balasubramaniam AS, Huang M, Bolton M, Oh EYN, Bergado DT, Phienweij N (2007) Interpretation and analysis of test embankments in soft clays with and without ground improvement techniques. *J SEAGS* 9(4):149–162
3. Bjerrum L (1967) Engineering geology of Norwegian normally-consolidated marine clays as related to settlements of building. Seventh Rankine Lecture. *Geotechnique* 17:81–118
4. Chai J, Carter JP, Liu MD (2014) Methods of vacuum consolidation and their deformation analyses. *Proc Inst Civ Eng - Ground Improv* 167(1):35–46
5. Das BM (2014) Principles of foundation engineering, 6th edn. CENGAGE Learning, USA
6. Madhav MR, Charan VV, Srikar G (2015) Estimation of non-homogeneities in in-situ compressibility and consolidation parameters of soft ground. In: Proceedings of international conference on geotechnical engineering (ICGE). Colombo, Sri Lanka, pp 267–270

Granular Soil Relationship Between Angle of Internal Friction and Uniformity Coefficient



Mindaugas Zakarka  and Šarūnas Skuodis 

Abstract The strength characteristics of the sand and gravel are influenced by the size of the grains, their distribution and packaging. The theoretical approach states that the sand angle of internal friction decreases if the uniformity coefficient increases. There are insufficient data for gravel correlation between the uniformity coefficient and the angle of internal friction. Consolidated drained triaxial compression tests (CD) were conducted to determine the strength parameters of remolded sand and gravel samples. These samples were classified as sands and gravels. The optimal water content and density were determined by standard Proctor compaction test and used for these samples. Consolidated drained triaxial compression test gives more reliable data that idealize the soil behavior in the real situation. Three different confining pressures of 20, 50 and 70 kPa were applied to restore horizontal stresses for the soil specimens imitating embankment behavior affected with traffic load. The results indicate that the sand angle of internal friction decreases if the uniformity coefficient is increased. The gravel angle of internal friction does not correlate with the uniformity coefficient.

Keywords Angle of internal friction · Particle size · Uniformity coefficient · Sand · Gravel · Triaxial compression test

1 Introduction

Due to their strength, compressibility and permeability properties, cohesionless soils are widely used for the installation of road structures [14]. Shear strength parameters are very important for the design of a safe and economical road structure. It was observed that the shear strength parameters are affected by the relative density, gradation, particle strength, size, shape, and degree of saturation of the specimen

M. Zakarka (✉) · Š. Skuodis

Department of Reinforced Concrete Structures and Geotechnics, Vilnius Gediminas Technical University, Saulėtekio al. 11, LT-0223 Vilnius, Lithuania
e-mail: mindaugas.zakarka@vilniustech.lt

[19, 20]. Particle size has been identified as an important factor in shear strength, and its effects have been studied for the last few decades [2, 14, 15].

The angle of internal friction is specifically emphasized as the most important parameter of sandy soils. The shear strength can be determined using Mohr's circle failure criterion [4]. A soil's angle of internal friction describes the shear resistance of a soil with presence of normal effective stress at which shear failure occurs [13]. Different methods were used to determine the relation of particles size with angle of internal friction: direct shear test [1, 7], triaxial test [8], 2D and 3D discrete element method analysis [6]. Sufficiently contradictory conclusions were obtained. At low sandy soil densities, the angle of internal friction decreases with increasing effective diameter (d_{10}) [5]. Sandy soils have a direct relationship between the angle of friction and the coefficient of uniformity [14]. The grain size distribution can greatly affect shear strength characteristics in sandy soils [17]. Although the investigations concluded that there is a relationship between size of the particles and angle of internal friction, the further investigations are needed.

Consolidated drained triaxial compression tests were applied to restore horizontal stresses for the soil specimens, imitating embankment behavior affected with traffic load. This research is oriented to road constructions, therefore three different confining pressures of 20, 50 and 70 kPa were applied [21]. For this study, three sand and three gravel types were analysed, differing from each other in terms of both the mean grain size and uniformity. The objective of this study is to assess granular materials relationship between the size of particle and the angle of internal friction.

2 Sample Preparation and Testing

For this investigation, three different types of sandy and gravelly soils were selected from different locations in Lithuania. A detailed laboratory investigation was carried out to determine the physical properties of the soil samples. Determination of particles size distribution was conducted according to LST EN ISO 17892-4:2017, Proctor compaction was conducted according to LST EN 13,286-2:2015. The physical properties of the soils are presented in Table 1, particle size distribution is presented in Fig. 1. Samples symbols given in Table 1 correspond LST 1331:2015.

Soil specimens for triaxial test apparatus were remolded with water content determined by standard Proctor compaction test. To each different soil, three sets of cylinder samples were prepared, the diameter of which 10.0 cm, height—20.0 cm. The tests were chosen to run under unsaturated conditions. Samples were prepared at Proctor water content without additional saturation. Three different cell pressures were used for consolidation: 20, 50, 70 kPa. The water can drain during the test. All of these conditions were selected according to LST EN ISO 17892-9:2017. All samples were consolidated for 30 min. The vertical strain velocity 0.950 %/min was accepted, based on consolidation time according to LST EN ISO 17892-9:2017. The tests were conducted by deforming the specimen until 15% of the vertical deformation. This research is oriented to road constructions, therefore the experiments used

Table 1 Physical properties of the soils

Sample no.	Sample symbol	Soil type	Water content determined by standard proctor compaction test $w, \%$	Density of specimen determined by standard proctor compaction test $\rho, \text{g/cm}^3$
1	GrP	Poorly graded gravel	3.0	1.90
2	GrP	Poorly graded gravel	3.5	1.83
3	GrM	Medium graded gravel	7.5	2.08
4	SaP	Poorly graded sand	14.3	1.65
5	SaP	Poorly graded sand	8.0	1.75
6	SaM	Medium graded sand	8.8	1.98

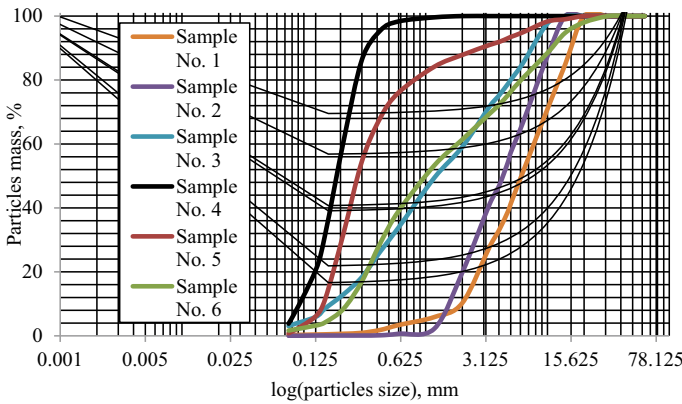


Fig. 1 Particle size distribution curves

the following cell pressures: $\sigma_3 = 20, 50, 70 \text{ kPa}$. The Mohr–Coulomb criterion $\tau = \sigma' \tan\phi' + c'$ was applied for results interpretation [3].

3 Results

Triaxial compression test results of different soil samples are presented in Table 2. The samples failure shape presented in Fig. 2. For samples Nos. 1–2, it is impossible to take photographs after the test without a membrane because the soils are too sensitive and collapse immediately. To make the results comparable, gravels (Nos. 1–3) and sands (Nos. 4–6) were separated.

As observed from test results, sands angle of internal friction ranges from 41.92° to 43.93° . The angle of internal friction of the sandy soil increases as the coefficient of uniformity of the samples decreases (Fig. 3). The same dependency was obtained

Table 2 Physical and mechanical properties of the soils

Sample no.	Sample symbol	d_{10}	d_{30}	d_{50}	d_{60}	C_U	C_C	φ'_o	c' , kPa
1	GrP	1.95	3.62	6.13	7.94	4.08	0.85	44.95	10.7
2	GrP	1.54	2.64	4.31	5.37	3.48	0.84	43.16	3.1
3	GrM	0.17	0.51	1.23	2.10	12.35	0.73	42.35	14.5
4	SaP	0.09	0.15	0.19	0.21	2.25	1.08	43.93	0
5	SaP	0.14	0.21	0.28	0.35	2.45	0.85	43.88	0
6	SaM	0.23	0.44	1.05	1.86	8.17	0.46	41.92	0

**Fig. 2** The shape of failure from the left: sample No. 1; sample No. 2; sample No. 3; sample No. 4; sample No. 5; sample No. 6

with the average particles size d_{50} , which is the opposite of what is found in the literature [16, 18].

Gravels' angle of internal friction varies from 42.35° to 44.95° . Figure 4 shows that angle of internal friction increased with the increasing average size of the particles d_{50} .

Fig. 3 The relationship between the coefficient of uniformity and the angle of internal friction for sands

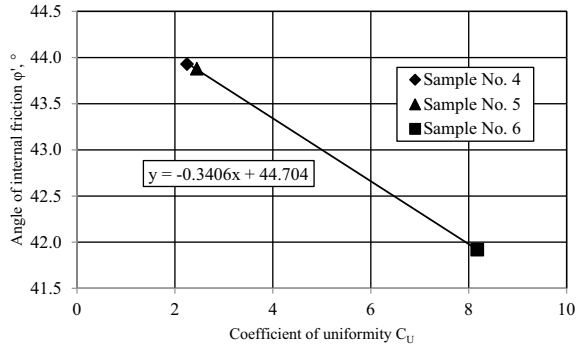
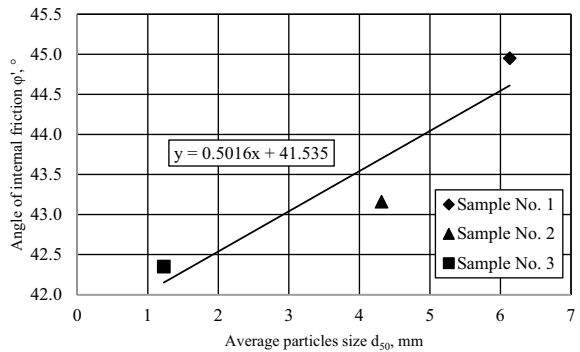


Fig. 4 The relationship between the average size of particles and the angle of internal friction for gravels



For investigated gravels there is no relationship between friction angle and coefficient of uniformity.

Correlation that can be established between coefficient of uniformity and angle of internal friction in sandy soils is graphically presented in Fig. 3. Another correlation established between average particle size d_{50} and angle of internal friction in gravelly soils is graphically presented in Fig. 4.

4 Conclusion

Since all the specimens were tested under the same experimental conditions (optimal water content, cell pressure, etc.), grain size distribution was the only physical parameter varying from one test to another. After the tests and analysis of tests results such conclusions can be made:

1. Increasing the coefficient of uniformity in sandy soil decreases the angle of internal friction;
2. Increasing the average particles size d_{50} in gravelly soil increases the angle of internal friction;

3. There is no direct relationship between the size of particles d_{50} and the angle of internal friction in investigated sandy soils;
4. There is no direct relationship between the coefficient of uniformity and the angle of internal friction in investigated gravelly soils.

The relationship between the particle size distribution and the angle of internal friction for granular materials is still debatable.

References

1. Afrazi M, Yazdani M (2021) Determination of the effect of soil particle size distribution on the shear behavior of sand. *J Adv Eng Computation* 5(2):125–134
2. Deng Y, Yilmaz Y, Gokce A, Chang CS (2021) Influence of particle size on the drained shear behavior of a dense fluvial sand. *Acta Geotech* 16:2071–2088
3. Dirgėlienė N, Skuodis Š, Vasys E (2022) The behaviour of stress variation in sandy soil. *Open Geosci.* 14(1):13–23
4. Heyman J (1972) *Coulomb's memoir on statics*. Cambridge University Press, London
5. Islam M, Badhon FF, Abedin MZ (2017) Relation between effective particle size and angle of internal friction of cohesionless soil. In: *Proceedings of international conference on planning, architecture and civil engineering*
6. Islam M, Siddika A, Hossain B, Rahman AN, Asad MA (2011) Effect of particle size on the shear strength behavior of sands. *Australian Geomechanics.* 46(3):85–95
7. Kara EM, Meghachou M, Aboubekr N (2013) Contribution of particles size ranges to sand friction. *Eng, Technol & Appl Sci Res* 3(4):497–501
8. Kirkpatrick WM (1965) Effects of grain size and grading on the shearing behaviour of granular materials. In: *Proceedings of the sixth International conference on soil mechanics and foundation engineering*, vol 1. Canada, pp. 273–277
9. LST 1331:2015 (2015) *Gruntai skirti keliams ir jų statiniams. Klasifikacija*. Vilnius, Lietuvos standartizacijos departamentas
10. LST EN 13286-2:2015 (2015) *Unbound and hydraulically bound mixtures—Part 2: test methods for laboratory reference density and water content—Proctor compaction*. Vilnius, Lietuvos standartizacijos departamentas
11. LST EN ISO 17892-4:2017 (2017) *Geotechnical investigation and testing—Laboratory testing of soil—part 4: Determination of particle size distribution*. Vilnius, Lietuvos standartizacijos departamentas
12. LST EN ISO 17892-9:2017 (2017) *Geotechnical investigation and testing—Laboratory testing of soil—part 9: Consolidated triaxial compression tests on water saturated soils*. Vilnius, Lietuvos standartizacijos departamentas
13. Mitchell JK, Houston WN, Scott RF, Costes NC, Carrier WD, Bromwell LG (1972) Mechanical properties of lunar soil: Density, porosity, cohesion and angle of internal friction. In: *Proceedings of the lunar science conference*, pp. 3235–3253
14. Rasti A, Adarmanabadi HR, Pineda M, Reinikainen J (2021) Evaluating the effect of soil particle characterization on internal friction angle. *Am J Eng Appl Sci* 14(1):129–138
15. Sharma V, Kumar A, Priyadarshree A, Chhotu AK (2019) Prediction of shear strength parameter from the particle size distribution and relative density of granular soil. In: *Agnihotri A, Reddy K, Bansal A (eds) Environmental geotechnology. Lecture notes in civil engineering*, vol 31. Springer, Singapore
16. Vangla P, Latha GM (2015) Influence of particle size on the friction and interfacial shear strength of sands of similar morphology. *Int J Geosynth Ground Eng* 1(6)

17. Viggiani G, Küntz M, Desrues JJM (2001) An experimental investigation of the relationships between grain size distribution and shear banding in sand. In: Continuous and discontinuous modelling of cohesive-frictional materials. Lecture notes in physics, vol 568. Springer, Berlin, pp 111–127
18. Wang JJ, Zhang HP, Tang SC, Liang Y (2013) Effects of particle size distribution on shear strength of accumulation soil. *J Geotech Geoenvironmental Engi-Neering* 139(11):1994–1997
19. Whalley WB (1979) Discussion on ‘Effect of sand grain shape on interparticle friction’’. *Geotechnics* 29(3):341–350
20. Yu X, Ji S, Janoyan KD (2006) Direct shear testing of rockfill material in soil and rock behavior and modeling. Geotechnical Special Publication, American Society of Civil Engineers, pp 149–155
21. Zakarka M (2022) Analysis of the traffic load—induced stresses of embankment. *Mokslas—Lietuvos ateitis* 14: 1–7

Mechanical Strength Tests of Building Blocks of the Historical British Government Building in Famagusta, North Cyprus



Salih Saner and Hasan Okaygun

Abstract Damage assessments and strength tests of building blocks of the British Government Building in Famagusta have been carried out. A total of 40 core samples, three or four-inches in diameter, were drilled from different spots, and mechanical strength tests were performed applying standard laboratory procedures. The building in question is made of Pliocene–Pleistocene age calcarenite (granular limestone) blocks whose trade name is Saritas, which means yellow stone. As a result of a fire, ceilings and roofs of the building collapsed, steel beams bent, wooden beams and other wooden elements burned, interior plasters fell. The compressive strengths of overall core samples varied between 1.01 and 21.85 MPa. The mean value for the formation is 6.86 MPa. The porosity of the samples varies between 16.74 and 50.44%. Porosity versus compressive strength revealed an inverse correlation between the two parameters. Collected samples were grouped into three facies based on their petrographic analysis. These are 1. Fine-grained calcarenite, 2. Coarse-grained calcarenite, and 3. Vuggy calcarenite. Compressional strength dependency on lithology type has been studied and the coarser the rock texture the weaker the rock strength is concluded.

Keywords Building blocks · North Cyprus · Calcarenite · Compressive strength

1 Introduction

The British Government Building was constructed in 1937 by British colonial administration and was ruined by a fire in 1974 (Fig. 1a). Damage assessments and strength tests of building blocks were the objectives of this study. The site was visited several times for damage inspection and core sampling for laboratory testing.

S. Saner (✉)
Engineering Faculty, Near East University, Nicosia, North Cyprus
e-mail: salih.saner@neu.edu.tr

H. Okaygun
Engineering Labs, Middle East Technical University, Kalkanlı, North Cyprus
e-mail: hokaygun@metu.edu.tr

© The Author(s), under exclusive license to Springer Nature Switzerland AG 2023
C. Atalar and F. Çinicioğlu (eds.), *5th International Conference on New Developments in Soil Mechanics and Geotechnical Engineering*, Lecture Notes in Civil Engineering 305, https://doi.org/10.1007/978-3-031-20172-1_9

113



Fig. 1 Various views of the British Government building: **a** Present view; **b** Bended steel beams due to heat expansion; **c** Oblique cracks in the Northeastern corner extending along joints without cross-cutting the blocks; **d** All wooden beams, ceilings and flammable materials were burned, interior gypsum plasters were unwrapped; **e** Rectangular building blocks used for exteriors are in good conditions; **f** On the southern front of the building 5–10 cm deep carvings formed by alteration in the 75–80 cm interval above the ground

1.1 *Extent of Devastation*

The building has been left uncontrolled without any repair work since 1974. In the fire, the wooden floor sections and ceilings burned down, steel beams bended due to thermal expansion (Fig. 1b). All wooden beams, ceilings and flammable materials burned except beams in the main entrance of the building. The status of walls which built of stones and foundation were the concerns of this study in order to initiate a restoration work for the building.

The northeast round corner is the most severely damaged wall. Here oblique cracks are continuous from ceiling to floor (Fig. 1c). Three parallel cracks are extending along the joints without cross-cutting the blocks.

Gypsum plasters on the walls are fallen but stone walls are in good condition (Fig. 1d). In an earlier restoration of the building, the arched doors and window heads reshaped into an angular geometry were damaged as a result of burning of the supporting wooden beams under arch fillings. No damage is observed to the arches and walls at the main entrance.

1.2 Foundation and Bed Rock

Hand excavations in four locations around the building validated that the building is sitting on a consolidated bedrock. A tough shell called caliche has developed on the upper surface of this rock. Soil overlying the bedrock in the area is 30 to 50 cm in thickness. In a pit opened inside the building, soil is overlain by wood coals and ceiling debris at the top. The thickness of this bedrock in nearby outcrops is 20 to 40 m. In the building site no foundation or ground failure was observed.

1.3 Status of Building Blocks

The British Government Building is made of calcarenitic limestone of Pliocene–Pleistocene age. This rock is extensively found and was historically widely used in constructing walls surrounding old cities, castles, churches, mosques, bridges and houses. Geologically they are also called grainstone, whose structure consists of the sand-size calcite particles (CaCO_3) being attached with natural calcite cement. Most often, due to granular texture, mistakenly they are called sandstone. Here, major grains are skeletal particles or small shells of organisms called Foraminifera.

This limestone is geologically very young and has not been buried deeply. Hence, its porosity is high due to negligible compaction. Some samples are hard and durable whereas some others are friable. The strength of the rock depends on inter-grain cementation degree.

Because of its yellow color, it is known as Saritaş (yellow stone) in the market. Saritas is easy to cut and shape in rectangular blocks. The wall thickness of the British Government Building is about 50 cm. Rectangular blocks were used for exterior decorations whereas irregular stones were used for the interiors to increase the wall thickness to 50–60 cm. (Fig. 1e).

1.4 Atmospheric Decomposition

Some building-blocks on the exteriors of the building have undergone environmental decomposition. This alteration effect is only up to 75–80 cm height above the ground (Fig. 1f). It is also noted that the decomposition is effective on the southern face where an asphalt road is passing along the wall. Weathered surfaces of the stones crumbled and carved to form up to 5–10 cm deep cavities. Two important dynamics can most likely be assumed for these occurrences: 1. Reaction of carbonate rock with acidic water, and 2. Splash of water on the walls due to passing vehicles and winds. There is no severe alteration at upper levels of the walls and the walls which are not adjacent to an asphalt road.

2 Laboratory Methods

In this research work, drilling core samples from altered and unaltered different lithology types was targeted. A total of 40 horizontal cores in 3 and 4-inch diameter were drilled.

2.1 Sample Preparation

After delivery of samples to the laboratory, photographs were taken, geological descriptions and lithofacies definitions were conducted, and those suitable for testing were designated. The diameters, lengths, bulk volumes (V_b) and weights (W) of all specimens were routinely measured and recorded.

Since most samples are composed of pure calcite, their matrix volumes (V_m) and pore volumes (V_p) have been calculated assuming the matrix density (ρ_m) is 2.71 g/cm^3 . Pore volume (V_p) was determined using Eqs. (1) and (2).

$$V_m = W/\rho_m \quad (1)$$

$$V_p = V_b - V_m \quad (2)$$

The samples deemed suitable for the test were dried in a vacuum oven at 90°C for 48 h. Plug sizes and numbers are as follows:

- a. 3-in diameter 14 plug samples
- b. 4-in diameter 9 plug samples
- c. 1.5-in diameter 7 dry plug samples
- d. 1.5-in diameter 7 wet plug samples.

Tests were performed complying with to ASTM standards [2, 3]. Length/diameter ratio was considered accordingly.

2.2 Test Equipment

UTEST brand UTM-8300 Electronic Universal Material Tester was used for mechanical tests. The device is fully automated with a capacity of 300 kN adjustable loading speed, instant (real time) graphics display, and computerized control features.

By compressing cylindrical samples from two circular surfaces, strain was recorded until the failure point and the strength (σ) in MPa was calculated by dividing the force (F) in kN to the circular surface area (A) in m^2 , as seen in Eq. (3) [3, 4].

$$\sigma = (F/A)^{10-3} \quad (3)$$

3 Rock Typing

The building blocks of the British Government Building are highly porous carbonate grainstones and their physical properties vary depending on textural changes. In this study, the samples were grouped into three distinctive textural lithofacies (Fig. 2).

1. Coarse grained homogeneous calcarenite: Consists predominantly of 2–4 mm size Mollusc shell fragments and Foraminifera shells. This rock is commercially known as Saritas which means yellow stone. They are easily cut and shaped. Rectangular blocks are used in giving a decorative appearance at the exteriors of the building. Although this facies is typically light yellow in color, it also has brownish yellow and white colors with the same texture as well.
2. Fine-grained homogeneous calcarenite: This litho facies is formed of fine bioclast particles. Unlikely, fine grains are subjected to compaction that reduced porosity, increased bulk density, and thus increased rock strength.
3. Vuggy-sandy calcarenite: In this facies, Mollusc shells and Foraminifera grains are dominant, but it contains sand size quartz and rock fragments in changing ratios. Rarely sand ratio increases over 50%. Due to bioturbation, primary depositional structures and texture have completely disappeared leaving behind a heterogeneous texture. Over the time, moldic or vug-type cavities (pores) were developed by dissolution of some particles with groundwater.

Compressive-strength versus porosity plots and linear trendline parameters of sample groups are seen in Fig. 3. Because of limited number of samples Correlation coefficients are low, but distinctive clustering is seen for the each sample group.

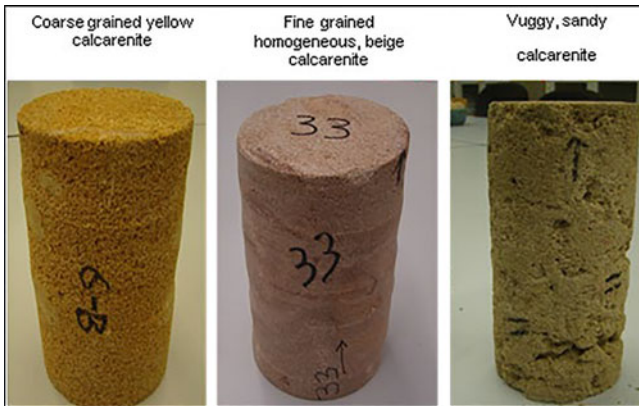
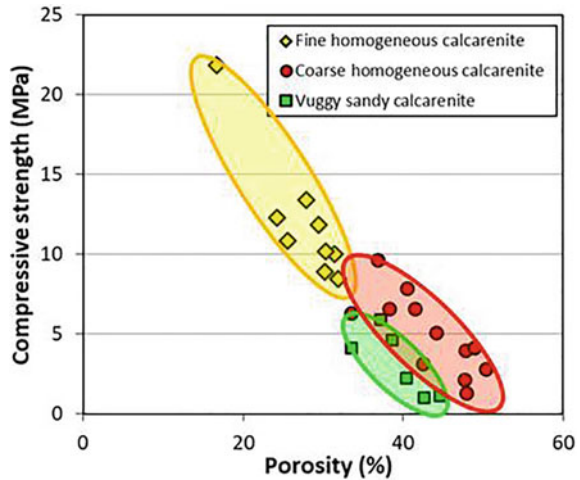


Fig. 2 Typical examples of three differentiated litho-facies groups

Fig. 3 Compressive strength versus porosity distributions for the three lithofacies



4 Test Results

According to ASTM standards [2, 3] it is recommended that the length to diameter ratio of cylindrical samples to be 2. If this ratio is lower than 2, it is recommended to correct the value found by multiplying it by a coefficient corresponding to the length-diameter ratio.

The tested samples are notable for their high porosity. Calculations showed that the porosity ranged from 16.74 to 50.44% and the average was 37.07% (Table 1). The compressive strengths of the tested overall samples ranged from 1.01 to 21.85 MPa. The mean value is 6.86 MPa. It is observed that the compressive strength values (σ) are directly proportional to the bulk density. However, there is an inverse linear correlation with the porosity (ϕ) as shown in Fig. 3. Using parameters for overall samples, if porosity approaches zero compressive strength could be 24.9 MPa. However, 1.5% porosity means no strength or almost disintegrated sample.

The highest compressive strength was 21.85 MPa which was measured against 16.74% porosity. All other measurements were below 14 MPa. Compressive strength is related not only to porosity percentage, but pore geometry, rock texture and composition as well. In Fig. 3 fine-grained calcarenite and the coarse-grained calcarenite

Table 1 Porosity and compressive strength averages of the three defined lithofacies groups

	Porosity (%)				Compressive strength (MPa)			
	Fine calcarenite	Coarse calcarenite	Vuggy calcarenite	Overall	Fine calcarenite	Coarse calcarenite	Vuggy calcarenite	Overall
AVG	27,53	43,41	37,50	37,07	11,98	4,98	4,15	6,86
MAX	31,89	50,44	44,67	50,44	21,85	9,60	7,30	21,85
MIN	16,74	33,55	29,46	16,74	8,43	1,30	1,01	1,01

porosities are within the same porosity range, but compressive strengths of the two groups are different due to the pore geometries. The mean, maximum and minimum values for the three facies groups are presented in Table 1.

Compressive Strength Results of Fine Grained Calcarenite Samples. This rock type has experienced more compaction than other groups. The average porosity is 27.53% and ranges from 16.74% minimum to 31.89% maximum. On the other hand, the compressive strength ranged from 8.43 to 21.85 MPa, averaging 11.98 MPa.

Photographs of cores are recorded before and after each mechanical test. After test, longitudinal tensional cracks appeared in the cores (Fig. 4). Diagonal shear fractures occurred in two cores and in some cores small edge-fractures under the circular upper surface have been observed. In some samples, longitudinal but radial fractures are interpreted as an indicator of partial barreling type plastic deformation [6].

Compressive Strength Results of Coarse-Grained Calcarenite Samples. These coarse-textured rocks have a spongy appearance with visible porosity. Porosity is between 33.55 and 50.44% and the average is 43.41%. Pressure strength tests ranged between 1.30 and 9.6 MPa with an average value of 4.98 MPa.

In some cores, deformation types at the termination of test could not be observed because deformation was completed with the collapse of some thin-walled shell cavities. Characteristically, there were edge fractures occurred where grain disintegrations were observed.

Compressive Strength Results of Vuggy Samples. The Compressive strength of samples from this facies is low like in the previous coarse-grained facies. Pores are usually inter-granular, but some pores form cavities up to 2–3 cm in diameter causing weakness zones in the rock.

Fig. 4 Various fracture geometries observed after compressive strength tests



Despite the oversized pores, the porosity is slightly lower than the coarse calcarenite facies. An average of 37.50% was achieved at a range of 29.46–44.67%. The measured compressive strength distribution trend is very parallel to that of coarse calcarenite facies in a lower position in Fig. 3. Compressive strength for vuggy facies ranges from 1.01 to 7.30 MPa. The average is 4.15 MPa.

Vertical and diagonal fracturings are commonly recorded. During the compression test of some samples, transversal fractures were developed due to the collapse of large-diameter vugs and as a result, edge fractures and disintegration occurred.

5 Conclusions

In order to interpret the compressive strength of the building, a calculation based on the overall average strength of the building stones can be misleading. It would be more realistic to take into the account three rock groups that have been defined. The load of the building consists of the weight of the building stones, weight of ceiling plates and the live load during usage. The average bulk density of building stones is 1.695 g/cm³ and the unit weight of the wall is 1.700 ton/m³. If the wall height is assumed to be 15 m, a load of 25.5 tons/m² will be applied on the foundation. If the roof load and live load are added to this a load of 50 tons/m² can be estimated. The compressive strength of the stones that will meet this load should be 0.5 MPa. However, the compressive strength values presented in Table 1 are 4.15 MPa even for the weakest vuggy calcarenite. Hence no strength problem is expected.

A disregarded issue is the damage that might occur due to beams sitting directly on some stones without base plates. Tensional fractures can occur if the beam load exceeds the tensional strength of the stone. Tensile Strength tests are recommended.

Acknowledgements Authors are grateful for engineering point of views given by Ass. Prof. Dr. Ceren İnce. Appreciations are extended to Mr. Abdullah Önal for his contributions in sample handling and laboratory experiments.

References

1. API Recommended Practice 40: Second Edition, 1220 L Street, N.W., Washington, D.C. (1998)
2. ASTM C1583-04 (2004) Standard test method for tensile strength of concrete surfaces and the bond strength or tensile strength of concrete repair and overlay materials by direct tension (Pull-Off Method). ASTM International, West Conshohocken, 100 Barr Harbor Drive, PO Box C700, Pennsylvania
3. TerraTek (1990) Basic applied rock mechanics. University Research Park, Utah
4. Yuming S, Guowei L (2000) Experimental study on dynamic and static parameters of rocks under formation conditions. *J Chengdu Coll Geol Technol* 27(3):249–255
6. Griggs DT, Handin J (1960) Observations on fracture and a hypothesis of earthquakes. *Geol Soc Am Mem* 79:347–364

Using Compression and Swelling Indices to Characterize Expansive Soils



Sergio Andrew Manigniavy, Yosra Bouassida, Dalel Azaiez,
and Mounir Bouassida

Abstract Expansive soils are a worldwide problem. The volume variation of this soil is depended on its moisture content. A new approach to characterize this kind of soil is based on the oedometer test results, performed on compressible soils, either expansive or non-expansive. The C_c/C_s ratio is determined, where C_c is the compression index and C_s is the swelling index. Zones delimited by a C_c/C_s value and a swelling pressure (σ_s) value are identified to differentiate expansive soils from non-expansive soils. When C_c/C_s ratio is higher or equal to 15, the swelling pressure is practically equal to zero.

Keywords Expansive soils · Characterization · Oedometer test · Compression index · Swelling index

1 Introduction

Expansive soils are globally widespread geological and natural hazard. This type of soil is currently found in arid or semi-arid areas. It can cause several damages to constructions. Clays, in particular the montmorillonite, are belong to the expansive soils. The shrink-swell behavior of this latter develops according to the variation of water content. Therefore, the expansive soils topic is of high interest for the six continents: Africa, Asia, Europe, Oceania, North and South America.

To understand the behavior of this category of soils, researchers are looking to suitable approaches to characterize it and to mitigate the swelling phenomenon.

The change in volume of expansive soils depends on the water content. The clay structure and the saturation of soils take a major place in this phenomenon. The liaison between montmorillonite clay particles is weak. During the swelling process, the water molecules and other cations carried by the water force the passage between

S. A. Manigniavy (✉) · Y. Bouassida · D. Azaiez · M. Bouassida
Ecole Nationale d'Ingénieurs de Tunis, Laboratoire d'Ingénierie Géotechnique et de Géorisque,
Université de Tunis El Manar, LR14ES03, Tunis, Tunisia
e-mail: sergioandrew.manigniavy@etudiant-enit.utm.tn

clay particles by pushing them apart. This leads to an increase in swelling pressure [6].

Several buildings are constructed on swelling clays and represent damages that are due to the swelling phenomenon in the North of Africa, in particular in Tunisia and Algeria. Therefore, a research program to characterize expansive soils suitably and to formulate countermeasures and construction methods is needed to help civil engineers in the safe design and construction of foundations on the swelling soils [1].

2 About Expansive Soils

The shrink-swell behavior of clays is an extremely destructive phenomenon and leads to huge repair costs. Therefore, it is crucial to find methods to characterize expansive soils.

First, expansive soils are one of the most hazardous natural disaster [2]. Slope instability, tunnel collapse, differential heavy and buckling of building, fissures on structures and destruction of hydraulic structures can result from the presence of swelling soils [6].

Second, around the world, a lot of money is wasted due to extensive damage to buildings caused by the effect of swelling phenomenon every year. In many countries, financial assessment of the extra-costs, like repairing and maintenance, due to swelling soil problems has not yet been carried out. In Sudan, the cost of damage to buildings and light structures due to swelling soils is estimated more than 6 million dollars [14]. Many countries are affected by the damage of this problematic soil: in United States, losses due to expansive soils are about 13 billion dollars in damage to buildings, roads, airports and other infrastructures each year [15]. In United Kingdom and Saudi Arabia, this cost varies in the range of 300 to 450 million dollars [5, 16].

Third, to deal with this type of soil, there are some improvements proposed, like the use of granular materials, chemical and soil mixture treatments. The granular piles technique is a practical and promising technique. Their installation is possible at any season. The reduction in swelling provided by the use of a granular piles varied from 10 to 45% [10]. The use of a granular material as a separation layer between the foundation and an expansive soil revealed a potential solution to reduce the swelling effect [1]. In addition, noted also that chemical treatments revealed of interest as well. According to Mahamedi and Khemissa [12], mixture of swelling clay with respectively cement and lime in an amount of 10% reduces the swelling potential and decreases liquid limit by 41 and 43% respectively. Soil sensitivity to water has been reduced by the lime treatment. This is due to decrease of moisture content after lime hydration [11]. As cement contains about 60% lime, mixing with cement gives approximately the same result as mixing with lime. Moreover, according to Gueddouda et al. [7], about the soil mixture, the addition of dune sand leads to an important reduction of the swelling parameters. With 45% sand, for the swelling potential, this reduction is about 65% and for the swelling pressure exceeds 85%.

This addition is involved in the increase of the pore size in the swelling soil mass that is owed to the reduction of these expansion effects. The evolution of suction is proportional to that of shear strength. Further, Tiwari et al. [18] recommended the use of coir geotextile which reduces the swelling pressure by about 27% and also reduces the speed of swelling. It is noted that, approximately, the same results are found with a silica fume treated coir geotextile. A reduction of 55% for the swelling pressure and 79% for the percentage of expansion are observed when using a coir geotextile treated with lime. Finally, according to Kalantari [9], the three most commonly used techniques are the soil substitution, use of enough strong structures and the separation between the structure and the swelling clay.

3 Characterization Methods

Due to damages caused by expansive soils, several researchers made an effort to develop approaches to characterize this type of soil in order to know it better and to prevent the problems it can cause. Sridharan and Prakash [17] proposed two kinds of characterization methods:

- by identifying the soil mineralogy using X-ray diffraction analysis, differential thermal analysis, dye adsorption, chemical analysis and scanning electron microscopy;
- by inferential testing using indirect or direct methods.

There are some indirect methods: clay fraction method, Atterberg limits tests and activity A_c method. Some classifications are referred to direct methods like the oedometer swell test, free swell tests and suction method.

4 Approach to Characterize Expansive Soils from Oedometer Test Results

Compression index (C_c) and swelling index (C_s) are currently determined from oedometer tests, which performed with submerged specimens to ensure a full saturation during the experiments. By an oedometer test, both indices C_c and C_s , can be measured for any compressible soil, either expansive or non-expansive.

The data used for this study are oedometer test results provided by specialized geotechnical engineering offices or published by researchers in technical papers. The method to characterize expansive soils using the C_c/C_s ratio relied on data collected from four case studies, comprising twenty-nine specimens from Tunisia, Algeria, Canada and United States. These data are presented in Table 1. The C_c/C_s ratio is an indicator of the change in volume quantifying the degree of soil compression versus swelling [1]. This volume variation is linked the swelling pressure (σ_s).

Table 1 Oedometer test results (update of Bouassida et al. [1])

Country	Site	Sample	Cc	Cs	Cc/Cs	σ_s (kPa)	Expansive	Non-expansive
Tunisia	Béja	BH1	0.160	0.024	6.667	110	x	
		BH2	0.140	0.026	5.385	230	x	
		BH3	0.150	0.018	8.333	90	x	
		BH4	0.180	0.037	4.865	120	x	
		BH5	0.160	0.035	4.571	140	x	
		BH6	0.140	0.010	14.000	40		x
		BH7	0.150	0.012	12.500	40		x
		BH8	0.130	0.019	6.842	140	x	
		BH9	0.220	0.030	7.333	130	x	
		BH10	0.180	0.039	4.615	80	x	
		G109-BH1-2	0.226	0.086	2.628	204	x	
		G109-BH1-3	0.176	0.035	5.029	108	x	
		Centre Urbain du Nord—Tunis	0.158	0.012	13.167	0		x
		BH1-US1-1	0.123	0.009	13.667	0		x
		BH1-US1-2	0.129	0.008	16.125	0		x
		BH2-US2-1	0.097	0.022	4.409	90	x	
		BH1-US11	0.040	0.004	10.000	95	x	
		BH1-US12	0.124	0.021	5.905	220	x	
		BH1-US13	0.114	0.027	4.222	185	x	
		BH2-US21	0.173	0.009	19.222	0		x
		BH3-US31	0.055	0.003	18.333	0		x

(continued)

Table 1 (continued)

Country	Site	Sample	Cc	Cs	Cc/Cs	σ_s (kPa)	Expansive	Non-expansive
		BH3-US33	0.156	0.040	3.900	275	x	
	Jardin El Menzah 1—Tunis	BH1-US1	0.140	0.017	8.235	160	x	
		BH1-US2	0.140	0.025	5.600	190	x	
		BH2-US2	0.140	0.017	8.235	150	x	
		BH3-US2	0.140	0.011	12.727	20		x
		BH4-US1	0.190	0.041	4.634	70	x	
		BH4-US3	0.200	0.061	3.279	180	x	
Algeria	Médéa ^a	S-1-1	0.140	0.045	3.111	400	x	
		S-4-1	0.400	0.100	4.000	70	x	
		S-4-3	0.350	0.140	2.500	80	x	
		S-10-1	0.150	0.100	1.500	420	x	
		S-10-2	0.080	0.070	1.143	800	x	
USA	Louisiana	–	0.360	0.110	3.273	170	x	
Canada	Lake Agassiz	B	0.73	0.23	3.174	54	x	
	Northern Alberta	C	0.12	0.07	1.714	429	x	
	Regina ^a	D	0.17	0.05	3.400	965	x	
		E-1	0.1	0.04	2.500	547	x	
		E-2	0.08	0.04	2.000	526	x	

^a Updated; BH: borehole; US: undisturbed sample; S: sample

The variation of swelling pressure with respect to the C_c/C_s ratio from the data, given by Table 1, is shown in Fig. 1. From this figure, non-expansive soils are in the side where C_c/C_s ratio is above 10 and the swelling pressure is under 50 kPa. The swelling pressure of expansive soils belong to the side where C_c/C_s ratio is under 10, is higher than 50 kPa. This approach is approved by Chen [3] and Coduto [4] who affirmed that when the swelling pressure is under 50 kPa, the swell potential is low, hence insignificant. Furthermore, when C_c/C_s ratio is higher than 15, the swelling pressure is practically equal to zero. A classification between expansive and non-expansive soils is shown in Table 2. If the compression index (C_c) is about 10 times larger than the swelling index (C_s), then the swelling potential of this soil is low. For Tunisian non-expansive soils, the swelling index is around or lower than 0.010. So, this value represents the low degree of soil to swell in North Tunisia. Note that all non-expansive Tunisian soils in Table 1 or in Fig. 1 are sandy or silty clays which may approve that the mixture of sand or silt with a swelling clay can reduce the soil swelling potential.

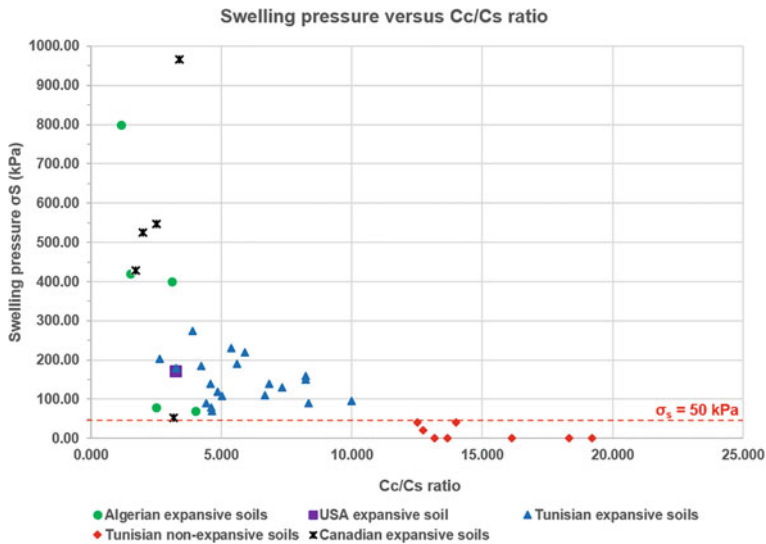


Fig. 1 Swelling pressure versus C_c/C_s ratio (updated from Bouassida et al. [1])

Table 2 Classification of expansive soils using oedometer test results [1]

Type of soil	C_c/C_s	σ_s (kPa)
Expansive	<10	>50
Non-expansive	>10	<50

5 Conclusion

The objective of this work is to characterize expansive soils using oedometer test results. This method is related to compression and swelling indices and carried out with thirty-nine (39) data from two continents, North America and Africa. The soil is considered to be non-expansive when the swelling pressure is under 50 kPa. If the C_c/C_s ratio is less than 10, Civil engineer should not underestimate the swelling pressure of the soil and should take it into their calculations. And, they should not forget the shrink—swell behavior of the soil.

The perspective of this work is to collect a lot of oedometer test results to have more precision in this characterization method and also to estimate the swelling pressure of a soil from these data.

References

1. Bouassida M, Manigniauy SA, Azaiez D, Bouassida Y (2022) New approach for characterization and mitigation of the swelling phenomenon. *Front Built Environ* 8:836277. <https://doi.org/10.3389/fbuil.2022.836277>
2. Chen FH (1975) *Foundations on expansive soils*. Elsevier Scientific Publishing Company Inc., New York
3. Chen FH (1988) *Foundations on expansive soils*. Elsevier Publisher B.V.
4. Coduto DP (2001) *Foundation design: principles and practices*, 2nd edn. Prentice Hall, New Jersey
5. Driscoll R, Crilly M (2000) *Subsidence damage to domestic buildings. Lessons learned and questions asked*, Building Research Establishment, London, UK
6. Elarabi H (2010) Damage mechanism of expansive soils. In: *Proceeding of the 2nd international conference on geotechnical engineering ICGE'10*. Hammamet, Tunisia, pp 125–131
7. Gueddouda MK, Goual I, Lamara M, Goual S (2013) Amélioration des propriétés physico-mécaniques des argiles gonflantes stabilisées par ajout de sable de dune. 3ème Conférence Maghrébine en Ingénierie Géotechnique CMIG'13, Alger, Algeria, pp 221–226
8. Hardy RM (1965) Identification and performance of swelling soil types. *Can Geotech J* 11(2):141–153. Printed in Canada
9. Kalantari B (2012) Foundation on expansive soils: a review. *Res J Appl Sci Eng Technol* 4(18):3231–3237
10. Kay JN (1990) Use of liquid limit for characterisation of expansive soil sites. CE32 No. 3
11. Kechouane Z, Nechnech A (2015) Characterization of an expansive clay treated with lime: effect of compaction on the swelling pressure. In: *The 4th international congress in advances in applied physics and materials science (APMAS 2014)* AIP conference proceedings 1653, 020057-1-020057-8. <https://doi.org/10.1063/1.4914248>
12. Mahamedi A, Khemissa M (2013) Cement and lime stabilization of compacted expansive clay. In: *Proceedings of the 3rd international conference on geotechnical engineering ICGE'13*, Hammamet, Tunisia, pp 369–377
13. Medjnoun A, Bahar R (2016) Shrinking–swelling of clay under the effect of hydric cycles. *Innov Infrastruct Solut* 1(1). <https://doi.org/10.1007/s41062-016-0043-6>
14. Osman MA, Charlie WA (1983) *Expansive soil in Sudan*. BBRI current papers. No. CP/3/83. Building and Road Research Institute. University of Khartoum, Sudan
15. Puppala AJ, Cerato A (2009) Heave distress problems in chemically-treated sulfate-laden materials. *Geo-Strata* 10(2):28–30, 32

16. Ruwaih IA (1987) Experiences with expansive soils in Saudi Arabia. In: Proceeding of 6th international conference on “Expansive soils,” central board of irrigation and power, New Delhi, India, pp 317–322
17. Sridharan A, Prakash K (2016) Expansive soil characterization: an appraisal. *INAE Letters* 1(1):29–33. <https://doi.org/10.1007/s41403-016-0001-9>
18. Tiwari N, Saytam N, Patva J (2019) Experimental study on the swelling behavior of expansive soil reinforced with coir geotextile. In: Proceedings of the Indian geotechnical conference 2019: IGC–2019, vol 4. India. https://doi.org/10.1007/978-981-33-6564_11
19. Wang JX (2016) Expansive soils and practice in foundation engineering. In: Louisiana transportation conference. Baton Rouge



Dr. Mounir Bouassida is a professor of civil engineering at the National Engineering School of Tunis (ENIT) of the University of Tunis El Manar where he earned his B.S., M.S., Ph.D., and doctorate of sciences diplomas, all in civil engineering. He co-supervised 23 Ph.D. and 32 Masters of Science graduates. His research focused on soil improvement techniques and the behavior of soft clays. Dr. Bouassida is the (co)author of more than 100 papers in refereed international journals; 180 conference papers including 27 keynote lectures and several book chapters. Further he co-authored three books and three patents as well as book series conferences.

He is Associate Editor of *Innovative Infrastructure Innovative Solutions and Ground Improvement (ICE)* journals, *Geotechnical-Geological journal*, *International Journal of Geosynthetics and Ground Engineering* and the GE section of the *Frontiers and Built Environment journal*.

As a 2006 Fulbright scholar, Dr Bouassida elaborated a novel methodology for the design of foundations on reinforced soil by columns. He is a co-developer of the software *Columns 1.01* used for the design of column-reinforced foundations. He was awarded the 2006 S. Prakash Prize for Excellence in the practice of geotechnical engineering.

In 2008, Dr Bouassida launched a Tunisian consulting office in geotechnical engineering, *SIMPRO*. As such, he contributed for the design of more than hundred projects.

Prof. Bouassida held the office of the vice president of *ISSMGE* for Africa (2005–2009) and then and appointed member of the *ISSMGE* board (2017–2022). He benefited from grants as a visiting-invited professor in several institutions in the USA, Canada, Europe, Australia and Asia. In 2018, he became a Director of the *International Press-In Association*.

Since 2019, the launch of the You Tube channel « Mounir Bouassida » gained lot of interest from than 1430 subscribers. Fifty nine uploaded videos, in English and French, to this channel cover themes focusing on soil mechanics, modelling and the study of the behavior of geotechnical engineering structures.

Probabilistic Interpretation of CPTu-DMT Data for Soil Profiling



Stefano Collico, Marcos Arroyo, and Amadeu Deu

Abstract Cone Penetration Test (CPTu) and flat Dilatometer Test (DMT) are widely employed in-situ tests for ground unit profiling in terms of Soil Behavior Type Index I_C and Material Index I_D . CPTu provides a nearly continuous data profile with respect to DMT, making it more appealing for soil unit identification, leaving DMT data for qualitative comparison. This work proposes a first attempt of integrating CPTu-DMT data within soil profiling task, aiming to probabilistic assess congruence and discrepancy between the two sets of data. A semi-automated CPTu-DMT bivariate data interpretation tool is here presented aiming to facilitate communication of layer delimitation while eliciting the heuristics that designers apply in this process. Conventional classification class boundaries –here taken from (Robertson, 2009) and Marchetti, (2001) chart– are applied with user-specified refinements. The proposed algorithm is applied to CPTu and DMT sounding records performed at Barcelona harbor (Spain).

Keywords Probabilistic soil profiling · Semi-automated tool · CPTu-DMT · Soil behavior type index · Material index I_D

1 Introduction

Cone Penetration tests (CPTu) and Dilatometer Tests (DMT) have become methods of choice for soil delineation. The cone penetration test can be conceived as a model of a pile mainly providing accurate predictions of the vertical capacity of a pile [1] lateral resistance (i.e., sleeve friction) and pore pressure due cone probe insertion are

S. Collico (✉) · M. Arroyo
Universitat Politècnica de Catalunya, BCN, Barcelona 08034, Spain
e-mail: stefano.collico@upc.edu

M. Arroyo
e-mail: marcos.arroyo@upc.edu

A. Deu
Geoscience and Maritime Exploration, Barcelona, Spain
e-mail: amadeu@gemigeo.com

also measured, making such tool a three-independent parameter test. The flat-plat dilatometer test (DMT) is recognized as a deformation test [2] allowing to predict accurate estimate of settlement [3, 4], and horizontal capacity of a pile. DMT is recognized as two-parameters test both related to soil characteristics as stiffness and stress history.

Each test has its own advantages [2, 5] and both tests do not allow to recover soil samples and use measured test responses to classify soils. This is most frequently done using Soil Behaviour Type, SBT charts where empirically pre-established boundaries separate different soil types [2, 6]. When both tests are performed at the same location, it is a common practice to compute soil profiling from each in-situ test independently. The CPTu-based profile is usually taken by practitioners as a final soil profiling leaving DMT-based one for qualitative comparison.

However, in the last decades, different works exploit and highlight the effectiveness of multi-test and multivariate analysis for site characterization [7]. Following the same line of thinking, a bivariate approach is here applied to derive in-situ tests-based soil profiling, exploiting the joint dependence of Soil Behaviour Type Index I_C , (CPTu) and Material Index I_D (DMT) parameters. Previous works on the topic using only CPTu data were made [8, 9]. This study provides an extension of such works for CPT-DMT data application.

2 Methodology

As a first step, due to the different amount of recorded data during these two tests (CPTu each 2–5 cm, DTM each 20–50 cm), the assessment of CPTu-DMT dependence requires the reconstruction of DMT profile to obtain paired I_D and I_C data. Several approaches could be applied. The simplest one concern a polynomial interpolation of DMT measurements. For facilitate the illustration of the proposed methodology such approach is applied in this study (i.e., spline interpolation).

Concerning CPTu, one of the most popular SBT charts is the [7] one. Class boundaries are approximated by a concentric circle whose radius is quantified by the unified parameter I_C (Soil Behavior Class):

$$I_C = [(3.47 - \log(Q_{tn}))^2 + (\log(F_R) + 1.22)^2]^{0.5} \quad (1)$$

with:

$$Q_{tn} = [Q_t - \sigma_{v0})/p_a] (p_a/\sigma'_{v0})^n \quad (2)$$

$$n = 0.381I_C + 0.05] (\sigma'_{v0}/p_a) - 0.15 \quad (3)$$

where $n \leq 1$ is a soil-type dependent exponent which normalizes for the effect of stress level on resistance.

The DMT allows to compute soil profiling in terms material index I_D and dilatometer modulus E_D , [2], (Fig. 1b). I_D and E_D are computed from the two measured parameters p_0, p_1 as:

$$I_D = p_1 - p_0 / (p_0 - u_0) \tag{4}$$

$$E_D = 34.7(p_1 - p_0) \tag{5}$$

with p_0 = lift-off pressure, p_1 = pressure to move the center of the membrane of 1.1 mm and u_0 pre-insertion in-situ pore pressure.

The I_C and I_D -based chart can then be combined generating the chart reported in Fig. 1c (see [6]). Such chart distinguishes between Sand-Like (SL), (i.e., drained soil response), Clay-Like CL (i.e., undrained response) and Soil Mixture SM (partially drained soil response). The red areas of Fig. 1c are representative of same soil classes predicted by both CPTu and DMT (i.e., matched classes). The remaining soil types highlight the discrepancy between CPT and DMT soil classification (i.e., mismatched classes). It is worth noticing that the mud and/or Peats class is not considered since this would require to account for the parameter E_D . The chart is here considered

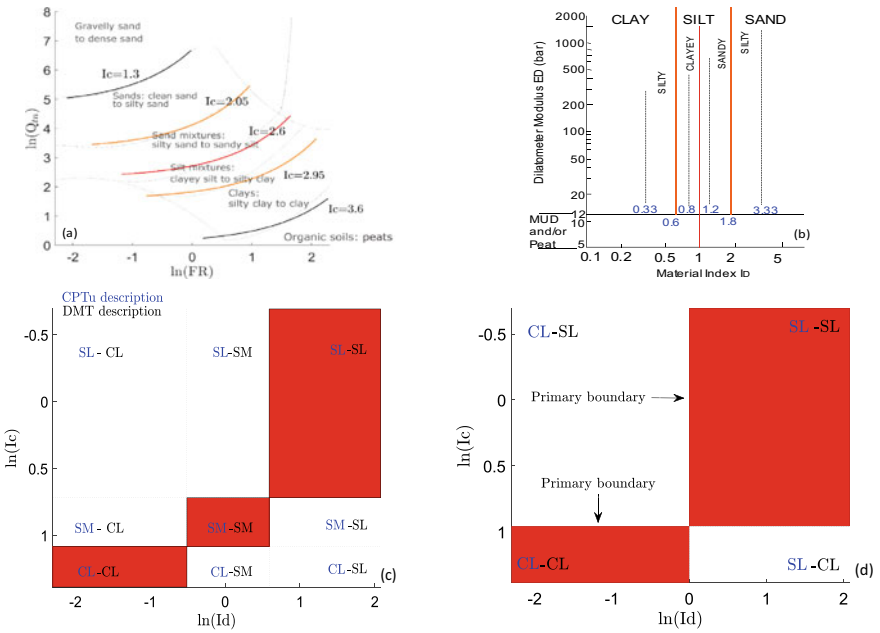


Fig. 1 a Soil Behavior Type chart based on Soil behavior Type Index I_C . b Soil Behavior Type chart based on Material Index I_D . c Combined I_C - I_D chart. d) Soil Behavior Type chart based on I_C and I_D , Level 1

in terms of natural logarithm, since the joint dependence of I_C , I_D is assumed to be lognormally distributed (Fig. 1c).

In some circumstances simpler classifications might appear more suitable to the analyst. This possibility has been enabled in this work introducing a staged classification procedure, in which SBT-based classifications of progressive refinement are introduced sequentially.

The coarser level uses a dual classification (Fig. 1d), distinguishing only between Clay-like behavior (CL) and Sand-like behavior (SL). These two soil classes, representative of undrained and drained response for CL and SL respectively, are identified by the I_C boundary value 2.6, and $I_D = 1$, (Fig. 1a, b). That boundaries are here onwards designed as a primary boundary. The second, more refined, level of classification is reported in Fig. 1c. The analyst might choose directly a particular classification level or might run sequentially through all levels.

When plotting CPTu-DMT observations classified by SBT, inherent variability and measurements errors, generate some data scatter (Fig. 2b). In this study a bivariate normal distribution is fitted to SBT data of a given stretch of CPTu-DMT (Fig. 2c):

$$f(\ln I_C, \ln I_D) = \frac{1}{2\pi\sigma_{\ln I_C}\sigma_{\ln I_D}\sqrt{1-\rho^2}} \exp\left(-\frac{1}{2(1-\rho^2)}\left[\frac{\ln I_C - \mu_{\ln I_C}}{\sigma_{\ln I_C}} + \frac{(\ln I_D - \mu_{\ln I_D})}{\sigma_{\ln I_D}} - \frac{2\rho(\ln I_C - \mu_{\ln I_C})(\ln I_D - \mu_{\ln I_D})}{\sigma_{\ln I_C}\sigma_{\ln I_D}}\right]^2\right) \quad (6)$$

with $\mu_{\ln I_C}$, $\mu_{\ln I_D}$, $\sigma_{\ln I_C}$, $\sigma_{\ln I_D}$ mean and standard deviation of $\ln(I_C)$ and $\ln(I_D)$ data sample respectively and $\rho =$ linear Pearson's correlation coefficient.

The interplay between this interval and SBT class boundaries is exploited to obtain a systematic procedure for layer identification.

Once the CPTu-DMT SBT values corresponding to a particular stretch are fitted to a bivariate normal distribution, the fitted data will be assigned to the soil class in which the bivariate mean is found. Two user-specified acceptance thresholds (i.e., model parameters) are used to divide the CPTu-DMT records into different stretches: Noise-threshold parameter, **P** and class-mixture tolerance parameter, **m**.

The **P** parameter (Fig. 2c) is introduced to account for extreme values of $I_C - I_D$ within the dataset. As an example, **P** = 0.25 contains 75% of the underlying data and 25% will be considered as noise. The class-mixture tolerance parameter **m** (Fig. 2d) explicit how strictly adhered to are pre-established class boundaries when the CPTu-DMT is subdivided into layers (see [8, 9]).

The CPTu cone is only able to unambiguously identify layers above a minimum layer resolution of 150–200 mm. A simplified practical approach to deal with this difficulty is to merge layers below the minimum thickness (here taken equal to 200 mm) with adjacent ones of similar soil behavior type [10]. This strategy is also adopted here, by merging thin layers based on the closeness on mean value of $I_C - I_D$ [9].

The output soil profiling will likely have layers assigned to mismatched classes, say SL-CL at Level 1 (i.e., SL from CPTu and CL from DMT) or CL-SL (i.e., CL from CPTu and SL from DMT). As a final step, to derive a soil profiling coherent with

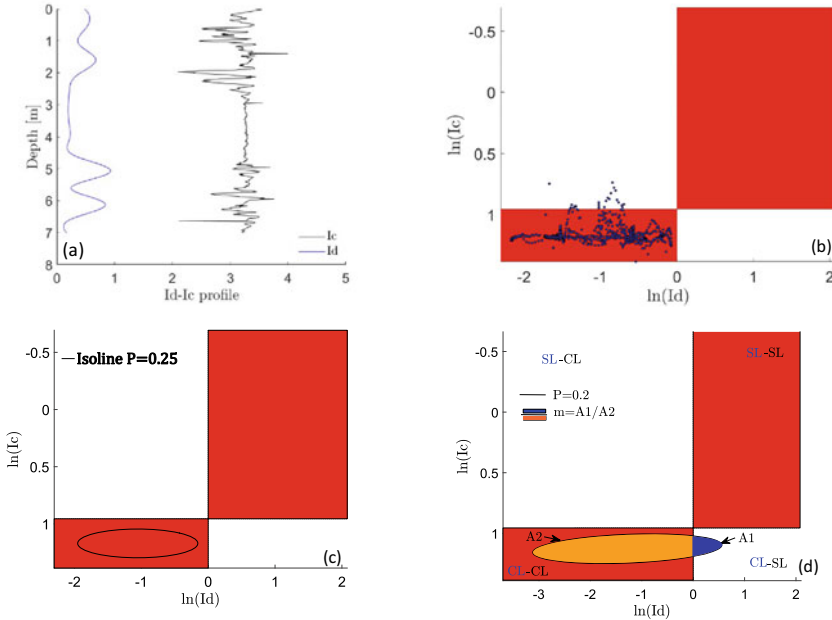


Fig. 2 a Synthetic I_C , I_D records. b data scatter on $I_C - I_D$ chart at Level 1. c Corresponding isoline 0.25 of fitted bivariate normal distribution. d Example of class assignment criterion for $m = 0.1$ and $P = 0.2$

analyst desire (i.e., each layer exclusively assigned to SL or CL class) a Bayesian perspective is introduced. Let consider a soil unit classified as SL-CL. The analyst might believe that CPTu assignment is more trustable due to the higher amount of data collected. To account for that, probabilities P (soil unit_{CPTu} = SL) and P (soil unit_{DMT} = CL) such that P (soil unit_{CPTu}) + P (soil unit_{DMT}) = 1 are introduced. This allows analyst to explicit their belief on CPT-based and DMT-based classification. The exclusively assignment is performed by computing the Bayes factor:

$$B = \frac{P(\text{soil unit}_{CPTu} | x_{Ic})}{P(\text{soil unit}_{DMT} | x_{ID})} \tag{7}$$

with P (soil unit_{CPTu} | x_{Ic}), P (soil unit_{DMT} | x_{ID}) = posterior probability of soil unit to be assigned as SL or CL given the $x_{Ic} = \ln(I_c)$ and $x_{ID} = \ln(I_d)$ data within the soil unit:

$$P(\text{soil unit}_{CPTu} | x_{IG}) = K \cdot P(x_{IG} | \text{soil unit}_{CPT}, \mu_{xIC}, \sigma_{xIC}) \cdot P(\text{soil unit}_{CPTu}) \cdot P(\mu_{xIC}) \cdot P(\sigma_{xIC}) \tag{8}$$

with K normalizing constant that does not depend on soil unit_{CPTu}, μ_{xIC} , σ_{xIC} , which normalize the posterior probability to one: $K = \int P(x_{Ic} | \text{soil unit}_{CPTu}, \mu_{xIC}, \sigma_{xIC})$

$\cdot P(\text{soil unit}_{\text{CPTu}}) \cdot P(\mu_{\text{xIC}}) \cdot P(\sigma_{\text{xIC}}) d\mu_{\text{xIC}} d\sigma_{\text{xIC}}; P(I_C | \text{soil unit}_{\text{CPT}}, \mu_{\text{xIC}}, \sigma_{\text{xIC}})$, likelihood expressed by Eq. (6); $P(\text{soil unit}_{\text{CPT}}) \cdot P(\mu_{\text{xIC}}) \cdot P(\sigma_{\text{xIC}})$ prior knowledge, which express the analyst's belief on soil profiling from CPTu.

In this work the assumption that $P(\mu_{\text{xIC}}) \cdot P(\sigma_{\text{xIC}}) = P(\mu_{\text{xID}}) \cdot P(\sigma_{\text{xID}}) = \text{constant}$ is made (equal uninformative knowledge). $B \geq 1$ will assign the identified layer to CPTu classification, to DMT one otherwise.

2.1 Single CPTu Analysis Workflow

The analyst has to feed in a CPTu record to analyze and select the level of classification, minimum layer resolution and the \mathbf{P} and \mathbf{m} values. The code can then start analyzing the CPTu-DMT input records by selecting a segment of CPTu-DMT data pairs long enough to fit an initial PDF ($\ln(I_C)$, $\ln(I_D)$). The bivariate is then updated by adding the next I_C - I_D data points, moving downwards through the record. Such updating allows the joint bivariate density to move on the SBT space until the representative \mathbf{P} surpasses any class boundaries by a larger proportion than that allowed by \mathbf{m} . At that time, data that fed the bivariate density are assigned to the identified layer, whose soil class is assigned depending on location of the mean value of bivariate distribution. The procedure resumes by analyzing the next segment in the CPTu record until all the record is analyzed (see [9]).

3 Illustrative Example: Llobregat Delta Site

The proposed methodology is tested on CPTu and DMT records obtained at Barcelona harbor (Spain). The CPTu and DMT sounding profiles (CPTu95, DMT164), each up to 40 m depth from seabed surface (Fig. 3a) are analyzed. An independently established soil layer profile was available for the site, which was derived from cores retrieved at the same location where CPTu95 was performed. Laboratory samples were retrieved each 5 m depth and core description followed UNE-EN ISO 14688-1 from which a detailed soil profile was derived (Fig. 3a). The boundaries identified carried significant uncertainty due to the complex structure and strong heterogeneity of the site.

The procedure previously described is applied to the CPTu95 record. The \mathbf{P} and \mathbf{m} model parameters were varied to try to match the blunter core-based delineation (Level 1, Fig. 3a). By considering $\mathbf{P} = 0.2$ and 0.05% threshold mixture, core-based boundaries were all identified (Fig. 4a). However, several additional layers were detected as expected within the first 10 m depth. To illustrate the effect of varying the fitting control parameters, the same record is reanalyzed using the $\mathbf{m} = 0$ value and $\mathbf{P} = 0.8$ (Fig. 4c). The parameters of the reanalysis result in a simpler profile, but it is noticeable that the layers disappearing are not simply the thinner ones (e.g.,

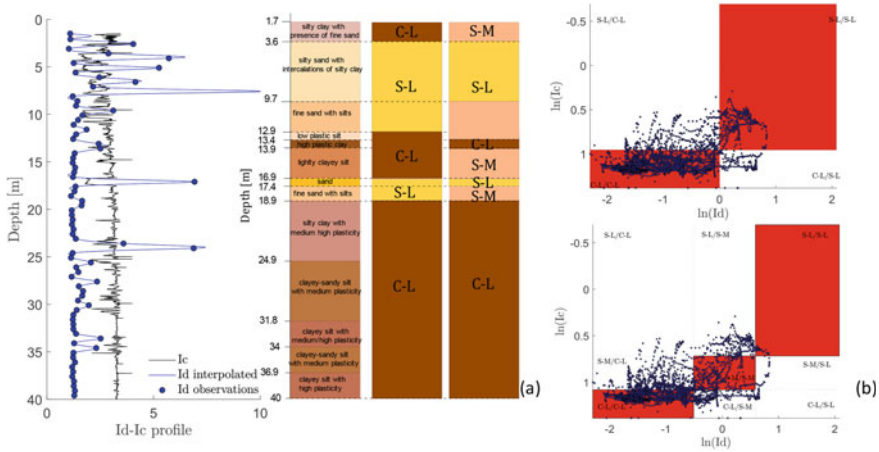


Fig. 3 a IC-ID profile and core-based delineation. b Data scatter on SBT chart at Level 1 and Level 2

at 3 m depth) but others (e.g., at 16.5 m depth) that were less statistically contrasted with their neighbors.

It can be observed that within the more heterogenous depth interval [0–11 m] several layers are assigned as SL–CL highlighting a mismatch between CPTu and DMT classification. Such mismatch can be also observed by comparing solely CPTu and DMT soil profiling by assuming equivalent **P** and **m** value within a univariate approach (Fig. 4d, e) (see [9] for univariate approach illustration).

Finally, the Bayesian perspective is introduced. Output soil profiling is reported in Fig. 5 by assuming for CPTu a prior probability of 0.7 and 0.3 for DMT classification. It can be observed that mismatched soil classes are assigned as SL class (Fig. 5a)

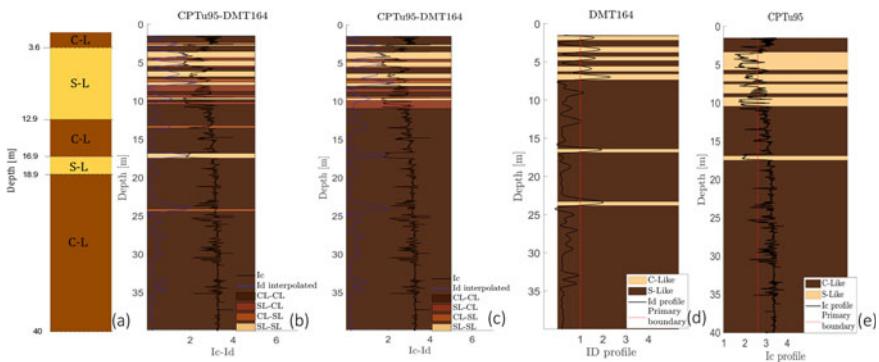


Fig. 4 a Core-based soil profiling. b Soil profiling at level 1 ($P = 0.2$; $m = 0.05$); c Soil profiling at level 1 ($P = 0.8$; $m = 0$). d) Solely CPTu-based soil profiling at level 1; e) Solely DMT-based soil profiling at level 1

resulting more coherent with CPTu-based soil profiling (Fig. 4d). By applying a prior of 0.5 to both tests the exclusively assignment of layer is solely dependent on likelihood function (Eq. 6). Finally, the prior 0.1, 0.9 is applied for CPTu and DMT respectively resulting in a soil profiling (Fig. 5c) more coherent to the DMT-based classification (Fig. 4e). The algorithm is then run for Level 2 by assuming the same values of P and m defined at Level 1 ($P = 0.2$; $m = 0.05$). Results in terms of soil profiling are reported in Fig. 6b. It can be observed that the mismatched between CPT-DMT classification increase with respect to Level 1. This is particularly relevant for the depth interval [0–11 m] where several layers classified as CL-SM or SL-SM are obtained. This does not come as surprise since previous study [2] show that DMT might classify clay as silt and viceversa. However, by applying a prior 0.7 and 0.3 for CPTu and DMT respectively, it can be observed a soil profiling more consistent with core-based one (Fig. 6a, c) and mostly of mismatched layers are now assigned to SM class.

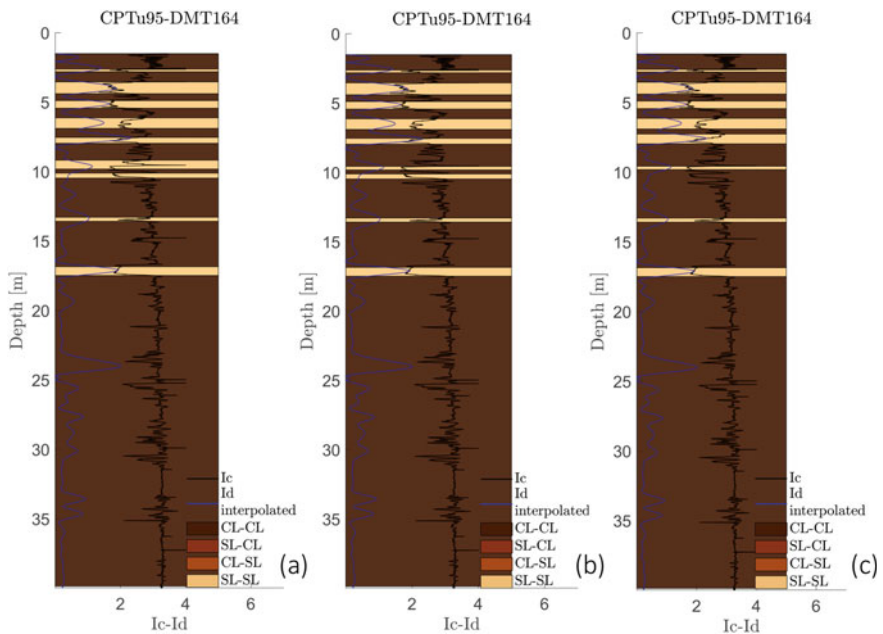


Fig. 5 Soil profiling at level 1 ($P = 0.2$; $m = 0.05$) after Bayesian perspective: a) $P(\text{soil unit}_{\text{CPTu}}) = 0.7$, $P(\text{soil unit}_{\text{DMT}}) = 0.3$; b) $P(\text{soil unit}_{\text{CPTu}}) = 0.5$, $P(\text{soil unit}_{\text{DMT}}) = 0.5$; c) $P(\text{soil unit}_{\text{CPTu}}) = 0.1$, $P(\text{soil unit}_{\text{DMT}}) = 0.9$

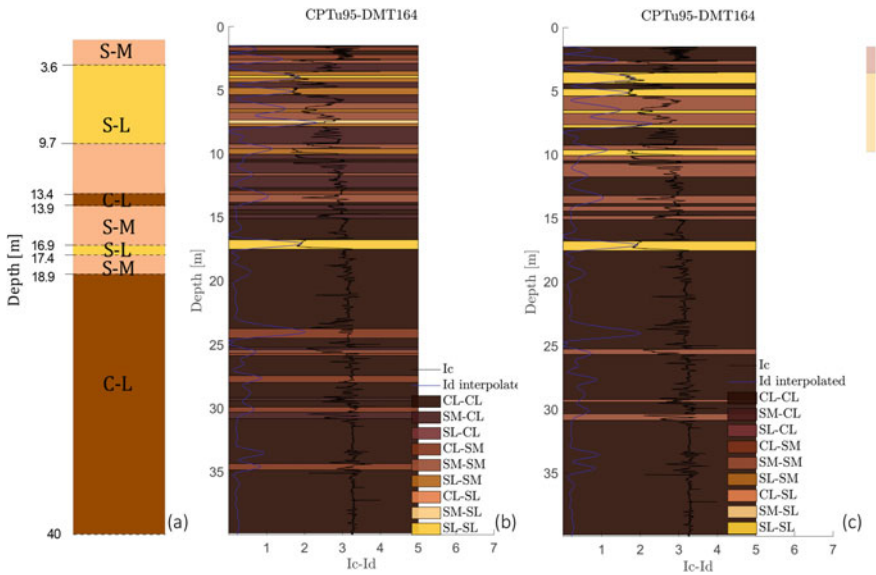


Fig. 6 a Core-based soil profiling at level 2; b CPTu-DMT soil profiling at level 2 for $P = 0.2$ and $m = 0.05$; c CPT-DMT based soil profiling for $P = 0.2$ and $m = 0.05$ applying a prior of 0.7–0.3 for CPTu and DMT respectively

4 Conclusions

This study proposes a first attempt of integrating CPTu-DMT data for soil profiling. A bivariate approach is applied, which quantified the dependence of I_C and I_D data while eliciting assumption and heuristics that analysts apply to soil profiling and explicating the belief of analyst about the two in-situ tests for soil profiling purpose. Once quantified the values of P and m , the same value can then be applied to different locations. At level 1 results highlight a good agreement between CPTu-DMT classification. At level 2 the discrepancy between CPTu-DMT classification increase. By introducing the Bayesian prospective the output soil profiling will result coherent with analyst’s requirement with a good match with-core-based description. The approach can be then systematically applied to other location within the project site area and/or multiple CPTu sounding records.

References

1. Bustamante M, Gianceselli L (1982) Pile bearing capacity prediction by means of static penetrometer CPT. Proceedings of the second European symposium on penetration testing, Amsterdam, pp 493–500
2. Marchetti S, Monaco P, Totani G, Calabrese M (2001) The flat dilatometer test (DMT) in soil investigations. In-Situ 2001, international conference on in situ measurement of soil properties, 95–131
3. Arroyo M, Mateos T (2006) Embankment design with DMT and CPTu: prediction and performance. Proceedings from the Second International Flat Dilatometer Conference, January 2006, 62–68
4. Monaco P, Totani G, Calabrese M (2006) DMT-predicted vs. observed settlements: a review of the available experience. In: Proceedings of the 2nd international flat dilatometer conference, Washington D.C., April 2006, pp 244–252
5. Robertson PK (2017) Closure to “CPT-DMT correlations ” by P . K . Robertson Discussion of “ CPT-DMT Correlations ” by. April 2011. [https://doi.org/10.1061/\(ASCE\)GT.19435606.0000488](https://doi.org/10.1061/(ASCE)GT.19435606.0000488) (Robertson, 2009a)
6. Robertson PK (2009) Interpretation of cone penetration tests—a unified approach. *Can Geotech J* 46(11):1337–1355. <https://doi.org/10.1139/t09-065>
7. Ching J, Phoon K, Chen C (2014) Modeling piezocone cone penetration (CPTU) parameters of clays as a multivariate normal distribution, 77–91
8. Collico S, Arroyo M, Deu A, Devincenzi M, Rodriguez A (2020) Semi-automated probabilistic soil profiling using CPTu. 6th international conference on geotechnical and geophysical site characterisation
9. Collico S, Arroyo M, Deu A, Devincenzi M, Rodriguez A (2022) Probabilistic delineation of soil layers Soil behaviour Type Index I_c . 5th symposium on cone penetration testing-bologna (in review)
10. Ganju E, Prezzi M, Salgado R (2017) Algorithm for generation of stratigraphic profiles using cone penetration test data. *Comput Geotech* 90:73–84

Clay Soil Stabilization Using Xanthan Gum and Sodium Alginate as Biopolymers



Ayberk Temurayak  and Tugba Eskisar 

Abstract This study deals with the effect of xanthan gum and sodium alginate biopolymers on the consistency, compaction, and strength properties of clay. Atterberg limits tests, standard proctor compaction tests, and unconfined compression tests were performed. The curing time of the specimens varied from 7 to 56 days. Xanthan gum ratios were %0.5, %1, %1.5, %2, %3 and sodium alginate ratios were %1, %2, %3, %4. As a result, a noticeable increase in liquid limit was observed in both biopolymers. Plastic limit and plasticity index of the specimens showed minor changes compared to the liquid limit of the soil specimens. Optimum water content of the clay specimens with additives was %2 higher compared to that of the untreated clay. Maximum dry density slightly decreased compared that of the untreated clay. The results of unconfined compressive tests showed that using xanthan gum and sodium alginate biopolymers had the beneficial effect of increasing the strength of the soils.

Keywords Xanthan Gum · Sodium alginate · Unconfined compressive strength · Compaction

1 Introduction

The application of different soil improvement techniques improves the properties of problematic soils. Large settlements and bearing capacity problems of the problematic soils can be alternatively solved with the help of stabilizers. Conventionally, cement, lime, and fly ash are used as stabilizers. Cement is largely consumed in soil stabilization projects, but it causes environmental and sustainability issues. During the production of cement, significant amounts of carbon dioxide and nitrogen oxide gases are emitted, with a certain level of air emissions in the form of cement dust, which exhibits another potential environmental problem [1]. In the recent past, it has been discovered that biopolymers of the food industry could also be an alternative as

A. Temurayak · T. Eskisar (✉)

Faculty of Engineering, Civil Engineering Department, Ege University, Bornova, İzmir, Turkey
e-mail: tugba.eskisar@ege.edu.tr

© The Author(s), under exclusive license to Springer Nature Switzerland AG 2023
C. Atalar and F. Çinicioğlu (eds.), *5th International Conference on New Developments in Soil Mechanics and Geotechnical Engineering*, Lecture Notes in Civil Engineering 305, https://doi.org/10.1007/978-3-031-20172-1_12

139

a stabilizing agent in the soil stabilization. Xanthan gum, guar gum, sodium alginate, and chitosan are some of the biopolymers used in the geotechnical applications.

Xanthan gum is a natural anionic polysaccharide and is the result of aerobic fermentation of sugars by the *Xanthomonas Campestris* bacteria [2]. It is used as a stabilizer and thickener additive in the food industry. It has high thickening properties even in low concentrations. Due to these features, it can be used as an additive for the soils. Soil stabilization with xanthan gum is a sustainable substitute to conventional additives in fine-grained soil improvement [2].

Sodium alginate is the sodium salt of alginic acid, the main source of which is brown algae. It is also used in the food industry because it prevents the spoilage of foods and provides a gel consistency. Sodium alginate forms a heat-resistant and irreversible gel. It is also used to increase the plasticity of materials such as cement, plaster and mortar.

In this study, xanthan gum and sodium alginate treated clay specimens were prepared and the changes in the soil consistency, compaction, and strength properties of the treated clay specimens were evaluated.

2 Materials and Method

The clay soil used in this study was composed of mainly kaolinite as determined from the chemical analysis. The soil was available in powder form with particles smaller than 75 μm . The liquid limit of the soil was 51%, and the plastic limit of the soil was 36.5%. The soil was classified as MH according to the unified soil classification system of ASTM D-2487 [3]. The specific gravity of the clay soil was 2.68. The optimum water content and the maximum dry density of the soil were 31%, and 1.64 t/m^3 , respectively.

Xanthan gum was a pale white powder with non-corrosive and environmentally friendly properties. This gum was preferred due to its pseudo-viscous and bio-clogging properties, and availability. On the other hand, sodium alginate was a yellowish white powder and it was preferred as the second biopolymer of the study as it dissolved slowly in water, forming smooth-pouring solutions.

The wet mixing method was preferred to prepare the specimens in all tests. According to wet mixing method, the biopolymers were first dissolved in the water and then added to the dry soil. In this study, xanthan gum and sodium alginate were prepared in solutions of 0.5–3%, and 1–4%, respectively. After that, the additive in solution was thoroughly mixed with the dry soil until a homogenous mixture was achieved. The unconfined compressive test specimens were prepared at the optimum water contents of the specimen groups. The specimens were cured for 7, 28 and 56 days.

The liquid limits and the plastic limits of the specimens were determined according to ASTM D4318 [4]. The standard Proctor compaction tests were performed according to ASTM D698 [5]. The unconfined compression test specimens were 100 mm in height and 50 mm in diameter. The unconfined compression tests were

held in accordance with ASTM D2166 [6]. The load was applied with a loading rate of 1.42 mm/min. The strain rate was chosen in a way that the time to complete testing of a single specimen did not exceed 15 min. The loading continued until the load values decreased with increasing strain, or until 15% strain was reached.

3 Results and Discussion

3.1 Atterberg Limits

Xanthan gum and sodium alginate additives increased the liquid limit of the treated soil specimens. The liquid limit increased by 34% with the addition of 3% xanthan gum, and the increment of the liquid limit was over 100% with the addition of 4% sodium alginate. At the highest concentration of sodium alginate which was 4%, the rapid change in viscosity led to a nonlinear increase of the liquid limit. A similar trend was also observed and reported by Nugent [7].

The plastic limit of the specimens had a linear increment with the addition of xanthan gum and sodium alginate. The plastic limit of the pure soil increased from 36.5% to 38.7% and 40.7% with the additions of xanthan gum and sodium alginate, respectively.

The plasticity indexes increased with the addition of both biopolymers. While the increase was 203% with the addition of 3% xanthan gum, it increased 414% with the addition of 4% sodium alginate. Increasing the water capacity of biopolymer added soils activated the monomers of the biopolymers and formed ionic and covalent bonds with soil particles. Thus, monomers required more water, which raised the liquid limit and plasticity index of the soil specimens [8]. This effect was more pronounced in 4% sodium alginate-treated soils. Atterberg limits of xanthan gum and sodium alginate treated specimens are presented in Fig. 1 a, b, respectively.

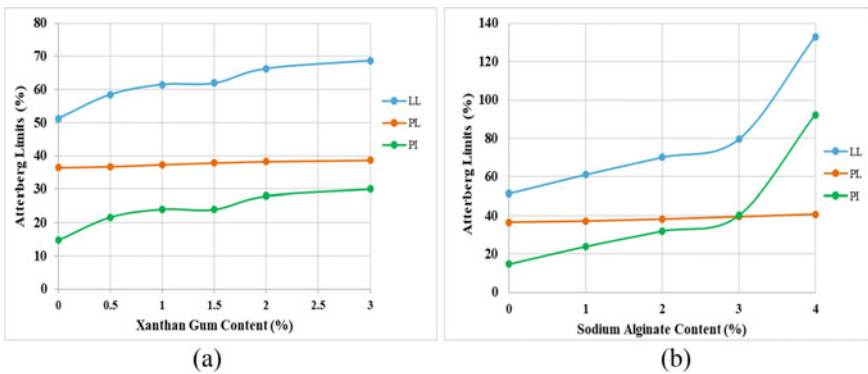
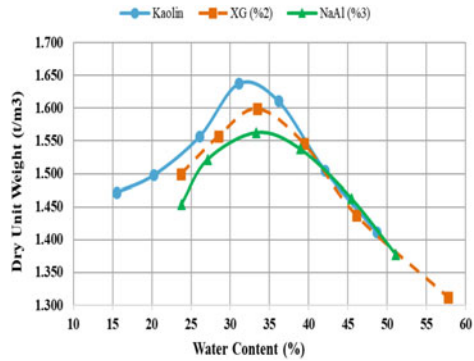


Fig. 1 Atterberg limits of a xanthan gum b sodium alginate treated clay

Fig. 2 The compaction properties of untreated clay and biopolymer treated clay (XG: Xanthan Gum, NaAl: Sodium Alginate)



3.2 Compaction Properties

The maximum dry unit weight and the optimum water content of untreated clay, clay with 2% xanthan gum, and clay with 3% sodium alginate additives are shown in Fig. 2. The optimum water content of 2% xanthan gum treated soil was 33%, and the maximum dry unit weight of the same specimen was 1.60 t/m³. The optimum water content of 3% sodium alginate treated soil was 33%, and the maximum dry unit weight was 1.56 t/m³. The decrease in the maximum dry unit weight and the increase in the optimum water content were due to the fact that the monomers located in the spaces between the soil particles absorbed more water and caused a net decrease in particle interaction [9].

3.3 Unconfined Compressive Strength

When stabilization with biopolymers is a concern, the success of soil improvement is affected by the type and composition of the soil, the type and amount of the biopolymer, curing time, and the mixing conditions [2]. Figures 3 and 4 show the unconfined compressive strength (UCS) values of 7, 28, and 56-day specimens which were treated with xanthan gum and sodium alginate, respectively. The UCS of untreated clay was 280 kPa. The UCS increased with the curing time and with an increase in the xanthan gum and sodium alginate contents. Higher biopolymer content led to a larger and thicker gum-soil matrix and more gum-soil interactions in the fine soils [1]. While the increase of the UCS was 2.6 times in 56-day specimens treated with %2 xanthan gum, and the increase was 3.8 times in 56-day specimens treated with 3% sodium alginate compared to that of untreated soil. The formation of cross-link elements and hydrogen bonds rendered the soil matrix stiffer, increasing its resistance to load resulting in higher unconfined compressive strength of the soil at all investigated percentages of xanthan gum [9]. As the rate of the sodium alginate increased, the soil strength also increased in a range of 1%-3% sodium alginate.

Zhao et al. [10] reported that the addition of sodium alginate at a rate between 1 and 3%, significantly improved the UCS of the soil in compliance with the findings of this study. The presence of the biopolymer due to the added sodium alginate to soils increased the bonding and cross-linking between the particles. As a result, a stiffer soil structure forms, leading to an increase in the soil stiffness and strength.

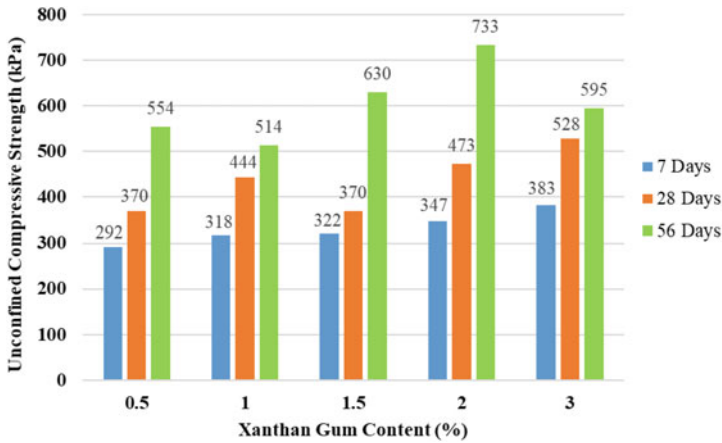


Fig. 3 The UCS of xanthan gum treated clay specimens

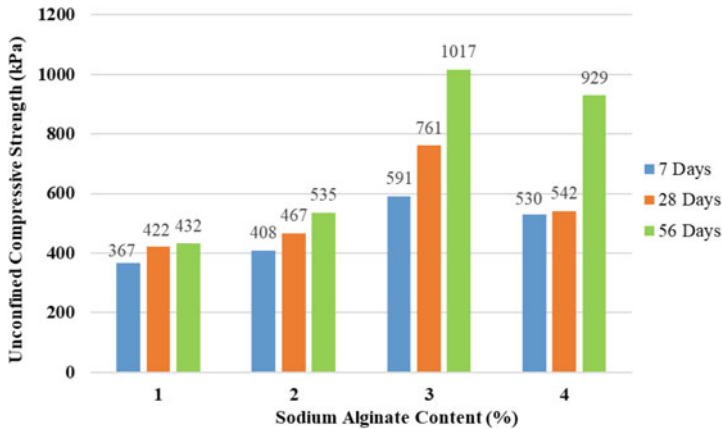


Fig. 4 The UCS of sodium alginate treated clay specimens

4 Conclusions

This study investigated two types of biopolymers as alternative soil stabilizers. Atterberg limits, compaction, and unconfined compression strength tests were performed with varying concentrations of these biopolymers. The effect of xanthan gum and sodium alginate were determined and Atterberg limits, compaction characteristics, and the strength of the specimens were compared with each other. The main outcomes of this preliminary study are summarized as follows:

- The liquid limit increased in both biopolymer additives; this effect was more pronounced in sodium alginate.
- The plastic limit increased continuously with sodium alginate and the xanthan gum addition to the specimens.
- The plasticity index increased in both biopolymers.
- The optimum water content increased by %2 in the specimens with both biopolymer additives. On the contrary, the maximum dry unit weight decreased in specimens with both biopolymer additives.
- The unconfined compressive strength of the specimens with a xanthan gum content of 2% and a sodium alginate content of 3% were the highest among 56-day specimens.

The preliminary investigation on xanthan gum and sodium alginate added clay soils showed that these additives could be beneficial for geotechnical site applications.

References

1. Chang I, Im J, Prasadhi AK, Cho GC (2015) Effects of Xanthan gum biopolymer on soil strengthening. *Constr Build Mater* 74:65–72
2. Dehghan H, Tabarsa A, Latifi N, Bagheri Y (2019) Use of xanthan and guar gums in soil strengthening. *Clean Technol Environ Policy* 21(1):155–165
3. ASTM D2487 (2006) Standard practice for classification of soils for engineering purposes, 12
4. ASTM D4318–17e1 (2018) Standard test methods for liquid limit, plastic limit, and plasticity index of soils, 20
5. ASTM D698–12 (2014) Standard test methods for laboratory compaction characteristics of soil using standard effort (12400 ft-lbf/ft³(600kN-m/m³)), 13
6. ASTM 2166–00 (2017) Standard test method for unconfined compressive strength of cohesive soil, 6
7. Nugent RA, Zhang G, Gambrell RP (2009) Effect of exopolymers on the liquid limit of clays and its engineering implications. *Transp Res Rec* 2101(1):34–43
8. Moghal AAB, Vydehi KV (2021) State-of-the-art review on efficacy of xanthan gum and guar gum inclusion on the engineering behavior of soils. *Innov Infracr Solut* 6(2):1–14
9. Sujatha ER, Atchaya S, Sivasaran A, Keerdthe RS, Enhancing the geotechnical properties of soil using xanthan gum—an eco-friendly alternative to traditional stabilizers
10. Zhao Y, Zhuang J, Wang Y, Jia Y, Niu P, Jia K (2020) Improvement of loess characteristics using sodium alginate. *Bull Eng Geol Env* 79(4):1879–2189

Estimation of OCR and Compression Index by Different Methods



Zeeshan Firdous, V. Padmavathi, and M. R. Madhav

Abstract Preconsolidation stress (σ'_c) is an important parameter to understand the stress history of the soil and in calculating settlements. Accurate determination of settlement depends largely on the accuracy of σ'_c . Several researchers have proposed different methods to obtain σ'_c from e-log σ' plot. Determination of preconsolidation stress relies on the graphical approach of Casagrande method. This method depends on identification of the point of maximum curvature on the e-log σ' curve which is highly subjective and leaves room for errors. Several methods have been proposed in the literature for interpretation of preconsolidation stress based on curve fitting rather than subjective judgment. These approaches are based on graphical interpretation of void ratio (e) versus effective stress (σ'), log e versus log σ' , log (1 + e) versus log σ' plots. The methods used in this study are semi-logarithmic [1, 2, 3, 4], bi-logarithmic [5, 6, 7] and based on variation of constrained modulus with effective stress [8]. In this study, test data taken from the three (Egypt, California and India) different locations around the world is analysed. Compression index (C_c) and over consolidation ratio (OCR) are determined using the above methods and the variation is studied.

Keywords Preconsolidation stress · Void ratio · Effective stress · Compression index and OCR

Zeeshan Firdous (✉)
Geotechnical Engineering, Department of Civil Engineering, JNTUH College of Engineering,
Hyderabad, India
e-mail: zeeshanf97@gmail.com

V. Padmavathi
Department of Civil Engineering, JNTUH College of Engineering, Hyderabad, India

M. R. Madhav
JNT University, IIT Hyderabad, Hyderabad, India

1 Introduction

Oedometer test provides one-dimensional soil deformation behaviour. Soil exhibits a bilinear response, when the oedometer test data is plotted on a semi logarithmic graph. The deformations are small below certain effective stress and beyond it, the deformations are large which lead to more compressed structure of the soil. That particular effective stress is known as preconsolidation stress, σ'_c and is required to estimate the consolidation settlement of soft soils. The ratio between σ'_c and in-situ vertical effective stress, σ'_0 , is known as Over Consolidation Ratio (OCR). The concept of preconsolidation stress and its importance is well defined in geotechnical engineering. Hence, different methods have been proposed by researchers to estimate preconsolidation stress from Oedometer test results. Methods proposed by Casagrande [1], Pacheco Silva [3], [5], Schmertmann [4], Nagaraj et al. [2], Oikawa [6], Sridharan [7] and Janbu [8] are analysed in this paper by considering the data from three (Egypt, California and India) sites available in the literature. These methods have a common assumption that the soil response varies from stiffer to softer at σ'_c . The present work also compares the variation of OCR and C_c based on the above mentioned methods.

2 Interpretation of σ'_c

Casagrande [1] estimated preconsolidation stress from the e-log σ' curve. This method interprets a large range of estimated preconsolidation stress, if the point of maximum curvature is not well defined. As illustrated in Fig. 1a, a point B on the curve is selected at maximum curvature. Horizontal and tangential lines are drawn passing through point B. A bisector is drawn at the same point, bisecting the angle between horizontal and tangential lines. Virgin compression line is extended backward and the intersection point of this line with the bisector is located at point D. The stress corresponding to point D is preconsolidation stress, σ'_c . According to Silva [3] method, a horizontal line AB, is drawn passing through initial void ratio, e_0 , of the specimen on the e-log σ' plot as illustrated in Fig. 1b. A line, CD is drawn from the straight line portion of the virgin compression curve until it intersects the line AB at point C. A vertical line is dropped down from the point C, until it intersects the e-log σ' curve at point E. Another line is extended in horizontal direction from the point E, to line CD to get an intercept, F. The stress corresponding to the point F, is preconsolidation stress. Figure 1c describes Nagaraj et al. [2] method, σ'_c is obtained from the point of intersection of a horizontal line from e_0 , and a line normal to the laboratory e-log σ' curve at the point of maximum curvature. A horizontal line passing through $0.4e_0$ intersects the virgin compression curve at point C. Compression index is obtained from the line joining point D and point C. Schmertmann [4] has proposed a method to correct the compression curve from soil samples subjected to disturbance. The method is detailed in Fig. 1d. Point C is marked at the

intersection of virgin compression curve with a horizontal line drawn from void ratio of $0.4e_0$. The backward extension of the linear portion of the curve ABC meets the horizontal line DE at point F. A smooth curve EG is drawn from point E, parallel to the recompression curve. The stress corresponding to point G is preconsolidation stress σ'_c .

Oikawa [6] method (Fig. 1e) summarises that, a compression curve is drawn for σ' on logarithmic scale and $\log(1 + e)$ on linear scale along X and Y axes respectively. The linear parts of compression curve are extended to get an intersection point A as shown in Fig. 1. The stress corresponding to the point A is σ'_c . The same procedure [6] is followed by Butterfield [5], Fig. 1f, to find σ'_c , with $\ln \sigma'$ and $\ln(1 + e)$ along X and Y axes respectively. Sridharan [7], illustrated the interpretation of σ'_c from the intersection of linear fit lines of 'e - σ' ' curve plotted on logarithmic (base 10) scales as illustrated in Fig. 1g. Janbu [8] proposed that the preconsolidation stress is determined from a plot of constrained modulus, M, which is inverse of coefficient of volume compressibility, versus the effective stress on a linear scale as shown in Fig. 1h. The stress corresponding to a marked drop of M, is the preconsolidation stress, σ'_c .

3 Results and Interpretation

The preconsolidation stress, OCR and Compression index are estimated using the methods specified in Sect. 2 for the e-log σ' curves taken from three sites located in Egypt [], California [9] and India [10]. The e-log σ' data was obtained from samples collected from Egypt site at depths of 15 m, 23 m and 30 m in a borehole, also at 8 m and 10 m depths from different bore holes. Profile of California site marks the presence of soft soil deposits with ground water table at ground level. Top layer of soil consists of highly plastic (CH) and low plastic (CL) clays of varying compressibility. e-log σ' plots are given for samples at various depths taken from boreholes at several locations.

3.1 Comparison of OCR Obtained from Different Methods

Overconsolidation ratio is estimated using the preconsolidation stress obtained from the different methods proposed by Casagrande [1], Silva [3], Nagaraj et al. [5, 2], Oikawa [6], Sridharan [7], Schmertmann [4] and Janbu [8] and presented in Table 1.

Results from Silva [3] method show small variation from those of Casagrande [1] method. This is because Silva [3] method is independent of the drawing scale while Casagrande [1] method is scale dependent. Nagaraj et al. [2] and Schmertmann [4] methods predict true in situ OCR by making corrections to sample disturbance. OCR obtained from Janbu [8] method are lower than the values from Casagrande [1] method for all the three sites. Janbu [8] method results in the highest deviations

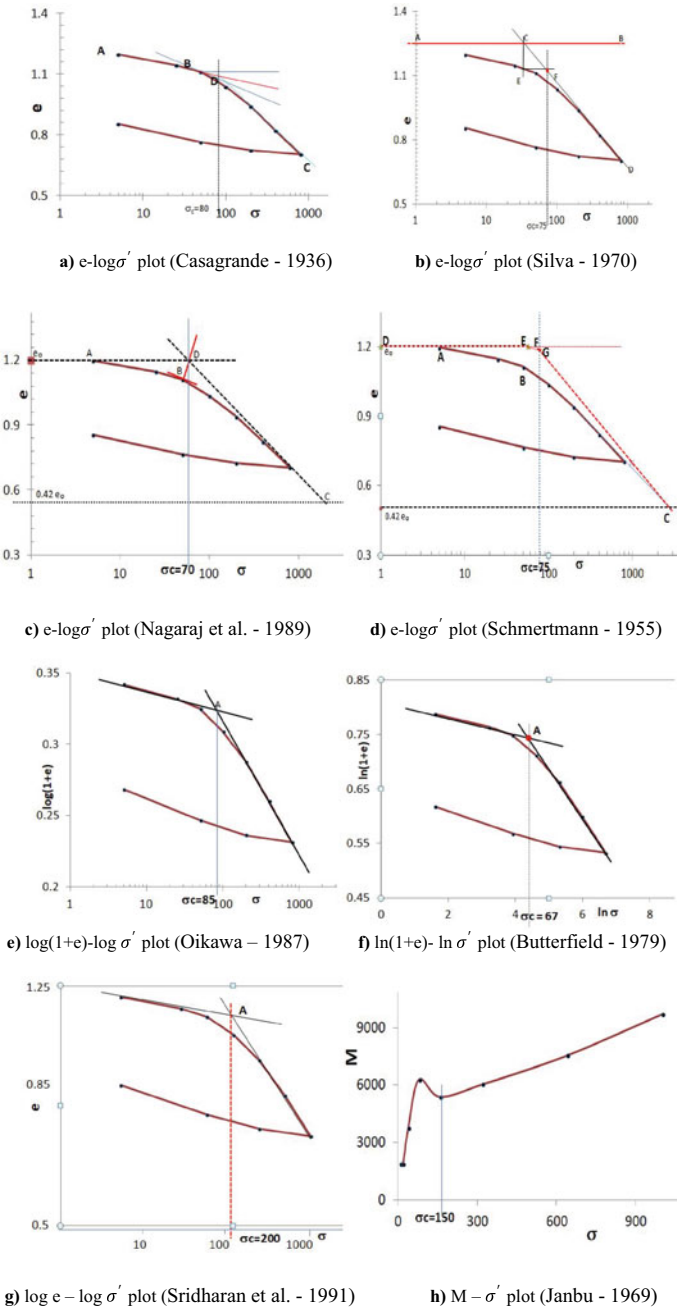


Fig. 1 Different methods for interpretation of σ'_c

Table 1 OCR obtained from different methods

Site	Casagrande [11]	Silva [3]	Nagaraj et al. [12]	Butterfield [1]	Oikawa [6]	Sridharan [7]	Schmertmann, [4]	Janbu [8]
Egypt	1.40	1.10	1.60	1.25	1.40	1.90	1.20	0.90
	0.75	0.43	1.25	0.76	0.75	1.06	1.00	1.00
	0.95	1.00	1.10	1.17	0.81	0.95	1.00	1.00
	3.57	3.07	3.54	2.59	2.71	2.86	3.93	2.14
	1.80	1.55	1.30	1.30	1.25	1.50	1.30	0.90
California	17.39	14.78	16.52	14.78	14.78	14.35	13.04	13.91
	1.96	1.43	1.70	2.63	2.38	2.14	1.31	1.90
	21.43	18.57	17.14	21.36	18.57	19.29	29.29	5.71
	3.70	2.59	4.07	5.19	4.63	5.56	2.22	1.48
	2.77	2.13	2.04	3.94	3.83	4.00	1.38	1.06
	2.26	1.66	1.72	2.20	2.60	3.10	1.56	3.20
	15.26	13.84	8.68	13.95	14.47	14.47	21.05	8.42
	33.33	33.33	18.33	31.11	33.33	33.33	44.44	35.56
India	9.34	9.87	7.42	7.89	7.89	8.16	9.47	2.89
	1.40	1.23	1.05	1.18	1.30	1.58	1.32	1.40
	2.08	1.89	1.60	1.89	1.79	1.75	1.70	1.42
	2.34	2.20	1.70	2.34	2.10	2.30	2.30	1.00
	1.01	1.04	0.83	1.03	1.01	1.04	1.00	1.04
	3.60	3.60	2.80	3.00	3.00	3.00	4.40	5.20
	1.15	1.27	1.09	1.07	1.00	1.13	1.13	1.00
	2.34	2.66	1.70	2.34	2.13	2.34	4.36	1.60
	1.10	1.34	1.00	1.32	1.22	1.46	1.95	1.10

as it does not clearly specify the steps to follow for graphical interpretation. Hence, it depends on the user’s experience and judgement. The values show more variation for high σ'_c and higher OCR. This might be due to higher recompression up to the point at which it reaches σ'_c . Virgin compression occurs beyond σ'_c . This unloading–reloading process might cause more disturbances and hence the deviation is observed. Butterfield [5], Oikawa [6] and Sridharan [7] methods give comparable values of OCR.

Table 2 illustrates the variation in OCR obtained from Silva [3], Nagaraj et al. [2], Butterfield [5], Oikawa [6], Sridharan [7], Schmertmann [4] and Janbu [8] methods with those from Casagrande [1] method.

The range of variation of OCR presented in table 2 is from –30% to 20%, –40% to 20%, –30% to 40%, –28% to 42%, –31% to 38%, –20% to 33% and –50% to 44% for the results obtained from Silva [3], Nagaraj et al. [2], Schmertmann [4], Butterfield [5], Oikawa [6], Sridharan [7] and Janbu [8] methods respectively. Minimum range of deviation is noticed from Silva [3] and Sridharan [7] methods.

Table 2 Variation of OCR from Casagrande [11] method

Methods	Average variation of OCR from Casagrande [11] method (%)	Range of variation of OCR from Casagrande [11] method (%)
Silva [3]	−8	−30 to 20
Nagaraj et al. [12]	−15	−40 to 20
Schmertmann [4]	4	−30 to 40
Butterfield [1]	2	−28 to 42
Oikawa [6]	−2	−31 to 38
Sridharan [7]	10	−20 to 33
Janbu [8]	−23	−50 to 44

Butterfield [5], Oikawa [6] and Sridharan [7] methods yield similar range of results. Hence, their application would be more conservative in estimation of σ'_c . Janbu [8] method shows a greater deviation of OCR from −50% to 44%.

3.2 Comparison of C_c Obtained from Different Methods

Compression index, C_c , is estimated from the Eq. 1 by Casagrande [1], Silva [3], Nagaraj et al. [2] and Schmertmann [3] methods.

$$C_c = \frac{\Delta e}{\Delta \log \sigma'} \quad (1)$$

Compression index, C_c , from Butterfield [5] and Oikawa [6] methods is estimated from the relationship between C_c and C_c' given by Eq. (2). Sridharan [7] established a relationship between C_c and C_c'' as shown in Eq. (3).

$$C_c = \frac{C_c' - 0.0192}{0.19} \quad (2)$$

$$C_c = \frac{C_c'' - 0.1067}{0.23} \quad (3)$$

where C_c' —slope of $\log(1 + e)$ vs $\log \sigma'$ plot (Fig. 1) or slope of $\ln(1 + e)$ vs $\ln \sigma'$ plot (Fig. 1).

C_c'' —slope of $\log e$ vs $\log \sigma'$ plot (Fig. 1)

C_c —Compression index.

The compression index values thus estimated are presented in Table 3.

Casagrande [1] and Silva [3] methods predict identical estimates of Compression index. Results from Nagaraj et al. [2] and Schmertmann [4] methods show greater deviation from those of Casagrande [1] method. This is because these two methods

Table 3 Compression index obtained from different methods

Site	Casagrande [11]	Silva [3]	Nagaraj et al. [12]	Schmertmann [4]	Butterfield [1]	Oikawa [6]	Sridharan [7]
Egypt	0.55	0.52	0.68	0.66	0.55	0.54	0.69
	0.49	0.47	0.63	0.66	0.48	0.49	0.73
	0.57	0.60	0.68	0.67	0.59	0.61	0.16
	0.31	0.30	0.41	0.38	0.30	0.32	0.20
	0.42	0.45	0.67	0.50	0.39	0.41	0.35
California	0.30	0.31	0.38	0.30	0.28	0.30	0.31
	0.20	0.21	0.27	0.24	0.23	0.22	0.15
	0.48	0.47	0.53	0.49	0.54	0.45	0.48
	0.31	0.32	0.41	0.35	0.36	0.33	0.41
	0.18	0.20	0.24	0.22	0.23	0.22	0.24
	0.17	0.17	0.20	0.19	0.18	0.17	0.29
	0.16	0.16	0.18	0.26	0.16	0.15	0.09
	0.25	0.24	0.25	0.31	0.25	0.26	0.19
India	0.30	0.33	0.35	0.39	0.28	0.30	0.30
	0.38	0.38	0.41	0.45	0.33	0.37	0.41
	0.22	0.20	0.22	0.23	0.22	0.18	0.13
	0.42	0.43	0.44	0.46	0.48	0.47	0.74
	0.33	0.32	0.32	0.31	0.30	0.34	0.34
	0.36	0.37	0.38	0.40	0.36	0.37	0.38
	0.29	0.31	0.36	0.35	0.30	0.30	0.33
	0.27	0.29	0.32	0.43	0.24	0.23	0.14
	0.38	0.41	0.31	0.49	0.28	0.30	0.28

make corrections to sample disturbance. Butterfield [5] and Oikawa [6] methods predict similar values of compression index as both the methods study bilogarithmic variation between specific volume and effective stress.

Table 4 illustrates the variation in C_c obtained from Silva [3], Butterfield [5], Schmertmann [4], Nagaraj et al. [2], Oikawa [6], Sridharan [7] and Janbu [8] methods with those from Casagrande method.

From table 4, the range of variation of C_c from Silva [3], Nagaraj et al. [2], Schmertmann [4], Butterfield [5], Oikawa [6] and Sridharan [7] is from -10% to 9% , -18% to 33% , -7% to 62% , -27% to 54% , -21% to 10% and -49% to 50% respectively. The minimum range of deviation is observed for Silva [3] and Oikawa methods. The maximum range of deviation is for Sridharan [7] and Schmertmann [4] method.

Table 4 Variation of C_c from Casagrande method

Methods	Average variation of C_c from Casagrande [11] method (%)	Range of variation of C_c from Casagrande [11] method (%)
Silva [3]	2	−10 to 9
Nagaraj et al. [12]	18	−18 to 33
Schmertmann [4]	20	−7 to 62
Butterfield [1]	3	−27 to 54
Oikawa [6]	3	−21 to 10
Sridharan [7]	1	−49 to 50

4 Conclusions

Preconsolidation stress, σ'_c , is estimated from eight methods mentioned in the literature. The OCR and C_c estimated from different methods are compared with the values obtained from Casagrande [1] method. Results from Casagrande [1] method varied with those from Silva [3] method on the basis of drawing scale, otherwise both the methods predict similar results. The results from Schermtmann [4] and Nagaraj [2] method can be utilised in obtaining true in situ behaviour of soil. Among all the methods considered, Butterfield [5], Oikawa [6] and Sridharan [7] methods provided the most comparable estimates. Values from Janbu [8] method show greater deviation.

References

1. Casagrande A (1936) The determination of the preconsolidation load and its practical significance. Proc First Int Conf Soil Mech Found Eng 3:60–64
2. Nagaraj TS, Murthy BRS, Vatsala A, Joshi RC (1990) Analysis of compressibility of sensitive soils. J Geotechn Eng 116(01):105–118
3. Silva PF (1970) A new graphical construction for determination of the pre-consolidation stress of a soil sample. Proceedings of the 4th Brazilian Conference on Soil Mechanics and Foundation Engineering, Rio de Janeiro, Brazil, 225–232
4. Schmertmann JNM (1955) The undisturbed consolidation behavior of clay. From Research to Practice in Geotechnical Engineering, Transactions of the American Society of Civil Engineers, American Society of Civil Engineers (ASCE), 1201–1233
5. Butterfield R (1979) A natural compression law for soils (an advance on e-log p'). Geotechnique 24(04):469–479
6. Oikawa H (1987) Compression curve of soft soils. Soils Found 27(3):99–104
7. Sridharan JBT (1991) Improved technique for estimation of preconsolidation pressure. Geotechnique 41(2):263–268
8. Janbu N (1969) Settlement calculations based on the tangent modulus concept. Soil Mechanics and Foundation Engineering, The Technical University of Norway, Trondheim 32
9. Robb ESM, Judd K, Gregg LF (2016) Teaching consolidation: case study of preloading with vertical drains. Int J Geoen Case Histories 4:222–233
10. Madhav MR (2022) Personal contacts

11. Donatas U, Ieva L, Domas G (2016) Over consolidation ratio determination of cohesive soil. historical experience and challenges of geotechnical problems in Baltic sea region. Proceedings of 13th baltic sea geotechnical conference, lithuanian geotechnical society, Lithuania, pp 22–24, September 2016
12. Santagata MC, Germaine JT (2002) Sampling disturbance effects in normally consolidated clays. *J Geotechn Geoenviron Eng* 128(12):997–1006
13. Kirstein A, Liu J (2017) Evaluation of different methods for identification of Preconsolidation pressure for Champlain sea clay using CRS tests. *Geo Ottawa conference paper*, October 2017
14. Yang X, Jia Y, Liu H, Shan H (2009) Characteristics and causes of the Preconsolidation stress of soils in the yellow river delta. *J Ocean Univ China* 08(3):215–221

Shallow and Deep Foundations

Limit Load Exemplary Analyses of Foundations Accidentally Placed on Sand Underlain by Peat Using Their Various Parameters



Łukasz Kaczmarek , Maria Grodzka-Łukaszewska ,
and Grzegorz Sinicyn 

Abstract The interaction of underlying organic soils with buildings and infrastructure is an important aspect of environmental engineering. Especially since these soils have a particularly important role in the ecosystem, as well as because of the great variety of their mechanical and permeability characteristics. This limit load study concerns the hypothetical situation of accidental direct foundation of a building on a layer of sands under which are peats (and the unconfined groundwater table). The analyzed case is a common situation in the vicinity of rivers and lakes, especially in areas with high urban pressure. In the calculations, the finite element method (FEM) was used to model the strip foundation of a residential building in a plane strain approach. The peat parameters were derived from various literature analyses of different locations (specifically from Poland, Nederland, and Turkey,) to provide a range of possible soil failure load scenarios. This type of analysis identifies the most undesirable variant and gives an idea of the scale of the issue.

Keywords Organic soil · Building foundation · FEM · Shear strength · Stress state

1 Introduction

Environmental concerns on the one hand and urban pressures on the other cause interactions which, without analysis, result in ecological damage and engineering constructions. To achieve sustainable development, it is very important to carry out even preliminary analyses which enable crucial risks to be identified. One of such risks is the danger of exceeding the bearing capacity of the ground, or even too large settlements causing the inability to exploit. Based on the results of a pre-linear analysis it is possible to customize the following detailed studies (and optimize their financial costs of them).

Ł. Kaczmarek (✉) · M. Grodzka-Łukaszewska · G. Sinicyn
Faculty of Building Services, Hydro and Environmental Engineering, Warsaw University of
Technology, Warsaw, Poland
e-mail: lukasz.kaczmarek@pw.edu.pl

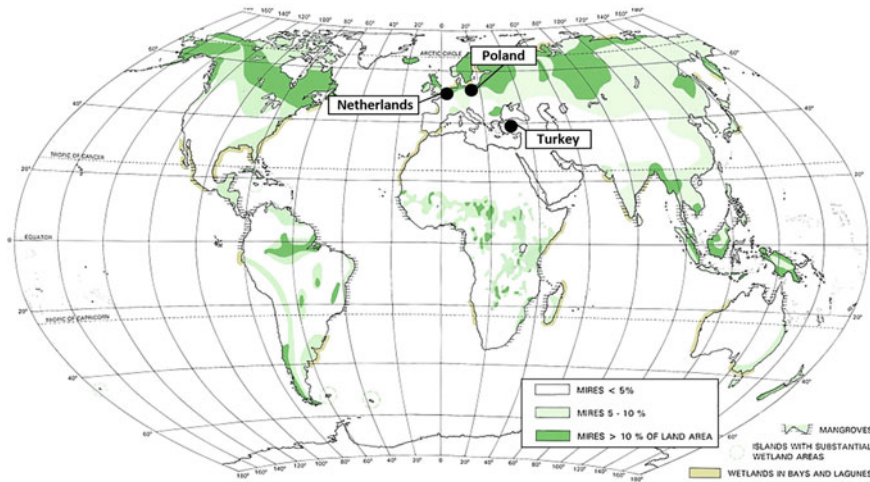


Fig. 1 Peats locations of used archival studies on the background of peatlands distribution (modified from [1])

An example of above would be housing buildings accidentally placed on weak peat soils. These soils are mostly located in wetlands, where there is also the problem of high groundwater table. Figure 1 shows area where peatland might be an issue in described context what gives some overview of the issue scale. This map shows selected peatland locations characterized in the literature (Poland, Netherlands, Turkey), which geotechnical parameters were used in this study to demonstrate the building foundations on peatlands failure loading hazards.

The objective of this limit load study by rough and non-sublime numerical calculations is to demonstrate the consequences of poorly designed or accidental foundations on peats.

2 Material Model

A model consisting of a direct foundation of a building on a layer of sands under which are peats (Fig. 2) was used to perform comparative numerical calculations. Below peat there are alluvial sands. The unconfined groundwater table is on the top surface of peat layer. Four variants of this model were considered, differing in parameters of 1 m peat layer. There were used 3 sets of peat parameters defined in 3 different publications referring to three different areas of analysis—Poland, the Netherlands and Turkey. The fourth variant concerned a model where in place of peat layer a layer of medium sands #1 was introduced. Thanks to this a reference point was obtained.

The analyzed study reflected one of the cases which occurred in the area adjacent to a lake and a small watercourse—i.e. construction of a building, where the foundation

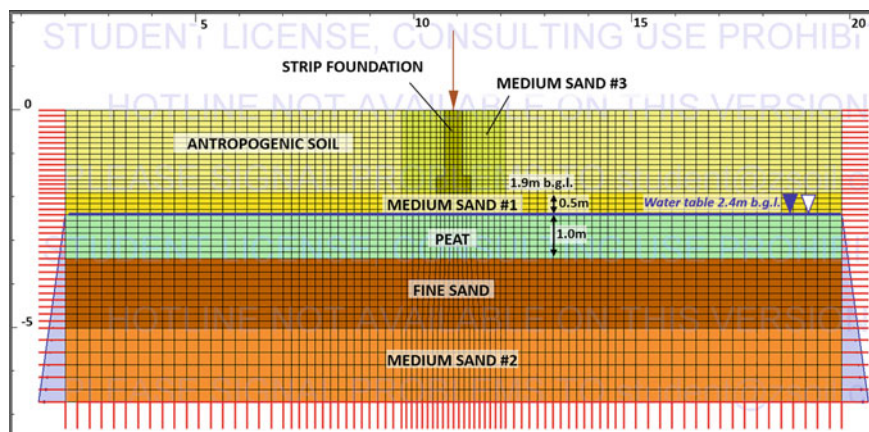


Fig. 2 Numerical model of analysed case study

level was located on sands below the layer of anthropogenic soils. As it turned out later, these sands were only 0.5 m thick, and under them there was a 1 m thick layer of peat. Thus, from the assumed not the worst ground conditions, it appeared that the building was located in complex conditions. This situation became the inspiration for this study, in order to illustrate the possible exceeding of the load-bearing capacity.

The model in the topic assumed a footing depth of 2.9 m below ground level, where the footing width was 0.8 m. In the footing excavation, the input of #3 medium sands was reconstructed.

Peats are soft organic soils, which geotechnical parameters are strongly varied, making difficult their characteristics, improvement or removing. For this reason, in this study three exemplary sets of peat parameters were selected (Table 1), which were used to carry out calculations of soil limit load in the situation of accidental direct foundation on peat. Their geotechnical parameters were derived from various studies in different locations (Poland, Netherland and Turkey) to provide a range of possible failure loading scenarios.

3 Methods

In the calculations, the finite element method (FEM) by Zsoil v.2018 software was used to model the strip foundation of a two-story residential building in a plane strain approach. That simplified limit load analysis of rigid footing problem has been done with use of Coulomb-Mohr model for soils (the yield criterion) and elastic model for foundation. The applied model is an elastic perfect plastic material model. The soil is regarded as an ideal elastic-plastic material and the associated flow law is adopted. The widely known set of parameters for the CM model contributes to the popularity of this type of preliminary analysis and estimation. The material models used were

Table 1 Materials parameters of geotechnical layers

No	Soil type	Bulk density, γ [kN/m ³]	Angle of internal friction, ϕ [°]	Cohesion, c [kPa]	Young's modulus, E [MPa]	Poisson ratio, ν [–]	Hydraulic conductivity, k [m/day]
1.1	Localization of exemplary peat characteristics	13.0	18.0	10.0	2.00'	0.37	5×10^{-4}
1.2		11.0	25.0	1.4	1.34*	0.26	1.6×10^{-2}
1.3		11.4	16.2	1.6	2.75	0.30^	9×10^{-6}
2	Antropogenic soil	17.0	30.0	0.0	34	0.27	1
3	Medium sand #1	18.5	33.0	0.0	85	0.25	0.5
4	Fine Sand	19.0	31.0	0.0	55	0.30	0.1
5	Medium sand #2	20.0	33.5	0.0	95	0.23	0.4
6	Medium sand #3	20.0	34.0	0	100	0.24	0.45
7	Concrete	25.0	–	–	30,000	0.20	0

applied as a rough initial approach of limit analyses. For more detailed analyses it is necessary to use large deformation continuum approach (due to significant finite elements geometry changes; [5]). Moreover, in order to carry out complex bearing capacity and serviceability analysis, the mentioned model cannot be used due to its limitations. Then, dedicated models of soft soils are necessary [4, 7, 8].

The mesh of the analyzed problem contained 3698 regular 4-noded elements (mainly rectangles). In this FE model standard box-type solid boundary conditions were generated. The hydrostatic pressure distribution was applied along define flow boundaries on model sides (Fig. 2). It was done through the pressure head value with special seepage elements. The axial loaded rigid strip footing is related to interfaces.

The numerical calculations included excavation, insertion of the footing along with sand filling, and then application of the force. The force was increased gradually until the loading limit was exceeded. The analysis of the results focused on comparing the maximum loads applied to the footing model, the corresponding stress distributions in the soil medium (especially the stress values affecting the peat layer), and the resulting failure surface.

4 Results

The most important reaction of the subsoil to the new load application is the loss of bearing capacity or settlement in case of not exceeding it. Therefore, the basic deliverables of this study are values of limit loads—Table 2. The highest values of limit load correspond with the highest values of cohesiveness which are characteristic of chosen studied peats in Poland. These soils do not have the highest value of internal friction angle. The highest value of friction angle was found for soil from the Netherlands—the maximum force, in this case, was 34.5 kN per 1 m of footing lower than in the parameters variant of soil from Poland. The lowest parameters were characteristic for the selected soils from central Turkey. As a result of such values of shear strength parameters, the difference in limit load was about 50 kN per 1 m of footing. The obtained load capacity results were 4–5 times lower than in the case of the assumed profile, in which there would be no peats (presence of fine sands only).

The obtained values of limit load were determined by the distribution of effective additional stress at maximum load. At the level of peat top surface, in the case of soils from Poland, it was about 90 kPa. In the case of soils from the Netherlands

Table 2 Limit loads calculation results

No	Localization of peat parameters archival case study	Limit load, Q [kN]
1	Poland	199.7
2	Nederland	165.2
3	Turkey	153.7
4	No peat case (MSa #1 parameters instead)	786.8

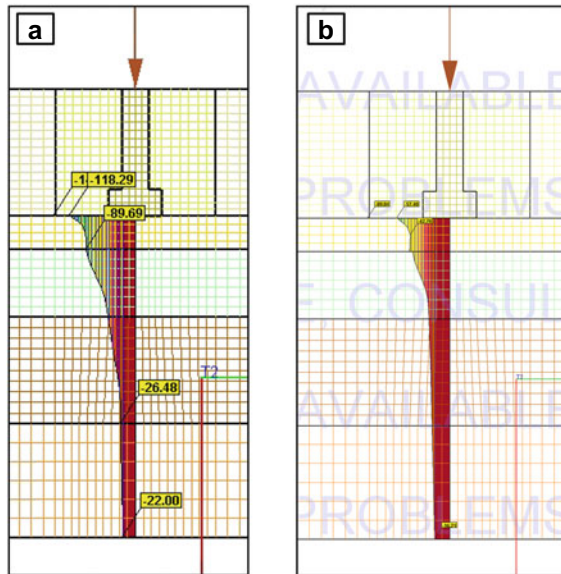


Fig. 3 Effective additional stress due to external limit loading in function of depth: **a** profile with geotechnical parameters of peat from Poland; **b** profile with geotechnical parameters of peat from Netherlands

and Turkey, the values of additional stress were over two times lower and equalled about 40 kPa (Fig. 3). On the receive bearing capacity of analysed soft soil, not only do soil strength properties have an impact, but also influence soil stiffness and their bulk density [5].

Analyzing the failure load results (Table 2) the load from the weight of the foundation itself was also taken into account (in the analyzed cases 53,2 kN of additional load). Thus, for example in case of peats from Turkey, where the lowest values of limit load were obtained, juxtaposing this value to the result of constant increase of axial force (100,5 kN per meter of footing), this load was approx. 50%.

The results confirm the key role of compressibility of peats (Fig. 5)—both from the physical perspective and further settlements as well as from the numerical perspective, where large deformations of finite elements occur (Fig. 4).

In this short paper, the immediate effects of exceeding or not exceeding the ultimate limit state are analysed, keeping in mind that in the case of organic soils (here peats) long-term settlements causing exceeding the serviceability limit state are a serious concern. In the case of a comprehensive analysis of the issue, calculations of short-term settlements as well as those developing in time are essential.

The described situation should be avoided by performing soil replacement or indirect foundation on a proper subsoil. However, if in case of residential buildings one can try to avoid the considered accidental foundation on peats (increasing reliable of ground investigation by drilling to several meters below the foundation level and

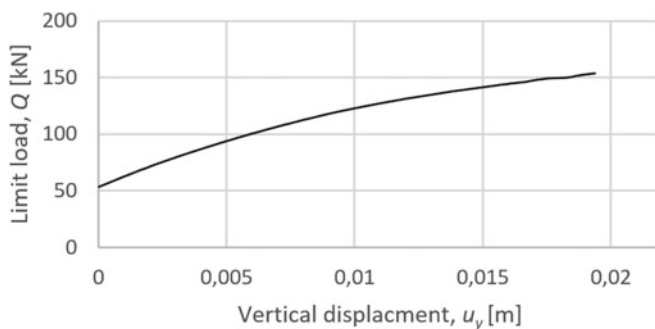


Fig. 4 Loading in Turkey peat parameters case

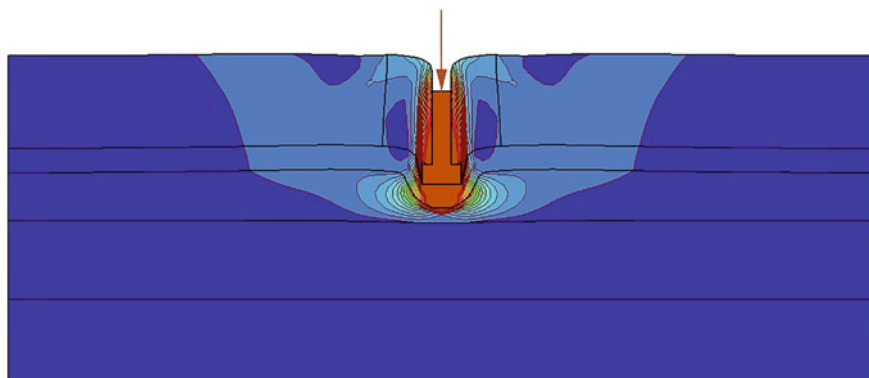


Fig. 5 Effect of soil displacement due to exceeding the ultimate state

choosing the optimal location), then for example in case of communication constructions of not too high rank, they can cause big difficulties in long-term exploitation. In case of realization of the investment and finding the problems caused by occurrence of peats, the main method of ground reinforcement are injections (associated with higher costs).

5 Conclusions

Peats are soft organic soils which geotechnical parameters are highly variable, making them difficult to strengthen and use in construction. In engineering practice in regions where organic soils such as peats may be present, it is worthwhile to carry out variant calculations of bearing capacity in case of unexpected occurrence of weak soils shallow under the layer of mineral soils. Therefore, it is very important to have a good knowledge of the strength, stiffness, and filtration characteristics of

such soils up to several meters below the foundation level. The effect of bad-scenario situations maybe even 5 times lower limit loads of soil. In the case of full geotechnical engineering analyses of ultimate and serviceability limit states, they provide the possibility to adjust the proper reinforcement method for failure-free exploitation of building objects.

Acknowledgements The study results presented in the article were carried out thanks to funding from the Dean's grant obtained at the Faculty of Building Services, Hydro and Environmental Engineering Warsaw University of Technology and co-financed by the Norwegian Financial Mechanism 2014–2021 (GRIEG FORCE research grant: 2019/34/H/ST10/00711).

References

1. Lappalainen E (1996) Global peat resources. The International Peat Society, Jyskä
2. Dłużewski JM (1997) Hydro-Geo: finite element program for geotechnical, hydro and environmental engineering. PW, Warszawa
3. Dłużewski JM, Popielski P, Sternik K, Gryczmański M (1999) Modelling of consolidation in soft soils. In: Proceedings of the 7th international symposium on numerical models in Geomechanics, NUMOG VII, pp 569–572. Balkema, Rotterdam
4. Papadaki E (2013) Modelling of peat compressed under sand bodies: experimental and numerical approach. TUD, Delft
5. Teunissen H, Zwanenburg C (2017) Modelling strains of soft soils. *Procedia Eng* 175:165–174
6. Ulusay R, Tuncay E, Hasancebi N (2010) Geo-engineering properties and settlement of peaty soils at an industrial site (Turkey). *Bull Eng Geol Environ* 69:397–410
7. Wheeler SJ, Näätänen A, Karstunen M, Lojander M (2003) An isotropic elastoplastic model for soft clays. *Can Geotech J* 40:403–418
8. Den Haan EJ, Kruse GAM (2007) Characterisation and engineering properties of dutch peats. In: Proceedings of the 2nd international workshop of characterisation and engineering properties of natural soils, pp 2101–2133. Balkema, Rotterdam

Interaction of Laterally Loaded Free Head Barrette Pile in Elastic Soils



Yasar Taner and Gurkan Ozden

Abstract Barrette piles are usually preferred over circular piles where larger bearing capacity, stiffness, and structural capacity are needed. Currently, design work with such piles is usually made assuming an equivalent circular pile diameter. Previous research did not cover pile-soil-pile interaction among piles with rectangular sections. In this study, the soil is assumed as elastic and the three-dimensional nature of the problem necessitated the establishment of 3D numerical analysis models. Piles are modeled as volume elements so that shape effects are properly studied. In this respect, the effects of cross-section and orientation of piles, spacing between piles, stiffness of the soil, and the magnitude of the loading were investigated on the behavior of group barrette piles. Considering these effects, interaction factors were calculated for different pile orientations in a group. Since barrette piles have rectangular cross-sections, the most important factor in their interaction with each other is the resistance of pile on the direction along which the load is acting on the pile. Circular and barrette group piles have been analyzed under horizontal loads. Analyses results showed that unlike circular piles, which have an equal moment of inertia in all directions the barrette piles were highly affected by loading direction and their orientation inside the group. This study emphasized that it is critical to determine the disposition of the piles considering the loading direction if less interaction among piles is desired.

Keywords Interaction factor · Barrette pile · Elastic soil · Pile orientation · Pile-soil-interaction interaction

Y. Taner (✉)

Graduate School Student, Natural and Applied Sciences Institute, DEU, Izmir, Turkey
e-mail: taner.yasar@ogr.deu.edu.tr

G. Ozden

Department of Civil Engineering, DEU, Izmir, Turkey
e-mail: gurkan.ozden@deu.edu.tr

1 Introduction

Foundations that transfer structural loads to deeper soil layers are rarely designed with single piles. The interaction between a single pile and surrounding soil is relatively simpler than pile groups since complex interaction patterns exist among the piles and the soil inside a group.

Pile-soil-pile interaction has long been studied since the late sixties and early seventies. The pioneering work is attributed to H. G. Poulos, who studied interaction among group piles under vertical and lateral loads [5–7]. Following Poulos, contributions to the field were also made [1, 3, 8]. Kaynia and Kausel [2] extended Poulos' approach to dynamic loading conditions.

Previous research did not fully cover pile-soil-pile interaction among piles with rectangular sections. Currently, design work with such piles is usually made assuming an equivalent circular pile diameter. In this study, findings of finite element-based research are presented regarding the influence of loading direction, pile spacing, and the position of a pile in the group on pile-soil-pile interaction. The three-dimensional nature of the problem necessitated establishment of 3D numerical analysis models. Piles are modeled as volume elements to study shape effects appropriately.

2 3D Numerical Analyses

Pile groups consisting of 3×3 piles with rectangular cross-sections are subjected to finite element modeling in this study. The finite element model comprises three-dimensional 10-noded wedge elements to discretize the volume piles and the soil profile. The aspect ratio of the pile cross-section is set as $L/B = 3.5$, where L and B stand for length and width of the pile section, respectively. This assumption is based on the fact that barrette piles are usually constructed with $L = 280$ cm and $B = 80$ cm sectional dimensions. Only very deep super piles attain plan width that is $B \geq 100$ cm.

In numerical analysis, two-layer profile is considered for barrette piles where stiffness of the upper layer was one half of that of the bottom layer. The thickness of the upper layer (h_1) is 10 m and the total thickness of the soil profile (h) is 40 m. Both soils are assumed to exhibit linear behavior under pile head lateral loading. The elastic soil parameters assigned to the soil layers of the model is shown in Table. 1.

The auto-meshing algorithm of the FE analysis software [4] is utilized while establishing the 3D-FEM model. The pile length to diameter ratio is kept equal to $L_{\text{pile}}/B = 25$ throughout the analyses. A 3D view of the model with solid piles is

Table 1 Elastic model parameters

E (kN/m ²)	γ_{unsat} (kN/m ³)	γ_{sat} (kN/m ³)	N
30,000	17.0	19.8	0.3/0.5
60,000	19.0	20.6	0.3/0.5

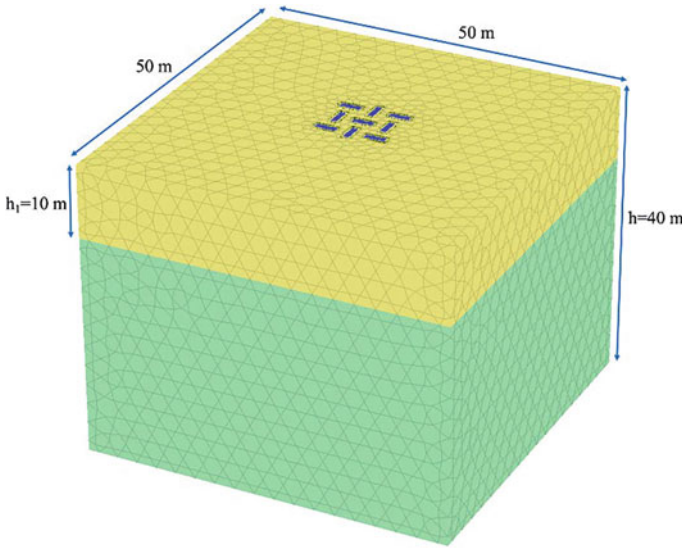


Fig. 1 FEM mesh for 3 × 3 barrette pile group (10-noded 31,028 elements)

shown in Fig. 1. It can be seen in this figure that the piles are positioned orthogonal to each other in the model.

The edge-to-edge orthogonal distance, s , between any two consecutive piles changes in direct proportion to the plan width of the pile (i.e. $s = 2B - 8B$). Each pile is horizontally loaded at the head in both x and y directions.

Poulos’ theory is based on some assumptions. First of all, the pile is assumed to be a thin rectangular vertical strip of width d , length L with a constant flexibility $E_p I_p$. It is also assumed that the pile and soil are fully compatible, ignoring the relative motion of the pile and soil. The soil is assumed to be elastic. The side shear, which is expected to be quite influential on lateral pile response for rectangular cross-sections, is not accounted for in Poulos’ solution. Interaction factor is defined according to Poulos as in Eq. (1):

$$\alpha = \frac{\text{Additional displacement caused by adjacent pile}}{\text{Displacement of pile under its own load}} \tag{1}$$

The source pile was loaded by means of a distributed lateral load at the pile head with a magnitude of 100 kPa for an 80 × 280 barrette pile. Interaction factors are determined depending on pile orientation for rectangular cross-sections since loading the piles along their strong or weak axis would generate different effects on adjacent piles (Case-1 and 2). In Case-1 and 2, the source piles interact with each neighboring pile, and the amount of interaction varies depending on the position of each receiver pile, as shown in Fig. 2. The source and receiver piles in similar positions with respect to the loading direction are linked to the source pile with the same color.

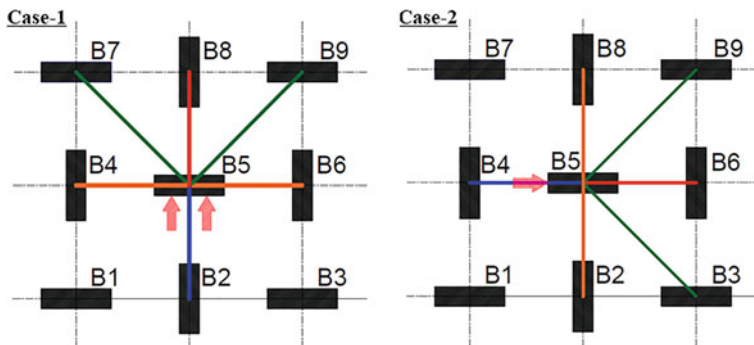


Fig. 2 Case-1 (loading along weak pile axis), and Case-2 (loading along strong pile axis)

Analyses revealed that the location and orientation of the receiver pile with respect to the source played an essential role on the lateral interaction factors. It was found that whether the strong axis of the receiver pile was parallel or perpendicular to the loading direction made the largest difference in pile response. While investigating the influence of pile position, it was noticed that the piles behind and in front of the receiver yielded same interaction factors irrespective of the pile spacing. Similar response existed for other pile pairs (i.e. B4 & B6; B7 & B9). This behavior may be attributed to the elastic nature of the soil medium and full bonding assumed between the soil and the pile.

Poisson's ratio affected pile response, albeit minor, causing larger lateral deformations resulting in larger interaction factors at the edge piles of the group. Interaction factors are plotted as a function of pile spacing and Poisson's ratio in Figs. 3 and 4 for Case-1 and 2, respectively. Figures 3 and 4 show that the piles are clustered as leading-trailing and side piles with respect to the central one (B5) on which the load is applied. It may be concluded upon elastic analyses that the orientation of the source pile or the piles positioned around the source is the dominant factor. For instance, if the source pile is loaded along its strong axis, its displacement decreases as compared with other direction resulting in higher interaction factors as shown in Fig. 4. This is also true for the receiver piles indicating that the bending stiffness governs pile response.

The interaction factors computed for 3×3 circular and barrette pile groups are compared in Figs. 5 and 6. It should be mentioned that the edge-to-edge spacing between two piles in a group is the same for both cases. It has been stated above that the interaction between the barrette piles varies according to the position of the pile just in front of the loaded pile. The authors found that in the analyses made with circular piles that have a sectional area equivalent to those of the barrettes, loading direction did not affect the interaction between the circular piles since they have the same inertia in all directions. It is clear from Figs. 5 and 6 that Case-1, in which the receiver pile was loaded along the weak axis, yielded lower interaction factors.

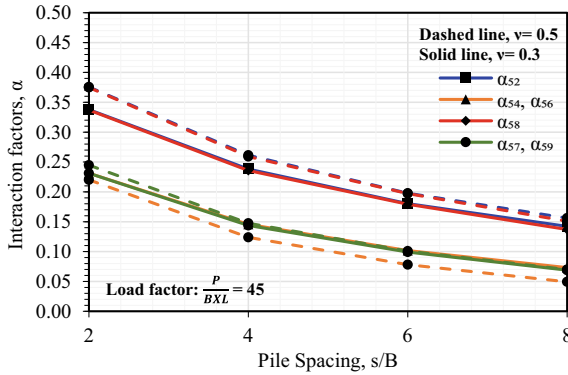


Fig. 3 Interaction factors between source pile B5 and receiver piles with different Poisson ratio in Case-1

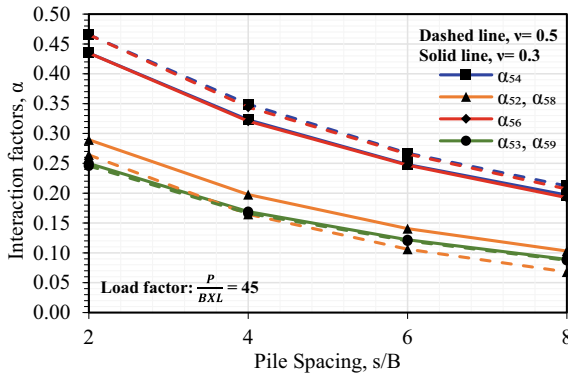


Fig. 4 Interaction factors between source pile B5 and receiver piles with different Poisson ratio in Case-2

The authors believe that the receiver pile exhibited larger displacement causing lower computed factors according to Eq. (1). In Case-2, however, the source pile has larger stiffness in the loading direction experiencing smaller displacement leading to higher interaction factors. Another aspect of barrette and circular pile group comparison is that the flexibility matrix is no longer symmetric for barrette piles whereas it is the opposite for circular piles. It may be concluded that what matters in elastic three-dimensional pile group analyses is the relative stiffness between the source and receiver piles.

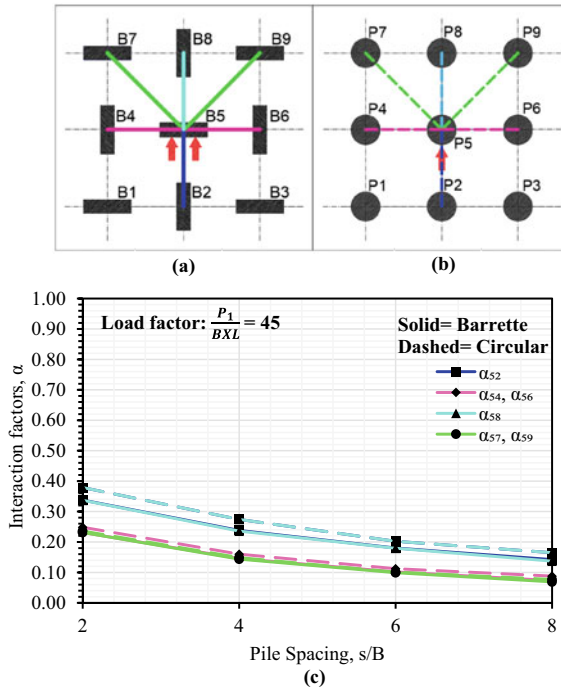


Fig. 5 a y-direction loading of barrette pile group, b y-direction loading of circular pile group, c Comparison of interaction factors for circular and barrette piles in y-direction loading

3 Conclusions

In this study, the pile-soil-pile interaction aspects of horizontally loaded barrette piles were studied based on numerical analysis models. While establishing the models, orientation and spacing of the piles in a group were set as basic variables. A 3×3 pile group was considered as the smallest possible unit cell in which orthogonal pile pairs are represented. among the pile head loading. Double layer soil profile was studied, and analyses were conducted assuming linear soil response. Besides, the piles were set as free head in a group. Following are the achieved results and recommendations for further studies.

Since barrette piles have rectangular cross-sections, the most critical factor in their interaction is the pile’s potential in resisting the induced displacement along the loading direction. This potential is found to be strongly related with the pile’s bending stiffness. Considering that the interaction factor between any two piles is defined as the ratio of the displacement of the receiver pile to that of the source pile (i.e. the head loaded pile), the pile that resists the loading with its stronger axis greatly affects the value of the interaction factor. This influence is prominent for cases where the receiver pile resists the loading with its stronger axis. Therefore, it can be said that

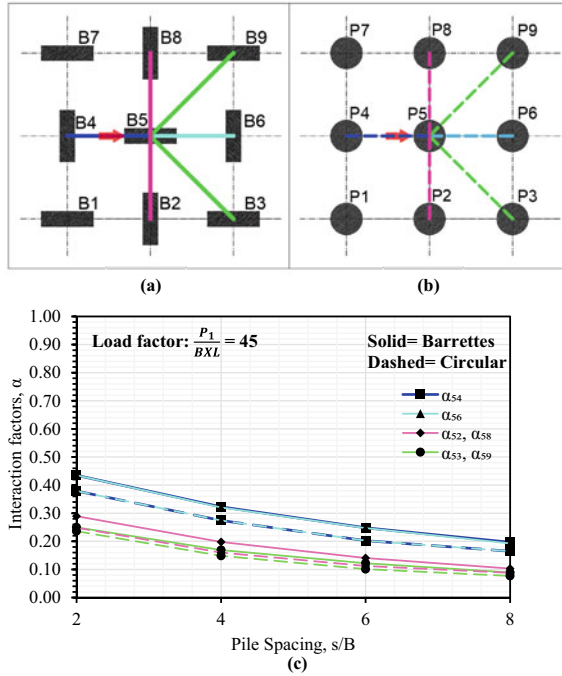


Fig. 6 **a** x-direction loading of barrette pile group, **b** x-direction loading of circular pile group, **c** Comparison of interaction factors for circular and barrette piles in x-direction loading

piles’ orientation in a group is one of the critical factors for pile-soil-pile interaction. Comparing the response of the circular and barrette piles, it can be stated that groups with rectangular pile sections behave quite differently than circular piles. First of all, the stiffness matrix becomes asymmetric due to pile orientation. Circular piles in a group, on the other hand, yield always symmetric stiffness matrix for elastic soil conditions.

In addition to strong influence of the loading direction, it is believed that findings of elastic finite element analyses shed lights on further non-symmetric pile response in a group when soil nonlinearity is also accounted for. Consideration of nonlinear soil response is expected to be quite essential on determining lateral load–deflection curves (i.e. p-y curves) along the strong and weak axes of the barrette pile. The authors believe that pile head fixity will affect the pile group response and load share, and this effect will be better observed in nonlinear soil.

Sectional dimensions of the barrette piles are fixed at $L/B = 3.5$ in the research. L/B ratios other than 3.5 shall also be studied in future research to gain more insight on the influence of pile flexibility on pile-soil-pile interaction.

References

1. Banerjee PK, Davies TG (1978) The behaviour of axially and laterally loaded single piles embedded in non-homogeneous soils. *Geotech* 30(1):309–326. <https://doi.org/10.1680/geot.1980.30.1.88>
2. Kaynia A, Kausel E (1980) Dynamic stiffness and seismic response of sleeved piles. TRID Database. <https://trid.trb.org/view/162450>
3. Mylonakis G, Gazetas G (1998) Settlement and additional internal forces of grouped piles in layered soil. *Geotech* 48(1):55–72. <https://doi.org/10.1680/geot.1998.48.1.55>
4. PLAXIS 3D (2019) Geotechnical engineering software. Plaxis BV, Delft, Netherlands. <https://virtuosity.bentley.com/product/plaxis-3d>
5. Poulos HG (1968) Analysis of the settlement of pile groups. *Geotech* 18(4):449–471. <https://doi.org/10.1680/geot.1968.18.4.449>
6. Poulos HG, Davis EH (1980) Pile foundation analysis and design book, Chapter 7–8. Wiley
7. Poulos HG (1979) Group factors for pile-deflection estimation. *J Geotech Eng Div, ASCE* 105(12):1489–1509. <https://doi.org/10.1061/ajgeb6.0000902>
8. Randolph MF, Wroth CP (1979) An analysis of the vertical deformation of pile groups. *Geotech* 29(4):423–439

Environmental Preservation, Water, and Energy

Influence of Thermal Cycles on the Volume Change of Ulexite Added Sand-Bentonite Mixtures



Sukran Gizem Alpaydin and Yeliz Yukselen-Aksoy

Abstract Bentonite and sand-bentonite mixtures are recommended as engineered barriers. In waste disposal facilities, especially radioactive waste, a significant temperature increase occurs. The engineering properties of sand-bentonite mixtures change depending on temperature. Sand-bentonite mixtures used as buffer material should be able to maintain their properties unchanged at high temperatures and under thermal cycles. In the present study, the volumetric deformation behavior of sand-bentonite mixtures containing 10% bentonite was investigated under room temperature and thermal cycles. In addition, ulexite, one of the boron minerals known for its high resistance to high temperature and low thermal expansion coefficient, was added to these mixtures at rates of 10 and 20% by dry weight. The compression-swelling behavior of ulexite added sand-bentonite mixtures under room temperature and thermal cycles was investigated. According to the results of the present study, when ulexite was added to the sand-bentonite mixture, the compression amount increased at room temperature, while the swelling amount decreased. However, the total compression amounts were reduced by half when thermal cycles were applied compared to the tests performed at room temperature.

Keywords Sand-Bentonite mixtures · Ulexite · Volume change · Thermal cycles

1 Introduction

Soils exposed to high temperature and temperature changes are an important topic to be investigated in geotechnical engineering. Soils surrounding energy geo-structures, which are exposed to long-term temperature changes, undergo thermal, hydraulic and mechanical changes during time. In order to prevent problems that may arise at the end of the long term, thermal, hydraulic and mechanical changes of the soil must be examined. For this, it can be determined how the soils will behave in the long term under high temperature with laboratory studies and numerical models.

S. G. Alpaydin (✉) · Y. Yukselen-Aksoy
Dokuz Eylül University, 35390 Izmir, Turkey
e-mail: alpaydin.sukrangizem@ogr.deu.edu.tr

© The Author(s), under exclusive license to Springer Nature Switzerland AG 2023
C. Atalar and F. Çinicioğlu (eds.), *5th International Conference on New Developments in Soil Mechanics and Geotechnical Engineering*, Lecture Notes in Civil Engineering 305, https://doi.org/10.1007/978-3-031-20172-1_16

Earlier studies on clayey soils were reported that volume of soils decreased at elevated temperatures in drained conditions [1–3]. In the study by Sinha and Kusakabe [4], the volumetric deformation of sand-bentonite mixtures at high temperature (up to 75 °C) was investigated. It was reported that the change in pore water pressure is temperature dependent under normally consolidated conditions. In other words, the void ratio changes with the temperature change [4]. While the volume of normally consolidated clays contracts with increasing temperature, the volume of over consolidated clays can even show expansion with increasing temperature [5, 6]. Plum and Esrig [7] observed a contraction in two clays with different plasticity at normally consolidated (NC) or low over consolidated ratio (OCR) condition. However, no volume change was observed in OCR = 1.7 [7] Baldi et al. [5] also showed that the transition between contraction and expansion increased when OCR = 2.5 at 58 °C [5].

Volumetric deformation of soils may cause damage around energy geo-structures. For that reason, additives can be added to buffer materials (bentonite/sand-bentonite) in order to minimize the damages that may occur. Boron mineral, which has low thermal expansion, can be considered as an additive material. Industrially important boron compounds are under the main grouping of borax (tincal, sodium-based boron compounds), colemanite (calcium-based boron compounds), ulexite (sodium-calcium-based boron compounds). Since boron reduces the expansion, it increases the resistance to thermal shocks. It also has an important place in the production of heat-resistant glassware and high-quality glasses to be used in electronics and space exploration, as it significantly reduces the thermal expansion of the boron glass, protects the glass against acid and scratching, and provides resistance to vibration, high temperature and heat shocks [8].

In the present study, boron mineral namely; ulexite, was added to 10% bentonite–90% sand mixture. Volume deformation of the mixtures was examined under room temperature (25 °C) and thermal cycle (25–80–25 °C).

2 Materials and Methods

2.1 Materials

In this study, sand-bentonite mixture and boron mineral, namely; ulexite, were used. The bentonite was a sodium (Na) containing bentonite with a high liquid limit value. The Na-bentonite was supplied from Eczacıbaşı Esan Mining Company. Ulexite was gathered from Eti Mining Operations General Directorate of Turkey. The sand was classified as well-graded (SW) according to the Unified Soil Classification System (USCS) [9]. The physico-chemical properties of the materials are summarized in Table 1.

The Na-bentonite and sand samples were used after drying for 24 h in the oven (105 °C). The sand and bentonite were used by sieving through No. 6 (3.35 mm) and

Table 1 Physico-chemical properties of the materials

	Sand	Na-bentonite	Ulexite
Specific gravity	2.63	2.70	1.98
Liquid limit (%)	–	476	33
Plastic limit (%)	–	70	25
Plasticity index (%)	–	406	8
pH	–	9.50	9.13
No. 200 (%)	1.64	100	100

No. 200 (0.075 mm), respectively. Ulexite was used in its natural water content (7%) as its structure changes with temperature. The natural water content of the ulexite was considered at the sample preparation.

2.2 Test Methods

The oedometer tests [10] were performed on additive-free sand-bentonite mixture (10% bentonite–90% sand and 10 and 20% ulexite added sand-bentonite mixtures (9B-81S-10U and 8B-72S-20U). The tests were conducted at room temperature (25 °C) and under thermal cycle (25–80–25 °C). The samples were prepared at the 2% wet side of the optimum water content and compacted in three layers in a ring. After the ring was placed in a water-filled cell, a seating pressure of 6.9 kPa was applied for 24 h. In the tests at room temperature, loading steps were applied as 24.5, 49, 98, 196, 392 and 784 kPa. After the consolidation was completed, the sample was unloaded to the vertical stress to 196 kPa and then to 49 kPa.

The oedometer test system was modified for thermal cycle tests. A specially designed heat ring was used to get high temperature and temperature control was provided using thermostat. A rubber membrane was placed on the cell to minimize evaporation. In addition, with low flow rate of water was provided to the cells from the water tank continuously, so that the water level would not decrease during the tests. Temperatures were controlled by means of K-type thermocouples.

Before the thermal cycle was applied, the test was performed at room temperature under the vertical stress of 196 kPa and then temperature was increased to 80 °C. As soon as the test reached equilibrium in terms of deformation, the temperature was reduced back to room temperature. When the compression/swelling behavior were over as a result of the thermal cycle, the vertical stress was increased to 392 kPa for ulexite added samples and to 785 kPa for additive-free mixture. Then, to examine the swelling behavior of the samples under thermal cycles, the stress was reduced to 196 kPa and thermal cycling (25–80–25 °C) was applied again.

3 Test Results

In the present study, oedometer tests of the sand-bentonite and ulexite-added sand-bentonite mixtures were performed at room temperature and under thermal cycle. The compression and swelling behavior of the samples were determined according to the test results. The compression curves of 10% bentonite–90% sand (10B-90S) mixtures in the presence of ulexite at room temperature are shown in Fig. 1. The amount of compression increased when ulexite was added to the 10B-90S mixture. The compression amount of the 10B-90S mixture increased from 6.6 to 8.1% in the presence of 10% ulexite, and to 12.4% with 20% ulexite.

It was seen that the amount of swelling decreased when ulexite was added to 10B-90S mixtures. The amount of swelling decreased to 1.14% in the presence of 10% ulexite and 1.09% in the presence of 20% ulexite. Increasing the amount of ulexite from 10 to 20% did not significantly change the swelling deformation amount.

The compression-swelling curves of ulexite added sand-bentonite mixtures under thermal cycles are presented in Fig. 2. The deformation amounts in the compression-swelling stages for ulexite added 10% bentonite samples under thermal cycling were almost the same and the values were very low. In other words, 9B-81S-10U and 8B-72S-20U mixtures did not show significant deformation under thermal cycling. However, compared to the tests performed at room temperature, the total compression amount was reduced by half. The samples, which were not very affected by the increase in temperature to 80 °C (0.1%), were slightly more compressed (0.4%) at room temperature.

The compression amount of sand-bentonite mixtures increased at room temperature in the presence of ulexite. The increase in fine content ratio may be the reason for this (sand-bentonite content was decreased as much as the percentage of ulexite).

When the behavior of ulexite added mixtures with the effect of thermal cycling was examined, the deformation amount decreased compared to the room temperature. Permanent deformation occurred during the compression phase when the cycle was

Fig. 1 Stress–strain curves of sand-bentonite mixtures in the presence of ulexite at room temperature

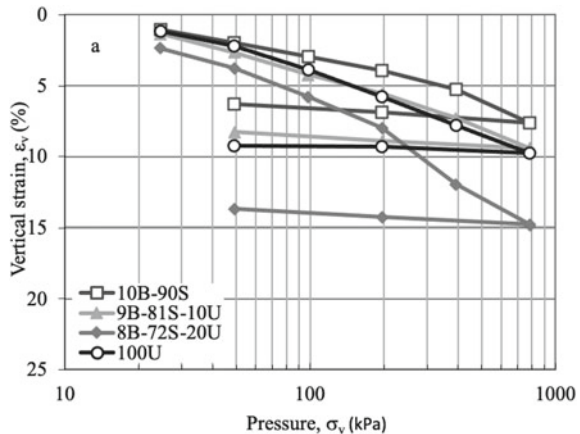
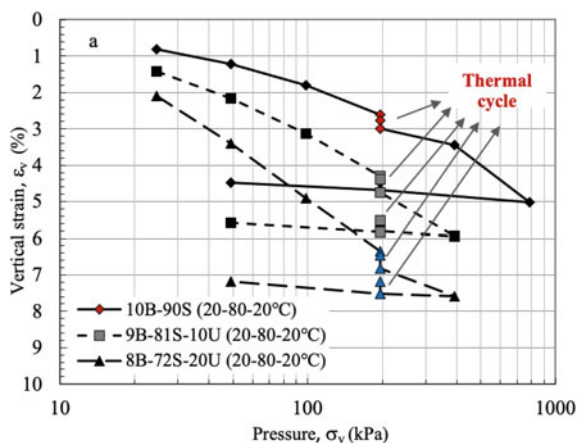


Fig. 2 Stress–strain curves of sand-bentonite mixtures in the presence of ulexite under thermal cycles



applied, and this behavior was not reversed by reducing the temperature. Paaswell [11] explained that under high temperature, the adsorbed water molecules move more easily from the diffuse layer, and when the water molecules ejected, the double layer thickness decreases, causing an irreversible volume reduction by approaching the clay particles [11].

4 Conclusions

In the present study, the volume deformation behavior of ulexite added sand-bentonite mixtures at room temperature and thermal cycles (25–80–25 °C) was investigated. Based on the results obtained, the following conclusions can be drawn:

1. The compression amount of sand-bentonite mixtures with the addition of ulexite increased significantly at room temperature.
2. The effect of ulexite on the compression amount of sand-bentonite mixtures under thermal cycles was negative (increasing) for 10B–90S mixtures.
3. The total compression amounts of additive free sand-bentonite mixture and ulexite added sand-bentonite mixtures under thermal cycles decreased compared to those at room temperature.
4. It was observed that ulexite additives reduce the swelling amount of sand-bentonite mixture under thermal cycles.
5. For boron added mixtures, vertical deformation continued when the temperature was increased to 80 °C under thermal cycling, and even the decrease in the void volume continued when the temperature was returned to room temperature. This indicates that high temperature causes irreversible deformation.
6. For the swelling stage, the deformation at high temperature was generally reversed by decreasing the temperature.

Acknowledgements This study is supported by The Scientific and Technological Research Council of Turkey (TUBITAK) (Grant no: 217M553). The authors are grateful for this support. The authors would like to thank 100/2000 The Council of Higher Education (YÖK) scholarship.

References

1. Campanella RG, Mitchell JK (1968) Influence of temperature variations on soil behaviour. *J ASCE Soil Mech Found Div* 94(SM3):709–734
2. Demars KR, Charles RD (1982) Soil volume changes induced by temperature cycling. *Can Geotech J* 19:188–194
3. Desideri A (1988) Determinazione sperimentale dei coefficienti di dilatazione termica delle argille. In: *Proceedings, convegno del gruppo nazionale di coordinamento per gli studi di ingegneria geotecnica sul tema: Deformazioni dei terreni ed interazione terreno-struttura in condizioni di esercizio*, vol 1. Monselice, Italy, pp 193–206
4. Sinha AN, Kusakabe O (2008) Temperature effects on volume change of bentonite-sand liner. *Aust Geomech J* 43:75–85
5. Baldi G, Hueckel T, Pellegrini R (1988) Thermal volume changes of mineral – water system in low-porosity clay soils. *Can Geotech J* 25(4):807–825
6. Romero E, Gens A, Lloret A (2001) Temperature effects on the hydraulic behaviour of an unsaturated clay. *Geotech Geolog Eng* 19:311–332
7. Plum RL, Esrig MI (1969) Effects of temperature on some engineering properties of clay soils. In: *Proceedings of an international conference on effects of temperature and heat on engineering behavior of soils*. Highway research board, Special Report 103 Washington, DC, pp 231–242
8. Özkan ŞG, Çebi H, Delice MD (1997) Bor minerallerinin özellikleri ve madenciligi. 2. Endüstriyel Hammaddeler Sempozyumu. İzmir, Türkiye, pp 224–228
9. ASTM:D2487–17 (2017) Standard practice for classification of soils for engineering purposes (Unified soil classification system). ASTM International, West Conshohocken, PA, USA, pp 1–10
10. ASTM D2435/D2435M–11 (2011) Standard test methods for one-dimensional consolidation properties of soils using incremental loading. ASTM International, West Conshohocken, PA, USA
11. Paaswell R (1967) Temperature effects on clay soil consolidation. *J Soil Mech Found Div* 93:9–22

Assessment of Climate Impact and Costs Comparing Two Railway Embankment Fill Methods



Ida Samuelsson, Johan Spross, and Stefan Larsson

Abstract Emissions from infrastructure projects and construction projects have a large impact on the environment. Construction activities and materials, including geotechnical engineering works, account for a great share of that impact and the monetary costs of the projects. In railway projects, crushed bedrock is often used as fill material in the embankments, and less suitable soil is excavated and transported to a landfill causing emissions. Despite that, sustainability assessments are rarely made when comparing the crushed bedrock fill method with other alternative methods, when the geotechnical engineer is designing an embankment. This paper, therefore, shows how climate impact and monetary costs can be compared for two fill methods in a railway embankment in Sweden, namely crushed rock fill and fill made of cement-stabilized sandy till. A comparing life cycle assessment (LCA) of climate impact and a life cycle cost analysis (LCCA) of monetary costs were made for the two methods. Activities and materials used in the production and construction stages were assessed. The results show that the stabilized sandy till method had both a smaller climate impact and lower life cycle cost (LCC) than the crushed bedrock fill method.

Keywords Soil stabilization · Geotechnical engineering · Life cycle assessment · Life cycle cost analysis · Climate impact

1 Introduction

The amount of greenhouse gas (GHG) emissions in the atmosphere is rising [1]. The construction and real estate sector in Sweden accounts for about 11.7 billion kg CO₂eq, which corresponds to 21% of the total GHG emissions in Sweden in 2019 [2]. Globally the building and construction sector account for almost 40% of energy-related and process-related CO₂ emissions in 2018, 11% of which resulted from manufacturing building materials and products [3]. Geotechnical engineering is

I. Samuelsson (✉) · J. Spross · S. Larsson
Division of Soil and Rock Mechanics, KTH Royal Institute of Technology, Stockholm, Sweden
e-mail: idasam@kth.se

© The Author(s), under exclusive license to Springer Nature Switzerland AG 2023
C. Atalar and F. Çinicioğlu (eds.), *5th International Conference on New Developments in Soil Mechanics and Geotechnical Engineering*, Lecture Notes in Civil Engineering 305, https://doi.org/10.1007/978-3-031-20172-1_17

181

an important part of the construction and infrastructure sector, and foundation works require material such as concrete, steel, and fuel, which produces GHG emissions when produced and used. Despite that, assessments of environmental impact, e.g. Life Cycle Assessment (LCA), are rarely made in the geotechnical design stage. Samuelsson et al. [4] found only 24 papers including both LCA and geotechnical engineering works. For ground improvement, only five papers included executed LCAs and only three included a calculation of monetary costs using the method Life Cycle Cost Analysis (LCCA). Praticò et al. [5] used LCCA and developed a model to select stabilizer and stabilization techniques for subgrade soil for low-volume roads with the lowest Life Cycle Cost (LCC). Da Rocha et al. [6] compared different binder contents and densities for soil stabilization using LCA. Raymond et al. [7] compared five different ground improvement methods using LCA and LCCA. The published research often includes the use of LCA and LCCA to assess the environmental impact and LCC for different stabilizers or different soil improvement methods. The soil improvement methods are however rarely compared to other geotechnical methods for example replacement of soil masses, embankment piling, use of lightweight material etc. using LCA and LCCA.

This paper addresses this gap in research by using LCA to assess the climate impact and LCCA to calculate the costs of two different fill methods in a railway embankment: a conventional filling of crushed bedrock and a stabilized filling of sandy till. Both are two possible methods in the geotechnical design work.

2 Methodology

The assessments of the climate impact and life cycle cost concerned a part of the high-speed railway project New Main Lines run by the Swedish Transport Administration (STA). The methods used in the assessment, LCA and LCCA, along with the system boundaries are presented in this chapter.

2.1 *Studied Part of the High-Speed Railway Project “New Main Lines”*

The studied part of the high-speed railway project New Main Lines is 70 km between the two cities Hässleholm and Lund in Sweden. The project is in an early stage and no final route has been decided. The railway will in this part alternate between embankments and cuts along the current planned route because of the changes in ground elevation. The availability of crushed bedrock, which is often used as embankment fill material, is limited. Because of the lack of bedrock, the STA is considering stabilizing the current soil, a sandy till, and using it instead of crushed bedrock. The two

alternatives are evaluated regarding several aspects during the project. Two aspects, the assessments of climate impact and costs, are presented in this paper.

We analyzed the soil mass quantities along the part in Geokalkyl 3 for ArcMap 10.7.1, which is a software owned by the STA. This indicated a surplus of 480,000 m³ of sandy till. This soil would need to be removed from the project if an embankment with crushed bedrock fill were to be used and the amount of the surplus sandy till is therefore used in the LCA and LCCA in this paper. The density of the crushed bedrock is assumed to be 2200 kg/m³ and the sandy till 1700 kg/m³.

2.2 Life Cycle Assessment Method

The method LCA quantifies a product's or a process's potential environmental impact during its life cycle. The method is standardized in ISO 14040:2006 [8] and ISO 14044:2006 [9]. The core rules for construction products are stated in the European standard EN 15,804:2012+A2:2019/AC:2021 [10].

An LCA consists of four phases: (1) goal and scope definition, (2) life cycle inventory analysis (LCI), (3) life cycle impact assessment (LCIA) and (4) interpretation [8, 9]. In the goal and scope definition, the system boundary needs to be specified and a functional unit on which the calculations are based must be decided. In the LCI, the input and output data of the system are collected and calculated. During the LCIA, the output data from the LCI phase are multiplied by its corresponding emission factor to assign it to impact categories. The last phase is an interpretation where the results from the LCI and/or the LCIA are summarized and discussed. According to the European standard [10], a life cycle includes the stages and sub-stages: production (denoted A1–A3), construction (A4–A5), use (B1–B7) and end of life (C1–C4). This standardization makes LCA calculations similar to each other, which makes the interpretation of the results more credible.

For the LCA calculations in this paper, the software Klimatkalkyl version 7.0 and Microsoft Excel were used, and the result is presented in the unit kg CO₂eq.

2.3 Life Cycle Cost Analysis Method

The method LCCA quantifies a product's or a process's monetary cost during its life cycle. LCCA has no international standard on how it should be performed. It can differ between countries and projects. The analysis in this paper is performed according to the STA's guidelines [11]. The life cycle stages that are included in an LCCA are investment costs (corresponding to A1–A5 in the LCA), future operation and maintenance costs (corresponding to B1–B7 in the LCA), and external costs.

For the LCCA calculations in this paper, Microsoft Excel was used, and the result is presented in SEK (Swedish krona) where 1 euro corresponds to 10.5 SEK.

2.4 System Boundaries and Functional Unit

The functional unit is an embankment with a total volume of 480,000 m³. The embankment has a length of 7400 m, an average width of 19 m and a height of 3.4 m. The climate impact (CO₂eq) and monetary costs (SEK) are to be assessed.

The life cycle stages that were included in this LCA and LCCA calculations are the product stage (A1 Raw material supply, A2 Transport and A3 Manufacturing) and the construction stage (A4 Transport and A5 Construction-installation process). The use stage and end-of-life stage were not included. The activities and materials that are included within the system boundary are presented in Fig. 1 for the crushed bedrock alternative and Fig. 2 for the stabilized sandy till alternative.

Crushed bedrock method. The bedrock is extracted from quarrying (A1–A3) and the transport distances (A4) with lorries to the construction site are 15, 25, 25 and 35 km depending on which of the four nearest quarries is chosen. The fill stage (A5) requires an excavator that builds up the embankment. The compaction (A5) of the crushed bedrock is made in layers of 0.5 m thickness with 14 overruns, using a work machine Dynapac CA5000D [12]. The excess sandy till is excavated with an excavator and transported (A5) 50 km on lorries to a landfill (A5). We investigated the effect of the degree of contamination of the till by altering it in three degrees: uncontaminated, little contaminated, and very contaminated.

Stabilized sandy till method. The amount of cement (A1–A3) needed to stabilize the sandy till is assumed to be 4.5% based on the dry density of the soil [13]. The three cement types used in the calculations is Infracement CEM I 42.5 N-SR3 MH/LA, Miljøsement CEM II/B-S 52,5 N and Lavvarmesement CEM III/B 42,5 L-LH/SR (na). CEM I is a Portland cement, CEM II is a Portland cement with 30% blast furnace slag, and CEM III is a Portland cement with 64% blast furnace slag. The cement is

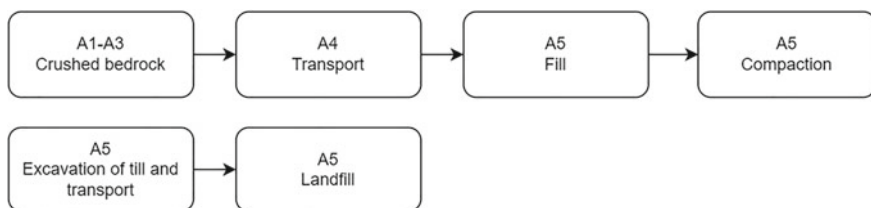


Fig. 1 The process for the crushed bedrock method. The top row shows the structuring of the embankment, and the bottom row shows the handling of the residual till

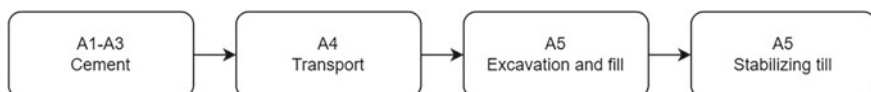


Fig. 2 The process for the stabilized sandy till method

transported (A4) 60 km from the factory in Malmö, Sweden, to the construction site. The excavation of the sandy till and construction of the embankment (A5) is assumed to take place close to each other, so no transport is included in this stage. For the stabilizing of the till (A5), the fuel consumption for all equipment used is 0.7 l diesel/m³ soil according to CimBeton [14]. The cost calculation for the stabilization assumes embankment layers that are 0.35 m thick.

3 Life Cycle Inventory Analysis (LCI)

The input data for the LCA and LCCA are taken from Environmental Product Declarations (EPDs), Geokalkyl, Klimatkalkyl or from experts when no other data is available and are presented in Tables 1 and 2. The output data is presented in Chap. 4. The two methods are assumed to take the same amount of time to complete. Therefore, there are no future cash flows to discount and the use of present values is not included in the calculations.

One emission factor (*EF*) and two conversion factors (*CF*) are related to fuel:

- $CF_{Transport} = \text{transport with lorries} = 2.5 \text{ MJ/tkm}, 43.25 \text{ MJ/liter diesel}$
- $CF_{Excavator} = \text{excavator} = 0.19 \text{ L diesel/m}^3 \text{ soil}$
- $EF_{Diesel} = \text{diesel} = 2.8 \text{ kg CO}_2\text{eq/liter diesel [15]}$.

Table 1 Emission factors, conversion factors and costs for the crushed bedrock method

Life cycle stage	Emission factors and conversion factor	Cost
A1–A3 crushed bedrock	0.004 kg CO ₂ eq/kg [15]	120 SEK/1000 kg [16]
A4 transport	$CF_{Transport}, EF_{Diesel}$	38 SEK/1000 kg (25 km) [17]
A5 fill	$CF_{Excavator}, EF_{Diesel}$	200 SEK/m ³ [17]
A5 compaction	EF_{Diesel}	22 SEK/m ² [17]
A5 excavation of till and transport	$CF_{Excavator}, CF_{Transport}, EF_{Diesel}$	250 SEK/m ³ [16]
A5 Landfill	0 kg CO ₂ eq/m ³ (uncontaminated) [16]	200 SEK/m ³ (uncontaminated)
	–	375 SEK/m ³ (Little contaminated)
	–	1250 SEK/m ³ (Very contaminated) [16]

Table 2 Emission factors, conversion factors and costs for the stabilized sandy till method

Life cycle stage	Emission factors and conversion factor	Cost
A1–A3 cement	817 CO ₂ eq/1000 kg (CEM I) [18]	–
	537.7 CO ₂ eq/1000 kg (CEM II) [19]	958 SEK/1000 kg (CEM II) [21]
	223.2 CO ₂ eq/1000 kg (CEM III) [20]	–
A4 transport	$CF_{\text{Transport}}$, EF_{Diesel}	90 SEK/1000 kg [22]
A5 excavation and fill	$CF_{\text{Excavator}}$, EF_{Diesel}	80 SEK/m ³ [17]
A5 stabilizing till	EF_{Diesel}	SEK/m ³ [17]

3.1 Crushed Bedrock Method Input Data

The emission factors and conversion factors and costs that are used are presented in Table 1. The amount of crushed bedrock in A1–A3, A4 and A5 Fill is 480000 m³ equivalent to $1056 * 10^6$ kg. The area of A5 Compaction is 984200 m² and the volume of sandy till in A5 Excavation of till and transport and A5 Landfill is 480000 m³. One unique cost is used for each of the three degrees of contamination in the A5 landfill.

3.2 Stabilized Sandy till Method Input Data

The emission factors and conversion factors and costs that are used are presented in Table 2. The amount of cement in A1–A3 and A4 is $36720 * 10^3$ kg. The volume of sandy till in the two A5 stages is 480000 m³. One unique emission factor is used for each of the three cement types in A1–A3.

4 Results

The climate impact and cost results, which are the output from the LCI, are presented in this chapter.

4.1 Climate Impact

The climate impacts of the two methods are presented in Fig. 3. The climate impact from the CEM III alternative is the lowest, $9.7 * 10^6$ kg CO₂eq, compared to the

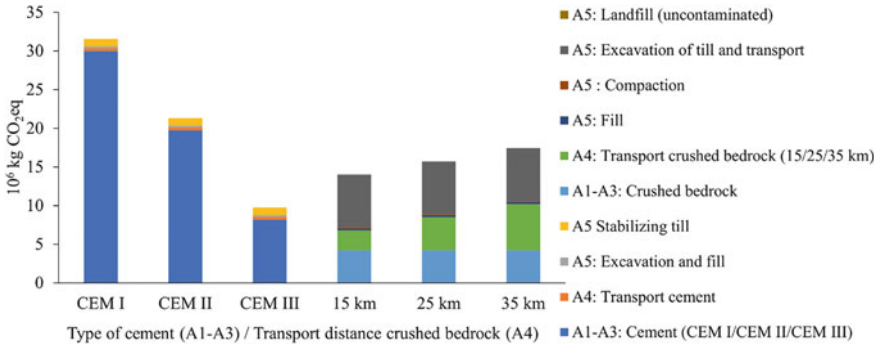


Fig. 3 The climate impact result from the LCA. The three cement stabilization method results on the left side and the three crushed bedrock method results on the right side

highest, CEM I, 31.6*10⁶ kg CO₂eq. For the crushed bedrock method, the result varies between 14 –17.4 * 10⁶ kg CO₂eq depending on the transport distance. The cement (A1–A3) accounts for 84–95% of the total climate impact of the stabilizing till method. For the crushed bedrock method, the highest impact comes from the crushed bedrock (A1–A3), the transport (A4) and the excavation of till and transport (A5).

4.2 Life Cycle Cost

The life cycle costs for the two methods are presented in Fig. 4. The cost of the CEM II alternative is the lowest, 159 million SEK, compared to the alternatives for the crushed bedrock method where the result varies between 500 and 1004 million SEK. For the stabilized till method, the highest cost comes from the actual stabilization of the till. For the crushed bedrock method, the cost is more evenly distributed over several activities, where the degree of contamination of the till affects the result significantly.

5 Discussion

The results in Figs. 3 and 4 indicate that the use of stabilized till instead of conventional crushed bedrock fill can reduce both the climate impact and costs from the production and construction stages. The assessments of the use and end-of-life stage are not included in this paper but can be added to get the total life cycle impact and

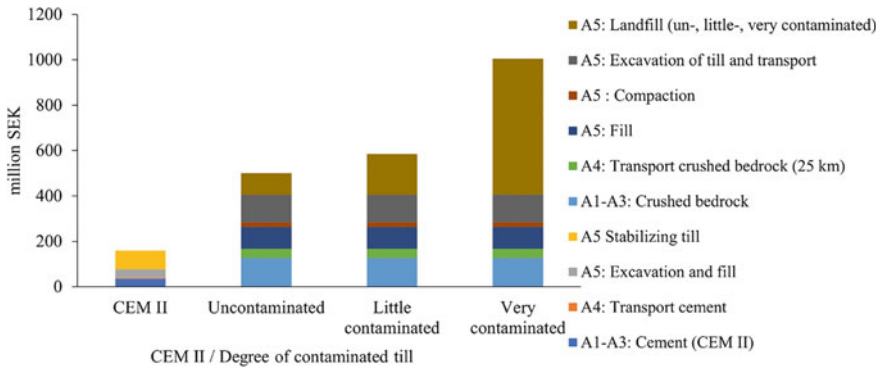


Fig. 4 The cost result from the LCCA. The one cement stabilization method result on the left side and the three crushed bedrock method results on the right side

cost which can affect the concluding results. The climate impact is lower for the CEM III regardless of available transport distances for the crushed bedrock in the project. If CEM III is not available, the crushed bedrock method will be a better choice regarding climate impact. The climate impact from materials and transport is the highest, so the designer should focus on those parts to reduce the climate impact if possible. The cost is the lowest for the stabilized till method: about 30% of the cost of the crushed bedrock method including uncontaminated till. As a general observation, we note that the input cost data can alter between manufacturer, location and over time which contributes to uncertainty in the results.

6 Concluding Remarks

This paper shows that assessing the climate impact and life cycle cost using LCA and LCCA is possible when comparing embankment fill methods. The geotechnical engineer designing railway embankments can, besides fulfilling the technical aspects, also choose the method, material and activities within these methods, based on their climate impacts and life cycle costs. This paper shows how an LCA and LCCA can be done by comparing two embankment fill methods, cement stabilized sandy till and crushed bedrock. The results from the LCA and LCCA can help the designer to make choices that reduce the climate impact and life cycle cost.

Acknowledgements The presented research was funded by the Sven Tyréns Foundation and the STA. Their support is gratefully acknowledged. Initial calculations were presented in a report by Tyréns Sverige AB [23]. They were in this paper further developed with more activities and a more detailed assessment and presentation.


References

1. IPCC (2018) Global warming of 1.5°C—An IPCC special report. In: Masson-Delmotte VP et al. (eds). Incheon
2. Boverket Homepage. <https://www.boverket.se/sv/byggande/hallbart-byggande-och-forvaltning/miljoindikatorer--aktuell-status/vaxthusgaser>. Accessed 9 Mar 2022
3. Global Alliance for Buildings and Construction, IEA and the UN Environment Programme (2019) 2019 global status report for buildings and construction: Towards a zero-emission, efficient and resilient buildings and construction sector
4. Samuelsson I, Larsson S, Spross J (2021) Life cycle assessment and life cycle cost analysis for geotechnical engineering: review and research gaps. In: IOP conference series: earth and environmental science, vol 710, no 1. IOP Publishing, p 012031
5. Praticò F, Saride S, Puppala AJ (2011) Comprehensive life-cycle cost analysis for selection of stabilization alternatives for better performance of low-volume roads. *Transp Res Rec* 2204(1):120–129
6. da Rocha CG, Passuello A, Consoli NC, Samaniego RAQ, Kanazawa NM (2016) Life cycle assessment for soil stabilization dosages: A study for the Paraguayan Chaco. *J Clean Prod* 139(2016):309–318
7. Raymond AJ, DeJong JT, Kendall A, Blackburn JT, Deschamps R (2021) Life cycle sustainability assessment of geotechnical ground improvement methods. *J Geotech Geoenvironmental Eng* 147(12):04021161
8. International Organization for Standardization (2006) ISO 14040:2006—Environmental management—Life cycle assessment—Principles and framework. Geneva
9. International Organization for Standardization (2006) ISO 14044:2006—Environmental management—Life cycle assessment—Requirements and guidelines. Geneva
10. European Committee for Standardization (2021) EN 15804:2012+A2:2019/AC:2021 Sustainability of construction works—Environmental product declarations—Core rules for the product category of construction products. Brussels
11. Swedish Transport Administration (2020) Stöd för arbete med livscykelkostnadsbedömningar och LCC-vid planering och projektering av vägar och järnvägar, v. 3.0 [Support for work with LCA and LCC-in planning and design of roads and railways]. Borlänge
12. Cramo Homepage. https://www.cramo.se/sv/category/anlaggning_valtar_envalsvalt/product/envalsvalt---16-ton-45-kg-cm-min.stat-linjelast-dynapacca5000d. Accessed 9 Mar 2022
13. Swedish Transport Administration: Data from Per Lindh, STA (2021)
14. CimBeton (2009) Comparative study in road engineering—Soil treatment vs unbound granular materials—Graphic method for environmental and economic comparison, T30
15. Swedish Transport Administration: Klimatkalkyl version 7.0
16. Tyréns Sverige AB (2021) Data from experts at Tyréns Sverige AB
17. Swedish Transport Administration: Geokalkyl 3 for ArcMap 10.7.1
18. Schwenk Sverige AB (2020) EPD—Infracement CEM I 42.5 N-SR3 MH/LA. Program operator: Næringslivets Stiftelse for Miljødeklarationer, Decl. No.: NEPD-2204-1015-NO
19. Cemex AS (2018) Cemex, Miljøsement, Cem II/B-S 52,5 N. Program operator: Næringslivets Stiftelse for Miljødeklarationer, Decl. No.: NEPD-1545-531-NO
20. Schwenk Norge AS (2020) Schwenk Lavvarmesement, Cem III/B 42,5 L-LH/SR (na). Prog. Op.: Næringslivets Stiftelse for Miljødeklarationer, Decl. No.: NEPD-2209-995-NO
21. Cementa (2021) Reference price for CEM II/A-LL 42,5 R
22. Cementa (2021) Reference price for transport from Malmö 60 km
23. Tyréns Sverige AB (2021) Höghastighetsjärnväg-Förstudie, Bankfyllning LCA/LCC-perspektiv, slutrapport [High speed railway—Early study, Embankment fill LCA/LCC-perspective, final report]

Modelling

Field Trial to Rapidly Classify Soil Using Computer Vision with Electric Resistivity and Soil Strength



Y. J. Eugene Aw , Soon-Hoe Chew, Yeow-Chong Tan, Pei-Ling Goh, Cheng-Soon Teo, Danette S. E. Tan, and Mei-Lin Leong

Abstract In Singapore, large volumes of excavated soils from the construction industry are sustainably re-purposed in land reclamation projects as fill material. The excavated soils are trucked to Staging Ground (SGs), where they are received and categorized into two broad groups (“Good Earth” and “Soft Clay”). The soil type categorization is traditionally done using properties such as particle size distribution (PSD) and water content (w). However, due to the heterogeneity of soils and non-uniform mixing during the excavation and truck loading process, the actual excavated soils in each truckload received at the SGs may vary. As such, visual checks of each truck are presently implemented at the SGs, which is labour-intensive and can be subjective. Therefore, an objective rapid classification method is required at the SGs. This can be achieved through an innovative system using computer vision complemented by in-situ probe measurement to perform non-destructive and instantaneous soil classification on-site. An accurate classification of excavated soils is critical in maximizing the recovery and reuse of natural resources in land reclamation projects for long-term sustainability. This paper presents the assessment of rapid soil testing methods that are suitable for integration with a recently developed novel rapid soil classification using computer vision. The objective of this complementary soil parameter measurement is to enhance the soil type prediction accuracy, as well as the capability to detect soil type with depth. The methods that are deemed suitable are the four-probe soil electrical resistivity measurement, cone penetration test (CPT) and moisture content test using time-domain reflectometer (TDR).

Keywords Computer vision technique · Cone penetration test · Electrical resistivity · Rapid and non-destructive · Soil classification

Y. J. Eugene Aw (✉) · S.-H. Chew

Department of Civil and Environmental Engineering, National University of Singapore, Queenstown, Singapore

e-mail: ceeayje@nus.edu.sg

Y.-C. Tan · P.-L. Goh · C.-S. Teo · D. S. E. Tan · M.-L. Leong

Building and Infrastructure Group, Housing and Development Board, Toa Payoh, Singapore

1 Introduction

1.1 Background

Staging Grounds (SGs) in Singapore performs two main roles—receiving excess excavated soil from construction sites, as well as supplying suitable fill material for land reclamation projects. Unwanted excavated soils are transported via dump trucks (Fig. 1) from construction sites to SGs located along the coast of Singapore. Subsequently, the soil is loaded onto barges and transported to land reclamation sites to be used as infill material. For proper use and appropriate treatment methods, the type of the excavated soils must be identified. With hundreds of trucks arriving at the SGs daily, SG operators are looking into ways to improve the quality of inspection and optimization of on-site operations in classifying soil received.

Excavated soils received at the SGs can be broadly classified into two groups, namely “Good Earth” and “Soft Clay”, despite the varying geologies over Singapore. Soil classification is made largely based on Particle Size Distribution (PSD) and water content. According to the SGs’ classification criteria, “Good Earth” soils contain at least 65% by weight of coarse particles ($>63 \mu\text{m}$) and water content of less than 40%. “Good Earth” soils generally have a higher percentage of coarse particles and relatively low water content.

On the other hand, soils categorized as “Soft Clay” have a higher percentage of fine particles, or a high water content, or both. These soils experience slow gain in shear strength and large settlement over time, requiring more costly ground improvement techniques to be effectively used as the infill material.



Fig. 1 (left) Excavated soil transported by dump trucks to the Staging Grounds, (right) Excavated soil loaded onto barges for transportation offshore

1.2 Current Classification Methods

Housing and Development Board (HDB) operates two Staging Grounds (SGs) in Singapore with daily throughput of thousands of truckloads. The current practice of soil classification primarily uses the borehole log information obtained before the excavation activities. After excavation, the excavated soil will be loaded onto trucks which were tagged with “Good Earth” (GE), or “Soft Clay” (SC) based on soil information obtained earlier. When truck arriving at the SGs, the weigh-bridge operator will perform a quick visual inspection of the soil in the truck via Closed-Circuit Television (CCTV) camera. In the case where the soil in the truck tagged with “Good Earth” label was found to have a visibly high water content, it would be downgraded to a “Soft Clay” soil.

The current practice fails to account for the highly varying geological formations in some parts of Singapore, and possible mixing of different soil types during the excavation activities on-site. Substantial amount of “Good Earth” soils may have been misclassified as “Soft Clay” soils. In this case, the relatively useful sandy soil that could have been used for revetment bunds were inefficiently utilized as general infill material, which is a waste of resources. On the other hand, there may be an occasion that “Soft Clay” was mistaken as “Good Earth” of which no treatment was conducted, which resulted in poor foundation and/or excessive settlement.

This calls for a need to improve the soil classification operation at the SGs. In addition, the current system is also very time-consuming and labour-intensive. Hence, a rapid in-situ soil classification method that is automatic, non-destructive and objective is explored for suitable use at the SGs. The research on the development of such method using non-destructive techniques was conducted on a near-full scale, and the initial version using computer vision technique was successfully developed [1].

2 Literature Review

2.1 Previous Research

In the first version of such rapid classification method, an Artificial Neural Network (ANN) model was established using back-propagation network tested with 40 soil samples collected from Tanah Merah Staging Ground (TMSG). It was found that the trained ANN model was able to differentiate between “Good Earth” and “Soft Clay” soils in less than a minute.

This has led to further research on using Grayscale Co-Occurrence Matrix (GLCM) textural features as inputs (Contrast, Correlation, Entropy), Generalized Delta learn rule and Sigmoid transfer function to refine the ANN model. A further 101 soil images and samples were obtained and used for training, which led to an improved version of ANN model. Comparing the predicted soil type against the actual soil type (determined by conventional laboratory testing), it was observed that

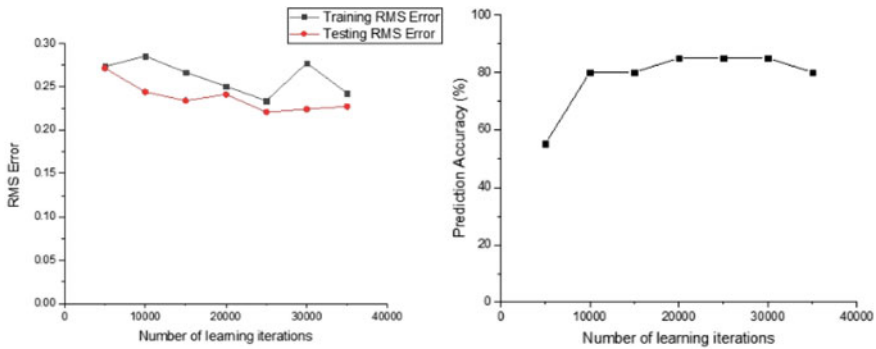


Fig. 2 Prediction accuracy using Improved ANN model developed in previous research

the optimal improved ANN model occurs at 25,000 learning iterations with an overall prediction accuracy of 85% on the selected representative soil images (Fig. 2).

However, this current improved version of the ANN model and its associated hardware system can only capture data of the top surface of the soil mass in the truck, and does not consider the variation of soil type with depth that may be possibly present beneath the surface. This paper presents a complementary scheme, that make use of additional soil parameters determined in-situ that can complement the computer vision system to obtain a better soil classification of soil at various depth in the truck. Apparent resistivity, moisture content and CPT strength were chosen to be possible soil parameters.

2.2 Apparent Resistivity

By Ohm' Law, the apparent resistivity of soil ρ (in a two-electrode soil box method) can be calculated based on the following Eq. (1):

$$\rho = \frac{V A}{I L} \quad (1)$$

where V = potential difference between two electrodes, I = current, and L and A are the length and area of the conducting cross section of soil. Wet to moist sand has a typical apparent resistivity of 20–200 Ωm , while that of clay ranges from 1 to 20 Ωm [2].

2.3 *Moisture Content*

Time-Domain Reflectometer (TDR) is an instrument which is capable to measure in-situ moisture content and provide results almost instantaneously. By sending out a fast-rise voltage pulse through the waveguides, wave propagation distance and speed are used to calculate the velocity of propagation, where the apparent dielectric constant can be derived. This apparent dielectric constant is subsequently used to estimate the volumetric moisture content drawn from a relationship supported by calibration data from numerous sources. A linear relationship was established, as shown in Eq. 2 [3], to relate volumetric moisture content, θ_v , and apparent dielectric constant, ϵ_{ra}

$$\theta_v = 0.115\sqrt{\epsilon_{ra}} - 0.176 \quad (2)$$

2.4 *Cone Penetrometer Test (CPT)*

Cone penetration testing (CPT) is a common soil profiling technique and is a quick and convenient testing method that may be suitable for rapid on-site soil classification. CPT is performed by inserting a cone into the soil mass. CPT tip resistance q_t is generally approximated by the cone tip resistance q_c at shallow soil depth [4] where pore water pressure is ignored, which is applicable in the context of this application where the expected measuring depth is <1.5 m.

3 *Methodology*

3.1 *Experimental Setup*

A series of tests were performed to investigate the feasibility of the three soil parameter determination (apparent resistivity, moisture content, CPT strength) in classifying soils at the SGs. The experimental setup mainly consists of a near-full scale soil box with metal and plywood walls measuring 180 (L) \times 1200 (W) \times 1200 mm (H) (see Fig. 3), sensors (discussed in further sections), soil mass filled up to a thickness of about 1000–1200 mm thick in the soil box, and a frame with actuators to push the sensors into the soil mass.

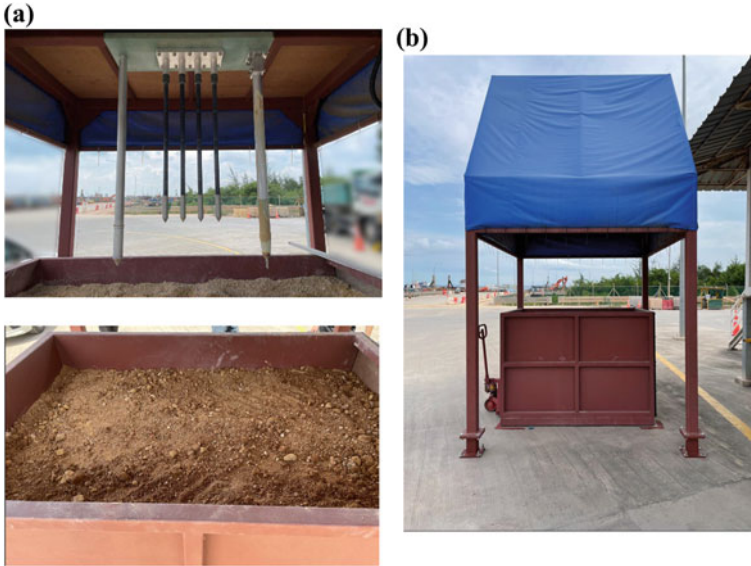


Fig. 3 a Test set-up sensors atop soil box b Test frame atop soil box

3.2 Apparent Resistivity Using Wenner's Array

Four electrodes were arranged with equal spacing, and current is passed through the outer two electrodes (A and B). Potential difference between the two inner electrodes (C and D) is measured (Fig. 4).

The apparent resistivity is calculated using the following Eq. 3:

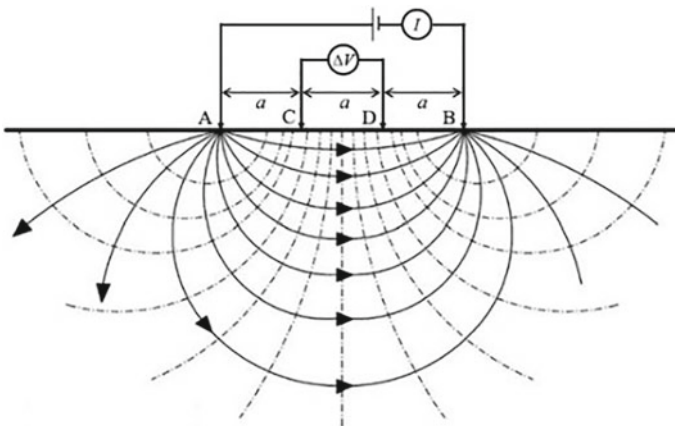


Fig. 4 Schematic diagram of Wenner's array

$$\rho = \frac{4\pi a R}{1 + \frac{2a}{\sqrt{a^2+4b^2}} - \frac{2a}{\sqrt{4a^2+4b^2}}} \quad (3)$$

where ρ = apparent resistivity (Ωm), a = electrode spacing (m), b = depth of electrode (m) and R = resistance (Ω), which is given by potential difference (ΔV) divided by current (I).

3.3 Moisture Content Using TDR

The TDR sensor is inserted into the soil mass together with the other sensors. As the volumetric moisture content measured is the average value across the entire waveguide length, the value is taken to be at the mid-point of the waveguides. The volumetric moisture content is measured and stored using a commercial datalogging software.

3.4 In-House CPT Cone

CPT was performed using an in-house CPT cone, and data is captured continuously every second. The CPT cone is 40 mm in diameter with a 60° tip and a shaft of 40 mm diameter and 120 mm length. It measures both tip and shaft resistances via the installed strain gauges. The penetration rate of the CPT cone during measurement is 8 mm/s, which is much lower than the standard rate of 20 ± 5 mm/s used in field CPT test to ensure better sensitivity in a soil mass with shallow thickness in this case.

4 Results and Discussion

Five (5) number of tests were conducted for this study. The configuration of the tests is listed in Table 1.

Table 1 The configuration of tests conducted

Test no	Homogenous or layered	Soil type
Test 1	Homogenous soil mass	Good earth (GE)
Test 2	Homogenous soil mass	Soft clay (SC)
Test 3	Layered soil	GE on top, SC below
Test 4	Layered soil	SC on top, GE below

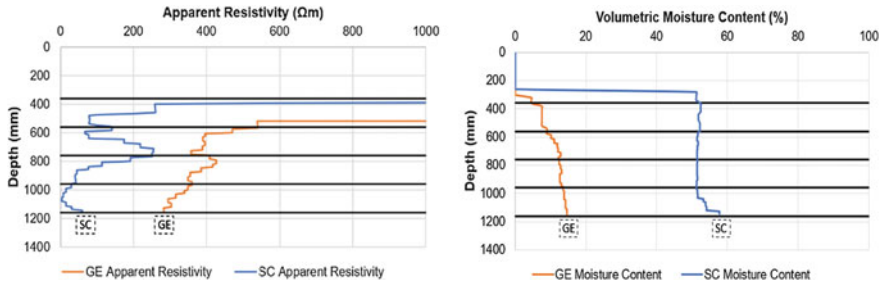


Fig. 5 (left) Apparent resistivity with depth for GE and SC, (right) volumetric moisture content with depth for GE and SC

4.1 Homogeneous Soil (Test 1 with GE and Test 2 with SC)

The apparent resistivity and moisture content with depth for Test 1 (GE) and Test 2 (SC) are plotted in Fig. 5. Soil parameter data is captured from 400 to 1200 mm depth.

Apparent resistivity is intuitively inversely proportional to moisture content, as a higher moisture content would allow more ions to carry electrical charges and conduct electricity. As the top part of soil mass is usually drier and uneven (presence of voids), apparent resistivity registered is comparatively higher.

Comparing the results of the two soil types, it can clearly be seen that GE soils have higher range of apparent resistivity and lower range of moisture content than SC soils. These range of values can be used as guiding values for distinguishing between the two.

Figure 6 shows the cone tip and shaft resistances as well as the friction ratio with depth for GE and SC. It is to be noted that shaft resistance values are much smaller than tip resistance values. Due to overburden pressure, soil at the bottom experiences greater stresses. Hence, tip resistance is found to be increasing with depth for GE, while that for SC is much less prominent, which is consistent with the understanding for sandy and clayey soils respectively. The two soil types can also be clearly distinguished from the difference in friction ratio (1% for sandy soil GE, 4–6% for clayey soil SC).

4.2 Layered Soil (Test 3 with GE-SC and Test 4 with SC-GE)

The apparent resistivity and moisture content with depth for Test 3 and Test 4 are plotted in Fig. 7, where GE-SC refers to “Good Earth” soil atop of “Soft Clay” soil, while SC-GE refers to “Soft Clay” soil atop of “Good Earth” soil.

From Fig. 7, the layering feature of the soil mass can be identified by the sudden change in resistivity and moisture content. It can be identified that GE soils show

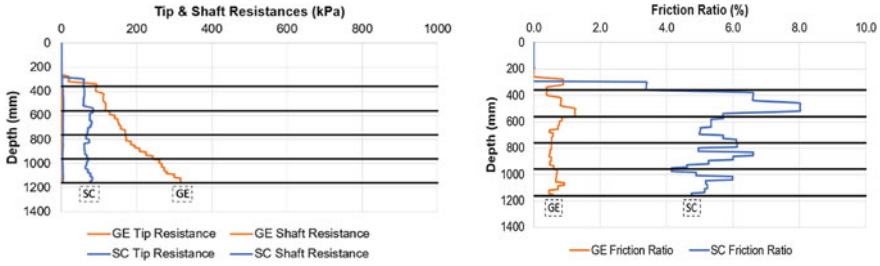


Fig. 6 (left) Tip and Shaft Resistances with depth for GE and SC, (right) Friction Ratio with depth for GE and SC

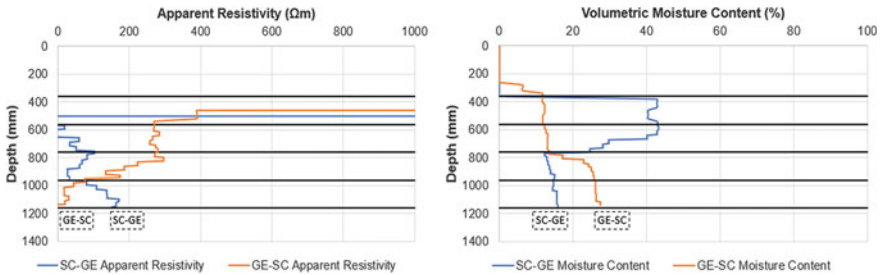


Fig. 7 (left) Apparent Resistivity with depth for GE-SC and SC-GE, (right) Volumetric Moisture Content with depth for GE-SC and SC-GE

a higher range of apparent resistivity and lower range of moisture content than SC soils. For example, in SC-GE where GE soil is atop SC soil, apparent resistivity drops from 300 Ωm to less than 100 Ωm at lower depth, while the moisture content increases from ~15% at the top, to ~40% at the greater depth.

Figure 8 shows the tip and shaft resistances as well as the friction ratio with depth for Test 3 and 4. Tip resistance is found to be increasing with depth for GE (sandy soil), while that for SC (clayey soil) is much more uniform. The difference in friction ratio is also very apparent (1% for sandy soil GE, 4–8% for clayey soil SC). Again, the layering feature of soil mass can be identified from these plots.

5 Conclusion

This paper has presented the preliminary findings from the three soil parameter determination: (i) apparent resistivity, (ii) moisture content, and (iii) CPT strength with the objective of complementing the newly-developed rapid soil classification technique using computer vision to classify excavated soils into “Good Earth” or “Soft Clay”. This near-full scale proof-of-concept has shown the feasibility of the

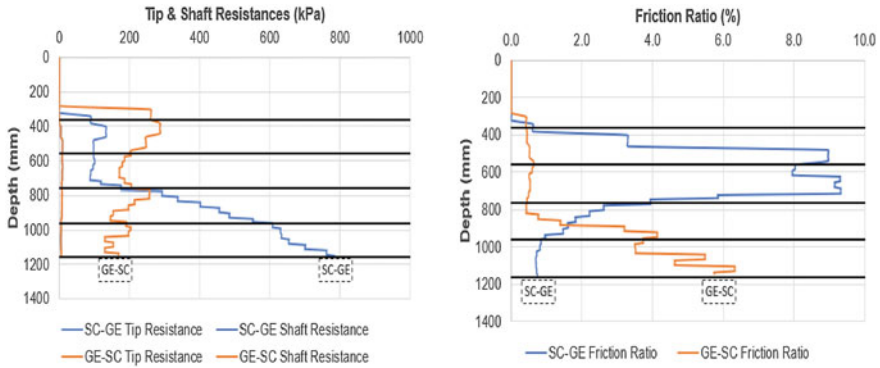


Fig. 8 (left) Tip and shaft resistances with depth for GE-SC and SC-GE, (right) friction ratio with depth for GE-SC and SC-GE

above three methods to distinguish between the two different soil types and identify certain foreign material located within the soil.

Further testing will be performed to obtain more data for calibration of models to further refine the range of soil property values for “Good Earth” and “Soft Clay” soils. An actual full-scale testing will be conducted to capture data with test dimensions that resemble actual operations at the SGs.

In future, the soil parameter determination can be combined with the existing computer vision method at the SGs to improve operational productivity, optimize use of excavated soils and contribute to the long-term sustainability for land reclamation projects and the construction industry in Singapore.

Acknowledgements This research is supported by the Singapore Ministry of National Development and the National Research Foundation, Prime Minister’s Office under the Cities of Tomorrow (COT) Research Programme (COT Award No. COT-V3-2019-1). Any opinions, findings and conclusions or recommendations expressed in this paper are those of the author(s) and do not reflect the views of the Singapore Ministry of National Development and National Research Foundation, Prime Minister’s Office, Singapore.

References

1. Aw YJE, Koh JW, Chew SH, Tan SED, Cheng LM, Yim HMA, Ang LJJ, Chua KE (2020) Application of computer vision technique for rapid soil classification. In: 10th International Conference on geotechnique, construction materials and environment. Melbourne, Australia
2. Department of Army, U.S. Army Corps of Engineers (2015) Geophysical exploration for engineering and environmental investigations, scholar’s choice
3. Knappett J, Craig RF (2020) Craig’s soil mechanics. CRC Press
4. Topp GC, Ferré T (2005) Time-domain reflectometry. In: Encyclopedia of soils in the environment. Elsevier, pp 174–181

Influence of Excess Pore Pressure Development on Inertial Pile Response



Hande Yumuk and Gurkan Ozden

Abstract The behavior of piles in submerged and liquefiable sandy soils under earthquake loads attracted attention of researchers since 1980s. In this study, behavior of soil surrounding piles in such soils was investigated. In the study, response of the piles under inertial loads was considered, and it was assumed that the soil was in passive terms of during the earthquake. In other words, kinematic and inertial interactions are separated in soil-pile interaction. In the three-dimensional finite element analysis, harmonic loading was applied to the pile head. As a liquefiable soil layer, sandy soil whose liquefaction model parameters were determined at the California Wildlife Test Site was considered. In the analyzes made under different horizontal loads and frequencies, it was determined that the stresses transferred from the pile to the soil can force the soil up to liquefaction by causing excess pore water pressure to change in the soil, and its reflection on the horizontal load–displacement curves (p–y curves) is discussed. The results of the analysis revealed that the loading frequency had some effect on soil behavior and development of excess pore water pressure significantly affected the horizontal load- displacement curves.

Keywords Liquefiable soils · Laterally loaded pile · Excess pore pressure · Pile-soil interaction

1 Introduction

Earthquake response of foundation piles have long attracted attention of researchers since pile damages were observed several times in past earthquakes [1]. Such observations accelerated research and major contributions to the field were already made

H. Yumuk (✉)

Natural and Applied Sciences Institute, Dokuz Eylul University, Izmir, Turkey

e-mail: hande.yumuk@ogr.deu.edu.tr

G. Ozden

Department of Civil Engineering, Dokuz Eylul University, Izmir, Turkey

[2, 3]. However, it is still necessary to get more insight on excess pore pressure development around piles in liquefiable soils [4]. In this study, a nonlinear dynamic finite element analysis campaign was pursued to study excess pore pressure regime developing around a pile loaded at the head in saturated liquefiable silty sands. Achieved results indicate that considerable pore pressure develops within the soil surrounding the pile thereby reducing soil resistance by a large margin as a result of inertial interaction.

2 Numerical Analysis Model

Two separate finite element analysis models were established to investigate lateral load–displacement and excess pore pressure pattern around a pile on which cyclic lateral load was applied. The pile diameter was set as 60 cm with an assigned elasticity modulus of 30×10^6 kPa. The 30 m deep first model consisted of a slender pile with a length to diameter ratio of $L/B = 15/0.6 = 25$. The second model, on the other hand, involved a 1.0 m long pile section where influence of effective stress was taken care of uniform applied vertical stress on the surface of the model, which was consolidated before application of the cyclic load. Lateral load was applied as a traction on pile heads along y-axis. Viscous absorbent boundaries were provided on the sides of both models with plan dimensions of 20m x 20m. Fine mesh was applied while discretizing the models with 32,771 ten node wedge elements provided for the long pile model and 82,358 elements for the pile section one Fig. 1a, b. A mesh quality check revealed that over 99% of the elements had Quality Sphere or Quality SICN values larger than 0.5.

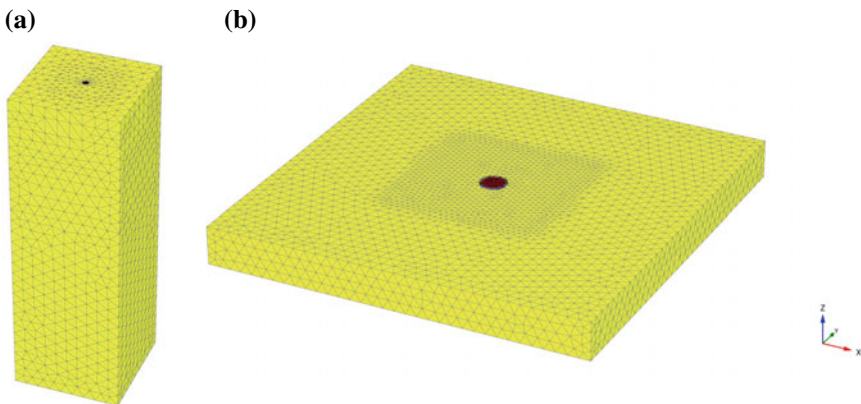


Fig. 1 Finite element model connectivity plots **a** $L/B = 25$ pile **b** 1.0 m long pile section

Table 1 UBC3D-PLM material model parameters

Parameters	Unit	Value
Young Modulus	kPa	7.28×10^4
Poisson's ratio	–	0.3
Void ratio	–	0.740
Constant volume friction angle	(°)	22
Peak friction angle	(°)	22.765
Cohesion	kPa	1.0×10^{-4}
Elastic shear modulus factor ^a	–	854.6
Plastic shear modulus factor ^a	–	250
Elastic bulk modulus factor ^a	–	598.2
Failure ratio	–	0.811
Densification factor	–	0.2
Post liquefaction factor	–	0.02
SPT-N ₁₆₀	–	7.65

^aModulus index values were assigned as 0.5 for elastic, plastic, and elastic bulk factors

3 Soil Characteristics and Material Model Parameters

As the study essentially targets pile response in saturated cohesionless soils Wildlife National Geotechnical Instrumentation Site was chosen as the parent site to obtain material model parameters pertaining to liquefaction analysis. University of British Columbia sand model was the preferred material model due to the availability of calibrated UBC3D-PLM and soil profile parameters for the Wildlife Site in the literature [5]. Soil parameters assigned to the FEM model is given in Table 1. Physical meanings of the parameters and details of the model may be reached out elsewhere [6]. The pile was modeled as an elastic volume element using non-porous material model.

4 Results of Numerical Analyses

Finite element analyses were realized for the full pile length and pile section models. In this respect general trend is to model the pile with its full length and driving the p–y curves along the pile length either through the interface or analyzing the induced stresses inside the soil in the immediate vicinity of the pile [7]. Some researchers, however, indicate that soil resistance is affected by the rotation and flexibility of the pile. It is suggested to restraint displacement of the pile along the loading direction so that pure lateral displacement is achieved [8]. It is considered that pile section model in which the 100 cm pile is only allowed to displace along y-direction would serve this purpose. The effective stress level acting along a pile length is represented by means

of an applied surface load. Here, it is aimed to limit the deformations on the interface by keeping the interface strength parameter very low. Soil resistance to the laterally deforming pile was obtained along the interface stress points. Monotonic and cyclic surface traction was applied at the pile head. Loading intensity varied between 25 and 200 kPa in cyclic loading undrained analyses. Cyclic loading frequency was set as 1 and 2 Hz. Monotonic loading analyses, on the other hand, progressed till 300 kPa (i.e. 25~300 kPa corresponding to $\approx 7\text{--}85$ kN of lateral point load at the pile head) beyond which soil body collapsed due to excessive pore water pressure and plastic point development (i.e. $H = 113$ & 141 kN).

4.1 Excess Pore Water Pressure Response

Excess pore water pressure (Δu_e) generation regime because of the lateral displacement of the pile towards and away from the surrounding saturated loose sand is one of the expected outcomes of undrained analyses. Results of monotonic loading tests are presented in Fig. 2a, c for a depth of 3 m below the ground surface. On this figure variation of Δu_e with horizontal strain ϵ_{yy} is plotted for stress points selected adjacent to the pile as well as 1B and 3.8B away the pile axis parallel to the loading direction. It may be followed on the figure that pore pressure development is associated with dilative soil response adjacent to the pile (Fig. 2a) whereas it is almost completely positive for all loading levels 3.8B away the pile. It is noteworthy that excess pore pressure generation is not highest for larger loads. This trend is related with dilation taking place as loading level increases. At $H = 113$ and 141 kN, however, negative pressure development ceases at about $\epsilon_{yy} = 4.5 \times 10^{-3}$ and 7.8×10^{-3} , respectively due to soil body collapse. Influence of head loads less than 42 kN is negligible on excess pore water pressure development.

The figures obtained via undrained monotonic analyses demonstrate excess pore pressure generation potential due to pile displacement. Both dilative and compressive soil response related pressure development tendency increases with loading intensity. Higher positive excess pore pressures are generated 1B away the pile section surface and they quickly diminish at 3.8B distance. At the pile-soil interface dilative soil response is observed as a result of passive wedge development. Maximum induced pore pressure, however, did not induce liquefaction at 1B distance since initial effective vertical stress was $\sigma'_{v0} = 37.3$ kPa as opposed to $\Delta u_{\max} = 27.8$ kPa.

Influence of loading frequency and intensity on the achieved results are presented in terms of p' - q plots at a depth of 3 m below the model surface. It may be followed in Fig. 3 that a slight influence of loading frequency (1 Hz and 2 Hz) on deviatoric stress is pronounced in three-dimensional full length pile analysis. A two-cycle analyses showed that 2 Hz cyclic loading with an amplitude of 42 kN (i.e. 150 kPa pile head cyclic traction) resulted in more than 30% decrease in deviatoric stress as compared with the 1 Hz case. Although loading intensities are not the same with the full pile length analyses, pile section runs at 1 Hz and 2 Hz cyclic loading with a magnitude of yielded a similar trend. It is interesting to note that deviatoric stresses are comparable

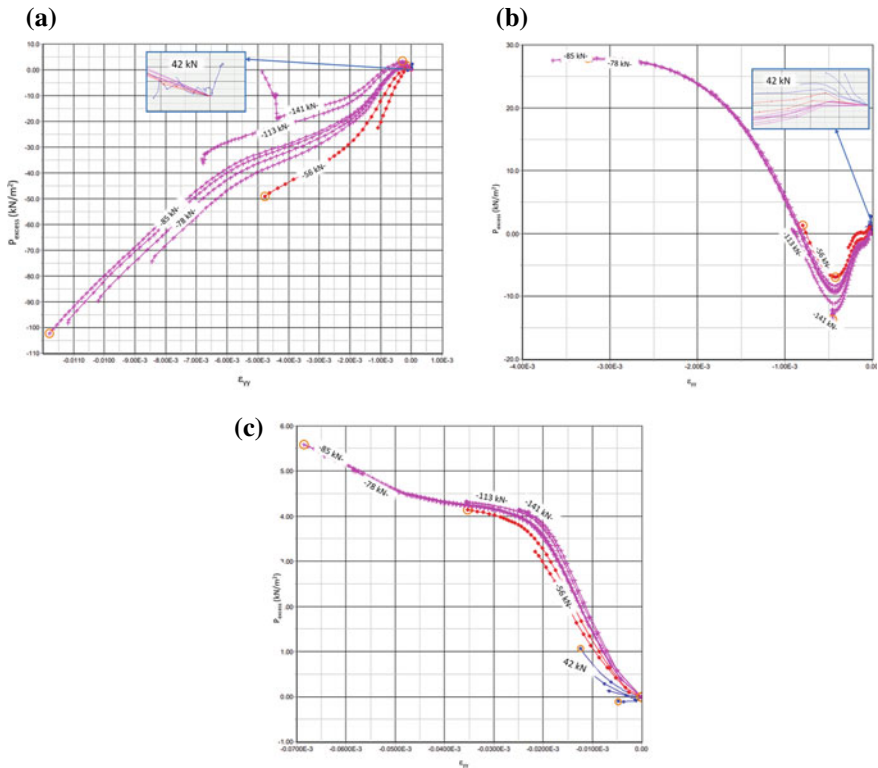


Fig. 2 **a** Excess pore water pressure with respect to horizontal strain adjacent to the pile surface. **b** Excess pore water pressure with respect to horizontal strain 1B away the pile surface. **c** Excess pore water pressure with respect to horizontal strain 3.8B away the pile surface

for both cases probably since same initial effective stresses are achieved in pile section analyses (Fig. 4). A better insight may be captured by applying head loading as a cyclic displacement pattern with a magnitude equal to full pile length analyses. Loading intensity effects on deviatoric and mean effective stress levels are observed in Fig. 5. It is clear that excess pore water pressure generation reduces shear strength especially with lower loading intensities (i.e. 25 kPa and 75 kPa) where a steady decrease towards failure takes place. At larger loading levels, however, dilation takes place at a certain level and shear strength recovery occurs. Dilative tendency quickly disappears with the distance from the pile surface.

4.2 Load–displacement Curves

The load–displacement curves, namely, p–y curves are derived for drained and undrained monotonic loading cases to form backbone curves that would degrade

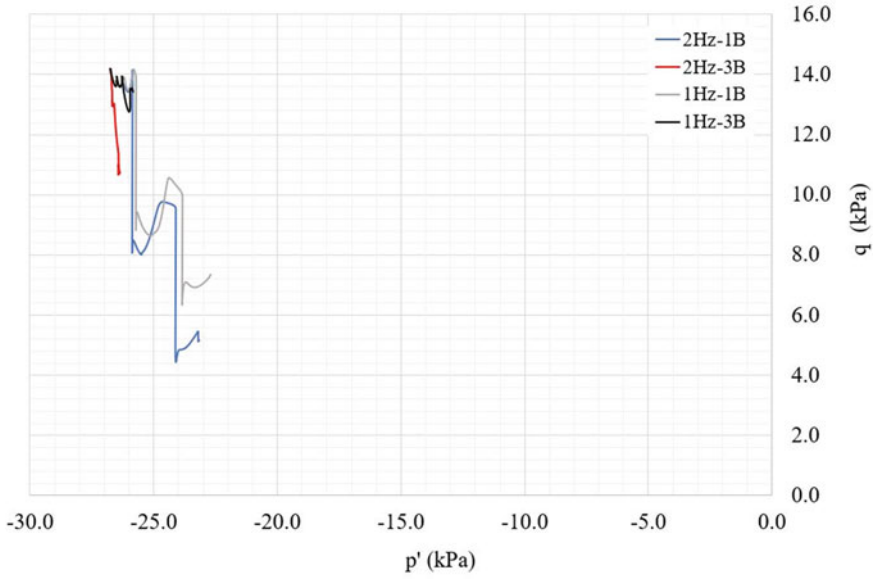


Fig. 3 Variation of deviatoric stress with mean effective stress in full pile length analyses (150 kPa loading amplitude at 2 Hz & 1 Hz frequency)

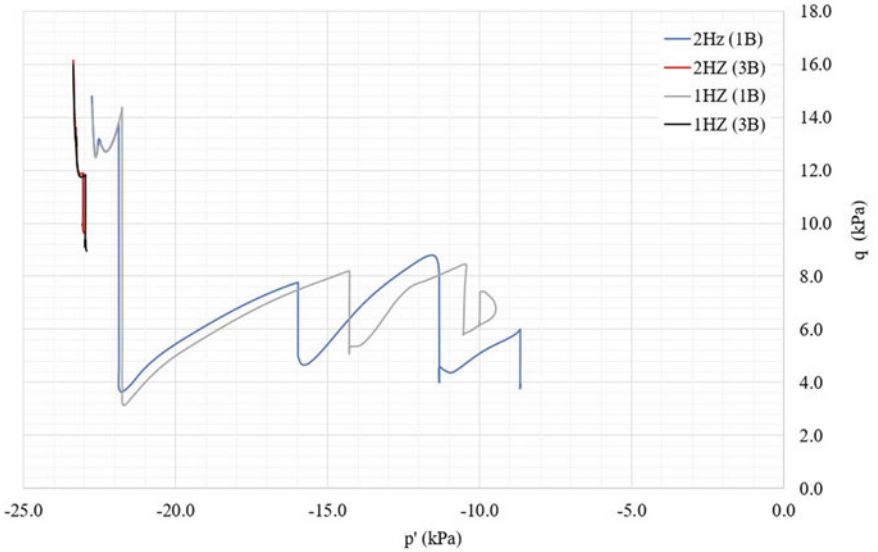


Fig. 4 Variation of deviatoric stress with mean effective stress in pile section analyses (200 kPa loading amplitude at 2 Hz & 1 Hz frequency)

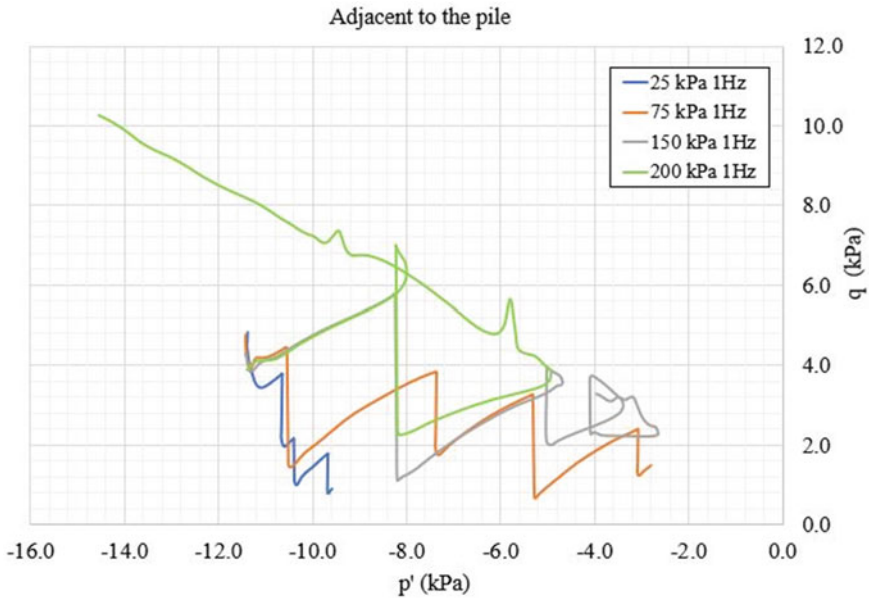


Fig. 5 Influence of loading intensity on variation of deviatoric stress with mean effective stress in pile section analyses (stress points adjacent to the pile)

as effective stress decreases as a result of excess pore water pressure accumulation under inertial cyclic loading conditions (Fig. 6). One may note that API p–y curve fits the drained p–y curve if API model parameters are adjusted accordingly. Further effort is necessary to obtain a p–y curve model that would work for undrained cyclic inertial loads.

5 Conclusions

Finite element analyses results presented herein show that UBC3D-PLM model can be utilized in soil-pile interaction research that targets excess pore pressure accumulation in very loose sandy soils if care is spent on the established numerical model since UBC model may be quite sensitive to boundary value problems. Pile section analyses are found to be applicable to the inertial cyclic loading cases. Full pile length and pile section analyses yielded similar but not the same results. Although spatial redistribution of excess pore water pressure can be handled in pile section model, high gradients parallel to the pile surface along the interface cannot be handled for the time being. As a result of this generated excess pore water pressures are less and soil strength reduction is not that sharp in 3D full pile length model. Both full length and pile section models showed that high pressure gradients take place at the soil-pile interface and dilative response occurs at larger loading amplitudes. Presented

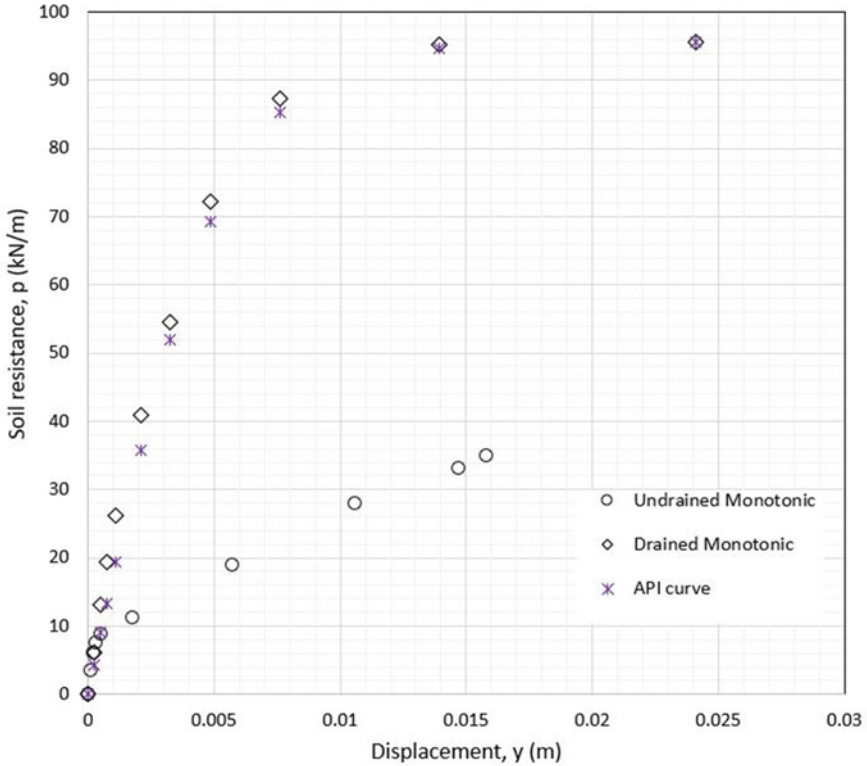


Fig. 6 p–y curves for monotonic drained and undrained loading cases (pile section analyses that correspond to a depth of 3 m below the surface)

p′–q plots and p–y curves belong to a case where soil depth is 3 m below the model surface. Findings of the ongoing research will be shared in future publications.

References

1. Mizuno H (1987) Pile damage during earthquakes in Japan (1923–1983). Response of pile foundations during earthquakes, Atlantic city spring convention, ASCE, pp 53–78
2. Kagawa T, Kraft LM Jr (1981) Lateral pile response during earthquakes. J Geotechn Eng Div ASCE 107(12):1713–1731
3. Kagawa T, Kraft LM (1980) Seismic p–y responses of flexible piles. J Geotechn Eng ASCE 106(GT8):899–918
4. Choi JI, Kim MM, Branderberg SJ (2015) Cyclic p–y plasticity model applied to pile foundations in sand. J Geotech Geoenviron Eng, ASCE, 04015013–1–9
5. Youd TL, Bartholomew HAJ, Proctor JS (2004) Geotechnical logs and data from permanently instrumented field sites: garner valley downhole array (GVDA) and wildlife liquefaction array (WLA). Report to NEES, Dept. of Civil and Env. Eng., Brigham Young University
6. Petalas A, Galavi V (2012) Plaxis liquefaction model UBC3D-PLM. Plaxis B.V., 45 p

7. Wolf TK, Rasmussen KL, Hansen M, Roesen HR, Ibsen LB (2013) Assessment of p–y curves from numerical methods for a non-slender Monopile in Cohesionless soil. Department of Civil Engineering, Aalborg University, DCE Technical Memorandum, No. 024
8. Pradhan DL (2012) Development of P–Y curves for monopiles in clay using finite element model Plaxis 3D foundation. MSc Thesis, Norwegian University of Science and Technology Department of Civil and Transport Engineering, 58 p

Numerical Study of Uplift Induced Levee Failure for the Design of a Centrifuge Test



Veronica Girardi , Elena Dodaro, Roberta Ventini, Marianna Pirone, Carmine Gerardo Gragnano, Daniela Giretti, Francesco Zarattini, and Fabio Gabrieli

Abstract In geotechnical engineering, physical and numerical models seek to shed light on multiphase phenomena that threaten earth structure stability. This is the case of river levees: when subjected to non-ordinary hydraulic loads, local and global failures with consequent floods could occur. If, on one hand, centrifuge models can replicate the real phenomena, exploiting the enhanced gravity, while scaling geometrical features and time, on the other, numerical models extend the possible case studies by capturing key elements, governing the hydro-mechanical behaviour of the earthworks. However, the two techniques could complement and benefit each other. In this research, a potential failure mechanism, induced by the development of uplift pressures beneath the toe of a levee characterized by a peculiar stratigraphic profile, is investigated. The foundation consists of a shallow weak low-permeability layer, overlying a coarser and more permeable one, this latter acting as a hydraulic preferential flow path between riverside and landside. Results of a preliminary numerical study carried out with different methods are presented and discussed. The study aims to improve understanding of complex failure mechanisms and to encourage the development of more robust forecasting methods. Indeed the results have provided fundamental guidance for a centrifuge experimental set up.

Keywords Levee · Geotechnical centrifuge · Numerical modelling

V. Girardi (✉) · F. Zarattini · F. Gabrieli
Department of Civil, Environmental and Architectural Engineering, University of Padova, Padova, Italy
e-mail: veronica.girardi.1@unipd.it

E. Dodaro · C. G. Gragnano
Department of Civil, Chemical, Environmental and Materials Engineering, University of Bologna, Bologna, Italy

R. Ventini · M. Pirone
Department of Civil, Building and Environmental Engineering, University of Napoli Federico II, Napoli, Italy

D. Giretti
Department of Engineering and Applied Science, University of Bergamo, Bergamo, Italy

1 Introduction

Water retaining geostructures, such as river levees, require continuous development of risk mitigation strategies to cope with the current and prospective increase of hydraulic loads acting on these structures. This study is focused on the geotechnical behaviour of levees, protecting urbanized territories from river flooding. Among several failure modes, those possibly emerging when a levee foundation is characterized by a shallow soft fine-grained deposit, overlying a highly permeable sandy layer, are still partially unknown, and thus unpredictable. The coarser layer may be directly interconnected with the river, acting as a hydraulic preferential conduit between riverside and landside. If the water level increases, high overpressure can build up at the interface between the fine-grained and sandy layer, exceeding the overburden stress of the shallow soil stratum on the landside. This circumstance may determine localized toe uplift on the ground level and, simultaneously, favour the progression of a slip surface in the levee body, resulting in a subsequent earth structure collapse, as reported by Refs. [1, 2]. The joint use of centrifuge testing and numerical modelling could be useful to investigate in details these phenomena. In fact, centrifuge modelling is a well-established approach in geotechnics research, still challenging when employed in this context, due to the well-known difficulties to recreate certain stratigraphy and apply time-dependent hydraulic boundary conditions on earth structures. On the other side, the application of various numerical techniques aids in getting a broader picture of the potential instability occurring in the experiment.

This research work seeks to shed light on complex potential failure mechanism that could develop when a preferential flow path establishes in the levee foundation. In particular, predictions determined by different numerical approaches are shown, hence providing guidance for their prospective use in safety assessment practice. It is worth noting that the experimental design of centrifuge tests, besides the numerical outcome, is based on a balanced compromise among physical features of the equipment, time and costs constraints. These aspects will be underlined during the final discussion.

2 Numerical Modelling

Three different methods are compared in the safety assessment of the levee model: (i) the *Limit Equilibrium Method* (LEM), implemented in the commercial software SLOPE/W [3], which was easily combined with transient seepage analysis performed by SEEP/W, included in the same software suite; (ii) the *Van Method*, available in the D-Stability code [4]; (iii) the *Strength Reduction Routine*, used by PLAXIS 2D [5], which was applied to the results of a coupled seepage-deformation analysis. The

numerical modelling was carried out to properly support the design a centrifuge test, however all the simulations have been performed at the prototype scale, in keeping with the geometrical similitude [6] expressed by Eq. (1):

$$L_m/L_p = 1/N \quad (1)$$

where N is the scale factor for gravity (i.e. $g_m = N g_p$), L_m and L_p are respectively characteristic lengths of model and prototype. The acceleration that is planned to be applied in the centrifuge test is 50-gravities. The calculation phases in FE model mimic the whole centrifuge test from the acceleration stage, passing through the self-weight equilibrium (during which consolidation takes place), to the flooding stage. Whereas, in LEM and Van Method only the processes occurring after consolidation are reproduced. A parametric study on the thickness of foundation layers is carried out to support the design of the physical model, to be tested under an enhanced gravity field and highlight the crucial role of the stratigraphy on the overall stability of the levee.

2.1 Geometry and Materials

A plane strain section, designed to be suitable for investigating the potential failure mechanism aforesaid and concurrently easily reproducible as a small-scale physical model, is considered in the numerical study. The prototype levee body is characterized by a height of 7.50 m, a 3.00 m wide crown and slopes inclination of 1H:1V and 1H:1.5V for the riverside and the landside, respectively (Fig. 1). The foundation consists of a fine-grained deposit overlying a layer made of a coarser material, which extends 3 m beyond the landside toe and is hydraulically connected to the water retained on the riverside. The parametric study consists of a variation of the first subsoil layer thickness, between 2.0, 2.5 and 3.0 m, maintaining constant the total foundation height (5.0 m). Hence, the sandy layer changes its thickness accordingly.

The filling material selected for the levee body, typically constituted by a heterogeneous mix of sands and silts, is a compacted mixture of 70% by weight of Ticino Sand (TS) and 30% of Pontida Clay (PON). The optimum moisture content ($w = 8.8\%$) and dry density ($\gamma_d = 20.60 \text{ kN/m}^3$), determined using the Standard Proctor compaction energy, are taken as reference as the initial state of the TS70-PON30% mixture. For the upper and bottom layers of the subsoil, which frequently consists of clayey and silty strata deposited in a floodplain environment, a homogeneous consolidated layer of PON and a compacted TS are considered. A pre-overburden vertical effective stress of 800 kPa has been considered for the PON layer and a relative density equal to 80% of ($\gamma_d = 15.74 \text{ kN/m}^3$) with a water content of 5.0% has been assumed to define the initial conditions of the TS layer. Soil index and physical main properties are determined for the three materials and can be found in Ventini et al. [7].

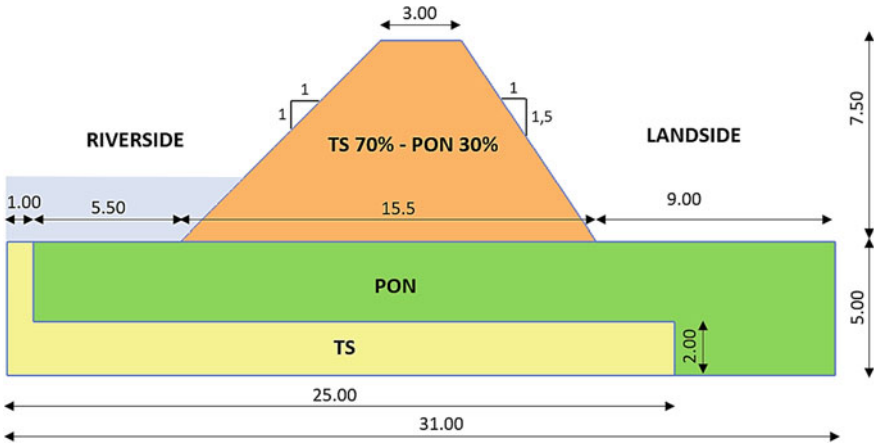


Fig. 1 Geometry of levee section numerically analyzed, in the case of 3.0m-thick PON layer (length unit in m)

2.2 Hydro-Mechanical Soil Properties

The full modelling of the time-dependent hydraulic behaviour is allowed in SEEP/W and PLAXIS 2D, whose results in terms of pore water pressure distributions are respectively used as input of LEM analysis and Strength Reduction method, while D-Stability doesn't account for transient seepage flow. In this last case, total hydraulic heads need to be directly specified for each material and the depicted situation can be considered as a steady-state condition.

Hydraulic and retention properties of the mixture and the clayey silt material, accurately estimated from specific laboratory procedures and extensively discussed in Ventini et al. [7], are listed in Table 1, together with the hydraulic conductivity of the TS, that is considered fully saturated during the entire duration of the analyses. The Mualem-van Genuchten model has been adopted for modelling the soil water retention curves (SWRCs) and hydraulic conductivity functions.

For this preliminary application, in SEEP/W, soil porous medium is assumed rigid under partially saturated conditions. Conversely, in PLAXIS 2D, the Hardening Soil (HS) hyperbolic formulation, developed by Duncan and Chang [8] is considered for modelling the mechanical behaviour of the mixture and the sand layer. Whereas,

Table 1 Hydraulic and retention parameters used for the seepage analyses in SEEP/W and PLAXIS 2D

Material	k_{sat} (m/s)	S_{res} (-)	S_{sat} (-)	α_{VG} (kPa)	n_{VG} (1/m)	l (-)
TS70%-PON30%	$1.23 \cdot 10^{-7}$	0.057	1.000	11.9	1.240	-3.347
PON	$6.67 \cdot 10^{-10}$	0.000	1.000	142.8	1.455	-0.584
TS	$3.45 \cdot 10^{-5}$	-	-	-	-	-

Table 2 Mechanical and physical parameters assigned to the levee body and foundation units in PLAXIS 2D, according to Hardening Soil and Soft Soil constitutive models

Material		TS70%-PON30%	PON	TS
Constitutive model		Hardening soil	Soft soil	Hardening soil
γ_{unsat}	kN/m ³	20.8	18.85	15.74
γ_{sat}	kN/m ³	22.3	21.85	16.53
e_{init}	–	0.30	0.44	0.67
E_{50}^{ref}	kN/m ²	22.52·10 ³	6.00·10 ³	19.80·10 ³
$E_{\text{oed}}^{\text{ref}}$	kN/m ²	10.00·10 ³	4.50·10 ³	14.14·10 ³
M	–	0.5	1	0.5
c'	kN/m ²	5.00	2.5	0.0
ϕ'	°	46.00	33	41.00
K_0^{NC}	–	0.287	0.455	0.344
N	–	0.223	0.20	0.256
λ^*	–	–	0.053	–
κ^*	–	–	0.016	–
M	–	–	1.702	–

for the fine-grained subsoil layer, the Soft Soil model [9] is used. In all the numerical techniques used in this study, a Mohr–Coulomb failure criterion with drained strength parameters is considered. Soil mechanical properties, derived from standard oedometer tests and triaxial tests are reported in Table 2. Further information on the hydro-mechanical characterization of the three materials can be found in Ventini et al. [7] and Fioravante and Giretti [10].

2.3 Initial and Boundary Conditions and Testing Sequence

The definition of realistic initial conditions in terms of suction and pore water pressure distributions represents a crucial aspect for transient seepage analyses of earthen structures. In PLAXIS 2D, starting from a uniform value of matric suction of about 5 kPa, representative of the physical model preparation state, a constant outflow is assigned to the crest and sides, to reproduce the progressive drying occurring during the centrifuge test. An initial water level, equal to 1.5 m, is supposed to be maintained constant during the in-flight acceleration and consolidation stages, for the time required to attain the equilibrium of pore water pressures (Fig. 2a). The same initial conditions after consolidation in PLAXIS 2D are imposed in SEEP/W.

Regarding boundary conditions, since the model is supposed to be contained in a rigid steel box, in the FE analysis, the bottom horizontal, right, and left vertical sides of the subsoil are assumed to be impermeable, with fully and horizontally fixed constraints, respectively. A time-dependent hydrometric condition is imposed on the

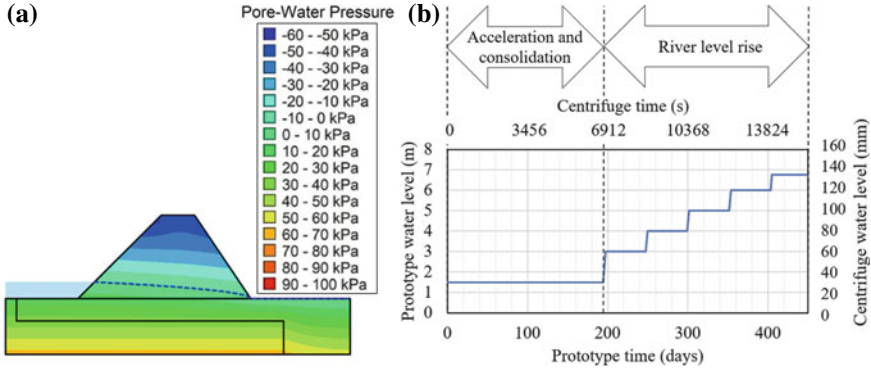


Fig. 2 **a** Initial pore water pressure distribution for transient seepage analyses (isoline increment = 10 kPa), phreatic surface in dashed blue line; **b** Hydraulic head boundary condition assumed in the numerical study, at both prototype and centrifuge scale

inner side of the levee. The goal is to identify the critical hydraulic head which would likely trigger a toe uplift mechanism, thus, the effect of five incremental river stages is investigated (Fig. 2b). Each water level is reached with a rate of 0.5 m/days and maintained for a period of 50 days, corresponding to about 30 min at the model scale, according to centrifuge scaling laws [6], to guarantee the establishment of a stationary flow regime within the levee body at each step. As mentioned in Sect. 2.2, D-Stability does not allow for the analysis of transient seepage processes, thus, the water levels are simply sketched, to determine the pore pressure distribution used in the following stability analysis. Two hydrometric heads are used: a higher one which guarantees high pressures only in TS, in agreement with the investigated river stages, while above TS pressures are controlled by the lower water level (see Fig. 5a), to mimic an undrained response of the system with a pressure leap between TS and PON.

2.4 Results and Discussion

Figure 3 shows FEM numerical results, considering a 3.0-m-thick PON layer with reference to three significant time steps. Following the first water level increment, a sudden increase of pore water pressures occurs in the sand layer. Then, the water level persistence leads to a progressive saturation of the lower part of the levee body and, simultaneously, to a slow rise of pore pressures even in the fine-grained layer. The total deviatoric strains, which appear extremely low at the beginning of the flooding stage and concentrated at the interface between PON and TS, tend to increase, with the advancement of the phreatic surface within the levee and the contextual decrease of vertical effective stresses in the PON layer, highlighting the shape of a possible slip surface. The number of plastic failure points tends to dramatically increase,

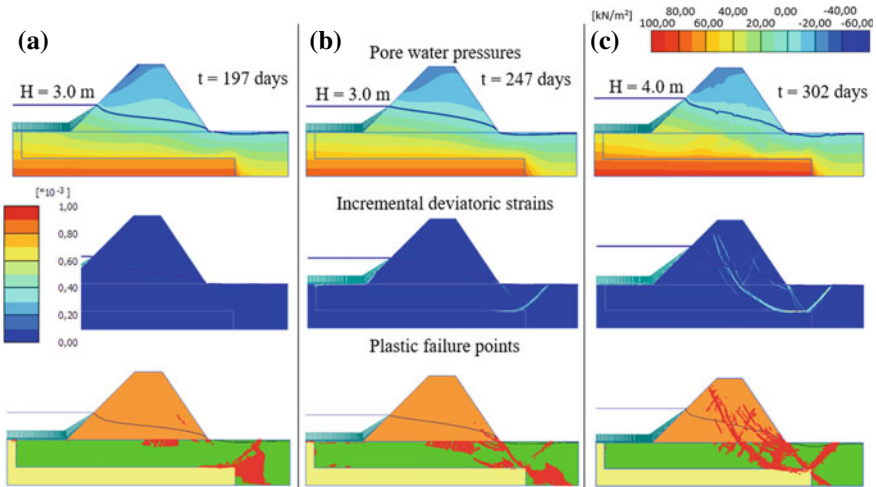


Fig. 3 Pore pressures, total deviatoric strains and plastic failure points at different stages during FEM analysis carried out by means of PLAXIS 2D: **a** at the beginning of the first water level increment ($t = 197$ days); **b** at the end of the first water level increment ($t = 247$ days); **c** during the persistence of the critical water level, associated to the failure mechanism ($t = 302$ days)

as the hydrometric level rise to 4.0 m, suggesting a significant weakening of the levee section, especially in correspondence of the landside toe, leading to the failure condition.

The correlation between river stages and their effects in terms of stability is particularly evident observing the evolutions of the Factor of Safety (FS) over time for FEM and LEM in Fig. 4a. For Van Method FS is correlated with the hydraulic head (Fig. 4b). In FEM and LEM analyses, as soon as the river stage rises to 3.0 m, the increase of pore pressures causes a reduction of shear strength, resulting in a significant decrease of FS, which tends to further reduce during the persistence of the water level (Fig. 4a). Potential failure conditions, identified by a FS minor than one, are achieved at different time steps and hydrometric loads for the three methods. In particular, in FE analyses, the 2.0 m thick PON layer encounters a critical condition for stability towards the end of the first water level persistence; while for thicknesses 2.5 and 3.0 m of the PON layer the critical hydraulic heads are higher, respectively 3.8 and 4.0 m. Indeed, FEM simulations do not converge anymore after these critical water levels are reached, evidencing that outcomes are strongly controlled by the hypothesis of small-displacements. In LEM, critical heads are generally higher than those obtained with FEM analyses, thus potential failure occurs for all the geometries but with a certain delay. However, it must be noted that the shape of the slip surface, assumed in these LEM calculations might be not representative of the investigated mechanism. Lastly, in Van Method, FS reduces with the progressive increase of the water level, but only for PON thickness equal to 2.0 m FS is less than the unit. In the other cases FS results greater than 1, probably due to the approximated pore pressure

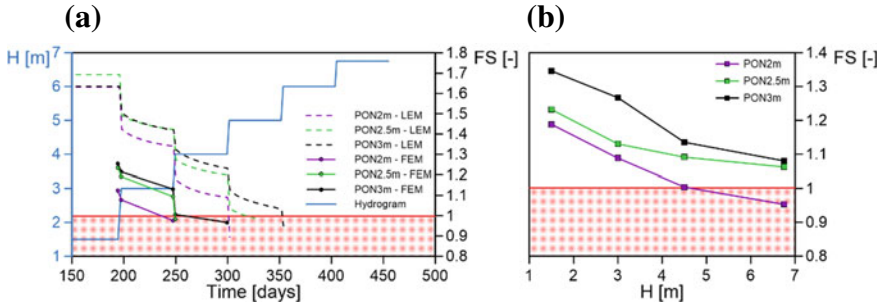


Fig. 4 Variation of FS for the three investigated foundation thicknesses: **a** over time for LEM and FEM analysis; **b** respect to hydraulic heads for Van Method

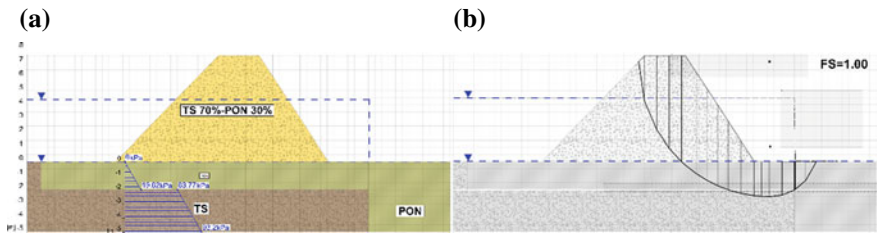


Fig. 5 Van Method results: **a** piezometric levels and resulting pore pressure distribution; **b** slip surface for FS = 1 in the case of PON thickness equal to 2 m

distribution, which results only in high pressure in TS, rather than in PON. Moreover, the location and shape of the slip surface (Fig. 5b) are similar to those observed in FEM (as visible from the increment of deviatoric strains of Fig. 4).

Nonetheless, nothing can be said in terms of deformation for LEM and Van method; hence they are affected by a generally higher level of simplification compared to FEM, which accurately reproduces the coupled flow-deformation behaviour, as long as the small displacement hypothesis stands. Therefore, since all the three approaches are unable to analyze the post-failure behaviour, the exploration of the entire failure event is demanded to the centrifuge test.

3 Remarks and Conclusions

In this work, the results of a numerical study carried out to investigate a river levee failure mechanism induced by toe uplift are presented and discussed. The study provides guidance for the definition of geometrical features of the physical model and in particular for the selection of foundation layers thicknesses. Based on FEM and LEM outcomes, the configuration characterized by a PON layer of 3.0 m seems to be the most suitable to replicate the instability of interest and, at the same time, to

investigate the effect of a time-dependent boundary condition on the safety performance of the levee. Furthermore, the research confirms that the proposed hydrograph, easily reproducible in the centrifuge apparatus, allows for identifying critical hydraulic heads which may trigger failure. In the light of the simulation outcomes, the following monitoring instruments devoted to pick the noteworthy aspects of the phenomena, are recommended: tensiometers in the levee body and on the landside, near the toe; pore pressure transducers in the foundation soils, in both layers; LVDT on the levee crest and near the toe and roto-translative transducers on the landside slope.

Acknowledgements The authors would like to acknowledge the financial support from MIUR (Redreef—PRIN 2017 Call, prot. 2017YPMBWJ).




References

1. Van MA, Koelewijn AR, Barends FB (2005) Uplift phenomenon: model, validation, and design. *Int J Geomech* 5:98–106. [https://doi.org/10.1061/\(ASCE\)1532-3641\(2005\)5:2\(98\)](https://doi.org/10.1061/(ASCE)1532-3641(2005)5:2(98))
2. Bezuijzen A, Kruse G, Van M.A. (2005) Failure of peat dikes in The Netherlands. In: international conference on soil mechanics and geotechnical engineering. <https://doi.org/10.3233/978-1-61499-656-9-1857>
3. Geo-slope (2017) Stability modeling with GeoStudio. GEO-SLOPE International Ltd., Calgary, Canada
4. Der Meij V.R. (2021) D-stability—computer software
5. PLAXIS 2D Connect Edition V21: Reference Manual (2020) Bentley systems Incorporated. Delft, The Netherlands
6. Garnier J, Gaudini C, Springman SM, Culligan PJ, Goodings D, Konig D, Kutter B, Phillips R, Randolph MF, Thorel L (2007) Catalogue of scaling laws and similitude questions in geotechnical centrifuge modelling. *Int J Phys Model Geotech* 7(3):1–23. <https://doi.org/10.1680/ijpmg.2007.070301>
7. Ventini R, Dodaro E, Gagnano CG, Giretti D, Pirone M (2021) Experimental and numerical investigations of a river embankment model under transient seepage conditions. *Geosciences* 11:192. <https://doi.org/10.3390/geosciences11050192>
8. Duncan JM, Chang CY (1970) Nonlinear analysis of stress and strain in soil. *J Soil Mech Found* 96:1629–1653
9. PLAXIS 2D Connect Edition V21: Material Models Manual (2020) Bentley systems Incorporated. Delft, The Netherlands
10. Fioravante V, Giretti D (2016) Unidirectional cyclic resistance of Ticino and Toyoura sands from centrifuge cone penetration tests. *Acta Geotech* 11:953

Emerging Subjects in Geotechnical Engineering

Prediction of Load Capacities of Closed-Ended Piles Using Boosting Machine Learning Methods



S. Karakaş , M. B. C. Ülker , and G. Taşkın 

Abstract In this study, a novel data-driven model is developed using boosting-type machine learning algorithms with the aim of predicting the ultimate load-bearing capacities of closed-ended piles. A comprehensive database is gathered using the full-scale load test data with four features. Special boosting type machine learning methods are trained and tested with the database. Once predictions are made, a newly developed machine learning algorithm called Shapley method is utilized to decide the effectiveness of the selected features in predicting pile capacities. Results indicate that the pile cross-section area and length features are sufficient to achieve accurate predictions covering the parameters on the pile side and the CPT-based tip resistance is the only parameter needed on the soil side. While different boosting methods result in different levels of accuracy in predicting the load bearing capacities of closed-ended piles, it is generally possible to determine the minimum number of features necessary to satisfy a high goodness of fit. In the end, optimum number of features are determined in the prediction process using the Shapley method through the boosting algorithms giving us a valuable prediction tool for estimating the bearing capacity of closed-ended piles.

Keywords Boosting algorithms · Closed-ended piles · CPT test · Load-bearing capacity · Machine learning · Shapley method

1 Introduction

Axially loaded piles are widely used as deep foundations for transferring structural loads to stiffer load-bearing soils or rock layers. These piles can be classified based on their material types, installation methods, or areas of use. Bearing capacity of piles

S. Karakaş
Department of Civil Engineering, Istanbul University-Cerrahpaşa, 34320 Istanbul, Turkey

M. B. C. Ülker (✉) · G. Taşkın
Institute of Disaster Management Earthquake Engineering Program, Istanbul Technical University, Istanbul, Turkey
e-mail: mbulker@itu.edu.tr

© The Author(s), under exclusive license to Springer Nature Switzerland AG 2023
C. Atalar and F. Çinicioğlu (eds.), *5th International Conference on New Developments in Soil Mechanics and Geotechnical Engineering*, Lecture Notes in Civil Engineering 305, https://doi.org/10.1007/978-3-031-20172-1_21

225

subjected to axial loading has been investigated since the early days of geotechnical engineering. The methods used for estimating the bearing capacity need local soil conditions. Cone Penetration Test (CPT) reveals such information on soils. Machine Learning (ML) is particularly used as a prediction tool to estimate load capacity of piles.

Samui [3] uses the Support Vector Machine (SVM) in pile foundations where their model predicts the friction capacity in clayey soils from pile geometry, stress history, and undrained shear strength. Ebrahimiyan and Movahed [4] develop an ML based genetic algorithm to predict axial capacity of piles. Their database consists of data from open-ended piles, h-section piles, and drilled shafts. Ghorbani et al. [1] develop a model that predicts pile capacity with CPT results using the Adaptive Neuro-Fuzzy Inference Systems (ANFIS) method. Kardani et al. [5] use six different ML methods to estimate pile bearing capacity again with a small number of data, where they find out that the optimized methods improve the performance. Pham et al. [6] develop Deep Learning Neural Network (DLNN) for bearing capacity estimation. In a recent study, Harandizadeh et al. [2] perform similar work on different databases with an optimized ANFIS method. Approximately 80% of examined studies conduct ML analysis with less than 100 pile samples [4], Harandizadeh et al. [2]. Studies show that ML methods provide a satisfactory performance, while they exhibit a highly complex black-box structure limiting their interpretability. Explainability of models is important in geotechnical engineering in that more reliable interpretations can be made if it is known how the model produces such results. To address this issue, the Shapley Additive Explanation (SHAP) method is introduced to quantify the ability of ML methods in interpreting their predictions. Wang et al. [7] use the boosting methods to perform seismic slope stability analysis investigating the importance of four features with the SHAP. Nasiri et al. [8] predict the uniaxial compressive strength and Young's modulus using XGBoost, Random Forest and SVM where they use the explainability of ML methods via SHAP. Other most recent methods that use the SHAP are Liang et al. [9], Kannangara et al. [10]. In this study, the bearing capacity of closed-ended piles is predicted with the help of the boosting methods of XGBoost, LightGBM and CatBoost. The five-fold cross validation method is used in the training of the methods. More importantly, the features that play the most important role in making such a prediction are determined through the SHAP method.

2 Database Collection

In this study, the closed-ended pipe piles (CEP) are considered and related database is gathered from the available load-deformation relationships of full scale static pile load tests and cone penetration tests (CPT). Data from both driven piles and drilled shafts take place in the databases, where concrete and steel piles with various cross sections are all considered. The CEP database involves a total of 219 pile load data. Four input features in our analyses are determined as the pile length (L), pile cross-sectional area (A), cone resistance from CPT at the pile tip ($q_{c,end}$), and the cone

Table 1 CEP database statistical values

	Feature	Count	Mean	Std	Min	25%	50%	75%	Max
Input	L	219	14.56	8.72	5.60	8.55	11.50	16.68	45.00
	A	219	0.25	0.35	0.06	0.10	0.13	0.21	2.54
	$q_{c,end}$	219	9.42	7.63	0.17	4.30	7.61	12.18	65.95
	$q_{c,ave}$	219	5.64	4.43	0.38	2.70	4.34	7.13	24.64
Output	Q_u	219	2202.76	2228.75	210.00	884.82	1320.00	2775.00	14,590.17

resistance along the pile length ($q_{c,ave}$). The only output is the pile bearing capacity (Q_u). Table 1 shows the statistical parameters of this database.

3 Machine Learning Methods

3.1 *eXtreme Gradient Boosting (XGBoost)*

XGBoost is a high-performance version of the Gradient Boosting (GB) algorithm optimized with various modifications. The algorithm designed by Chen and Guestrin [11] is used in Kaggle competitions due to its high predictive performance.

3.2 *Light Gradient Boosting Machine (LighGBM)*

LightGBM is a boosting algorithm developed by Ke et al. [12] as part of the Microsoft’s Distributed Machine Learning Toolkit (DMTK) project. Compared to other boosting algorithms, it has a high processing speed, large data processing, less computational resource usage and parallel processing. According to Ke et al. [12] LightGBM is twenty times faster than two versions of XGBoost, LightGBM.

3.3 *Categorical Boosting (CatBoost)*

Catboost is an open-source ML algorithm based on GB developed by Prokhorenkova et al. [13]. It was introduced as an alternative to XGBoost and LightGBM, which are developed to increase the performance of GB. High learning speed, ability to work with numerical, categorical and text data, GPU support and visualization options are the most distinguishing features of Catboost, which builds a symmetrical tree structure.

4 Feature Selection via a Model Interpretability Method

The feature importance of ML models is quantified with the Shapley Additive Explanation (SHAP) method, which allows to determine the importance of inputs towards their prediction success. ML methods quantify the feature importance themselves also called the Gini Importance (GI). GI calculates the importance of each feature as a sum of the number of splits across all trees, which are then compared to the SHAP importance values. Ultimately the aim here is to identify which inputs are more important towards the prediction of load-bearing capacity of closed-ended piles.

4.1 Shapley Additive Explanation (SHAP) Method

SHAP provides the necessary interpretability of tree-based algorithms and explains how the model predicts a value through the feature selection methodology [14]. Given a model, v , Shapley for each input feature can be computed as:

$$\phi_i^S(v) = \sum_{S \subseteq N \setminus \{i\}} \frac{|S|!(n - |S| - 1)!}{n!} [v(S \cup \{i\}) - v(S)] \quad (1)$$

where i is the selected feature, S is a subset of features that excludes the i th feature, N is the number of all features in the input, and n is the total number of features. SHAP exhibits local/global interpretability with the effects of features on each observation.

5 Results

In this study, three boosting ML methods are applied to the CEP database. In both databases, 20% of the data, which is not used for cross-validation, is randomly selected and reserved for testing phase, while the rest is used for training. In the training phase the *fivefold cross validation method* is used for model tuning. Following the training/testing of the databases, the interpretability of the predictions of ML models are obtained through the SHAP analyses. Here, SHAP values for individual features as well as feature combinations are obtained. Figure 1 shows the flow diagram of the ML predictions adopted in this study.

Standard deviation is calculated to quantify the quality of training/testing separation. The purpose of the separation is to satisfy a certain level of uniform representation in the characteristics of the data included in the entire database. When the statistical properties of the training and test data are different from one another, it is observed that the two sets behave differently, where the model performs poorly on the test data. In this study, the training and test set is separated by a *random*

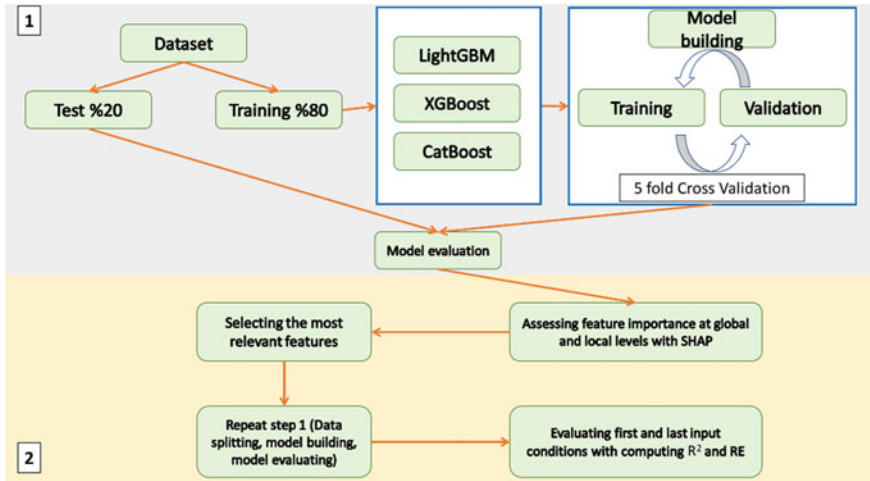


Fig. 1 Flow diagram of ML models constructed and the prediction process

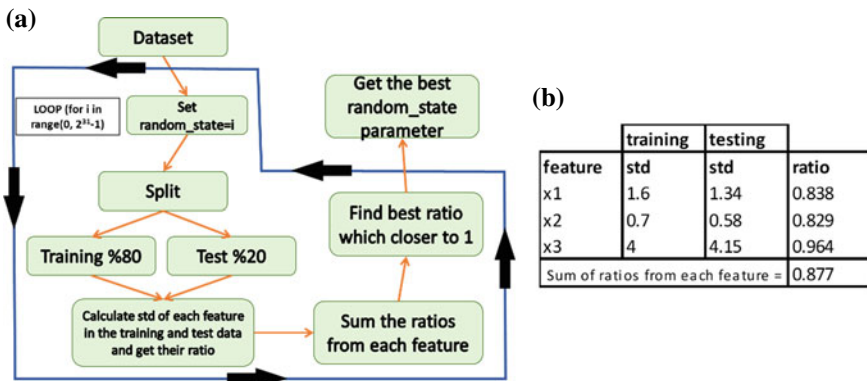


Fig. 2 a Quantification of suitability in splitting training/testing, b Calculation of this process

state hyper-parameter. Figure 2a shows this process in a related flowchart. Figure 2b shows an example of this process.

5.1 Analysis with CEP Database

The ratio of statistical parameters of training and test data for the obtained random-state value is given in Table 2, while the performance of each ML method on the test dataset in terms of R^2 and RE scores are presented in Table 3. We observe from Table 3 that the boosting-based methods, LightGBM, CatBoost and XGBoost

perform similarly. The effect of each feature on the ML models are then analyzed with the SHAP method, whose results are presented in Fig. 3.

In Fig. 3, the XGBoost model gives out the pile ‘cross section area’ about 70% importance, while the SHAP method gives that to be slightly less. The model gives less importance to other inputs, while the Shapley values indicate otherwise. Similarly, the LightGBM model results in the area feature to have more than 30% importance, while SHAP mentions that to be more. The importance given to other inputs in terms of predicting the pile load capacity (Q_u) is less important for the CatBoost model. The XGBoost’s SHAP shows significance placed on the area feature compared to others.

Table 2 Ratio of statistical properties for training and test dataset splitting in of CEP database

	Feature	Std	Mean	Max	Min
Input	L	0.99	0.99	0.82	0.96
	A	0.89	0.94	0.69	1.00
	$q_{c,end}$	0.99	0.94	0.45	0.33
	$q_{c,ave}$	0.99	0.91	0.67	0.89
Output	Q_u	0.98	0.89	0.83	0.67

Table 3 Performances of each ML method on the test dataset of CEP database using four features

	LightGBM	Catboost	XGboost
R ²	0.8	0.8	0.76
RE	0.37	0.36	0.33

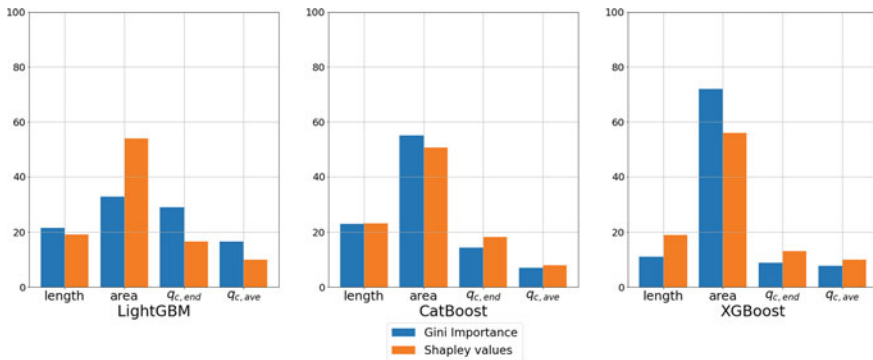


Fig. 3 Gini Importance and Shapley values computed for each ML method on the CEP database

5.2 Global Interpretation

Figure 4 shows the variations of the SHAP values for each model. These are the summary plots that combine feature importance values with feature effects. Each point on the summary plot is a Shapley value for a certain feature, and the color code represents the value of the feature from low to high importance. The area feature shows similar behavior in all the ML models. That is, all models show that the pile cross section area is crucial in predicting the bearing capacity, which gives a low SHAP at low feature values. According to the length and $q_{c,ave}$ feature graphs, such a behavior for the $q_{c,end}$ is clear, which gives SHAP close to zero in mean with a narrow bandwidth. Shapley values of the $q_{c,ave}$ in medium-sized data gather around zero.

According to these SHAP results, the length, area and $q_{c,end}$ features are sufficient to estimate the pile bearing capacity. That is, two geometric features attributed to piles (area and length) and a single feature for soil ($q_{c,end}$) seems to be sufficient in predicting the CEP load capacity.

With the detection of the most important features, models are trained and tested again with only these features (area, length and $q_{c,end}$). The split of the dataset into training/testing is carried out the same way for both cases (old 4 features and new 3 features). Once the training is finished, the performances of the predictive ML models are evaluated with the test data. Table 4 shows the new RE and R^2 values.

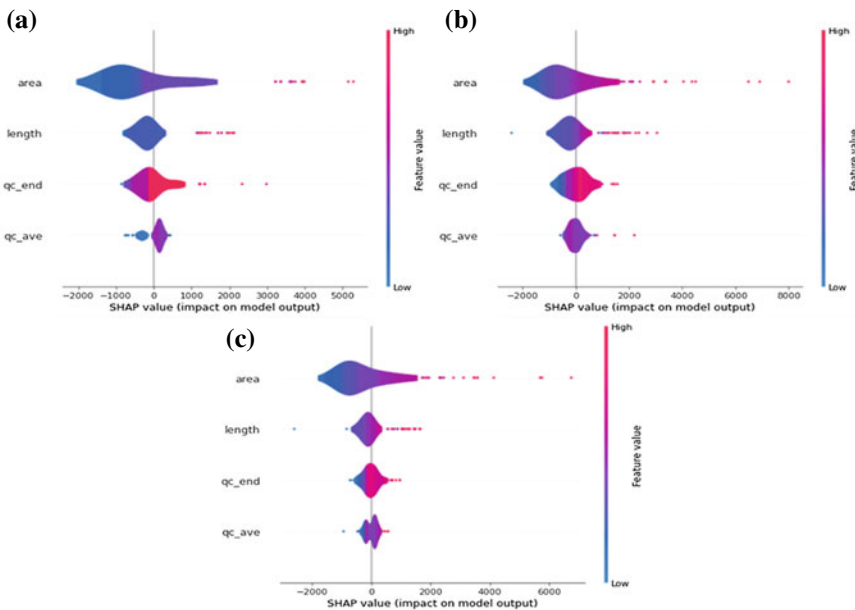


Fig. 4 Global SHAP values of features in a LightGBM, b CatBoost, c XGBoost for the CEP

Table 4 Load bearing capacity predictions of four ML methods with three features

	LightGBM	CatBoost	XGBoost
R ²	0.85	0.83	0.87
RE	0.47	0.36	0.42

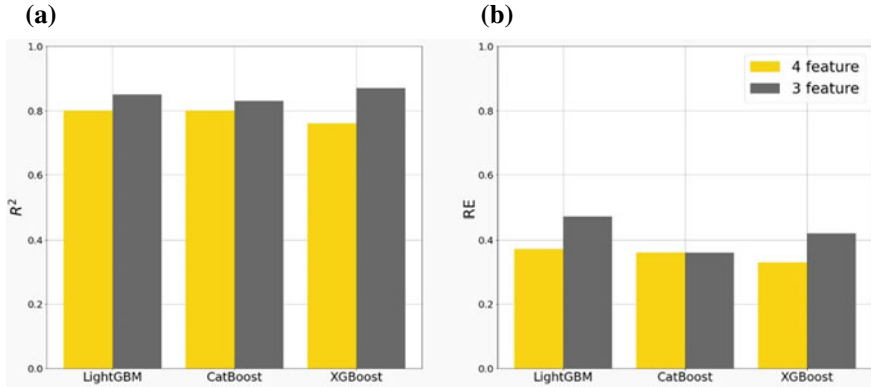


Fig. 5 a R² values and b RE values of the model predictions for two different feature selections

The performance variations between the models trained with the features suggested by these methods and the ones trained with the four features are in Fig. 5a, b. The three-feature sets result in better predictions in all the ML methods compared to the four-feature ones. Thus, two geometric pile parameters and a single soil parameter are indeed sufficient to predict the pile bearing capacity with a high accuracy.

6 Conclusions

Ultimate load-bearing capacity of closed-ended piles is predicted through boosting machine learning algorithms. The LightGBM, CatBoost and XGBoost methods are used and the importance of features are investigated with a model explainability method called SHAP. Upon analyses, the area, length and $q_{c,end}$ are determined to be the crucial ones in making fairly accurate predictions towards load-capacity of closed-ended piles.

References

1. Ghorbani B, Sadrossadat E, Bolouri Bazaz J, Rahimzadeh Oskooei P (2018) Numerical ANFIS-based formulation for prediction of the ultimate axial load bearing capacity of piles through CPT data. *Geotech Geol Eng* 36(4). <https://doi.org/10.1007/s10706-018-0445-7>

2. Harandizadeh H, Jahed Armaghani D, Khari M (2021) A new development of ANFIS–GMDH optimized by PSO to predict pile bearing capacity based on experimental datasets. *Eng Comput* 37(1)
3. Samui P (2008) Support vector machine applied to settlement of shallow foundations on cohesionless soils. *Comput Geotech* 35(3)
4. Ebrahimian B, Movahed V (2017) Application of an evolutionary-based approach in evaluating pile bearing capacity using CPT results. *Ships Offshore Struct* 12(7). <https://doi.org/10.1080/17445302.2015.1116243>
5. Kardani N, Zhou A, Nazem M, Shen SL (2020) Estimation of bearing capacity of piles in cohesionless soil using optimised machine learning approaches. *Geotech Geol Eng* 38(2)
6. Pham TA, Tran VQ, Vu HLT, Ly HB (2020) Design deep neural network architecture using a genetic algorithm for estimation of pile bearing capacity. *PLoS One* 15:e0243030
7. Wang L, Wu J, Zhang W, Wang L, Cui W (2021) Efficient seismic stability analysis of embankment slopes subjected to water level changes using gradient boosting algorithms. *Front Earth Sci* 9
8. Nasiri H, Homafar A, Chelgani SC (2021) Prediction of uniaxial compressive strength and modulus of elasticity for Travertine samples using an explainable artificial intelligence. *Results Geophys Sci* 8
9. Liang M, Chang Z, Wan Z, Gan Y, Schlangen E, Šavija B (2022) Interpretable ensemble-machine-learning models for predicting creep behavior of concrete. *Cem Concr Compos* 125
10. Kannangara KKPM, Zhou W, Ding Z, Hong Z (2022) Investigation of feature contribution to shield tunneling-induced settlement using Shapley additive explanations method. *J Rock Mech Geotech Eng*. Published online February 12, 2022
11. Chen T, Guestrin C (2016) XGBoost: a scalable tree boosting system. In: *Proceedings of the ACM SIGKDD international conference on knowledge discovery and data mining*
12. Ke G, Meng Q, Finley T et al (2017) LightGBM: a highly efficient gradient boosting decision tree. In: *Advances in neural information processing systems*, vol 2017-December
13. Prokhorenkova L, Gusev G, Vorobev A, Dorogush AV, Gulin A (2018) Catboost: Unbiased boosting with categorical features. In: *Advances in neural information processing systems*, vol 2018-December
14. Lundberg SM, Lee SI (2017) A unified approach to interpreting model predictions. In: *Advances in neural information processing systems*, vol 2017-December

Shear Strength Behavior of Perlite Added Sand-Bentonite Mixtures Under Room Temperature and Thermal Cycles



Esra Güneri and Yeliz Yukselen-Aksoy

Abstract The present study investigates the shear strength behavior of perlite added sand-bentonite mixtures under room temperature and thermal cycling. The increase in the number of energy structures causes interaction of soils with high temperature. Thermally durable soil material is needed around energy geo-structures. In this study, it was aimed to obtain a new buffer material to be used around energy structures by adding 10 and 20% perlite additive to 20% bentonite-80% sand mixtures (20B-80S). The direct shear tests were conducted under temperature cycling (8 hrs heating-16 hrs cooling). As a results of the compaction tests, it was seen that the perlite additive decreased the maximum dry unit weight ($\gamma_{\text{dry-max}}$) and increased the optimum water content (w_{opt}). The test results showed that perlite additive reduced the shear strength of the mixture under thermal cycles but with 20% perlite additive reached higher strength than 10% perlite additive.

Keywords Compaction · Perlite · Shear strength · Thermal behavior · Thermal cycle

1 Introduction

The demand for sustainable energy sources and structures is increasing due to the growing population and the need for energy. Solid waste and nuclear waste storage areas, buried power cables, geothermal energy plants, heat piles are the structures and facilities that cause temperature changes in the soil. Materials are needed which keep their engineering properties unchanged under thermal effects.

It is known that many engineering properties of soils change with temperature. For instance, temperature affects shear strength depending on thermal history, stress

E. Güneri (✉) · Y. Yukselen-Aksoy
The Graduate School of Natural and Applied Sciences, Dokuz Eylül University, 35390 İzmir,
Turkey
e-mail: esra_cetinorgu@hotmail.com

Y. Yukselen-Aksoy
Dept of Civil Engineering, Dokuz Eylül University, Izmir, Turkey

© The Author(s), under exclusive license to Springer Nature Switzerland AG 2023
C. Atalar and F. Çinicioğlu (eds.), *5th International Conference on New Developments in Soil Mechanics and Geotechnical Engineering*, Lecture Notes in Civil Engineering 305, https://doi.org/10.1007/978-3-031-20172-1_22

235

history and drainage conditions [1, 2]. The consequences of this effect vary depending on whether drainage is allowed during the heating phase. The shear strength of normally consolidated and slightly overconsolidated saturated clays heated in drained conditions increases. It was observed that the shear strength decreases due to the expansion of the soil and the excessive pore water pressure increases in undrained conditions [1, 3, 4]. Laloui [5] investigated the properties of saturated fine-grained soils such as compressibility, permeability and shear strength change due to temperature. Laloui [6] conducted the triaxial test at different temperatures (25, 70, and 90 °C) and at different temperature histories (25-70-25 and 25-90-25 °C) in undrained conditions. It was observed that the maximum deviatoric stress increased with the effect of temperature [5]. Cekerevac and Laloui [4] investigated that the shear strength of the kaolinitic soil with increasing the temperature. It was observed that the shear strength of kaolin clay increases in the presence of increased temperature from 22 to 90 °C [4]. In another study, triaxial compression tests were performed using Pontida silty clay and it was observed that the shear strength decreased when the temperature increased from 18 to 115 °C [6].

As a buffer material bentonite or sand-bentonite mixtures are currently used. Thermally resistant materials like perlite may improve thermal durability of buffer materials. Perlite is a highly porous additive material of volcanic origin, which is widely used in the construction industry, especially preferred for thermal insulation. Silicon dioxide, aluminum oxide, iron (III) oxide, calcium oxide, sodium oxide, potassium oxide, magnesium oxide are compounds found in the chemical structure of perlite [7].

In the present study, it was aimed to obtain a new buffer material by adding perlite additive to sand-bentonite mixtures as an alternative to these materials. The compaction and direct shear tests were conducted on the 20% bentonite-80% sand mixture (20B-80S) in the presence of 10 and 20% perlite additives. Direct shear tests were performed in two different conditions: room temperature and temperature cycle.

2 Materials and Methods

2.1 Materials

In this study, sand-bentonite mixture and perlite were used. These materials were supplied from local companies. The bentonite was Na-bentonite. The physico-chemical properties of the materials are given in Table 1 and grain size distributions of the samples are given in Fig. 1.

The sand used in the experiments was dried in an oven. In addition, it was sieved through No.6 sieve and used. While preparing the mixtures, 20% bentonite and 80% sand were used. Perlite was added to mixture in 10 and 20% contents.

Table 1 Physico-chemical properties of materials

	Bentonite	Sand	Perlite
Specific gravity	2.70	2.63	1.50
Liquid limit (%)	476	—	375.0
Plastic limit (%)	70	—	N.P
pH	9.5	—	8.96

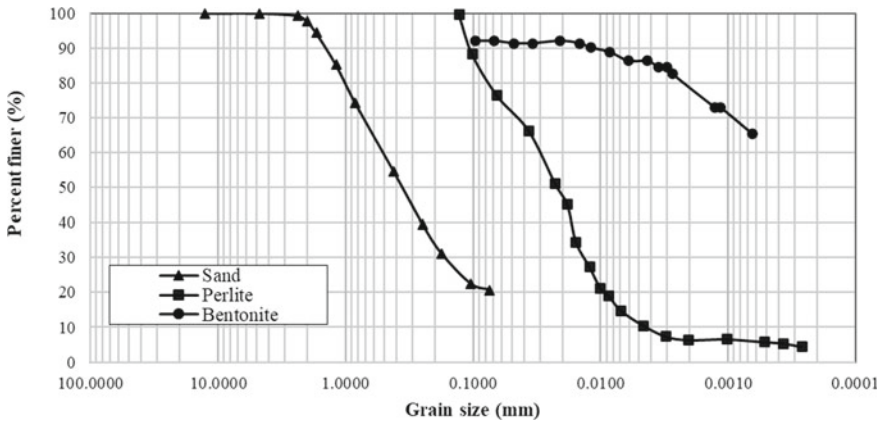


Fig. 1 Grain size distributions of the samples

2.2 Methods

Standard Proctor tests were conducted to determine the maximum dry unit weight and optimum water content of the mixtures. Compaction tests were performed according to ASTM D698-12 [8]. While preparing the mixtures, 10 or 20% of the total dry weight was determined as perlite, 20% of the remaining part was added as bentonite and the remaining part was sand.

Direct shear tests were performed according to ASTM D3080 [9]. Direct shear test samples were prepared at 2% wet side of the optimum water content. Samples were placed in 2 cm height and 6 × 6 cm² square molds. The samples were kept in submerged condition in water for 24 h, in order to prevent swelling weight was placed on the samples. Experiments were carried out under room temperature and temperature cycling. The temperature during heating was 80 °C, the temperature was provided with the help of the heat rod placed in the shear box and a thermostat was used to stabilize the temperature (Fig. 2). Inside the cell temperature was measured and recorded by means of a thermocouple placed in both the soil and the water. The shearing rate was chosen according to the oedometer test results in order to allow to drainage.

In the experiments with thermal cycle, the consolidation stage was started at 80 °C and after 8 h of heating, the samples were allowed to cool for 16 h. At the end of this

Fig. 2 Direct shear test apparatus for thermal cycle



period, the samples were sheared under a stress of 196 kPa. The temperature was room temperature (22–25 °C) during the shearing phase.

3 Results

In this study, compaction tests of 20B-80S mixture in the presence of perlite additives and direct shear tests under room temperature and temperature cycling were performed. The compaction parameters ($\gamma_{d,max}$ and w_{opt}) values of 20B-80S mixtures were given in Table 2. The compaction test results showed that the perlite additive decreased the dry unit weight of the mixtures and increased the optimum water content (Fig. 3). The specific gravity of perlite has a very low value of 1.5 causes a decrease in the dry unit weight, and its multi-void structure increases the water absorption capacity, leading to an increase in the optimum water content.

The direct shear test results of the mixtures showed that as the perlite content increased, the internal friction angle of the 20B-80S mixture also increased and the cohesion value decreased under room temperature (Table 3). Silanol (Si–OH) groups on the perlite surface are held by the clay surface by binding to hydroxyl groups at the edges of the clay plates [10]. Thus, the shear strength of the sand-bentonite mixture increases with the addition of perlite (Fig. 4).

Table 2 The Compaction parameters of 20B-80S mixtures

Mixtures	$\gamma_{d,max}$ (kN/m ³)	w_{opt}
20B-80S	15.6	17.5
18B-72S-10PE	11.1	25.0
16B-64S-20PE	8.8	50.0

Fig. 3 Compaction curves of the perlite added sand-bentonite mixtures

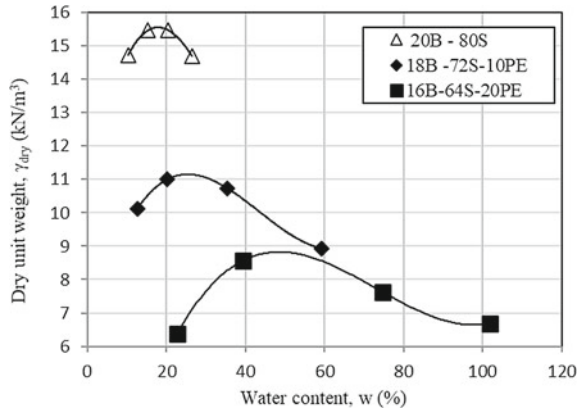


Table 3 Φ (°) and c (kPa) values of 20B-80S mixtures under room temperature

Mixtures	Φ (°)	c (kPa)
20B-80S	7.0	38.5
18B-72S-10PE	20.0	17.6
16B-64S-20PE	23.3	31.1

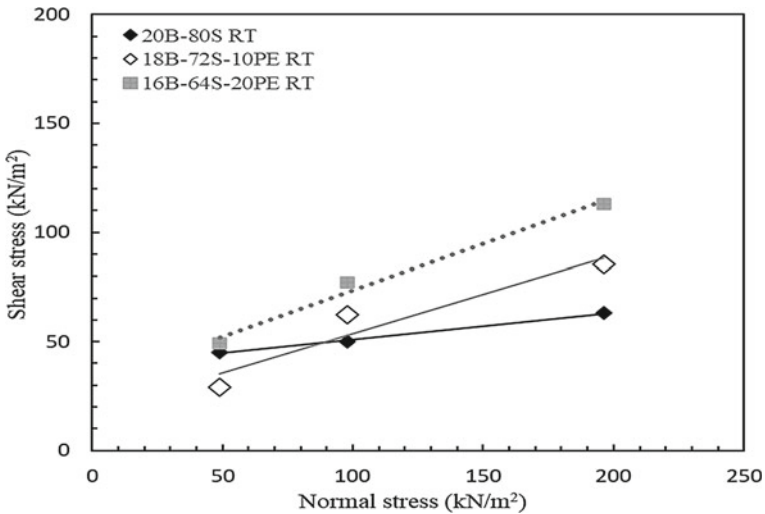


Fig. 4 τ - σ graph of the perlite added sand-bentonite mixtures under room temperature

In Fig. 5, the τ - ϵ_h graph of perlite added 20B-80S mixtures obtained from direct shear tests under temperature cycle (25-80-25°) and 196 kPa normal stress were given.

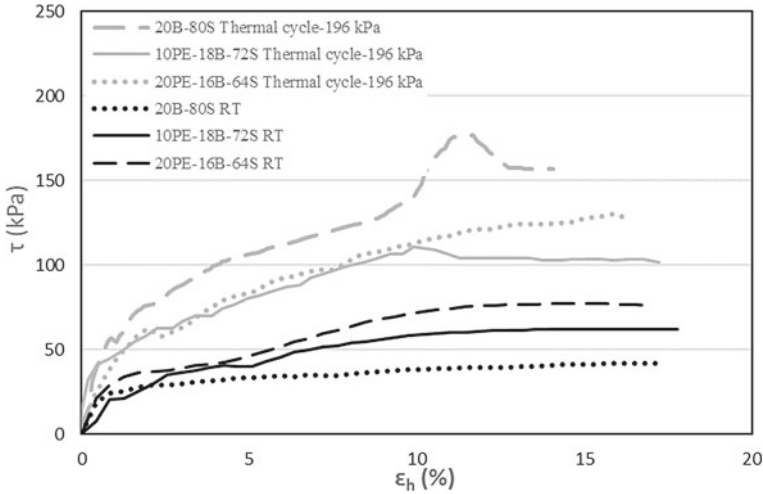


Fig. 5 τ - ϵ_h graph of the perlite added sand-bentonite mixtures under thermal cycle and room temperature

In the presence of perlite, the shear strength parameters were obtained of 20B-80S mixtures by consolidating under 8 h heating-16 h cooling cycle. The maximum shear stress value of the 20B-80S mixture was determined 176.1 kPa. This value decreased to 111 kPa with 10% perlite and 130 kPa with 20% perlite at room temperature. In addition, perlite additive decreased the shear strength of the mixture, but with 20% perlite additive reached higher strength than 10% perlite additive. The lower bentonite ratio in the 20% perlite added mixture causes the higher shear strength when compared with 10% perlite added mixture. In addition, the porous structure of perlite is one of the main reasons (material displacement) for this decrease in the strength of the sand-bentonite mixtures under thermal cycles.

As can be seen in Fig. 5, the perlite additive had an increasing effect on the shear stress of the additive free mixture under room temperature. Silanol (Si-OH) groups on the perlite surface were held by the clay surface by binding to hydroxyl groups at the edges of the clay plates [10] and this exchange causes increase in shear strength. However, this effect was not observed under temperature cycling. The fact that the voids formed in the structure of perlite with increasing temperature are irreversible when the mixture is returned to room temperature and it causes decrease in shear stresses. On the other hand, when the same mixture is taken into account, the stress value under the temperature cycle is higher than the value at room temperature can be explained by the increase in ductility [4]. In other words, because of ductility the mixture can sustain more deformation under the applied normal stress in the presence of high temperature.

4 Conclusions

In the present study, compaction and direct shear tests were performed in the presence of 10 and 20% perlite additive on the sand-bentonite mixtures. Direct shear tests were conducted under two different conditions, room and temperature cycle.

According to results of this study, when perlite additive was added to the 20B-80S mixture, it increased the optimum water content while decreased the dry unit weight of the mixture. The direct shear test results performed at room temperature revealed that perlite has an increasing effect on the shear strength of the mixture. In addition, the results of the direct shear test performed under the temperature cycle showed that both perlite ratios have a reducing effect on the shear stress value of the mixture. The shear strength improvement effect of perlite on sand-bentonite mixtures was found to be significant under room temperature but insignificant under thermal cycles.

References

1. Campanella RG, Mitchell JK (1968) Influence of temperature variations on soil behavior. *J Soil Mech Found Div* 94 (3):709–734
2. Xiao S, Suleiman MT, Al-Khawaja M (2019) Investigation of effects of temperature cycles on soil-concrete interface behavior using direct shear tests. *Soils Found* 59(5):1213–1227
3. Mitchell JK, Soga K (2005) *Fundamentals of soil behaviour*, 3rd edn Wiley, New Jersey
4. Cekerevac C, Laloui L (2004) Experimental study of thermal effects on the mechanical behaviour of a clay. *Int J Numer Anal Methods Geomech.* <https://doi.org/10.1002/nag.332>
Author
5. Laloui L (2001) Thermo-mechanical behaviour of soils. *Revue Française de Génie Civil*
6. Hueckel T, Baldi G: Thermoplasticity of saturated clays: experimental constitutive study. *J Geotech Eng* (1990)[https://doi.org/10.1061/\(ASCE\)0733-9410\(1990\)116:12\(1778\)](https://doi.org/10.1061/(ASCE)0733-9410(1990)116:12(1778))
7. Mekaddem N, Ben Ali S, Fois M, Hannachi A (2019) Paraffin/expanded perlite/plaster as thermal energy storage composite. *Energy Procedia*
8. ASTM D698-12 (2012) Standard test methods for laboratory compaction characteristics of soil using standard effort (12 400 ft-lbf/ft³ (600 kN-m/m³)). ASTM International West Conshohocken, PA, USA, pp 1–13
9. ASTM D3080/D3080M-11 (2011) Standard test method for direct shear test of soils under consolidated drained conditions, ASTM International West Conshohocken, PA, USA, pp 1–9
10. Ogawa M, Okutomo S, Kuroda K (1998) Control of interlayer microstructures of a layered silicate by surface modification with organochlorosilanes. *J Am Chem Soc* 120:7361–7362. <https://doi.org/10.1021/ja981055s>

Role of BIM for Different Phases of Geotechnical Investigation of the Transport Infrastructure



Ivan Vaníček and Martin Vaníček

Abstract The paper deals with application of BIM—Building Information Modelling and is focused on different phases of the Geotechnical Investigation, preferably for Transport Infrastructure. The result is combined 3D model of the Ground and Geotechnical structure—embankment of the motorway which enables to the construction partners not only discussed technical problems but also construction time schedule, financial flow.

Keywords BIM · Geotechnical investigation · Geotechnical design · Geotechnical model · Earth structures · Transport infrastructure

1 Basic Principles of BIM

In the last decade, with the process of digitization in construction, a process called BIM—Building Information Modelling—has come to the fore. BIM is a shared source of knowledge about construction, creating a reliable basis for decision-making during its life cycle, defined from the first concept to demolition.

In principle, it is a 3D model of the structure divided into the smallest details. Therefore, it was first applied to the field of mechanical engineering or energy/electronic structures, where the smallest detail, simply put, begins with the screw itself. This gradual division is easier for building structures—building Engineering, especially for the area of technical equipment of buildings than for the area of Civil Engineering. For building construction, division into unified parts is more common and allows their subsequent repetition. For civil engineering, this unification is significantly smaller.

I. Vaníček (✉)
Czech Technical University in Prague, Prague, Czech Republic
e-mail: ivan.vanicek@cvut.cz

M. Vaníček
Geosyntetika Ltd., Prague, Czech Republic

The 3D BIM model can be applied from the first beginning to the end of the construction life. It therefore has a clear development, of which the phase of completion of construction and presentation of the BIM model of the actual construction is important, which is then used throughout the life of various repairs, reconstructions and in its final phase serves to evaluate energy consumption not only for construction, but also operation and subsequently demolition of the building, Refs. [1–6].

The BIM model thus serves not only for the discussion of the individual construction participants in the design phase but also for the construction phase in terms of construction time schedule, financial flows, etc. Therefore, the abbreviation BIM in these cases of use is also interpreted as Building Information Management.

2 Role of Geotechnical Engineering in BIM Process

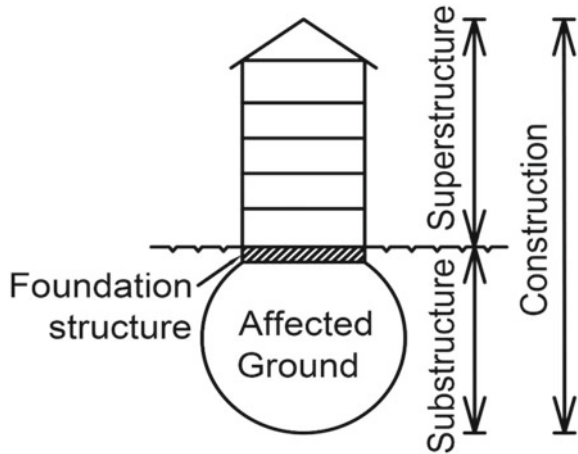
The role of geotechnical engineering occupies two basic positions in the whole BIM process:

- A role of a substructure that interacts with a superstructure.
- The role of the superstructure itself, which, however, also interacts with the substructure.

It should be emphasized here that the term substructure mainly represents the rock environment—ground—with which the superstructure interacts, but also the foundation structures by which the interaction of the superstructure with the rock environment—ground—is ensured. The relationship is shown in Fig. 1, and it follows that the term construction includes not only superstructure but also substructure, when the extent of the rock environment, which is still part of the whole construction is the part that is affected by the proposed construction. It therefore represents an area that needs to be sufficiently explored, as it must be considered when solving the limit states of the geotechnical structure, in this case the foundation structure. This corresponds to the most common definition of a construction, in which it is necessary to include not only the superstructure, but also the area of the affected rock environment—ground—including the foundation structures.

The above scheme applies to practically all building structures, but also to some engineering structures, such as bridges. On the one hand, there is the initial idea of the architect or building/structure engineer about superstructure and on the other hand, the initial idea of the geotechnical engineer about the rock environment—ground. Gradual specification of geotechnical properties for the rock environment—especially to the extent affected by the construction—leads to more precise ideas about the foundation structure that ensures the interaction. In most cases, the foundation structures will adapt to the original assumptions, but their optimization may lead not only to requirements for the ground improvement, but also to the design of superstructures with lower sensitivity to the limit states of geotechnical structures.

Fig. 1 Schematic representation of the term building—consisting of superstructure, foundation structure and ground affected by the whole structure



Thus, the following comes to the fore:

- Significance of individual phases of geotechnical survey corresponding to individual phases of geotechnical investigation of geotechnical structure
- Importance of close cooperation structural and geotechnical engineers, as are together responsible for safety, stability and economical design of structure.

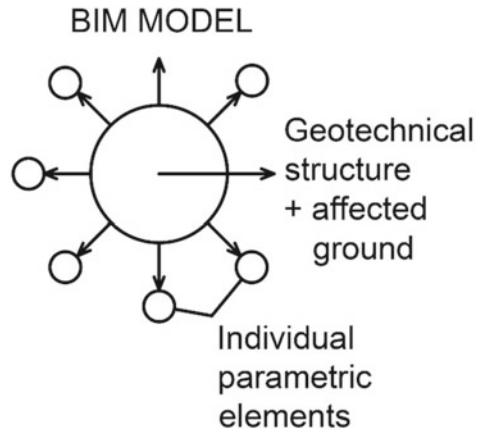
In particular, the second point leads to the requirement to connect 3D models of the superstructure and 3D model of the rock environment from the very beginning. The hitherto common separation of the 3D superstructure model, for example by an architect without a connection to the rock environment, is insufficient to meet the new requirements, even from the point of view of digitization and final construction. The new requirements require the connection of both models, which gradually leads to the refinement of the 3D model of the foundation structure that provides the interaction. However, the centre of the 3D model is the building (or bridge) itself, and the foundation structure with the rock environment forms an individual parametric element.

3 BIM Process for Transport Infrastructure

In the case of Transport Infrastructure, all 3 basic geotechnical structures come to the fore:

- Foundation structures, especially for the cases of bridge foundations, which were in principle described in the previous chapter.
- Earth structures, which include road or railway embankments and cuts, airports, parking lots, Refs. [7, 8].
- Underground structures—especially tunnels.

Fig. 2 Layout diagram of the BIM model, in the centre of which is a geotechnical structure (earth or underground with affected ground)



In the last two cases, the geotechnical structure itself is in principle characterized as a superstructure and it is a direct interaction of the earth or underground structure with the rock environment. The geotechnical engineer is thus not only involved in determining the geotechnical properties of the rock environment, but is also responsible for meeting the limit states as required for geotechnical structures in Europe in Eurocode 7-EN 1997 “Geotechnical design”. The centre of the 3D BIM model is both the earth structure and the underground structure, Fig. 2.

4 Relationship Between the Phases of Geotechnical Investigation and Geotechnical Design

This relationship is important for all structures, because each structure solves the interaction with the rock environment, in the form of foundation structures. Therefore, it is a general principle, the closer knowledge of which is important not only for geotechnical engineers who are engaged in investigation or design, but for all other participants in the construction process, starting with investors and ending with the contractor.

Currently, in the final phase of Eurocode 7 Geotechnical design of the second generation, there are 5 main phases of Geotechnical/Ground Investigation (GI), when the third phase, referred to as “Design Geotechnical/Ground Investigation”, is used for the actual design of geotechnical structure (GD). Subsequent phases are referred to as Supplementary GI or Confirmatory GI and serve both in the case of changes (modifications) to the geotechnical structure, or when finding at the beginning of the structure execution that the conditions of the rock environment differ significantly from those anticipated. Confirmatory GI is in principle a documentation of the exposed rock environment during structure execution and is part of the GCR—Geotechnical Construction Report, Ref. [9].

Table 1 Relationship between individual phases of geotechnical survey and design of geotechnical structure

Ground/geotechnical investigation GI	Geotechnical design
Desk study	Study—investment project (idea)
Preliminary GI	First step project documentation for planning inquiry
Design GI	Design (GDR)—documentation for building permit
Supplementary GI	Design modification—for construction
Confirmatory GI	GCR—Geotechnical construction report

The general relationship between the GI phase and the GD phase is given in Table 1.

Further attention will be focused on the first three phases. Their scope and focus are governed by the general principle. The care given to the survey and the design itself is governed by the risk associated with the proposed design and execution. For very undemanding constructions, realized in a simple rock environment and thus associated with a small to negligible risk, it is even possible to combine the individual phases into one, just confirming the original assumptions obtained on the basis of previous experience.

For common structures, especially for Transport Infrastructure, the assumption of 3 phases is justified. It is advisable to start with the requirements for the third phase, the Design Geotechnical/Ground Investigation. In the Design GI report, the geotechnical structure designer should receive basic information about the rock environment, its division into quasi-homogeneous lithological layers/geotechnical units including discontinuities with a summary of all the knowledge gained for each of them. Design GI report also contains information on groundwater, especially with regard to its changes over time, problem which is not part of this paper.

Subsequently, the designer selects from the data file the so-called representative/characteristic value of the geotechnical property, which he/she then uses in his Calculation Model. The selection is cautious and mainly considers the sensitivity of the partial property to the solved limit states. The reliability of the delivered set of properties within the Design GI, including the selection of representative values, can then be compared with the properties found primarily within the Confirmatory GI, how credible the investigation or the selection of the representatives/characteristic values was.

5 First Three Phases of the Geotechnical Investigation for Transport Infrastructure

Geotechnical structures for Transport Infrastructures are usually connected with relatively high risk, namely for foundation of bridges, for tunnels, and for earth structures with high embankments or deep cuts. The division of GI into 3 basic phases is therefore fully justified and has a direct link to geotechnical design, when in accordance with Table 1 it can be divided into:

- Investment project (idea), feasibility studies require a survey in the search of all available information (desk study) supplemented by personal site visit.
- First step project, documentation for planning inquiry requires preliminary GI and
- Design—Geotechnical Design Report—documentation for building permit requires detailed -Design GI

The main focus is the gradual refinement of the rock environment model up to the stage used by the geotechnical structure designer for his Geotechnical Design model. At the beginning, the geological view prevails, but over time, with the acquisition of information about the geotechnical properties of individual lithological layers of the rock environment, the geotechnical view prevails, not only in terms of the needs of the designer, but also the needs of the structure execution.

It is obvious that close cooperation is required not only of the GI developer and the designer of the geotechnical structure, but also of the investor and the builder/contractor of the construction.

5.1 Desk Study

Desk study, supplemented by a visit of the area of interest, is a relatively fast and undemanding way to obtain initial data. It mainly uses existing map data, where the main importance is geological, engineering geological and hydrogeological maps, in some countries as Finland also by geotechnical maps. In some states, it is possible to rely on a larger list of maps. In the Czech Republic, there are up to 17 sheets of so-called geological and environmental maps. The maps are supplemented by other archival documents, such as construction activities in the area of planned construction or the impact of the war years. The previous experience with the application of similar constructions in the vicinity is of great importance, especially in terms of geotechnical properties and experience with construction execution. In the case of Transport Infrastructure, especially line constructions, the amount of existing information obtained in the vicinity of cities that are connected by transport infrastructure will differ from information from places with limited existing development.

The result of the desk study should be the creation of the first initial stage of the geological model, but above all:

- Evaluation of the impact of the proposed construction on the rock environment, which is one of the primary materials for the EIA process—Environmental Impact Assessment—today a practically necessary requirement in most countries for the Transport Infrastructure.
- Evaluation of the impact of the rock environment on the proposed structure, emphasizing the potential geotechnical risks associated with this rock environment—thus using existing experience with the rock environment and experience with the implementation of similar structures in a similar rock environment.

As a result, it forms an important basis for deciding on the route of highways, railways, respectively. To choose between the considered variants of the communication route. If the designer defines a 3D terrain model, it is very useful to enter the initial geological model.

5.2 Preliminary GI

Preliminary GI—occupies a particularly important position in the whole process, not only in terms of its preparation—planning, but also in terms of its evaluation.

The main goal of preliminary GI planning is to define the area of the rock environment that will be affected by the proposed construction, both in the vertical direction (depth) and in the direction perpendicular to the communication route. Exploration points, especially boreholes and field exploration methods after determining their area and depth range will firstly specify the initial Geological model. Geophysical methods can also make a significant contribution to the rock environment model. However subsequently with the help of the obtained results of the geotechnical parameters the first Geotechnical model will be proposed. With new distribution of the layers in the rock environment, called in proposal of the second version of EN 1997—geotechnical units, for which it is approved that these units are quasi-homogeneous in terms of geotechnical properties. That the geotechnical properties for individual geotechnical unit create a closed set. In the Geotechnical model, these sets (files with obtained results) are assigned for each layer—geotechnical unit.

For the preliminary GI phase, it is sufficient if this quasi-homogeneity is demonstrated on the basis of index and descriptive properties of soils and rocks. This possibility significantly influences the initial decision on defining the required category of sampling methods and about laboratory quality classes of samples according to EC 7 Geotechnical design (also EN ISO 22475-1).

The basis of quasi-homogeneity verification is the grain size composition with the help of triangular diagram with percentage of fine (f), sand (s) and gravel (g) fractions—Fig. 3. For fine-grained soils, the verification should be supplemented by a plasticity diagram, Fig. 4. Evaluation of the clay activity index I_A is also useful, Fig. 5.

Fig. 3 Quasi-homogeneity verification based on grain size composition

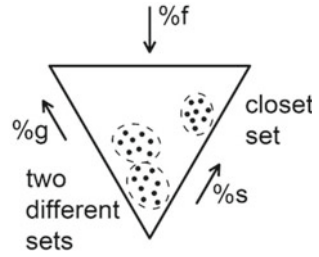


Fig. 4 Fine-grained soils, quasi-homogeneity verification based on plasticity

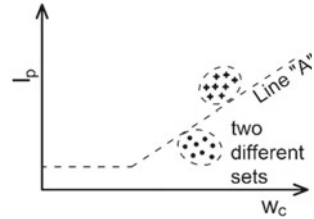
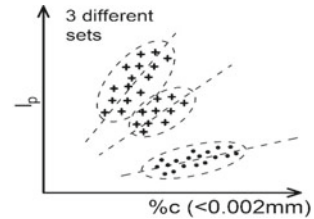


Fig. 5 Verification of quasi-homogeneity based on clay activity index I_A



From the point of view of determining the boundaries for various geotechnical properties, the determination of the state characteristics is also of great importance, the Consistency index I_c for fine-grained soils or the Index of density I_D (at least indicative) for coarse-grained soils.

One of the goals of the geotechnical model in the case of a relatively complex geological profile is to try to reduce the number of layers, but with the use of a certificate of quasi-homogeneity. For example, from the geologist's point of view, it is important to determine the interface between the Quaternary and the weathered bedrock. However, if the character of the rock eluvium is very similar in terms of geotechnical properties with the Quaternary, this possibility exists here.

The same applies to the cases of tunnels or deep cuts made in rock. Aspects of properties (e.g. simple compressive strength) predominate over aspects of geological development or detailed petrographic composition. The question of the degree of weathering also plays a very important role.

The joint discussion of the participating partners on the Geotechnical Model after the end of the Preliminary GI phase leads mainly to:

- Specification of the traffic route level, for fills, cuts, tunnels;
- Preparation of a project for documentation for planning inquiry, especially using derived geotechnical parameters for the geotechnical structures (using soil classification and table values, parameters derived from the application of field survey methods, or parameters derived from the previous experience—from a similar construction under similar geological conditions);
- To evaluate the ratio of excavations and embankments, including the suitability of the extracted material for embankments;
- The first valuation of land purchase entitlements for the final route management;
- Discussion on the implementation of the principles of Sustainable Construction, consisting in lowering of land consumption, as well energy together with CO₂ footprint and natural aggregates, their potential replacement by non-standard aggregates/waste materials, Ref. [10].
- Specification of requirements for the next phase of GI (Design GI).

5.3 *Design GI*

For the design of the geotechnical structures of Transport Infrastructure, it is necessary in the third phase of GI to ensure a sufficient number of results of measurements of mechanical-physical properties for each quasi-homogeneous layer/geotechnical unit for statistical evaluation. The areal and depth distribution of investigation points is based on the evaluation of the previous stage and is focused on places where there is greater uncertainty in order to specify it.

The Design GI phase is associated with greater demands on sampling and their quality. In principle, these are drilling applications with the collection of virtually intact samples and subsequent laboratory tests. Or the application of ground investigation methods, (e.g. penetration, pressure meter tests). Their mutual combination is optimal, when the depth sequence of layers can be visually observed on the drilling core, while ground investigation methods provide continuous information with depth with respect to the measured parameters from which mechanical-physical properties can be derived using verified correlations.

This phase of the GI also provides information on the geotechnical properties of soils after compaction and application to embankments.

The discussion of the BIM geotechnical model of the rock environment together with the marked geotechnical structure—embankment, cut, tunnel, foundations of bridge abutments and pillars is focused on evaluating the complexity of this phase with attention to the most sensitive places associated with geotechnical risk, including the view of the designer and contractor. However, the main goal of the Design GI is to ensure a safe and economical design of the geotechnical structure and its subsequent execution.

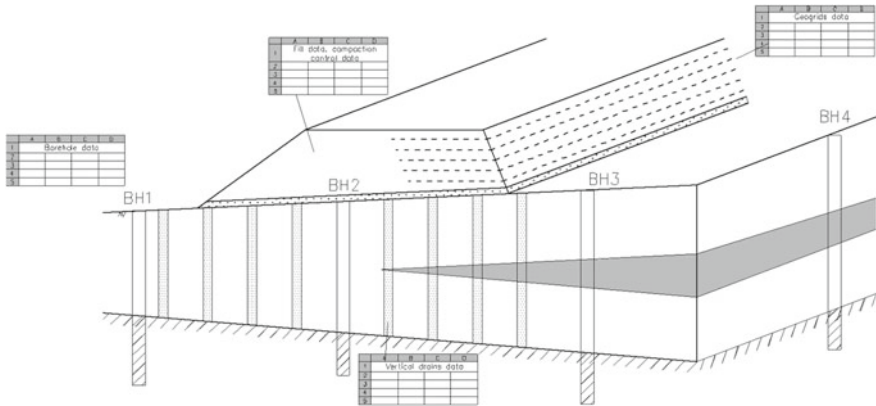


Fig. 6 BIM model of the real communication embankment (according to [5])

5.4 BIM Model of the Real Geotechnical Structure Execution

From the point of view of a geotechnical engineer, the final BIM model contains not only final Geotechnical model of the rock environment but also the model of the realized geotechnical structure as specified in the Geotechnical construction report.

An example of such a final 3D BIM model is the communication embankment on the subsoil improved by vertical geo-drains to accelerate consolidation, and it is possible to obtain additional information about all findings within the GI, about all construction materials used as well the results of quality control of the embankment construction, Fig. 6.

Such a BIM model is used throughout the life of the structure, most often about 120 years, and is used not only for maintenance and repairs of the structure but also for future potential interactions, whether it is an interaction with a new structure or a newly created interaction, such as during natural disasters or accidents caused by human activity, Ref. [11]. An example could be a truck accident with a hazardous substance when quickly choosing to protect the rock environment and the structure itself from contamination.

6 Conclusion

The paper primarily proves that the rock environment is an integral part of the construction, because the demonstration of safety and stability of the construction itself is also related to the demonstration of safety and stability of the rock environment, which is affected by the construction itself. The BIM model of the solved interaction of the bedrock and the geotechnical structure is gradually specified for individual phases of the Geotechnical investigation and design of the geotechnical

structure. It serves for closer cooperation of all partners in the construction process to ensure an optimal design adapted to the risk, specifically to Geotechnical categories according to Eurocode 7 Geotechnical design. At the same time, it represents a new element of construction documentation in digital form with easy use as needed in the future within the lifetime of the geotechnical structure itself.

References

1. McInerney J (2016) Implementing BIM on large infrastructure projects. Engineers Ireland cork region annual seminar 2016
2. Moryn G (2016) Geotechnical BIM: applying BIM principles to the subsurface. Autodesk University
3. Svensson M, Friberg O (2021) Full geotechnical BIM—a must for urban areas. Invited Lecture Nordic Geotechnical Meeting Helsinki
4. Van Nederveen GA, Tolman FP (1992) Modelling multiple views on buildings. *Autom Constr* 1(3):215–224
5. Vaníček I, Jirásko D, Vaníček M (2020) Modern earth structures for transport engineering. Engineering and sustainability aspects. CRC Press, Taylor and Francis Group
6. Vaníček I, Jirásko D, Vaníček M (2021) Role of geotechnical engineering in BIM process modelling. In: 14th Baltic Sea region geotechnical conference. Helsinki
7. Vaníček I, Vaníček M (2008) Earth structures in transport, water and environmental engineering. Springer, p 637
8. Vaníček I (2016) Specific position of earth structures in geotechnical structures design. Keynote lecture. In: Proceedings of the 4 ICNDSMGE. Nicosia
9. Vaníček I, Rockbeck Y, Bredeveld J, Jirásko D, Vaníček M (2021) Present demands on earth structures in transport engineering in Europe. In: 4 ICTG, Chicago, vol 3. Springer, pp 699–713
10. Vaníček I, Jirásko D, Vaníček M (2016) Added value of transportation geotechnics to the sustainability (Design Approach). Special lecture. 3 ICTG guimarães. *J Procedia Eng* 143:1417–1424
11. Vaníček I, Jirásko D, Vaníček M (2018) Interaction of transport infrastructure with natural hazards (landslides, rock falls, floods). Keynote Lecture. XVI DECGE, vol 1. Wiley Ernst & Sohn, Skopje, pp 135–164

Use of Neural Networks to Predict Correlations Between CPT and PMT Tests for Clay and Marl Soils



Mohamed Khiatine and Ramdane Bahar

Abstract The Menard pressuremeter (PMT) and the cone penetrometer (CPT) are the most widely used in situ tests for geotechnical investigations of sites in Algeria. Due to the quick and accurate results, they allow for field surveys, geotechnical design parameters and quality control assessments. Numerous correlations of geotechnical parameters measured from these two tests have been established in the literature. In this work, it is proposed to establish correlations between the geotechnical parameters deduced from the pressuremeter and the cone penetrometer tests for the clays and marls of the Algiers region in Algeria using the artificial neural networks approach (ANN). The parameters taken into account are the cone resistance of the CPT, the deformation modulus and the limit pressure deduced from the PMT. The results obtained will be discussed and compared to empirical relationships in the literature. The obtained correlations are relatively low compared to those from the literature.

Keywords Correlations · Pressuremeter · Cone penetrometer · Clay · Marl · ANN

1 Introduction

The geotechnical engineer is often confronted with heterogeneous soils during geotechnical investigations. This heterogeneity makes the mission more difficult, costly and increases the error of soil characterization. Geotechnical investigations are generally based on in-situ and laboratory tests. In this context the use of correlations between the different geotechnical parameters is essential in order to obtain more reliable results. In the practice of soil mechanics, correlations between parameters are also used as a means of controlling the results of in situ and laboratory tests,

M. Khiatine
Yahia Fares University of Medea, Medea, Algeria

M. Khiatine · R. Bahar (✉)
Faculty of Civil Engineering, University of Sciences and Technology Houari Boumediene (USTHB), LEEGO, Algiers, Algeria
e-mail: rbahar@usthb.dz

and as a means of producing complementary values for certain parameters in relation to others, especially for preliminary evaluation and design purposes.

In Algeria, among the wide range of in-situ tests, the cone penetrometer test (CPT) and the Menard pressuremeter (PMT) are distinguished, which occupy an important place in a geotechnical investigation campaign. Because of their rapidity of implementation and quickness of results obtained, their cost and because they adapt to most of the soils present on the surface, especially when these soils are generally soft and clayey. The CPT provides continuous evaluation of the subgrade profile with improved repeatability and reliability of test data. It measures continuous profiles of cone tip resistance (q_c) and sleeve frictional resistance (f_s). The PMT is an important field test that can be used to determine soil settlement and bearing capacity by direct measurement of the geotechnical properties of the soil, such as deformation modulus and limit pressure [1]. In the majority of projects, to minimize the costs associated with geotechnical testing, the investigation campaign often involves only one type of testing, which justifies the need to use specific correlations for each type of soil. The objective of this paper is to establish correlations between the geotechnical parameters derived from the CPT and PMT tests for the clay and marl formations encountered in the Algiers region using neural networks.

2 Review of Existing PMT-CPT Correlations

Several geotechnical researchers have presented relationships between the two most commonly used in-situ soil investigation tests, the PMT and CPT. These relationships allow engineers to take an empirical approach to evaluating and analyzing soil properties by converting the available database from either test into the parameter(s) of the other tests. Many studies have focused on fine soils (clays and silts) and have interpreted a number of correlations between PMT and CPT such as those published by several authors [1–5]. In general, these correlations are based on the ratio of the cone tip resistance (q_c) of the CPT and the limit pressure (P_l) of the PMT. The ratio of the net values q_c^*/P_l^* , would be more representative. The (q_c^*) and (P_l^*) are the net cone resistance of the CPT and the net limit pressure of the PMT, respectively, and can be calculated from:

$$q_c^* = q_c - q_0 \quad (1)$$

$$P_l^* = P_l - P_0 \quad (2)$$

q_0 and P_0 are total vertical stress and total horizontal pressure in the ground respectively.

Jezequel et al. [2] studied the influence of the depth on q_c^*/P_l^* on hydraulic fill dikes of a tidal power project in Rance, France [2]. The fill used was composed of clean sand with a dry density equal to 1500 kg/m^3 . The ratio q_c^*/P_l^* in the top 1.5 m

Table 1 The ratio (q_c^*/P_1^*) for different soil types according to Baguelin et al. [3]

Soil description	q_c^*/P_1^*
Very soft to soft clays	Close to 1 or From 2.5 to 3.5
Firm to very stiff clay	From 2.5 to 3.5
Very stiff to hard clay	From 3 to 4
Very loose to loose sand and compressible silt	From 1 to 1.5 and From 3 to 4
Compact silt	From 3 to 5

Table 2 The q_c/P_1 ratio for different soil types according to Briaud et al. [2]

Soil type	PMT parameter	Correlation to CPT
Clay	P_1	0.2 q_c
	E_m	2.5 q_c
Sand	P_1	0.11 q_c
	E_m	1.15 q_c

of fill was from 9.11 to 12.03. Although q_c varied from 2 to 10 MPa, q_c^*/P_1^* was approximately 6.7 in the rest of the 20 m thick backfill. According to [3] soil type has the greatest effect on q_c^*/P_1^* , and for depths of about 5–20 m there appears to be a close correlation between q_c^* and P_1^* . Baguelin et al. [3] consider that reasonable averages of q_c^*/P_1^* can be considered as those presented in Table 1. Wambekce [6] proposed, based on theoretical and experimental studies, that q_c/P_1 ratio be equal to 3 [6]. A total of 82 PMT borehole data from various projects from 1978 to 1985 were collected by Briaud et al. (1992) and the correlations in Table 2 were proposed [4]. Furthermore, many correlations have also been proposed to relate Menard’s modulus (E_m) to cone tip resistance (q_c) in a form of a ratio E_m/q_c in the literature [7, 8].

Many studies have been carried out on clays and silts. According to a study carried out on 165 comparative tests, Cassan [7] proposes an E_m/q_c ratio of between 2.5 and 3.3 [7]. Bahar et al. [8] propose from a campaign of tests conducted in Algeri-an clays values of E_m/q_c between 3.0 and 4.9 [8].

2.1 Situation, Geological and Hydrogeological Contexts of Studied Site

The study area is located in the region of Baraki, about 10 km East of the capital Algiers and relatively close to the coast of the Mediterranean Sea (around 5 km). The site covers an area of nearly 45 ha is intended for the future project of Baraki stadium and its associated structures. Within the framework of this project, several geotechnical investigation campaigns have been conducted between 2007 and 2013. The selected data were obtained from soil studies that were carried out in 2013 for the

four megapiles supporting the roof of the stadium. Geologically, the main formations encountered are brownish to greenish clays, grayish muds, blackish peats, deposits of coarse sand with the presence of gravels and pebbles (alluvium with passage of conglomerate) and marls. According to the hydrogeological map of the Algiers region, the study area is characterized by a generally high permeability with important water resources.

2.2 Geotechnical Data and Soil Properties of the Site

Several geotechnical investigation campaigns have been completed since 2007 for the project. The first was carried out in 2009 and the second in 2013. The results of the second campaign have been exploited in this communication [9]. In the site of interest, the geological formations outcropping are essentially constituted by clays and alluvium (filling of the Mitidja plain). The synthesis of the boreholes carried out allowed distinguishing in general two horizons. A superficial horizon from 0 to 12 m or even 30 m deep in the right of the East mega pile composed of brownish to greenish marly clays slightly pebbly, greyish vases and blackish peat in some places. The second horizon, beyond 6.0–30 m depth in some places consisting of alluvium resting on marl. Beyond about 30 m depth, the main formation encountered is the layer of yellowish grayish marl with grey stain little to pebbly becoming grayish with yellowish stain in depth (Pliocene marly substratum). The piezometric water level were made varied from -2.0 to -10.0 m.

Samples collected from boreholes at different depths were subjected to physical–mechanical tests in the laboratory. The results of these tests are shown in Table 3. The main formations encountered in site are essentially fine soils (Fig. 1). The results of the laboratory tests reveal formations not very dense to dense, not very plastic to plastic with the presence of some very plastic formations on the surface, soft to consistent, moderately compressible with passages rather to highly compressible by place, not swelling to relatively swelling.

In addition to the boreholes and laboratory tests, the following measurements were also made the pressuremeter tests (08) and CPT (08). The selected data were obtained from PMT and CPT tests that were performed as part of a soil investigation program at the four stadium mega-piles. The minimum and maximum depths of the CPT tests were 7.0 and 30 m respectively. However, PMT test depths were performed to 30 and 45 m. The obtained results in term of pressuremeter parameters (P_1 and E_m) are shown in Fig. 2. Also, the results obtained of cone penetrometer test parameters (q_c) is illustrated in Fig. 2. The type of the penetrometric machine employed on the site is Gouda type of 20 tons. The tip of the cone has an angle of 60° and a base area of 10 cm^2 . The sleeve lateral surface is 150 cm^2 , placed on top of the cone, in the zone influenced by the displacement bulb. The assembly is driven into the ground by means of a hydraulic system at a speed of 2 cm/s . The measurements of the characteristics are made every 20 cm.

Table 3 Physical and mechanical characteristics of the main formations of soils

Characteristics of the soil	Marly clay brownish to greenish with yellowish spots	Grayish marl (Pliocene marly substratum)
Horizon	Superficial horizon	Second horizon
Classification	Fine soil	Fine soil
γ_d (kN/m ³)	13.80 – 16.30	15.30 – 19.00
γ_h (kN/m ³)	18.65 – 20.05	19.20 – 21.00
w (%)	18.80 – 46.50	9.40 – 34.20
Sr (%)	92.00 – 100.00	48.00 – 100.00
w _L (%)	43.30 – 52.30	34.00 – 63.75
I _p (%)	19.65 – 25.40	16.50 – 33.00
φ (°)	4.95 – 13.44	8.05 – 25.93
C (kPa)	38.00 – 74.00	48.00 – 120.00
Compressibility	Medium to very compressible	Low to medium compressible

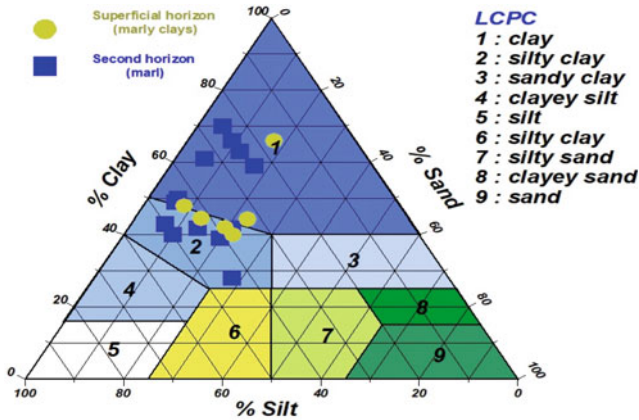


Fig. 1 Textural soil classification in a ternary diagram with LCPC denomination

From the examination of the lithological profiles of the PMT and CPT soundings, we can see that the soil is essentially constituted by two horizons, characterized by distinct pressuremeter and cone penetrometer parameters. The first horizon of very low to low resistance from 0 to 5 MPa (occasional exceeding 8 MPa) with an average of about 2.1 MPa, represented by the brownish to greenish marly clays and the second horizon with an average to quite resistant from 3 to 7 MPa up to exceed 9 MPa or even 10 MPa corresponding to the greyish marls (substratum). The first horizon, also characterized by limit pressures varying between 0.3 and 0.9 MPa with an average of 0.45 MPa and deformation modulus varying between 2 and 20 MPa with an average of about 5 MPa. E_m/P_1 ratio indicates subconsolidated to normally consolidated clays. Whereas the second horizon, which corresponds to the yellowish

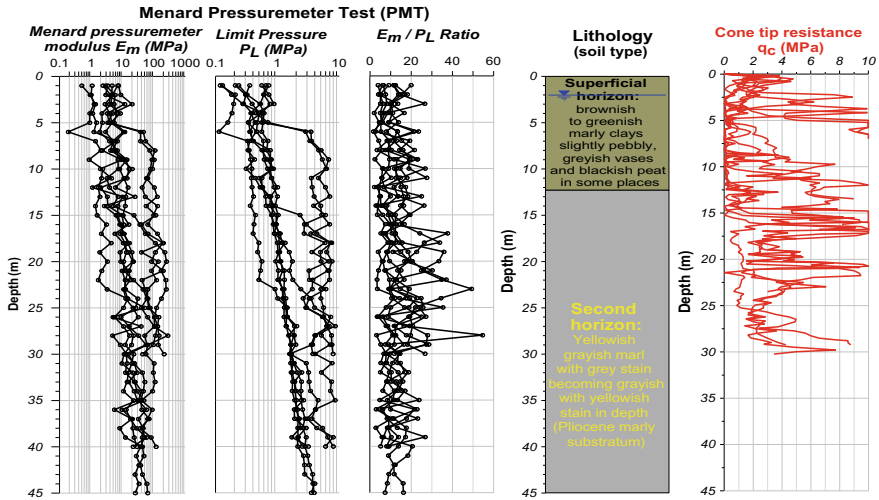


Fig. 2 Pressuremeter and penetrometric parameters results measured in the study area

to grayish marls, characterized by pressure limits ranging from 0.4 to 2.9 MPa with an average of 1.25 MPa, and pressure modulus ranging between 65 and 500 MPa with an average of around 140 MPa. The second horizon, E_m/P_1 ratio indicates mainly marls normally consolidated to over consolidated.

2.3 Analysis of CPT and PMT Data Using ANN

The practice of ANNs (Artificial Neural Net-works) in geotechnical engineering has developed considerably over the past decades. Several studies have suggested that neural networks were used for evaluating pile capacity prediction, soil behavior modeling, slope stability calculations, etc. [10]. It should be noted that soil engineering properties have a wide variety of uncertainties due to the heterogeneity of soil associated behavior. The ANNs are likely the best option for establishing a reliable relationship model with nonlinear data points. Recently, several studies have been conducted on the correlation of soil engineering properties with geotechnical and geophysical parameters of soils by incorporating neural networks [11].

ANNs are systems capable of adjusting their own internal configurations according to the desired objective. They are specially designed to solve problems with nonlinear variables. The processing elements of neural networks are called “nodes”, which is the basic element of this technique. The system consists of the various input and output nodes that communicate with other nodes or with the environment provided by the network. In addition, each network has its own functions that transform input into output, as shown in Fig. 3. In this study, the training process was performed by MATLAB, which includes a number of training algorithms, including

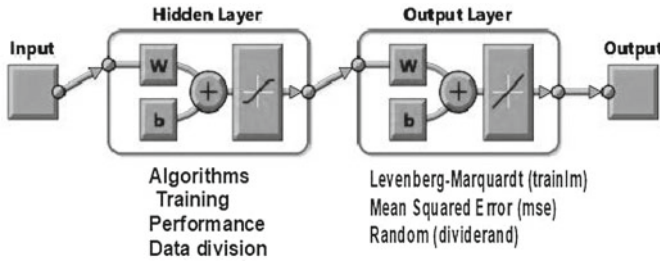


Fig. 3 Schematic showing a processing element containing a neuron to compute an output from an input

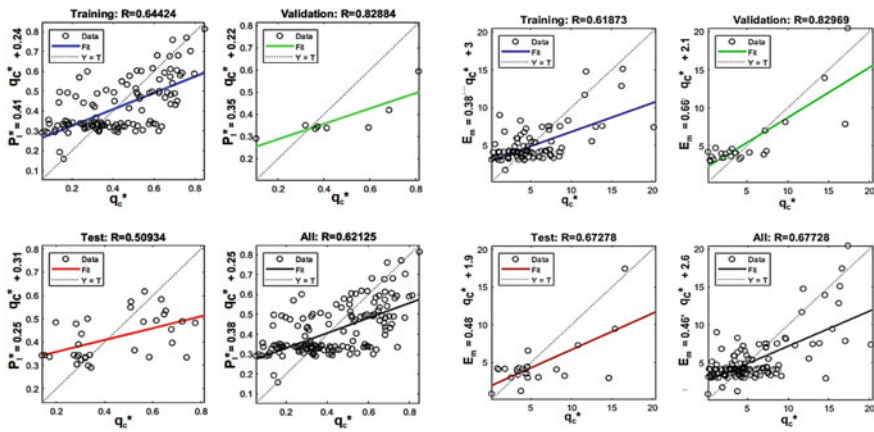


Fig. 4 Correlations q_c^* (MPa) versus P_1^* and q_c^* (MPa) versus E_m (MPa) in the superficial horizon (clay and marl clay) using ANN

the back propagation training algorithm. The collection of measurements from PMT and CPT tests performed on the two different soil horizons (surface horizon: marl clay and second horizon: marl), located in the province of Baraki, Southeast of the capital of Algiers. Figures 4 and 5 show the results obtained from the cone tip resistance with net pressure limit and pressuremeter modulus for the two different types of soil horizons encountered mainly on site.

2.4 Result and Discussion

A total of 165 sets of clay and marly clay and 140 sets of marl soil data from site were collected using the results of the CPT and PMT tests. Data subdivided in three sets: 15% of the data for testing, 15% of data for validation and the remaining 70% of the data were used for training. According to the trend shown in the graphs above,

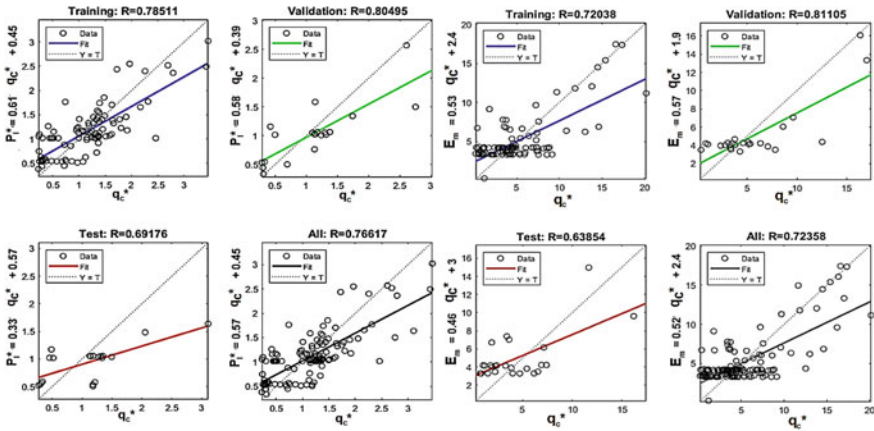


Fig. 5 Correlations q_c^* (MPa) versus P_1^* and q_c^* (MPa) versus E_m (MPa) in the second horizon (marl) using ANN

the limit pressure and pressure modulus increase with the cone tip strength and the re-regression coefficient R^2 is from 0.80 to 0.82 for the validation data, from 0.61 to 0.78 for the training and between 0.62 and 0.76 for all the tested values. This result can be considered a good regression value. The adjustment relation obtained between the net limit pressure (P_1^*) and the net cone tip resistance (q_c^*) for the very soft marly clays is of the form: $P_1^* = 0.38 q_c^* + 0.25$ and for the marl is of the form: $P_1^* = 0.57 q_c^* + 0.45$. However, the adjustment relation obtained between the pressuremeter modulus (E_m) and the net cone tip resistance (q_c^*) is as follows: $E_m = 0.46 q_c^* + 2.6$ for clays and marly clays and for marls is of the form: $E_m = 0.52 q_c^* + 2.4$.

3 Conclusions

The correlation between CPT and PMT parameters was studied using ANN for a heterogeneous site, located in the province of Baraki, South-East of the capital of Al-giers. For clays and marly clays examined, the average E_m/q_c ratio is about 3.47, this value is in agreement to those proposed by Bahar et al. (1999) and Van Wambekce. The average q_c^*/P_1^* ratio is about 2. This value is relatively lower compared to the literature, due to the marly clay studied which is very soft. For the marl studied (1982), it has been shown that, the ratio q_c/E_m is in the order of 1.5 and ratio q_c^*/P_1^* is 1.3. This range is lower compared to the literature, due to the marl studied which is soft. The work will continue for other marls in the study area with a bigger database in the future for a more reliable characterization of this formation.

References

1. Van Wambeke A (1962) Méthodes d'investigation des sols en place – étude d'une campagne d'essais comparatifs. *Sols-Soils* 2:9–18
2. Jezequel J, Lemasson H, Touze J (1968) Le pressiomètre Louis Ménard: Quelques problèmes de mise en oeuvre et leur influence sur les valeurs pressiométriques. *Bull Liaison LCPC* 32:97–120
3. Baguelin F, Jezequel J, Shields D (1978) The pressuremeter and foundation engineering. Trans Tech Publications, Stafa-Zurich
4. Briaud J (1992) The Pressuremeter. AA Balkema. Rotterdam, Netherlands
5. Van Wieringen J (1982) Relating cone resistance and pressuremeter test results. In: *Proceeding of the 2nd European symposium on penetration testing*. Amsterdam
6. Van Wambeke F (1982) Correlations between the results of static or dynamic probing and the pressuremeter tests. In: *Proceedings of the 2nd European symposium on penetration testing*. Amsterdam
7. Cassan M (1978) *Les essais in situ en mécanique des sols*. Eyrolles, Paris
8. Bahar R, Kaoua F, Aissaoui T (1999) Quelques corrélations entre essais in situ et essais de laboratoire pour certaines argiles Algériennes. In: *Geotechnics for developing Africa*. CRC Press, pp 255–262
9. LCTP (2013) *Complementary geotechnical investigations 40 000 places stadium*, Baraki, Algiers
10. Shahin MA, Jaksá MB, Maier HR (2001) Artificial neural network applications in geotechnical engineering. *Aust Geomech* 36(1):49–62
11. Ataeia OA, Moghaddasa NH, Lashkaripoura GR, Nooghabib MJ (2018) Predicting shear wave velocity of soil using multiple linear regression analysis and artificial neural networks. *Scientia Iranica* 25(4):1943–1955

Stability of Slopes and Landslides

Numerical Analysis of Slope Instability Due to Water Pipe Leakage



K. H. Park and G. Ramnauth

Abstract Buried pipe leakage can initiate landslides in road slopes. This study deals with stability analysis of a clayey slope subjected to water pipe leakage. A case study of landslides is considered for slope in Chatham Village of south Trinidad. Numerical analyses were conducted in two ways: (1) unsaturated seepage analysis using SEEP/W software to obtain the porewater pressure distribution and (2) slope stability analysis using SLOPE/W to calculate the factor of safety during water leakage. The results demonstrate that most important observations in water flow and stability responses of unsaturated clayey soil slope under water pipe leaking condition can be reasonably well simulated using the proposed numerical procedure.

Keywords Slope failure · Clayey slope · Water pipe leakage · Unsaturated flow · Stability analysis

1 Introduction

Trinidad is a tropical island of approximately 4,827 km², located at the south fringe of the Caribbean Sea. The climate is tropical and seasonal with a dry season from January through May, and a wet season from June through December. The annual temperature varies from 21–30 °C with average temperature of 25 °C. The rainfall averages 1520 mm. Topographically, the island is divided by three mountain ranges separated by undulating land, plains and swamps: the Northern Range, the Central Range, and the Southern Range. The majority of recorded landslides in the Northern Range are along the Maracas Road, caused by slope-disturbing activities where roads cross steep slopes, and triggered by intense rainfall [1]. In the Central and Southern Ranges, slope failures are prone to occur when high plasticity clays alternate with silty clays of medium to high plasticity with varying thickness and plasticity [2–5]. Around 76% of Trinidad and Tobago's landslips are in central and south Trinidad. Clayey soil, especially combined with excess water, contributes to the prevalence of

K. H. Park (✉) · G. Ramnauth
University of the West Indies, St. Augustine, Trinidad and Tobago
e-mail: KyungHo.Park@sta.uwi.edu

© The Author(s), under exclusive license to Springer Nature Switzerland AG 2023
C. Atalar and F. Çinicioğlu (eds.), *5th International Conference on New Developments in Soil Mechanics and Geotechnical Engineering*, Lecture Notes in Civil Engineering 305, https://doi.org/10.1007/978-3-031-20172-1_25

267



Fig. 1 Location of landslides

landslips. Such water may come from heavy rainfall, nearby homes including cesspits and soakaways, leaking WASA pipes, deforestation and vegetation clearance, etc.

Chatham Village is in the south-western Siparia region of Trinidad and is connected to the rest of the island by one road, the Southern Main Road (Fig. 1). There have been several slope failures along the ridge of the Southern Main Road, especially with two major failures (Fig. 1). These landslips along the Southern Main Road threaten to disconnect residents in Chatham Village from the rest of the island. Despite attempts to remediate the area, landslips continue to occur, and the causes of these slope failures have not been adequately determined. One constant factor among all of the slope failures has been leakages in buried water pipes.

The objective of this study is to investigate the effect of a progressive water leakage in buried pipe on slope stability.

2 Methodology

2.1 *Slope Model and Soil Properties*

After the landslides occurred, the geotechnical investigation was conducted by EISL [6] on December 14–15, 2015 at the request of the government agency. In this study, the typical section of slope for the analysis and soil properties are determined using the results of field survey, SPT and laboratory tests conducted by EISL. This study focuses on the stability analysis of Landslide B. Figure 2 shows the typical section of slope in clayey soils with buried pipe (0.4 m diameter water pipeline).

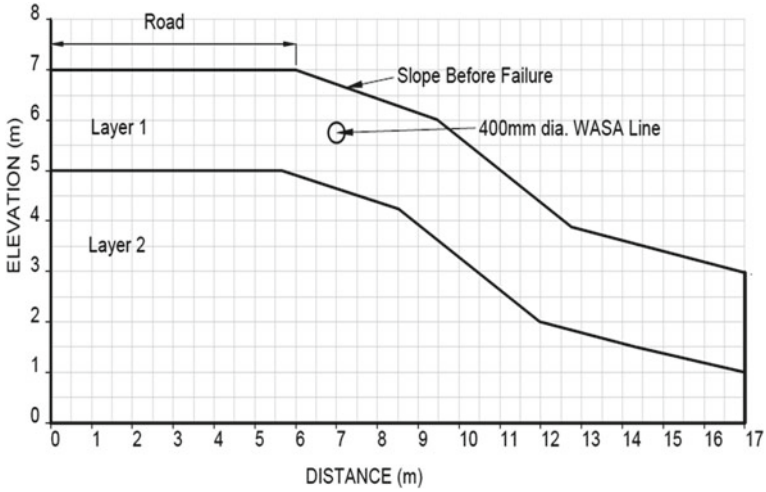


Fig. 2 Geometry of Landslide B (before failure) [6]

The basic soil properties of the soils are summarized in Table 1. The soil-water characteristic curve (SWCC) equation was obtained by a functional parameter regression model, such as [7, 8]

$$a = 32.835 \times \ln(wPI) + 32.438 \text{ (kPa)} \tag{1}$$

$$n = 1.421 \times wPI - 0.3185 \tag{2}$$

$$m = (-2.04 \times 10^{-4}) \times wPI + 2.22 \tag{3}$$

Table 1 Soil properties used in this analysis [6]

Parameter	Layer 1	Layer 2
USCS classification	CH	SC
Sand (%)	40.1	79.3
Silt & Clay (%)	59.5	13.8
Liquid limit (%)	57	34
Plasticity index (%)	45	23
Unit weight (kN/m ³)	18	19
Effective cohesion (kPa)	5	0
Angle of internal friction (°)	25	30
Saturated permeability (m/s)	5×10^{-8}	5×10^{-7}

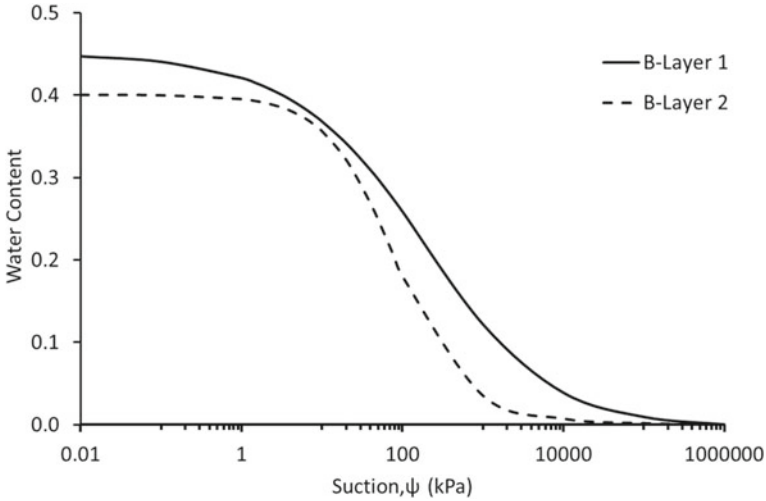


Fig. 3 SWCC used in this study

$$wPI = PI \times P_{200}/100 \tag{4}$$

where, a , n , and m = curve-fitting parameters for Fredlund and Xing’s [9] SWCC equation, PI = plasticity index (%), and P_{200} = percent of soil passing US standard sieve # 200 (%). The SWCC used for the analysis is shown in Fig. 3.

2.2 Seepage and Stability Analyses

To obtain porewater pressure distribution, a transient seepage analysis was conducted using SEEP/W [10]. Pipe leakage was modelled by applying a flow rate at the pipe source. The range of $1 \times 10^{-10} - 1 \times 10^{-6} \text{ m}^3/\text{s}$ can be considered as a single undetected leak to a very large leak [11]. Most pipe leakages begin as small leaks and then progress to become larger leakages. To simulate the progression of the pipe leakage, the flow rate was progressively increased from $1 \times 10^{-7} - 7 \times 10^{-7} \text{ m}^3/\text{s}$ at 5-day intervals to a maximum of 35 days, as summarized in Table 2. The modelling mesh is shown in Fig. 4.

SLOPE/W [12] was used to conduct the limit equilibrium stability analysis using the Morgenstern-Price method. The slip surface was set up by the entry and exit method considering the actual failed surface.

Table 2 Time step flow rates and duration

Step	Flow rate (m ³ /s)	Duration (day)
1	1×10^{-7}	5
2	2×10^{-7}	5
3	3×10^{-7}	5
4	4×10^{-7}	5
5	5×10^{-7}	5
6	6×10^{-7}	5
7	7×10^{-7}	5

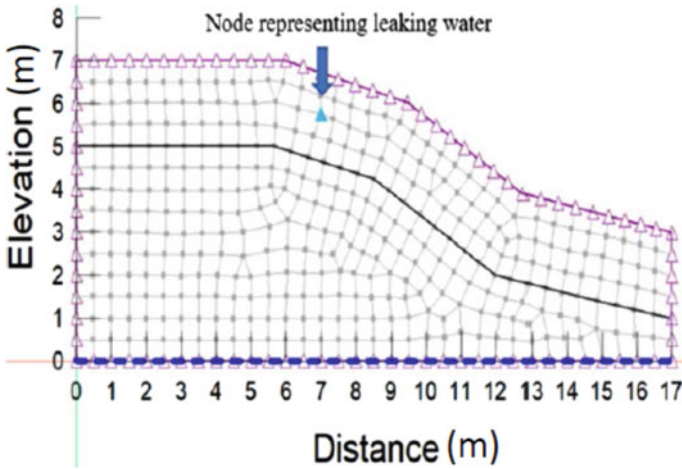


Fig. 4 Modeling mesh

3 Results and Discussion

3.1 Effect of Flow Rates

The changes in factor of safety with respect to time at different flow rates are shown in Fig. 5. At time 0 day, the factor of safety is at its highest irrespective of the flow rate because the shear strength of the soil is greater than the overburdened stress at the initial dry condition. The factor of safety fell below 1.0 at a flow rate of 1×10^{-6} and 5×10^{-7} m³/s at days 9 and 57 respectively. However, for flow rates of 2×10^{-7} and 1×10^{-7} m³/s, there was no failure within 180 days.

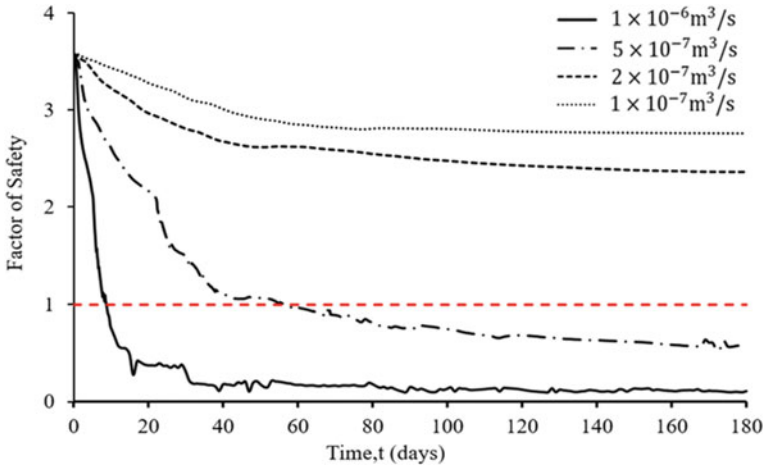


Fig. 5 Variation of factor of safety for different flow rates

3.2 Effect of Progressively Increasing Flow Rate

The change of the safety factor due to progressively increasing flow rate in Table 2 is shown in Fig. 6. For every change in the flow rate, there is gradual change in factor of safety up to 25 days. Thereafter, the factor of safety decreases significantly and drops below 1.0 at approximately day 33.

Small leakages in buried water pipes are difficult to detect. However, if these small leakages are not repaired early, the damage can progress and lead to slope instability.

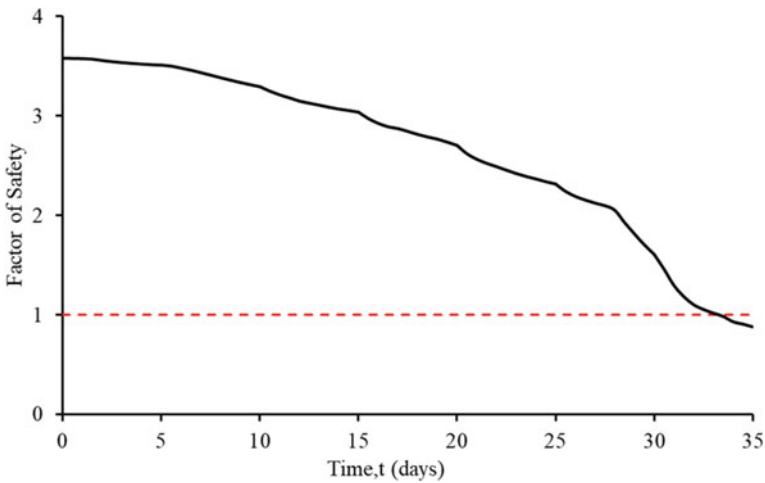


Fig. 6 Variation of factor of safety for progressively increasing flow rate

For the given slope, as the leakage of the buried water pipe progressed, the slope become unstable.

4 Conclusions

Numerical analysis was performed to investigate whether leakage of water pipes buried along the clay slope of Chatham Village affect the slope failure. The effect of progressively increasing leakage on slope failure was also investigated.

The results indicate that water pipe leakages can result in slope instability and the rate of leakage is an important factor that should be considered during slope stability analysis. The progressively worsening leakages can lead to slope failure. Thus, it is important to repair damages to leaking buried water pipe early and before it becomes worse.

References

1. Al-Tahir R, Thompson NA (2009) The use of photogrammetry for landslide inventory in the Northern Range, Trinidad. *Caribb J Earth Sci* 40:25–31
2. Kanithi V, Kanhai C (2006) Landslides in Trinidad – a geotechnical study. In: Fourth LACCEI international Latin American and Caribbean conference for engineering and technology (LACCET'2006). Mayaguez, Puerto Rico
3. Park KH, Beerapat N (2021) A case study of slope failure in central Trinidad due to water pipe leakage. ASEM21 Congress, August 23–27. Seoul, Korea
4. Alexander DVA, Park KH, Gay DA (2020) An estimation of the soil water characteristic curves of Trinidad's expansive clays. In: 4th European conference on unsaturated soils, October 19–21. Lisbon, Portugal
5. Alexander DVA, Gay DA, Park KH (2020) Development of a thornthwaite moisture index map for Trinidad and Tobago. In: 4th European conference on unsaturated soils, October 19–21. Lisbon, Portugal
6. EISL Ltd (2016) Chatham landslide LP 1983–86 landslide investigation report. Trinidad and Tobago
7. Perera YY, Zapata CE, Houston WN, Houston SL (2005) Prediction of the soil-water characteristic curve based on grain-size-distribution and index properties. *Geotechnical Special Publication*. 130:49–60
8. Chai J, Khaimook P (2020) Prediction of soil-water characteristic curves using basic soil properties. *Transportation Geotechnics*. 22:100295
9. Fredlund DG, Xing A (1994) Equations for the soil-water characteristic curve. *Can Geotech J* 31:521–532
10. Geo-Slope International Ltd.: Seepage modeling with SEEP/W. Calgary (Alta), Canada (2012).
11. Schwaller J, van Zyl JE (2015) Modeling the pressure-leakage response of water distribution systems based on individual leak behaviour. *J Hydraul Eng ASCE* 141(5):04014089
12. Geo-Slope International Ltd (2012) Stability modeling with SLOPE/W. Calgary (Alta), Canada

GIS Susceptibility Maps for Shallow Landslides: A Case Study in Shawinigan, Quebec, Canada



Michael Barbosu and James Gray

Abstract Landslides on various scales represent an important category of morphological processes in Quebec, playing an important role in the evolution of slopes, as well as causing instability problems for infrastructures and occasionally, loss of life. In this paper, we present the potential for shallow landslides, within the La Bissonnière amphitheatre, near Shawinigan, itself created progressively over the last 10,000 years, by a combination of episodic quick clay flows and fluvial downcutting of the St Maurice River and its tributaries. An infinite slope model, using the so-called factor of safety was used to produce GIS shallow landslide susceptibility maps for the area and the validity of the model was confirmed through field observations and comparisons with orthophotos.

Keywords Landslides · GIS susceptibility maps · Factor of safety · Shawinigan

1 Introduction

In the lowland areas of Quebec, covered at the end of the last glacial period by sensitive marine clays, slopes created by the fluvial incision of streams and rivers have created conditions favorable to catastrophic quick clay flows of varying magnitudes [12, 13].

Marine clays have indeed created the main pre-conditions for the larger, more deep-seated landslides, but for shallow, superficial landslides, other factors need also to be taken into account.

This paper evaluates these factors and uses them to design a GIS-based shallow landslide susceptibility map for the large La Bissonnière amphitheater, along the St Maurice River, near Shawinigan, Québec.

M. Barbosu (✉)
Rochester Institute of Technology, Rochester, NY, USA
e-mail: mxbsma@rit.edu

J. Gray
University of Montreal, Montreal, QC, Canada

2 Previous Studies

The deglaciation of the middle and lower St Lawrence Valley and the concomitant invasion of the lowlands by the Champlain Sea have been described in detail in [17].

Many authors have described landslides or quick clay flows in the region, some of catastrophic proportions [3, 5, 8, 12, 13].

The St Lawrence Lowlands descends gently from the Canadian Shield to the present St Lawrence River by a series of terraces, cut during recessive phases of the Champlain Sea invasion. The combination of initial relief between the margins of the Canadian Shield and the Saint Lawrence River, the thick blanket of sensitive marine clays and overlying sands, silts and clays, created ideal pre-conditions for both deep-seated quick clay flows and also for shallow landslides. Most slopes are adjacent to the hydrographic network and this is the source of the differences in altitude, while the process of embankment of the rivers lead to the destabilization of slopes. Several case studies in the area emphasize abundant precipitation or rapid snow-melt as triggering factors for such landslides [3, 7]. Moreover, higher water tables create zones susceptible to shearing [14] and therefore to mass movements.

For the St. Lawrence Valley, mass movements were classified into four major categories [13]:

- (a) Rotational landslides, where the fracture plane corresponds to an arc of a circle and the movement of the material occurs in a rotation, having deeper fracture surface and considerable debris volume.
- (b) Retrogressive landslides, which essentially have the same mechanisms as rotational landslides, except for the fact that there is a succession of ruptures; this type of landslides can cause the clay to liquefy.
- (c) Clay flows, characterized by a very strong retrogression and major liquefaction of the clays.
- (d) Shallow landslides, that can be up to 2–4 m deep and are mainly generated by the water saturation of the soil. They develop in marine sediments and they occur in large numbers each year, especially along rivers and steep escarpments, in clayey terrain [9]. These landslides are a consequence of changes in the stress on the slope and many of them represent a preliminary step for a progressive failure, which can develop into a large-scale mass movement.

The current work concerns shallow landslides in the South Shawinigan region of Quebec.

3 The Study Area

The Shawinigan region of Quebec is notorious for the landslides that have taken place here and the several scars from clay flows [5, 12]. The sites of old landslides in marine clay show a high susceptibility to new, superficial ones, along the stream

gullies; they can cause local instability and then spread over larger areas, [15]. The unconsolidated deposits in the region are composed of sand at the surface, clayey silt at depth, and an irregular layer of till at the base, as presented in [8]. These deposits rest on a substratum made up of Precambrian rocks and crossed by the Saint-Cuthbert fault. The region is also characterized by a series of stepped terraces on both sides of the Saint-Maurice River, that are cut across by the amphitheater mentioned above.

Our particular study area, described in detail in [8], is located in the Mauricie area of Quebec, on the site of the La Bissonnière amphitheater, outlined below in Fig. 1a.

For the La Bissonnière amphitheater we also generated the Digital Elevation Model (DEM), presented in Fig. 1b.

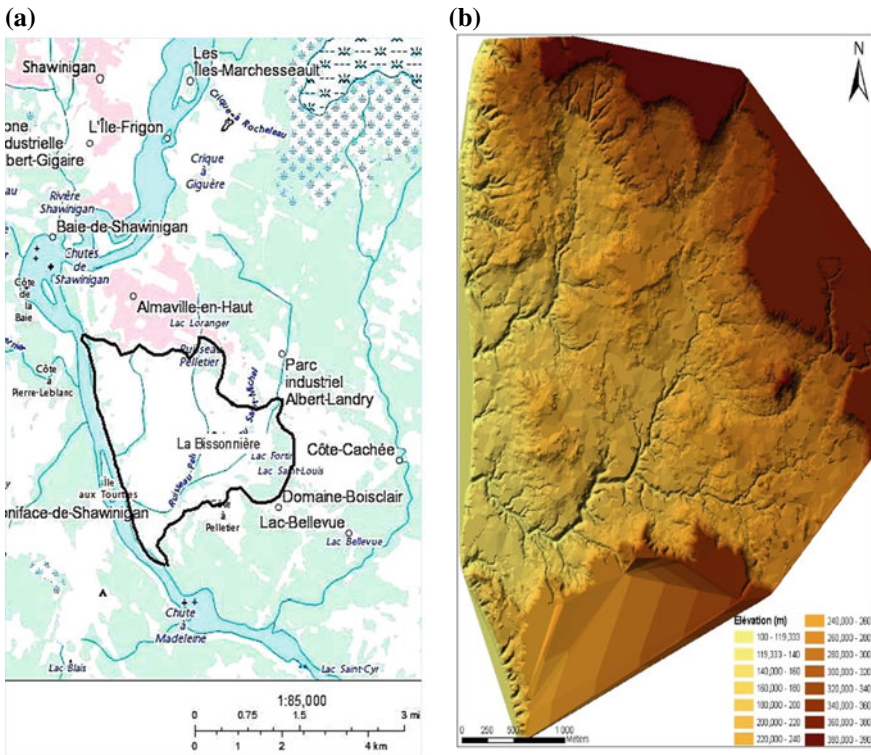


Fig. 1 a Study area with approximate boundary of La Bissonnière Amphitheater © Open Government License—Canada, 2022. b DEM generated for the study area, in La Bissonnière Amphitheater

4 Methodology

Our goal is to develop and implement a model used to create GIS-based shallow landslide susceptibility maps for the La Bissonnière amphitheater.

Landslide susceptibility was defined by [4] as the tendency of a landslide to occur in a specific region in the future and there are several indicators used to suggest whether a site is susceptible to mass movements.

The slope angle is one of them, and in the context of a temperate climate, the angle of equilibrium for clays is around 20°, so slopes with an inclination greater than this value are more likely to become unstable [11].

Changes in the position of the water table is another important factor to consider, because it induces a change in pore pressure and can generate shear planes in cracks that exist in clays [10, 11]. In fact, when any variable that influences the slope stability undergoes a strong variation in a very short period of time, it can generate a destabilization of the material and cause a land slip or reactivate a pre-existing one [2, 20].

It may be, for example, an exceptional rainfall event, leading to water saturation and erosion, a seismic shock, or an anthropogenic action—like building new road embankments or trenches at the bottom of the slope, etc.

Shallow landslides—which represent the focus of our study—have the plane of failure oriented parallel to the surface of the slope, are translational, and can have a thickness of up to 2–4 m. To obtain the susceptibility map for an area to shallow landslides we used the infinite slope model [16, 19].

This model comes with the following assumptions, applicable to our study area:

- we assume that the failure occurs as a single layer and the failure plane is infinitely wide, with a shearing surface and a water table parallel to the ground surface;
- we also assume that all parameters involved in the model are continuous functions, allowing us to perform spatial interpolation between the sample points;
- finally, we consider that susceptibility to landslides is a constant over time, which is true for shorter periods of time, as is our case, but over long time periods, there is some temporal variability [6].

In the present study of the Shawinigan region, the information we had and collected on the subsoil, along with the existence of large-scale topographic maps allowed us to opt for an approach of generating landslides susceptibility maps based on this infinite slope model, with a spatial evaluation of the factor of safety, FS.

FS is the ratio between two contradictory forces acting on a slope: the frictional force (resistance) and the inertial force (movement); here we used the formula [16, 18]:

$$FS = \frac{c + hg \cos^2 \theta (\rho_{\text{mat}} - \rho_{\text{water}}) \tan \phi}{\rho_{\text{mat}} h g \sin \theta \cos \theta} \quad (1)$$

where:

c = cohesion of the material (kPa)

ρ_{mat} = density of the material (kg/m^3)

ρ_{water} = water density = 1000 (kg/m^3)

θ = slope angle (degrees)

h = thickness of the sliding mass (meters)

Φ = angle of internal friction (degrees)

g = gravitational acceleration = 9.81 m/s^2

$m = d/h$, the ratio between the vertical distance d (from the sliding surface to the phreatic surface) and h (defined above). This way, m varies between $m = 0$ if the water table is at or below the slide surface and $m = 1$ if the water table is at the ground surface.

Note that even if in theory, $\text{FS} = 1$ would be the limit for slope stability/instability, in practice, $\text{FS} = 1.5$ is accepted as a critical threshold state because of the approximate nature of Eq. (1), given the limited number of measurable parameters and the fact that other factors, like the influence of vegetation cover, etc., are ignored. In our current study and in the subsequent maps we took 6 classes of susceptibility:

- very high susceptibility (FS less than 1);
- high susceptibility (FS between 1 and 1.5);
- moderate susceptibility (FS between 1.5 and 2);
- low susceptibility (FS between 2 and 3);
- very low susceptibility (FS between 3 and 4);
- stable areas (FS greater than 4).

This classification indicates areas with different degrees of stability, where landslides may occur. The prediction based on measurable parameters is very complex, [1], because of the uncertainty concerning some initial conditions, like the thickness of the sliding mass, the properties of the materials, and the hydraulic conditions, like the position of the water table, which is highly variable over time.

Given the variety and amount of data that involve landslide processes, the most appropriate approach for generating landslide susceptibility maps is with Geographic Information Systems (GIS). Here we used the ArcGIS software with Spatial Analyst and the Raster Calculator. The algorithm developed to generate the susceptibility maps for shallow landslides involved the following steps:

- topographic maps were digitized and the DEM, shown in Fig. 1b, was obtained; then, the DEM layer in Triangulated Irregular Network (TIN) format was converted to a raster format, each raster cell having 1 m^2 ;
- samples from 45 points (with a range of depth between 2–4 m) in the La Bissonnière amphitheater were collected and soil geotechnical analyses were performed; these lead to ranges of the angle of internal friction (22° – 34°), cohesion of material (10–30 kPa) and density of material (545–1420 kg/m^3). Particular values determined for the 45 points along with interpolated/extrapolated values for all other points in the region were used in the equation of FS.

Finally, FS was fed into the Raster Calculator and susceptibility maps were generated at a scale of 1:5000, showing instability of slopes for each pixel.

Our final result has an interactive character, which allows the modification of certain parameters. In the current paper, this latest feature is exemplified with two scenarios concerning the position of the water table: $m = 0$ (water table at or below the slide surface) and $m = 1$ (water table at the ground surface); these two situations are illustrated in Figs. 2 and 3, respectively.

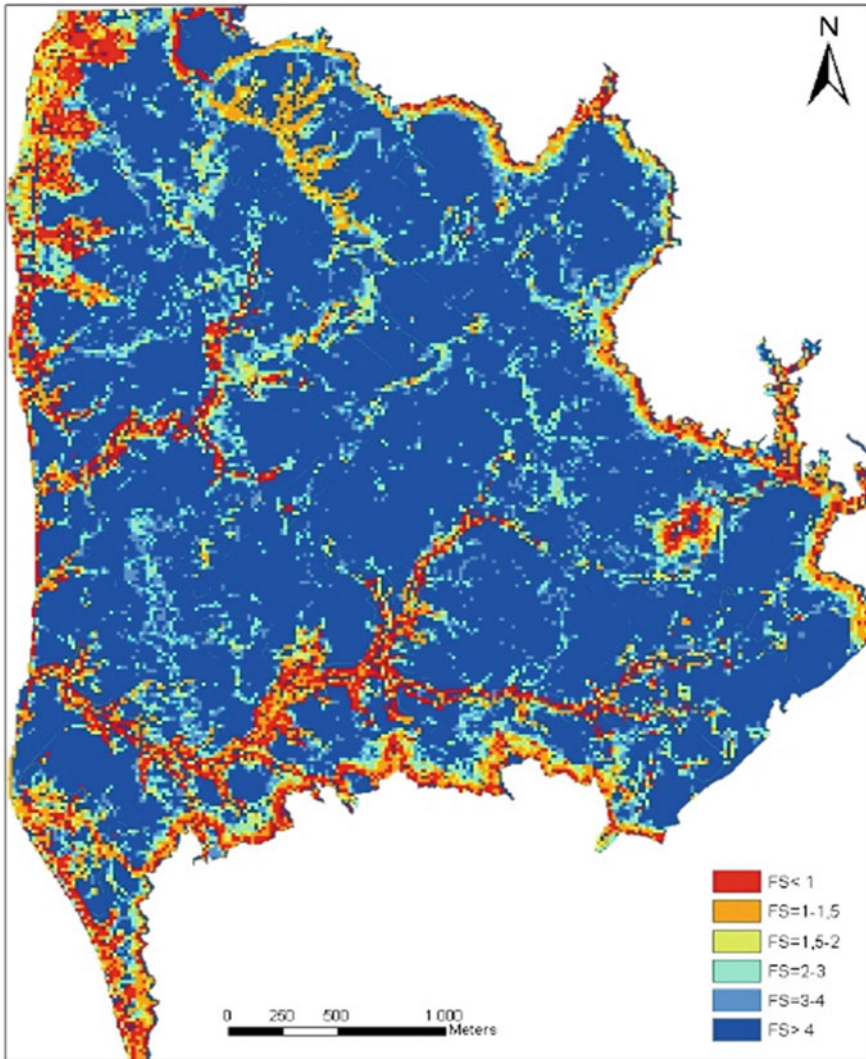


Fig. 2 Landslide susceptibility map for La Bissonnière, when $m = 0$

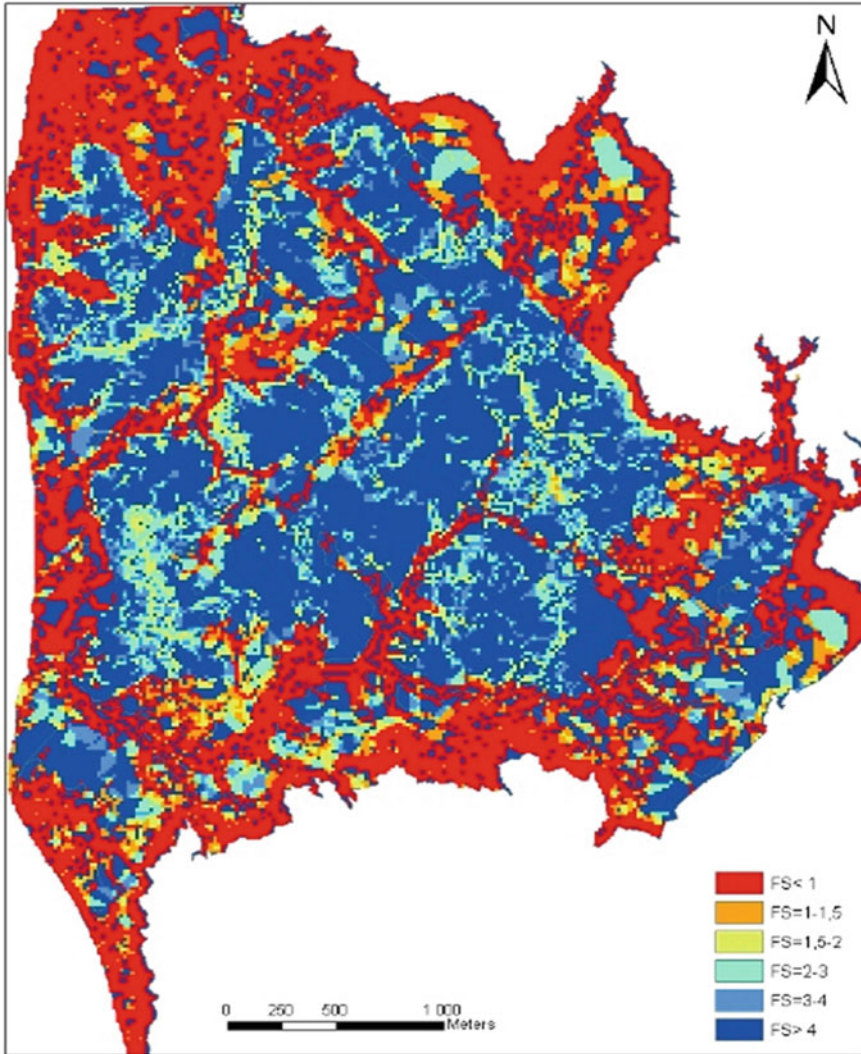


Fig. 3 Landslide susceptibility map for La Bissonnière, when $m = 1$

5 Results and Conclusions

The current work shows the potential of the GIS spatial analysis technique used along with the infinite slope model to assess susceptibility to shallow landslides. GIS is very efficient for handling and processing a large amount of data in a short time and at a relatively low cost. Changes in input parameters, certain human activities, and

seasonal climate variations can also be incorporated into the model, updating and improving landslide susceptibility maps almost in real-time.

Based on the methodology described in the previous section, in Fig. 2 and Fig. 3 we generated maps of susceptibility to shallow landslides for La Bissonnière; they are the final output of our model and represent, as mentioned above, the two extreme scenarios for the position of the water table, i.e. for $m = 0$ and $m = 1$.

Maps from Figs. 2 and 3 indicate that most regions in the La Bissonnière amphitheater are relatively stable, except for some sections occupied by escarpment and small ravines, which are subject to small superficial landslides. In percentages, zones affected by these shallow landslides vary from 6% when $m = 0$ to 35% when $m = 1$. As expected, most regions of high and very high susceptibility correspond to areas with steep slopes. However, we can identify sectors susceptible to landslides that are not necessarily related to slopes, but to soil properties, under conditions of high humidity. These areas are located in the N and NE part of the amphitheater and are distinguished by the low cohesion of materials and the higher content of clays. We also notice that, while overall this ancient landslide amphitheater has returned to a state of relative equilibrium, with a very low risk of large-scale quick clay flow or landslide, shallow landslides still occur. They are associated with direct or indirect anthropogenic impacts and as indicated in [14], about 80% of landslides that occur each year are the result of the erosion of a watercourse at the base of a slope, while the remaining 20% result from inappropriate human interventions. Therefore, in the current context of climate change, the whole issue of risk assessment and susceptibility to landslides should be monitored and constantly reassessed.

We checked and confirmed the validity of the model through comparisons of our susceptibility maps with orthophotos and recurrent field observations; besides, the latest landslide we visited, occurred in the city of Shawinigan on October 24, 2021, at the north of our study area, leading to the evacuation of 4 houses situated on the Boisclair street.

Acknowledgements We would like to extend our special thanks to our friends and collaborators, Professor Alexandru Imbroane and Researcher Corina Nicorici for their help, support and feedback, throughout this work.

References

1. Anderson MG, Richards KS (1989) Slope stability. Edition Wiley & Sons Ltd., London
2. Atkinson PM, Massari R (1998) Predicting the relative likelihood of landsliding in the central apennines. Italy. *Comput Geosci* 24:373–385
3. Bégin C, Evans SG, Parent M, Demers D, Grondin G, Lawrence DE, Aylsworth JM, Michaud Y, Brooks GR, Couture R (1996) Le glissement de terrain d'avril 1996 à Saint-Boniface-de-Shawinigan, Québec: observations et donnés préliminaires. *Nat Resources Canada*, 215–223
4. Brabb E (1984) Innovative approaches for landslide hazard evaluation. *Proceedings of the 4th international symposium on landslides, Toronto*, 307–323
5. Chagnon J-Y, Lebuis J, Allard D, Robert J-M (1979) Sensitive clays, unstable slopes, corrective works and slide in the Québec and Shawinigan area. *Geological A Canada B-11:1–38*

6. De Boer DH (1992) Hierarchies and spatial scale in process geomorphology: a review. *Geomorphology* 4:303–318
7. Demers D, Leroueil S, d'Astous J (1999) Investigation of a landslide in Maskinongé. *Revue Canadienne de Géotechnique* 36(6):1001–1014
8. Desjardins R (1980) Tremblements de terre et glissements de terrain: corrélation entre des datations au 14c et des données historiques à Shawinigan. Québec. *Géographie physique et quaternaire* 34(3):359–362
9. Dionne JC (1997) Bilan vicennal des connaissances sur la Mer de Goldthwait au Québec. *Bulletin de l'AQQUA* 23(1):6–20
10. Geertsema M, Torrance JK (2005) Quick clay from the mink creek landslide near terrace, British Columbia: geotechnical properties, mineralogy, and geochemistry. *Can Geotech J* 42:907–918
11. Holtz RD, Kovacs WD (1991) Introduction à la géotechnique. Éditions de l'École polytechnique de Montréal
12. Karrow PF (1972) Earthflows in the Grondines and Trois Rivières areas. Québec. *Canadian J Earth Sci* 9:561–573
13. Lajoie G (1974) Les coulées d'argile dans les basses terres de l'Outaouais, du Saint-Laurent et du Saguenay. *Rev Géogr Montréal* 28:419–428
14. Landry B, Mercier M (1992) Notions de géologie. Modulo Éditeur, 3e édition
15. Mollard JD, Janes JR (1985) La photointerprétation et le territoire canadien. Centre d'édition du Gouvernement du Canada, Hull, 425 p
16. Nicorici C, Gray J, Imbroane AM, Barbosu M (2012) GIS susceptibility maps for shallow landslides: a case study in Transylvania, Romania. *Carpathian J Earth Environ Sci* 7:83–92
17. Parent M, Occhietti S (1988) Late Wisconsinan deglaciation and Champlain Sea Invasion in the St. Lawrence Valley, Quebec. *Geogr Phys Quat* 42(3):215–246
18. Skempton AW, Delory FA (1957) Stability of natural slopes in London clay. *Proceedings of the 4th international conference on soil mechanics and foundation engineering*, vol 2, pp 378–381
19. Van Westen CJ, Terlien MTJ (1996) An approach towards deterministic landslide hazard analysis in GIS. A case study from Manizales (Colombia). *Earth Surface Processes Landforms* 21:853–868
20. Wu W, Siddle RC (1995) A distributed slope stability model for steep forested basins. *Water Resour Res* 31(8):2097–2110

Determination of Critical Height of Unsupported Vertical Cuts Using Experimental and Numerical Methods



Z. Nil Kutlu, Gregory Brennan, and Won Taek Oh

Abstract Stability of unsupported cuts are commonly analyzed numerically as a 2-dimensional problem using commercial geotechnical software such as SLOPE/W. This is also true for the unsupported cuts excavated into unsaturated soils. However, limited experimental studies have been undertaken to validate the numerical approaches in estimating the critical heights of unsupported cuts in unsaturated soils. To bridge this gap, laboratory test was conducted using a large-scale soil tank ($W \times L \times H = 1.5 \times 2.2 \times 2.4$ m) to determine the critical height of an unsupported vertical cut in sand with water table at 0.7 m from the surface. Excavation was simulated by removing 0.1 m height retaining panels until general failure took place. The matric suction profile in sand above the water table was established based on the suction values measured from various depths with high capacity tensiometers (i.e., T5X). The critical height determined in the laboratory test was compared with the one estimated using PLAXIS (3D).

Keywords Unsupported vertical cut · Critical height · Stability analysis · Matric suction · Numerical analysis

1 Introduction

In many cases, geotechnical projects such as construction of foundations and pipelines are initiated by excavating unsupported cuts. It is common practice for field workers to enter the unsupported cuts during the construction; hence, the design of unsupported cuts should be carried out with the utmost caution since the collapse of even 1.5 m height of an unsupported can suffocate the field workers [1, 2]. Two factors should be taken into account in designing an unsupported cut: critical height

Z. N. Kutlu (✉)
Maltepe University, 34857 Istanbul, Turkey
e-mail: zehranilkutlu@maltepe.edu.tr

G. Brennan · W. T. Oh
University of New Brunswick, Fredericton, New Brunswick, Canada

and stand-up time. Critical height is a maximum depth of an unsupported cut that can be excavated without failure, while stand-up time is defined as time elapsed from the instant a trench is excavated until it fails. Unsupported cuts are typically excavated in soils that are in a state of unsaturated conditions. This indicates that stability of unsupported cuts is governed by the matric suction distribution with depth in field. Recently, several research has been undertaken to estimate critical height [3–6] and stand-up time [7] of unsupported vertical cuts in unsaturated fine- and coarse-grained soils. However, these previous studies were limited to analytical and numerical (2-dimensional) estimations of critical height and stand-up time of unsupported cuts without experimental validation.

In the present study, a large-scale soil tank ($W \times L \times H = 1.5 \times 2.2 \times 2.4$ m) available at the Geotechnical Lab, UNB is used to experimentally determine a critical height of an unsupported cut in a sand. The soil tank was designed in a way that both saturated and unsaturated conditions can be achieved in sand by adjusting the level of water. The experimentally determined critical height was compared with the one estimated using the finite element software, PLAXIS (3D) to check the validity of numerical approach.

2 Testing Program

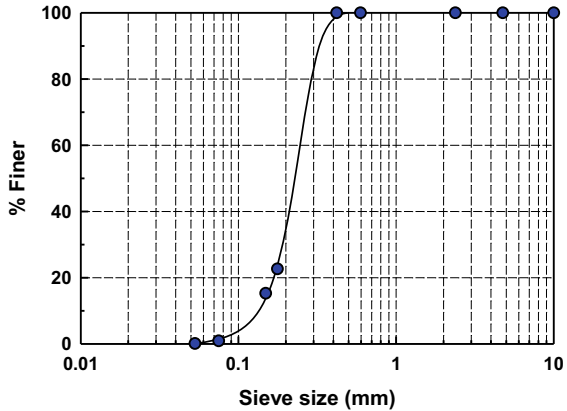
The critical height of unsupported vertical cut was determined in Unimin 7030 industrial sand (hereafter referred to as sand). Basic soil properties of the sand are summarized in Table 1. The grain size distribution of sand is shown in Fig. 1.

Figure 2a shows initial set-up in the soil tank to determine the critical height of an unsupported vertical cut in sand. The sand was first fully saturated using upward flow

Table 1 Basic soil properties of Unimin 7030 sand [8]

Property	Value	Remark
Plasticity index, I_p	NP	
Saturated unit weight, γ_{sat} (kN/m ³)	20.4	
Saturated volumetric water content, θ	0.387	
Void ratio, e	0.63	
Effective cohesion, c' (kPa)	0	
Effective internal friction angle, ϕ' (°)	36.2	
Elasticity modulus, E^* (kPa)	10,000	Assumed value in numerical analysis
Poisson's ratio, ν^*	0.33	Assumed value in numerical analysis

Fig. 1 Grain size distribution curve of Unimin 7030 sand



of water from the bottom of the tank. The unsaturated condition was then obtained by lowering water table to the targeted level (i.e., 0.7 m from the soil surface in this study). The matric suction values measured from different depths using T5X (i.e., high capacity tensiometers; METER Group) indicated that hydrostatic negative pore-water pressure (i.e., matric suction) distribution can be assumed without introducing significant error. To simulate vertical excavation, 0.1 m height retaining panels were removed one by one until general failure took place. Failure in sand was observed when the eighth panel was removed, which indicates that the critical height is between 0.7 and 0.8 m. The plan view at the moment of failure in sand is shown in Fig. 2b.

3 Numerical Analysis

The testing program detailed in Sect. 2 was also simulated with PLAXIS 3D (2018) to estimate a critical height of an unsupported vertical cut extending finite element method considering boundary effects. The sand was modelled as a Mohr–Coulomb material with effective shear strength parameters and unit weight as shown in Table 1 for saturated condition. The standard Mohr–Coulomb model is sufficient for the performed stability analysis since the stress dependent stiffness behaviour is not included in the safety type calculations in Plaxis 3D. The water table in the soil tank was set to a constant value of 0.7 m from the soil surface by defining water head. This generates negative and positive hydrostatic pore-water pressure distributions in soils above and below water table, respectively. The negative hydrostatic pore-water pressure above water table is also supported by the T5X tensiometer measurements.

The Soil–Water Characteristic Curve (Fig. 3) in PLAXIS 3D was established using van Genuchten [9]’s model (Eq. (1)) based on the measured data [9].

$$S(\psi) = S_{res} + (S_{sat} - S_{res})[1 + g_a|\psi|^{g_n}]^{g_c} \quad g_c = \left(\frac{1 - g_n}{g_n}\right) \quad (1)$$

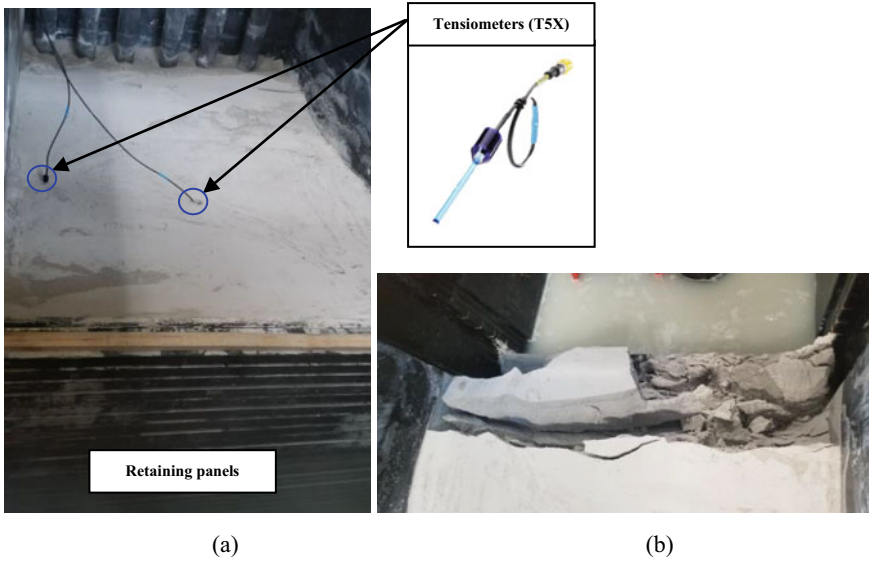


Fig. 2 Laboratory test in a soil tank to determine the critical height of unsupported cut; **a** initial set-up with water table at 0.7 m from the soil surface, **b** plan view after failure in sand

where S_{res} , S_{sat} = saturation for residual and full saturated conditions, respectively, g_a , g_n , g_c = fitting parameters, and ψ = matric suction.

Vanapalli et al. [10] proposed a model that can be used to estimate the variation of total cohesion with respect to matric suction (Eq. (2)). The fitting parameter, κ is a function of plasticity index, I_p and $\kappa = 1$ can be used for cohesionless soil. Similar approach is adopted in PLAXIS 3D to consider the influence of matric suction on cohesion by introducing the term, effective suction. The total cohesion values that are normalized in terms of the maximum cohesion C_{max} , obtained at 0.25 m, is shown

Fig. 3 Soil–water characteristic curve of Unimin 7030 sand

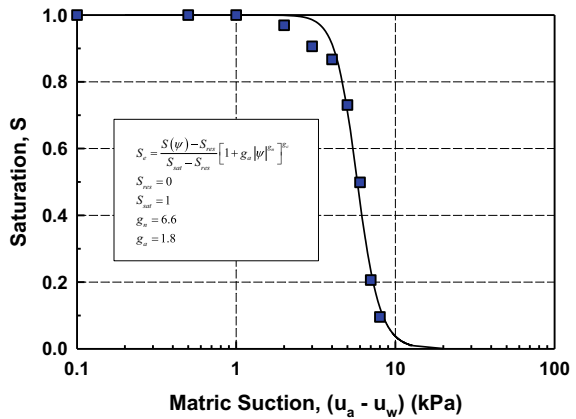
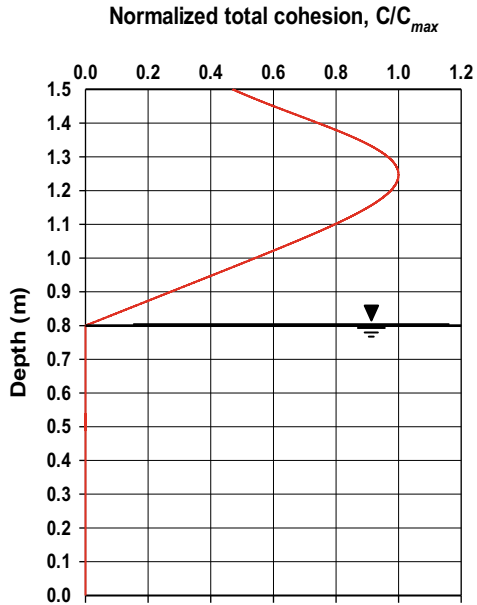


Fig. 4 Variation of normalized total cohesion (C/C_{max}) values with depth



in Fig. 4 with depth, for GWT at 0.7 m from the soil surface.

$$C = c' + (u_a - u_w)(S^\kappa) \tan \phi' \tag{2}$$

where C is total cohesion, c' is effective cohesion, u_a is pore-air pressure, u_w is pore-water pressure, $(u_a - u_w)$ is matric suction, S is degree of saturation, κ is fitting parameter ($\kappa = 1$ for NP), and ϕ' is effective internal friction angle.

The front retaining panels (0.1 m in height each, Fig. 2) were modelled as elastic structural elements ($E = 2.1 \times 10^8 \text{ kN/m}^2$, $\gamma = 78.5 \text{ kN/m}^3$). Deformation fixities (horizontally fixed) boundary conditions were assigned to simulate sides of soil tank, which can reduce the stiffness difference effect on results at the boundaries. The problem was divided into several groups of phases and staged construction was performed in the analysis to simulate the removal of the retaining panels in the experiment until the soil collapses as a vertical cut. The 3D geometry model, meshes, and boundary conditions are shown in Fig. 5.

Stability of unsupported vertical cut during excavation was estimated by calculating the global safety factor ($\sum M_{sf}$) using the ϕ'/c reduction method (Eq. (3)). Table 2 summarizes the global safety factors after each excavation in Plaxis 3D.

$$\sum M_{sf} = \tan(\phi'_{input}) / \tan \phi'_{reduced} = c'_{input} / c'_{reduced} \tag{3}$$

The global safety factor dropped to 1.15 after the seventh panel was removed in the model. Removal of eighth panel caused failure in the unsupported cut. This indicates that the critical height is between 0.7 and 0.8 m, which coincides with

Fig. 5 3D model geometry, meshes and boundary condition used in Plaxis 3D

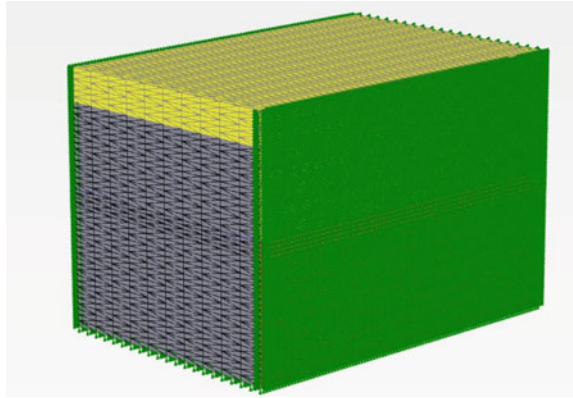


Table 2 Global safety factor versus excavation depth obtained in Plaxis 3D

Depth of excavation (m)	$\sum M_{sf}$
0.1	5.80
0.2	3.67
0.3	2.77
0.4	2.26
0.5	1.82
0.6	1.51
0.7	1.15
0.75	1.04
0.8	Failure

the experimental result. Additional stability analysis was carried out by dividing the eighth panel into two 0.05 m height panels and the global safety factor was determined to be 1.04 at the excavation depth of 0.75 m (see Fig. 6).

The deformed mesh and failure wedge after the removal of seventh panel shown in Fig. 7 The failure plane in the soil wedge makes angle of 62° with the horizontal. This angle matches the angle of slip line for active case. The disturbed soil zone formed an arc shaped area in the plan view (Fig. 8), which is the indication of the boundary effect at the interface between the soil and sides of tank. However, this boundary effect was not observed in the experiment.

4 Summary and Conclusions

Laboratory test was conducted using a large-soil tank ($W \times L \times H = 1.5 \times 2.2 \times 2.4$ m) to investigate the critical height of an unsupported vertical cut in unsaturated sand. Excavation was simulated by removing 0.1 m high panels subsequently until

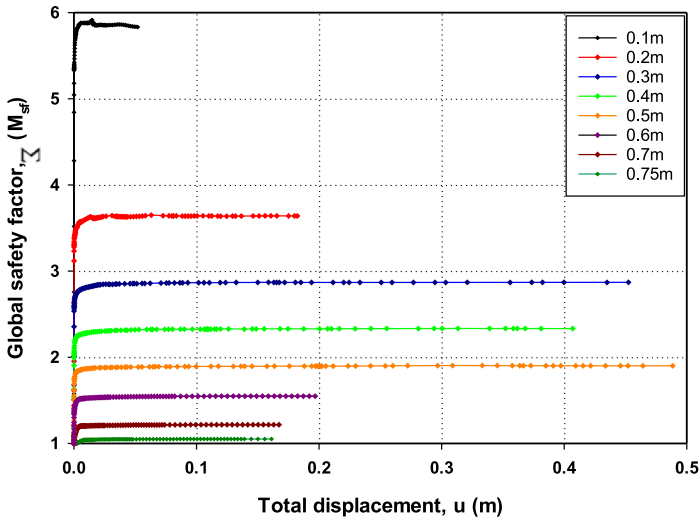


Fig. 6 Global safety factor, $\sum M_{sf}$ versus total displacement, u relationship for each excavation depth

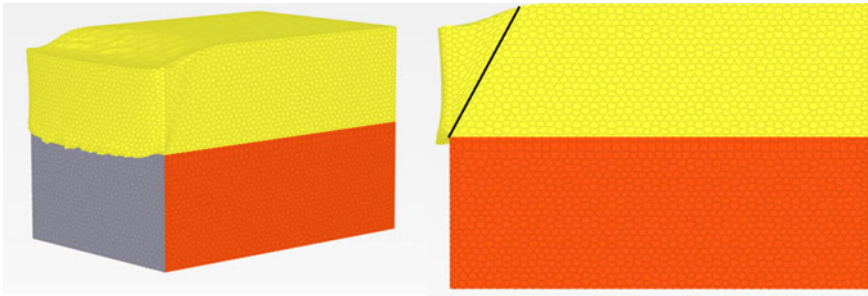


Fig. 7 a Deformed mesh and b failure wedge (excavation depth = 0.75 m, $\sum M_{sf} = 1.04$)

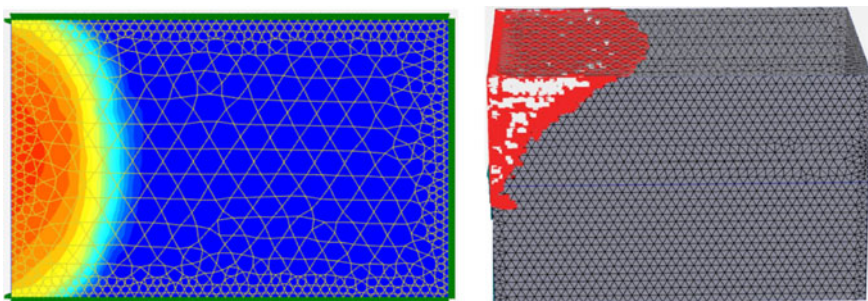


Fig. 8 Plastic points and extension of the disturbed zone due to excavation (excavation depth = 0.75 m, $\sum M_{sf} = 1.04$)

failure took place in the soil. The critical height was determined to be between 0.7 and 0.8 m with the water table at 0.7 m. Similar results were obtained from the the stability analysis undertaken with PLAXIS 3D. This good comparison indicates that the critical height of unsupported vertical cut in unsaturated soils can be reliably estimated through numerical approach by considering the influence of matric suction on the shear strength based on the measured suction distribution profile.

References

1. National Institute of Occupational Safety and Health (NIOSH) (2013) Trenching and excavation-workplace safety and health topic. US department of health and human services
2. Arboleda C, Abraham D (2004) Fatalities in trenching operations-analysis using models of accident Causation. *J Constr Eng Manag* 130(2):273–280
3. Richard A, Oh WT, Brennan G (2020) Estimating critical height of unsupported trenches in vadose zone. *Can Geotech J* 58(1):1–17
4. Brennan G, Oh WT, Nasir O (2020) Stability analysis of unsupported vertical cuts in the vadose zone using 2D and 3D numerical methods. In: 4th European conference on unsaturated soils proceedings, Lisboa
5. Richard A, Brennan G, Oh WT, Ileme V (2017) Critical height of an unsupported vertical trench in an unsaturated sand. In: 70th Canadian geotechnical conference proceedings (CD), Ottawa
6. Yanamandra G, Oh WT (2021) Influence of excavation time, tension crack, and rainfall on the stability of unsupported vertical cuts in unsaturated soil. *Int J Geomech* 21(10):1–17
7. Ileme V, Oh WT (2019) Estimating the stand-up time of unsupported vertical trenches in vadose zone. *KSCE J Civ Eng* 23(2):4259–4273
8. Mohamed FMO, Vanapalli SK (2006) Laboratory investigations for the measurement of the bearing capacity of an unsaturated coarse-grained soil. In: 59th Canadian geotechnical conference proceedings, Vancouver
9. van Genuchten MT (1980) A closed-form equation for predicting the hydraulic conductivity of unsaturated soils. *Soil Sci Soc Am J* 44(5):892–989
10. Vanapalli SK, Fredlund DG, Pufahl DE, Clifton AW (1996) Model for the prediction of shear strength with respect to soil suction. *Can Geotech J* 33(3):379–392

Slope Stability Analysis of Open-Pit Mines Using Statistical Methods



Petra Olah and Péter Gorog

Abstract A non-traditional method of slope stability calculation is presented, which often occurs during geotechnical design. The possible occurrence of slope failure is not illustrated by a safety factor but by the probability of failure. The result is the percentage of failure or, the safety of the stability that can be expected for a given slope. Unlike the deterministic calculation, not a constant value is given for each input parameter but statistical variables according to the distribution belonging to the sample data set, such as mean, standard deviation, relative minimum, and relative maximum. An approach is taken to how slope resistance calculations can be performed on a probabilistic basis through a case study. The subject of this case study is Hungary's largest open-pit lignite mine in Visonta, eastern Hungary. On the optimised sections using the deterministic method, the slope resistance test was performed on a probabilistic basis. The analysis of statistical parameters is also presented as the most important step of the investigation. To determine the input parameters for the probabilistic analysis, the first step is collecting the shear strength values (in this case, friction angle and cohesion) and then deriving a statistical distribution, carrying out the goodness of fit test finally determining the parameters.

Keywords Slope stability · Open-pit · Probability · Statistics · Geology

1 Introduction

Slope stability analysis is the area of geotechnical design where most uncertainties are present. Geological anomalies, spatial variability of soil parameters, lack of

P. Olah (✉) · P. Gorog
Budapest University of Technology and Economics, Budapest, Hungary
e-mail: olahpetra@edu.bme.hu

P. Gorog
e-mail: gorog.peter@emk.bme.hu

© The Author(s), under exclusive license to Springer Nature Switzerland AG 2023
C. Atalar and F. Çinicioğlu (eds.), *5th International Conference on New Developments in Soil Mechanics and Geotechnical Engineering*, Lecture Notes in Civil Engineering 305, https://doi.org/10.1007/978-3-031-20172-1_28

293

representative data, changes in environmental conditions, unexpected failure mechanisms, simplifications and approximations in geotechnical models, and human errors in design and construction all contribute to the uncertainty of the calculations [1].

Probability-based slope stability analysis (PSSA) was first introduced in the 1970s [2]. The deterministic slope stability analysis does not consider the uncertainty; it relies on conservative parameters. Probabilistic analyses allow uncertainty to be quantified and reasonably incorporated into the design.

In addition to calculating uncertainty, PSSA is a useful method for estimating the frequency of hazards in risk analysis, especially in the absence of representative empirical data [1]. In slope design work, the most common acceptance criterion is the safety factor (FS), often supplemented with the probability of failure (PF) or sensitivity analysis to deal with uncertainty. Adams [3] FS is the result of a deterministic concept that does not describe the real uncertainty of slope stability. An FS of 1.0 describes the point at which the total slope load is equal to the total slope capacity on each material for a given failure mode. However, the failure of a slope is much more complex than LEM models. In practice, failure does not occur simultaneously on a single discrete surface, but localised material defects gradually develop into increasing copper failure. A basic prerequisite for the PF (Probability of Failure) concept is to determine a statistical distribution (probability density function) for each input parameter to analyse slope stability. Probabilistic modelling is a method that considers the uncertainty associated with the input parameters in the analysis and results in a statistical distribution of FS instead of a single deterministic value [3].

2 Methodology

2.1 Probabilistic Analysis

Uncertainty can be considered by sensitivity analysis when examining the effect of changes in individual parameters on slope stability. This study presents an alternative method, the probability modelling. This method requires knowledge of the uncertainty associated with the input parameters, and the result will be a function of the statistical distribution of FS. The most important step in statistical analysis is correctly entering the input parameters. In order to this, a pretty large data set is required. The first step is to use a test called Goodness of Fit to determine the type of distribution that best fits the dataset. The distribution fitting analysis is followed by the determination of the expected value (mean), the standard deviation, and the absolute (characteristic) maximum and absolute minimum values based on the most appropriate distribution type. The relative minimum and relative maximum indicate the distance from the average. There are several methods for calculating slope resistance in a probabilistic way: the Monte-Carlo simulation and the Latin-Hypercube method are the most common. Using the Monte-Carlo method, we evaluate the

problem from multiple runs from random input data, but the type of failure must be determined. The Latin-Hypercube method is very similar to the Monte-Carlo simulation, the difference is that it is based on stratified sampling, much fewer runs are enough for a result like Monte-Carlo, so the calculation takes less time.

2.2 Softwares

The available data set (strength parameters of the different layers) was analysed by the EasyFit and CumFreq software. EasyFit is a data analysis program designed to provide fast statistics with probabilistic results.

A significant number of distribution types are available and can be selected by users according to their preferences. One of the add-on software of the EasyFit, the StatAssistant is able to perform additional calculations on the data set [6]. CumFreq provides an estimate of the cumulative frequencies in the variable data sets, allowing the most appropriate probability distribution to be determined. It lists the averages of the absolute values of the differences between the distributions according to the literature and the fitted one in percentage. The lower the average, the better the fitted distribution. Cum-Freq creates a list of distributions ranked by fit accuracy [7]. The stability analyses on the sections were performed with the Slide2 software of the Rocscience program family, basically with a two-dimensional slope stability analysis program, which can be used to calculate the safety factors and failure probabilities of a slope using different failure surfaces. Slide2 also has extensive probabilistic modelling and analysis features. Almost all input parameters can be defined as random variables to calculate the probability of failure and to perform sensitivity analysis [8]. The calculation method chosen is the global minimum analysis. The statistical method is Latin Hypercube analysis, the number of test runs is $N = 1000$. The program recalculates the safety factor N times to the lowest safety slider globally while randomly generating shear strength variables. The Probability of Failure (PF) is the number of analyses in which the safety factor divided by the total number of samples is < 1.0 .

3 Case Study

3.1 The Investigated Area

Visonta is located at NE region of Hungary, where opencast lignite has been extracting since the 1970s. There are three mining areas one is already recultivated, the second is under recultivation, and the third one is still cultivated. The name of cultivated mine is Eastern no. III, where it was necessary to design high-altitude slopes and ensure their stability before mining began [4]. The end slope has 3–3 sections on

the north and south sides, which are shown in section 1–3–5 (southern slope) and 21–24–27. (northern slope).

3.2 Geology

The studied mining area is a significant part of the lignite area in Northern Hungary, and within it in Mátraalja [5]. The area of lignite occurrence consists of Pliocene Formations covered with a Quaternary layers. The geological structure of the area is basin-like, the bedrock of it consists of Miocene formations of the Mátra Mountains, mainly various andesite formations. The Pliocene layers which are hundreds of meters thick, are settled on this base. The lignite within the Pliocene layers are included in the upper Pannonian age series. Sand, sandy silt/silty sand layers between lignite deposits are well-graded shallow-sea, coastal sediments. In some places, there are fine-grained layers such as coarse silt and fine grained sands which are prone to liquefaction [5].

The most important layers in the strata in addition to lignite are: clays (with intermediate and high plasticity sometimes with some sand and silt), silts (sandy silt, coarse silt, clayey silt) sand (mainly silty sand), and there are some bentonite layer as well. There were some silt and clay layers with notable organic content. Soil layers can be seen in Fig. 1. Since the studied open pit lignite mine is dewatered in the calculations showed below no ground water were considered.



Fig. 1 Soil layers of the border slope in Eastern no. III. mine, Visonta

3.3 Input Data

Several investigatory boreholes were drilled in the investigated area. After sampling, direct shear strength tests were done, which provided enough data for statistical analysis. The cohesion, internal friction angle, unit weight and the saturated unit weight of each soil layer can be specified as variables in the program. There were enough data for the statistical calculations for the most important seven layers: Quaternary high plasticity clay, silty clay, sandy clay, high plasticity organic clay, clayey silt, organic silty clay with high plasticity, bentonite clay. The optimisation of the slope should be done in six sections; three are on the Northern side and three on the Southern side of the mine. One of the six calculated sections is on Fig. 2 and Table. 1.

From the above mentioned layers, there were only 5, which had sufficient data for statistical calculations:

The quarter fat clay layer: for cohesion normal distribution is used, the mean is .80.1 kPa, standard deviation is 45.7 kPa, relative minimum is 76.9 kPa and 13.4 kPa as relative maximum and for friction angle lognormal statistical distribution is used, 12.8° is the mean, 6.2° the standard deviation, the relative minimum is 6.1° and the relative maximum is 0.4°.

For the -2. cover silty clay the cohesion is considered as a lognormal distributed data set, the mean value is 40.2 kPa, the standard deviation is 3.8 kPa, the relative minimum is 4.4 kPa and the relative maximum is 54 kPa. For the internal friction angle uniform distribution is used, the mean is 10.8°, the standard deviation is 5.7°, and the relative minimum is 4.8°, while the relative maximum is 1.2°.

The -1.0 clayey silt's cohesion values have normal distribution type, the mean is 28.3 kPa, the standard deviation is 6.7 kPa, the relative minimum is 11.1 kPa, the relative maximum is 18.2 kPa. For the internal friction angle with a statistical distribution of uniform, the mean is 21.2°, the standard deviation is 2.2°, the relative minimum is 2.6°, and 1.2° as a relative maximum.

For the 0.0 clayey silt for the cohesion normal distribution is taken, the mean is 25.3 kPa, the standard deviation is 14.4 kPa, the relative minimum is 23.3 kPa and the relative maximum is 46.5 kPa. For the internal friction angle the distribution

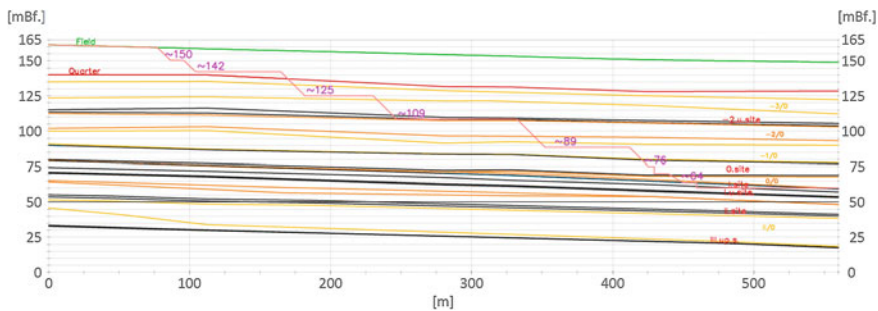


Fig. 2 Geometry of Section 24

Table 1 Material properties of the layers used in the calculation.

Layer's sign, name	Unit weight (kN/m ³)	Cohesion (kPa)	Friction angle (deg)
Quarter fat clay	19.1	80.1	12.8
Quarter clayey silt	20	18	14
–3./0 coarse silt	20	34	20
–2. cover silty clay	20	40.2	10.8
–2. site lignite	13	100	26
–2./0 silt	20	27	26
–1./0 clayey silt	19.5	28.3	21.2
0. cover fat clay	19.5	27	15
0. site lignite	13	100	26
0./0 clayey silt	20	25.3	19.3
I. cover silty fat clay	20.3	29.4	9.7
I. site lignite	13	100	26
I./0 medium plasticity clay	20	36	14
I.a. site lignite	13	100	26
I.a/0. sandy silt	20.3	20	20

type is lognormal, the mean value is 19.3°, the standard deviation is 5.9°, the relative minimum is 5° and the relative maximum is 1.4°.

Finally, the I. cover silty fat clay is used as statistically distributed layer. For cohesion, mean value is taken as 29.4 kPa, the standard deviation is 21 kPa, the relative minimum is 18.4 kPa and the relative maximum is 42 kPa. The distribution type is lognormal. For the internal friction angle the statistical distribution of uniform is used, the mean is 9.7°, the standard deviation is 4.6°, the relative minimum is 3.8°, and relative maximum is 0.4°.

3.4 Results

Six sections were calculated, three from the Northern side and three from the Southern side of the mine. In this paper only one is introduced, which gave interesting results. This is the Section 24 from the Northern slope (Fig. 3).

In the case of section 24, although the cross-section is safe according to deterministic calculation, since FS (deterministic) = 1.551 and the mean FS of the probabilistic calculation is also good FS (mean) = 1.338 (Fig. 4), but the probability of

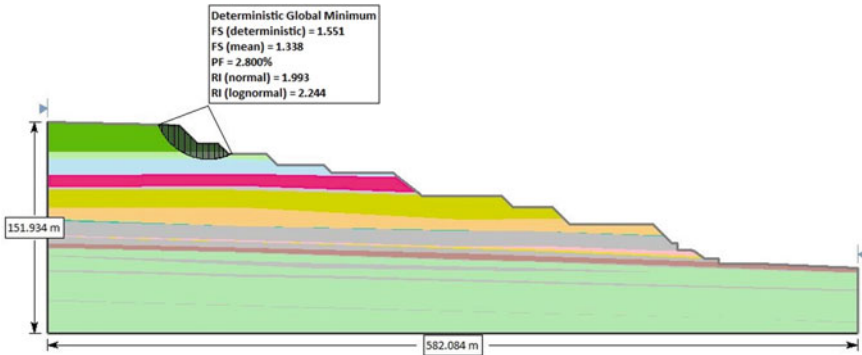


Fig.3 Result of the statistical calculation of the Section 24 (Bishop)

failure is $PF = 2.800\%$. This means that in 28 cases out of 1000 runs performed by the program, the safety of the most critical slip surface did not reach $FS = 1.0$. This is also proved by the reliability index, as neither the RI calculated with the normal distribution, nor the RI value calculated with the lognormal distribution ($RI = 1.99$) reaches the recommended value which is 3. The probability calculation can be very useful in such cases. Both the deterministic result which was calculated the optimised profile, reaches $FS = 1.35$ and the mean value of the FS determined by the statistical method, also close to the $FS = 1.35$ value, but there are still 28 out of 1000 cases where it does not reach the minimum safety, so the FS is below 1.0.

In Fig. 5. You can see the distribution function of the samples run. The inflection point gives the mean of the Factors of Safety according to the simplified Bishop method.

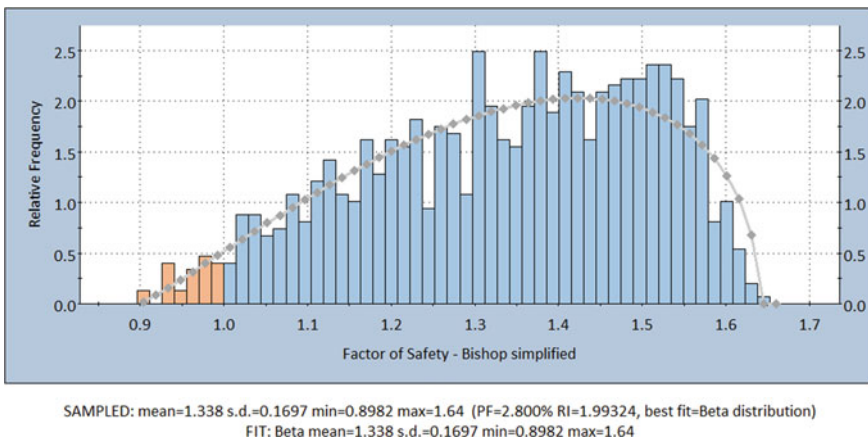
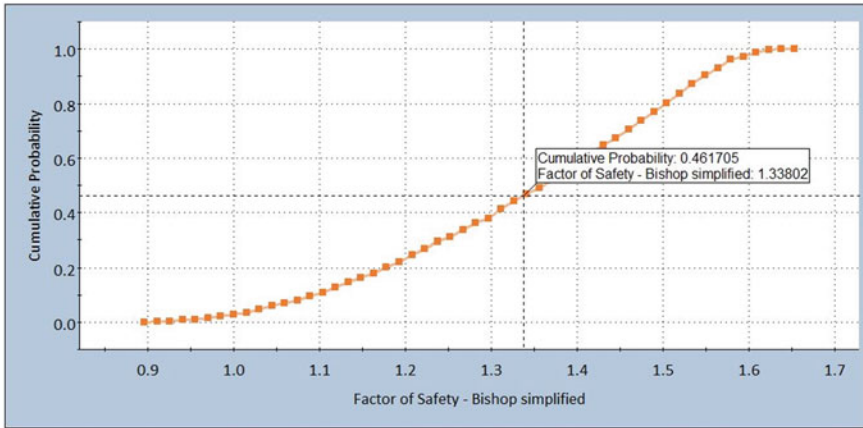


Fig. 4 Histogram of safety factors for section 24



SAMPLED: mean=1.338 s.d.=0.1697 min=0.8982 max=1.64 (PF=2.800% RI=1.99324, best fit=Beta distribution)

Fig. 5 Distribution function of the safety factors of section 24

Figure 6 shows the change in the probability of failure according to the Janbu method for section 24. The graph shows that as the number of samples increases, the curve converges to a constant value. The worst possible combination of input parameters is at run 177, when the probability of slope failure is 14.12%. It is important to note that this value is also understood here for the 1000 samples. Thus, according to calculation no. 177, in approximately 141 of the 1000 cases, the FS will be < 1.0.

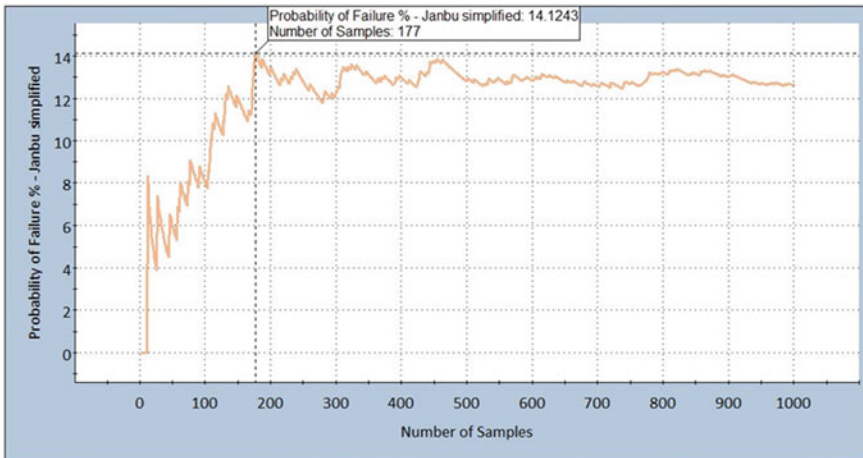


Fig. 6 Evolution of the probability of failure of section 24 according to the Janbu method

4 Conclusion

Slope resistance calculation is the area of geotechnics where the greatest uncertainty prevails in the input parameters. For example, in the case of a long cut, it is not necessarily a guarantee that all sections have the same geological conditions. Geological variations, variability of soil properties, lack of certain information, changes in environmental conditions, unexpected events, approximations used in geotechnics in design or the human errors inherent in the implementation all carry the fact of uncertainty in themselves, which reduces the reliability of the deterministically chosen variables. The disadvantage of probabilistic analyses is that they require significantly more computational energy than deterministic analyses, but their application pays off.

Uncertainty should never be ignored in slope stability analysis. If the data set of the material properties has such distribution where the low values occurs higher density (such as lognormal, gamma, beta, exponential distribution), the safety factor may differ significantly from the deterministic safety factor. This deviation is always negative, so the real safety is lower than the deterministic one.

The introduced case study prove that, the deterministically calculated safety factor of the most critical slip is above 1.3, and therefore it can be considered acceptable. However, after running the calculation on a probabilistic basis, it can be seen that the probability of failure was relatively high. At section 24, the simplified Janbu method gave a 14.12% chance of slope failure, which means that in 141 cases out of 1000 runs, the slope would slip because the safety factor did not reach 1.0 in these 141 cases. This is not considered acceptable for the Visonta lignite mine. Full assurance is provided by supporting the slope compliance with a statistical method. The design of the slope geometry is finished, when the probability of failure is as close as possible to 0%. The same is true when examining an existing slope (soil or rock slope): The stability of the slope cannot be stated after a satisfactory result obtained by a deterministic calculation, it is worth supporting this result with a probability calculation.

I would like to thank the Department of Geology and Hydrology of Mátrai Erőmű Zrt. for the data provided and the help provided for the preparation of the article.

References

1. El Ramly et al. (2002) Probabilistic slope stability analysis for practice. *Can Geotech Journal*. 20 pages, p 2
2. Alonso EE (1976) Risk analysis of slopes and its application to slopes in Canadian sensitive clays. *Géotechnique* 26:453–472
3. Adams BM (2015) Slope stability acceptance criteria for opencast mine design, Australia New Zealand. In: *Conference on geomechanics*. Wellington, New Zealand, p 120
4. Mátrai Erőmű Zrt (2012) Brief geological information in the Visonta lignite area, K-II. the area of the eastward continuation and the tailings area (in Hungarian)

5. Kabai I (1997) Verification geotechnical expert opinion on Visonta K-II. on the establishment of a border slope system for the mine—Budapest (in Hungarian)
6. EasyFit (2020) <https://easyfit.informer.com/>
7. CumFreq (2020) <https://en.wikipedia.org/wiki/CumFreq>
8. Rocscience Slide2 (2020) <https://www.rocscience.com/software/slide2>

Investigation of Ground Stability of the Surroundings of the “Statue of Peace and Freedom”, Alsancak-North Cyprus



Salih Saner

Abstract The Peace and Freedom Monument is about seven kilometers to the west of Girne on the main road to Güzelyurt. It was built in 1977 by the Ministry of Public Works and Transport of the State of North Cyprus, in memory of the 1974 Peace Operation on the beach where Turkish soldiers first set foot on the island of Cyprus. Due to some adverse ground conditions and repair deficiencies to date, some foundation-related damages and structure depreciations occurred. This study includes foundation damages observed and assessment of the mass movements that might occur in the ground allocated for construction of the Beach Project in the nearby area. Geomorphological, geological, and groundwater aspects affecting the ground durability have been brought to the attention of engineers.

Keywords Ground stability · Land sliding · Statue of peace · North Cyprus

1 Introduction

The Peace and Freedom Monument, was built in 1977 by the Turkish Federated State of Cyprus, Ministry of Public Works and Transport, to commemorate the 1974 military operation at the point where Turkish soldiers first set foot in Cyprus (Fig. 1a). The Monument suffered some damage due to ground movements and due to the wear of the reinforced concrete structure over the time.

The marble floor around the monument in the ceremonial area, was tilted and got broken. There were bendings and collapses on the floor along the fractures that occurred in places. In fact, no serious damage was observed, but it was left out of control without preventive maintenance. On the other hand, damages that seem insignificant today may cause major damages in the future. In this study, it is aimed to investigate the extent of damages and advise necessary precautions to protect the structure against natural disasters.

S. Saner (✉)
Engineering Faculty, Near East University, Nicosia, North Cyprus
e-mail: salih.saner@neu.edu.tr

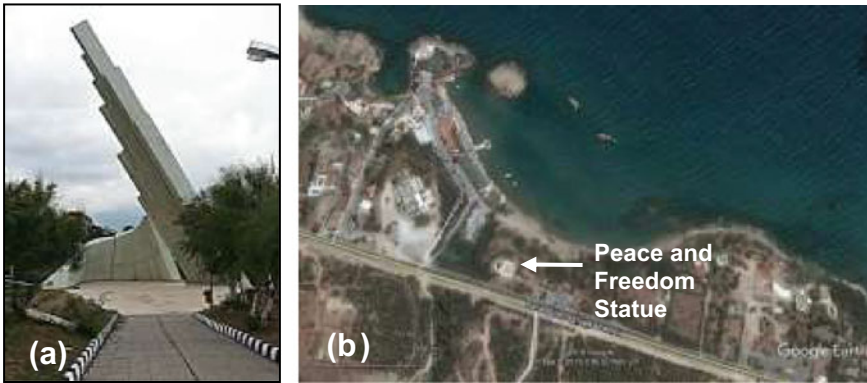


Fig. 1 **a** View of the Peace and Freedom Monument, **b** Satellite view of the Yavuz Landing Beach area to be developed as a public beach. The western part of the beach is called Escape beach and the eastern part is designated as Alsancak Municipality Beach.

Alsancak Municipality has planned to develop not only the monument, but also the entire beach area called “Yavuz Landing Beach” seen in Fig. 1b. The project includes a parking lot, beach facilities, a restaurant and a buffet. Another car park will be built in the south of the asphalt road. Two parking lots on both sides of the road will be connected with a tunnel passage.

Project file and drawings prepared in 1977 could not be obtained, but Alsancak Municipality provided two study reports made by Istanbul Technical University (ITU). The first report includes the soil mechanics test results of the cores taken from two wells [1]. The second report includes damage observations on the monument and ground slip parameters. Tensile cracks and slip circles were examined and shear modeling was carried out using the available data [2].

2 Mass Movements and Ground Problems

Mass movement is flow or slide of the rock and soil materials down the slope by gravity. The factors controlling these movements are the steepness of the topographic slope angle, the mechanical properties of the rock or soil type, the strike and dip of formation bedding, ground and surface waters and vegetation.

2.1 Geomorphological Features of the Study Area

The Statue of Liberty was built on the edge of a plateau gently dipping northward between the Besparmak Mountains and the coast line. Its topographic elevation is about 20 m. The average topographic slope from the monument to the coast is 15–20°

(26–36% slope). The slope from the monument to the Anıt Creek valley in the West is more than 30° (57%).

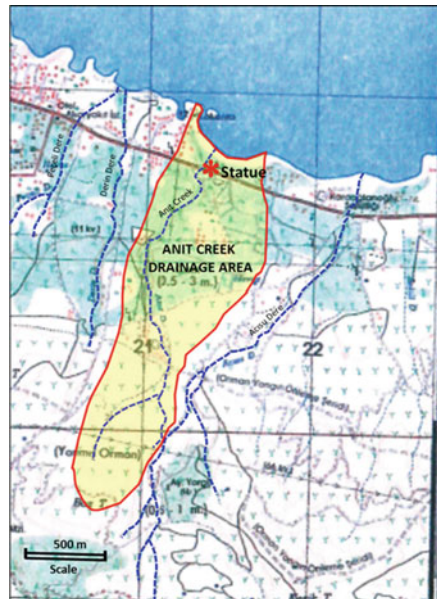
Drainage Network. The coastal plateau extending along the Beşparmak Mountains is cut by parallel streams flowing from South to North. Anıt Creek, which passes 20 m west of the Statue of Liberty and reaches Yavuz Landing Beach, is the only stream that can directly impact the project area.

The drainage area of the Anıt Creek is approximately 2 square kilometers (Fig. 2). If the average precipitation is 460 L per square meter, yearly 960 thousand tons of rain falls in the Anıt Creek drainage area. Assuming that one third of this will flow on the surface, it can be said that an average of 320 thousand tons of water flows in this stream annually.

Since the drainage area of the creek is small and does not extend to the Beşparmak Mountains, any major flooding is not expected. However, during a thunderstorm high speed and high flow rate of the stream is able to carry pebble size gravels. Recent pebbles in the fluvial deposits of the Anıt Creek are clues of mass flows. These pebbles are not derived from the Beşparmak mountains, but from the conglomerate interbeds in the calcarenite (locally called havara limestone) which forms the plateau.

Surficial Drainage. Water and geological factors are most significant effects in all mass movements. The slope area in the Alsancak Beach Project area is about 50 thousand square meters. The rain falling on the slope area is 23 thousand tons, annually. Infiltration of rain-water into shale-soil causes local accumulation on the underlying shale interface and may cause slip or mass flow. It can also cause disintegration of the shale.

Fig. 2 Drainage map of the Anıt Creek



2.2 Geological Features

Two geological units and several soil types differentiated in the study area. The Geological map which has been prepared and a cross section are given in Fig. 3.

Calcarenite Limestone. The coastal plateau up to Besparmak Mountains consists of granular limestone called calcarenite. It is Pliocene to Pleistocene occurrence which different facies are given different formation names. Most commonly, Nicosia Formation name is used [3]. Stratification is dipping 2–4° northward. About 4 m thick outcrops reach 25 m on the plateau in south. Due to its hardness, it forms steep scarps along the 200 km edge of the coastal plateau in the northern coast of the island (Fig. 4a). It unconformably sits on the inclined shale layers (Fig. 4b) and forms Girne aquifer where infiltrating rain water accumulates.

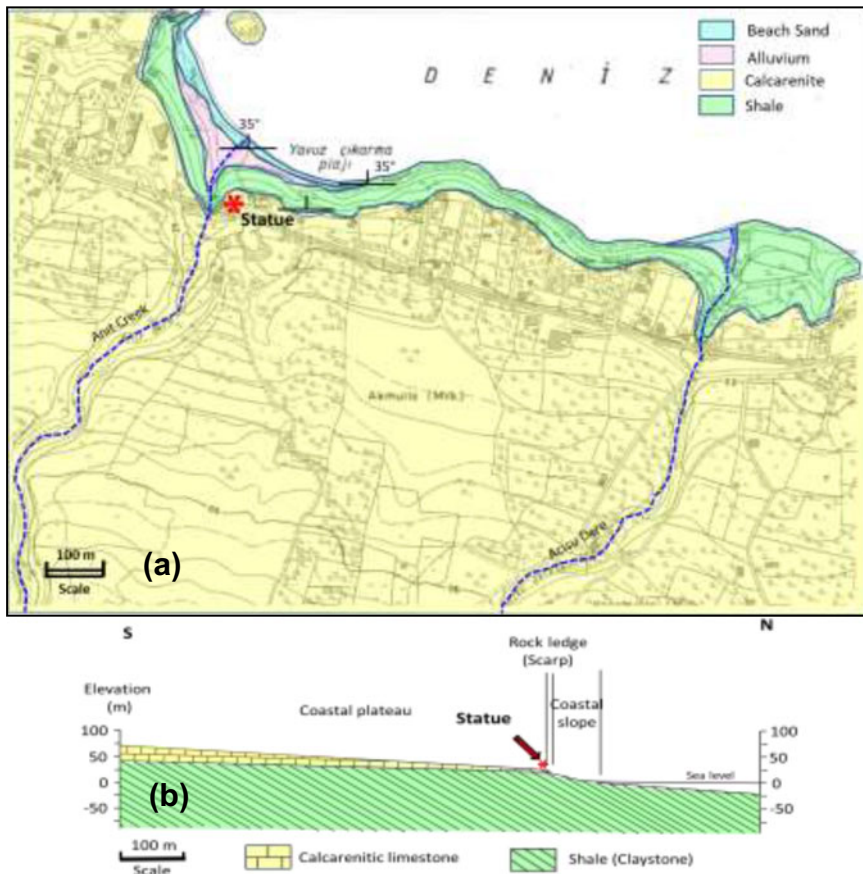


Fig. 3 a. Geological map of Yavuz Landing Beach Area; b. North–South geological cross section through the Statue of Liberty

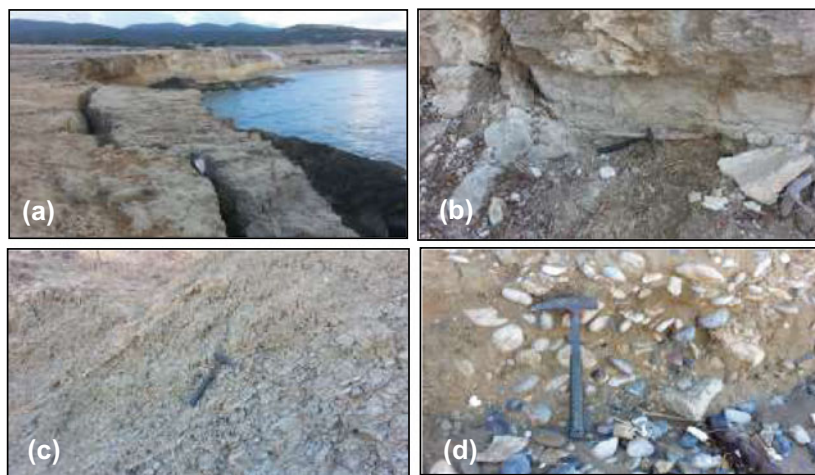


Fig. 4 **a** Calcarenite unit forms a coastal plateau with a rock ledge along the Northern coast of Cyprus. Along the scarps gravity fractures and rock falls are very common; **b** Calcarenite overlies the shale unit with a distinct angular unconformable contact marked by hammer tip; **c** Shale (Gonno) unit consists of claystone and siltstone thin layers which are dipping northward with 35–40°. **d** Pebbles seen in the alluvium at the mouth of Anit Creek

Shale. This flysch sequence is known as Degirmenlik Formation deposited in Middle Miocene [3]. The lower part contains proximal turbiditic sands [4], whereas it is mainly claystone in the upper part. It consists very thin claystone layers locally called “Gonno” (Fig. 4c). Sequence is dipping 35–40° to the north and are overlain unconformably by the younger calcarenite unit. This shale becomes slippery, like a soap, when it is wet. Grains get disintegrated in water. Two samples placed in the tap water in the laboratory were completely dispersed in 30 min.

Shale Weathering Soil. When the shale comes into contact with water and atmosphere, it decomposes rapidly and its surface is covered with impervious clay. This forms a kind of protective sheath for the underlying unweathered shale against air and water. If this soil is excavated or removed, the underlying shale will decompose again, perhaps resulting in slope instability and mass movements.

Alluvial Soil. High slope rate of the upper Anit Creek vally is not suitable for alluvial deposition, but alluvial accumulation is seen in the small plain where Anit Creek meets the sea. This soil consists of a mixture of weathered calcarenite and shale material. Pebbles shown in (Fig. 4d) indicates deposition by a flooding.

Beach Sand and Gravel. Yavuz Landing Beach is famous for its fine sand. Pebbles and cobbles can be seen around the mouth of Anit Creek. As seen in the map the sandy beach is not continuous Eastward up to Acisu Creek.

3 Mobility Observations on the Foundation of the Statue

Some damages seen in foundation and reinforced concrete structure are indications of ground mobility. These observations are mentioned below:

1. Stone pavement adjacent to the statue in the north has broken apart (Fig. 5a).
2. Fractures, thrusts, and buckling of the retaining walls indicate a mass force downhill towards the north (Fig. 5b).
3. The upper surface of the northern wall of the ceremonial square bows down in the middle which indicates a vertical subsidence.
4. The central part of the ceremonial square collapsed about 10 cm (Fig. 5c). Damages are more evident along the drainage channels.
5. The concrete floor above the drainage channel between the two pillars of the monument collapsed due to slight downward slip of the western wall.
6. In the seating stands to the east of the ceremonial square, bending is the indicator of ground subsidence.
7. Below the wall joint in the south of the monument, there is a 2 cm open fracture in the foundation (Fig. 5d). With little rotational movement walls were separated by 3 cm in the upper part.
8. A fracture occurred in the foundation under the wall joint on the west of the monument. The bars connecting the two walls forced the concrete as a result of the relative movement.



Fig. 5 Some damages observed: **a.** The stone pavement adjacent to the monument is separated from the monument towards the north; **b.** Buckling of the retaining wall by the load forcing from north to south; **c.** Partial subsidence formed in the Ceremony Square especially extends along the drainage channels; **d.** The fracture in the foundation under the two concrete joints

9. In the southwest of the ceremonial square north–south compression uplifted floor marbles forming tepee structures.

4 Factors Affecting Ground Mobility in the Vicinity of the Peace and Freedom Statue

In terms of mass movements, the slope region between the cost line and the plateau is a critical area. Movements that can be seen here are 1. Landslide (slump), 2. Rock slide, 3. Rock fall, 4. Debris flow, 5. Earth flow, and 6. Creep.

There are three main factors that may cause mobility in the area, namely ground rock type, water effect, and gravity effect.

4.1 Ground Rock Type

Around Yavuz Landing Beach, only calcarenite unit is suitable as bedrock for constructions. Shale sequence is a formation dominated by clay minerals. Therefore it is undesirable as a bedrock for three reasons: 1. Easily slide downhill along a bedding surface or along a fracture; especially when it is wet, 2. Swelling in wet and shrinkage in dry conditions causing cracks in structures; 3. Alteration and disintegration of clay with water, forms a plastic mud on the ground.

Shale layers are dipping with an angle of 35° in the same direction with the topographic slope, which is undesirable. The topographic slope is about $15\text{--}20^\circ$. If the topographic slope is more than the dip angle, it will be even more undesirable in terms of landslides. Therefore, high slopes creation during excavations should be avoided or a retaining wall should be built immediately.

4.2 Water Effect

The only stream that can be active in the Yavuz Landing Beach area is Anıt Creek, which sometimes flows in winter. Normally, it is not expected to cause any damage, but in case of flooding, it may cause mass movement on the Anıttepe slope.

Groundwater accumulation at the interface of shale and calcarenite, meets a significant amount of water requirement for usage and irrigation in the Girne region. Excess water from the aquifer flows in the direction of the interface dip, creating springs and small seeps along the Northern coast of Cyprus. The Girne coast line is covered with green vegetation due to these water seepages.

Since the shale–calcarenite interface is generally above sea level, sea water cannot enter the aquifer even though excessive water-pumped from the aquifer. Another fact is that, water infiltration seeping from septic wells joins this aquifer causing pollution.

4.3 Gravity Effect

Rocks from cliffs easily slide on clay accumulated on the shale formation. The slopes are suitable for gliding of rock blocks towards the coast due to gravity effect. Allochthonous limestone blocks of different sizes scattered on the slope are of this type.

5 Conclusions and Recommendations

The results of the study are summarized below:

1. Although there are some movements and related damages on the floor of the Peace and Freedom Monument, no major slippage has been observed. However, precautions should be taken and maintenance should be done so that these small movements do not turn into a big disaster in the future.
2. The land on the coast, where the Yavuz Landing Beach project will be built, has a risk of ground slipping and flowing since it consists of shale formation. During implementation of the project, it is recommended not to disturb the slope angle of the ground, but to strengthen them.
3. Since calcarenite limestone ledges shelter the shale formation from atmospheric weathering, they must be protected from human destruction.
4. The soil on the shale formation in the Yavuz Landing Beach area should not be excavated as it is forming a protective sheath for the underlying shale.
5. Since uncontrolled surface waters rather than groundwater pose a danger in the region, their controlled flows should be ensured.
6. Afforestation, in the of Yavuz Landing Beach Project area, will both enrich the environment and provide stability to the ground as well.

Acknowledgements Author would like to thank to Mr. Hasan Okaygun for his constructive review and improvement of the manuscript.

References

1. ITU (2008) Cyprus statue of liberty laboratory report. ITU Civil Engineering Faculty Hamdi Cheesecioglu Soil Mechanics Laboratory, Ayazaga, Istanbul
2. ITU (2010) Geotechnical report on the freedom monument of the Turkish Republic of Northern Cyprus. ITU faculty of civil engineering, Department of civil engineering, Ayazaga. Istanbul
3. Hakyemez HY (2014) Main geological characteristics of Northern Cyprus. TAPG Bull 26(2):7–44
4. Weiler Y (1964) Some remarks on the Kythrea Flysch. Ann Rep Geol Surv Dpt for 1963. pp 53–56, 1 fig

Dynamic Response Analysis of Highway Embankments



Yasin S. Toksoy and Ayşe Edinçliler

Abstract As the severity and the occurrence rate of natural disasters, such as earthquakes, increases; highway embankments become more susceptible to related hazards. However, highway embankments are considered to be an important life-line which must be in continuous operation under any circumstances. In light of the recent advances and latest research, geosynthetics can successfully and effectively be used to reinforce highway embankments against the primary and secondary effects of earthquake induced damages. It is important to estimate the approximate dynamic behaviour of engineering structures via numerical simulations before the experimental studies. This study covers numerical modelling of the dynamic response of full-scale highway embankments using the Mobile Seismic Shaker (MSS) in the field as a dynamic source. This numerical simulation phase has been used to ensure the true structural design and true instrumentation. The numerical simulations have been performed implementing the FEM technique using PLAXIS 2D software and includes the dynamic response analysis of dimensionally identical unreinforced and geogrid reinforced highway embankment models. Revealed numerical results clearly show that, geogrid reinforcement can successfully reduce the total displacements and transmitted accelerations at crest level which are key structural performance indicators.

Keywords Highway embankments · Seismic performance · Geosynthetics · Numerical modelling

Y. S. Toksoy (✉) · A. Edinçliler
Earthquake Engineering Department, Boğaziçi University, Kandilli Observatory and Earthquake
Research Institute, Istanbul, Turkey
e-mail: yasin.toksoy@boun.edu.tr

© The Author(s), under exclusive license to Springer Nature Switzerland AG 2023
C. Atalar and F. Çinicioğlu (eds.), *5th International Conference on New Developments
in Soil Mechanics and Geotechnical Engineering*, Lecture Notes in Civil
Engineering 305, https://doi.org/10.1007/978-3-031-20172-1_30

311

1 Introduction

The consideration of the role of roads and highways to provide required safety and emergency needs in case of a natural disaster such as earthquakes, highlights the importance of dynamic performance of highway embankments especially in earthquake prone areas. Because roads and highways are considered to be very important lifelines and lifelines must be in continuous operation under any circumstances [1–3].

Mitigating earthquake hazards and risks of engineering structures have always attracted researches. However, the dynamic performance of highway embankments is one of the important topics in the literature although these structures are clearly vulnerable to earthquake induced damages. It is very important to improve the seismic performance of highways as well as to mitigate earthquake related hazard to provide continuous operation of such lifeline structures [4].

Highway embankments, slopes or dam like structures and their static and dynamic stability and durability must be maintained in early construction stages. The required stability conditions shall be achieved with the implementation of various engineering applications to reinforce this kind of structures. There are a number of improvement techniques by means of static and dynamic performance available in the literature for the reinforcement of highway embankments but this study particularly concentrates on geosynthetic reinforcement.

The integration of geosynthetic materials to the civil, geotechnical and earthquake engineering applications has become an advantageous and cost-effective way to achieve the required stability conditions of related structures. Geosynthetics are synthetic materials that are commonly used to solve civil and geotechnical engineering problems. The use of these materials is not limited to static load conditions. Geosynthetics are capable of absorbing dynamic forces and transmitting less dynamic forces to engineering structures [3–5].

Due to the primary and secondary effects of earthquakes, highway embankments experience minor to major scale of damage all around the world constantly. Due to the additional tensile strength provided and the soil-structure interaction, it is a common practice to use geosynthetics to improve the seismic performance of earth structures like embankments [6]. In the literature, it is possible to find many kinds of different studies on geosynthetic reinforcement of different geotechnical structures [7–12].

Previous studies related with the dynamic performance of highway embankments and slopes are generally based on numerical simulations and shaking table experiments. A few shaking table experiments related to the seismic behavior of reinforced slopes and embankments are also provided in the literature [13]. Provided experimental and numerical studies aim to determine the effect of slope angle on the results. In a research, the effect of frequency on seismic response of reinforced soil slopes was studied. Clayey soil was used for the experiments and reinforced and unreinforced slopes with two different slope inclinations of 45° and 60° were tested in a laminar box. Biaxial geogrids were used for reinforcement of slopes and models were excited dynamically under 0.3 g of acceleration with different frequency values

of 2, 5 and 7 Hz. It was concluded that the increase in frequency values leads to an increase in displacement values [14].

In an experimental study, scaled highway embankment models were 1-g shaking table tested under different dynamic motions with different frequency and amplitudes in addition to the real earthquake records. Dimensionally identical unreinforced and geotextile-reinforced highway embankment models were subjected to input dynamic motions (2–14 Hz 40 cycle and scaled Düzce Eqe. record) to determine the effect of the inclusion of geosynthetics on the dynamic response of highway embankment models. Results clearly show the geosynthetic reinforcement successfully reduced the settlements and transmitted accelerations up to 85% and 56%, respectively [15].

In a full-scale shaking table experiment, the dynamic response of highway embankments reinforced with flexible container bags was studied. The method is basically placing the flexible container bags (with different configurations) at the toe of the embankment for earthquake resistance purposes. Instrumented full-scale models were shaking table tested under 5 Hz 40 cycle of harmonic motion. Results of the study suggests that proposed method improves the dynamic response of highway embankment models [16].

Regarding the previous experience and expertise, the aim of this research is to determine the effects of geogrid reinforcement on the seismic performance of highway embankments numerically prior to field scale tests. The study is parametric in a way that the seismic performance of the highway embankments is investigated by performing seismic performance analyses using the same dynamic input which Mobil Seismic Shaker (MSS) is capable of applying in field scale. The MSS is a very special and expensive device which is specifically developed for research purposes. There are only few MSS' around the world and there is only one in Turkey, which is operated by the Earthquake Engineering Department of Boğaziçi University in KOERI.

The native soil parameters were determined by a series of geophysical tests including Pressuremeter tests, Multichannel Analysis of Surface Waves (MASW) tests, Electrical Resistance Tomography (ERT) tests and laboratory tests. By using the tested field data, two different highway embankment models with and without geogrid reinforcement were modelled and obtained results were compared under the same dynamic motion.

2 Numerical Study

Numerical simulations of the proposed field scale seismic performance tests have been performed using the commercially available PLAXIS 2D Connect Edition software with finite element modelling technique. Mobile seismic shaker (MSS) operated by KOERI Earthquake Department is going to be used as a seismic source for the proposed field experiments. So that, a selected input dynamic motion of which MSS is capable of applying is also used in numerical analysis. MSS is capable of applying 27 kN of force between 0–225 Hz both vertically and horizontally. A point load which

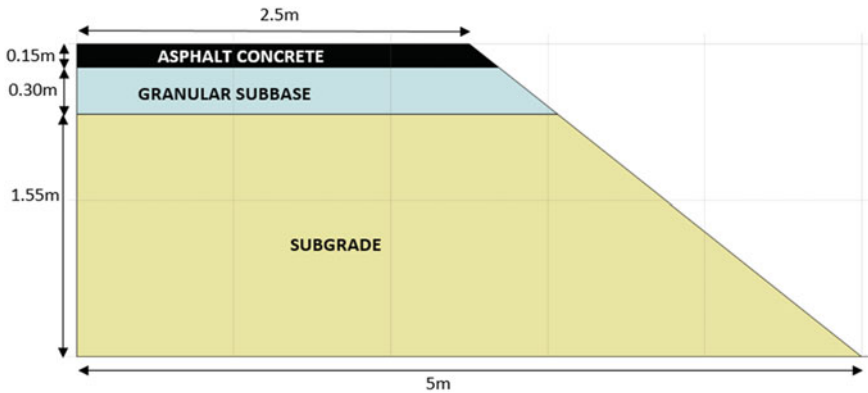


Fig. 1 Unreinforced highway embankment model

is located 1 m away from the toe of the embankment models is used to mimic the MSS as a seismic source. As the embankments models are symmetric, only the right half has been modelled and subjected to dynamic excitations. Dynamic response analysis requires special boundary conditions to avoid reflection of seismic wave which may possibly cause distortions and unrealistic results. Thus, viscous boundaries are defined to the edges of the mesh. The unreinforced embankment model and its dimensioning identical to the field models are represented in Fig. 1. The geogrid reinforcement used in the numerical analysis has an ultimate tensile strength of 40 kN/m^2 . However, PLAXIS use axial stiffness (EA) parameter instead of T_{ult} value. Provided from the design charts, the axial stiffness value of the proposed geogrid material under 5% strain level has been calculated as 2000 kN/m and used as an input value. The geogrid reinforced embankment model and its dimensioning is represented in Fig. 2.

The details of all the materials, material models and related properties are given in Table 1. These parameters are compatible with the related studies in the literature.

An input dynamic motion of incremental 0–100 Hz sinusoidal motion with a peak acceleration value of 1.1 g is selected for the numerical analysis. This input is going to be used for the field experiments as well. The acceleration-time history of the record is given in Fig. 3.

3 Results

Numerical results taken from two models are represented by means of total displacements and transmitted acceleration values. The possible sensor locations in field tests were approximated and the similar locations were defined in the software prior to the analysis. Total displacement distributions of unreinforced and Geogrid reinforced highway embankment models are represented in Figs. 4 and 5.

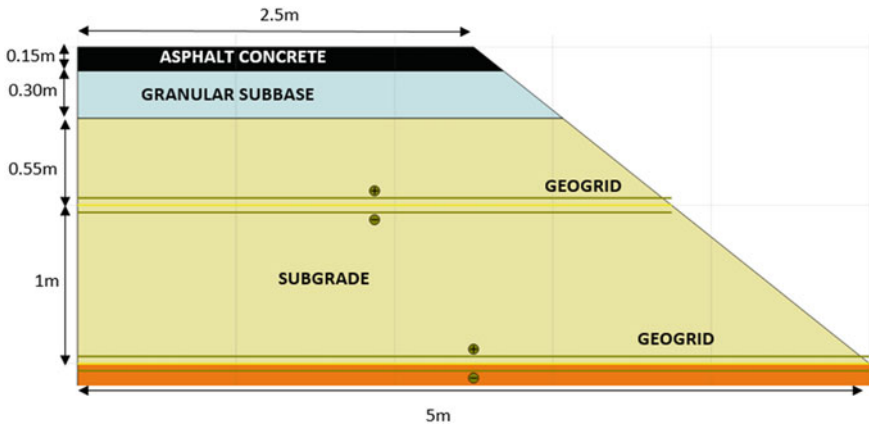


Fig. 2 Geogrid reinforced highway embankment model

Table 1 Material properties used in finite element modelling

	Asphalt concrete	Granular subbase	Subgrade material	Very firm silty clay (Baltaliman formation)
Material model	Linear Elastic	Mohr–Coulomb	Mohr–Coulomb	Mohr–Coulomb
γ_{unsat} (kN/m ³)	24	22	18	18
E' (kN/m ²)	2.1 E ⁶	100 E ³	25 E ³	50 E ³
Poisson ratio	0.4	–	0.34	–
Cohesion (kN/m ²)	–	0.01	40	17
ϕ	–	45°	30°	12°

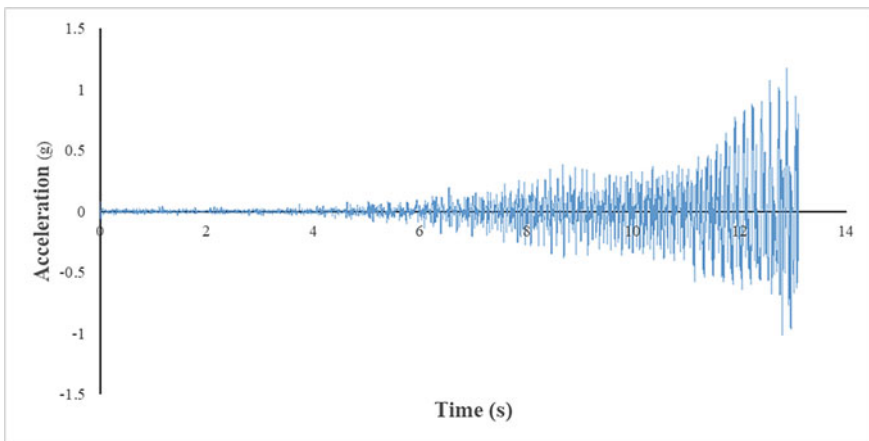


Fig. 3 Input motion of 0–100 Hz harmonic motion

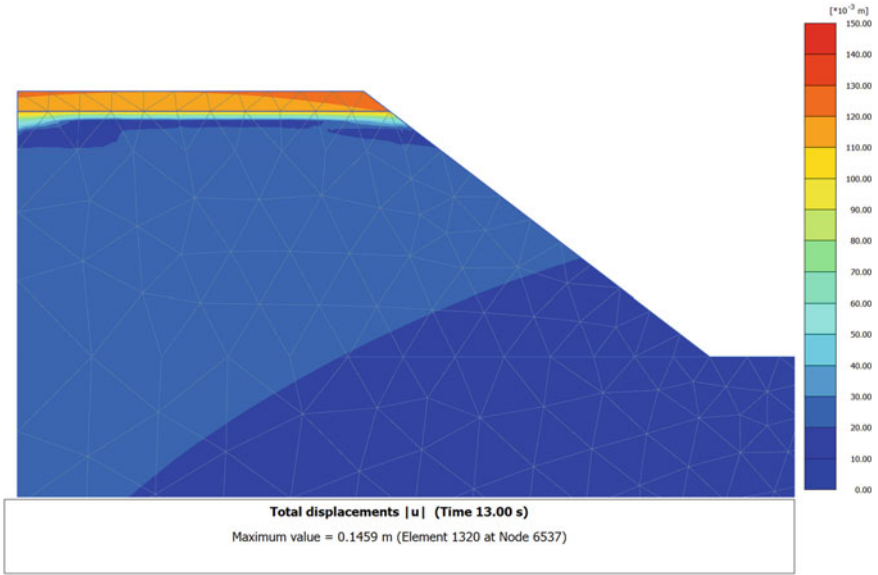


Fig. 4 Total displacement distributions of unreinforced model

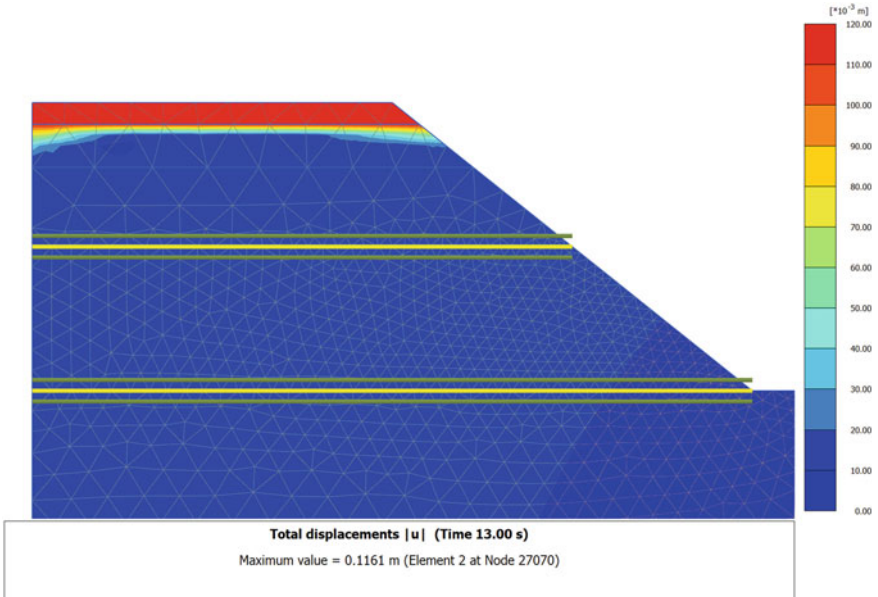


Fig. 5 Total displacement distributions of geogrid reinforced model

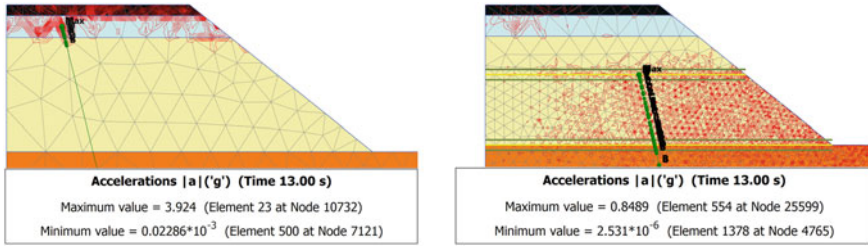


Fig. 6 Total acceleration distributions of unreinforced and geogrid reinforced models

Table 2 Summary of numerical results at the crest

	Total displacements (cm)	Total accelerations (g)
Unreinforced model	15	3.92
Geogrid reinforced model	12	0.85

As can be inferred from the displacement distribution figures, unreinforced model displaces approximately 15 cm. It is seen that the settlement is only concentrated at the crest level. As can be seen in Fig. 5, the geogrid reinforced model displaces approximately 12 cm, which is also observed at crest level. Transmitted acceleration distributions of unreinforced and Geogrid reinforced highway embankment Models are represented in Fig. 6.

It is obvious from the total acceleration distribution figures that the geogrid reinforcement can successfully absorb the dynamic energy and transfer less dynamic motion to the highway embankment model. Observed maximum acceleration value in the unreinforced model is 3.92 g around the crest level. However, the maximum acceleration value observed in geogrid reinforced model is only 0.85 g. Aforementioned results are tabulated in Table 2, for ease of comparison.

4 Conclusions

This paper presents the numerical part of the study which involves the field-scale dynamic response of highway embankment models. Determination of the dynamic response of full-scale highway embankments using the Mobile Seismic Shaker (MSS) in the field as a dynamic source was studied. This numerical study is the simulation of the field-scale testing in which the input parameters are based on previously performed geophysical tests. Obtaining the approximate dynamic behavior of the highway embankment models before the field-scale construction phase is an essential tool to estimate the effectiveness of the geogrid reinforcement on the seismic

performance of the embankment model. This numerical simulation phase has also been used to ensure the true structural design and true instrumentation.

Performed dynamic response analysis of the proposed embankment models reveal that the geogrid reinforcement can substantially and successfully reduce the total displacements and transmitted accelerations at crest level, which are key structural performance indicators. Due to the additional tensile strength provided from the geogrid layers, the geogrid reinforced model displaces 20% less than the unreinforced case. Also, peak transmitted acceleration value on the reinforced embankment model is 78% less than the unreinforced model. Presented results highlighted that the geogrid reinforcement is an effective reinforcement element to mitigate the earthquake hazards of the highway embankments.

Acknowledgements This research has been supported by Boğaziçi University Research Fund Grant Number D15901.

References

1. Edinçliler A (2017) Using waste tire–soil mixtures for embankment construction. In: International workshop on scrap tire derived Geomaterials “opportunities and challenges”. Kanto Branch Jpn Geotechn Soc, 319–328
2. Edinçliler A, Baykal G, Saygılı A (2010) Influence of different processing techniques on the mechanical properties of used tires in embankment construction. *Waste Manage* 30:1073–1080
3. Edinçliler A, Toksoy YS (2017) Physical model study of the seismic performance of highway embankments with and without geotextile. *J Earthq Tsunami* 11(2). <https://doi.org/10.1142/S1793431117500038>
4. Toksoy YS (2014) Investigation of the seismic performance of reinforced highway embankments. MSc Thesis, Boğaziçi University, Istanbul, Turkey
5. Edinçliler A, Toksoy YS (2018) Effects of improvement techniques on seismic performance of highway embankments. In: 16th European conference on earthquake engineering (16ECEEE) proceedings, 18–21 June, Thessaloniki, Greece
6. Koseki J (2012) Use of geosynthetics to improve seismic performance of earth structures. *Geotext Geomembr* 34:51–68
7. El-Emam ME, Bathurst RJ (2004) Experimental design, instrumentation and interpretation of reinforced soil wall response using a shaking table. *Int J Phys Model Geotechnics* 4:13–32
8. El-Emam ME, Bathurst RJ (2007) Influence of reinforcement parameters on the seismic response of reduced-scale reinforced soil retaining walls. *Geotext Geomembr* 25:33–49
9. Yegian MK, Kadakal U, Catan M (1999) Geosynthetics for earthquake hazard mitigation. *Indian Fabrics Assoc Int* 1:87–100
10. Perez A, Holtz RD (2004) Seismic response of reinforced steep soil slopes: results of shaking table study. In: *Geotechnical engineering for transportation projects*, ASCE geotechnical special publication (126), pp 1664–1672
11. Lin YL, Leng WM, Yang GL, Li L, Yang JS (2015) Seismic response of embankment slopes with different reinforcing measures in shaking table tests. *Nat Hazards* 76:791–810
12. Wartman J, Seed RB, Bray JD (2005) Shaking table modeling of seismically induced deformations in slopes. *J Geotechn Geoenviron Eng* 131(5):610–622
13. Lin ML, Wang KL (2006) Seismic behavior in a large-scale shaking table test. *Eng Geol* 86:118–133

14. Srilatha N, Latha GM, Puttappa CG (2013) Effect of frequency on seismic response of reinforced soil slopes in shaking table tests. *Geotext Geomembr* 36:27–32
15. Edinçliler A, Toksoy YS (2017) Shake table tests to measure the dynamic performance of geotextile-reinforced embankment. *Periodica Polytechnica Civil Eng* 61(4):803–814
16. Nakazawa H, Kawamata Y, Shibuya S, Kato S, Jeong K, Baek J, Lohani TN, Morita A, Take-moto O, Moriguchi Y (2020) Full-scale experiment of earthquake resistant embankment using flexible container bag. *J Disaster Res* 15(6):765–781

Motion Analysis of Ground Failure Considering Rainfall and Ground Water Migration in Sandy Slopes



Yan Liu, Hemanta Hazarika, Divyesh Rohit, Sahibbi Ali,
Yasuhide Fukumoto, Masanori Murai, Nguyen Thi Hoai Linh,
and Yurika Taguchi

Abstract Failure of sandy slopes during heavy rainfall is often attributed to the rise of the groundwater table, which causes the slope to gradually transition from an unsaturated to a saturated state. Conventional methods for evaluating the stability of slopes under the influence of rainfall neglected the migration of groundwater and the dynamic motion of particles. In the current study, a model test is conducted to evaluate the trend of the groundwater table migration. In addition, a framework for partially saturated and unsaturated slopes is proposed for the dynamic process based on the analytical method. The results of the study show that based on the data analysis of the model tests, the upward trend of the groundwater table can be determined. Furthermore, the factor of safety (F_s) calculated from the analytical method shows that, F_s decreases sharply due to the upward migration of the groundwater table. The motion analysis provides the soil displacement and particle trajectory. This study provides an effective and practical method for evaluating the stability of unsaturated slopes under rainfall conditions, which can also be used for preliminary analysis in the early warning process.

Keywords Factor of safety · Model test · Motion analysis · Rainfall · Sandy slopes

Y. Liu (✉) · H. Hazarika · D. Rohit · S. Ali
Graduate School of Engineering, Kyushu University, Fukuoka, Japan
e-mail: liu.yan.441@s.kyushu-u.ac.jp

Y. Fukumoto · N. T. H. Linh
Institute of Mathematics for Industry, Kyushu University, Fukuoka, Japan

M. Murai
Shimizu Corporation, Tokyo, Japan

Y. Taguchi
School of Interdisciplinary Science and Innovation, Kyushu University, Fukuoka, Japan

1 Introduction

The whole world is suffering from an increasing risk of natural disasters due to frequent rainfall, which poses a significant threat to human life and property. It has been observed that, between 2004 and 2016, nearly 4,000 landslide disasters occurred due to heavy rainfall and 55,997 people were killed in these rainfall disasters [1]. Statistics on the regional distribution of rainfall disasters show that Asia accounts for 75% of all landslides, and Japan also suffers greatly from the increasing impact of rainfall [2]. Therefore, appropriate measures for early detection of landslides are the need of the hour to ensure the safety of the population.

There are three main methods for evaluating the stability of rainfall slopes. The first one is based on numerical analysis, such as FEM and SPH, which can build various models and provide dynamic failure processes [3]. The second method, which has been widely used in slope stability analysis, is the analytical method, which provides the factor of safety (F_s) of the slope based on the theory of slip surface or force balance [4], where the sliding surface of the slope can be assumed as a straight line, polyline or logarithmic spirals. Some classical studies rely mainly on experimental simulation [5]. Rainfall model experiments can provide an analysis of the soil mechanical performance and slope failure mode under rainwater infiltration and serve as a reference for the early warning models.

Therefore, in order to provide a more comprehensive analysis of the slope stability under the influence of rainwater migration, this study carried out a model test on sandy slope with artificial rainfall and the numerical calculation of the F_s on a cell-by-cell basis. In addition, motion analysis and particle tracking by an image processing software was also performed.

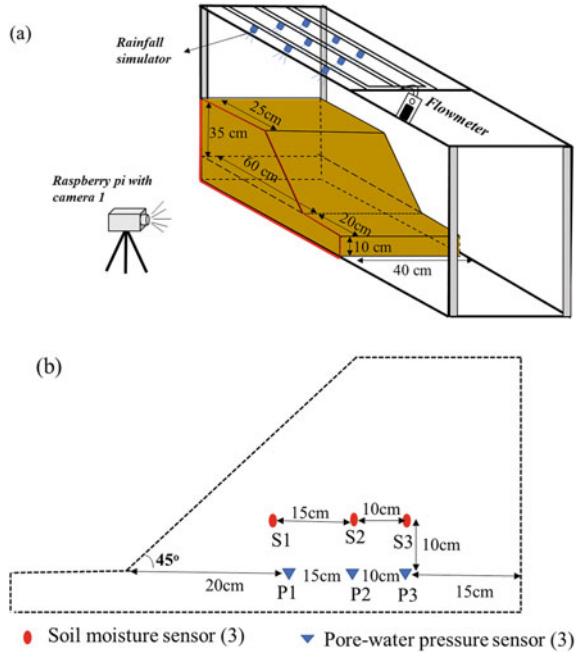
2 Model Test Set-Up and Derivation of F_s

2.1 Test Set-Up

AS shown in Fig. 1a, a sandy slope model with 80 cm length, 45 cm height and 40 cm wide was built in a rectangular box, the slope angle was set as 45° , and 9 spray nozzles were supplied from the top and a flowmeter was taken to control the rainfall intensity as 100 mm/h. Sensors used in this model test are 3 soil moisture sensors (SEN0193) and 3 pore-water pressure sensors (KPG-PA) located at the bottom, as shown in Fig. 1b. Raspberry pi with cameras can provide continuous picture taking on the side view (camera 1). Motion analysis and Particle Image Velocimetry (PIV) analysis can be used to capture the slight slope displacement and motion trail based on real-time pictures from cameras.

Kumamoto sand K7 is chosen to build the model in this study. It has the uniformity U_c of 2.96 and a void ratio e of 0.866. The median grain size (D_{50}) is 0.17 mm and

Fig. 1 Layout of artificial rainfall model test: **a** Model test set-up; **b** Sensors layout



the specific gravity (G_s) of K7 is 2.62. The effective cohesion $c' = 0$ and effective internal friction angle $\varphi' = 40^\circ$. The initial volumetric moisture content is 17% in this research.

2.2 Derivation of F_s

Although infinite-slope stability analysis is always used for shallow landslides, in which shallow slope failure is controlled by an increase in the groundwater table. This method has also been used in past to perform the analysis of unsaturated slopes [6]. F_s as a function of depth below ground surface and time can be denoted as:

$$F_s(Z, t) = \frac{\tan \varphi'}{\tan \beta} + \frac{c' - \sigma_s(Z, t) \tan \varphi'}{(\gamma + \gamma_w * w(Z, t)) * Z * \sin \beta * \cos \beta} \quad (1)$$

Here Z refers to the depth below the ground surface (as shown in Fig. 2), t is the measuring time, β ($^\circ$) is the angle of slope, φ' ($^\circ$) is the soil friction angle for effective stress and c' (kPa) is the soil cohesion for effective stress, γ (N/m^3) is the soil unit weight, γ_w (N/m^3) is the unit weight of groundwater, w is soil moisture content, and σ_s (kPa) defined by [7] for the saturated state and [8] for the unsaturated state:

Fig. 2 Water distribution in an unsaturated slope

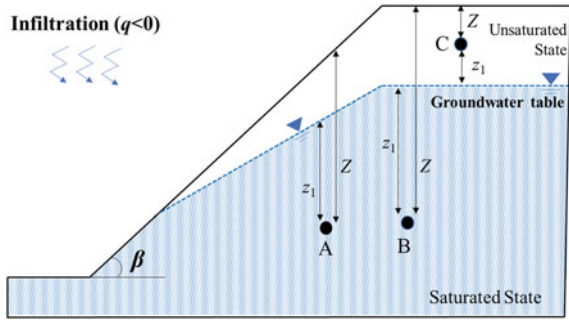


Table. 1 Soil parameters for the slope stability analysis

Parameter	Symbol	Value
Soil unit weight	γ/kNm^{-3}	14 to 18
Inverse of the air entry pressure	a/kPa^{-1}	150 g
Pore size distribution	N	5
Vertical specific discharge	q/ms^{-1}	$-3.14 \cdot 10^{-8}$
Saturated hydraulic conductivity	k_s/ms^{-1}	$3 \cdot 10^{-5}$

$$\sigma^s = \begin{cases} r_u \gamma z_1 & (u_a - u_w) \leq 0 \\ \frac{1}{\alpha} \frac{\ln[(1+q/k_s)e^{(-\gamma_w \alpha z_1)} - q/k_s]}{(1 + \{-\ln[(1+q/k_s)e^{(-\gamma_w \alpha z_1)} - q/k_s]\}^n)^{1-1/n}} & (u_a - u_w) > 0 \end{cases} \quad (2)$$

u_a is pore-air pressure, which is usually 0, u_w is pore-water pressure, a , n are related parameters of soil water characteristic curves. q is vertical specific discharge; k_s is the saturated hydraulic conductivity, and z_1 is the net distance from the general point to the groundwater table, as shown in Fig. 2. r_u is the coefficient of pore-water pressure, it presents an overestimation of the pore-water in the part of hillslopes [9]. In slope stability analyses, the coefficient r_u is usually assumed to be smaller than 0.6. Finally, unsaturated parameters are selected as shown in Table 1.

3 Result and Discussion

3.1 Soil Moisture Content and Pore-Water Pressure

The trend in Fig. 3 depicts the soil moisture content and porewater pressure variation with different. Soil moisture sensor 1 (S1) was recorded to be influenced by the rainwater quicker than S2-S3, because S1 was located closest to the slope. The soil moisture content stayed constant for a short period of time near the threshold of 28%. And S1 also re-increased faster than other sensors because the wetting front went up from the base of the slope, and the moisture content in all the sensors peaked to 38%

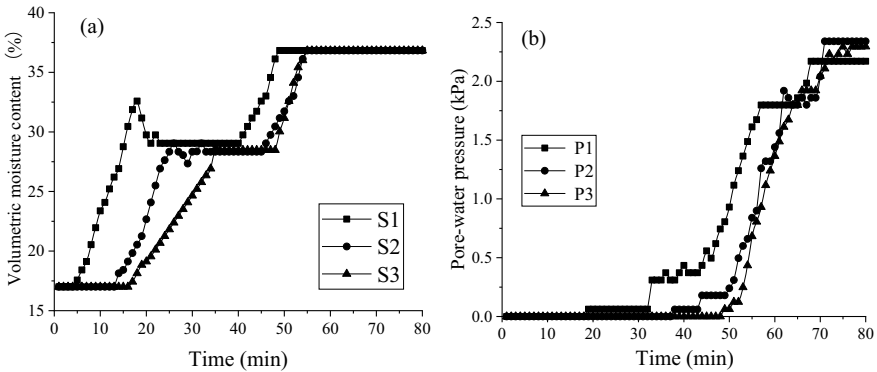


Fig. 3 Sensor data from model test: **a** Soil moisture content; **b** Pore-water pressure

in turn as soil slope gradually became saturated state. Similarly, at the beginning of the test, the pore water pressure did not respond because the infiltrated rain did not reach the bottom of the slope. Then the pore-water pressure sensor 1 (P1) reflected faster than that of P2, due to its proximity to the slope surface. However, P2 tends to show highest water pressure magnitude.

3.2 Safety Factor of Slope and Groundwater Migration

Through this study, it could be highlighted that the increase in soil moisture content during the process of rainfall infiltration, does not have an excessive impact on the F_s , while the rise of the groundwater level led to a rapid reduction of the safety factor. Since S1 is the first sensor to react to the change in soil moisture content and increase of porewater pressure, its safety factor is reduced faster than S2, while S3 is still the last sensor to show a decrease. Furthermore, it is also observed that the time of instability ($F_s < 1.000$) at three sensors was 55 min, 59 min and 62 min (Fig. 4).

Based on the data from different sensors, the migration of groundwater table at different time duration is plotted, and for each moisture sensor, this study marks the F_s to provide the local factor of safety in Fig. 5. It can be clearly observed that with the effects of rainfall continuing, the groundwater table continues to rise. It's obvious that for a sandy slope, although the whole slope is not completely saturated, the slip surface may occur in the saturated zone.

3.3 Motion Analysis

In this research, a camera is stationed on the front of the model to capture the entire process of initiation of the landslides. The camera transmits real-time photos or

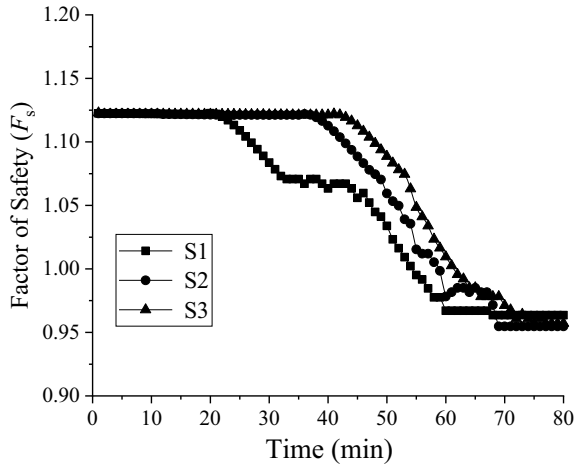


Fig. 4 Factor of Safety of each monitoring point

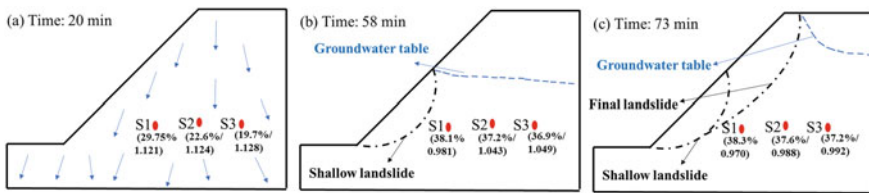


Fig. 5 Real-time state of each monitoring point

videos to the cloud in a convenient and low-cost manner. Embed the motion trajectory calculation into the system to capture the micro displacement. As already shown, sand slopes always induce multiple shallow landslides. Research presents the front view at different duration times during rainfall intensity 100 mm/h. As the initial state is shown in Fig. 6, from the side view, 7 tracking points were marked in the slope, of which 4 points (Point 1-Point 4) are along the slope and 3 points (Point 5-Point 7) are on the far side of the slope edge. Research defines three slope failures based on obvious movement captured by motion analysis, which occurred successively from bottom to top. Here, motion analysis provides real-time displacement of monitoring points, motion trajectory and deflection of monitoring point coordinates, etc. Figure 7a shows that point 1 and point 5 have the earliest response, while Point 1, Point 2 and Point 3 have longer displacement than other points. Because point 1 and point 5 are located in the first shallow landslide area, prompting them to move the earliest. Since Point 1- Point 3 are close to the slope surface and are in the landslide area, the resulting displacement is higher. Motion analysis also records the tilt angle of point coordinates. It is also easy to understand that the tilt angle observed in the upper part are significantly larger than that in the lower area due to the steep slope

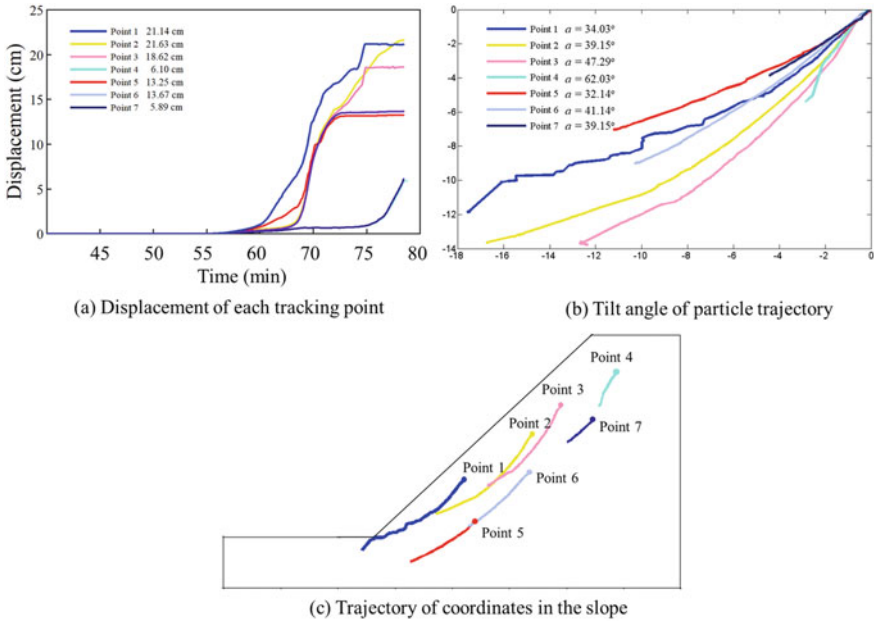


Fig. 6 Motion analysis under rainfall intensity 100 mm/h

of 45° and the landslide mass is accumulated at the slope toe, so it is more likely to generate a larger tilt angle. It can be clearly seen that after the first landslide occurs, it will quickly spread to multiple landslides, and eventually produce extremely violent long-distance landslides. As observed from Fig. 6, more than 50% of the sliding distances of the monitoring points are derived from the last deep landslide. The time of each shallow landslide is 59 min, 65 min and 73 min. Furthermore, the results from PIV (Particle Image Velocimetry) at three different landslides are shown in Fig. 7, it can be seen clearly that at each failure time, the main particle flows are distributed at the bottom, middle, and top, respectively, which is consistent with our expected results.

4 Conclusions

In this study, the stability analysis of sandy slope under rainfall is carried out through model test, analytical method and software analysis, and the following conclusions are obtained:

- (1) Obviously, under the action of rainfall, the slope will lead to the increase of soil moisture content and the rise of the water table, and as the groundwater level rises, the factor of safety (F_s) of the slope decreases rapidly.

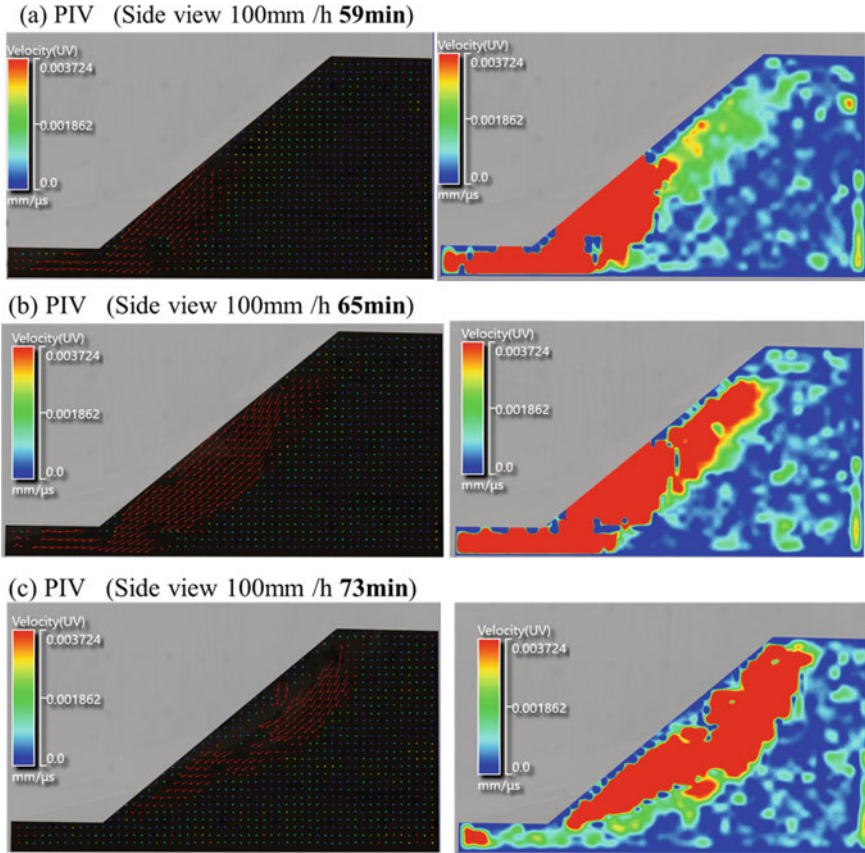


Fig. 7 Motion analysis under rainfall intensity 100 mm/h: a 59 min; b 65 min; c 73 min

- (2) It takes 4 min from the $F_s < 1.0$ to the first shallow landslide because semi-infinite slope calculation theory is easy to produce a lower F_s than the actual state. The faster time to reach the failure state can also be used as an early warning indicator.
- (3) Through the motion analysis, it can be ascertained that, after the initial landslide, the displacement will accumulate rapidly, and multiple landslides will occur in a short period of time to the final deep landslide. The time from the initial landslide to the final landslide is 14 min, as observed this study.

The failure mechanism and instability process of sandy slopes under rainfall conditions are analyzed in detail, and the relevant research results can be used as important indicators in the construction of early warning systems.

Acknowledgements The study is supported by IMI Short-term Joint Research Project (2022a024 and 2022a025) and the MAEDA ENGINEERING FOUNDATION. We would also like to thank Prof.

Haruichi Kanaya (Kyushu University, Japan), Dr. Kazuaki Tanaka (Kyushu Institute of Technology, Japan) and Mr. Keisuke Yamashita (Cross Media Networks, Japan) for their technical support.

References

1. Froude MJ, Petley DN (2018) Global fatal landslide occurrence from 2004 to 2016. *Nat Hazard* 18(8):2161–2181
2. Hazarika H, Kazama M, Lee WF (2016) *Geotechnical hazards from large earthquakes and heavy rainfalls*. Springer
3. Su Z, Wang G, Wang Y, Luo X, Zhang H (2021) Numerical simulation of dynamic catastrophe of slope instability in three Gorges reservoir area based on FEM and SPH method. *Nat Hazards*, 1–16
4. He Y, Liu Y, Hazarika H, Yuan R (2019) Stability analysis of seismic slopes with tensile strength cut-off. *Comput Geotech* 112:245–256
5. Xu J, Ueda K, Uzuoka R (2022) Evaluation of failure of slopes with shaking-induced cracks in response to rainfall. *Landslides* 19(1):119–136
6. Lu N, Wayllace A, Oh S (2013) Infiltration-induced seasonally reactivated instability of a highway embankment near the Eisenhower Tunnel, Colorado, USA. *Eng Geol* 162:22–32
7. Bishop AW, Morgenstern N (1960) Stability coefficients for earth slopes. *Geotechnique* 10(4):129–153
8. Van Genuchten MT (1980) A closed-form equation for predicting the hydraulic conductivity of unsaturated soils. *Soil Sci Soc Am J* 44(5):892–898
9. Michalowski RL (2018) Failure potential of infinite slopes in bonded soils with tensile strength cut-off. *Can Geotech J* 55(4):477–485

**Excavations, Support Systems,
Earth-Retaining Structures
and Underground Systems**

Experimental Investigation and Visualization of Failure Surfaces in Pipe-Soil Interaction Problems Using PIV Technique



Selçuk Bildik, Peter Rogenbuke, Gizil Tak, Baran Tulan,
and Özer Çinicioğlu

Abstract In this study, the effect of relative density on bearing capacity was investigated for cases in which a pipe is buried within the zone of influence. As a novelty, failure mechanisms are experimentally determined using Particle Image Velocimetry (PIV). Within the scope of the study, six different physical model experiments were carried out for this purpose. In these experiments, the load imposed on the neighboring surficial foundation model and the resulting displacements relationship were also determined. The results suggest density dependency of the distribution of deformations.

Keywords Relative density · PIV method · Pipe-soil interaction · Bearing capacity · Failure surface

1 Introduction

Infrastructures such as buried pipeline systems have great importance in daily life. Sewer systems enable people to process the municipal waste, and oil pipelines contribute to transporting petroleum products.

S. Bildik (✉) · G. Tak
Department of Civil Engineering, Nisantasi University, İstanbul, Turkey
e-mail: selcuk.bildik@nisantasi.edu.tr

G. Tak
e-mail: giziktak@gmail.com

P. Rogenbuke · B. Tulan · Ö. Çinicioğlu
Department of Civil Engineering, Bogazici University, İstanbul, Turkey
e-mail: peterogenbuke@gmail.com

B. Tulan
e-mail: baran.tulan@boun.edu.tr

Ö. Çinicioğlu
e-mail: ozercinicioğlu@boun.edu.tr

One of the most common materials used for such systems is PVC pipes. The most important reasons are that they are cheaper and non-corrosive, and due to the that fact, they are less susceptible to microbiological growth. Furthermore, their durability is competitive with other materials such as steel.

The analysis and design of such systems require the consideration of soil-structure interaction [1]. When designing buried pipeline systems, estimating parameters such as displacements, internal stresses caused by transported materials, and external stresses caused by the surrounding soil are necessary.

In the literature, many researchers conducted experiments to evaluate the performance of buried pipes, focusing on the load–displacement behavior of pipes [2–7]. Additionally, there is limited research about pipe-soil interaction in terms of bearing capacity [6, 8, 9].

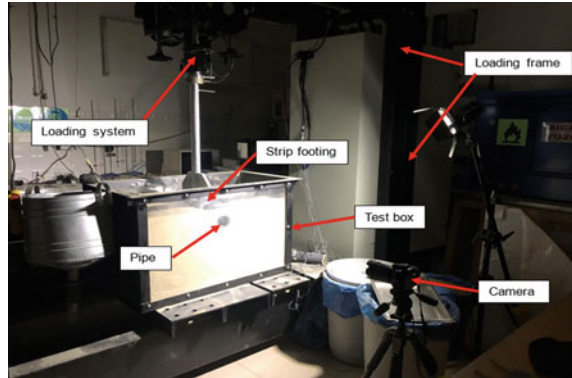
One of the most popular techniques for image analysis, called Particle Image Velocimetry (PIV), was used for the analyses of the images captured during the model tests conducted in this study. PIV is a non-invasive velocity measuring procedure that adapts to geotechnical applications [10]. In this study, MATLAB based GeoPIV_RG software [11] was used. The software operates by dividing a reference image into user-defined meshes and calculates displacements between consecutive images regarding the reference image. This way, displacement vector field can be determined. With the GeoPIV_RG algorithm, the formation of the failure surface in the soil can be observed with a map consisting of different colors indicating different displacement surfaces. The obtained results are presented and discussed.

2 Experimental Studies

2.1 Experimental Setup

Physical model tests were carried out in a rigid box that contains backfill of target density with a pipe buried. Pipe location was varied between experiments. In the tests, a model surficial continuous footing was loaded to observe backfill-pipe-foundation interaction.. The model tests were designed to examine the effect of pipe embedment depth. The tests were recorded by employing different types of data recorders which can measure both load acting on the foundation model and the resulting displacements. The steel frame in which the model tests are conducted allows the preparation of a model backfill with dimensions 100 cm × 50 cm × 60 cm. The front and back sides of the frame are made of plexiglass for capturing consecutive images of soil deformations. For this purpose a Nikon D90 camera was used and the images are later analyzed using GeoPIV-RG. In the model tests, a strip foundation model is placed with dimensions of 50 cm × 10 cm × 3 cm on the backfill and loaded using a loading piston. Foundation loads and the resulting displacements were measured using a load cell and LVDT transducers, respectively. Furthermore, pipe strains were measured using TML brand strain gauges. All measurements are and recorded via

Fig. 1 Overview of the test setup



National Instruments (NI) modules equipped with NI developed LabView software. Three different load cells having different capacities of 500 kg, 1 tonne, and 2 tonnes were used throughout the experiments. LVDT stroke length is 150 mm, and the strain gauges are GFLA-6-50-4L type. Strain gauges were attached to the PVC pipe with a unique cyanoacrylate adhesive. Experimental setup is shown in Fig. 1.

The rate of the loading piston was kept constant at 10 mm/min. The images were captured with a rate of one photo for every 12 s. This corresponds to 2 mm of piston displacement per image making it easier to translate pixel-based displacements to actual displacements. After the completion of the tests, captured images were analyzed using GeoPIV_RG using the initial image as the reference which is meshed with 50px × 50px-sized patches (Fig. 2). The results were expressed in millimeters. As a result, the stress–displacement curves were presented are plotted with 2 mm intervals up to 10 mm displacement, which corresponds to the 10% of the foundation width, due to adopted failure criterion [12].

Fig. 2 PIV analysis area and mesh

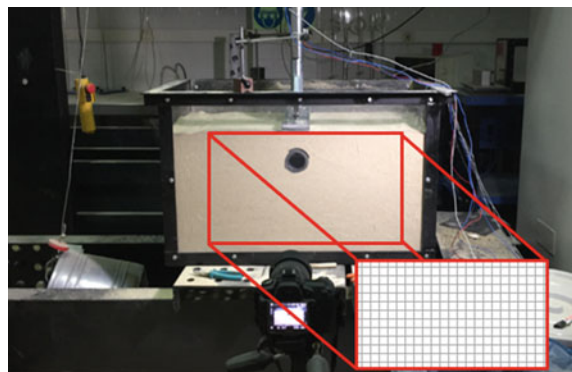
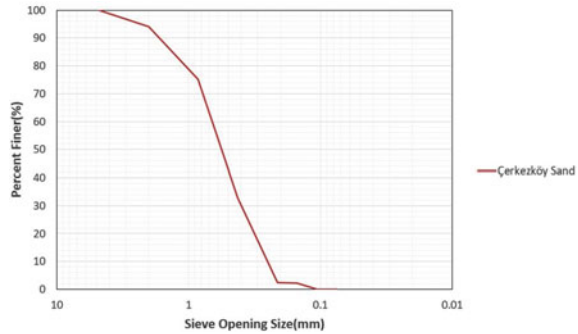


Table 1 Index properties of Çerkezköy sand

Soil property	Value
Classification	SP
Median particle size (D_{50})	0.64
Coefficient of uniformity (C_u)	2.37
Coefficient of curvature (C_c)	0.93
Specific gravity (G_s)	2.62
Maximum void ratio (e_{max})	0.83
Minimum void ratio (e_{min})	0.50
Average sphericity (S_{ave})	0.560
Average roundness (R_{ave})	0.749

Fig. 3 Grain size distribution of Çerkezköy sand



2.2 Soil Properties

For this research, sand obtained from Çerkezköy region of İstanbul was used. Index properties of Çerkezköy Sand are summarized in Table 1 and (Fig. 3).

2.3 Experimental Method

In the scope of this experimental study, 6 model tests were conducted, in which them of them were with the pipe being buried at an embedment ratio of $H/D = 1$ and the other three were without the buried pipe. Each case was examined for different relative densities (D_r) of 35, 50 and 65%. The configuration of the tests are illustrated in Fig. 4 where H is the vertical distance between the bottom of the foundation and the crest of the pipe and D is the pipe diameter which is constant as 75 mm. The required relative density of the sand soil was established by calculating the total soil mass necessary for the whole volume of the frame, then placing and compacting it in ten layers, each layer corresponding to 1/10 of the volume of the frame hence 1/10 of the required soil mass. Details of the model tests conducted are given in Table 2.

Fig. 4 Pipe embedment

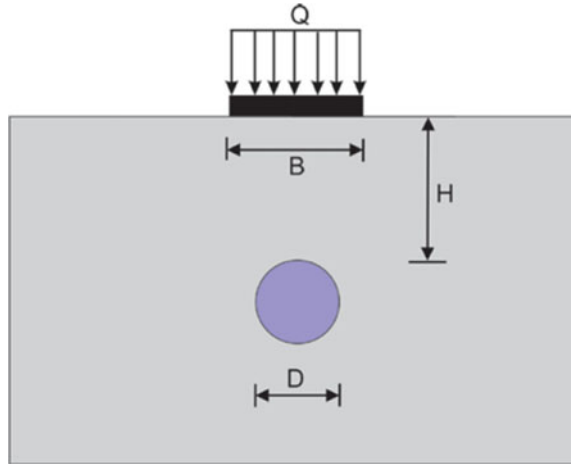


Table 2 Test program

Test no	Relative density of sand (D_r)(%)	Embedment ratio of pipe (H/D)
1	35	–
2	35	1
3	50	–
4	50	1
5	65	–
6	65	1

3 Results and Discussion

This study aims to examine the effect of the buried pipe and different sand relative densities on the bearing capacity of neighboring surficial strip foundations. Figure 5 shows the experimental distribution of vectorial displacements and resultant displacement contours obtained from GeoPIV_RG analyses for 10 mm foundation settlement, which corresponds to 10% of the foundation width that is considered to correspond to failure in this study. It is clear from the analysis results that pipe affects the wedge size and stress distribution due to creating a non-continuous soil zone. Also, resultant contours indicate that displacement zones created just below the pipes and the lowest relative density Çerkezköy sand have the largest displacement zone just below the pipe, as expected.

Figure shows the stress-displacement behavior at 10 mm displacement, which corresponds to 10% of the foundation width of the Çerkezköy Sand with and without the presence of the pipe. As expected, for the case without pipe, the highest load is carried when the relative density is the highest. For the case with pipe, the loading

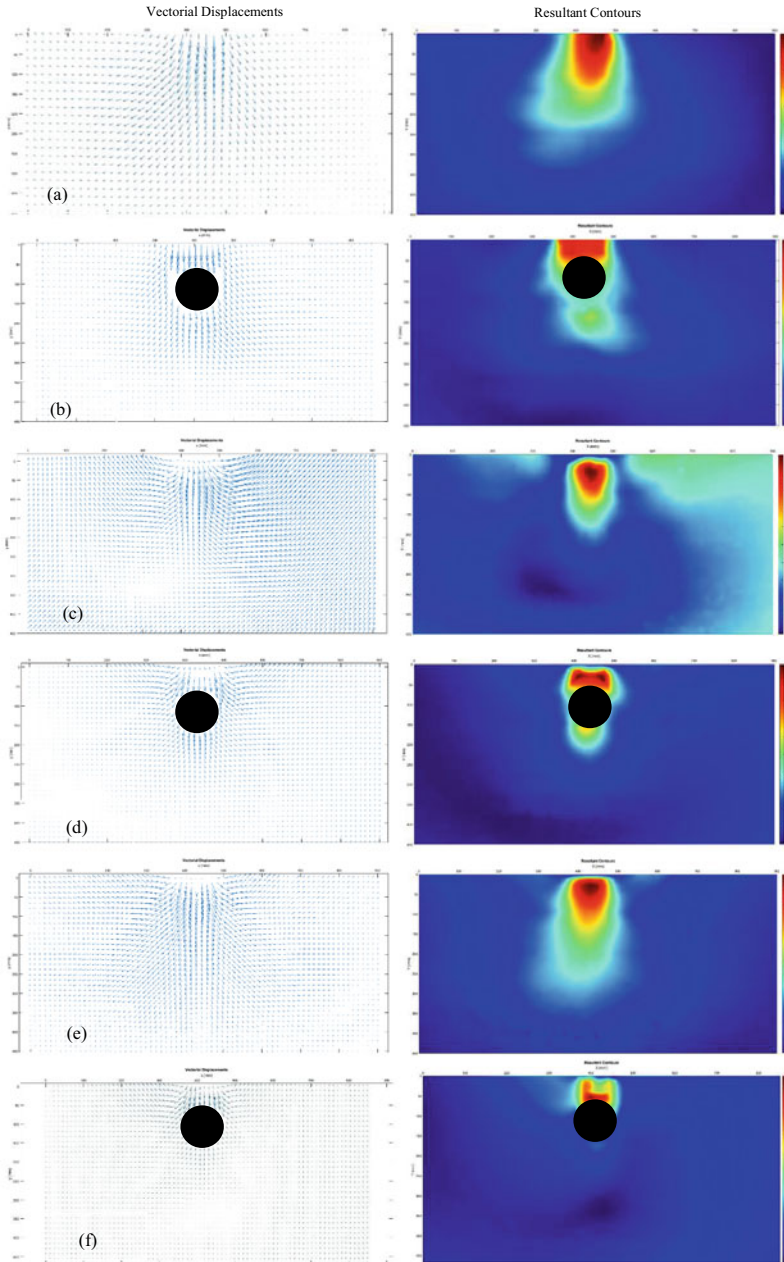


Fig. 5 Vectorial displacements and resultant displacement contours from GeoPIV_RG. **a** Dr: 35% without pipe, **b** Dr: 35% H/D: 1, **c** Dr: 50% without pipe, **d** Dr: 50% H/D: 1, **e** Dr: 65% without pipe, **f** Dr: 65% H/D: 1

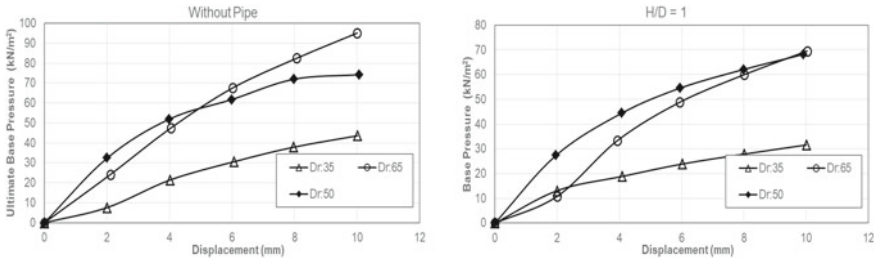


Fig. 6 Stress- displacement behavior of Çerkezköy sand with and without pipe

capacity of the soil at 35 and 65% relative densities drops around 70%, whereas 50% relative density drops around 90% of the case without pipe load values (Fig. 6).

4 Conclusions

In this study, six physical model tests and GeoPIV_RG analyses were conducted to observe the effects of the presence of the pipe and relative density on the deformation of the soil-pipe-foundation system under loading. Pressures and displacement acting on the model foundation were measured, and deformation of the soil strata was visualized by using GeoPIV_RG analyses. GeoPIV_RG analysis accurately envisioned the deformation zones of different sand relative densities. It is understood from the correct separation of the sizes and geometries of the displacement fields obtained from three different analysis results from each other. Furthermore, PIV_analyses were also accurate in visualizing the deformation zones with pipe since it can be seen that from the results, pipe leads to separate deformation fields in sands of different relative densities as expected.

Further studies could be carried out to investigate the effect of geosynthetic on deformation fields and bearing capacity of soil-pipe-foundation system under loading by using GeoPIV_RG analyses. Moreover, further research could examine different soil types using strain contours which can be provided by GeoPIV_RG analyses.

Acknowledgements The work presented in this paper was carried out with funding from TUBITAK (The Scientific and Technological Research Council of Turkey) grant number 116R020.

References

1. Richard A (1973) Parmelee Investigation of soil-structure interaction of buried concrete pipe. Highway Res Board 443:32–39
2. Selig ET, DiFrancesco LC, McGrath TJ (1993) Laboratory tests of buried pipe in hoop Compression, Buried Plastic Pipe Technology, (ASTM STP 1222). PA, USA, pp 119–132

3. Brachman RWI (1999) Structural performance of Leachete collection pipes. PhD thesis, Department of Civil and Environmental Engineering, University of Western Ontario, London, ON, Canada
4. Cho S: Behaviour of flexible plastic pipes with flowable backfill in trench conditions. PhD thesis, University of Houston, Houston, TX, USA
5. Cameron DA (2005) Analysis of buried flexible pipes in granular backfill subjected to construction traffic. PhD thesis, Graduate School of Engineering, University of Sydney, Sydney, Australia
6. Terzi NU (2007) Investigation of the effects of vertical and lateral loads on the stability of buried pipes. PhD thesis, Institute of Natural and Applied Science, Yıldız Technical University, İstanbul, Turkey
7. Talesnick ML, Xia HW, Moore ID (2011) Earth pressure measurements on buried HDPE pipe. *Geotechnique* 61(9):721–732
8. Brachman RWI, Krushelnitzky RP (2005) Response of a landfill drainage pipe buried in a trench. *Can Geotech J* 42(3):752–762
9. Bildik S (2013) Investigation of buried pipe systems in different soil and loading conditions. PhD thesis, Institute of Natural and Applied Science, Cukurova University, Adana, Turkey
10. Lesniewska D, Wood DM (2011) Granular materials at meso and macro Scale: photo-elasticity and digital image correlation. In: *Advances in bifurcation and degradation in geomaterials*, Springer Series in Geomechanics and Geoengineering, vol 11
11. Stanier SA, Blaber J, Take WA, White DJ (2015) Improved image-based deformation measurement for geotechnical applications. *Can Geotech J* 53(5):727–739
12. Vesić A (1975) Bearing capacity of shallow foundations. In: Winterkorn, HF, Fang HY (eds) *Foundation engineering handbook*. Van Nostrand Reinhold, New York, pp121–147

Earthquake Geotechnical Engineering and Associated Problems

P-Y Curves for Piles in Sand Based on the SPT Test–Parametric Study and Practical Recommendations



Abdesselem Laouedj and Ali Bouafia

Abstract ULS and SLS limit state design of pile foundations under lateral loads is often undertaken on the basis of the P-Y curves concept. Since more than half a century, the methods of P-Y curves have been subject of an extensive research work worldwide. Nowadays, the P-Y curves parameters, namely the reaction modulus and the soil lateral resistance, are derived by correlation with geotechnical parameters measured by laboratory test or in-situ tests like the cone penetration test. The contribution of the standard penetration test SPT to the direct construction of P-Y curves is however not demonstrated in the literature. The paper aims at presenting an original semi-empirical method of construction of the P-Y curves along the pile directly based on the N-value measured by the SPT. On the basis of a detailed parametric study it was highlighted some key factors affecting the pile load–deflection behavior.

Keywords Pile · Lateral load · P-Y curve · SPT test · Sand

1 Introduction

The load–deflection behavior analysis of a pile foundation based on the P-Y curves is a practical approach allowing powerful analysis of the forces and displacements of the pile under a horizontal load. These curves are constructed as prescribed by geotechnical standards such as the API and Eurocode 7, following empirical or semi-empirical correlation to the geotechnical parameters measured by the laboratory or in-situ tests (AFNOR [1], API [2]).

The P-Y curve describes a local constitutive law between the lateral soil reaction P undertaken by a spring at the pile/soil interface at a given depth along the pile, and the lateral pile deflection Y at this depth. As shown in Fig. 1, the P-Y curve

A. Laouedj
National Marine Science and Coastal Planning School University, Dély Ibrahim, Algeria

A. Bouafia (✉)
University Saâd Dahleb of Blida, Ouled Yaïch, Algeria
e-mail: ali.bouafia@univ-blida.dz

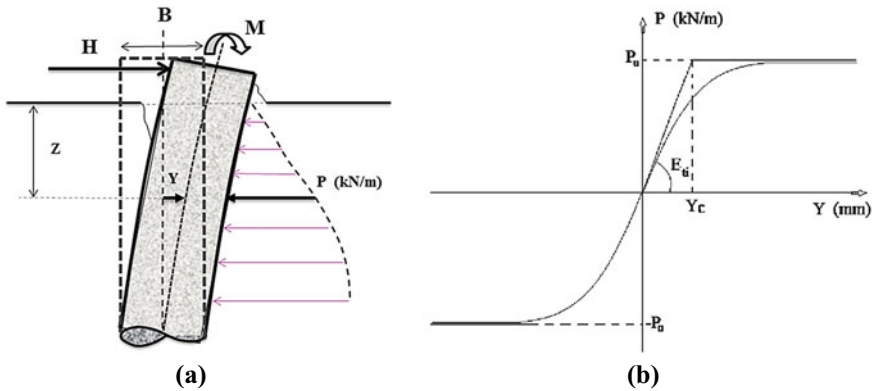


Fig. 1 Schemes of forces balance and the P-Y curves [3]

is non-linear shaped and characterized by an initial slope called the lateral reaction modulus denoted E_{ii} , and a horizontal asymptote P_u corresponding to the lateral soil resistance [3–5].

In spite of the large number of applications of the standard penetration test (SPT) in foundation engineering, it is rarely mentioned in the literature how to use directly the N-value measured by the SPT test to analyze the load–deflection behavior of piles.

This paper aims at presenting a practical method of direct construction of the P-Y curves for piles in sandy soil on the basis of the SPT test.

2 Parameters of the P-Y Curve

The experimental P-Y curve, at a given depth z , derived from the analysis of fully instrumented full-scale test piles by Laouedj and Bouafia [6] were fitted by the hyperbolic function given by Eq. (1), where the two parameters of the P-Y curve E_{ii} and P_u were correlated to the N_{spt} value and the pile characteristics.

$$P(z) = \frac{Y(z)}{\frac{1}{E_{ii}(z)} + \frac{|Y(z)|}{P_u(z)}} \tag{1}$$

The first parameter of the P-Y curve E_{ii} is called the initial lateral reaction modulus and expressed as follows:

$$E_{ii} = K_E N_{spt} \sigma_v' \tag{2}$$

The second parameter of the P-Y curve is called the lateral soil resistance and defined as follows:

Table 1 Values of the parameters K_E and K_N

Above water table	Below water table
$K_E = 207$	$K_E = 156$
$K_N = 21$	$K_N = 17$

$$P_u = K_N \sigma_v' B \tag{3}$$

The coefficients K_E and K_N are respectively called “the modulus number” and “the lateral resistance coefficient”. It was shown they may be directly correlated to the N_{spt} value. In Table 1 are summarized the values of K_E and K_N depending on the position of pile segment with respect to ground water table [6].

Laouedj and Bouafia [7] found out for all the test piles studied that the embedded length D was greater than 3 times the elastic length L_0 ($D > 3L_0$), which leads to classify their behaviour as of flexible piles, and consequently limits the results presented here to the category of flexible piles [7].

3 Parametric Study

3.1 Dimensional Analysis of the Problem

In studying the mechanics of piles under a horizontal force H_0 , the deflection at the grand surface Y_0 of the pile can then be determined. The P-Y curve parameters may be correlated to vertical overburden stress σ_{v0} and N_{spt} the properties of the soil around the geometric properties of the pile, namely the pile flexural stiffness $E_p I_p$, the embedded length D , and the diameter B (or the dimension perpendicular to the lateral load direction), according to the following general equation at a given depth z :

$$f(H_0, Y_0, E_p I_p, B, D, \sigma_{v0}(z), N_{spt}) = 0 \tag{4}$$

Dimensional analysis of this equation according to the Buckingham’s theorem leads to the dimensionless equation:

$$g\left(\frac{Y_0}{B}, \frac{H_0}{\sigma_{v0}(D)BD}, \frac{D}{B}, N_{spt}\right) = 0 \tag{5}$$

The first term is called the normalized displacement, the second is the normalized lateral load, and the third is the pile slenderness ratio. The parametric study presented hereafter focuses on the effect of the following parameters: the pile slenderness ratio, the groundwater level, and the sand density.

3.2 Features of the Model

In this parametric study, the load–deflection curve of a single pile embedded within a homogeneous deep sandy layer having different densities (loose, medium, or dense) was investigated. The model is a steel pipe pile with 0.5 m in diameter, a flexural stiffness of 50 MN.m² and an embedded length varying from 5 to 25 as summarized in Table 2. The lateral load H load is applied at 1 m above the ground surface.

The soil unit weight (submerged or dry) depending on the position of the water table was estimated by empirical correlations with the N_{spt} value as recommended in geotechnical literature.

Terzaghi [8] suggested to correlate the N_{spt} with the in-situ state of density of the sandy deposits as shown in Table 3, and the Table 4 summarizes the physical and mechanical characteristics of the sandy soil used in this parametric study.

Four possible groundwater levels are studied, namely: dry sand without water table, submerged sand (water table at ground level), sand with a water level at mid-length of pile, say D/2, and sand with a water level at a depth of D/4.

The P-Y curves for a given model of pile/soil system were generated and input in the software SPULL (Single Pile Under Lateral Load) developed at the University of Blida.

Table 2 The geometric characteristics of the pile

Embedded length (m)	Diameter	Slenderness ratio D/B	Flexural stiffness
D = 5.0	B = 0.5 m	10	E _p I _p = 50,000 kN.m ²
D = 10.0		20	
D = 25.0		50	

Table 3 Relation between N_{SPT} and density of the sand (after Terzaghi [8])

N value	Relative density
4–10	Loose
10–30	Medium
30–50	Dense

Table 4 The characteristics of the sandy soil model

N value	Dry unit weight (kN/m ³)	Submerged unit weight (kN/m ³)
N _{SPT} = 5	γ _d = 13.91	γ' = 8.66
N _{SPT} = 20	γ _d = 14.98	γ' = 9.33
N _{SPT} = 40	γ _d = 16.28	γ' = 10.13

3.3 Discussion of the Parametric Study Results

3.3.1 Effect of the Pile Slenderness Ratio

Load–deflection curves are illustrated in Fig. 2 which demonstrates the important effect of the pile slenderness ratio on the pile response. In Fig. 2a and b related to the cases of dry and saturated loose sand respectively, the difference of deflections for $D/B = 10$ and 20 is about 92.5%, and for $D/B = 10$ and 50 , the difference of is about 99.7%. Consequently, the D/B ratio has considerable effect on the pile deflections. One can conclude that for a given lateral load, an increase in slenderness ratio results in an important increase of the pile deflection, whatever the density of the sand and its degree of saturation.

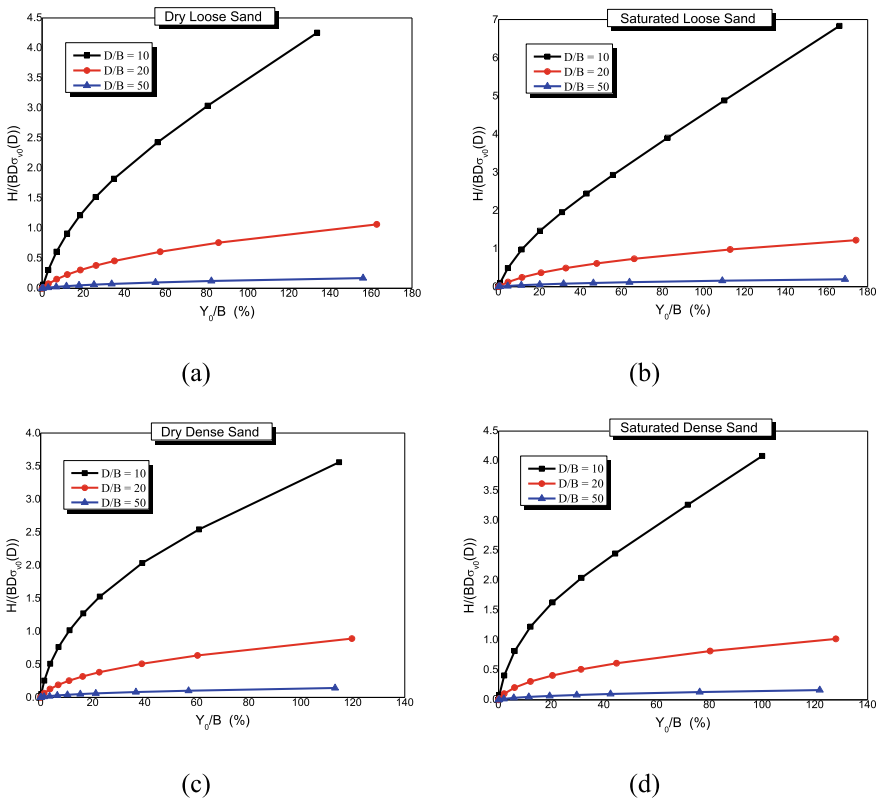


Fig. 2 The effect of pile slenderness on the behavior of the soil/pile system in sand: **a** pile in dry loose sand; **b** pile in saturated loose sand; **c** pile in dry dense sand; **d** pile in saturated dense sand

3.3.2 Effect of the Sand Density

Density is a key parameter governing the behavior of any sandy soil. This study includes three level of density: loose, medium and dense sand are illustrated in Fig. 3.

The influence of the density is correlated with N_{SPT} and its effect is studied with different parameters listed in Table 4. The lateral soil resistance is one of the most important factors that directly influences the pile response under lateral load. In Fig. 3a and b, the effect of the sand density on the pile deflection is shown for a pile slenderness ratio varying from 10 to 50. The other two figures Fig. 3c and d illustrate the same sand density and same slenderness ratio for a saturated sand.

At the same normalized of the pile top deflection, the normalized lateral load of medium and dense sand is quite equal, and the normalized deflection in a loose sand is larger by 14% than those in dense sand with a pile slenderness ratio of 10. For the

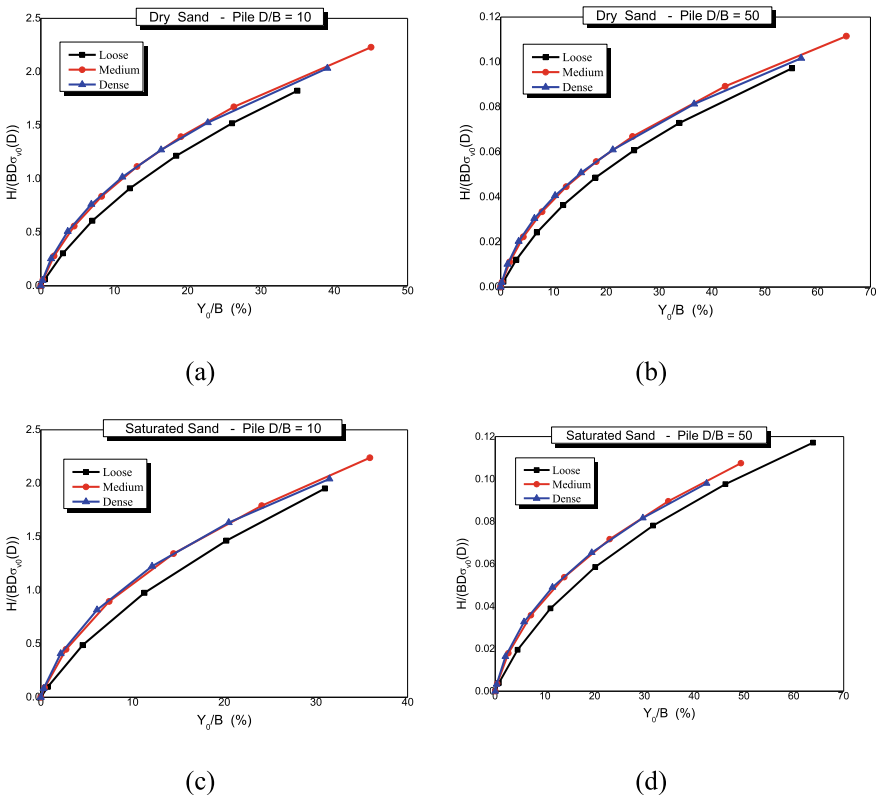


Fig. 3 The effect of sand density on the behavior of the soil/pile system: **a** pile of $D/B = 10$ in dry sand; **b** pile of $D/B = 50$ in dry sand; **c** pile of $D/B = 10$ in saturated sand; **d** pile of $D/B = 50$ in saturated sand

slenderness ratio of the pile equal to 50 in loose sand, the deflection is larger 17% than those in medium or dense sand.

In the saturated sand, for a slenderness ratio of 10, the comparison of the normalized deflection due to the same normalized lateral load gives an excess of 11% in loose sand compared to medium or dense sand, and with a slenderness ratio of 50, an excess of 14.5% is noticed for the same comparison.

It can be concluded that the sand density plays a major role in the behavior of piles under lateral loading. It can also be seen from these figures that the single pile in medium or dense sand shows practically the same displacements, regardless of the pile slenderness ratio and the saturation degree of the sand. The reduction in displacements is therefore observed only when passing from loose sand to a medium-dense sand. When the density of the sand increases, the displacement of the pile decreases, regardless of the degree of saturation of the sand and the slenderness ratio of the pile.

3.3.3 Effect of the Groundwater Level

In this study, the performance of a laterally loaded single pile embedded in a sandy soil with different ground water levels is presented. Four water table cases we simulated. Accurate ground water level information is then needed for the estimation of the soil density as well as the parameters K_N and K_E as shown in Table 1.

From Fig. 4 it can be seen that the effect of groundwater position on the pile top deflection. The lateral soil resistances along the pile in medium and dense sands are larger than those in loose sand. Whatever the slenderness ratio of the pile and the density of sand, the relative differences in pile top deflection are within 10%, the load–deflection curves being practically merged, regardless of the level of the water table. In other words, for low levels of lateral load, the position of the water table has practically negligible influence on the pile deflections as long as they are less than 10% of B .

4 Conclusion

A detailed parametric study was undertaken in order to investigate the effects of the pile slenderness ratio, the sand density, and the position of the groundwater. The main results from this study are summarized as follows:

1. The pile top deflection decreases with the increase of the pile slenderness ratio (D/B), which is then an unfavorable effect on the stability of the pile/soil system.
2. The increase in sand density leads to a decrease in the pile top deflection. It can be concluded that the sand density plays a favorable key role in the design of laterally loaded piles.

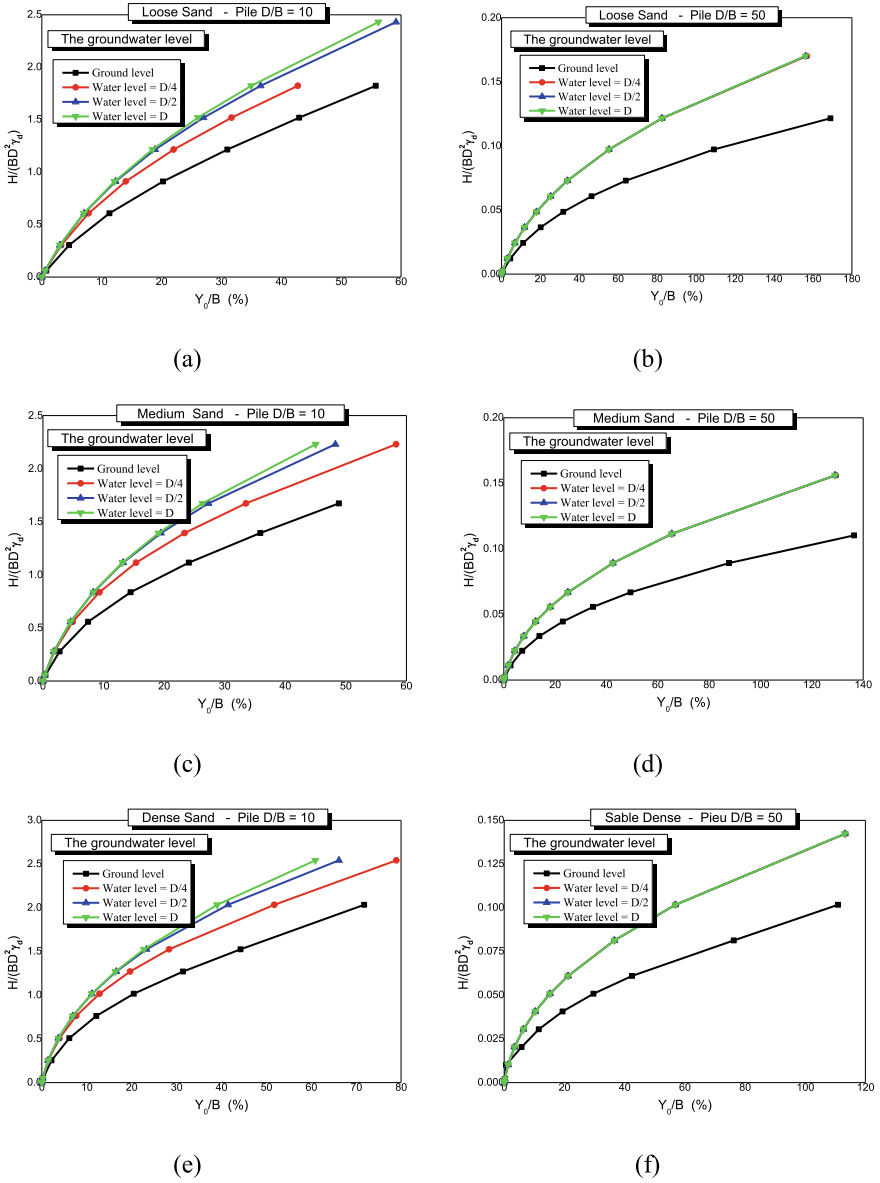


Fig. 4 The effect of groundwater level on the behavior of the soil/pile system: **a** pile with D/B = 10 in loose sand; **b** pile with D/B = 50 in loose sand; **c** pile with D/B = 10 in medium sand; **d** pile with D/B = 50 in medium sand; **e** pile with D/B = 10 in dense sand; **f** pile with D/B = 50 in dense sand

3. The increase in the level of the water table with respect to the ground level in sandy soil has negligible influence on the pile top deflection under small level of lateral loads. For deflections greater than 10% of B, the effect of the existence of the groundwater generates an amplification of deflections with a rise of the ground water level to the soil surface.

References

1. AFNOR: (2012) Fondations Profondes, Norme française NF, pp 94–262
2. API (2014) Petroleum and Natural Gas Industries-Specific Requirements for Offshore Structures, Part–4: Geotechnical and Foundation Design Considerations
3. Bouafia A, Lachenani A (2004) Courbes P-Y des pieux isolés dans le sable–Détermination à partir de l’essai pressiométrique (in French). *Rev Fr Geotech* 108:5–15
4. Bouafia A (2009) Analysis of P-Y curves for single piles from the cone penetration test. In: Proceedings of the 17th International conference on soil mechanics and geotechnical engineering. Alexandria, Egypt, pp 1103–1106
5. Bouafia A, Lachenani A (2005) Analysis of P-Y curves for single piles from the prebored pressuremeter. In: Proceedings of the 16th International conference on soil mechanics and geotechnical engineering. Osaka, Japan, pp 1955–1958
6. Laouedj A, Bouafia A (2017) Pieux isolés sous charges latérales–Construction des courbes P-Y à partir de l’essai SPT (in French). *Rev Fr Geotech* 12(4):1–9
7. Laouedj A, Bouafia A (2017) Design and analysis of single piles under lateral loads in cohesionless soils based on the standard penetration test (SPT). In: Proceedings of 17th international conference on advances in sustainable construction materials and civil engineering systems, MATEC Web Conference, vol 120(06001). EDP Sciences, pp 1–8
8. Terzaghi K (1955) Evaluation of coefficients of subgrade modulus. *Geotechnique* 5(4):297–326

Behaviour of Embedded Beam Formulations Under Dynamic Loading



Andreas-Nizar Granitzer and Franz Tschuchnigg

Abstract Fully-coupled dynamic finite element analyses (FEA) of pile foundation structures are computationally demanding; hence, they are rarely performed in practice. Due to their exceptional ability to circumvent this obstacle, dimensionally reduced beam-type-elements (BTE), such as embedded beam formulations (EBF), have gained popularity in dynamic FEA of related problems. The current engineering approach assumes a high level of compliance in the predicted dynamic response across different pile modelling techniques. However, static FEA have shown that this assumption is not generally warranted, primarily due to limitations of the line-to-volume coupling scheme employed in classical BTE. This raises an obvious questions about their general applicability to dynamic FEA of pile foundation structures, which generally require a realistic representation of dynamic soil-structure interaction. Subsequently, comparative dynamic FEA are carried out considering different embedded beam formulations. The credibility of results is numerically validated based on direct comparisons with the well-accepted standard FE approach. In this regard, EBF capture the free vibration behaviour with high accuracy. Special care must be taken when using EBF for the prediction of kinematic amplification ratios close to resonance.

Keywords Embedded beam formulations · Harmonic excitation · Finite element · Dynamic soil-structure interaction · Free vibration

1 Introduction

In many cases, the design of pile-supported structures has to consider the potential occurrence of time-varying loads. Broadly, the latter are divided into two main categories: loads applied directly to structures, such as wave forces or machine loads, and loads acting on structures through the soil, presumably originating

A.-N. Granitzer (✉) · F. Tschuchnigg
Institute of Soil Mechanics, Foundation Engineering and Computational Geotechnics, Graz
University of Technology, Graz, Austria
e-mail: andreas-nizar.granitzer@tugraz.at

© The Author(s), under exclusive license to Springer Nature Switzerland AG 2023
C. Atalar and F. Çinicioğlu (eds.), *5th International Conference on New Developments in Soil Mechanics and Geotechnical Engineering*, Lecture Notes in Civil Engineering 305, https://doi.org/10.1007/978-3-031-20172-1_34

353

from earthquake loads, blast effects or distant vibrating sources [1, 2]. Owing to arising dynamic soil-structure interaction effects (DSSI), neither the ground motion nor the structural response are independent of each other, but in turn depend on various factors including the mass of the superstructure, the stiffness of the soil or damping phenomena of the soil-structure system [3]. Consequently, the analysis of related problems poses a multidisciplinary task at the interface between geological, geophysical, structural and geotechnical disciplines [4].

In practice, the investigation of related problems is carried out under the assumption of a fixed based structure, thereby ignoring the development of DSSI [5]; see Fig. 1a. It is widely recognized that this assumption constitutes an over-simplification that may lead to unsafe and, respectively, uneconomic design as it neglects contributions stemming from soil deformability, material or radiation damping [6]. In particular for flexibly-supported slender structures founded on soft soil deposits, the predominant importance of DSSI has been clearly highlighted by well-documented experimental tests and post-earthquake field investigations [7]. From the above discussion, it is evident that dynamic calculations have to consider DSSI with sufficient accuracy.

Although relevant design codes, such as Eurocode 8 [8], assert a potentially relevant significance of DSSI in the design of sensitive structures, there is no general guidance on how to assess the influence of DSSI [5]. At present, the prominent type of dynamic analysis procedures are based on numerical and analytical approaches that utilize either simplified multi-step methods (MSM) or the single step method (SSM) [7]. Unlike MSM, the SSM considers both inertial effects (due to vibration of the superstructure) and kinematic effects (imposed by lateral ground displacements) simultaneously through fully-coupled soil-structure models; see Fig. 1b. This makes the SSM particularly suitable for the dynamic analysis of piled foundations, which generally provide a higher dissipation of energy compared to shallow foundations.

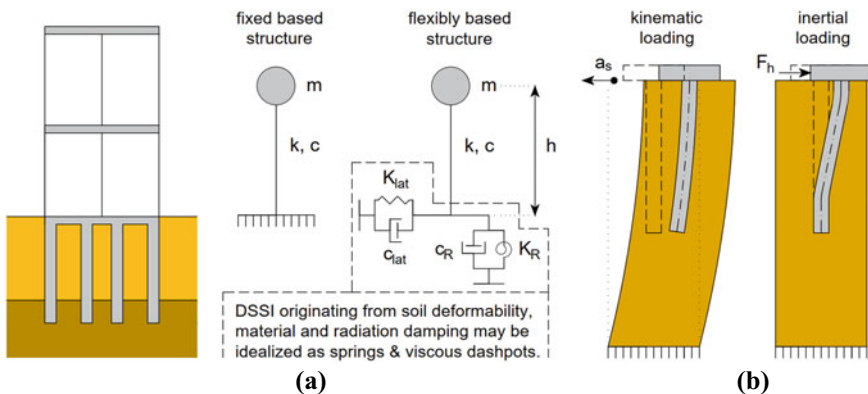


Fig. 1 a Approximation of a pile-supported slender structure as equivalent oscillator with one dynamic DOF on fixed/flexible base; b kinematic and inertial type loading

The latter aspect renders the determination of frequency-dependent springs and dashpots associated with MSM more problematic [5]. On the contrary, the SSM requires higher computational resources, and is therefore rarely performed in practice [7].

In many instances, the SSM is realized employing the finite element (FE) method; hence, the rate of convergence is closely linked to the mesh configuration [9]. As dynamically induced forces depend on the displacements rather than their derivatives as it is the case for their static counterparts, coarser discretizations may be selected for elastic dynamic FE analyses (FEA) than for static ones [1]. This allows to reduce the size of the system of equations derived from the dynamic equation of motion:

$$\mathbf{M}\ddot{\mathbf{u}} + \mathbf{C}\dot{\mathbf{u}} + \mathbf{K}\mathbf{u} = \mathbf{f} \quad (1)$$

In Eq. (1), \mathbf{M} is the mass matrix, \mathbf{C} the damping matrix, \mathbf{K} the stiffness matrix, \mathbf{u} the displacement vector and \mathbf{f} the load vector. Moreover, idealizing foundation piles by means of dimensionally reduced discretizations instead of the standard FE approach (SFEA) [10] may serve as powerful strategy to improve the computational efficiency of the SSM. In this context, previous contributions suggest the application of beam type elements (BTE) where the beam-to-solid coupling is either established via conforming mesh discretizations, explicit or implicit interfaces; see [9, 11, 12]. Despite the modern trend towards dynamic FE calculations using BTE, their performance in dynamic response analysis of pile foundation systems has not been thoroughly investigated. Related studies documented in the literature are restricted to the local pile behaviour as a function of different beam-cap connection types as well as the existence of explicit interface elements [9, 13], thereby ignoring the deterioration of numerical fidelity due to the inconvenient application of BTE. However, recent studies concerning pile-soil interaction phenomena under static loads have showcased limitations associated with certain BTE; hence, the compliance of numerical predictions obtained with different pile modelling approaches is not generally warranted [10]. This raises an obvious questions about the suitability of widely adopted BTE in dynamic FE analysis.

The present contribution aims at providing insight to the significance of the pile modelling approach in the dynamic analysis of pile foundation constructions. In view of their intended use (i.e., to capture the behaviour of SFEA piles [14]), the performance of two BTE is numerically assessed based on comparisons with the SFEA benchmark; namely, the widely adopted embedded beam with line interface (EB) [14] and the novel embedded beam element with interaction surface (EB-I) [10]. To this end, the remainder of this paper is organized as follow: Sect. 2 introduces the numerical model characteristics of a conceptually simplified pile foundation construction, whereas special emphasis is placed on the pile modelling approach. In Sects. 3 and 4, the dynamic response sensitivity is investigated based on its behaviour under free vibration and dynamic excitation. Section 5 closes with the main conclusions.

2 Numerical Model Characteristics

To study the performance of BTE in the numerical evaluation of the dynamic response of pile foundation structures, FEA are carried out in both the time and frequency domain using the FE software code Plaxis 3D [15]. Broadly, the boundary value problem under investigation has been subject of numerous previous studies [16, 17] and constitutes a single degree of freedom structure supported by four flexible piles; see Fig. 2a. In accordance with [17], FEA are performed considering the linear visco-elastic constitutive model for the piled foundation and the Mohr–Coulomb visco-elasto-perfectly-plastic constitutive model for the soil, respectively; see Table 1. Damping of the soil and the structure material is introduced through frequency-dependent Rayleigh damping, where the damping matrix C results from a combination of mass matrix M and stiffness matrix K ; see Eq. (2).

$$C = \alpha \cdot M + \beta \cdot K \tag{2}$$

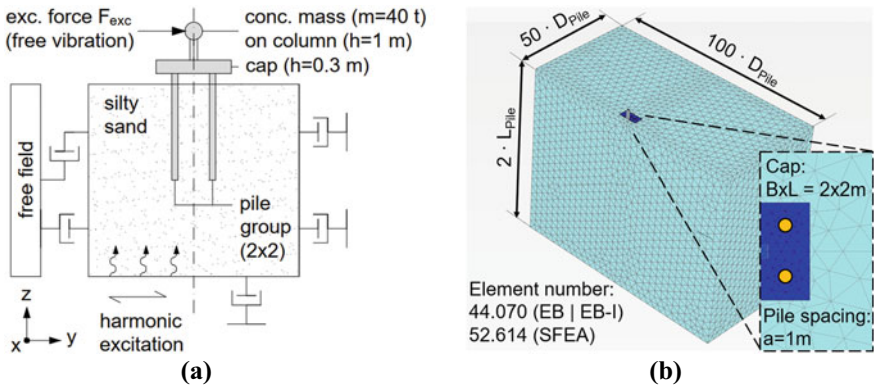


Fig. 2 a Model geometry, adopted from [17], and b mesh discretization of EB | EB-I model. Taking advantage of the symmetry conditions, only half of the problem is analysed

Table 1 Pile parameters (above) and soil parameters (below)

Unit weight	Axial stiffness	Poisson ratio	Damping factor	Diameter	Length
$\gamma_{pile} \text{ (kN/m}^3\text{)}$	$E_{pile} \cdot A_{pile} \text{ (MN)}$	ν_{pile}	ξ_{pile}	$D_{pile} \text{ (m)}$	$L_{pile} \text{ (m)}$
24	1078	0.3	2%	0.25	10
Unit weight	Young's modulus	Poisson ratio	Damping factor	Cohesion	Friction angle
$\gamma_{soil} \text{ (kN/m}^3\text{)}$	$E_{soil} \text{ (MPa)}$	ν_{soil}	ξ_{soil}	$c' \text{ (kPa)}$	$\varphi' \text{ (}^\circ\text{)}$
17	10	0.3	10%	0	30

According to [4], the Rayleigh damping constants are evaluated as $\alpha = \xi \cdot \omega$ and $\beta = \xi \div \omega$, being ω the angular frequency of the system and ξ the damping ratio of respective materials. The dynamic equations of motions are integrated based on the well-known implicit Newmark time integration scheme. In the free vibration FEA, viscous boundary conditions are considered to absorb outgoing wave energy, whereas a combination of compliant base and free-fields boundaries is applied in FEA concerning harmonic excitation.

The solid domain is discretized with 10-noded tetrahedral elements with quadratic element functions; see Fig. 2b. Since the dimension of the solid elements limits the value of the highest transferable input frequency, the average element size (AES, i.e. quotient formed by the total tetrahedral edge length divided by the number of edges) follows Eq. (3) [18]:

$$\text{AES} \leq V_{s,\min} / (8 \cdot f_{exc,\max}) \quad (3)$$

where $V_{s,\min} = 48$ m/s is the minimum elastic shear wave velocity in the soil and $f_{exc,\max} = 5$ Hz denotes the maximum excitation frequency used in the FEA. A series of sensitivity FEA concerning the domain dimensions have been conducted to ensure both minimum boundary effects and manageable computational effort. The compliant base is excited with harmonic loads in the form of horizontal acceleration amplitudes $\ddot{u}_{exc} = 0.2$ g of varying frequency $f_{exc} \in [f_{soil} = 0.6, 5]$ Hz.

To study the dynamic response sensitivity towards the pile modelling approach, the piles are idealized by means of EBs, EB-Is and the SFEA, whereas the latter serves as numerical benchmark [10]. Unlike EBs, EB-Is are equipped with a translational coupling scheme that defines beam kinematics based on the relative displacements between pairs of corresponding soil and beam nodes distributed across an implicit interaction surface instead of an implicit line surface. In this way, EB-Is enhance the credibility of numerical predictions compared to EBs [10]. For the sake of numerical consistency, the skin resistance is defined as layer-dependent, hence dependent of the stress state in the surrounding soil [14]. This allows to specify the pile-structure interaction similarly to the numerical SFEA benchmark. For the sake of brevity, the interested reader may refer to [17] for complementary modelling details.

3 Free Vibration Analysis

In seismic codes involving response spectrum analysis, both the equivalent viscous damping ratio ξ_{SS} and the natural frequency f_{SS} of the soil-structure system represent fundamental ingredients in the evaluation of the maximum spectral acceleration amplitude and the design base shear force, respectively [8]. With regard to flexibly-supported structures, DSSI render a priori predictions based on analytical solutions unreliable as the modal parameters may considerably differ from that of the fixed-base structure or the soil deposit alone [4]. Again, the SSM in combination with free vibration analysis have proved viable to determine ξ_{SS} and f_{SS} with high accuracy

[19]. In the present case, free vibrations are invoked via horizontal excitation forces F_{exc} of different magnitudes that are applied to the concentrated mass; see Fig. 2a. f_{SS} -values are obtained from the free decay responses after F_{exc} -release, which are recorded at the position of the concentrated mass. Accounting for an exponential decay of the displacement amplitude, ξ_{SS} -values are determined by means of the logarithmic decrement method as described in Eq. (4):

$$\xi_{SS} = 1/(2\pi) \cdot \ln(A_i/A_{i+1}) \tag{4}$$

where A_i and A_{i+1} are the amplitudes of vibration in two successive cycles.

Figure 3 shows the horizontal displacements u_y and accelerations \ddot{u}_y of the damped system recorded at the position of the concentrated mass. Despite a slight shift in amplitude and natural period towards lower values, the ability of both embedded beam formulations to capture the dynamic response of the SFEA benchmark is evident. More specifically, Fig. 4 deduces equivalent viscous damping ratios and natural frequencies as function of the excitation force magnitude from the calculated time-history records. Regardless of the pile modelling approach, ξ_{SS} -values increase with F_{exc} -magnitude, while f_{SS} -values show the opposite trend. The validity of these observations has been confirmed by numerous researchers and is mainly attributed to non-linear soil damping characteristics [3, 4]. Obviously, the modal parameters are in good agreement with the SFEA: $\|\xi_{SS,SFEA} - \xi_{SS,EB|EB-I}\|_\infty < 1\%$ and $\|f_{SS,SFEA} - f_{SS,EB|EB-I}\|_\infty < 0.1$ Hz.

It is worthy to note that the calculated f_{SS} -range does not encompass the natural frequency of the underlying soil ($f_{soil} = 0.6$ Hz); consequently, double resonance effects [7] that evolve under the condition $f_{SS}/f_{soil} \sim 1$ and lead to high-amplitude oscillations of the concentrated mass are avoided.

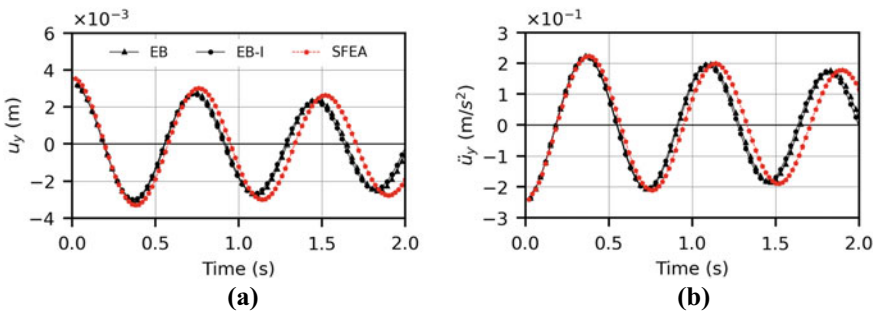


Fig. 3 **a** Horizontal displacement- and **b** acceleration-time-histories ($F_{exc} = 10$ kN)

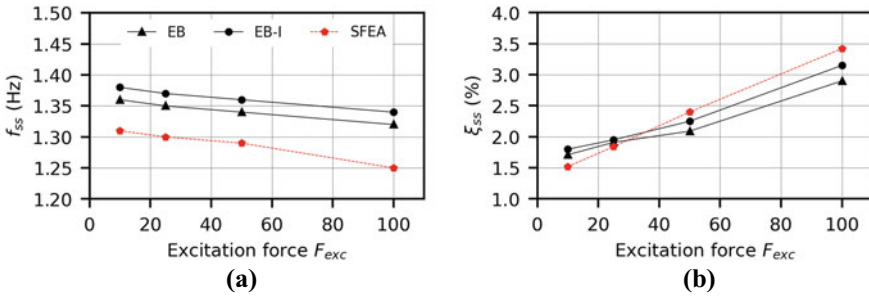


Fig. 4 a Natural frequency and b viscous damping ratio as function of excitation force

4 Response to Harmonic Excitation

Harmonic excitations imposed at the model base idealize vertically propagating shear waves [3]; see Fig. 2. The dynamic response of the pile-structure system is evaluated using widely-accepted amplification ratios: the mass-base amplification ratio $A_{m-b} = u_{mass}/u_{base}$ and the mass-free field amplification ratio $A_{m-ff} = u_{mass}/u_{ff}$, where u_{mass} , u_{base} and u_{ff} denote the steady-state horizontal displacement amplitudes at the position of the concentrated mass, model base and free field surface, respectively.

Both amplification ratios examined in Fig. 5 incorporate the combined effect of inertial and kinematic interaction. As a consequence, the latter are dominated by f_{soil} and f_{ss} : The maximum steady-state response to harmonic excitation develops near f_{ss} , commonly resulting in the evolution of maximum pile bending moments. If f_{exc} is equal to f_{soil} , amplification ratios are lowered due to the dominant role of soil resonance. It is worth noting that these variation patterns have been observed in experimental tests executed on comparable pile foundation systems [7].

In view of the sensitivity studies, the results provide evidence that the pile modelling technique has a considerable influence on the kinematic behaviour of the

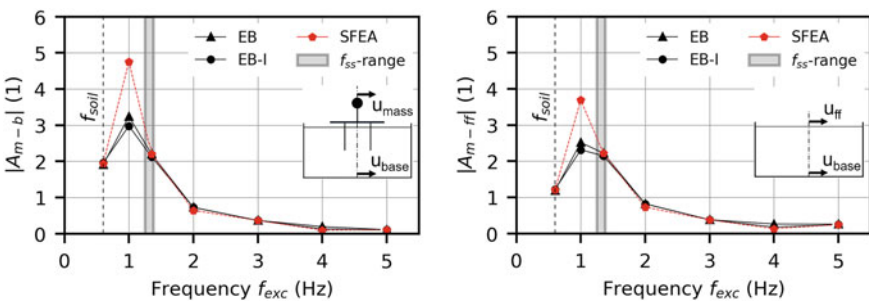


Fig. 5 a Mass-base amplification ratio A_{m-b} and b mass-free field amplification ratio A_{m-ff}

structure: While the amplification ratios are similarly damped if $f_{exc} \gg f_{ss}$, significant deviations in case $f_{exc} \sim f_{ss}$ are apparent, presumably due to the different soil-pile coupling schemes implemented in the pile modelling techniques studied [10]. At $f_{exc} = f_{soil}$, all pile modelling techniques show compliant results which is attributed to prevailing soil resonance. Above observations apply for both amplification ratios.

5 Conclusions

The present contribution comprises numerical sensitivity studies undertaken to assess the performance of different embedded beam formulations (EBF) in dynamic FEA of pile foundation structures. Partly, the presented results support the common belief that the dynamic response is non-sensitive to the numerical pile modelling technique, hence, justifying the substitution of computationally expensive 3D pile discretizations with EBF. The validity of this assumption is confirmed for free vibration analysis with the aim to quantify the natural frequency as well as the equivalent viscous damping ratio of conceptually simplified soil-structure system. Moreover, the results indicate a high level of compliance with respect to the structural kinematics under harmonic base excitation; however, at excitation frequencies close to the natural frequency of the coupled soil-structure system, EBF tend to underestimate widely adopted amplification ratios describing kinematic and inertial effects acting on piles.

In view of the wide application of embedded beam formulations in the seismic design of pile supported structures, further studies should be carried out to assess the credibility of critical pile stress resultants obtained with EBF. In addition, future work may concern the validation of embedded beam formulation under supplementary dynamic loading types traditionally employed in geotechnical engineering, such as impulse loading (dynamic pile load tests) or forced vibration (machine loads). Deduced recommendations regarding credible application areas may help numerical engineers to exploit the exceptional computational efficiency of EBF in dynamic FEA with more confidence, thereby allowing for a more realistic consideration of dynamic soil structure interaction effects in the seismic design of pile supported structures.

References

1. Wolf JP (1985) Dynamic soil-structure interaction: Prentice-Hall
2. Poulos HG, Davis EH (1980) Pile foundation and design
3. Kramer SL (1996) Geotechnical earthquake engineering, 1st ed. Pearson
4. Massimino MR, Abate G, Grasso S, Pitilakis D (2019) Some aspects of DSSI in the dynamic response of fully-coupled soil-structure systems. *Rivista Italiana di Geot* (1)
5. de Sanctis L, Iovino M, Di Laora R, Aversa S (2020) Relevance of dynamic soil-foundation-structure interaction for pile-supported buildings. *J Geotech Geoenviron Eng* 146(6):4020034

6. Mylonakis G, Gazetas G (2000) Seismic soil-structure interaction: beneficial or detrimental. *J Earthquake Eng* 4(3):277–301
7. Hussien MN, Tobita T, Iai S, Karray M (2016) Soil-pile-structure kinematic and inertial interaction observed in geotechnical centrifuge experiments. *Soil Dyn Earthq Eng* 89:75–84
8. Comité Européen de Normalisation (CEN) (2004) Eurocode 8: Design of structures for earthquake resistance: part 1 general rules, seismic actions and rules for buildings (EN 1998-1:2004)
9. Lopez Jimenez GA (2019) Static and dynamic behavior of pile supported structures in soft soil. PhD thesis. Grenoble, France
10. Granitzer A-N, Tschuchnigg F (2021) Practice-oriented validation of embedded beam formulations in geotechnical engineering. *Processes* 9(10):1739
11. Scarfone R, Morigi M, Conti R (2020) Assessment of dynamic soil-structure interaction effects for tall buildings: A 3D numerical approach. *Soil Dyn Earthq Eng* 128:1–14
12. Haddad ED, Choobbasti AJ (2019) Response of micropiles in different seismic conditions. *Innov Infrastruct Solut* 4(1)
13. Goit CS, Saitoh M (2018) Single pile under vertical vibrations in cohesionless soil. *Géotechnique* 68(10):893–904
14. Tschuchnigg F, Schweiger HF (2015) The embedded pile concept—verification of an efficient tool for modelling complex deep foundations. *Comput Geotech* 63:244–254
15. Bentley. PLAXIS Reference Manual: 3D-Connect Edition V21
16. Sadek M, Shahrour I (2006) Influence of the head and tip connection on the seismic performance of micropiles. *Soil Dyn Earthq Eng* 26(5):461–468
17. Ghorbani A, Hasanzadehshooiili H, Ghamari E, Medzvieckas J (2014) Comprehensive three dimensional finite element analysis, parametric study and sensitivity analysis on the seismic performance of soil–micropile–superstructure interaction. *Soil Dyn Earthq Eng* 58:21–36
18. Kuhlemeyer RL, Lysmer J (1973) Finite element method accuracy for wave propagation problems. *J Soil Mech Found Div* 99(5):421–427
19. Lombardi D, Bhattacharya S (2014) Modal analysis of pile-supported structures during seismic liquefaction. *Earthquake Eng Struct Dyn* 43(1):119–138

Estimation of Ground Motion at One of the Damaged Building Sites Following the October 30, 2020, Samos Earthquake



Doga Altunevlek and Gurkan Ozden

Abstract On October 30, 2020, an earthquake with a moment magnitude of 7.0 occurred on the Kaystrios fault in the north of Samos Island. Although the effects of the earthquake in İzmir were widespread in several districts, the majority of the damage was concentrated in alluvial sites, the Bayraklı-Manavkuyu region, which is approximately 70 km away from the epicenter being the most heavily affected area. The fact that none of the buildings as high as four storeys did not experience considerable damage in contrast with the heavily damaged or collapsed structures with a number of storeys varying between 8 and 12 demonstrated that longer period harmonics that were close to the natural periods of these taller buildings were amplified by deep and soft saturated alluvial soils. Strong ground motion stations available at the time of the earthquake in the Manavkuyu region were established on soft grounds where the engineering bedrock with a shear wave velocity of 760 m/s is seated at about 200–350 m. Therefore, it was necessary to conduct deconvolution analyses to come up with engineering bedrock motions that would further be used in convolution runs to come up with realistic ground motions at the sites of the collapsed buildings. Shear wave velocity data captured in seismic surveys, capable of providing reliable data from deeper soil layers, were utilized along with deep borehole logs while establishing the one-dimensional soil response models. A sequential series of deconvolution analyses were then made in order to come up with the engineering bedrock motions. Site response analyses were made on accordingly established 1D model at the site of one of the collapsed buildings yielding acceleration response spectra which were later modified to reflect kinematic soil-structure interaction that would take place underneath the considerably large foundation of the damaged building. It was found that significant soil amplification took place at the building site, and the base shear force obtained based on the kinematic SSI analysis was close to the one found with respect to the 1975 Turkish Seismic Design Code with which the building was designed for.

D. Altunevlek (✉) · G. Ozden
Civil Engineering Geotechnical Department, Dokuz Eylul University, Izmir, Turkey
e-mail: doga.altunevlek@ogr.deu.edu.tr

© The Author(s), under exclusive license to Springer Nature Switzerland AG 2023
C. Atalar and F. Çinicioğlu (eds.), *5th International Conference on New Developments in Soil Mechanics and Geotechnical Engineering*, Lecture Notes in Civil Engineering 305, https://doi.org/10.1007/978-3-031-20172-1_35

363

Keywords Site response analysis · Deconvolution · Soft soil · Deep alluvial deposit · Soil structure interaction

1 Introduction

Bedrock depths in İzmir vary in coastal districts such as Mavişehir, Karşıyaka and Bayraklı. The general trend in this variability is that the bedrock depth increases as the coastline approaches. The andesite bedrock, which was found to be 9 m deep in a very close location to the andesite formation outcropping in Bayraklı, goes down to 23 m depth in the Bayraklı coastal area towards the south. The strong ground motion station location coded TK 3513 goes deeper with a sudden drop. As a result of the drilling work carried out at this location, the bedrock could not be reached at 63.5 m according to TUBITAK 106G159 project [9].

In the Manavkuyu district, which is a district of the Bayraklı region and was affected by the Samos Earthquake, it is known that the bedrock depth varies between 200-and 220 m. This region comprises loose-characterized thick alluvial layers carried by the Laka, Bornova, and Manda creeks. Knowing the bedrock depth in the Bayraklı region is important for the foundation design and is a variable that affects the results in dynamic soil behavior analyses.

The site response analysis is performed using the outcropping motion recorded at a close distance to the area of interest. However, it is very difficult to realistically predict the earthquake motion on the ground surface in areas where engineering bedrock cannot be reached. In addition, even if the bedrock depth is known, the 2D and 3D effects and the uncertainties caused by geological conditions such as basin effect will be ignored in the 1D site response analyzes applied in the first evaluation. Therefore, in this study, the outcropping motion was estimated by a series of deconvolution processes found in the literature.

Estimated outcropping motion obtained from Camdibi strong ground motion station data, coded TK3522 was used in the site response analysis for strong ground motion station TK3513 and compared with the surface motion recorded in the Samos Earthquake. Since the results obtained are compatible, site response analysis was also carried out at the location of the collapsed buildings. Considering the damping in the system with the assumption of flexible foundation, the base shear force in a collapsed building was calculated and compared with the design load of the 1975 Turkish Seismic Design Code Locations of the strong ground motion stations used in the analyzes according to the region of the collapsed buildings are given in Fig. 1.

2 Deconvolution Process of Ground Motion

Silva [7] tried to estimate the surface motion records of earthquakes of equivalent magnitude at low strain and high strain levels in soft alluvial soil profiles using a series

Fig. 1 The map showing the strong ground motion stations and the site of collapsed buildings location



of equivalent-linear deconvolution analysis results and examined their coherency with the observed records. Based on the positive results of the coherency analyses, a series of deconvolution processes have been proposed.

The areas where the mentioned process is applied are alluvial deposits, soft soil deposits, and profiles with very deep engineering bedrock. In this section, the same analysis steps are applied for the soil profile of the Camdibi strong ground motion station, which is an alluvial soil profile. The steps followed are presented below:

1. Low-pass filtering was applied at 15 Hz and scaled 0.87 times, surface motion recorded at Camdibi strong ground motion station.
2. The motion obtained in step 1 was reduced to a layer determined as the control point below the surface by equivalent deconvolution analysis.
3. As a result of iteration, shear modulus reduction (G/G_{max}) and damping ratios (β) of each layer were obtained.
4. Linear deconvolution analysis was applied using the degraded soil data obtained in the 3rd step. For this analysis, motion recorded at a strong ground motion station at 15 Hz was applied to low-pass filtering, not scaling.

Linear deconvolution analyzes were performed in DEEPSOIL V.7 software [10] and equivalent linear deconvolution analyzes were performed in EERA software [1].

2.1 Deconvolution Process of Camdibi Sites

The Samos Earthquake, which occurred on October 30, 2020, and whose epicenter was in Izmir, was recorded by the Camdibi health center station with the code TK 3522, and the surface ground motion records were used in deconvolution analyses. The outcropping motion, which should be estimated to be used in site response analyzes in Bayraklı and Manavkuyu regions, was obtained by the deconvolution procedure performed for the Camdibi station. The reason for this location preference is that Camdibi station has a thick alluvial profile that also represents the Bayraklı and Manavkuyu regions, which can be evaluated at shallow depths. Another reason

is that the Camdibi profile in which the deconvolution process followed in this study is performed is quite similar to the study area in the literature. Low plasticity clay, clayey sand layers with fine content exceeding 20%, and clayey gravel layers are observed. The groundwater level is at 13 m for the Camdibi profile, lower than that of the Bayraklı region. The average shear wave velocity for the first 30 m is 258.2 m/s. According to the Turkish building seismic code 2018 [8], the site class is ZD. It corresponds to class D in NEHRP [5] and class D in Eurocode-8 [2]. The soil profile has data up to 40 m deep, and the engineering rock was inaccessible. It is seen that the shear wave velocity at 40 m is 525 m/s. The engineering bedrock could not be reached and ended with a ZC soil class. TK3522 Camdibi station soil profile and soil data are given Fig. 2.

In the equivalent linear deconvolution analysis, the free field motion is the motion at the surface of the soil deposit. Within motion is the motion at the base of the soil deposit. The outcropping motion is the motion that occurs where the rock exits the ground surface. Therefore, rock outcropping motion is not affected by soil amplification. In the deconvolution analysis, x and y components of the motion recorded at the strong ground motion station in the Samos 2020 Earthquake were used as surface ground motion. Equivalent linear deconvolution was performed separately for the E and N directions. The maximum shear strain, maximum stress, shear modulus reduction, and damping ratio were obtained under the gravelly clay layer at 40 m.

The third stage of the deconvolution procedure was completed with the damping ratios and shear modulus reduction obtained from the last iteration. The shear modulus was recalculated based on the shear modulus reduction ratio of the degraded soil. A new shear wave velocity was obtained for each layer by considering the softening caused by cyclic loading in the soil. The shear wave velocity obtained in the last case was used in the linear deconvolution analysis.

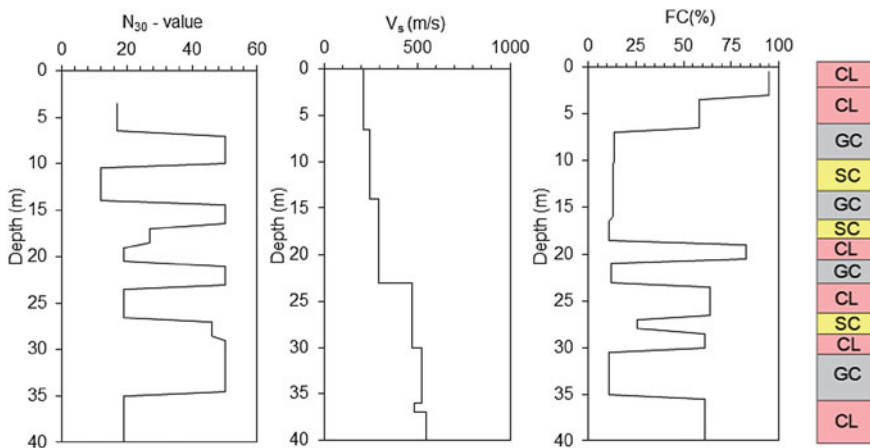


Fig. 2 Soil profile data of Camdibi strong ground motion station coded TK 3522

3 Validation of the Estimated Ground Motion

Surface ground motion data recorded at Camdibi strong ground motion station were converted into outcropping motions to be used for both directions as a result of the deconvolution process. The suitability of the estimated data as a result of this series of analyzes was checked with the site response analysis performed at Bayraklı station. The results were compared with the data recorded at the Bayraklı station during the Samos 2020 Earthquake. TK 3513 Bayraklı station soil profile and soil data are given in Fig. 4.

The groundwater level is at 2.00 m, and the average shear wave velocity is 186 m/s for the first 30. According to the Turkish building seismic code 2018, the site class is ZD. It corresponds to class D in NEHRP and class D in Eurocode-8. No engineering rock is encountered in the first 65 m, and the soil layer ends with ZC soil class. Results of the equivalent linear deconvolution analysis performed at TK 3522 Camdibi station are plotted in Fig. 3.

Effective stress-based non-linear site response analysis was performed in the Deepsoil software, and the MKZ soil model was used. Since the Camdibi profile, from which the estimated Outcropping motion record was obtained, ended at 525 m/s, the estimated motion from the layer with the same shear wave velocity was given to the Bayraklı profile. The results of the analysis were compared with the recorded at Bayraklı station.

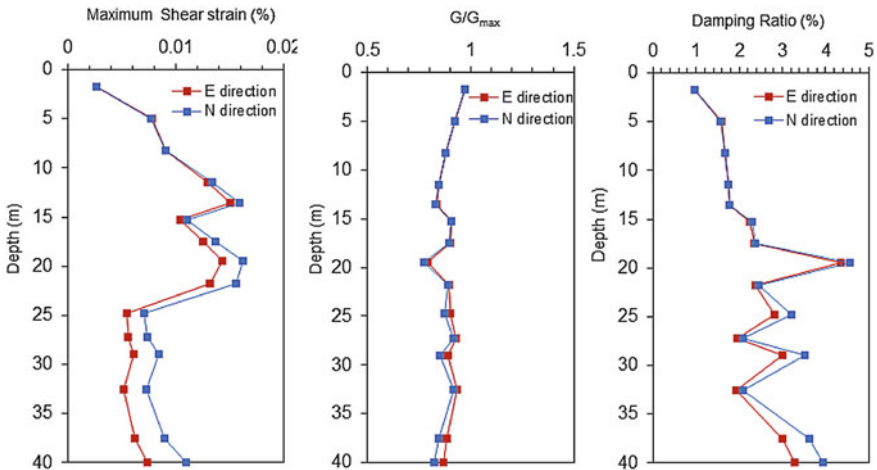


Fig. 3 Variation of damping ratio, maximum shear strain, and shear modulus reduction ratio with depth in equivalent linear deconvolution analysis

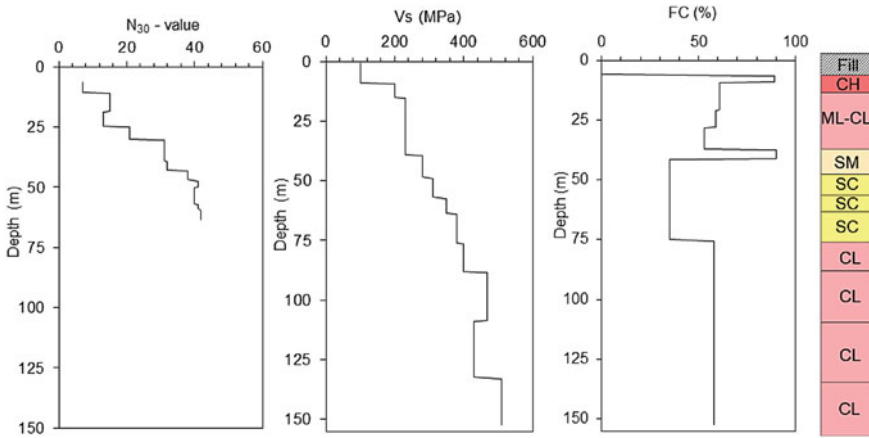


Fig. 4 Soil profile data of Bayraklı strong ground motion station coded TK 3513

3.1 Comparison of the Estimated and Recorded Motion

Spectral acceleration values recorded for the E and N directions of the earthquake during the Samos Earthquake at Bayraklı station were compared with the estimated spectral acceleration values. The non-linear analysis predicted that the shear wave velocity data could vary by $\pm 20\%$, and more consistent results were obtained with the shear wave velocities increased by 20% as shown in Fig. 5, consistent results were obtained after 2 s period, on the other hand, filtering between 0.3 and 0.7 s draws attention, and spectral accelerations could not be captured. Peak accelerations were achieved around the 1-s region. PGA values are below the measured value.

As can be seen in Fig. 6, a general acceleration spectrum trend was captured in the N direction, which is the perpendicular component to the earthquake, but a significant phase difference was observed. The analyzes were carried out with the estimated outcropping records due to the fact that peak accelerations could be

Fig. 5 Comparison of the spectral accelerations recorded for the E direction during the Samos earthquake at Bayraklı station with the estimated spectral acceleration values

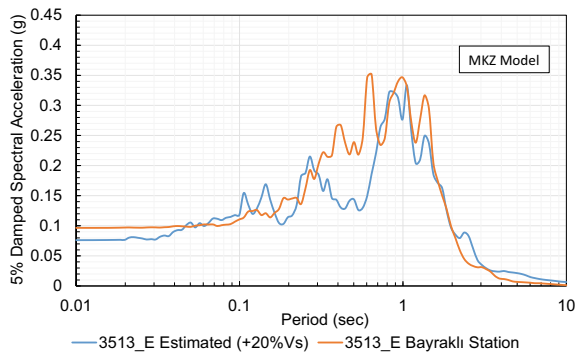
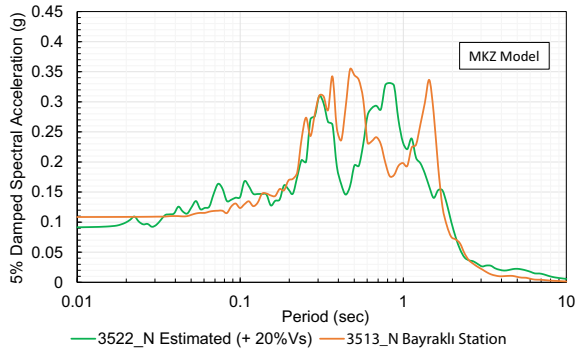


Fig. 6 Comparison of the spectral accelerations recorded for the N direction during the Samos earthquake at Bayraklı station with the estimated spectral acceleration values



captured in both earthquake direction there was no excessive amplification in the high period region and the PGA values were estimated very close.

4 Case Study: SSI Effect on a Nine Storey Building

Considering the compatible results obtained at Bayraklı strong ground motion station, site response analysis was performed for a building that collapsed in the 2020 Samos Earthquake. In order to evaluate the analysis results, the building was considered as a single degree of freedom system, and the flexible-base foundation was accepted. While calculating the natural vibration period of the system, the rigidity of the system was calculated by taking into account the maximum displacement measured by the recorded motion at the Bayraklı station. With the assumption of flexible foundation, the horizontal, vertical and rotational stiffness of the foundation are calculated and the effects of soil flexibility are taken into account. Static stiffness of foundation Gazetas [3], Mylonakis et al. [4], dynamic stiffness were calculated using the relations of Pais and Kausel [6] and period lengthening ratio were calculated using the relations of Veletsos and Meek [11] Collapsed building soil profile and soil data are given in Fig. 7.

From this point of view, the period lengthening ratio of the system was calculated using Eq. 1.

$$\frac{\tilde{T}}{T} = \sqrt{1 + \frac{k}{k_x} + \frac{kh^2}{k_{yy}}} \tag{1}$$

In addition, the period lengthening ratio, foundation damping and flexible-base foundation system damping were calculated by taking into account the degraded shear modulus and increased damping ratio for the 0.02% strain level, which is the maximum shear strain caused by the given input movement in the ground. Figure 8

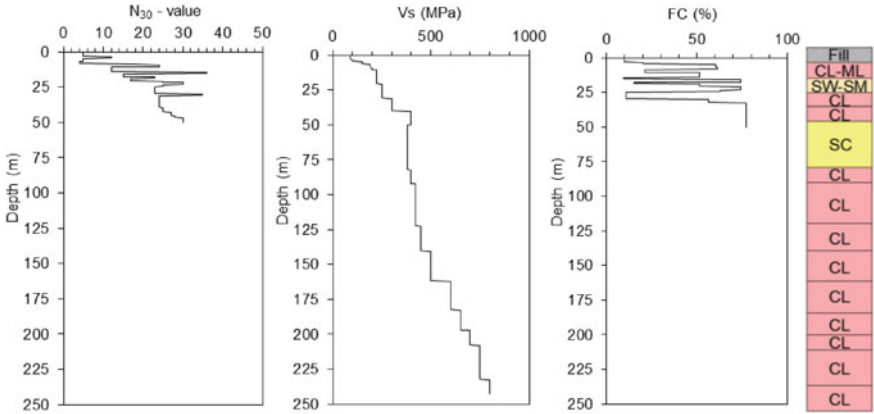
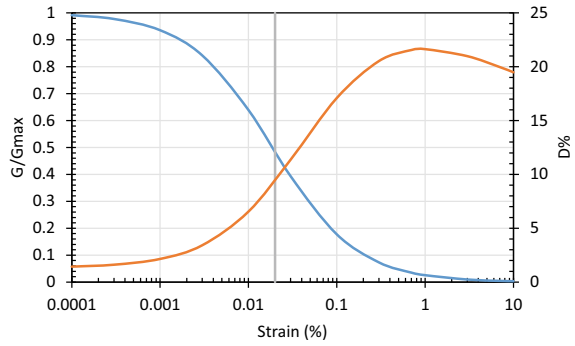


Fig. 7 Soil profile data for the site of a collapsed building located in Bayrakli region

Fig. 8 Shear modulus reduction and damping ratio curves



shows the modulus reduction and the damping ratio curves with the expected shear strain level of 0.02%.

Equations 2 and 3 were employed to estimate the foundation damping and the damping of the system with the consideration of soil-structure interaction.

$$\beta_f = \left[\frac{\left(\frac{\tilde{T}}{T}\right)^{n_s} - 1}{\left(\frac{\tilde{T}}{T}\right)^{n_s}} \right] \beta_s + \frac{1}{\left(\frac{\tilde{T}}{T_x}\right)^{n_x}} \beta_x + \frac{1}{\left(\frac{\tilde{T}}{T_{yy}}\right)^{n_y}} \beta_{yy} \tag{2}$$

$$\beta_0 = \beta_f + \frac{1}{\left(\frac{\tilde{T}}{T}\right)^n} \beta_i \tag{3}$$

The calculated values for the period lengthening and the variation of damping ratio due to the soil-structure interaction was summarized in Table 1.

Table 1 Overall system damping parameters and period lengthening results

T (sec)	\tilde{T} / T	\tilde{T} (sec)	β_s	β_i	β_f	β_o
0.84	1.65	1.38	0.089	0.050	0.061	0.072

Nonlinear ground response analysis was performed on the soil profile of a collapsed building with the estimated outcropping motions. The acceleration-response spectra obtained on the surface ground motion are presented in Fig. 9 for $D = 5\%$, and the damping ratio increased as a result of soil-structure interaction $D = 7.2\%$. In addition, spectral accelerations corresponding to $\tilde{T} = 1.38$ s, increasing period due to the result of soil-structure interaction, are also shown. Accordingly, the spectral accelerations corresponding to the estimated elongated structure period were found to be 0.41 and 0.47 g for the E and N directions, respectively (Figs. 9 and 10).

Fig. 9 Acceleration response spectra for the surface motion obtained in the site (for East direction)

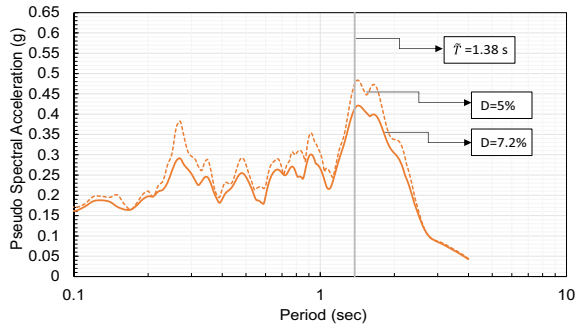
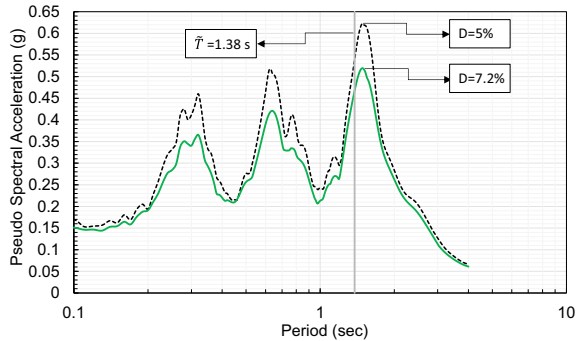


Fig. 10 Acceleration response spectra for the surface motion obtained in the site (North direction)



5 Conclusion

In this study, the surface motion was estimated for the locations where there is no strong ground motion station in the Bayraklı region and which were destroyed during the earthquake. For this, the outcrop record was estimated by using the strong ground motion station record of the Bayraklı region, the engineering rock of which is at a shallower depth. This estimation was made by a series of deconvolution processes found in the literature [7]. In addition, its validity was demonstrated by comparing it with the recorded surface motion at the Bayraklı strong ground motion station. From this point of view, ground-response analyzes were carried out in a destroyed building location in Bayraklı region. As a result of the ground response analysis, the accelerations that occur in the structure are estimated by considering the concept of structure-soil interaction. The horizontal design force corresponds to 10% of the building mass in the 1975 regulation to which the building is subject during construction. However, the predicted accelerations showed that the base shear force could be above the design value. This result showed the importance of the soil-structure interaction concept on a collapsed building.

References

1. Bardet JP, Ichii K, Lin CH (2000) EERA: a computer program for equivalent-linear earthquake site response analyses of layered soil deposits. University of Southern California, Department of Civil Engineering
2. EN 1998-1 (2004) Eurocode 8: design of structures for earthquake resistance
3. Gazetas G (1991) Foundation vibrations. In: Fang H-Y (ed) Foundation engineering handbook, 2nd edn, Chapter 15. Chapman and Hall, New York, New York
4. Mylonakis G, Nikolaou S, Gazetas G (2006) Footings under seismic loading: analysis and design issues with emphasis on bridge foundations. *Soil Dyn Earthq Eng* 26:824–853
5. NEHRP (2020) Recommended seismic provisions for new buildings and other structures. Prepared for the federal emergency management agency of the U.S. Department of Homeland Security (FEMA), Washington, D.C
6. Pais A, Kausel E (1988) Approximate formulas for dynamic stiffnesses of rigid foundations. *Soil Dyn Earthq Eng* 7(4):213–227
7. Silva W (1988) Soil response to earthquake ground motion: Final report. EPRI-NP-5747 ON: TI88920246
8. TBDY, Türkiye Bina Deprem Yönetmeliği, AFAD, Türkiye (2018)
9. TUBITAK 106G159 (2012) Modelling of seismic behavior of soils for safe design of buildings against earthquakes in İzmir Province, Aliğa and Menemen district, pp 45–46
10. University of Illinois (2011) DEEPSOIL V4.0, University of Illinois at Urbana Champaign. <http://deepsoil.cee.illinois.edu>. Accessed 2011
11. Veletsos AS, Meek JW (1974) Dynamic behavior of building-foundation systems. *Earthquake Eng Struct Dyn* 3:121–138

Analysis of the Pile Foundation Calculation Results Given the Action of an Earthquake and Soaking of the Loess Base



Nyamdorj Setev and Dashjamts Dalai

Abstract Purpose and task: On the territory of Mongolia, loess type subsiding soils are widespread and where seismic activity is 6–9 points according to the modified scale of Giuseppe Mercalli (Charles Richter) system. During the calculation of piles, the goal was to analyze the reduction in the bearing capacity of the pile foundation, depending on the activity of the earthquake and the water saturation of the soil of the building base in the operational stage. Brief description of the methodology: Based on the results of the analytical calculation, a comparative analysis of the reasons for the decrease in the bearing capacity of the pile foundation under action 6 was carried out; 7; 8 and 9 points and in the condition W_{sat} . A method was used to predict the probability of a risk from unacceptable and uneven settlement of buildings and structures. Results and conclusions: A quantitative assessment of the reduction in the bearing capacity of the pile foundation was obtained and the inequalities of the boundary conditions were revealed based on the results of comparative analyzes of numerical values, relevant factors of influence, such as an earthquake and wetting of the subsiding soil of the base. Conclusions are drawn on the basis of a quantitative assessment and comparative analyzes that when designing pile foundations in a mandatory laying, consider the problem of reducing and increasing uneven settlements, and make a design decision taking into account the coefficient of reduction in the bearing capacity of the foundation.

Keywords Humidity · Water saturation · Subsiding soils · Bearing capacity · Settlement

N. Setev (✉) · D. Dalai
Mongolian University of Science and Technology, Ulaanbaatar, Mongolia
e-mail: nyamdorj@must.edu.mn

D. Dalai
e-mail: ddashjamts@must.edu.mn

1 Introduction

According to the requirement of the development of urban planning and the development of a new territory where structurally unstable soils are common, such as subsidence loessal, swelling, bulk, seasonal and permafrost soils, the optimal use of pile foundations, taking into account the high activity of the earthquake according to the modified scale of Giuseppe Mercalli (Charles Richter), is acute. The experience of using pile foundations for buildings and engineering structures in the above-considered engineering geological conditions of Mongolia shows that there are certain opportunities to increase the economic efficiency of investments, reduce the duration of the zero-cycle technological work, complete mechanization, most importantly, ensure reliable stability of the base and foundation of the structure under construction and operational suitability during the estimated period.

According to the results of field tests of reinforced concrete piles of various lengths in low-moisture subsidence dusty sandy loam soil of the territory of the city of Darkhan, the bearing capacity decreases by 1.14–2.59 times after soaking to the state of water saturation in terms of moisture (Nyamdorj [1]).

2 Brief Description of the Methodology

Abelev Yu.M., Y., Broms B.B., Vesic A.S., Bakholdin B.V., Ishihara K., Grigoryan A.A., Kulhawy F.H., Nordlund R.L., Dashzhamts D., Ilyichev V.A., Stavnitser L.R., Tomlison M.J., Krutov V.I., Mangushev R.A., Jian Chu., Gotman A.L. and others studied the features of the work of piles and pile foundations in subsidence soils during soaking, taking into account earthquake activity and developed a theoretical justification for their calculation. Currently, more than 200 different types of piles have been developed and used in the world, and new research is ongoing to find better options. This circumstance confirms that the most effective constructive and technological options for pile foundations have not yet been found (Mangushev [2]; Ishihara [3]; Dashzhamts [4]).

In 1997, in the city of Hamburg, the Germans, leading researchers and specialists in the field of pile foundation engineering, set the goal at a meeting of the Technical Committee (TS-18) of the International Association for Soil Mechanics and Geotechnics (ISSMGE) as follows: “by modeling the calculation method of a pile foundation and designing according to optimal design solutions, save material costs and reduce the total estimated cost of buildings and structures”.

For example, in the soil conditions of the territory of Mongolia, piles are driven and embedded in subsiding soil with natural low humidity, in the future, in a long operational period, the moisture content of the base soil increases due to technogenic soaking, in other words, there is a high probability of increasing the degree of humidity to the value of water saturation ($S_r \geq 0,8$). If, under this condition, a seismic event occurs, that is, an earthquake, there can be great risk. At the current

level of development of geotechnical science in modeling using the finite element method, it is more possible to predict the patterns of subsidence deformation and changes in bearing capacity (Ilyichev [5]; Stavnitser [6]). The seismic behavior of piled foundations during soaking of the base soil and earthquake is widely discussed by many researchers from different countries in order to design more safely and economically.

Ishihara and Asuyuki Koga [7] studied the conditions of soil liquefaction and destruction of buildings and structures during the 1964 Nigata earthquake. Tokimatsu and Asaka [8] studied the negative effects of soil movements caused by liquefaction on the work of piles during an earthquake, established the causes of the destruction of the building and engineering communications of the city of Hyogoken-Nambu (Kobe) in 1995. Motosaka and Somer [9] established ground motion characteristics and structural damage of liquefied soils during the 1999 Kocaeli earthquake in Turkey. Motosaka and Wang [10] studied the vibration characteristics to the ratio of damage to the pile heads at the joints with the grillage structure of a high-rise building with a large span and a pile foundation based on microtremor observations of the Sendai (Fukushima) earthquake in 2011. It was established that soil liquefaction is the main cause of damage to building structures in seismically active areas.

Finn and Fujita [11] in his work "Pile in liquefying soils: seismic analysis and design issues" specific design cases are considered and illustrated. One is the reaction of the pile to a strong earthquake, accompanied by the development of high pore water pressures or liquefaction during shaking, and the other is the reaction to pressure caused by the lateral movement of the liquefied soil. An analysis was made of the results of model tests of pile foundations, which are used to demonstrate the current process of reducing the bearing capacity during strong shaking. Boulanger et al. [12] investigated the causes of damage to bridge support structures after an earthquake, that is, as a result of liquefaction of the soil of the base of the supports. Rostami et al. [13]. The regularities of the loss of the bearing capacity of the pile and the nature of the damage were studied and the place of formation of plastic hinges along the length of the pile was determined. The results of parametric studies have shown that a plastic hinge is formed at the boundaries of the fluidized and non-liquefied layers; however, many factors can influence the location, such as material properties, pile length, and thickness of the liquefied soil layer.

Janalizadeh and Zahmatkesh [14]. Studies were conducted using three-dimensional (3D) numerical modeling to determine various parameters such as soil stratification, kinematic and inertial forces, pile head boundary conditions, soil surface slope, and pile response. Comparing the results of numerical analyzes with the results of laboratory flume tests, it was concluded that the use of the p-y curve method for liquefied sand gives satisfactory results. In the work of Stolyarov [15] analyzes the effect of residual seismic soil displacements on the operation of traditional foundations, as well as on pile foundations with an intermediate cushion. It is proposed to use seismic-resistant foundations in seismic regions with an intensity of 7–9 and 9–10 points, the size of which takes into account the magnitude of residual soil displacements, It is shown that the accepted standard accuracy of setting the

intensity of an earthquake for settlements $-\Delta I = 1$ point, at which seismic displacements change by a factor of 6, is unprecedentedly low for science and technology. It is desirable to bring it to the Japanese accuracy of 0.1 points. Wang [16] investigates the seismic response of single piles in liquefying soil by testing on a laboratory shaker and numerical simulation. The main factors of influence on the behavior of piles in liquefied soil, as well as the dynamic connection of the inertial interaction of the structure and the pile, the mechanism of kinematic soil-pile interaction were established.

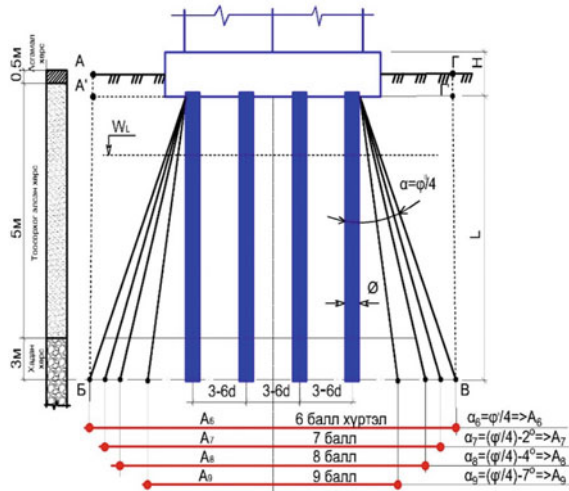
From the considered and cited works of researchers, it can be seen that the problem of the interaction of a pile and a liquefied soil is very complex and depends on many factors. Including the volume of laboratory and field work performed to determine the calculated physical and mechanical indicators, their reliability is very important. The clarity of the assignment for the performance of engineering-geological work is very important, it must be certain, subsequent work depends heavily on the reliability of certain calculated indicators of soil conditions until the expiration of the operational suitability of the constructed buildings and structures.

3 Methods and Materials

According to the methodology specified in BNbD 50.01-16 [17] and SP 24.13330-2011 [18] to determine the area of the base of the conditional pile foundation of buildings and structures built on subsidence soils, taking into account soaking to the value of W_{sat} and $S_r \geq 0.8$, in Depending on the activity of the earthquake, the angle of internal friction decreases as follows: with a 7-point earthquake, the values of φ^{II} by 2° ; at 8 points by 4° and at 9 points by 7° (where φ^{II} —is the angle of internal friction of water-saturated soil). As a result of the latter, the area of the base of the conditional pile foundation decreases to a certain extent, in such a case, in order to provide the criteria for calculating I for strength and II for deformation limit states, increase the depth of the piles and the distance between the piles that are part of the pile cluster foundation.

Developed a calculation scheme in accordance with the methodology under consideration, taking into account the moisture content of the base soil soaking and earthquake activity (Fig. 1). For the purpose of comparative analysis and identification of the dynamics of the decrease in bearing capacity, calculations were carried out in accordance with this methodology, taking into account the liquefaction of silty sandy loamy soil and an increase in seismic activity from 6 to 9 points, the results of which are analyzed and shown in the next part.

Fig. 1 Calculation scheme for determining the area of the base of a conditional piled pad foundation under the conditions of increasing seismic activity



4 Results of the Analytical Calculation

Let’s consider an example of calculating the bearing capacity (F_d) of a bored pile with a length of 8.0 m and a diameter of 0.6 m in subsiding dusty sandy loamy soil of the city of Darkhan, taking into account the water saturation of the base soil from technogenic soaking in the operational period and 7-point seismic activity according to microzoning according to the formula Grigoryan [19] and according to Appendix E of the SP norm [18], formula 16: The calculated characteristics of the soil condition are obtained from table 2 from (Nyamdorj et al. [20]).

$$F_d = \gamma_c(F_{1H} + F_{2H}); \tag{1}$$

where γ_c —is the working condition coefficient, $\gamma_c = 1.0$.

$F_{1H}-F_d = \gamma_c(F_{1H} + F_{2H})$; lateral resistance coming to the length $l_0 + l_H$,

$$F_{1H} = A_1 = U[\ell_0(0.5\xi \cdot \gamma \cdot \ell_0 \cdot tg\varphi'' + c) + (\xi \cdot \gamma \cdot \ell_0 \cdot tg\varphi'' + c)\ell_2]; \tag{2}$$

$U = 1.884$; $\xi = 0, 5$; $\varphi'' = 17^\circ - 2^\circ = 15^\circ$; $c'' = 6.8 k\pi a$, $l_2 = 7.7 - 1.0 = 6.7m$

$$l_2 = l + 2/d - l_0 - b - a = 7.7 + 0.6/2 - 2.0 - 0.23 - 1.0 = 4.77M$$

$l_0 = l_1 - a = 3.0 - 1.0 = 2.0 M$; $tg15^\circ = 0, 32$; $ctg15^\circ = 3.12$;

$l_1 = 12d$ or accepted not less than 6.0 m, accepted $l = 3.0 M$.

$$b = d/2 - (ctg\alpha - 1)ctg\varphi'' = 0.6/2 - (3.126 - 1) \cdot 3.126 = 30 - 6.65 = 23.35 \text{ cm}$$

Table 1 Results of calculating the dependence of the bearing capacity and settlements of bored piles on seismic activity

Seismic activity, Q	Length and diameter of piles, m	φ_{sat} soaked soil	The area of the sole of the conditional foundation-A, m ²	Bearing capacity of piles- F_d , tons	Decrease in bearing capacity Δ , in time
6 points	L = 8.0, $\varnothing = 0.6$	17°	23.75	71.97	1.0
7 points	L = 8.0, $\varnothing = 0.6$	15°	20.92	63.14	1.14
8 points	L = 8.0, $\varnothing = 0.6$	13°	16.46	52.48	1.64
9 points	L = 8.0, $\varnothing = 0.6$	10°	9.16	27.79	2.59

$$\alpha = 45^\circ - \varphi - x \cdot c = 45^\circ - 15^\circ - 0.2 \cdot 5.0 = 29^\circ, \operatorname{ctg} \alpha = \frac{0.674}{0.485} = 1.802, x = \frac{k}{l_0} = \frac{1.0}{5.0} = 0, 2$$

$$F_{1H} = 1.884[2.0(0.5 \cdot 0.5 \cdot 16.5 \cdot 2.0 \cdot 0.32 + 6.8) \cdot 4.77] = 12.46 \text{ mn}$$

$$F_{2H} = k\delta_1 A; \quad (3)$$

$$F_{2H} = 3.0 \cdot 59.69 \cdot 0.283 = 50.68_{TH}, \text{ if } k = 3.0$$

$$\delta_1 = \frac{\delta_3(1 + \sin\varphi) + 2c \cos\varphi}{1 - \sin\varphi} = \frac{16.5(1 + 0.485) + 2 \cdot 6.8 \cdot 0.874}{1 - 0.485} = 59.69$$

$$\delta_3 = \xi \gamma l_0 = 0.5 \cdot 16.5 \cdot 2.0 = 16.5.$$

$$F_d = 1, 0(12.46 + 50.68) = 63.14_T$$

The results of calculations performed in accordance with the above methodology to determine the dependence of the bearing capacity and settlement of bored piles on the angle of internal friction (φ_{sat}) and seismic activity are shown in Table 1.

5 Analysis of the Results

When the value of the angle of internal friction of subsidence low-moisture (i.e. with natural moisture) silty sandy loamy soil at $\varphi = 17^\circ$ and Q = 6 points, $A_6 = 23.75 \text{ m}^2$, $F_{d;6} = 71.97$ tons, when it decreases by 2° at $\varphi_{sat} = 15^\circ$ and Q = 7 points, it turns out $A_7 = 20.92 \text{ m}^2$ and therefore $F_{d;7} = 63,14$ tons or the bearing capacity decreases by 1.14 in times. For other cases, similar calculations were carried out: at

$Q = 8$ points $A_8 = 20.92 \text{ m}^2$; $F_{d;8} = 43.88$ tons or 1.64 times; with $Q = 9$ points $A_9 = 16.46 \text{ m}^2$; $F_{d;9} = 27.79$ tons or 2.59 times respectively decrease (Figs. 2, 3 and 4).

In the work of Ter-Martirosyan et al. [21] presented approximately similar results of a comparative analysis of analytical calculations and numerical solutions of the interdependence of a pile and a water-saturated base soil, taking into account soil liquefaction during an earthquake.

Fig. 2 Diagrams of the dependence of the area of a conditional pile foundation on the angle of internal friction, taking into account the activity of seismic $A = f(\varphi_{sat})$, (red curve) and the bearing capacity on the angle of internal friction, taking into account the activity of seismic $F_d = f(\varphi_{sat})$, (blue curve)

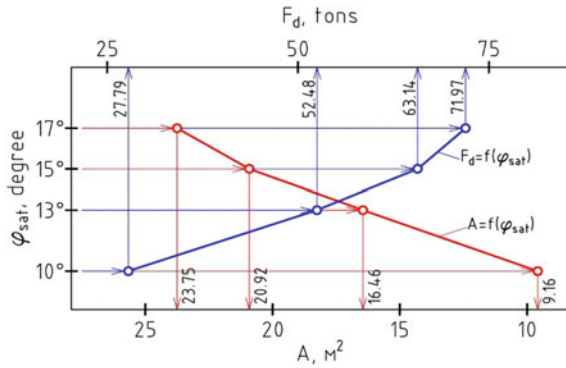


Fig. 3 Diagrams of the dependence of the area of a conditional pile foundation on the intensity of seismic, taking into account the angle of internal friction $A = f(Q)$, (red curve) and the bearing capacity of the pile foundation on the intensity of seismic $F_d = f(Q)$, (blue curve)

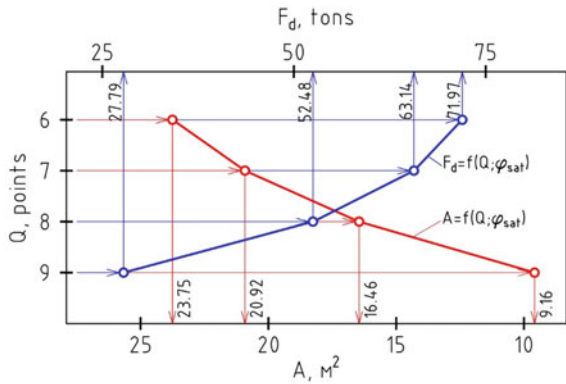
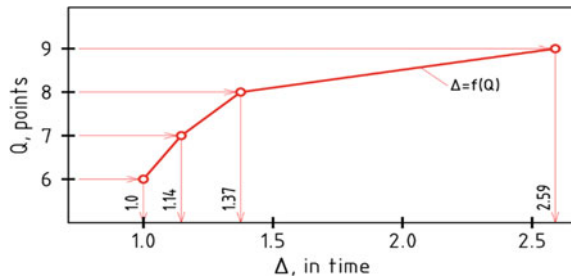


Fig. 4 Variation curve (Δ) of A and F_d values versus Q and φ_{sat} values



Based on the results of the calculation, diagrams were constructed for a preliminary assessment of the dependence of the decrease in the area of the base of the conditional foundation and the bearing capacity of bored piles with a length of 8.0 m and a diameter of 0.6 m in subsidence soils on seismic activity and the angle of internal friction of the soaked soil.

The main reason for the decrease in the bearing capacity of piles is the process of liquefaction of sandy-argillaceous soil with high humidity during an earthquake, which is shown in Fig. 3. The quantitative assessment of the negative impact of soil liquefaction on the calculated bearing capacity of a pile foundation under seismic impacts is not fully understood.

According to the results of the calculation and their analysis, it was established that the values of the numerical values of the variability (Δ) of the area (A) and the bearing capacity (F_d) depending on the seismic intensity (Q) and the angle of internal friction (φ_{sat}) are equal to.

The boundary condition of the bearing capacity determined by this calculation method is written:

$$F_{d;6} > F_{d;7}^{sat} > F_{d;8}^{sat} > F_{d;9}^{sat}, \quad (4)$$

where— $F_{d;6}$; $F_{d;7}^{sat}$; $F_{d;8}^{sat}$; $F_{d;9}^{sat}$ —bearing capacity pile according to 6–9 points.

As shown in Fig. 1, the numerical value of the area of the base of conditional pile foundations corresponds to the $A_6 > A_7 > A_8 > A_9$, then the following boundary conditions for calculating the settlement of the pile foundation should be provided:

$$S_u < S_6 < S_7^{sat} < S_8^{sat} < S_9^{sat}, \quad (5)$$

where S_6 – S_9 —pile foundation settlement, corresponding to 6–9 points, S_u —maximum allowable settlement.

The pile foundation is designed according to the conditions for fulfilling the criteria of these mathematical inequalities of the boundary conditions for calculating the bearing capacity and settlement. An analysis of the results shows that the fulfillment of the inequality criteria makes it possible to ensure the operational reliability of buildings and structures.

6 Conclusion

1. According to the results of calculation and analysis, it is established that there are many causes of the destruction of buildings and structures under the action of 7 and greater seismicity, but among them the most significant reasons are the liquefaction of the soaked soil of the pile foundation during an earthquake. In order to prevent this kind of risk, it is necessary to avoid fulfilling the inequality criterion (4) and (5).

2. Comparative analysis shows that under the condition of 6 point seismic, the bearing capacity of the pile foundation, without taking into account the influence of base soaking and earthquake, is 1.14 times greater than the bearing capacity determined taking into account soaking and 7point earthquake, and also at 8 and 9 points respectively 1.64 and 2.59 times more.
3. The main reason for the decrease in the bearing capacity of piles is the process of liquefaction of sandy-argillaceous soil with high humidity during an earthquake.
4. The use of the proposed diagrams is correct provided that the geometric characteristics of the pile and the calculated corresponding soil parameters of the foundation, taking into account the regional features of this territory of Mongolia.
5. The risk from an earthquake depends on many factors, including the possibility of a decrease in the bearing capacity with 7, 8 and 9 seismic points, from which great risks can be created. Unfortunately, in recent years, some strong earthquakes have occurred in different countries of the world and there have been huge risks, on the basis of the latter, it is necessary to draw the appropriate conclusions and make decisions on the obligatory consideration of these circumstances in the construction project.

References

1. Nyamdorj S (2021) Foundation and basement of buildings and structures in subsiding soils. Ulaanbaatar. Print. MUST, p 261
2. Mangushev RA (2018) Piles and pile foundations. Design, design and technology. In: Mangushev RA, Znamensky VV, Gotman AL, Ponomarev AB. DIA Publishing House, p 320
3. Ishihara K. 2006. Behavior of soils during earthquakes // Series "Achievements of modern geotechnics" / Translated from English by V.M. Ulitsky, A.G. Shashkin, M.B. Lisyuk. -St. Petersburg. 2006. 384p.
4. Dashjants D (1998) Theoretical basis for optimal solutions for designing basements and foundations of buildings in structurally unstable soils. Diss.doc. Tech Science (SC.D). UB 1998. SHUTS-1001, p 37
5. Ilyichev VA, Mongolov YuV, Shaevich VM (2010). Pile foundations in seismic regions. 1983.
6. Stavnitser LR (2010) Seismic resistance of foundations and foundations. Publishing House ASV, p 449
7. Ishihara K, Asuyuki Koga Y (1981) Smudies of liquefaction in the 1964 Nigata. Earthq Found 21(3). (Sept 1981, Japanese Society of Soil Mechanics and Foundation Engineering)
8. Tokimatsu K, Asaka Y (1998) Effects of liquefaction-induced ground displacements on pile performance in the 1995 Hyogoken-Nambu (Kobe) earthquake. Special Issue of Soils and Foundations, Sept 1998, pp 163–177
9. Motosaka M, Somer A (2002) Ground motion directionality inferred from a survey of minaret damage during the 1999 Kocaeli and Düzce, Turkey Earthquakes. J Seismol 6: 419–430. (Printed in the Netherlands)
10. Motosaka M, Wang X (2018) An investigation on vibration characteristics and relevance to damage on pile-heads of a tilted high-rise building with high aspect ratio and pile foundation based on microtremor observation. J Japan Assoc Earthq Eng 18(5). (Jan 2018)
11. Finn WDL, Fujita N (2002) Piles in liquefiable soils: seismic analysis and design issues. Soil Dyn Earthq Eng El 22(9–12):731–742. (Oct–Dec 2002)

12. Boulanger RW, Chang D, Brandenberg SJ, Armstrong RJ, Kutter BL (2007) Seismic design of pile foundations for liquefaction effects. In: *Earthquake geotechnical engineering*. Springer Theses University of California at Los Angeles USA, pp 277–302
13. Rostami R, Hytiris N, Bhattacharya S, Giblin M (2017) Seismic analysis of pile in liquefiable soil and plastic hinge. *Geotechn Res* 4(4): 203–213. E-ISSN 2052-6156
14. Janalizadeh A, Zahmatkesh A (2015) Lateral response of pile foundations in liquefiable soils. *J Rock Mech Geotech Eng* 7: 532–539. (Babol University of Technology Babol, Iran)
15. Stolyarov VG (2006) Residual seismic ground displacements, horizontal impacts on a building, seismic-resistant pile foundations. North Caucasian State Technical University, Stavropol, Jan 30, 2006, pp 70–74
16. Wang R (2016) Analysis of seismic single pile response in liquefiable ground. Springer theses Springer, Berlin, Heidelberg, pp 55–89. https://doi.org/10.1007/978-3-662-49663-3_3
17. BNbD 50-01-16 (2016) Norms and rules for designing bases and foundations. Ulaanbaatar, p 317
18. SP 24.13330.2011. Pile foundations. Act.ed: SNIp2.02.03-85, p 92
19. Grigoryan AA (2010) On the bearing capacity and settlements of bored piles for high-rise construction on clay soils, taking into account the new nature of the destruction of their foundations. In: *Proceedings of the international conference in geotechnics. Geotechnical problems of megacities*. T-4, pp 1220–1227
20. Nyamdorj S, Dashjamts D, Mangushev RA (2021) The work of bored piles on a horizontal load in wetted subsidence soils. In: *Sat. report international conferences: modern theoretical and practical issues: new materials, designs, technologies and calculation methods*. (GFAC 2021) St Petersburg, pp 73–81
21. Ter-Martirosyan AZ, Le Duc A, Manukyan AV (2020) Influence of soil liquefaction on the design bearing capacity of a single pile. *Vestnik MGSU, Mon J Constr Archit* 15(5): 655–664. [https://doi.org/10.22227/1997-0935.2020.5.\(rus\)](https://doi.org/10.22227/1997-0935.2020.5.(rus))

Proposal of a Model Setup for Verification of the Origin of High Frequency Motion in Soil



Piotr Kowalczyk 

Abstract High frequency components of motion are typically measured in laboratory tests on shaking tables when investigating the dynamic response of soil subjected to harmonic excitation. The source of these high frequency components is often thought to be related to uncertainties of experimental setups. In contrast, a group of numerical and theoretical research works suggested potential physical explanations to high frequency components of motion as related to soil mechanical behavior including soil fluidization, cyclic mobility, pounding or unloading elastic waves. This paper presents a finite element numerical study of an example model setup designed to verify the origin of high frequency motion in soil as potentially related to the presence of soil elastic waves in the steady state response of nonlinear hysteretic soil. The soil is modelled with an advanced soil constitutive model within the general framework of hypoplasticity to account in a reliable manner for soil cyclic behavior. The results show that high frequency motion can be observed in the computations in free field and on a simple structure even though a simple harmonic sinusoidal input motion is introduced at the base of the model setup. It is shown that apparently this high frequency motion can be representative of soil elastic waves released in nonlinear hysteretic soil in the steady state response.

Keywords Finite element modelling · Soil-structure interaction · Hypoplasticity · High frequency · Elastic waves · Wave propagation

1 Introduction

High frequency motion is often registered in experimental works on soil dynamic behavior carried out in flexible soil containers placed on shaking tables and subjected to simplified sinusoidal input motions. Although often this high frequency motion

P. Kowalczyk (✉)

Independent Researcher, Previously University of Trento (Italy), Trento, Italy

e-mail: pk.piotrkowalczyk.pk@gmail.com

is attributed to uncertainties of experimental setups, some attempts to recognize the source of the high frequency motion in the experimental works as related to physical phenomena were also made in the past. Different authors attributed the observed high frequency motion to various physical phenomena, for example, to soil fluidization [1], cyclic mobility in saturated soil [2] or pounding between soil and structure [3]. The most recent potential explanation to the experimental observations is the possibility of the release of soil unloading elastic waves in the steady state response of nonlinear hysteretic soil under harmonic excitation [4–7]. The author's previous works showed promising comparisons between advanced numerical studies and some benchmark experimental works supporting the idea of the presence of unloading elastic waves in the steady state response of soil. In fact, these findings may potentially explain why some experimentalists observe that their experimental tests were *destroyed* by elastic waves. On the other hand, one has to remind that experimental works are often aimed at studying complex boundary value problems and their setups include various structural elements, non-homogenous soil profiles or deal with saturated soil, all possibly inducing additional waves in the dynamic system. Moreover, the induced input motions may contain spurious high frequencies due to the imperfections of actuators. Finally, soil flexible containers tend to be rather small for the reasons of reduced experimental costs, however in such case the boundaries of the containers may more likely affect the measurements. Therefore, it appears that there is a need for a dedicated experiment to further advance the findings on soil unloading elastic waves, especially in regard to their impact on structures.

This paper presents a 2D finite element numerical analysis of an example model setup which could be considered as a *perfect experiment* for explicit verification of the existence of soil elastic waves potentially released in hysteretic soil in the steady state response. To this aim, homogenous dry soil is placed in a large flexible soil container and subjected to perfectly sinusoidal input motion of horizontal acceleration. The soil nonlinear behavior is accounted by an advanced soil constitutive model formulated in the framework of hypoplasticity to yield high-fidelity predictions. In addition, a small oscillator with its natural frequency close to the soil first natural frequency is placed in the middle of the soil container to allow further verification of the existence of soil elastic waves in the steady state response of soil.

2 Methodology

2.1 Numerical Model

The numerical model presented in this work is an example of a proposal of a *perfect experimental setup* where experimental uncertainties and imperfections are eliminated. To this aim, the flexible soil container in this work is assumed to be much

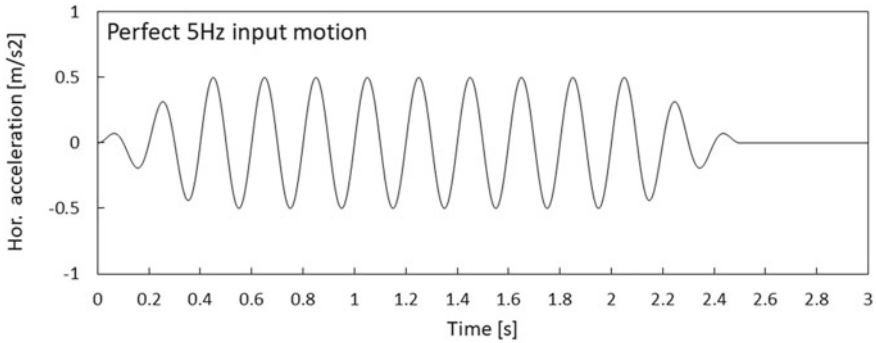


Fig. 1 Input motion of the driving frequency of 5 Hz introduced at the base of the soil specimen

larger than typically. For example, the size of the flexible soil container is assumed here to be 5 m long and 1 m high. The 5 m long soil container would allow reducing relatively the zone where the effects of boundary conditions and interaction between the container and the soil may occur, thus more reliable free field measurements could be obtained. The soil filling the container is dry sand, for example, Leighton Buzzard sand, fraction E. The assumed density is 1300 kg/m³, with the initial void ratio of 0.9, and the initial K₀ condition of 0.5. Soil natural frequency in the soil container for such assumptions is around 24 Hz. Finally, example perfectly sinusoidal input motion of 5 Hz and a moderate amplitude of up to 0.05 g is introduced in a smooth manner as shown on Fig. 1.

In addition, a relatively small example structure made of aluminum is placed in the center of the soil container. To this aim, an oscillator consisting of 200 g mass fixed on the top of a 0.1 m high aluminum column of 3 × 12 mm section and placed on 0.1 m size foundation is assumed. The natural frequency of such oscillator assuming fixed base is 26 Hz, thus it lies closely to the soil natural frequency. In fact, such close match between the natural frequencies of the soil and the structure is intended. The oscillator in the proposed experiment can act as an additional measuring instrument which can identify the presence of soil elastic waves in the steady state response of soil. Namely, if such waves are released in soil, the oscillator will vibrate in the steady state response with its natural frequency in addition to the driving frequency of the input motion. On the other hand, if the elastic waves are not released in soil, the oscillator should vibrate only with a single frequency, the one of the input motion.

Note that no common procedure of filtering data with low-pass filters is proposed in order to avoid the possibility of removing physical phenomena from the results.

In general, the presented example model setup is such, in which typically encountered experimental uncertainties and imperfections, related to close boundaries, non-homogenous soil profiles or numerous structural elements, are minimized. Therefore,

if carried out physically, one could expect unaffected response in free field and on the oscillator.

2.2 Constitutive Model

Hypoplastic sand model in the form developed by [8–10] and implementation available on *soilmodels.info* webpage [11] has been used in this work to ensure reliable soil mechanical response under seismic loading conditions and ease in replicating the numerical study by the interested Readers. The calibration of the model is practically the same as in the previous similar works of the author [4] with only slight modifications. The calibrated parameters with their descriptions are shown in Table 1.

Table 1 Model parameters for the hypoplastic sand model

	Parameter	Description	Value
Basic hypoplasticity	φ_c	Critical friction angle	33.0
	h_s	Granular hardness [MPa]	2500
	n	Stiffness exponent ruling pressure-sensitivity	0.42
	e_{d0}	Limiting minimum void ratio at $p' = 0$ kPa	0.613
	e_{c0}	Limiting void ratio at $p' = 0$ kPa	1.01
	e_{i0}	Limiting maximum void ratio at $p' = 0$ kPa	1.21
	α	Exponent linking peak stress with critical stress	0.13
	β	Stiffness exponent scaling barotropy factor	0.8
Intergranular strain concept	R	Elastic range	0.00004
	m_R	Stiffness multiplier	4.0
	m_T	Stiffness multiplier after 90° change in strain path	2.0
	β_R	Control of rate of evolution of intergranular strain	0.8
	χ	Control on interpolation between elastic and hypoplastic response	0.5
	ϑ	Control on strain accumulation	5.0

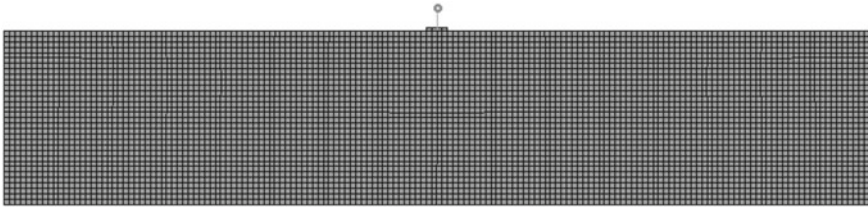


Fig. 2 Mesh discretization of the 2D finite element model

2.3 Discretization and Boundary Conditions

Abaqus finite element code [12] has been used to run the numerical model of the example experimental setup. The 2D mesh discretization is shown on Fig. 2. The size of a quadratic element of 0.05 m ensures reliable predictions for representing the problem of S-wave propagation.

The boundary conditions on the lateral sides comprise restricting corresponding nodes at the same height to have the same lateral displacement, i.e. to mimic the presence of a flexible soil container. Horizontal acceleration time history is introduced at the base.

The oscillator (i.e. the column and the foundation) are modelled with elastic material of properties of aluminum. Additional damping of 1% has been assumed for the elastic material of the oscillator.

Moderate numerical damping has been introduced to the Hilbert-Hughes-Taylor integration scheme [13], with its parameters set to: $\alpha = -0.41421$, $\beta = 0.5$, $\gamma = 0.91421$, in order to remove very high frequency (i.e. much higher than those studied in this work) oscillations in the computed accelerations.

3 Results

The results present the occurrence of high frequency motion in free field and on the oscillator in the computed horizontal accelerations (Fig. 3) and in the horizontal relative lateral displacements (Fig. 4) even though perfectly sinusoidal input motion has been applied (Fig. 1). Figure 5 shows the spectral response of the computed accelerations as evaluated in the steady state part of the motion (i.e. from 0.8 to 2.0 s) and reveal increased presence of the harmonic 25 Hz representative of soil elastic waves. In particular, one can observe very strong presence of high frequency motion on the oscillator. Note also the presence of other harmonics in the spectral response (e.g. 15 Hz). These are believed to characterize a distorted sinusoidal wave

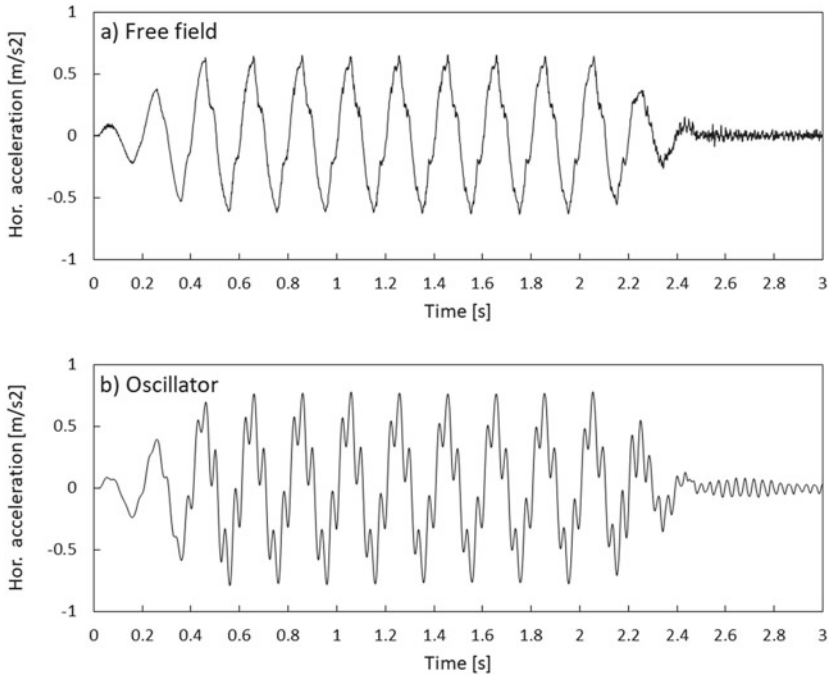


Fig. 3 Horizontal accelerations computed at the top of the soil in free field (a) and at the top of the oscillator (b)

as explained in the past, e.g. [14], and not representative of additional waves in the analyzed system.

Note that the presence of high frequency motion is the strongest in the steady state part of the motion, thus the presented effects can not be related to the transient response. In any case, any additional waves induced at the initiation of motion due to the transient response would be damped out as a result of material hysteretic damping (Fig. 6). On the other hand, apparently this damping is not sufficient to remove the high frequency motion (i.e. soil elastic waves) from the steady state response. Finally, note how high frequency motion remains in the *coda* part of the computations and is slowly damped out.

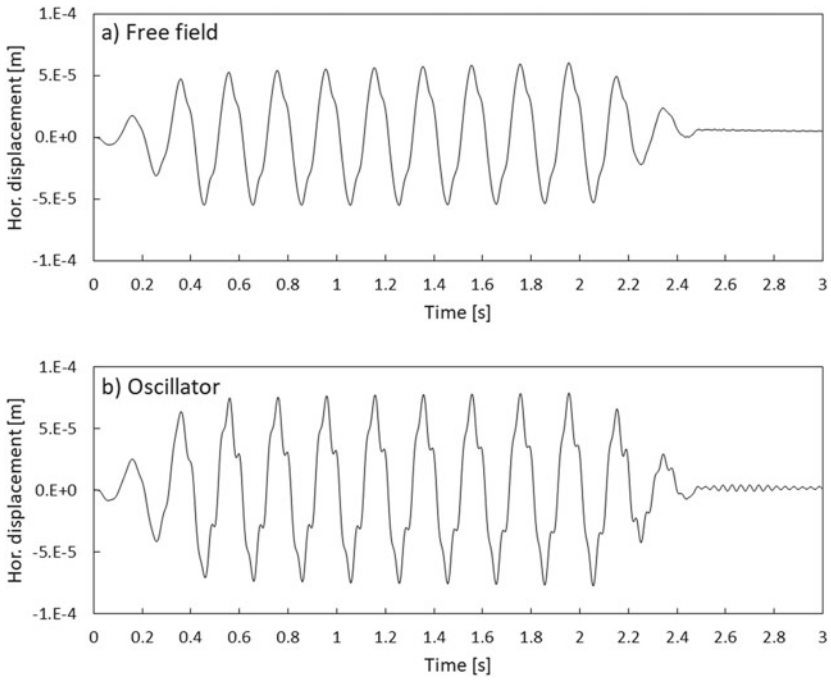


Fig. 4 Horizontal displacements computed at the top of the soil in free field (a) and at the top of the oscillator (b)

4 Summary

The numerical study in this work showed a proposal of an example model setup for the verification of the origin of high frequency motion often observed in soil specimens tested under sinusoidal input motions. The computed results indicated that soil elastic waves can be found in the steady state response of the soil and the structure. Further studies should involve experimental verification of these findings, for example, by physical modelling of the example model setup proposed in this work.

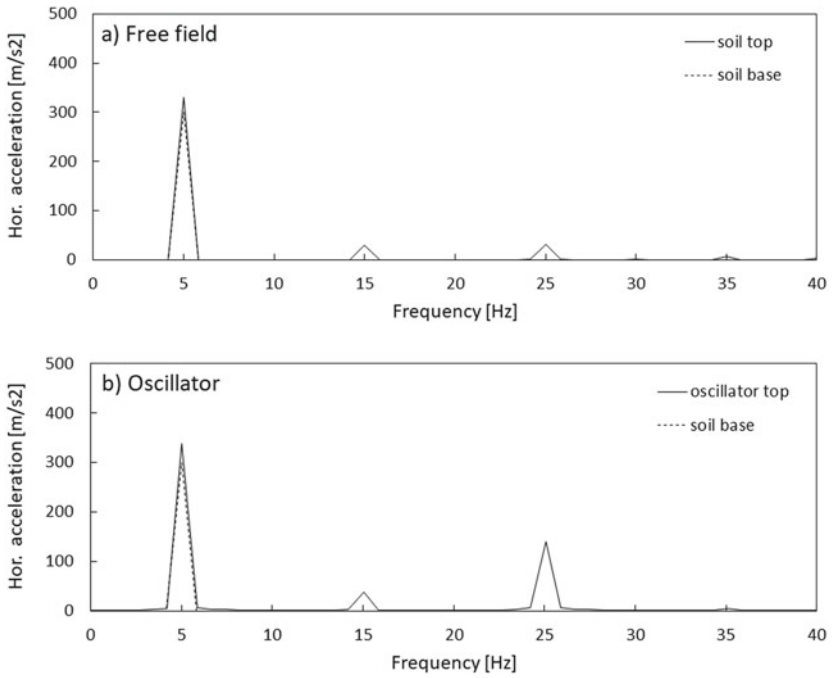


Fig. 5 Spectral response evaluated in the steady state response of the computed accelerations at the top of the soil in free field (a) and at the top of the oscillator (b)

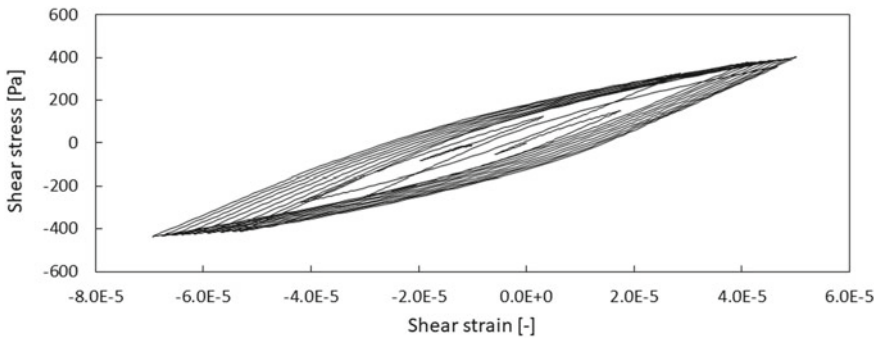


Fig. 6 Shear stress versus shear strain response computed at the mid-depth of the soil

Acknowledgements The author would like to acknowledge University of Trento for the provision of computational resources.

References

1. Dar AR (1993) Development of a flexible shear-stack for shaking table testing of geotechnical problems. PhD thesis. University of Bristol
2. Kutter BL, Wilson DW (1999) De-liquefaction shock waves. In: Proceedings of: 7th U.S.-Japan workshop on earthquake resistant design for lifeline facilities and countermeasures against soil liquefaction, Technical Report MCEER-99-0019, pp. 295–310
3. Chau KT, Shen CY, Guo X (2009) Nonlinear seismic soil-pile-structure interactions: shaking table tests and FEM analyses. *Soil Dyn Earthq Eng* 29:300–310
4. Kowalczyk P (2020) Validation and application of advanced soil constitutive models in numerical modelling of soil and soil-structure interaction under seismic loading. PhD thesis. University of Trento. https://doi.org/10.15168/11572_275675
5. Kowalczyk P, Gajo A (2022) Introductory consideration supporting the idea of the release of unloading elastic waves in the steady state response of hysteretic soil (Submitted)
6. Kowalczyk P (2021) New insight on seismic soil-structure interaction: amplification of soil generated high frequency motion on a kinematic pile. In: Proceedings of the 1st Croatian conference on earthquake engineering, 22–24 March. Zagreb, Croatia
7. Kowalczyk P (2022) Resonance of a structure with soil elastic waves released in nonlinear hysteretic soil upon unloading. *Studia Geotechnica et Mechanica*. <https://doi.org/10.2478/sgem-2022-0015>
8. Von Wolffersdorff PA (1996) A hypoplastic relation for granular materials with a predefined limit state surface. *Mech Cohesive Frict Mater* 1(3):251–271
9. Niemunis A, Herle I (1997) Hypoplastic model for cohesionless soils with elastic strain range. *Mech Cohesive Frict Mater* 2:279–299
10. Wegener D (2013) Numerical investigation of permanent displacements due to dynamic loading. PhD thesis. TU Dresden
11. Gudehus G, Amorosi A, Gens A et al (2008) The soilmodels.info project. *Int J Numer Anal Methods Geomechan* 32(12):1571–1572
12. Dassault Systèmes (2019) Abaqus Standard software package
13. Hilber HM, Hughes TJR, Taylor RL (1977) Improved numerical dissipation for time integration algorithms in structural dynamics. *Earthq Eng Struct Dyn* 5:283–292
14. Mercado V, El-Sekelly W, Abdoun T, Pajaro C (2018) A study on the effect of material nonlinearity on the generation of frequency harmonics in the response of excited soil deposits. *Soil Dyn Earthq Eng* 115:787–798

A Comparison Study Between 1D and 2D Site Response Analyses Based on Observed Earthquake Acceleration Records



Shima Shamekhi, Atilla Ansal, and Asli Kurtuluş

Abstract The objective of the present work is to evaluate the necessity of 2D site response analysis based on the comparison among the peak ground and spectral accelerations recorded by Istanbul Rapid Response Network and Istanbul vertical array stations during the $M_w = 6.5$ 24/5/2014 Gökçeada and $M_w = 5.9$ 19/5/2011 Kütahya earthquakes with the calculated accelerations by 1D and 2D site response analyses. The shear wave velocity profiles determined based on in-situ geophysical and geotechnical measurements and laboratory tests within the Istanbul Microzonation Project are reevaluated adopting a revision scheme to obtain the best fits between the recorded and calculated spectral accelerations by 1D site response analysis. These modified shear wave velocity profiles are later used for 1D and 2D site response analyses performed in North–South and East–West directions to model peak ground and spectral accelerations on the ground surface. Finally, by modelling different distances around boreholes the influence of variation of the soil profile in horizontal direction is investigated by 2D analyses.

Keywords 1D and 2D site response analyses · Effect of site conditions · Vertical strong motion arrays · Istanbul rapid response network · Horizontal heterogeneity

1 Introduction

The characteristics of the site conditions have a very significant influence on the variation of building damage during earthquakes, thus, it is essential to evaluate and analyze the effects of site conditions. One option is to conduct site-specific response analysis to calculate the response of the soil layers by using estimated acceleration records on rock outcrop, shear wave velocity profiles, shear modulus reduction, and damping ratio curves as inputs for the encountered soil layers. This is usually the first phase of a seismic study that allows geotechnical engineers to estimate amplification

S. Shamekhi (✉) · A. Ansal · A. Kurtuluş
Department of Civil Engineering, Ozyegin University, Istanbul, Turkey
e-mail: shima.shamekhi@ozu.edu.tr

© The Author(s), under exclusive license to Springer Nature Switzerland AG 2023
C. Atalar and F. Çinicioğlu (eds.), *5th International Conference on New Developments in Soil Mechanics and Geotechnical Engineering*, Lecture Notes in Civil Engineering 305, https://doi.org/10.1007/978-3-031-20172-1_38

393

of ground motion on the ground surface and to investigate the liquefaction potential and stability of slopes at the site [1–4].

Govinda et al. [2] conducted a case study of equivalent linear site response analyses during the Bhuj earthquake on January 26, 2001, at a site near the Sabarmati River belt in Ahmedabad city. The effects of soil amplification, settlement, and their relationship with acceleration of soil strata were investigated. Ansal et al. [5] performed 1D equivalent linear site response analyses using the modified version program SHAKE91 [6] based on the recorded accelerations from the Gökçeada earthquake by the Istanbul geotechnical vertical arrays (IGVA). The authors concluded that the recorded peak ground accelerations (PGA) are generally higher than the calculated values due to the simplifying assumptions of the 1D site response analysis procedure.

The objective of the present study is to compare 1D and 2D equivalent linear site response analyses on the ground surface to evaluate the need for 2D site response analysis. These comparisons would verify the role of shear wave velocity profiles as an effective factor in the site response analysis using DEEPSOIL [7] and QUAKE/W [8] computer codes. In addition, the effect of horizontal heterogeneity is investigated by 2D site response analyses.

2 Methodology

In the Istanbul Microzonation Project, geotechnical data were obtained based on 2921 soil borings with minimum depth of 30 m. Among these, there were 25 deep borings distributed over the whole area to locate the engineering bedrock and using PS logging for seismic wave velocity measurements. The engineering bedrock in all boreholes was calculated by combining geotechnical data and seismic survey profiles. The information about soil layers obtained from this project are used to perform the required analysis in the present study.

The Istanbul Rapid Response Network (IRRN) consists of one hundred free-field strong-motion stations. Fifty-five of these stations are located on the European side of the city and three Istanbul Geotechnical Vertical Arrays (IGVA) including Ataköy, Fatih, Zeytinburnu stations are located in the same area approximately five kilometers apart from each other, where very detailed site investigations were conducted during the installation of the vertical arrays (Fig. 1) [4, 5, 9].

Two medium size but distant earthquakes have been recorded by IRRN and IGVA stations. One of them was the Gökçeada earthquake of 24/5/2014 with $M_L = 6.5$, focal depth of 23 km and an epicentral distance of 166 km. All three IGVA stations (ATK, FTH, ZYT) recorded the accelerations at the bedrock level. In addition, there are acceleration records for the 23 IRRN stations located in the near vicinity. Another earthquake recorded by the three IGVA stations was the Kütahya earthquake of 19/05/2011 with $M_L = 5.7$, focal depth of 24.5 km and epicentral distance of 205 km. This earthquake was recorded by 22 IRRN stations [9, 10]. The input ground motions for 1D and 2D equivalent linear analyses are applied at the engineering bedrock level in two main directions, NS and EW. In the 2D analysis, in addition to the horizontal

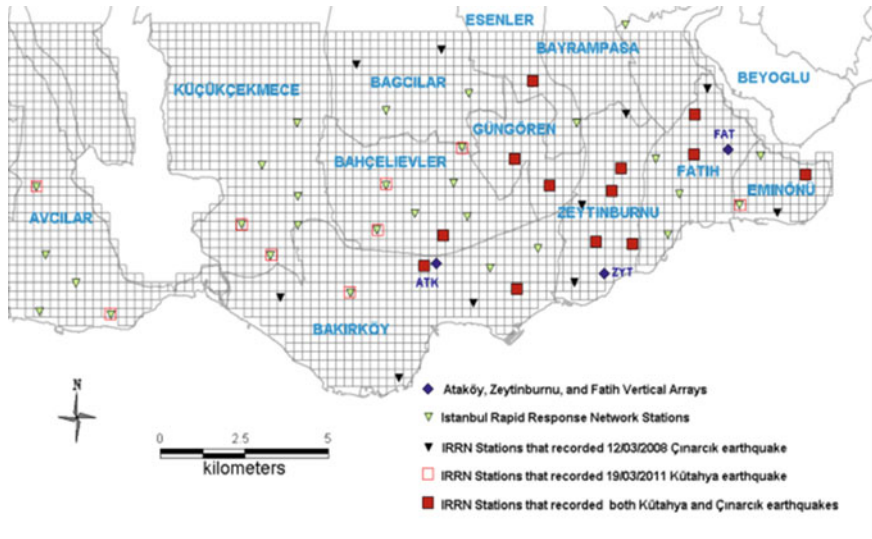


Fig. 1 IRRN and IGVA stations within the Microzonation area in Istanbul [10]

acceleration time histories, the vertical acceleration time histories are also used as input.

The one-dimensional methods are usually preferred for site response analysis. Most engineering projects designed using these methods in the past have survived earthquakes, so 1D site response methods have proven themselves and there is a belief that it provides conservative results. In addition, there are three main assumptions for this approach: all soil layers are horizontal and extend to infinity, the ground surface is level, and the input ground motions are spatially uniform, horizontally polarized shear waves that propagate vertically. There are some good reasons for using 1D analyses, such as: Stress waves propagate vertically from the bedrock toward the ground surface, while their velocity decreases. The main ground motions tend to be horizontal due to the structural design and soil layers are considered to be transversely isotropic in the horizontal direction, so the properties of soil layers can change very rapidly in the vertical direction. However, several cases have shown that the effects of location and variability of damage evaluated based on 1D site response analysis were not satisfactory [2, 10, 11].

The equivalent linear site response analysis was introduced by Schnabel et al. [12] transferring boundary; the input motion could be applied at any level of the soil layers. 1D and 2D equivalent linear site response analysis is generally performed in the frequency domain [7]. Two important advantages of equivalent linear modelling are the low computational cost and few input parameters compared to nonlinear calculations. There are common computer codes for this purpose such as SHAKE, DEEPSOIL, ERRA, Pro-Shake, GeoStudio, etc. Since the equivalent linear modelling is based on a total stress representation of soil behavior, the nonlinear stress-strain loop

is approximated by a single equivalent linear crossing of the shear modulus, which is a function of the shear strain [8].

All 1D simulations are performed using the DEEPSOIL program, based on an equivalent linear model. The EW and NS component of recorded time history acceleration at the bedrock level from Gökçeada and Kütahya earthquakes were used as inputs separately, as the bedrock motions.

As an improvement process and to reduce the difference of the spectral acceleration plots between the 1D calculated analyses and the values recorded at the IRRN stations, a Monte Carlo Simulation was performed in the range of $\pm 30\%$ of the measured values for the V_s value of each soil layer profile of the IRRN stations. First, 1000 shear wave profiles for each soil profile of the IRRN stations were generated, and then the best 30 of them were selected based on the reliability of the calculated V_s with respect to average shear wave velocity V_{s30} range, calculated shear wave velocity spikes and differences of shear wave velocities between consecutive soil layers. All calculations are based on the acceleration history records of the Gökçeada earthquake. Also, for the common IRRN stations that recorded both earthquakes, the basis of the calculations is the Gökçeada earthquake, except for the stations that recorded only the Kütahya earthquake, in which case the acceleration history of the Kütahya earthquake was used. In the next step, one-dimensional equivalent linear site response analyses are performed by using EW time history acceleration component of IGVA stations records, and the best fit with respect to the recorded spectral acceleration in EW direction is selected. The modified shear wave velocity profiles are also used as input for 2D equivalent analyses. GeoStudio-QUAKE/W software is used to model and perform 2D equivalent linear analyses. QUAKE/W is a part of the GeoStudio software. QUAKE/W is a geotechnical finite element code for analysis of ground and soil structures [8].

All required material inputs for 2D analyses are similar to 1D, for the maximum shear modulus G_{max} , required in 2D analysis, is calculated using the revised shear wave velocities. Additionally, the vertical components of the Gökçeada and Kütahya earthquakes recorded at stations ATK, FTH, and ZYT were used for the second component of the earthquakes input. The applied boundary condition for this type of analysis in the dynamic situation is a fixed horizontal displacement on the bedrock level and fixed in vertical displacement on the lateral edges. Moreover, the damping ratio for the rock level is the same as in the 1D situation. For the application of the finite element methods, the program was set to a mesh size of 10 m each. Based on the side boreholes of the main borehole, we tried to design the soil layering as accurately as possible, and if accurate information is not available, we estimated the thickness of the layers by linear interpolation considering the shear wave velocity in the layers. Considering the effects of soil profiles in horizontal distance on site response, the authors selected one IRRN station with approximately uniform soil types at approximately 1250 m apart at NS and EW toward the center of the station. This distance was then divided into 250, 500, 750, 1000, and 1500 m. Thus, the effect of site stratigraphy can be observed as an approximate relationship station.

3 Results

The recorded and calculated PGA for 1D site response analyses is compared for 45 IRRN stations. The calculated 1D results are obtained using the acceleration time history at the bedrock level of three IGVA stations of the Gökçeada and Kütahya earthquakes before and after the revision of shear wave velocities.

Figure 2 shows a comparison of the recorded and calculated PGA for 1D site response analyses on the ground surface in NS direction for the Gökçeada earthquake before and after the revision. It is easy to see that after the revision based on Monte Carlo simulations, the difference between the PGA values of the recorded and the equivalent linear 1D analyses in the NS directions decreased significantly in some stations such as AVIIO, BAVIO, and ZYTDK. This means that there is a significant variability in the measured and and/or empirically calculated V_s values. Moreover, there are large differences in soil type even at short distances. As shown in Fig. 2 in several stations the PGA and SA values are less than recorded values. This is due to simplification/approximation procedures of computer-aided programs and 1D methodologies during the analyses.

Figure 3 Compares of PGA values of 1D site response analyses calculated on the basis of records from the ATK IGVA station of Gökçeada earthquake on the ground surface after the V_s revision in NS-EW directions. The PGA values in NS direction are calculated based on improved V_s values of EW direction records. The obtained results clearly show that the difference between PGA values is not very significant. However, the presence of heterogeneity in the soil types at the sites in the normal directions leads to some disparity in site responses of the sites. At some stations, the predominant direction changed, demonstrating the importance of multidimensional investigation in studying site responses. In general, PGA values are higher in NS direction than in EW direction. Therefore, it should be considered more in the study of the mentioned zone.

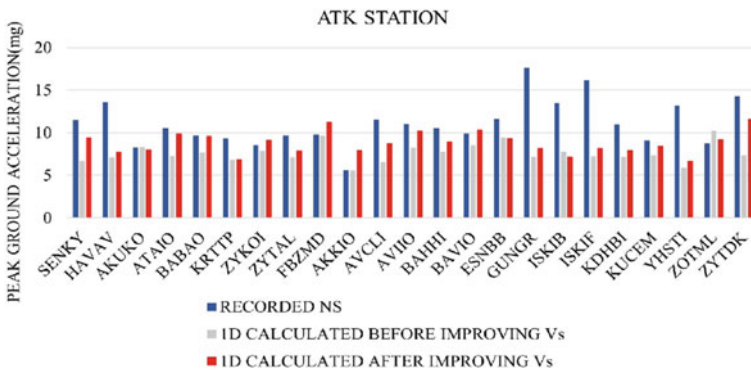


Fig. 2 Comparison of PGA recorded and 1D site response analyses calculated based records of ATK IGVA station of Gökçeada earthquake on the ground surface before and after shear wave velocity revision in NS direction

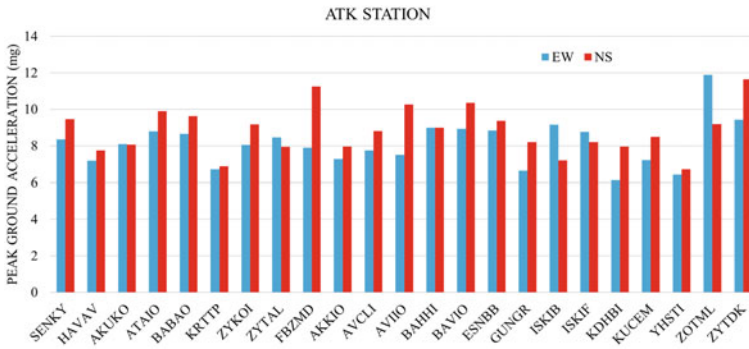


Fig. 3 Comparison of PGA values of 1D site response analyses calculated based on the records from the ATK IGVA station of Gökçeada earthquake on the ground surface after the Vs revision

The results reveal better agreement of 1D analysis for the IRRN stations closer to IGVA stations. For instance, the comparison of the recorded and calculated for the AKUKO, ATAIO and KRTPP stations are in better agreement using ATK bedrock records as the input. At the same time, regarding the spectral acceleration of all investigated IRRN stations at the bedrock level and calculated SA by equivalent linear analyses at the ground surface shows that there is a significant soil amplification in all soil profiles.

To better illustrate the role of improvement procedure to advance Vs profiles, the comparison of spectral acceleration between recorded on the ground surface, recorded at bedrock, 1D calculated before improvement, and 1D calculated after improvement are provided for one of the IRRN station i.e., KRTPP are shown in Fig. 4. The ATK-EW IGVA input data are used in this analysis. The figure shows the better fit of 1D calculated results after performing the revision of Vs profile approach regarding better capture the recorded spectral acceleration paths. Moreover, the comparison between the recorded values at bedrock level and the 1D calculated results shows a significant soil amplification presence through the soil layers in the KRTPP station.

In addition, the modeled soil profiles were analyzed with enhanced Vs values for IRRN stations of Kütahya earthquake using the Kütahya earthquake inputs. As can be seen in Fig. 5, there is an improvement in the short-period (0–0.5 s) spectral acceleration at the KRTPP station and the spectral acceleration values obtained are closer to the recorded values than before the improvement.

Furthermore, and as the main purpose of this study, calculated PGA and SA results by 1D and 2D analyses are compared with each other and reference values on the level of ground surface. It is noteworthy that for the case of 2D analyses the shear wave velocity values are enhanced using the improvement procedure as well. The difference between recorded, 1D and 2D analyses between of both earthquakes proves that 2D PGA results are more consistent with reference values rather than obtained 1D results. It should be noted that since 2D analyses has various parameters and these parameters are varying within small distances, it is not applicable to make

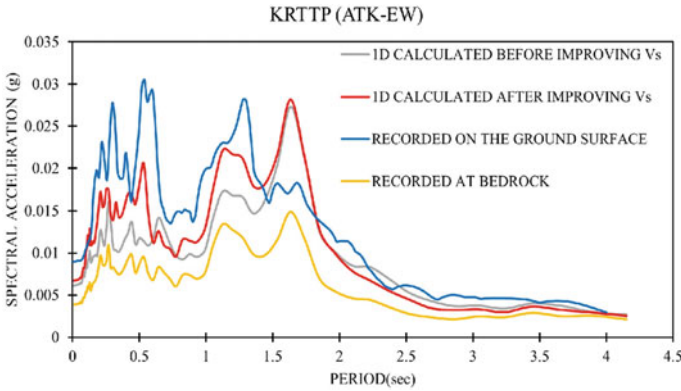


Fig. 4 Comparison of SA analyses between recorded, and 1D analyses using before and after Vs revision for KRTTP IRRN based on ATK Gökçeada records in EW direction

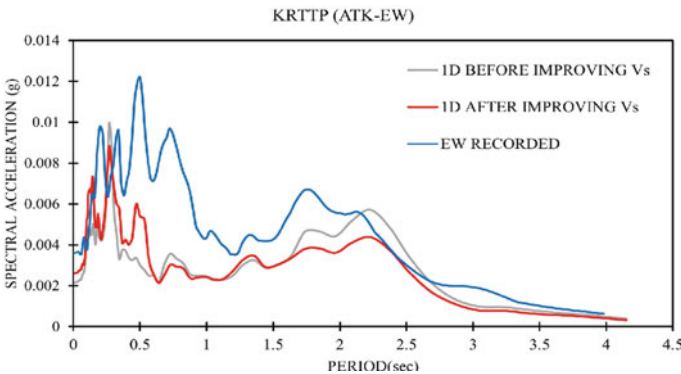


Fig. 5 Comparison of SA analyses between recorded, and 1D analyses using before and after versus revision for KRTTP IRRN based on ATK Kütahya records in EW direction

a relationship between them so There is a predictable amount of discrepancy with the recorded values. Finally, the influence of the horizontal heterogeneity on the 2D response for the selected boreholes is studied for both earthquakes. For this purpose, different symmetric distances from the borehole are chosen (i.e., 250, 500, 750, 1000, and 1250 m). Then, the optimal distance is determined by obtaining the minimum difference between the recorded and calculated SA values. It can be seen that the best convergence occurs at 750 and 1000 m away from the boreholes.

Figures 6, 7 show that the best 2D spectral acceleration results for the ATAIO IRRN station are obtained within 375 in each side totally 750 m of the borehole. In addition, it can be observed an amplification in response of the ATAIO station in terms of increasing horizontal distance. This may be due to the increasing depth of the soft soil layers around the main borehole.

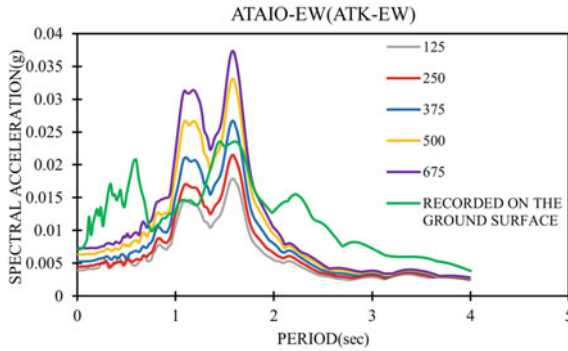


Fig. 6 Comparison of 2D site response analyses between various horizontal distances from location of ATAIO IRRN based on the records of ATK IGVA station of Gökçeada earthquake in EW direction

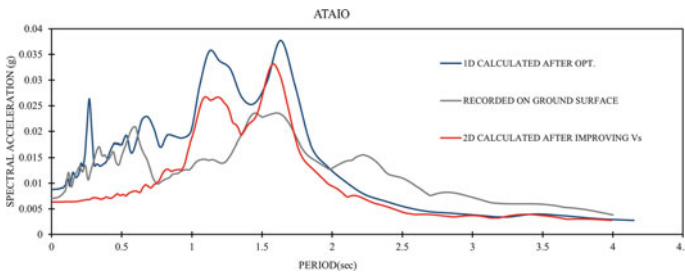


Fig. 7 Comparison of SA analyses between recorded, 1D and 2D analyses for ATAIO IRRN based on the records of ATK IGVA station of Gökçeada earthquake in EW direction

4 Conclusions

1D and 2D site response analyses of 45 different stations located in Istanbul are calculated and compared with observed earthquake acceleration records. Both 1D and 2D analyses utilize improved shear wave velocity values by a well-known optimization method so-called Monte Carlo simulation. As conclusion, the obtained results emphasize the efficiency and accuracy of 2D analysis regarding high consistency with recorded acceleration especially if the vertical arrays are closer to the considered IRRN station. In addition, this study evaluated the influence of horizontal heterogeneity for both selected earthquake records and showed that the effects of soil types and geotechnical features at horizontal extent are very significant for site response results.

Acknowledgements The financial support provided by the Scientific and Technological Research Council of Turkey (TUBITAK) under the grant No: 116M232 is greatly acknowledged.

References

1. Amoroso S, Gaudiosi I, Tallini M, Di Giulio G, Milana G (2018) 2D site response analysis of a cultural heritage: the case study of the site of Santa Maria di Collemaggio Basilica. *Bull Earthq Eng* 16(10):4443–4466
2. Govinda Raju L, Ramana GV, HanumanthaRao C, Sitharam TG (2004) Site-specific ground response analysis. *Curr Sci*:1354–1362
3. Makra K, Chávez-García FJ, Raptakis D, Pitilakis K (2005) Parametric analysis of the seismic response of a 2D sedimentary valley: implications for code implementations of complex site effects. *Soil Dyn Earthq Eng* 25(4):303–315
4. Parolai S, Ansal A, Kurtulus A, Strollo A, Wang R, Zschau J (2009) The Ataköy vertical array (Turkey): insights into seismic wave propagation in the shallow-most crustal layers by waveform deconvolution. *Geophys J Int* 178(3):1649–1662
5. Ansal MA, Kurtuluş A, Tonuk G (2014) Site response from Istanbul vertical arrays and strong motion network. In: *Proceedings of the 10th national conference in earthquake engineering*. Earthquake Engineering Research Institute (EERI)
6. Idriss IM, Sun JI (1972) 1992. Shake91, a computer program for conducting equivalent linear seismic response analysis of horizontally layered soil deposits, modified based on the original SHAKE program by Schnabel, Lysmer and Seed
7. Hashash YMA, Musgrove MI, Harmon JA, Groholski DR, Phillips CA, Park D (2016) DEEPSOIL 6.1, user manual. Urbana, IL, Board of Trustees of University of Illinois at Urbana-Champaign
8. Krahn, J.: *Dynamic modeling with QUAKE/W: an engineering methodology*. Calgary: GEO-SLOPE (2004)
9. Kurtuluş A (2011) Istanbul geotechnical downhole arrays. *Bull Earthq Eng* 9(5):1443–1461
10. Ansal A, Fercan Ö, Kurtuluş A, Tönük G (2017) 2D site response analysis of the Istanbul rapid response network. *Theme Lecture, PBD III, Vancouver*
11. Pehlivan M, Rathje EM, Gilbert RB (2012) Influence of 1D and 2D spatial variability on site response analysis. In: *Proceedings of the 15th world conference on earthquake engineering*, vol 24
12. Schnabel PB (1972) SHAKE: A computer program for earthquake response analysis of horizontally layered sites. EERC Report 72–12. University of California, Berkeley

Subsurface Study of Flowslide Liquefaction in Petobo, Palu, Indonesia



Togani Cahyadi Upomo, Muhsiung Chang, Rini Kusumawardani,
Galih Ady Prayitno, Ren-Chung Huang, and Muhammad Hamzah Fansuri

Abstract A huge flowslide due to liquefaction occurred at Petobo on September 28, 2018. Many building structures were collapsed, tilted, buried, or moved away up to a distance of 800 m or more. Flowslide occurred at slopes of around 3° and the affected area was approximately 1.64 km^2 . Magnitude and intensity of earthquake shaking, soil and groundwater conditions etc., would have contributed to the phenomena of the flowslide. Drilling, SPT with hammer energy measurements, laboratory testing on grain-size distributions and groundwater monitoring were performed after the incident. This paper discusses subsurface conditions and the assessment of liquefaction susceptibility. The geometry of ground surface was developed based on topographic survey and DTM data. Results show the materials at Petobo site consist primarily of loose silty sands and sandy silts in the middle and the debris flood areas. At the crown, the soils are mostly gravelly sands or sandy gravels. The groundwater is generally very close to the surface in the middle and the toe areas. The liquefaction susceptibility was assessed by Seed/NCEER method. At BH-1, located near the crown, liquefaction would be more susceptible in layers with depth generally more than 10 m. In the middle areas, BH-2 would likely be liquefied due to the earthquake at depth of less than 10 m. At BH-3, situated near the toe, the liquefaction susceptibility appears low, where only few separated depths are computed with low factors of safety.

T. C. Upomo (✉)

Graduate School of Engineering Science and Technology, National Yunlin University of Science and Technology (YunTech), Yunlin, Taiwan
e-mail: togani.cahyadi@mail.unnes.ac.id

T. C. Upomo · R. Kusumawardani

Department of Civil Engineering, Universitas Negeri Semarang (UNNES), Semarang, Indonesia

M. Chang · G. A. Prayitno · R.-C. Huang

Department of Civil and Construction Engineering, National Yunlin University of Science and Technology (YunTech), Yunlin, Taiwan

M. H. Fansuri

Department of Military Building, Construction Engineering, Universitas Pertahanan Indonesia (UNHAN), Bogor, Indonesia

Keywords Flowslide · Liquefaction · Subsurface exploration · Liquefaction assessment

1 Introduction

Soil liquefaction is a phenomenon of saturated sands become liquefied under transient or repeated load. When transient or repeated load is applied, the saturated sand could lose its strength or stiffness and behave like a liquid material. The increase in pore water pressure and decrease in effective strength are the main reasons for strength loss [1, 2]. Liquefaction would cause catastrophic damages to various buildings and infrastructures. Liquefaction is identified through the following phenomena, such as sand boils, lateral spreads, settlement, uplift, sinking, tilting, and buried structures, or even landslides.

During Palu Donggala earthquake ($M_w = 7.5$) on 28 September 2018, Petobo village, as seen in Fig. 1a, has suffered a dramatic flow slide due to liquefaction [4, 5]. Hundreds of buildings collapsed, tilted, buried, and moved away up to 800 m or more. The flowslide occurred at slopes of around 3° , with affected area of approximately 1.64 km^2 (Fig. 1b).

For determining subsurface conditions in Petobo, the site characterization activities include three boreholes, SPTs (Standard Penetration Test), and grain-size analyses. Figure 1b shows the study area and borehole locations, which are near the Moh. Soeharto road of the site. SPTs were conducted in the boreholes at a depth interval of 1.5 m. Additionally, grain-size as well as physical indices of soils were tested on the split spoon samples. Groundwater levels were measured weekly subsequently after the drilling.

This paper discusses the subsurface soil profile and the speculated of potential slip surface in the Petobo flowslide area. The soil profile was developed based on the boreholes, and liquefaction susceptibility zones were estimated by the Seed/NCEER method [6].

2 Seismicity

Palu city is situated on the island of Sulawesi, which is the capital of Central Sulawesi. Donggala and Sigi regencies border the northern and southern parts of Palu City. The eastern and western regions are bounded by Parigi Moutong and Donggala regencies and by Sigi and Donggala regencies [7].

Palu city is also traversed by Palu-Koro fault (PKF), which is well-known as one of Sulawesi's most active faults. In the past, several earthquakes included the 2018 Palu-Donggala earthquake, had centered on or near this fault (see Fig. 1a). PKF divides the Sulawesi island into Makassar and North Sula regions. The fault length is approximately 500 km, with an estimated slip rate of 34 mm/year [8].

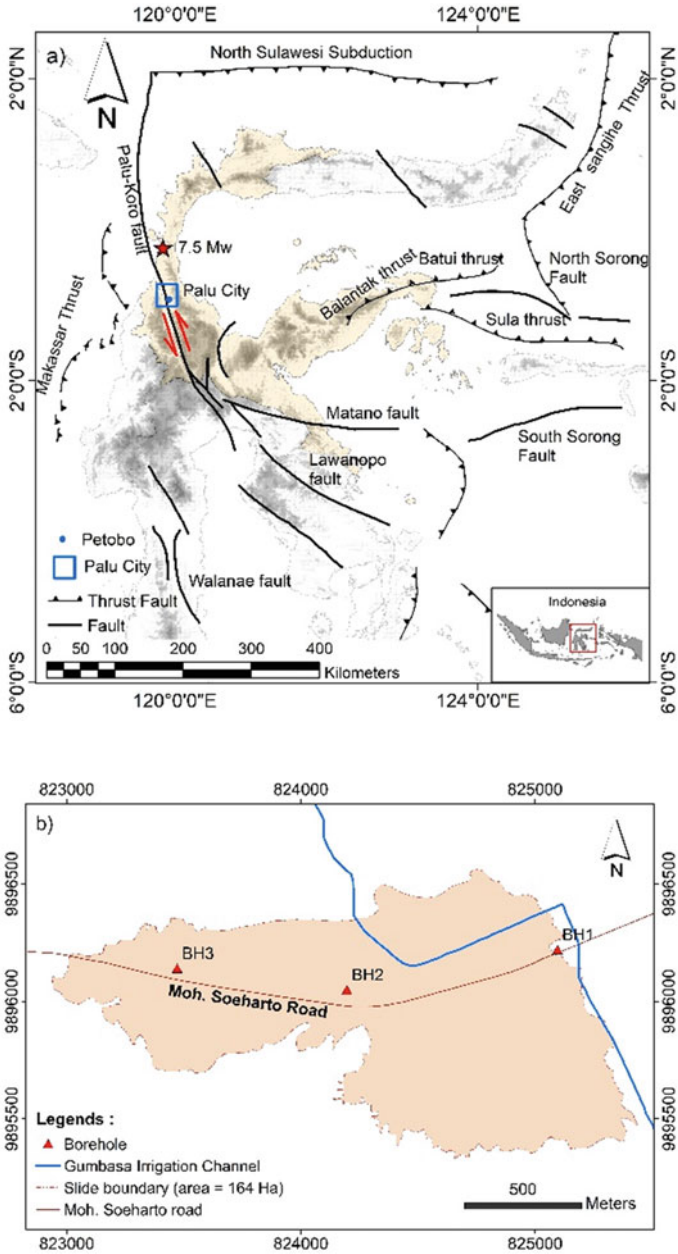


Fig. 1 **a** Regional tectonic map in Sulawesi, Indonesia and surrounding taken from [3]. Red star, blue rectangle and blue dot indicate the epicentre of main shock, locations of Palu city and Petobo village, respectively. **b** Locations of boreholes (BH-1, BH-2, and BH-3) at the Petobo flow slide area

During 2018 Palu-Donggala earthquake, MPSI (Station Mapaga, Sulawesi), located 66 km north of the mainshock, recorded a maximum peak ground acceleration (PGA) of 95.057 gal (0.142 g) in N direction [9]. However, the station of BMKG and JICA, located in Balaroa, recorded a PGA of 333 gal (0.34 g) [10].

3 Site Investigations

3.1 Soil Profile

Three boreholes (BH-1, BH-2, and BH-3) with SPTs were conducted in the slide area along Moh. Soeharto road. The soils were explored to a depth of 20–24 m. Table 1 shows the results of SPT-N and hammer energy ratio (ER) measurements. The SPT-N value and the results of ER varied about 3–71 and 58.3–77.7%, respectively. Results of the soil profiles are shown in Fig. 2.

Table 1 The SPT-N value and Energy measurements

Borehole No	SPT-N	ER (%)	ER average (%)
BH-1	8–71	59–77.7	70.9
BH-2	3–55	63.5–75.6	70.4
BH-3	4–44	58.3–69.7	64.8

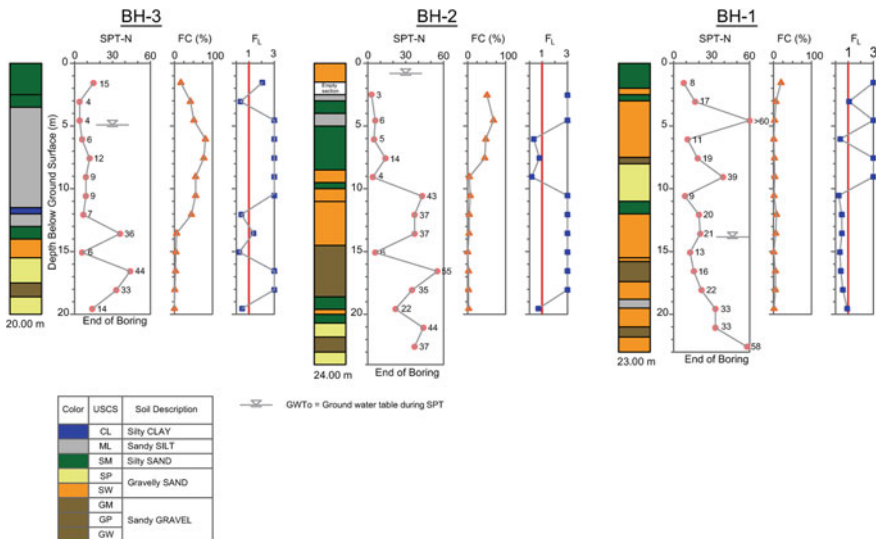


Fig. 2 SPT blow counts, fine contents and the computed safety factor in the boreholes

The soil layer in BH-1 are dominated by sand and gravel. Loose soils with N values of approximately 8–17 have been found at the top 4 m. Below this level, soils become denser with N values between 7–60. Fines content ranges from 1–20%.

The soil layer in BH-2 consists of silt and sand with fines content range of 40–70% for the top 8.5 m. N values vary from 3–14. The soils below 8.5 m are sand and gravel with N values ranged from 22–55.

At BH-3, debris materials were found at the top 2.5 m. Below the debris materials and down to 13 m deep, soils are dominated by loose to medium dense sand and silt with fines content 42–79%. N values vary from 4–12. The soil stratum below 13 m consists of sand and gravel with N values ranged 6–44.

A comparison of SPT blow counts and fines content shows that fines content appears to have a relationship with the N value. At BH-2 and BH-3 with fines content of > 20%, N values would be less than 10. In contrast, BH-1 has a fines content of < 20% and the N values would be more than 10.

3.2 Groundwater Monitoring

Groundwater levels were monitored during drilling and periodically after the drilling for a period started from 18 March 2020 to 24 March 2021.

During drilling, groundwater tables (GWTo) were measured. The groundwater tables at BH-1, BH-2, and BH-3 were –13.83, –0.82, and –4.91 m, respectively, from the ground surface.

As seen in Table 2, the average groundwater level (GWT) after drilling for BH-1, BH-2, and BH-3 are –13.18, –0.05, –3.83 m, respectively. The monitored groundwater levels of the boreholes appeared only minor changes with the values measured during the drilling.

At BH-1, located near Gumbasa irrigation canal, the GWT was found approximately 13–14 m below the ground surface. Although, three weeks after the Petobo flowslide incident, Kiyota et al. [10] observed that the GWT at area near the Gumbasa Irrigation canal was relatively close to the ground. In this case, Gumbasa irrigation canal and paddy fields had affected the GWT at this location before and during the earthquake. The water in irrigation canal and paddy fields would seep into the ground and saturate the soil. However, after the slide, Gumbasa irrigation canal dried out and GWT dropped to currently stable level of approximately 14 m below the ground surface.

Table 2 Results of groundwater table measurements (depth from ground surface)

Borehole no	GWTo (m)	Lowest GWT (m)	Average GWT (m)	Highest GWT (m)
BH-1	–13.83	–12.75	–13.18	–13.63
BH-2	–0.82	+0.34	–0.05	–0.38
BH-3	–4.91	–2.60	–3.83	–4.70

The GWT at BH-2 was <0.5 m below the ground surface. After sliding, many small ponds and swampy areas were found near the BH-2. Based on the characteristics of surface morphology, the area near BH-2 is judged to locate in the liquefaction flow area.

At BH-3, the groundwater table depth was around 4–5 m. In view of the accumulated debris materials of about 2.5 m, the GWT depth before sliding could be less than 3 m.

3.3 Liquefaction Evaluation

The liquefaction susceptibility has been analyzed using the simplified procedure by Seed/NCEER method [6] and spreadsheet program established by [11]. The liquefaction safety factor (F_L) at any depth is defined as the ratio between cyclic resistant ratio of soils (CRR) and cyclic stress ratio due to shaking (CSR), expressed as:

$$F_L = CRR/CSR \quad (1)$$

The CSR is computed with equation as:

$$CSR = 0.65 \frac{a_{max}}{g} \frac{\sigma_{v0}}{\sigma'_{v0}} r_d \quad (2)$$

where g is the acceleration due to gravity, r_d is a shear stress reduction factor, σ_{v0} is the total vertical overburden stress and σ'_{v0} is the effective vertical overburden stress. By using SPT data for clean sands, CRR can be expressed as

$$CRR_{M=7.5} = exp \left(\frac{(N_1)_{60}}{14.1} + \left(\frac{(N_1)_{60}}{126} \right)^2 - \left(\frac{(N_1)_{60}}{23.6} \right)^3 + \left(\frac{(N_1)_{60}}{25.4} \right)^4 - 2.8 \right) \quad (3)$$

where $CRR_{M=7.5}$ is the cyclic resistance ratio for a $M_w = 7.5$ earthquake and $(N_1)_{60}$ is the corrected SPT value of clean sand. The CRR and CSR should be adjusted with magnitude scaling factor (MSF) and overburden correction factor (K_σ).

The groundwater level for CRR evaluation uses the groundwater level during drilling (GWT₀) as suggested by [12]. For analysis of CSR , GWT is assigned for BH-1 by assuming 2 m below the ground surface. In view of a high groundwater table that might have been existing during the earthquake, GWTs in BH-2 and BH-3 are assumed the same level as the ground surface. The peak ground acceleration at the ground surface a_{max} is estimated as 0.30 g and the moment magnitude of Mw Palu-Donggala earthquake of 7.5 is adopted.

The computed safety factors are shown in Fig. 2. At BH-1, the soils with high liquefaction potential are at 6 and 11–18 m. Soil classifications for these depth

ranges are SP and SW. The grain-size distributions for samples of BH-1 can be seen in Fig. 3a, indicating the soils in this borehole are almost gravel and sand in size. Our onsite observations in the area around BH-1 did not clearly reveal the symptoms for soil liquefaction. However, numerous cracks and down-dropped ground surface are observable on the surface near to BH-1 area, dividing it into several soil blocks. This phenomenon could be triggered by ground shaking and/or lack of downslope support [14].

In BH-2, liquefaction is estimated to have occurred at a depth of 6–9 m, with soil classifications of SW and SM. As shown in Fig. 3b, the soils in this depth are almost silt and sand, and below 9 m then become sand and gravel. Based on our surface observations, flow liquefaction occurs in the location near BH-2. The SW and SM layers of the borehole are believed to have liquefied and the depth of about 9 m is speculated as the slip surface of this flowslide.

At BH-3, the safety factor of less than 1 occurs at depths of 12–15 m, with soil types of SM, ML, and SP. Observations on the surface of BH-3 are indicative of transported debris mixed with liquefied soils. By comparison with grading curves as shown in Fig. 3c, most of the soils are susceptible to be liquefied. The debris materials include soils, stones, and construction remains.

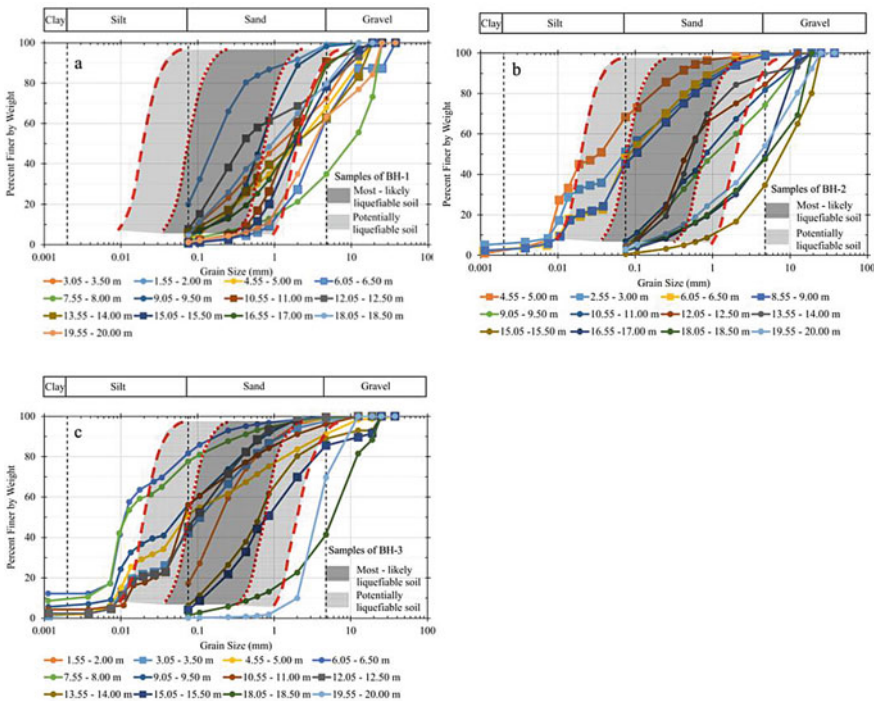


Fig. 3 Grain-size curves of SPT samples as compared with ranges of most-likely susceptible to liquefaction and potentially susceptible to liquefaction [13]

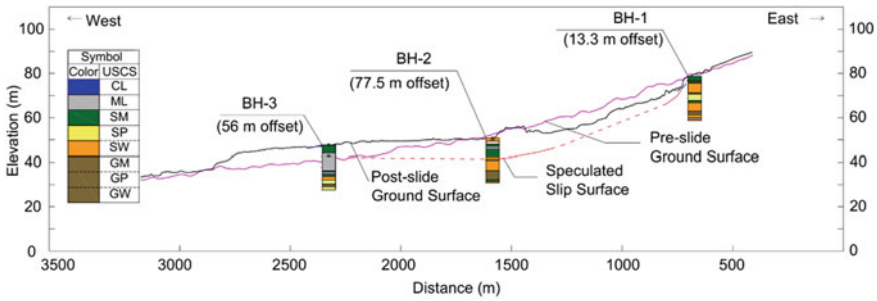


Fig. 4 Soil profile along Moh. Soeharto road. Bold red line and black line indicate post-slide and pre-slide, respectively

Figure 4 shows the soil profile along Moh. Soeharto road revealed after onsite exploration, as well as a potential slip surface estimated in association with the results of liquefaction assessment. The potential slip surface is speculated to locate with a maximum depth of approximately 13 or 10 m, respectively, below the pre-slide or post-slide ground surface.

4 Conclusions

This study aimed to reveal the subsurface conditions in Petobo sliding area. Site investigation, GWT monitoring and laboratory testing have been conducted. The study found sand, silt and gravel existed at the site. Sands and gravels dominate in the crown near irrigation canal. However, sands and silts are more often in middle and toe parts. Groundwater near the crown area would be around 14 m below the ground surface, after the earthquake and without the influence of infiltration by the canal and paddy fields. Moreover, groundwaters at middle and toe parts in the current post-slide period are close to the ground surface. The safety factor against liquefaction has been assessed by using Seed/NCEER method. At BH-1, located near the crown, liquefaction would be more susceptible in layers with depth generally > 10 m. In the middle areas, BH-2 would likely be liquefied due to the earthquake at a depth of < 10 m. At BH-3, situated near the toe, the liquefaction susceptibility would appear low and relatively stable, with only few separated depths computed with low safety factors.

References

1. Prakash S (1981) Soil dynamics. McGraw-Hill Companies, New York
2. Kramer SL (1996) Geotechnical earthquake engineering. Prentice-Hall, Upper Saddle River, New Jersey

3. Cipta A, Robiana R, Griffin JD, Horspool N, Hidayati S, Cummins PR (2016) A probabilistic seismic hazard assessment for Sulawesi, Indonesia. Geological Society, London, Special Publications
4. Irsyam M, Hanifa NR, Sahadewa A, Muntohar AS, Prakoso WA, Harninto DS, Djarwadi D, Ridwan M, Natawidjaja DH, Daryono M, Gunawan E, Meilano I, Pamumpuni A, Rudyanto A, Pramono S, Nazir R (2018) Damages associated with geotechnical problems in 2018 Palu earthquake, Indonesia. In: 20th SEAGC—3rd AGSSEA conference in conjunction with 22nd annual Indonesian national conference on geotechnical engineering, pp 5–14. Jakarta
5. Watkinson IM, Hall R (2019) Impact of communal irrigation on the 2018 Palu earthquake-triggered landslides. *Nat Geosci* 12:940–945
6. Youd TL, Idriss IM, Andrus RD, Arango I, Castro G, Christian J, Dobry R, Liam Finn WD, Leslie H, Hynes ME, Ishihara K, Koester J, Liao S, Marcuson WF, Martin GR, Mitchell JK, Moriwaki Y, Power MS, Robertson PK, Seed RB, Stokoe KH (2001) Liquefaction resistance of soils: summary report from the 1996 NCEER and 1998 NCEER/NSF workshops on evaluation of liquefaction resistance of soils. *J Geotech Geoenviron Eng* 127:817–833
7. BPS (2020) Palu municipality in figures 2020. BPS—statistics of Palu municipality. Palu
8. Walpersdorf A, Vigny C, Subarya C, Manurung P (1998) Monitoring of the palu-Koro fault by GPS. *Geophys Res Lett* 25:2313–2316
9. BMKG (2018) Ulasan guncangan tanah akibat gempa bumi Donggala 28 September 2018. In: BMKG. [https://www.bmkg.go.id/berita/?p=ulasan-guncangan-tanah-akibat-gempabumi-utara-donggala-sulteng-28-september-2018&lang=ID&tag=ulasan-guncangan-tanah](https://www.bmkg.go.id/berita/?p=ulasan-guncangan-tanah-akibat-gempabumi-utara-donggala-sulteng-28-september-2018&lang=ID&>tag=ulasan-guncangan-tanah). Accessed 24 Aug 2019
10. Kiyota T, Furuichi H, Hidayat RF, Tada N, Nawir H (2020) Overview of long-distance flow-slide caused by the 2018 Sulawesi earthquake, Indonesia. *Soils Found* 60:722–735
11. Chang M (2020) Soil liquefaction analysis spreadsheet program V05
12. Chang M, Chan MS, Huang RC, Upomo TC, Kusumawardani R (2020) Assignment of groundwater table in liquefaction analysis of soils. In: Proceedings of GeoMEast 2020. Giza, p 17
13. Tsuchida H, Hayashi S (1971) Estimation of liquefaction potential of sandy soils. In: Proceedings of the 3rd joint meeting, US–Japan Panel on wind and seismic effects. UJNR, Tokyo, pp 91–109
14. Kusumawardani R, Chang M, Upomo TC, Huang RC, Fansuri MH, Prayitno GA (2021) Understanding of Petobo liquefaction flowslide by 2018.09.28 Palu-Donggala Indonesia earthquake based on site reconnaissance. *Landslides* 18(9):3163–3182

Deformation of Earthquake Resistant Gravel-Tire Chips Mixture as Drains



Yutao Hu and Hemanta Hazarika

Abstract Gravel-tire chips mixture (GTCM) as an alternative geomaterial has been introduced in recent years. In addition to its low-carbon-released characteristics, other advantageous material characteristics include lightweight, excellent vibration absorption capability, and high permeability. A newly designed earthquake-induced liquefaction mitigation countermeasure has been proposed. This so-called GTCM drains technique utilized GTCM as the material for precast drains installed around existing infrastructures located on the liquefiable ground. During the earthquake, the excess pore water could be dissipated through the drains, therefore, mitigating the potential of liquefaction. However, the deformation characteristics which has a significant influence on foundation settling post-earthquake, are not clearly researched on such improved ground. In this research, based on modelling experiment on 1-g shaking table, Particle Image Velocimetry (PIV) has been used to track and analyse the deformation of the ground foundation during dynamic loadings. The results indicate that with GTCM drains installed, the movement and acceleration of the foundation beneath the on-surface structure were limited. Meanwhile, the excess pore water pressure increased much slower due to the combined effect of drainage and less ground deforming. This study on the deformation characteristics proves the effectiveness of such liquefaction mitigation technique from another perspective.

Keywords Liquefaction mitigation · GTCM drains · Ground deformation · PIV

1 Introduction

Every year, approximately 1 billion waste tires are produced in various parts of the world. In Japan, according to the report by JATMA [6], the total number of end-of-life tires produced was 86 million, which was near 1 million tons by weight in 2020. To recycle such industrial waste, scrap tire-derived materials (STDMS) have been utilized as geomaterials in recent years. In addition to its low-carbon-release

Y. Hu (✉) · H. Hazarika
Kyushu University, 744 Motoooka, Nishi-Ku, Fukuoka 819-0382, Japan
e-mail: hu.yutao.594@s.kyushu-u.ac.jp

© The Author(s), under exclusive license to Springer Nature Switzerland AG 2023
C. Atalar and F. Çinicioğlu (eds.), *5th International Conference on New Developments in Soil Mechanics and Geotechnical Engineering*, Lecture Notes in Civil Engineering 305, https://doi.org/10.1007/978-3-031-20172-1_40

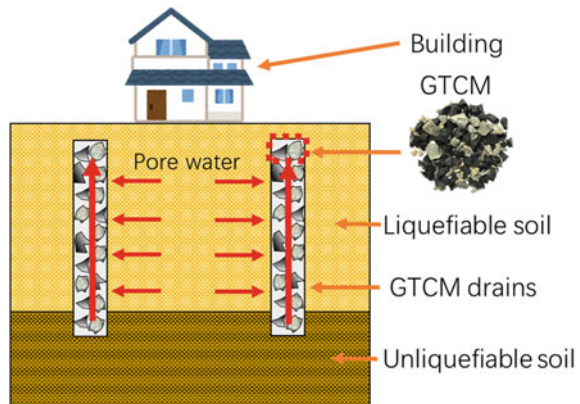
413

characteristics when used as geomaterials, other advantageous material characteristics of STDM include lightweight, excellent vibration absorption capability, and high permeability. Furthermore, unlike other granular geomaterials, these materials are non-dilatant in nature [1]. They can replace other traditional materials (such as gravel) in applications such as drainage, leachate removal in landfills, soil reinforcement, and so on because of these characteristics. Gravel-tire chips mixture (GTCM), as an alternative geomaterial, has been introduced by Hazarika et al. [2].

One of Large-scale earthquake-induced hazards, liquefaction, has become much too common in recent years, especially in Japan. During the 2016 Kumamoto Earthquake, as an example, several areas in the southern part of Kumamoto City experienced liquefaction causing damage to residential houses due to differential settlement [3]. To prevent the extreme damage to buildings caused by liquefaction during earthquakes, an appropriate and cost-effective disaster mitigation technique called GTCM drains has been proposed (Fig. 1). It utilized GTCM as material of precast drains installed around existing infrastructures located on liquefiable ground. During earthquake, the excess pore water could be dissipated through the drains therefore mitigate the potential of liquefaction.

In this paper, the deformation characteristics which has significant influence on foundation settling post-earthquake on GTCM drains improved ground are researched. Model test using 1-g shaking table facility was performed. Particle Image Velocimetry (PIV) has been used to track and analyse the deformation of ground foundation during dynamic loadings.

Fig. 1 Principle of GTCM drains technique



2 Model Experiment

2.1 Test Model

Model test was conducted using the 1-g shaking table facility at the geo-disaster laboratory of Kyushu University as shown in Fig. 2. Soil-structure-fluid interaction can be simulated using the scaling law proposed by Iai [5]. Since this research involves liquefaction induced damage to on-surface structure, it is the most suitable similitude relationship. A geometrical scaling factor of 1:32 was set based on this law in this model test.

Toyoura sand was used as foundation soil in these tests. A dense layer of such sand ($D_r = 90\%$, 200 mm in depth) representing non-liquefiable ground was constructed using both dry deposition and tamping techniques. The upper liquefiable layer ($D_r = 50\%$, 300 mm in depth) was constructed only using dry deposition technique. The saturation process could be performed by percolating water gradually and uniformly through 3 water inlets from the bottom of the container. GTCM with volumetric gravel fraction of 50% was used to make drains. The properties of the materials are shown in Table 1.

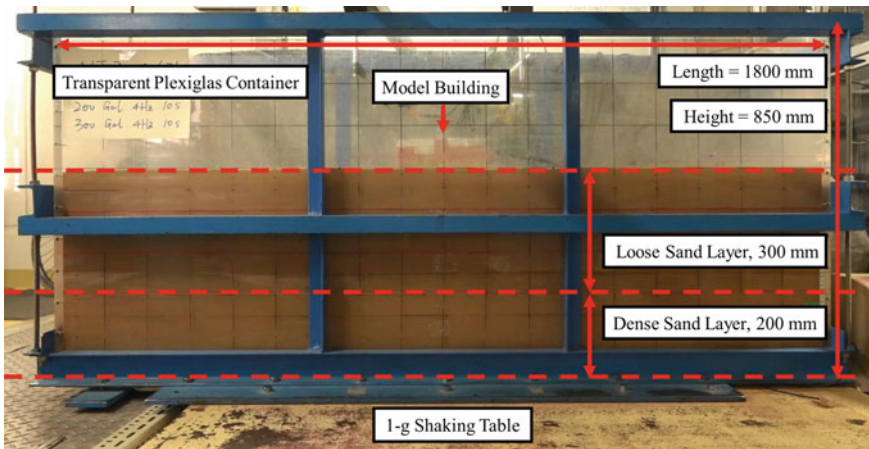


Fig. 2 Test model on 1-g shaking table

Table 1 Properties of materials in used

Material	G_s	Dry density (g/cm^3)	ρ_{max} (g/cm^3)	ρ_{min} (g/cm^3)	D_{50} (mm)
Toyoura sand	2.640	1.506	0.976	0.611	0.160
GTCM	1.910	1.022	1.036	0.842	4

2.2 Test Conditions

Figure 3 shows the layout of the test model in this research. Six vertical GTCM drains are arranged symmetrically along the long side of the model building, installed from the surface level up to the bottom of the loose sandy layer, and extended into the hard layer. Another four GTCM drains are inserted at 60 degrees diagonally along the short side of the model building. The diameter of these prefabricated GTCM drains is 50 mm with a height of 300 mm. Since heavy building could settle more due to its weight rather than the influence of liquefaction [4], a shallow foundation of a building with a bearing pressure of 3 kPa, represented by a rectangular block of brass material, with a cross-sectional area of 230×100 mm in model scale, is set upon the soil. In addition, there is a thick layer of gravel with 2 cm in depth between the model building and GTCM drains. A sinusoidal acceleration of 200 Gal with the frequency of 4 Hz and duration of 10 s is applied to the model. Several pore water pressure transducers are set in the location shown in Fig. 3b. Two motion analysis marks are located at two side of the model building.

3 Results and Discussion

3.1 Settlement

The model building suffered settlement due to the deformation of the loose sand foundation, as shown in Fig. 4a. Through motion analysis, the time history and trend of the building settling are obtained and drawn out in Fig. 4b. At D1, the maximum settlement is 37.45 mm. While at the other side (D2), the value is recorded as 32.32 mm. The rotation due to the uneven settlement was about 1.28° .

3.2 Excess Pore Water Pressure Ratio

Figure 5 shows the time history of excess pore water pressure ratio, defined as $R_u = u_{exp}/\sigma_{vo}$, recorded by PPTs at each location inside the loose sandy layer (shown in Fig. 3b). As a benchmark, in the shallow layer of free-field, with no influence from any drains, only P4 reaches the fully liquefied value of 1. Other than that, the R_u initiates a speedy increase as the earthquake started and remains in high value until the end of shaking at P3, P4, P7 and P8. On the contrary, the R_u at P1, P2, P5 and P6, surrounded by GTCM drains, remains at a low level. The GTCM drains, therefore, did effectively dissipate the excess pore water and make a great effort in preventing liquefaction. Since liquefaction was not observed beneath the building, the settlement described in the previous section is assumed to be caused only by the loose soil consolidation.

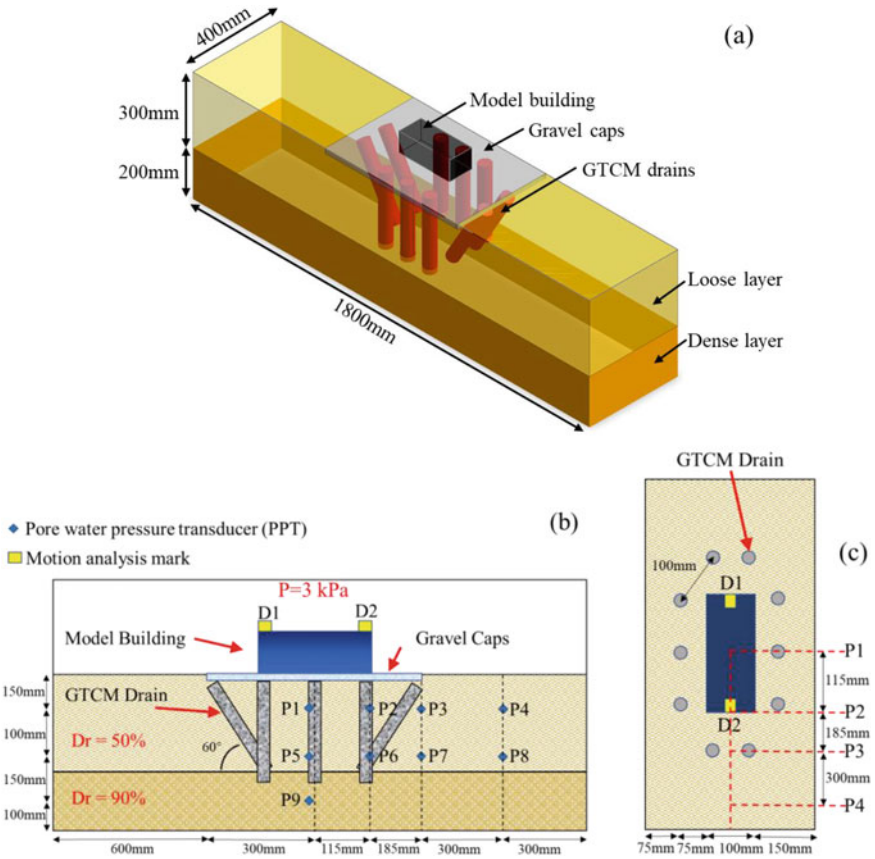
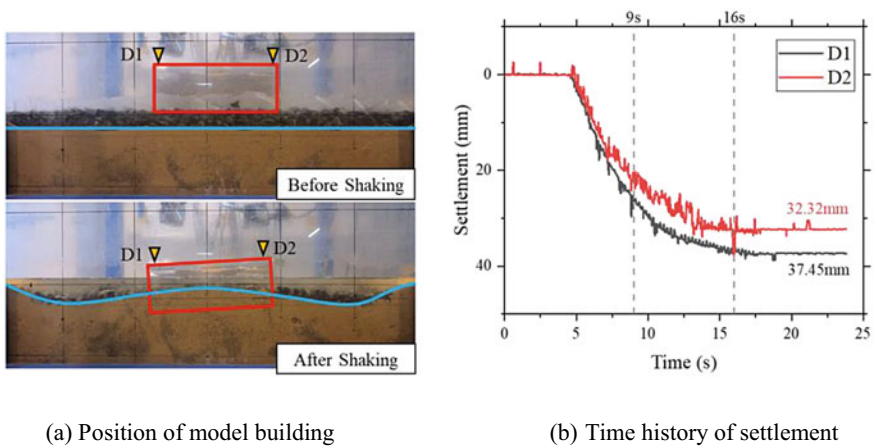


Fig. 3 Layout of test model: a 3D view; b Front view; c Top view



(a) Position of model building

(b) Time history of settlement

Fig. 4 Settlement of model building

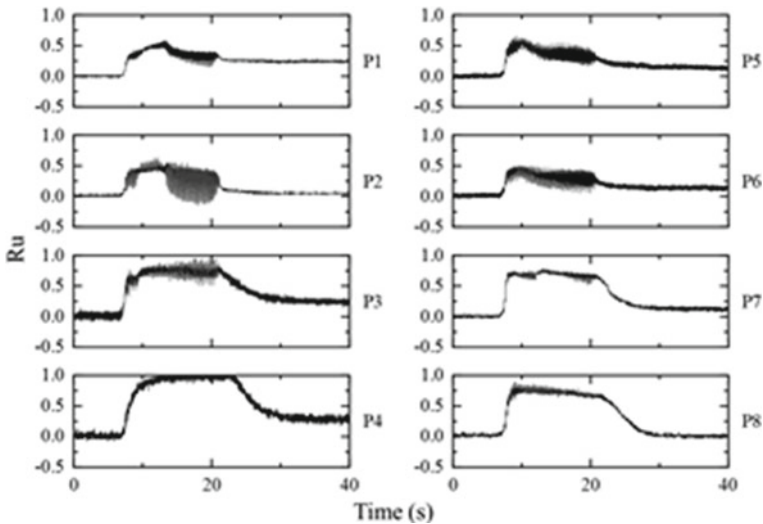


Fig. 5 Time history of excess pore water pressure ratio

3.3 Velocity Fields

Figure 6 depicts velocity fields during two cycles of sinusoidal dynamic loading, obtained from PIV analysis. The analyze area is 400×70 mm. Large velocities are observed in the loose sand soil foundation accompanied by the sinusoidal accelerating of the shaking table. Figure 6a shows the velocity field in a cycle after the shaking table reached the acceleration of 200 Gal ($t = 9$ s). As the shaking continued, the consolidation of the loose sandy ground results in the settling of the model building. The soil is also found to be pushed upward into the gravel cap layer simultaneously. As a comparison, Fig. 6b shows the velocity fields in a cycle during the post-consolidation phase ($t = 16$ s). Though large velocities are observed in areas, the foundation rocks much more slightly. Indeed, the velocity under the foundation is negligible compared to that further away, as well as the cycle described in Fig. 6a. However, due to the rotations of the shallow foundation, the upper soil of inclinedly-installed GTCM drains deforms more significantly. The after-deformation foundation surface, on the other hand, has the similar shape of the velocity fields of the soil beneath.

4 Conclusions

In this study, the deformation characteristics of GTCM drains improved ground under existing building was carried out through model test. The results indicate that with GTCM drains installed, the movement and deformation of foundation beneath the on-surface structure could be limited, especially during the post consolidation

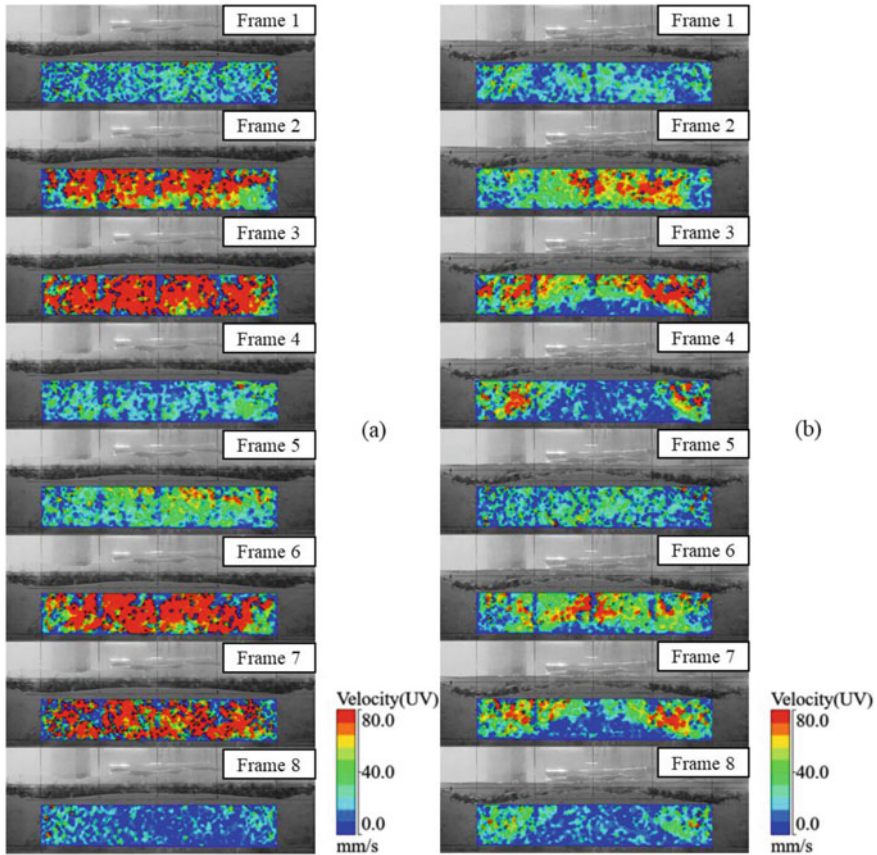


Fig. 6 Velocity fields of a dynamic cycle at: **a** $t = 9$ s; **b** $t = 16$ s

phase. Meanwhile, the excess pore water pressure increased much slower due to the combined effect of drainage and less ground deforming. However, the influence of GTCM drains arrangement to the ground deformation is significant. To figure out the deformation situation beneath the foundation, which could not be observed through model tests, the Finite Elements Method would be used to do numerical simulation in the following research. This study on the deformation characteristics proves the effectiveness of such liquefaction mitigation technique from another perspective.

Acknowledgements The authors would like to acknowledge the financial support provided by Kyushu University under Progress 100 project. This study was also supported by JST SPRING, Grant Number JPMJSP2136. Thanks to Mr. Yuichi Yahiro, technical assistant of Geo-disaster Prevention Laboratory of Kyushu University, for his help and support while conducting experiments.

References

1. Hazarika H (2013) Paradigm shift in earthquake induced geohazards mitigation-emergence of nondilatant geomaterials. In: Keynote lecture for the annual conference of Indian geotechnical society. Roorkee, India
2. Hazarika H, Abdullah A (2016) Improvement effects of two and three dimensional geosynthetics used in liquefaction countermeasures. *Jpn Geotech Soc Spec Publ* 2(68):2336–2341
3. Hazarika H, Kokusho T, Kayen RE, Dashti S, Fukuoka H, Ishizawa T, Kochi Y, Matsumoto D, Furuichi H, Hirose T, Fujishiro T, Okamoto K, Tajiri M, Fukuda M (2017) Geotechnical damage due to the 2016 Kumamoto earthquake and future challenges. *Lowl Technol Int* 19(3):189–204
4. Hu Y, Hazarika H, Pasha SMK, Haigh SK, Madabhushi GSP (2021) Effect of bearing pressure on liquefaction-induced settlement in layered soils. In: Hazarika H, Madabhushi GSP, Yasuhara K, Bergado DT (eds) *Advances in sustainable construction and resource management*, vol 144. *Lecture Notes in Civil Engineering*. Springer, Singapore, pp 261–270
5. Iai S (1989) Similitude for shaking table tests on soil-structure-fluid model in 1g gravitation field. *Soils Found* 29(1):105–118
6. Japan Automobile Tyre Manufacturers Association (2021) Tyre industry of Japan. Retrieved from http://www.jatma.or.jp/media/pdf/tyre_industry_2020.pdf

Special Subjects in Geotechnical Engineering

Evaluation of Relationships Between Strength Properties of Rock Samples and Drilling Rate Index



Efe Aslan, Hakan Köpüklü, and H. Turan Durgunoğlu

Abstract A comprehensive subsurface investigation program was conducted to delineate the soil, rock and groundwater conditions in subject area of the project site located in Gulf Region consisted mainly of land-based geotechnical drilling. In the scope of this study, the onshore site characterization is based on an integrated approach that combines the site specific data collected from borings, field and laboratory tests. Within the scope of laboratory studies, relationships between strength properties of rock samples and drilling rate index were examined. For this purpose, uniaxial compression test, Schmidt hammer rebound test and drillability test were conducted for the rock samples which were collected from different rotary drilling boreholes. The experimental studies have shown that the drilling rate index (DRI) decreases with the increasing uniaxial compressive strength (UCS) and Schmidt Hammer Rebound Hardness (SHRH).

Keywords Drilling rate index · Brittleness test · Sievers' J-Miniature drill test · Uniaxial compressive strength · Schmidt hammer rebound hardness

1 Introduction

An accurate estimation of drillability became a mandatory factor in planning, design and construction stages of underground projects. For the excavation phases in mining, tunneling and underground constructions, drilling progress, cutter wear and related costs are becoming compulsive elements [5]. Therefore, in parallel with the accurate estimations, rock cutting tools and equipment may be optimized and drilling rate may provide beneficial data for underground excavations such as using tunnel boring machines (TBMs) or other excavators. Selection of these tools without physical, mechanical, and mineralogical information of the planned construction area can cause major problems for all stages of projects.

E. Aslan (✉) · H. Köpüklü · H. T. Durgunoğlu
Zemin Etüd ve Tasarım A.Ş., Istanbul 34794, Turkey
e-mail: efe.aslan@zeminas.com.tr

© The Author(s), under exclusive license to Springer Nature Switzerland AG 2023
C. Atalar and F. Çinicioğlu (eds.), *5th International Conference on New Developments in Soil Mechanics and Geotechnical Engineering*, Lecture Notes in Civil Engineering 305, https://doi.org/10.1007/978-3-031-20172-1_41

Kahraman et al. [8], investigated the percussive blast hole drills in eight rock types and showed that uniaxial compressive strength (UCS), Brazilian tensile strength, point load strength and Schmidt hammer value were the dominant rock properties affecting the penetration rate of percussive drills. Yarali and Soyer [11], focused on relationships between DRI and strength properties were evaluated and stated that decreasing linear relationships were constituted between DRI and UCS, Schmidt rebound hardness, Shore scleroscope hardness, diametral and axial point load strength values. Adebayo and Adetula [1], conducted laboratory tests and stated that that UCS, texture and grain size, DRI and Equivalent Quartz Content (EQC) are important pa-rameters which affect drilling conditions. Demirdag et al. [7], studied the factors affecting the drilling rates in terms of physical and mechanical properties of the rocks. Uniaxial compressive strength, Brazilian tensile strength, impact strength, Bohme abrasion strength, P-wave velocity, porosity, unit volume weight, Schmidt hardness index and brittleness index values were correlated with the drilling rates. Shafique and Bakar [10], evaluated relations between DRI tests and porosity, density, P-wave velocity, UCS, Brazilian tensile strength and Schmidt hammer rebound number. Capik et al. [3], stated that DRI decreases with increasing UCS, point load strength, Bra-zilian tensile strength, and Schmidt rebound hardness. Yenice et al. [13], stated that correlations were found between DRI and uniaxial compressive strength and indirect tensile strength values. Yenice [14], studied the relation between UCS, Brazilian tensile strength and the DRI were determined using multiple regression analysis. Kamran [9], constituted a model for the evaluation of DRI by using the uniaxial compressive strength, Brazilian tensile strength, brittleness test, and Sievers' J-miniature drill values.

2 In-Situ Applications

2.1 Project Site Information

A comprehensive subsurface investigation program was conducted to delineate the soil, rock and groundwater conditions in subject area of the project site located in Gulf Region consisted mainly of land-based geotechnical drilling. Project site location is given in Fig. 1.

Wireline rotary drilling method has been employed utilizing PQ3 type core barrel equipment to generate high quality core samples with better core recovery. Exploratory boreholes were drilled vertically by rotary wash boring method producing core samples with nominal core diameter of 82 mm. A continuous coring was performed as per the BS 5930:2015. Core samples retrieved through each run were photographed first to show in situ position and orientation of cores without disturbance and then logged by geologist. The rock parameters were measured in-situ by the geologists. Samples were wrapped with plastic stretch to preserve natural water



Fig. 1 Project site location

content and were placed in proper core boxes for delivery purposes to laboratory. Appropriate sample selections were made for the laboratory tests.

2.2 Geotechnical Formations

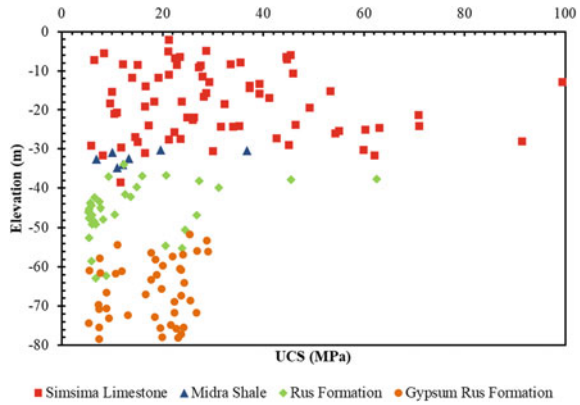
Cavelier [4], presented the basic structure for the project site. The formations of the Gulf region are entirely of Tertiary to Quaternary age. The subsurface soil/rock stratigraphy in project area, as encountered in the geotechnical boreholes presented in Table 1.

The greater part of the land consists of a uniform limestone horizon of middle Eocene age, the Simsima Limestone. The Simsima Limestone forms part of the Upper Dammam Formation and is underlain by the Midra Shales member of the Lower Dammam Formation from middle Eocene in age. This is in turn underlain by the Rus Formation, which is lower Eocene in age. The solid geology is overlaid by shallow cover of loose to medium dense silty, gravelly sand.

Table 1 Range of approximate observable thickness of formations encountered in boreholes

Geotechnical Formations	Observable thickness range encountered in boreholes	
	Minimum (m)	Maximum (m)
Fill Material/Made Ground	0.20	0.50
Quaternary Aeolian Sand	0.30	11.90
Quaternary Cap Rock	1.35	8.75
Weathered Simsima Limestone	0.30	7.50
Simsima Limestone	26.45	38.75
Midra Shale	1.70	5.90
Rus Formation Limestone	5.10	25.10
Rus Formation Gypsum	7.80	25.50

Fig. 2 Uniaxial compressive strength test results



3 Experimental Research

In the scope of this experimental research, rock samples which were collected from different formations were examined. Drillability tests, uniaxial compressive strength tests and Schmidt hammer rebound hardness tests were conducted to evaluate the relationships between strength properties and drilling rate index of rock samples.

3.1 Uniaxial Compressive Strength Test

Uniaxial compression tests were performed on 157 rock core samples which had a diameter of PQ size (82 mm) and length to diameter ratio of 2.0–2.5. The stress rate was applied within the limits of 0.5–1.0 MPa/s in accordance with ASTM D7012. Test results are given in Fig. 2.

In addition to that, compressive strength and elastic moduli of intact rock core tests were performed on 115 samples. Modulus of elasticity (E) was determined as the average value of tangent modulus of elasticity and secant modulus of elasticity. Poisson's ration (μ) determined as the ratio of the Modulus of elasticity (E) and slope of diametric curve. Test results are given in Fig. 3.

3.2 Schmidt Hammer Rebound Hardness Test

Schmidt hammer rebound hardness tests were performed on 95 rock specimens. Proceq silver rock L-Type Schmidt hammer having impact energy of 0.74 Nm was used in accordance with the ISRM. The orientation of hammer was on vertical downwards position and 20 impacts were conducted and separated by at least the diameter of the plunger. The lower %50 of the rebound values were eliminated and the average

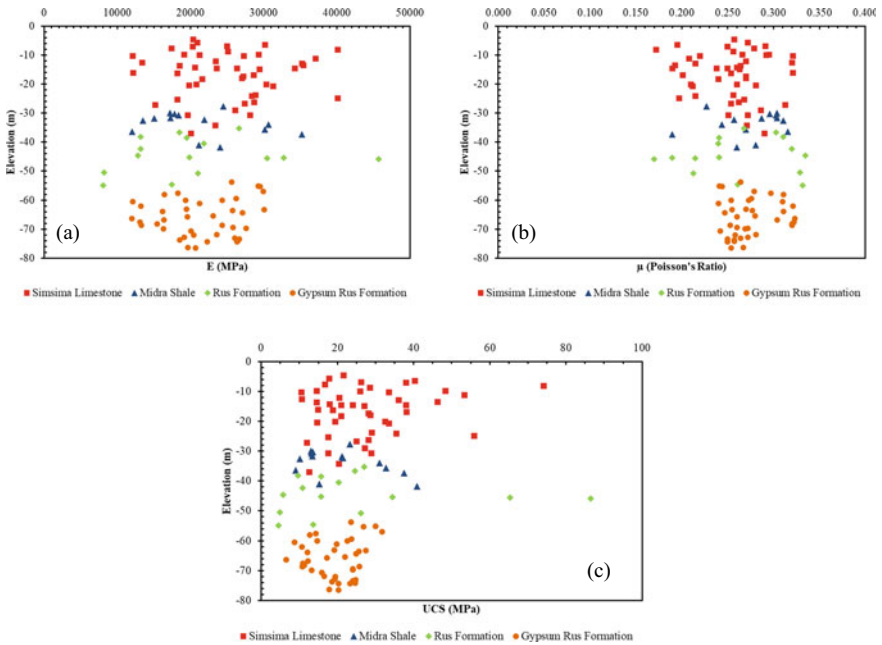
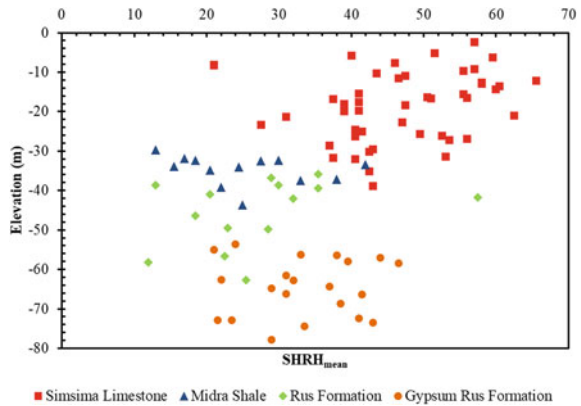


Fig. 3 Uniaxial compressive strength test results **a** E (MPa), **b** Poisson's ration (μ), and **c** UCS (MPa)

value was recorded as the Schmidt hammer rebound hardness ($SHRH_{mean}$) number. Test results are given in Fig. 4.

Fig. 4 Schmidt hammer rebound hardness test results



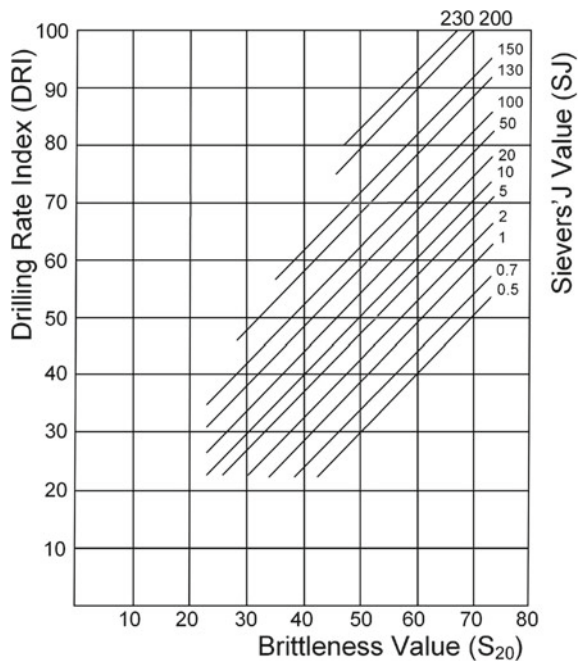
3.3 Drillability of Rock Core Samples

NTNU/SINTEF drillability test method was developed at the Department of Geology and Mineral Resources Engineering at NTNU in 1960s for evaluating drillability of rocks by percussive drilling [11]. The Drilling Rate Index (DRI) is assessed on the basis of two laboratory tests, the Brittleness Value (S_{20}) test and the Sievers' J-Value (SJ) miniature drill test. These indices are recognized as providing practical characterization of rocks applicable in time and cost prediction models available for hard rock tunneling and surface excavation. The chart which determines DRI value is given in Fig. 5.

Sievers' J-Miniature Drill Test. The Sievers drill test was developed by Sievers in the 1950s for estimating cutter life [12]. The Sievers' J-value is determined by using a rock sample drilled for a minute with 200 revolutions per minute of the 8.5 mm miniature drill bit under 20 kg of static load. Thereafter, the drill hole height was measured. SJ-value is determined as the mean value of the measured drill hole depth in 1/10 mm of 4–8 repetitive drill holes.

Brittleness (S_{20}) Test. The brittleness test was developed in Sweden for evaluation of the quality of aggregates [11]. The S_{20} value shows the resistance of a rock specimen to mechanical impacts. Rock sample was crushed in a jaw crusher and sieved through the 16 mm and 11.2 mm sieves. Crushed and sieved rock sample is used for the test. A hammer of 14 kg was dropped on the mortar containing rock material for 20

Fig. 5 Drilling rate index chart [6]



times. This procedure was repeated for three to five times for each rock sample. Afterwards, rock material was sieved through an 11.2 mm sieve. The percentage of material passing the sieve was determined as the S_{20} value [6].

Drilling Rate Index (DRI). Figure 5 was used for the evaluation of drilling rate index (DRI) which includes the brittleness value (S_{20}) and the Sievers' J-value (SJ_{mean}). The classification of each sample is given in Table 2.

4 Evaluation of Experimental Research

In this experimental research, 20 different rock core samples were tested for the drilling rate index in the laboratory. In order to evaluate the relations between strength properties of rock samples and DRI, the closest uniaxial compression test and Schmidt hammer rebound hardness test results were selected within a range of ± 2.0 m distance from the DRI test samples. The correlations between DRI and strength parameters of the rock samples are stated in Fig. 6. UCS results range from 5.8 to 55.9 MPa, modulus of elasticity range from 12,120 to 40,132 MPa, Poisson's ratio range from 0.197 to 0.335, Schmidt hammer rebound hardness range from 13 to 58. It was observed that the DRI values of all the tested rock specimens classified from medium to extremely high. DRI values of rus formation samples were classified as extremely high. In addition to that, gypsum samples were classified between high to extremely high. Dolomitic limestone samples were classified as medium to high.

5 Conclusions

The performance and cost evaluations in tunneling, mining and other underground projects are commonly attributed to drillability of rocks. Intact rock properties have a significant part in excavation.

In this study, the correlations between DRI and strength properties of rocks were investigated. Rock samples were collected from different geotechnical formations and the properties of all samples were determined by laboratory experiments. Then, correlations between these results were obtained. The DRI decreases with increasing UCS, $SHRH_{\text{mean}}$ and E. In addition to this, DRI increases with increasing Poisson's ratio. After all these interpretations, it can be stated that DRI and strength parameters can represent well correlations, although further studies should be conducted for improving these results. Further studies could investigate the mineralogical properties of rocks in order to determine their influences on the DRI. The estimation of the DRI could also be associated with in-situ tests by executing diagraphy drilling. Thus, experimental results could be supported with the field data where drilling speed (m/h) could be correlated with the varying geotechnical formations.

Table 2 Drillability tests summary

No	Depth (m)	Elevation (m)	Lithologic Unit	Formation	S ₂₀	SJ	DRI	Class
1	28.20	-26.45	Dolomitic Limestone	Simsima Limestone	58	84.80 ± 8.81	68	High
2	27.00	-25.28	Dolomitic Limestone	Simsima Limestone	44	92.00 ± 10.56	54	Medium
3	17.80	-16.01	Dolomitic Limestone	Simsima Limestone	47	89.60 ± 37.43	58	High
4	16.50	-13.61	Dolomitic Limestone	Simsima Limestone	53	78.8 ± 19.02	66	High
5	16.10	-13.52	Dolomitic Limestone	Simsima Limestone	37	111.25 ± 1.66	50	Medium
6	26.30	-23.72	Dolomitic Limestone	Simsima Limestone	42	104.00 ± 1.65	56	Medium
7	19.90	-18.21	Dolomitic Limestone	Simsima Limestone	56	95.80 ± 20.63	67	High
8	24.50	-21.35	Dolomitic Limestone	Simsima Limestone	54	83.80 ± 0.78	66	High
9	38.00	-36.08	Mudstone	Rus	75	158.00 ± 39.60	96	Extremely high
10	35.00	-33.56	Mudstone	Rus	72	124.25 ± 37.14	86	Extremely high
11	49.80	-47.73	Calcarenite	Rus	77	154.40 ± 2.92	96	Extremely high
12	54.90	-51.75	Calsisiltite	Rus	77	97.67 ± 0.40	88	Extremely high
13	36.80	-32.69	Limestone	Midra Shale	55	109.80 ± 0.61	70	High
14	46.10	-42.95	Limestone	Midra Shale	54	82.60 ± 0.59	65	High
15	58.60	-57.16	Gypsum	Gypsum Rus	59	86.80 ± 4.97	69	High
16	58.50	-56.71	Gypsum	Gypsum Rus	65	157.00 ± 37.42	92	Extremely high
17	67.70	-64.81	Gypsum	Gypsum Rus	57	79.60 ± 2.51	67	High
18	57.10	-55.41	Gypsum	Gypsum Rus	56	136.80 ± 12.79	74	Very high
19	65.00	-60.89	Gypsum	Gypsum Rus	53	151.25 ± 3.40	76	Very high
20	71.30	-68.15	Calsisiltite	Gypsum Rus	69	148.75 ± 1.31	79	Very high

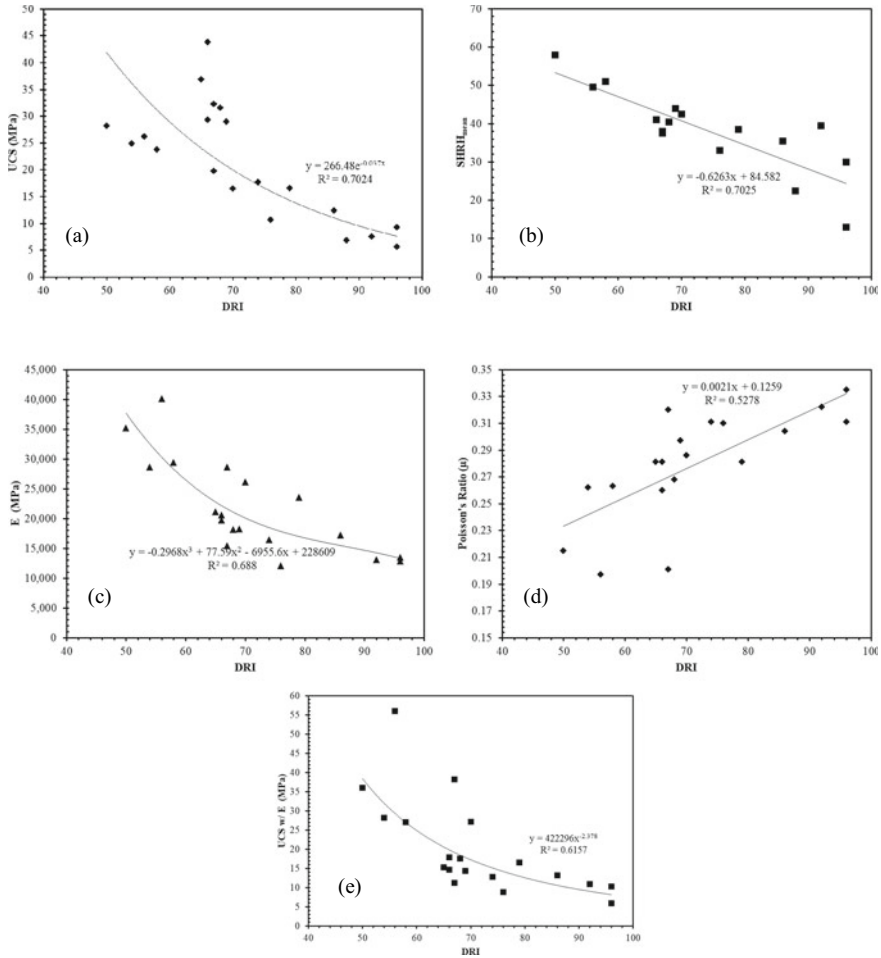


Fig. 6 Correlations between DRI and strength parameters **a** UCS and DRI, **b** SHRHL_{mean} and DRI, **c** E and DRI, **d** μ and DRI and **e** UCS w/E and DRI

References

1. Adebayo B, Adetula B (2013) Evaluation of physical and mechanical properties of rock for drilling condition classification. World J Eng
2. Aydin A (2008) ISRM suggested method for determination of the Schmidt hammer rebound hardness: revised version. In: The ISRM suggested methods for rock characterization, testing and monitoring: 2007–2014. Springer, Cham, pp. 25–33
3. Capik M, Yilmaz AO, Yasar S (2017) Relationships between the drilling rate index and physico-mechanical rock properties. Bull Eng Geol Env 76(1):253–261
4. Cavalier C (1970) Geological description of the Qatar Peninsula (Arabian Gulf). Qatar Department of Petroleum Affairs, p 39

5. Dahl F, Bruland A, Jakobsen PD, Nilsen B, Grøv E (2012) Classifications of properties influencing the drillability of rocks, based on the NTNU/SINTEF test method. *Tunn Undergr Space Technol* 28:150–158
6. Dahl F (2003) The Sugsted DRI, BWI, CLI Standards. NTNU, Angleggsdrift, Trondheim, Norway
7. Demirdag S, Sengün N, Uğur İ, Efe T, Akbay D, Altundağ R (2014) Variation of vertical and horizontal drilling rates depending on some rock properties in the marble quarries. *Int J Min Sci Technol* 24(2):269–273
8. Kahraman S, Bilgin N, Feridunoglu C (2003) Dominant rock properties affecting the penetration rate of percussive drills. *Int J Rock Mech Min Sci* 40(5):711–723
9. Kamran M (2021) A probabilistic approach for prediction of drilling rate index using ensemble learning technique. *J Mining Environ* 12(2):327–337
10. Shafique U, Bakar MA (2015) Evaluation of relationships between drilling rate index and physical and strength properties of selected rock units of Pakistan. *Nucleus* 52(2):79–84
11. Yarali O, Soyer E (2013) Assessment of relationships between drilling rate index and mechanical properties of rocks. *Tunn Undergr Space Technol* 33:46–53
12. Yarali O, Soyer E (2011) The effect of mechanical rock properties and brittleness on drillability. *Sci Res Essays* 6(5):1077–1088
13. Yenice H, Özdoğan MV, Özfırat MK (2018) A sampling study on rock properties affecting drilling rate index (DRI). *J Afr Earth Sc* 141:1–8
14. Yenice H (2019) Determination of drilling rate index based on rock strength using regression analysis. *Anais da Academia Brasileira de Ciências* 91

Unsaturated Geomechanical and Physicochemical Characterisation of Soils Used for Adobe Blocks



Jose Concha-Riedel  and Susana Lopez-Querol 

Abstract A mechanical and physicochemical characterisation of soil used for adobe block production is presented in this paper, considering a geomechanical framework. The main research objectives were to apply the partially saturated soil mechanics theory and obtain some of the soil's physicochemical characteristics. The soil used in this research was extracted from Putaendo, Chile, as it is representative of the vernacular building of that region. The soil was classified as silty sand, of low plasticity. Further inspection showed a 7% content of organic matter. The unsaturated shear strength of the soil was obtained using a conventional shear box test, coupled with the soil–water characteristic curve (which was obtained using the filter paper technique) to estimate suction values. The soil–water characteristic curve had a similar shape as for other sands previously reported in the literature, but with a higher air entry and residual values. Results show that shear strength increases for drier soil samples, reaching an asymptotic value after the air entry suction of the soil. It is concluded that shear box tests without suction control can be used to estimate the unsaturated strength of soils and that the organic matter in soils can influence its cohesive strength, although further research on this aspect is required.

Keywords Partial saturation · Adobe blocks · Earthen materials · Organic content · Shear box

1 Introduction

The mechanical behaviour of geomaterials is one of the principal concerns of the civil engineering discipline. Moreover, scientists are looking for alternative construction materials with lower environmental impacts that can help mitigate the effects of climate change. In that regard, earthen blocks arise as a very sustainable material for the construction of residential buildings. Several researchers have studied

J. Concha-Riedel (✉) · S. Lopez-Querol
University College London, Gower Street, London WC1E 6BT, UK
e-mail: jose.riedel.20@ucl.ac.uk

© The Author(s), under exclusive license to Springer Nature Switzerland AG 2023
C. Atalar and F. Çinicioğlu (eds.), *5th International Conference on New Developments in Soil Mechanics and Geotechnical Engineering*, Lecture Notes in Civil Engineering 305, https://doi.org/10.1007/978-3-031-20172-1_42

433

their unconfined compressive strength, to use them to build safer and more environmentally friendly structures. However, the complex mechanics that occur in the three-phased material usually found in earthen materials (soil, water, and air) are not fully understood yet.

Earth blocks have been extensively studied in recent years, with a special emphasis on the evaluation of the effect of fibres and binders on their mechanical and physical properties [1]. Different authors have measured the changes in flexural and compressive strength due to the inclusion of plant [2], animal [3] and industrial fibres [2], and have concluded that fibres increase the toughness of the mixture [2, 3]. However, different results have been observed with regards to peak flexural and compressive strengths, with some authors measuring its increase [1] while others observe its decrease [4]. One of the common points of the studies mentioned above is that most of them have employed a construction materials framework and measured failure properties, ignoring the soil mechanics perspective of the problem. In that regard, [5–7] have evaluated soil bricks under the soil mechanics framework. The first one observed that as the moisture content of the block increases, the unconfined compressive follows the opposite trend. This is in line with the increment of suction due to the reduction of water in unsaturated soils. On the other hand, [6, 7] considered an unsaturated soil mechanics approach to calculate the soil cohesion due to suction. Both authors found that the shear strength of the soil is proportional to the suction, obtained from the soil–water characteristic curve (SWCC).

A second challenge for the analysis of earthen blocks is the broad range of soils used for their production, as has been previously pointed out in the literature [8]. Low consensus on the optimal soil type for this use has been achieved, as some authors propose an amount of clay for the blocks [9], whilst others do not [8]. This hinders the ability to create standards for earth block production, as the physicochemical properties of each employed soil might vary vastly. As an example, in their study, [8] showed that soils with identical classifications can produce contrasting physical and mechanical properties when used for adobe blocks matrices production.

Hence, the objectives of the present research are: (i) to characterise the type of soil used for Chilean adobe block vernacular buildings, and (ii) to observe if the standard shear box test without suction control can be used to measure unsaturated shear strength.

2 Materials and Methods

2.1 Soil Sample

The soil used in this research was collected from an adobe manufacturing pit located in Putaendo (Chile) and air shipped to London (United Kingdom) for its analysis. The particle size distribution of the soil was obtained using a mechanical sieve shaker following the procedures stated in the British standards [10] and can be seen in

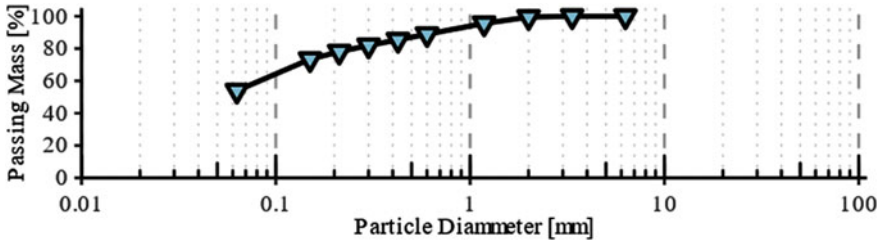


Fig. 1 Particle size distribution of the studied material

Fig. 1. Alongside this, using the same standards, the plastic and liquid limits were also obtained, which had a value of 35 and 40% respectively, and fall in the category of ML and OL in Casagrande's plasticity chart. Finally, the specific gravity of the soil was measured and resulted in a value of 2.54.

2.2 Organic Content

To obtain the organic content of the soil, a thermogravimetric analysis (TGA) was used. The soil was tested using a heating ramp of 20 °C/min, in three stages: (i) from 0 to 150 °C, (ii) from 150 to 550 °C, and (iii) from 550 to 950 °C as per the suggestions of [11]. After each stage was completed, the temperature was left constant for 30 min to ensure all the compounds were incinerated. The organic content of the soil was calculated as follows:

$$OC = \frac{(M_{150^\circ} - M_{550^\circ})}{M_{150^\circ}} \quad (1)$$

where OC is the organic content of the soil in percentage, M_{150° and M_{550° are the mass measurements at the end of the first and second stage respectively. Two samples of 30 μg each were used for this test.

2.3 Scanning Electron Microscope (SEM)—Energy Dispersive Spectroscopy (EDS)

To observe the differences between coarse and fine soil particles, a SEM coupled with an EDS were employed in this study to obtain both images and the chemical components of each part of the soil. Tests were performed on two specimens taken from the complete soil sample and two from the fractions that passed the 63 μm sieve; the weight of each sample was approximately 5 g.

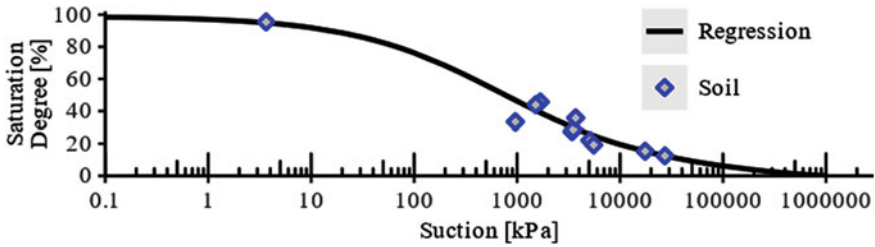


Fig. 2 Soil–water characteristic curve

2.4 Soil–Water Characteristic Curve (SWCC)

For this study, the SWCC was obtained for the soil using the non-contact filter paper method (total suction), as stated in the ASTM D 5298 standard [12], and was calibrated as per the suggestions of [13]. The suction was then correlated to the calibration curve and the moisture content of the paper. Figure 2 shows the SWCC, which starts at a suction value of 0.1 kPa, because the logarithmic scale diverges at 0. Initial voids ratios for unsaturated samples varied between 0.91 and 1.38, while their moisture content ranged between 5 to 23%. Values obtained using the filter paper technique are plotted in the figure, whereas the regression line using the model proposed by [14] is also represented. It is worth mentioning that two other points were obtained at saturations closely to 100% and were used to calculate the regression curve but are not plotted due to their low suction (i.e., 10^{-7} kPa).

2.5 Shear Box Test

To obtain the effective shear strength of the soil, the shear box test was used following the recommendations stated in the British Standard [15]. Normal stresses of 40, 177 and 354 kPa were used. Normal stresses of 40 and 177 kPa are common service conditions for walls in adobe houses, and the normal stress of 354 kPa was selected to evaluate high demand cases. Unsaturated tests were performed to evaluate the effect of suction on the soil with saturation degrees that ranged between 20 and 90%. All tests were performed using a displacement protocol of 0.5 mm/min, as the estimated permeability (with Hazen’s formula [16]) of the soil is approximately 10^{-5} m/s.

The specimens were prepared inside the shear box, by pouring a controlled amount of soil and measuring the height of the sample. This allowed calculating the initial voids ratio of each sample individually. For all samples, the soil was cooled down for 3 h under laboratory conditions after being oven-dried at 105 °C for 24 h and mixed with water to reach different moisture contents ranging between 5 to 30%. This was then let to homogenize for a period of 24 h under laboratory conditions

in a sealed container to avoid any moisture loss. The soil was then put inside the shear box to obtain an initial voids ratio of about 1.28, which is the value measured for plastic adobe samples. To evaluate the moisture content, an initial sample was taken from the container and this value was measured. After the test was concluded, a sample from the middle of each specimen inside the shear box was taken and its moisture content was also measured to check consistency between initial and final determinations.

3 Results and Discussions

3.1 SEM-EDS

Figure 3 shows the microscopy images of the soil sample. Coarse particles (between 2.31 mm and 63 μm) have the typical shape of sands, with angular edges (Fig. 3a). Fine particles (smaller than 63 μm) can be seen over the surface of the sand grains. When observing the fine particles, it can be noted that their shape is similar to peat soils [17], with a configuration of small webbed clusters. These particles have an average diameter of 40 μm , with a rough surface and angular edges.

Table 1 reports the mineralogical composition of the soil, which shows that the coarse particles are composed mainly of silica, aluminium, and ferrous oxides, which is consistent with the chemical compounds of silica sands [18]. On the other hand, fine particles are composed primarily of carbon and silica, which is consistent with organic soils.

The results obtained from the liquid and plastic limits, the particle size distribution, SEM, EDS and TGA test all indicate a lack of clay and some amount of organic

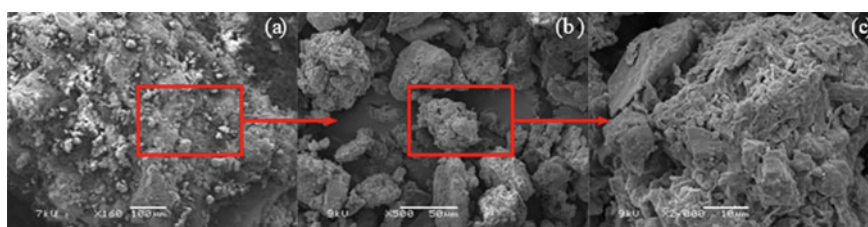


Fig. 3 SEM images of: **a** coarse grain, **b** fine particles and **c** close-up view of fine particles

Table 1 Soil chemical composition

Particles	Na ₂ O	MgO	Al ₂ O ₂	SiO ₂	K ₂ O	CaO	TiO ₂	C	Fe ₂ O ₃
Coarse	3.71	2.05	22.94	53.06	1.85	2.02	0.7	–	9.08
Fine	0.88	1.7	7.08	18.97	0.94	1.5	0.35	64.93	3.44

matter, which is different from what many researchers have found previously in their tested soils [1]. Although the cohesion of the soil for the saturated and dry shear box tests resulted in a low value (5.7 kPa), it could also be counted as a possible indication of organic matter. This is consistent with the results obtained for peat soils, which showed values for cohesion between 6 to 17 kPa [19]. However, due to the low accuracy of the shear box test, further study using triaxial tests is suggested to validate the latter.

3.2 Unsaturated Shear Strength

The unsaturated shear strength of the soil and suction are plotted in Fig. 4 for each normal stress (i.e., (a) for 40 kPa, (b) for 177 kPa and (c) for 354 kPa). Red triangles show the shear strength obtained at a failure state, whereas blue points represent the shear strength at a 20% shear strain state. Samples that had an initial voids ratio higher than 1.28 are plotted in grey. It is worth mentioning that the suction values were estimated using the SWCC, showed in Fig. 2. For the normal stress of 40 kPa, the shear stress varied between 35.7 and 42.1 for suction values of 360 and 7900 kPa respectively. Samples at vertical stress of 177 kPa had a peak shear strength between 119 and 144, for suctions between 33 and 8950 kPa respectively. Finally, samples at a normal stress of 354 kPa showed shear strength values between 229 and 263 kPa for suctions between 3 and 5750 kPa respectively. It is worth reminding that these values only consider the samples with an initial voids ratio approximately of 1.28.

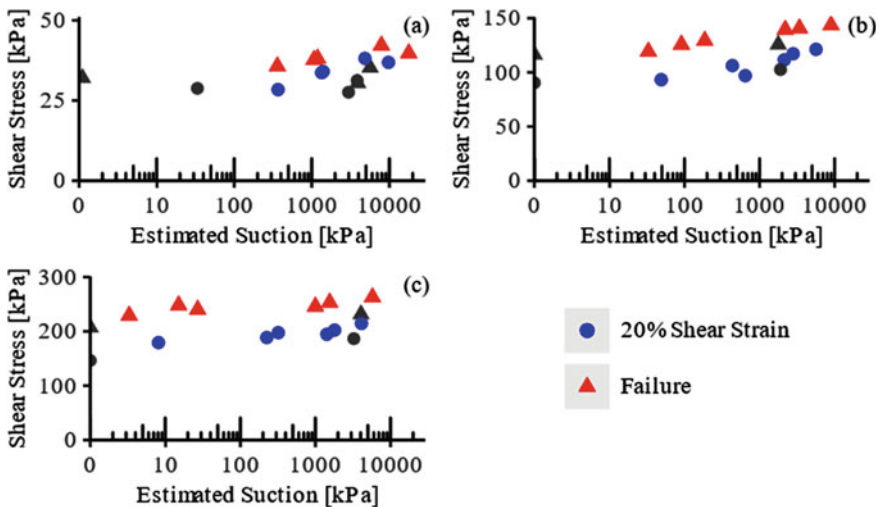


Fig. 4 Unsaturated shear strength at a normal stress of: a 40, b 177 and c 354 kPa

As suction increases, shear strength increases for almost all samples tested. The rate of increment is higher for suctions below the air entry value, of around 500 kPa, and continues to increase but at a lower rate, for suctions higher than 1000 kPa. The latter is consistent with the observations of [20, 21].

4 Summary and Conclusions

In this study, the partially saturated shear strength of a Chilean soil used in the production of adobe blocks was evaluated. A geotechnical characterization, the SWCC and the determination of the shear strength through the shear box apparatus were conducted. The major findings of this study are listed as follows:

1. The soil used in this study is a silty sand with low plasticity. Its composition is different from most studied soils for earth brick manufacturing purposes, as those usually have clay. It is suggested that the organic content of the soil might be helping in achieving the cohesive strength that allows the block to maintain its shape, but further research to confirm this assumption is needed.
2. The standard shear box test can be used to obtain the shear strength of unsaturated soils. However, it is suggested that another type of equipment, such as the triaxial apparatus, should be used, as the measurement of volumetric changes in the shear box apparatus might not be accurate enough.
3. The control of the initial conditions of the sample, mainly the voids ratio, has to be precise if accurate results are to be obtained. In general, it was observed that higher initial voids ratios resulted in lower shear strength values, even though suction was higher for those samples.

Acknowledgements The authors would like to thank Dr F.C. Antico, Dr B. Baudet and Dr P. Ferreira for their suggestions, which greatly improved this research. The authors would also like to thank Mr. Boorman and Mr. Wilkinson for their help with the testing equipment, and Mr. Arnaldo Puebla, for showing and teaching the traditional process of adobe manufacturing. Finally, the authors thank the Chilean National Agency for Research and Development (ANID) / Scholarship Program / DOCTORADO BECAS CHILE / 2020 – 72210077 for the founding of this research.

References

1. Laborel-Preneron A, Aubert JE, Magniont C, Tribout C, Bertron A (2016) Plant aggregates and fibers in earth construction materials: a review. *Constr Build Mater* 111:719–734. <https://doi.org/10.1016/j.conbuildmat.2016.02.119>
2. Concha-Riedel J, Antico FC, Araya-Letelier G (2020) Mechanical and damage similarities of adobe blocks reinforced with natural and industrial fibres. *Rev Mater* 25(4):1–11. <https://doi.org/10.1590/S1517-707620200004.1206>

3. Araya-Letelier G, Concha-Riedel J, Antico FC, Valdés C, Cáceres G (2018) Influence of natural fiber dosage and length on adobe mixes damage-mechanical behavior. *Constr Build Mater* 174:645–655. <https://doi.org/10.1016/j.conbuildmat.2018.04.151>
4. Pedergrana M, Elias-Ozkan ST (2021) Impact of various sands and fibres on the physical and mechanical properties of earth mortars for plasters and renders. *Constr Build Mater* 308(37):125013. <https://doi.org/10.1016/j.conbuildmat.2021.125013>
5. Bui QB, Morel JC, Hans S, Walker P (2014) Effect of moisture content on the mechanical characteristics of rammed earth. *Constr Build Mater* 54:163–169. <https://doi.org/10.1016/j.conbuildmat.2013.12.067>
6. Heath A, Walker P, Fourie C, Lawrence M (2009) Compressive strength of extruded unfired clay masonry units. *Proc Inst Civ Eng Constr Mater* 162(3):105–112. <https://doi.org/10.1680/coma.2009.162.3.105>
7. Beckett CTS, Augarde CE, Easton D, Easton T (2018) Strength characterisation of soil-based construction materials. *Geotechnique* 68(5):400–409. <https://doi.org/10.1680/jgeot.16.P.288>
8. Concha-Riedel J, Antico FC, López-Querol S (2021) Mechanical strength, mass loss and volumetric changes of drying adobe matrices combined with kaolin and fine soil particles. *Constr Build Mater* 312:125246. <https://doi.org/10.1016/j.conbuildmat.2021.125246>
9. Bouhicha M, Aouissi F, Kenai S (2005) Performance of composite soil reinforced with barley straw. *Cem Concr Compos* 27(5):617–621. <https://doi.org/10.1016/j.cemconcomp.2004.09.013>
10. British Standards Institution (1990) Methods of test for soils for civil engineering purposes — Part 2: classification tests. *Br Stand* 1:40
11. Bensharada M, Telford R, Stern B, Gaffney V (2021) Loss on ignition vs. thermogravimetric analysis: a comparative study to determine organic matter and carbonate content in sediments. *J Paleolimnol* 67(2):191–197. <https://doi.org/10.1007/s10933-021-00209-6>
12. ASTM International (2016) ASTM D 5298 - 16 Standard test method for measurement of soil potential (suction) using filter paper. https://compass.astm.org/EDIT/html_annot.cgi?D5298+16
13. Likos WJ, Lu N (2002) Filter paper technique for measuring total soil suction. *Transp Res Rec J Transp Res Board* 1786(1):120–128. <https://doi.org/10.3141/1786-14>
14. Fredlund D, Xing A (1994) Equations for the soil-water characteristic curve. *Can Geotech J* 31(4):521–532. <https://doi.org/10.1139/t94-061>
15. British Standard Institution (1990) Soils for civil engineering purposes: Part 7 : Shear strength tests (total stress). London, BS 1377, no. 1
16. Hazen A (2013) XXIII. Some physical properties of sands and gravels, with special reference to their use in filtration. In: *State sanitation: a review of the work of the Massachusetts state board of health, vol. II*. Harvard University Press, pp 232–248
17. Aminur M, Kolay PK, Linda SN, Taib D, Ibrahim M, Ahmad Kamal AA (2011) Physical, geotechnical and morphological characteristics of peat soils from Sarawak. *Inst. Eng. Malaysia* 72(4):5
18. Mckeague JA, Cline MG (1963) A. McKeague and M. G. Cline. *Adv Agron* 15(802):339–396
19. Kim Huat B (2006) Deformation and shear strength characteristics of some tropical peat and organic soils. *Pertanika J Sci Technol* 14(1 & 2):61–74
20. Gan JKM, Fredlund DG, Rahardjo H (1988) Determination of the shear strength parameters of an unsaturated soil using the direct shear test. *Can Geotech J* 25(3):500–510. <https://doi.org/10.1139/t88-055>
21. Vanapalli SK, Fredlund DG, Pufahl DE, Clifton AW (1996) Model for the prediction of shear strength with respect to soil suction. *Can Geotech J* 33(3):379–392

Soil Improvement

The Evaluation of Stone Column and Jet Grouting Soil Improvement by Conducting a Comprehensive Experimental Program



Arshiya Abadkon and Erol Güler

Abstract Ground improvement is an important requirement in today's construction industry as land reclamation is becoming increasingly popular. Many different ground improvement techniques have been developed over the past few decades to treat weak soil deposits. Two of commonly used techniques are jet grouting and vibro-stone column. The goal of this study is to investigate the advantages and disadvantages of both techniques using in-situ tests such as cone penetration testing, standard penetration testing, seismic wave velocity measurements and laboratory tests including direct shear tests, density and void ratio measurements on undisturbed samples obtained from the soil between produced columns. A test area including 25 jet grout columns with 1.8 m spacing and diameter of 60 cm was prepared to investigate the effectiveness of jet grouting method. A test area with same dimensions as it was for jet grout columns was prepared for stone columns. 25 stone columns with diameter of 1 m and spacing of 1.8 m were produced in the test area. Vibroflotation technique was used to produce stone column with top feeding method. In-situ and laboratory tests were carried out for these test areas to investigate the advantages and disadvantages of both techniques. The most important result obtained from in-situ tests was the better improvement of soil mass between stone columns than that of jet grout columns which plays a key role in reducing seismic risks and liquefaction hazards. Laboratory tests on undisturbed samples obtained from the soil between produced stone columns and jet grout columns also approved the findings from in-situ tests.

Keywords Ground improvement · Field study · Stone column · Jet-grout columns

A. Abadkon

Geosismik A.Ş. Formerly ELC/Royal Haskoning DHV, Istanbul, Turkey
e-mail: arshiya.abadkon@geosismik.com.tr

E. Güler (✉)

George Mason University, Fairfax, VA, USA
e-mail: fguler@gmu.edu

1 Introduction

Ground improvement is an important requirement in today's construction industry as land reclamation is becoming increasingly popular. Many different ground improvement techniques have been developed over the past few decades to treat weak soil deposits [1]. Two of commonly used techniques are the installation of jet grout columns and vibro-stone columns. Jet grouting soil improvement method was used since early 1970s. The technique of jet grouting uses high pressure/velocity jet fluids to erode the existing soil and then to mix the cuttings with cement slurry to form soilcrete columns. It is effective across the widest range of soil types of any grouting system. However, if the native soil is not completely mixed with slurry the resulting columns will have soil inclusions which can reduce the strength of the column. Also the achieved diameter of the column depends on the soil type and density of the soil [2].

Stone column method refers to columns of compacted, gravel size stone particles constructed vertically in the ground to improve the performance of soft or loose soils. This technique was invented in Germany in the early 1960s and is possibly the most natural foundation system in existence as it consists entirely of a gravel column that is formed in the subsoil. In addition stone columns are also more durable than most of the other soil improvement systems which involve use of cement or steel (Barksdale and Bachus 1983).

The goal of this study is to investigate the advantages and disadvantages of both techniques using in-situ tests such as cone penetration testing, standard penetration testing, seismic wave velocity measurements and laboratory tests including direct shear tests, density and void ratio measurements on undisturbed samples obtained from the soil between produced columns. Since there is liquefaction risk on this site, these evaluations were crucial. Literature cites that jet-grout columns can mitigate liquefaction risk [3]. Still the Engineer had several questions regarding the effectiveness of jet grouting techniques especially in seismic areas. In this paper seismic test results are also presented for stone column soil improvement technique.

2 Experimental Study

Experimental program in this study was conducted during soil improvement works of Ashgabat International Airport Project in Turkmenistan. Existing soil at the site consisted of mostly loose silty sand with thin clay layers. Due to weak soil conditions bearing capacity and settlement problems were foreseen during geotechnical evaluation of the project for structures transferring high loads to the ground such as Main Terminal, Cargo Terminal, Aircraft Hangars and etc. In addition, because of the cohesionless structure of the existing soil and high groundwater level liquefaction risk at the site was very high. Therefore, jet grout columns with 16 m length and 0.6 m diameter and stone columns with 16 m length and 0.8 m diameter were designed to remove the mentioned risks for the soils below the foundation of the

Table 1 Existing soil profile at test site

Depth (m)	Soil type
0–4.5	Silty sand
4.5–7.5	Lean clay
7.5–12.0	Silty sand
12.0–13.5	Lean clay
13.5–16.0	Silty sand

structures. Experimental study was carried out based on details provided by the alternative designs for the same site. Two test areas in the same region was established and in-situ and laboratory tests for the test areas including jet grout and stone columns were conducted. The existing soil profile at test areas is shown in Table 1. Both test areas have dimensions of 7 × 7 m, each including 25 columns with spacing of 1.8 × 1.8 m.

2.1 Experimental Study for Jet Grout Columns Test Area

A test area including 25 jet grout columns with 1.8 m spacing and diameter of 60 cm was prepared to investigate the effectiveness of jet grouting method. Single fluid jet grouting technique was used to produce jet grout columns. Slurry was injected to the ground with 400 bar pressure and water to cement ratio of one. Prior to production of jet grout columns one standard penetration test and one cone penetration test were conducted. Same tests were done after jet grout columns production in the same area in order to compare the results before and after improvement. Schematic plan of the test area and test points are given in Fig. 1.

Fig. 1 Plan of jet grout test area

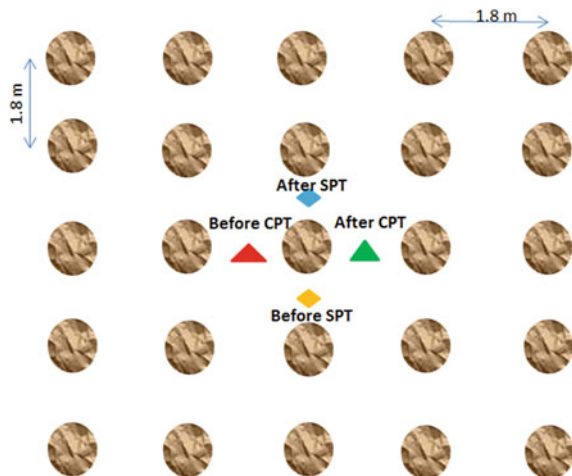




Fig. 2 Excavation around jet grout columns

After post production tests soil around the jet grout columns was excavated to measure the diameter of the columns (Fig. 2). In addition full length coring was conducted on some of the produced jet grout columns to check the integrity of the produced columns.

2.2 Experimental Study for Stone Column Test Area

A test area with same dimensions as it was for jet grout columns was prepared for stone columns. 25 stone columns with diameter of 1 m and spacing of 1.8 m were produced in the test area. Vibroflotation technique was used to produce stone column with top feeding method. Before stone column soil improvement SPT and CPT tests were conducted in the predetermined locations. Mentioned tests were done also after improvement in the same location to investigate the effect of stone column technique on the soil between the columns. Test plan is shown in Fig. 3.

Moreover, after conducting in-situ tests undisturbed sample (Shelby Tube) was obtained from the soil between the columns for laboratory tests. Shear strength parameters of the soil before and after stone column improvement were checked.

Seismic reflection tests were also conducted on this test area to compare the shear wave velocity of the soil before and after improvement (Fig. 4).

Fig. 3 Plan of stone columns test area

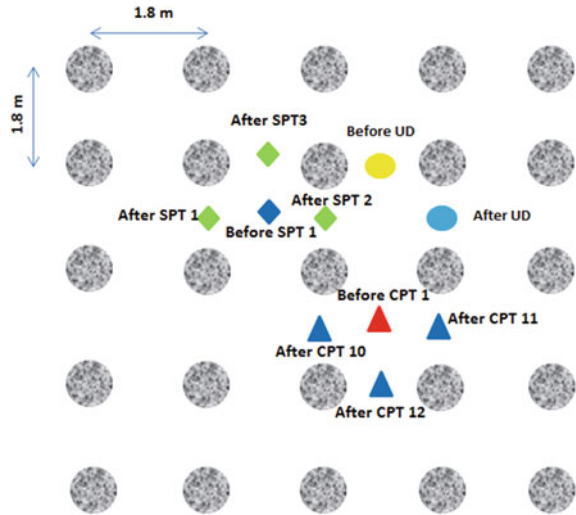


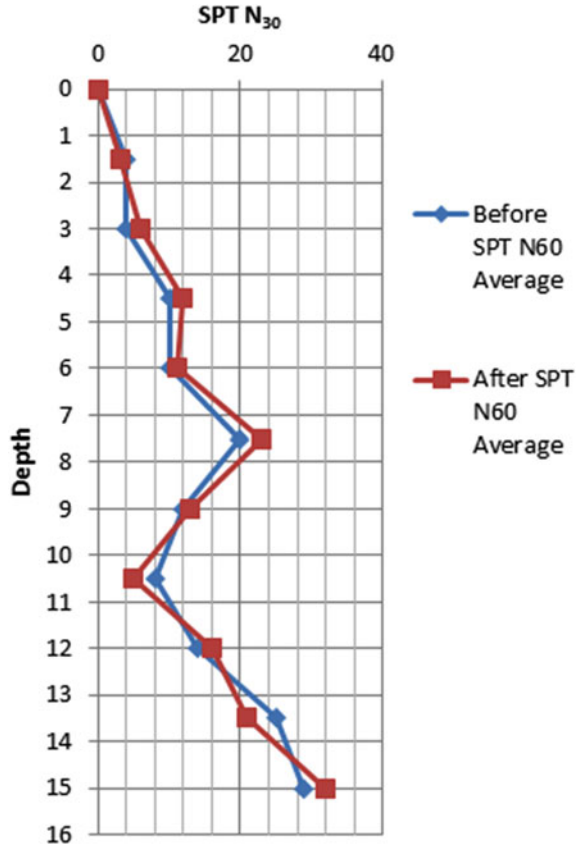
Fig. 4 Produced stone columns in test area

3 Test Results Study

3.1 Jet Grout Column Test Area Results

SPT and CPT test results showed almost no change in the strength of the soil between columns before and after jet grouting improvement. Results of SPT tests are shown in Fig. 5.

Fig. 5 SPT results for jet grout area



Results showed that there is not a homogeneous structure in the whole length of jet grout columns. Moreover, in some columns there were soil inclusions resulting from existence of hard clay which avoided jet grout slurry to mix with soil and produce the soil-crete columns. This might cause bearing capacity and settlement problems for the geotechnical design.

3.2 Stone Column Test Area Results

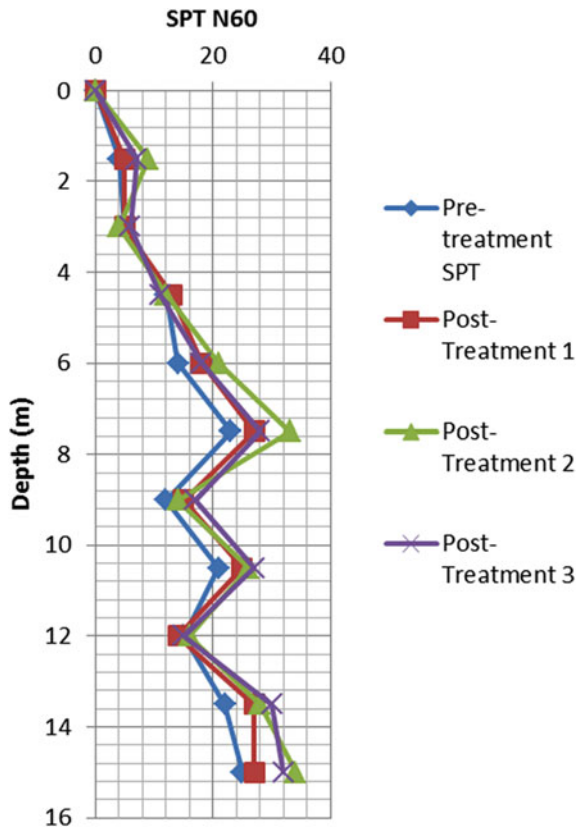
Standard penetration test results showed a slight increase in average SPT N60 values after stone column soil improvement which indicated that in addition to the area of the stone column itself, soil mass between columns has also been improved (Fig. 6). This plays a key role in reducing seismic risks and liquefaction hazards. CPT results also showed that strength parameters of the soil mass between stone columns have increased. The purpose was to determine the liquefaction risk before and after soil

improvement. The average values of the cone resistance are given in Fig. 7. Also the soil classification determined from the CPT test prior to stone column installation are given in the same figure.

In addition, direct shear and density tests were conducted on undisturbed soil samples obtained from soil between stone columns. Test results showed an important increase in friction angle of the soil and decrease in void ratio which confirms the in-situ test results. Results of laboratory tests are shown in Table 2.

Moreover, seismic tests as seen in Fig. 8 was conducted on site. The seismic tests showed that shear wave velocity of the soil increased from 170.4 m/s before improvement to 250.7 m/s after improvement which indicates a 47% increase. Average value of shear wave velocity until depth of 30 m was increased from 290 to 370 m/s after improvement.

Fig. 6 SPT results for stone column area



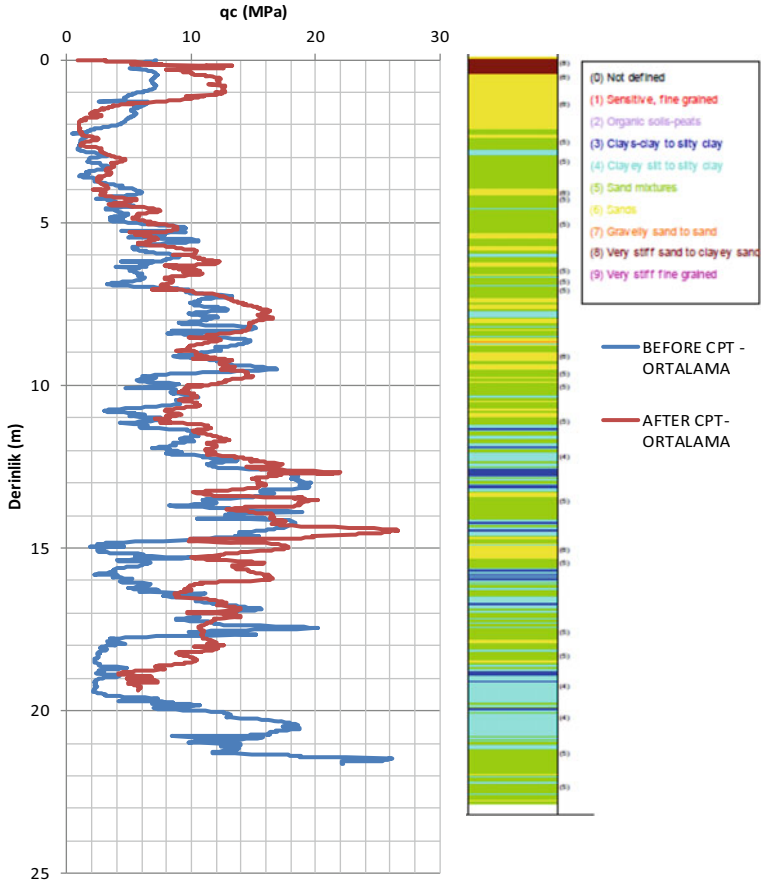


Fig. 7 CPT test results for stone column test area

Table 2 Laboratory tests results for soil between stone columns

	Wet density ρ_s (ton/m ³)	Dry density ρ_d (ton/m ³)	Specific gravity (Gs)	Void ratio (e)	Peak internal friction angle φ (°)
Before improvement	19.6	16.6	2.70	0.59	12.3
After improvement	21.3	17.9	2.71	0.54	29.4

Fig. 8 Seismic test for stone column test area



4 Discussion and Conclusions

In this paper jet grouting and stone column soil improvement techniques were evaluated by conducting in-situ and laboratory tests. Especially soil mass between jet grout and stone columns was tested to measure the effect of these methods on the improvement of the area between columns.

Post treatment test results show significant increase in friction angle of the soil between stone columns. This is because the soil is cohesionless and consists mainly of silty sand and is therefore affected by the vibration of the probe during stone column installation. This increase in internal friction angle means a denser soil which leads to reduction of liquefaction hazard especially for loose saturated soils. It was also observed that the structure of the soil obtained from post treatment Shelby tube is in general different than the soil obtained before improvement. In summary it can be said that there is an increase in density and internal friction angle of the soil in-between the stone columns. This indicates that stone columns provide a very efficient soil improvement in granular soils.

Another indication of the increased density was the significant increase in shear wave velocity by the use of stone column technique. Similarly the increase in shear wave velocity is an indication of a decrease in the risk of liquefaction hazards.

In case of jet grout columns practically no improvement was observed in the soil in-between the columns. Also full length coring results for jet grout columns showed

that there is a risk of soil inclusion or discontinuities within jet grout column length due to ground conditions.


Acknowledgements This study was done within the scope of Ashgabat International Airport Construction. Authors would like to acknowledge Polimeks Construction and contracting and ELC/Royal HaskoningDHV for providing support to this study.

References

1. Kirsch K, Bell A (2009) Ground improvement
2. Grace P, Flora A (2014) Jet grouting: technology, design and control
3. Martin JR, Olgun CG, Mitchell JK, Durgunoglu HT (2004) J Geotech Geoenviron Eng 130(6):561–571
4. Stark TO (2009) Soil inclusions in jet grout columns. DFI J 1(1)

Feasibility Study of Transforming Excavated Clayey Soil into ‘Sand-Like’ Material



Juan-Wei Koh , Sathyamoorthy Subramanian, Soon-Hoe Chew, Yeow-Chong Tan, Cheng-Soon Teo, Meng-Yang Charmaine Koh, Hui-Bin Grace Foo, Ting-Hong Hadley Cheung, Tamilselvan Thangayah, and Czha-Yheaw Tan

Abstract In order to upcycle clayey soil, which generally has poor strength properties, it was proposed to transform them into a more useable ‘sand-like’ material using sintering technology in this feasibility study. A muffle furnace was adopted to heat the clayey soil at different sintering schedules. The results showed that the well sintered ‘sand-like’ pallets had a friction angle (about 34–37°) in the same range as a typical medium dense sand. The sintered product’s permeability was found to be in the order of 1×10^{-3} m/s, which is similar to the gravel-sand mixtures category. The maximum dry unit weight and optimum moisture content in compaction behaviour were slightly lower than a typical silty sand-gravel. Mineralogy check and soil fabric check using X-ray diffraction (XRD) and scanning electron microscopy (SEM) showed that the kaolinite (weak mineral) had been transformed into metakaolinite (stronger mineral) in the ‘sand-like’ material. The sintered product was almost irreversible through the acid and saltwater dissolvability test. All the findings confirmed that it is feasible to produce “sand-like” material from excavated clayey soil through sintering technology.

Keywords Clayey soil · Sand-like material · Sintering

J.-W. Koh (✉) · S. Subramanian · S.-H. Chew
National University of Singapore, Queenstown 119077, Singapore
e-mail: ceekohj@nus.edu.sg

Y.-C. Tan · C.-S. Teo · M.-Y. C. Koh · H.-B. G. Foo · T.-H. H. Cheung
Housing and Development Board, Toa Payoh 310480, Singapore

T. Thangayah
NeWall Tech Pte Ltd, Singapore 638723, Singapore

C.-Y. Tan
GeoTests (S) Pte Ltd, Singapore 628708, Singapore

1 Introduction

Clayey soil of varying thicknesses can be found beneath about one-third of Singapore's surface. There are tons of clayey soil excavated from construction activities within Singapore every year. Often, the clayey soil has low strength properties, and it was primarily re-purposed to be used in land reclamation projects as infill material. Ground improvement works, commonly surcharge preloading aided with prefabricated vertical drains, must be staged on the clayey infills to strengthen the ground prior to other infrastructure construction. In practice, a few meters thick of bearing later made from sands must be laid on top of the clayey infills to support the weight of the ground improvement machinery.

Given the availability of abundant excavated clayey soil and the sand shortage problem, a feasibility study of transforming excavated clayey soil into 'sand-like' material using sintering technology is formulated. The "sand-like" material is aimed to partially replace the sands needed to form the bearing layer for ground improvement works. This paper discussed the production of the "sand-like" material and the physical properties and mineralogy of the 'sand-like' material.

1.1 Sintering

One of the established ways of transforming clay into a solid, coherent product is through a thermal treatment called sintering. Examples of solid, coherent products made from clay are ceramic, brick and light-weight aggregate (LWA). Among the products, LWA and the 'sand-like' material produced in this study may look similar, but there are differences. One of the key differences between LWA and 'sand-like' material is that the bloating agent and the raw material must be carefully selected and designed for LWA. Not all clayey material can be used for LWA. In addition, LWA is made to be lower in density and bigger in size (≥ 10 mm), while 'sand-like' material has a higher density than LWA and is smaller in size (1–5 mm).

The investigations on obtaining LWA from Singapore clayey soil had been reported in the past. The studies used Singapore's clayey soil and sludge to produce LWA [1–5]. Table 1 shows the key parameters obtained from the research studies on using Singapore clay as part of the ingredient to produce LWA.

Most of the studies adopted a very high heat treatment, where at least 1000 °C was adopted for the sintering stage. A higher temperature would consume more energy and have a more carbon footprint for the process. In addition, it can be found that a rotary kiln was preferred due to its efficiency in the sintering process as compared to a muffle furnace, where only 1–2 min are required in the rotary kiln [1] and 240 min for the muffle furnace [4, 5]. The studies concluded that LWA could be produced and potentially used in the construction sector with a proper mixture ratio between the clay and sludge. Although the research studies were claimed to be successful,

Table 1 LWA research studies using Singapore clayey soil as part of raw material

Materials		Red clay + Sludge	Marine clay + Sludge			
Granulation		The mixture was fired in a larger size before being broken down into about 20 mm	Rolled into 11–15 mm	Rolled into 10–20 mm		Hand-rolled into 10–15 mm
Preheating stage	Temperature (°C)	–	105	500	900	110
	Duration (min)	–	overnight	60	60	120–180
Sintering stage	Temperature (°C)	1050–1080	1135	1000–1300		1200
	Duration (min)	–	240	240		1–2
Sintering device		Brick firing kiln	Muffle furnace	–		Trefoil rotary kiln
References		[3, 6]	[4, 5]	[2]		[1]

no actual production of LWA using recycled clayey soil has been implemented in Singapore.

A muffle furnace was used for the “sand-like” material production reported in this study due to inaccessibility to a rotary kiln at that moment. It should be noted that a muffle furnace would be sufficient for this feasibility study because energy efficiency and cost-effectiveness will only be the focus in the future phase of the study after the feasibility study is satisfied.

2 Materials and Methods

2.1 Excavated Clayey Soil

The excavated clayey soil was soft, blue-grey, and contained gravel and sand. It is classified as inorganic clays of high plasticity, fat clays (C.H.), based on Unified Soil Classification System (USCS). Table 2 presents the Atterberg limits and particle size distribution of the raw material.

Table 2 Atterberg limits and particle size distribution of the excavated clayey soil

Parameters		Value
Atterberg limits	Water content (%)	70–80
	Liquid limit (%)	75–80
	Plastic limit (%)	33–38
Particle size distribution	Gravel (%)	1–3
	Sand (%)	2–18
	Silt (%)	31–43
	Clay (%)	35–56

2.2 Production of ‘Sand-Like’ Material

The clayey soil was rolled into cylindrical pellets with about 3 mm in diameter and a length of between 1 and 5 mm. It was air-dried for a day before sintered in a muffle furnace. Four series of sintering tests, with different sintering schedules, at two target sintering temperatures of 900 °C and 500 °C, were conducted (i.e., SLM1, SLM2, SLM3 and SLM4), as shown in Fig. 1. This resulted in 4 batches of sintered pellets, which is termed ‘sand-like’ material. The sintering temperatures of 900 and 500 °C were chosen as endothermic dehydroxylation would occur and produce metakaolin at a temperature around 500 °C; the dehydroxylation continued until 900 °C [7, 8]. Besides, different dwelling duration under similar sintering temperatures would show the effect of dwelling duration on the quality of the sintered product of ‘sand-like’ material.

2.3 Characterisation of Sintered Product ‘Sand-Like’ Material

Visual inspection was done after the sintered pellets cooled down. Selected samples of sintered pellet were then cut open, and the sintered percentage was evaluated based on the area inside the pellet where changes in colour was observed. The pellets with the highest sintered percentage were then sent for physical properties tests (i.e., density, friction angle, permeability, density-moisture relationship in compaction tests). In addition, mineralogy and soil fabric tests also conducted to examine the character of the ‘sand-like’ material—its mineralogy and its fabric. Lastly, the sintered pellets were soaked in acid and saltwater in two separated columns to check the dissolvability of the pellets.

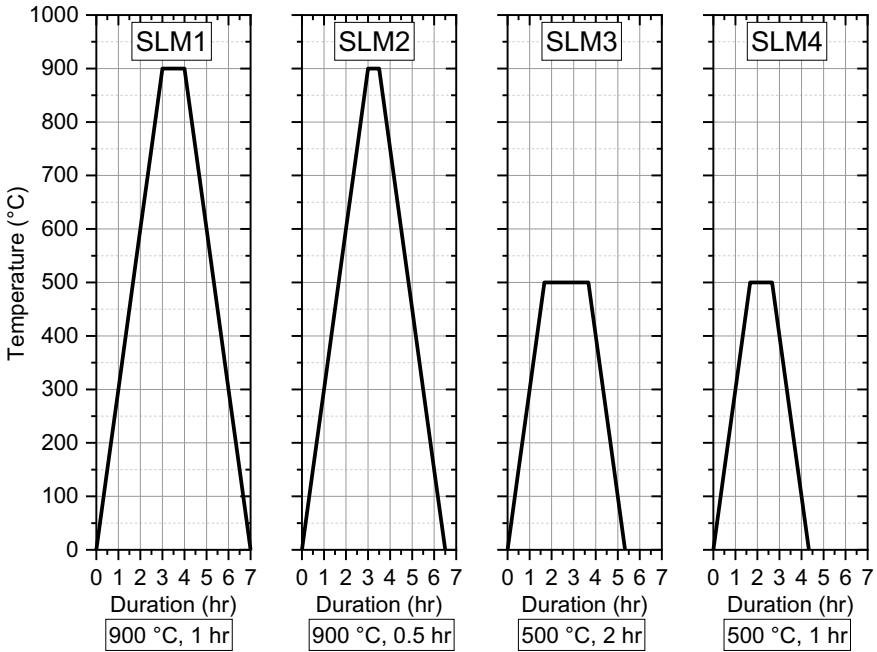


Fig. 1 Sintering temperature schedule

3 Results and Discussions

3.1 Sintered Percentage

A few random sintered pellets or ‘sand-like’ materials from each batch were broken down to check the sintered area inside the core. The “sintered percentage” was roughly estimated based on the colour changes: orange coloured represents sintered area while blue-grey colour (original colour of raw material) represents the non-sintered parts. Figure 2 shows the photograph of ‘sand-like’ material before and after cutting open. The calculated sintered percentage of SLM1, SLM2, SLM3 and SLM4 is close to 100, 70, 45 and 16%, respectively. This result shows that ‘sand-like’ material undergone 900 °C sintering achieved a higher sintered percentage than those produced under 500 °C sintering. The result also shows that a longer dwelling duration at sintering temperature gave a better-sintered quality. Among the batches tested, only SLM1 was fully sintered.

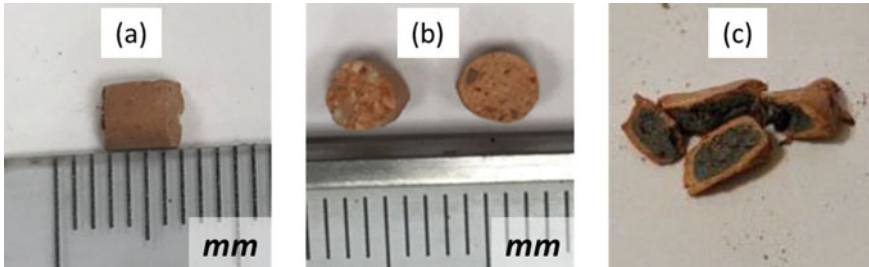


Fig. 2 Photograph of ‘sand-like’ material: **a** Intact pellet before cutting open, **b** fully sintered pellet after cutting open, and **c** not fully sintered pellet after cutting open

3.2 Physical Properties of “Sand-Like” Material

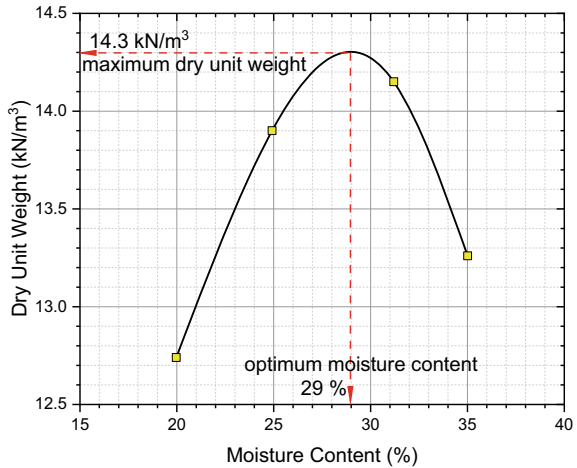
The fully sintered SLM1 ‘sand-like’ material was subjected to various physical properties tests. Table 3 states the physical properties of SLM1 sintered pellets.

The most loosely packed dry density of SLM1 sintered pellets is found to be in the range of 1139–1187 kg/m³, which falls within the category of light-weight fine aggregate (<5 mm size and <1200 kg/m³) [9]. Although there was no intention of creating a lightweight feature of the ‘sand-like’ material, the excavated clayey soil may possibly bloat during the sintering process and become “light-weight”. A series of consolidated drained triaxial tests were conducted to obtain the friction angle of SLM1 sintered pellets. The friction angle was computed as 34–37°, which falls within the range of medium dense sands [10]. This high value of friction angle of the ‘sand-like’ material is favourable if this material will replace the usage of sand in the land reclamation project in the future. The permeability of SLM1 sintered pellets was also determined through the constant head permeability test. It was found that the mean permeability of SLM1 sintered pellets was found to be 1.14×10^{-3} m/s. This permeability value indicated that this material is highly permeable and can be categorised as gravel-sand mixtures [10], meaning that its drainage properties is as good as gravel-sand mixtures and can experience immediate settlement when dumped in landfills. It is thus truly “sand-like”.

Table 3 Physical properties of SLM1 sintered product ‘sand-like’ material

Physical properties		Unit	Value
Most loosely packed dry density		kg/m ³	1139–1187
Effective friction angle		°	34.7
Permeability		m/s	1.14×10^{-3}
Compaction characteristic	Maximum dry unit weight	kN/m ³	14.3
	Optimum moisture content	%	29

Fig. 3 Density-moisture curve of SLM1 sintered product ‘sand-like’ material



In addition, a series of modified proctor tests were conducted to determine the density-moisture relationship, which indicates the compaction behaviour of SLM1 ‘sand-like’ material. Figure 3 shows the relation between moisture content and dry unit weight of SLM1. From the figure, the optimum moisture content is found to be 29%, while the maximum dry unit weight is 14.3 kN/m³. By comparing these values with the typical soil type, it can be categorised under diatomaceous or micaceous silts, which is slightly lower than the silty sands and gravels category (maximum dry unit weight = 14.7–19.6 kN/m³ and optimum moisture content = 10–20%) [11]. This result shows that SLM1 sintered product ‘sand-like’ material is able to be compacted, although it may be slightly lighter than the typical silty sands and gravels based on the maximum dry unit weight.

3.3 Mineralogy and Soil Fabric

The mineralogy of SLM1 ‘sand-like’ material was examined using X-ray diffraction (XRD). The XRD plot of SLM1 sintered pellet was compared with the raw material’s XRD plot (excavated clayey soil), as shown in Fig. 4. The primary minerals in the clayey soil are kaolinite, quartz and illite. In theory, kaolinite would transform into metakaolin at a temperature above 500 °C, where metakaolin is a stronger mineral than kaolinite. Therefore, reducing kaolinite minerals in SLM1 sintered pellets proved that some kaolinite may change to metakaolin.

In order to investigate the existence of metakaolin, a scanning electron microscope (SEM) was used because metakaolin is amorphous. The soil fabric of kaolinite and metakaolin is in layered structures, but the layer structure of metakaolin is more open than kaolinite [12]. Figure 5 illustrates the SEM image of the SLM1 ‘sand-like’ material. Although the SEM image may not clearly show metakaolin’s distinct

Fig. 4 XRD of raw material and SLM1 sintered product ‘sand-like’ material

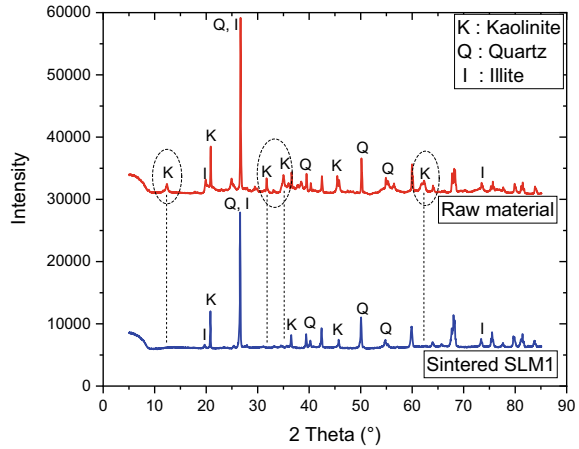
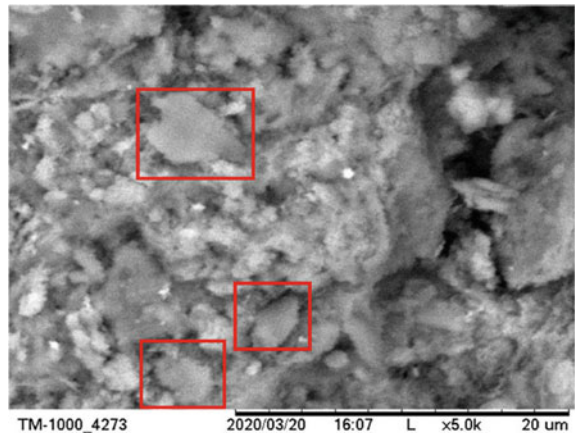


Fig. 5 SEM image of SLM1 sintered product ‘sand-like’ material



microstructure, the red square in the SEM image indicates the suspected metakaolin formed in SLM1 sintered product.

3.4 Acid and Saltwater Dissolvability

Since ‘sand-like’ material is likely to be used in the land reclamation works, it will be exposed to seawater and carbonic acid, carbonic acid formed when carbon dioxide in the air reacts with water. Hence, it is crucial to ensure that ‘sand-like’ material does not dissolve in seawater and acidic conditions. A quick check was carried out on the dissolvability of SLM1 sintered pellets in saltwater and acidic conditions. The pellets were soaked in seawater and pH 4 acid, in two separate columns for 28 days. The dry

weight of the intact pellets before and after soaking was measured, and the difference was calculated. The difference in dry weight of the pellets soaked in seawater is 0.6% of the original weight, while that of pellets immersed in acid is 1.0% of the original weight. It was found that the pellets have almost negligible differences in dry weight after soaking in the seawater and acidic conditions. Hence, it can be concluded that sintered clay does not dissolve in seawater and acid after soaking for 28 days.

4 Conclusions

The study investigates the feasibility of transforming excavated clayey soil in Singapore into ‘sand-like’ material to upcycle the clayey soil. One of the possible usages of ‘sand-like’ material is to replace the surface sand layer required during ground improvement works in the land reclamation project.

Four batches of 1–5 mm clayey soil pellets were subjected to different sintering programmes, and it was found that the sintered percentage is highest when the target sintering temperature is 900 °C and maintained for an hour. The sintered product is found to have high friction angle and high permeability, values comparable to typical sand-gravel mixtures. This material can also be compacted with a maximum dry density of 13.4 kN/m³ at an optimal moisture content of 29%. Furthermore, SEM and XRD studies confirmed the formation of reduction of kaolinite, and transformation of kaolinite into metakaolin in this sintering process, where metakaolin is a stronger mineral. Lastly, the pellets were almost un-dissolvable under seawater and acidic conditions for 28 days.

The findings derived from this phase I of the study suggest that well-designed sintering programme would produce a sintered product, which is “sand-like”, from excavated clayey soil. The subsequent phases of the study would include the energy efficiency, cost-effectiveness and environmental impact of employing sintering technology in the mass production of ‘sand-like’ material, which are crucial.

Acknowledgements This research is supported by the National Research Foundation, Singapore, and Ministry of National Development, Singapore, under its Cities of Tomorrow R&D Programme (CoT Award No.: COT-V3-2019-2). Any opinions, findings and conclusions or recommendations expressed in this material are those of the author(s) and do not reflect the views of National Research Foundation, Singapore and Ministry of National Development, Singapore.

References

1. Laursen K, White TJ, Cresswell DJF, Wainwright PJ, Barton JR (2006) Recycling of an industrial sludge and marine clay as light-weight aggregates. *J Environ Manage* 80(3):208–213
2. Show KY, Lee DJ, Tay JH, Hong SY, Chien CY (2005) Light-weight aggregates from industrial sludge–marine clay mixes. *J Environ Eng* 131(7):1106–1113

3. Tay JH, Yip WK, Show KY (1990) Clay-blended sludge as light-weight aggregate concrete material. *J Environ Eng* 117(6):834–844
4. Tay JH, Show KY, Hong SY (2002) Concrete aggregates made from sludge-marine clay mixes. *J Mater Civ Eng* 14(5):392–398
5. Tay JH, Show KY, Lee DJ, Hong SY (2004) Reuse of wastewater sludge with marine clay as a new resource of construction aggregates. *Water Sci Technol* 50(9):189–196
6. Tay JH, Show KY (1992) Reuse of wastewater sludge in manufacturing nonconventional construction materials—an innovative approach to ultimate sludge disposal. *Water Sci Technol* 26(5–6):1165–1174
7. Srikrishna K, Thomas G, Martinez R, Corral MP, Moya JS (1990) Kaolinite-mullite reaction series: a TEM study. *J Mater Sci* 25:607–612
8. Wang H, Li C, Peng Z, Zhang S (2011) Characterisation and thermal behavior of kaolin. *J Therm Anal Calorim* 105:157–160
9. Zhang H (2011) Concrete. In: *Building materials in civil engineering*. Woodhead Publishing Series in Civil and Structural Engineering, pp 81–423
10. Look BG (2007) *Handbook of geotechnical investigation and design tables*
11. Carter M, Bentley SP (2016) Density. In: *Soil properties and their correlations*. pp 49–67
12. Haddaji Y, Majdoubi H, Mansouri S, Tamraoui Y, Boulif R, Oumam M, Hannache H (2020) Effect of Sodium Hexafluorosilicate addition on the properties of metakaolin based geopolymers cured at ambient temperature. *Silicon* 13(5):1441–1451

Estimation of Modular Ratio and Modulus of Deformation of Granular Piles from in Situ Compression Tests Under Direct Loading



M. Najamuddin, M. R. Madhav, and V. Padmavathi

Abstract Granular piles have been and continues to be used extensively for improving the ground in terms of increased load carrying capacity, reduced settlements, for rapid dissipation of pore pressures, to mitigate liquefaction effects etc. The effective application of granular piles in soft ground necessitates the knowledge of deformation parameters of the ground and of the granular piles, for determining the behavior of granular piles in different soil conditions. This paper presents a method to estimate the modular ratio of granular piles and modulus of deformation of surrounding in situ soil from the load—settlement response obtained from the compression tests. The direct loading test cases in which the applied load is totally transferred onto the granular pile have been considered in this study.

Keywords Soft ground · Granular piles · Load tests · Settlement influence factor · Modulus of deformation · Modular ratio

1 Introduction

Granular Piles are often used as a ground improvement measure, and are very effective in increasing the load carrying capacity and contribute to reducing the settlements of the ground. Granular piles can usually be constructed using vibro-flotation or ramming techniques. Granular piles are often provided in groups to engineer large areas of ground.

M. Najamuddin (✉)

Geotechnical Engineering, Department of Civil Engineering, JNTUH College of Engineering, Hyderabad, India

e-mail: najamuddin7000@gmail.com

M. R. Madhav

JNT University, Hyderabad, India

IIT Hyderabad, Hyderabad, India

V. Padmavathi

Department of Civil Engineering, JNTUH College of Engineering, Hyderabad, India

The implementation of theoretical solutions to practical problems require sufficient knowledge of the shear and deformation parameters of the soil and granular piles. According to Poulos and Davis [1], the deformation parameters of soil can be determined from laboratory triaxial tests, full-scale load tests, and/or empirical correlations based on previous experiences. The results obtained from the small-scale laboratory tests may comprise of limitations and do not reflect the actual in situ conditions to determine the true in situ parameters. Hence, interpretation of in situ load tests is a better alternative to determine the deformation parameters.

Mattes and Poulos [2] employed linear elastic theory to analyze the behavior of a compressible floating pile of circular cross-section in an ideal elastic soil mass. Pile displacements are expressed conveniently in terms of dimensionless influence factors. Sharma [3] presented analysis of a single granular pile considering both vertical and radial displacement compatibility. Gupta and Sharma [4] considered the non-homogeneity of granular piles for the settlement analysis. Prasad and Madhav [5] presented a parametric study to quantify the percentage of load transferred on to the granular pile as a function of the relative sizes of the granular bed and the rigid plate with respect to the diameter of the granular pile, and relative stiffness of the granular pile with respect to that of in situ soil.

Fatahi et al. [6] proposed a method to determine the deformation modulus of granular pile using numerical simulation. Initially, deformation parameters were assumed in the finite element modelling and the numerical simulation results were compared with in situ test results. The deformation modulus of the granular pile was obtained iteratively based on the accuracy of prediction. In the proposed method, the settlement influence factors given by Mattes and Poulos [2] for a single compressible pile have been utilized in the back analysis for deformation parameters of granular piles and the ground.

2 Methodology

A compressible pile of length, L , and diameter, d , is installed in in situ soil which has modulus of deformation, E_s , and subjected to an applied axial load, P , as shown Fig. 1(a) Mattes and Poulos [2] expressed the settlement of compressible pile, S , shown in Fig. 1(a) by Eq. (1).

$$S = \frac{P}{E_s L} \cdot I_p \quad (1)$$

where I_p is settlement influence factor and depends on the length to diameter (L/d) ratio and the modular ratio (K) of the granular pile.

The relative stiffness or modular ratio of the granular pile is defined as the ratio of modulus of deformation of granular pile to that of the in situ soil ($K = E_{gp}/E_s$). A general load test on granular pile consists of loading arrangement as shown in

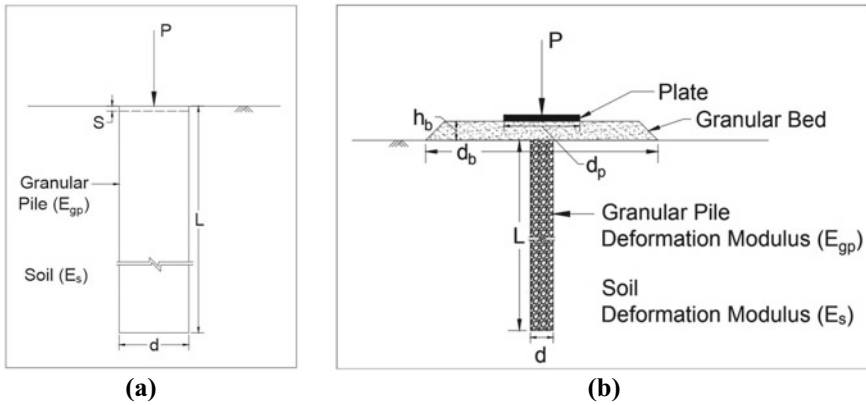


Fig. 1 a Settlement of compressible pile under axial load b Definition sketch for a load test

Fig. 1(b), which includes granular bed of diameter, d_b and thickness, h_b , underneath a test plate of diameter, d_p . The proportion of load transferred to a granular pile through a granular bed depends on the relative sizes of granular bed and test plate involved as discussed in Prasad and Madhav [5]. The entire applied load transmits to the pile, if the test plate and granular bed are of the same diameter as that of the granular pile in presence of granular bed and the test plate diameter is same as the pile diameter in absence of granular bed.

The soil deformation modulus, E_s , is evaluated from Eq. (2), by rewriting Eq. (1) in terms of E_s , in which the estimation of E_s requires knowledge of I_p which is a function of K . The length and diameter of the pile, applied load and settlement are obtained from load test details. Hence, as E_s and I_p are unknown in Eq. (2), the modular ratio is assumed, in order to determine I_p and estimate E_s .

$$E_s = \frac{PI_p}{SL} \tag{2}$$

The settlement influence factor, I_p , is obtained based on L/d and modular ratio, K , from Mattes and Poulos [2] as presented in Fig. 2. The settlement influence factors given by Mattes and Poulos [2] ranges from $K = 10$ to 100 , the I_p values with respect to L/d have been interpreted by extrapolating the curves for $K = 5$ and presented in Fig. 2. I_p is independent of K for an L/d of 5 and for higher L/d , it decreases with increase in modular ratio.

The following steps are proposed to estimate the modular ratio and deformation modulus of granular piles:

1. The settlement and applied load are to be obtained from load–displacement curve of compression test on pile of known length and diameter. The settlement influence factor is to be obtained from Fig. 2, for an assumed modular ratio and known L/d .

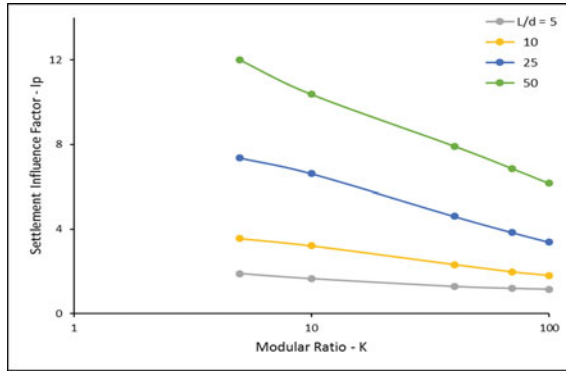


Fig. 2 Settlement Influence factors versus Modular Ratio for $L/d = 5$ to 50 and Poisson’s Ratio of 0.5

2. Deformation modulus of in situ soil, E_s , is to be estimated from Eq. (2) using the parameters in step-1.
3. A plot is to be drawn between E_s and assumed range of K (5–100).
4. A range of soil deformation modulus based on the type of soil present is to be drawn on the same plot.
5. The K versus E_s curve plotted in step-3 is to be used to determine the modular ratio of granular pile from the K values corresponding to the E_s range from step-4.
6. Finally, the range of deformation modulus of granular pile, E_{gp} , is determined based on the E_s and modular ratio K obtained from step-4 and 5 respectively.

3 Case Studies

The present analysis is carried out by collecting data from different case studies of compression test on granular pile. These individual test details are described in Sects. 3.1, 3.2 and 3.3.

3.1 Case Study 1

Hoque and Alamgir [7] studied the behavior of granular pile of 8.5 m length and 0.3 m diameter which were constructed using the rammed-displacement method at the KUET campus, Khulna, Bangladesh. Three load tests were carried out, one on natural soil, second and third on granular pile after one month and one year of installation respectively, to analyze the granular pile behavior and performance with time. A granular pile was tested with a 0.3 m diameter plate which is same as diameter of the pile by placing the plate directly on the pile, without granular bed under the plate. The load displacement response of the three tests are illustrated in Fig. 3(a).

The soil profile existing in site is shown in Fig. 3(b) and the layers are listed from ground level to 18 m depth starting with silty sand followed by clayey silt and organic clay. E_s is estimated for an applied load of 28 kN and corresponding settlement of 3.3 and 4.3 mm for one month and one year respectively from Fig. 3(a).

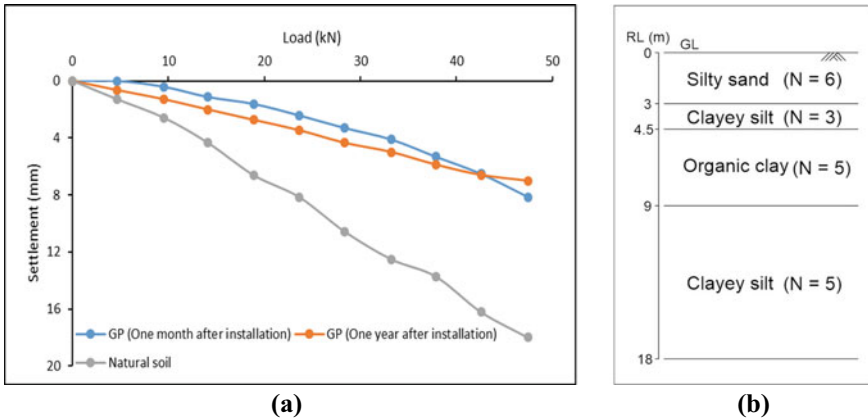


Fig. 3 a Load—Displacement plot from case study 1 b Soil profile—case study 1

3.2 Case Study 2

Bhosle and Vaishampayan [8] carried out load test on a granular pile of 20 m length and 0.9 m diameter, intended to improve the ground conditions for the construction of a container yard at Vallarpadam Island, Cochin, India. These granular piles were constructed using the vibro-replacement method. MS plate of 0.9 m diameter upon a 100 mm sand blanket layer was used in the test. The load settlement response is presented in Fig. 4(a). The settlement and applied load considered, in the estimation of E_s , are 4.2 mm and 230 kN respectively from Fig. 4(a). The subsurface stratification included layers of silty sand with shells, soft clay and fine sand as depicted in Fig. 4(b). The diameter of the sand blanket and the plate used in the test are same as that of the granular pile. Hence, the entire load applied on the plate was considered to be transferred onto the granular pile as the thickness of the sand blanket is less.

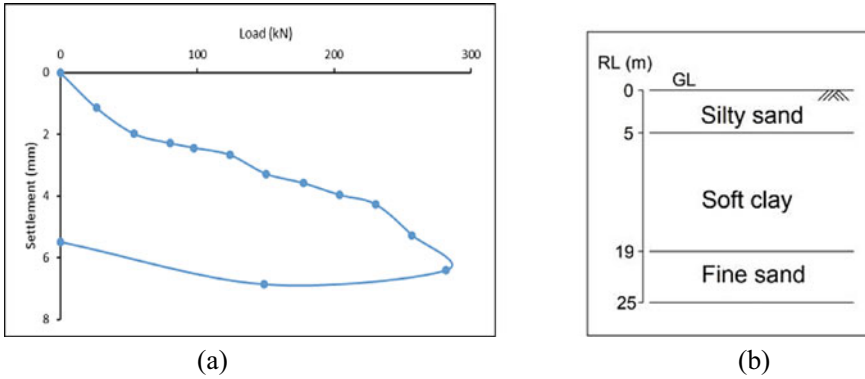


Fig. 4 a Load—displacement plot from case study 2 b Soil profile—case study 2

3.3 Case Study 3

Plate load test was carried out by Mokhtari and Kalantari [9] on granular pile constructed at four different locations (North, South, East, and West) of the site which was located at Bandar Abbas, Iran. The length and diameter of the pile were 12 and 0.8 m respectively. The plate size used for the test was 0.6 m diameter which was directly placed on the pile and the entire load applied is transferred onto the pile. The load displacement response and the soil profile are illustrated in Fig. 5a, b respectively. The applied load considered, in the estimation of E_s , from Fig. 5a for the South case is 12 kN for settlement of 2.3 mm.

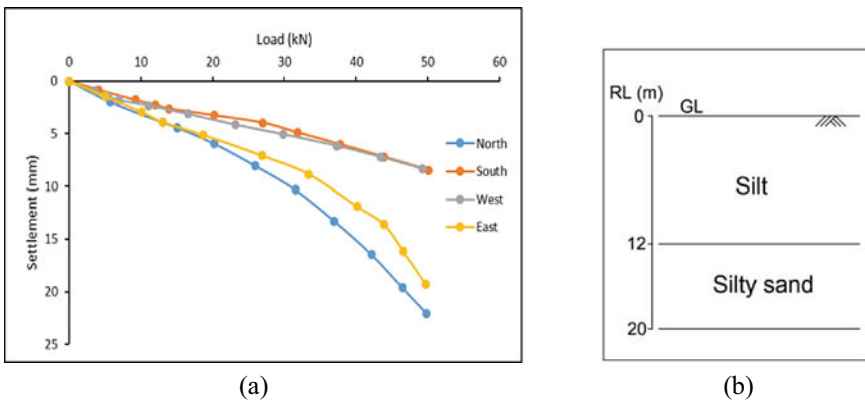


Fig. 5 a Load—displacement plot from case study 3 b Soil profile—case study 3

4 Results and Discussion

The estimated E_s for all the case studies is presented in Table 1 for the assumed modular ratio of 5–100. Table 2 presents the obtained deformation parameters of granular piles for the E_s range based on type of soil (Geotech Data [10]). The weighted average of E_s values along the length of granular pile has been considered by giving higher weightage to the top layer, if soil is stratified.

Table 1 Estimated Modulus of Deformation of Soil

Assumed modular ratio–K	Estimated soil deformation modulus– E_s (MPa)						
	Case study 1		Case study 2	Case study 3			
	Undrained	Drained		North	South	West	East
5	8	6.1	17.9	1.4	2.1	1.6	1.3
10	7.2	5.5	16.1	1.2	1.9	1.4	1.2
40	5.1	3.9	11.3	0.9	1.4	1	0.9
70	4.3	3.3	9.4	0.7	1.1	0.8	0.7
100	3.8	2.9	8.3	0.7	1	0.8	0.6

Table 2 Estimated Deformation Parameters of Granular Pile

Case study		E_s range based on type of soil (MPa)	Modular ratio–K	Deformation modulus of GP– E_{gp} (MPa)
1	Undrained	8–4.4	5–64	40–281.6
	Drained	6.1–4.4	5–28	30.5–123.2
2		14–8.3	22–100	308–830
3 (South)		2.1–1.5	5–31	10.6–46.5

4.1 Results–Case Study 1

The variation of soil deformation modulus with assumed modular ratios is plotted in Fig. 6(a) for the tests performed after one month and one year of installation as described in case study 1. The one-month and one-year behavior of the ground is expected to reflect an undrained and a relatively drained condition respectively. The deformation modulus varies from 8 to 3.8 MPa for the undrained condition and 6.1–2.9 MPa for the drained condition, for a modular ratio range of 5–100, as indicated in Table 1. The undrained E_s is greater than the drained E_s throughout the range of K for the same load-settlement response. Based on soil stratification—silty sand, clayey silt and organic clay, the E_s range from Geotech Data [10] is 4.4 to 9.3 MPa which

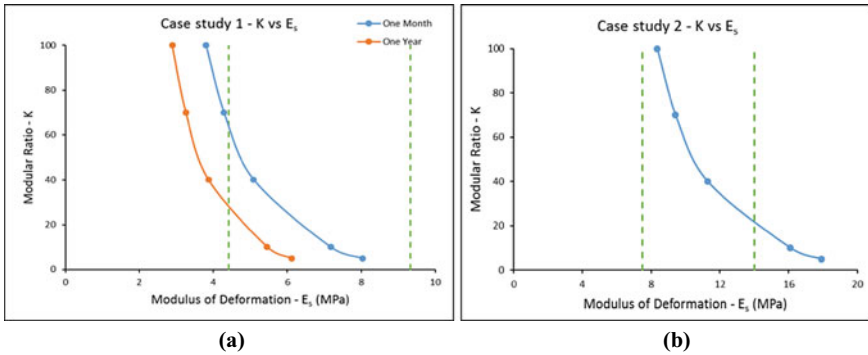


Fig. 6 a Variation of E_s with K for case study 1 b Variation of E_s with K for case study

is depicted in Fig. 6(a). The modular ratios obtained within this range, as presented in Table 2, for the undrained and drained conditions is 5–64 and 5–28 respectively. Hence, the granular pile deformation modulus is 40–281.6 MPa and 30.5–123.2 MPa for the undrained and drained condition respectively.

4.2 Results–Case Study 2

The soil deformation modulus for case study 2 is depicted in Fig. 6(b) which varies from 17.9 to 8.3 MPa for modular ratio of 5 to 100. An E_s range from Geotech Data [10] based on soil layers present—silty sand with shells, soft clay, and fine sand, which is 7.5–14 MPa. The modular ratio obtained from Fig. 6(b) for an E_s range of 14–8.3 MPa is 22 to 100 and the modulus of deformation of the granular pile (E_{gp}) obtained is 308–830 MPa.

4.3 Results–Case Study 3

The results for all the load tests involved in case study 3—North, South, West, and East are illustrated in Fig. 7(a). The estimated soil deformation modulus, for the load test conducted at the south side of the site, is 2.1–1 MPa for a modular ratio range of 5–100 respectively. The E_s range for silt from Geotech Data [10] is around 1.5–6 MPa. Hence, for the South side of the site, for an E_s of 2.1–1.5 MPa, the modular ratio from the Fig. 7(a) is 5 to 31 and the corresponding granular pile deformation modulus is 10.6 to 46.5 MPa as presented in Table 2.

The estimated soil deformation modulus in this case study tends to be lesser than the range of the E_s based on the type of soil. This might be due to the diameter of the plate (0.6 m) used for the load test being less than the granular pile diameter (0.8 m).

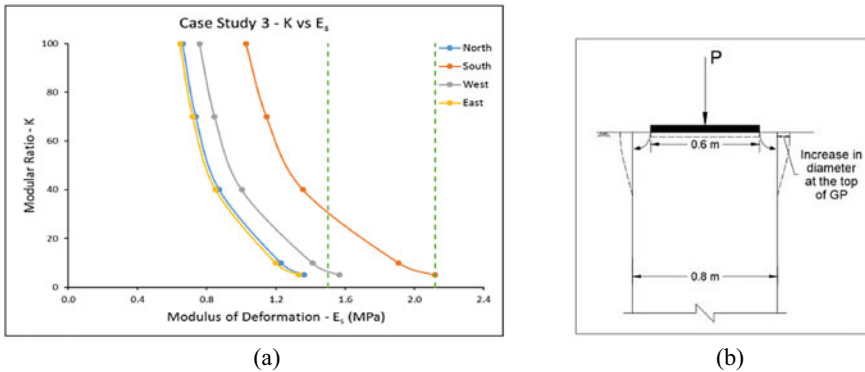


Fig. 7 a Variation of E_s with K for case study 3 b Case study 3 loading arrangement

As there is no confinement for the granular pile, due to the smaller plate size, on the application of load there might be squeezing out of granular pile material which increases the diameter at the top of the pile (Fig. 7(b)) and this affects the settlement influence factors. If the diameter at the top of the granular pile does not increase due to the squeezing out of pile material, then the influence factors will tend to be higher which in turn results in higher E_s values.

5 Conclusion

Efficient ground improvement using granular piles requires understanding of its settlement behavior. This settlement prediction depends on the deformation parameters of ground and granular piles. The method proposed in this study, aims to estimate the deformation parameters which reflect the actual in situ behavior of the reinforced ground. The design of granular pile can be enhanced by estimating the deformation modulus of the granular pile. The proposed method was validated using different case studies and it indicated that this method can be applied to back analyze deformation parameters from in situ load tests which helps in predicting the accurate settlement of granular piles.




References

1. Poulos HG, Davis EH (1980) Pile foundation analysis and design. John Wiley & Sons Inc., New York
2. Mattes NS, Poulos HG (1969) Settlement of single compressible pile. J Soil Mech Found Divis ASCE 95(1):189–207
3. Sharma JK (1999) Analysis and settlement of granular pile (s)—single, in group and with raft. A thesis submitted for the degree of Doctor of Philosophy to the Department of Civil

- Engineering, Indian Institute of Technology, Kanpur, India
4. Gupta P, Sharma JK (2018) Settlement analysis of non-homogeneous single granular pile. *Indian Geotechnic J* 48(1):92–101
 5. Prasad RGB, Madhav MR (2006) Load transfer through a granular bed onto a granular pile in soft ground. In: *Proceedings of international symposium of lowland technology*. Saga, pp 225–228
 6. Fatahi B, Basack S, Premananda S, Khabbaz H (2012) Settlement prediction and back analysis of Young's modulus and dilation angle of stone columns. *Aust J Civ Eng* 10(1):67–80
 7. Hoque MI, Alamgir M (2014) Study on the field performance of granular pile as a ground improvement technique. *J Eng Sci* 05(1):103–115
 8. Bhosle S, Vaishampayan VV (2009) Ground improvement using vibro stone columns—capacity of stone columns. In: *Proceedings of Indian Geotechnical Conference*. Guntur, pp 510–513
 9. Mokhtari M, Kalantari B (2019) Behavior of stone columns based on plate load test and FEM analysis on the north end of persian Gulf. *Electron J Geotech Eng* 24(05):1317–1326
 10. Geotechdata.info. Soil Young's Modulus. <http://geotechdata.info/parameter/soil-Young-s-modulus>. Accessed 29 June 2022

Resilient Modulus as a Technical Parameter for Evaluating the Cement-Stabilized Soil



Patryk Dobrzycki , Katarzyna Zabielska-Adamska ,
and Mariola Wasil 

Abstract The design and construction of road pavement substructures involves compacting aggregate in conditions close to optimum moisture content. The recommendation introduced by AASHTO, obliges designers to use mechanistic-empirical design methods by using the resilient modulus. The value of cyclic resilient modulus is determined based on cyclic triaxial tests, in which elastic axial strain and cyclic deviator stress are measured. Laboratory tests were performed on natural (gravelly sand) and chemically stabilised (CEM I 42.5 R) soil. The study compared the effect of different cement additives (1.5, 3.0, 4.5, 6.0%) on the resilient modulus tested on samples which were compacted using the Standard Proctor method. The addition of cement increased the stiffness of the soil and the resilient modulus, while the elastic axial strain has decreased. The samples were tested after 7 and 28 days of care. A longer period of treatment increased the resilient modulus. The gravelly sand stabilised with cement obtained high values of resilient modulus.

Keywords Resilient modulus · Cyclic load · Stabilised soil

1 Introduction

The road base is the part of the pavement structure whose main function during exploitation is to transfer and distribute the stress caused by the movement of vehicles on the road. Subbase layers may be made of asphaltic concrete, unbound mixtures or binder-bound mixtures. Depending on the type and position of the substructure in the structure, the materials permitted for their construction may be different [1]. The American Association of State Highway and Transportation Officials (AASHTO) standard introduced the resilient modulus (M_r) [2] as a basic parameter of mechanistic design for pavement and pavement layers to determine layer thickness and overall

P. Dobrzycki (✉) · K. Zabielska-Adamska · M. Wasil
Department of Geotechnics and Structural Mechanics, Białystok University of Technology,
Białystok, Poland
e-mail: p.dobrzycki@doktoranci.pb.edu.pl

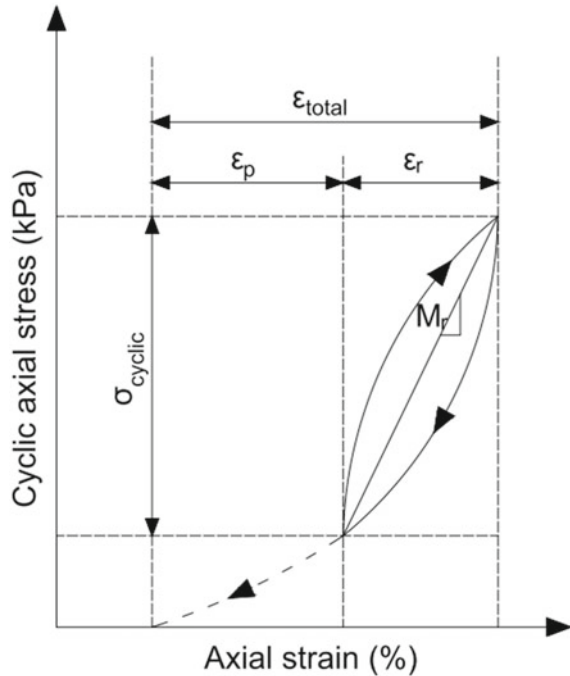
system response to traffic loads in the case of flexible pavements. The formula for determining M_r is related to applied cyclic axial stress (σ_{cyclic}) and relative resilient axial strain (ϵ_r).

$$M_r = \sigma_{cyclic} / \epsilon_r \tag{1}$$

Cyclic loading causes an increase in the resilient modulus of unsaturated soil. It is related to the plastic strengthening of the soil, which, as a result of successive cycles of the same stress, corresponds to a decrease in plastic deformation and an increase in elastic deformation [3]. In Fig. 1, it can be seen the stress in the test specimen changes during cyclic loading.

The review of the literature shows that many researchers have investigated the effect of different parameters on the resilient modulus of various types of soil. The elasticity of unbound materials is most often assessed using a triaxial apparatus, but other methods can also be used, including a simple shear test, torsional resonance column test, a hollow cylinder test and a true triaxial test. The most frequently studied parameters are the influence of deviator stress and confining pressure, the time and frequency of loading, the number of loading cycles, the grain size and density of the material and the degree of saturation [3]. In the literature, various mathematical models for predicting the elastic response of materials under repeated loading can

Fig. 1 Specimen response to cyclic loading during resilient modulus testing; ϵ_p is the constant relative deformation and ϵ_r is elastic relative deformations



also be found. They present, *inter alia*, the modelling of permanent deformation as a function of the number of load applications and stress conditions.

The significance of elastic modulus in design is discussed by Nazarian et al. [4]. They used different pavement design models to demonstrate the importance of resilient modulus values for the required pavement thickness and to prove the importance of obtaining a reliable elastic modulus measurement for mechanistic-empirical pavement design. Various pavement analysis algorithms and material models have been analysed to demonstrate the influence of resilient modulus on mechanistic-empirical pavement design. The study showed that inaccuracies in analysis algorithms and testing procedures have a significant impact on the design.

Another important parameter that affects the resilient modulus is the effect of the stabilizing additive. The vast majority of publications refer to lime-stabilised soils. The effect of lime addition and curing time on the modulus of elasticity is most commonly evaluated [5]. An increase in resilient modulus values was observed with the percentage of (0–8%). In the case of lime addition at 4, 6 and 8%, the effect of curing time is evident.

Significantly lower numbers of publications and literature refer to cement stabilization. The amount of cement used to stabilize the soil depends on the soil grain size, composition and requirements. Cement affects the cohesive soil by increasing its cohesion and reducing its water absorption and plasticity. Its content in stabilization is usually in the range of 4–10% [6]. Larger amounts of cement addition increase the strength but also increase the risk of shrinkage and cracking.

The aim of the research is to consider the impact of various percentages of cement additives: 1.5, 3.0, 4.5, and 6.0% on the resilient modulus and quick shear strength of non-cohesive soil used for the construction of road base and subbase.

2 Materials and Methods

2.1 Materials

Laboratory tests to determine the resilient modulus were carried out on soil–cement mixtures. The cement that was used as a stabilizer was Portland cement 42.5R. The cement was mixed with the soil in different proportions in the range of 1.5–6%. The cement percentage referred to the dry weight of the cement relative to the dry weight of the coarse soil in the test sample.

One of the basic tests to determine the granulometric composition was sieve analysis, which was performed in accordance with the EN 933–1 standard [7]. The results of the test are presented in Fig. 2.

Comparing the results with EN ISO 14688–1 [8], the tested soil is gravelly sand (grSa). In order to determine whether the soil is well-graded, the coefficient of homogeneity – C_U and the coefficient of curvature – C_C , were calculated from the grain-size curve. The values of $C_U = 5.45$ and $C_C = 0.87$ indicate that the tested soil is

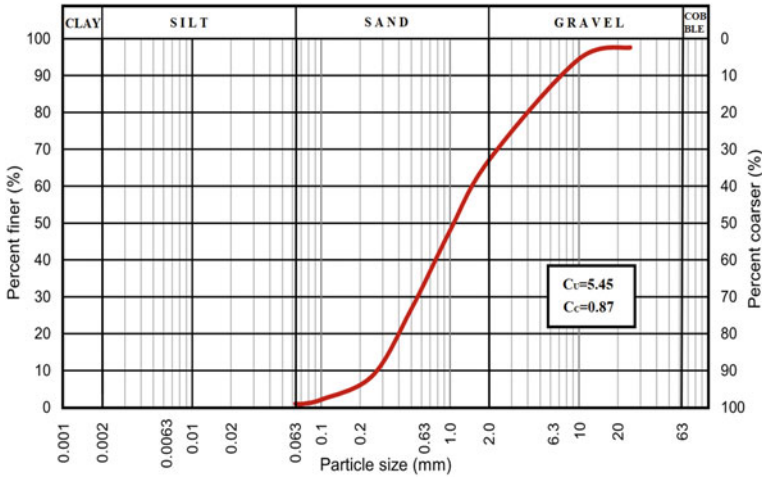


Fig. 2 The grain-size curve of tested soil

poorly graded [9]. The tested soil can be used as base or subbase course material (gradation D) with a lower percentage of fine fractions as it meets the requirements of EN 13,242 [10].

The gravelly sand is a post-glacial soil, which is characterized by a large variation in x of grain. The soil contains well-rounded quartz crumbs and angular grains, with significant lithic and feldspar particles [11].

Another laboratory test performed was the standard Proctor test, which was carried out in accordance with EN 13,286–2 [12]. It was carried out to determine the optimum moisture content (w_{opt}) and the maximum dry density ($\rho_{d max}$). Tests were conducted on gravelly sand and sand with different cement additions (1.5, 3, 4.5 and 6%). The results of the tests are presented in the compaction curves in Fig. 3.

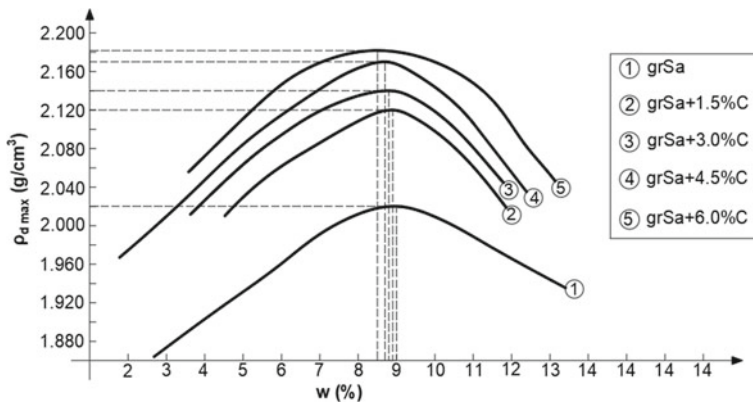


Fig. 3 Compaction curves of tested materials

Table 1 Geotechnical parameters of the tested materials

Material	w_{opt} (%)	$\rho_{d\ max}$ (g/cm ³)	e (-)	ρ_s (g/cm ³)
grSa	9.00	2.020	0.31	2.65
grSa + 1.5%C	8.90	2.120	0.25	2.66
grSa + 3.0%C	8.80	2.140	0.24	2.66
grSa + 4.5%C	8.70	2.170	0.23	2.67
grSa + 6.0%C	8.50	2.182	0.23	2.68

C-cement addition

Table 1 provides the compaction parameters (w_{opt} and $\rho_{d\ max}$), the initial void ratio $-e$ and the specific dry density $-\rho_s$.

The addition of cement increases the maximum dry density of soil and slightly decreases the optimum moisture content. A review of the literature shows that many researchers have also confirmed this relationship [13, 14]. The void ratio e decreases with increasing cement addition, while the value of ρ_s increases insignificantly.

2.2 Methods

Tests were performed on compacted specimens of gravelly sand with cement additions. Initially, the dried soil was mixed with cement, then sufficient amount of water was added to obtain the optimum moisture content for each material (see Table 1). The samples were prepared in a bipartite cylindrical mould by compacting the material in three layers. The height of the sample was approximately 140 mm, and the diameter was about 70 mm.

The main test apparatus was the Dynatriax Cyclic Triaxial System shown in Fig. 4, which allows full automation and control of all the parameters that are required to perform a cyclic triaxial test. Specimen deformations are measured using external LVDT sensors built into the actuator piston and at the top of the chamber.

The design manual introduced by AASHTO specifies the parameters to be used when testing the resilient modulus [2]. The specimen is loaded cyclically in 16 sequences in which parameters such as chamber pressure, axial stress, cyclic stress and contact stress are changed. The number of cycles for sequence 0 is 500–1000 cycles, and for the other sequences, the number of cycles is constant and is 100. Sequence “0” is the conditioning of the sample. In the next fifteen sequences confining pressures range from 20.7 to 137.9 kPa, and maximum axial stresses range from 20.7 to 275.8 kPa. The resilient modulus M_r for sequences from 1 to 15 is calculated as the average value from the past five cycles of each load sequence.

Fig. 4 Laboratory equipment



Once all sequences have been completed the quick shear tests have proceeded. The confining pressure in the chamber during the test was 34.5 kPa. The applied load generated axial deformation at a rate of 1% per min. The test was stopped when the specimen failed (drop in force, increase in deformation).

3 Results and Discussion

All stabilised specimens passed the cyclic loading tests, hence the calculation of the resilient modulus was possible, which was not obtained for gravelly sand alone [11]. The specimens failed only after the quick shear test. Figure 5 shows a graph of the change in resilient modulus during the execution of all loading cycles for a gravelly sand sample with 1.5% cement added, cured for 28 days. M_r increased rapidly at the beginning and became almost constant after 600 loading cycles, which can be observed in sequence 1. This behaviour may be due to the cyclic compaction of the sample under increasing maximum axial stress. Another observation is that the highest increase in modulus could be seen during the three sequences (sequences 0, 12 and 15) when the highest increase in axial stress occurred. The highest value of modulus for all the tested specimens was obtained in sequence 15. The reason for this is that confining pressure and max applied axial stress have the largest values and

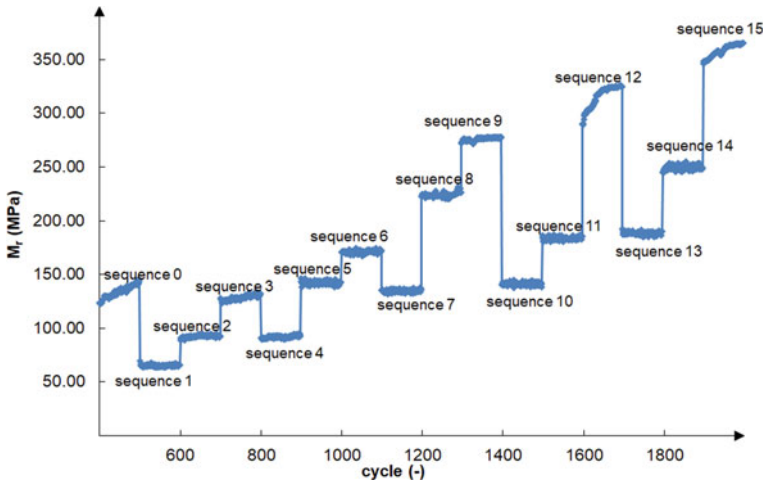


Fig. 5 The plot of change in resilient modulus during all load cycles for a specimen with 1.5% cement added and cured for 28 days

are respectively: 137.9 and 275.8 kPa. The lowest modulus values occurred during sequence 1, where σ_3 and σ_1 were the lowest and had the same values -20.7 kPa.

The resilient modulus increased as a result of increasing confining pressure and maximum axial load. Figure 6 shows the dependence of the resilient modulus on varying cyclic applied axial stress. It is shown in two plots as a function of specimen care length. The addition of cement has a significant effect on the increase of the elastic modulus values. Increasing the cement addition by 1.5% increased the resilient modulus values by around 50% in most cases evaluated for the same sequence. Another similarity is that samples cured for 28 days had a higher M_r value than those cured for 7 days. Samples stabilized with 1.5–6.0% cement addition achieved elastic modulus values in the range 63–789 MPa after 7 days of curing and 73–921 MPa after 28 days. Another relationship that can be deduced from Fig. 5 is that the lowest coefficients of determination R^2 , but explaining more than 50% of the variables, were for samples with cement additions of 4.5 and 6%. In both cases, this may be due to the drying of the samples during curing.

Table 2 shows the resilient modulus and quick shear strength (axial stress σ_1 at failure) as a function of the percentage of cement content and the length of care. It can be observed that both parameters increased with rising cement addition in the sample. A similar relationship was found for the length of care. Samples, after 28 days, achieved higher values of both parameters than those that were cared for 7 days. Samples with 1.5 and 3% cement addition achieved similar values despite the different lengths of care. The specimen with 6% cement addition, cured for 7 days, and the specimens with 4.5 and 6% of cement cured for 28 days, were not destroyed during the quick shear test performed after cyclic loading. The apparatus reached a maximum contact force of 10 kN.

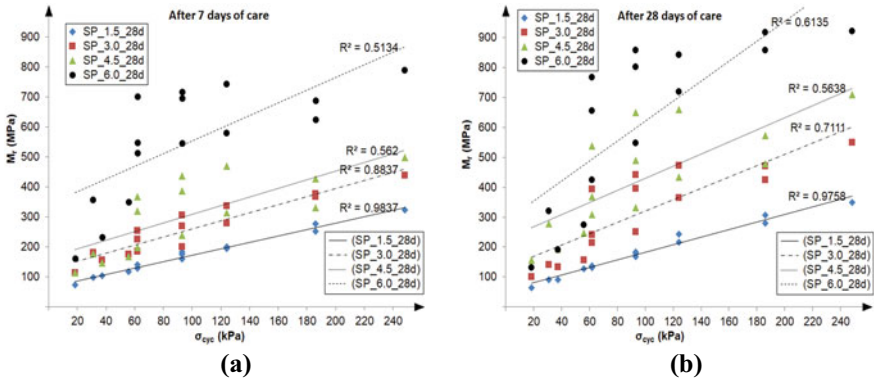


Fig. 6 Dependence of resilient modulus on cyclic applied axial stress after 7 and 28 days of care

Table 2 The resilient modulus and axial stress as a function of time of curing

Material	After 7 days of care		After 28 days of care	
	M_r (MPa)	σ_I (kPa)	M_r (MPa)	σ_I (kPa)
grSa + 1.5%C	324	855	349	1180
grSa + 3.0%C	439	1375	549	1518
grSa + 4.5%C	498	1572	709	>2600
grSa + 6.0%C	789	>2600	921	>2600

4 Conclusion

Based on the test results the following conclusions were reached:

- (1) The addition of cement significantly increases the resilient modulus values obtained and reduces the relative elastic axial strain. Increasing the cement addition by 1.5% resulted in approx. 50% increase in the resilient modulus value in most cases evaluated. Increasing the curing time of the sample from 7 to 28 days also has a positive effect on the resilient modulus value, increasing it.
- (2) The addition of cement, as well as the length of care, has an effect on the quick shear strength. All samples were subjected to 16 cyclic loading sequences and finally, the quick shear test was performed. The axial stress at failure increases with an increase in cement addition and time of curing.

References

1. Law H, Kinnear Clark D (2017) *The construction of roads and streets*, 3rd edn. Hanserbooks, Norderstedt, Germany
2. AASHTO T 307-99 (2021) Standard method of test for determining the resilient modulus of soils and aggregate materials. American Association of State and Highway Transportation Officials, Washington, DC, USA
3. Brown SF (1996) Soil mechanics in pavement engineering. *Geotechnique* 46:383-426
4. Nazarian S, Abdallah I, Meshkani L, Ke A (2003) Use of resilient modulus test results in flexible pavement design. ASTM International
5. Bhuvaneshwari S, Robinson RG, Gandhi SR (2019) Resilient modulus of lime treated expansive soil. *Geotech Geol Eng* 37:305-315
6. Saxena P, Tompkins D, Khazanovich L, Balbo JT (2010) Evaluation of characterization and performance modeling of cementitiously stabilized layers in the mechanistic-empirical pavement design guide. *Transp Res Rec* 2186:111-119
7. Tests for geometrical properties of aggregates—part 1: determination of particle size distribution—sieving method; EN 933-1:2012. (2012). European Committee for Standardization, Brussels, Belgium
8. Geotechnical Investigation and Testing. (2018). Identification and classification of soil. In: Identification and description; EN ISO 14688-1:2018. ISO, Geneva, Switzerland
9. Geotechnical Investigation and Testing. (2018). Identification and classification of soil—part 2; EN ISO 14688-2:2018-05. ISO, Geneva, Switzerland
10. Aggregates for unbound and hydraulically bounded materials for use in civil engineering work and road construction; EN 13242: 2007. (2007). European Committee for Standardization: Brussels, Belgium
11. Zabielska-Adamska K, Wasil M, Dobrzycki P (2021) Resilient response of cement-treated coarse post-glacial soil to cyclic load. *Materials* 14(21):6485
12. Unbound and hydraulically bound mixtures—part 2: test methods for laboratory reference density and water content—proctor compaction; EN 13286-2:2010. (2010). European Committee for Standardization, Brussels, Belgium
13. Shooshpasha I, Shirvani RA (2015) Effect of cement stabilization on geotechnical properties of sandy soils. *Geomech Eng* 8:17-31
14. Zabielska-Adamska K (2008) Laboratory compaction of fly ash and fly ash with cement additions. *J Hazard Mater* 151:481-489

Effect of Freeze–Thaw Cycles on the Strength of a Nanosilica and Lime Treated Clay



İsmail Taş  and Tugba Eskisar 

Abstract In this study, the unconfined compressive strength of a clay treated with nanosilica and lime was investigated under freeze–thaw conditions. The specimens were prepared at their corresponding optimum water contents and compacted under a standard Proctor compactive effort. The pure clay and the clay treated with 5% lime were subjected to freeze–thaw cycles to determine the strength changes of specimens. The maximum number of cycles applied to the specimens was 10. The cycles were applied in 12 h intervals and the temperature range was ± 18 °C. Subsequently, the clay was treated with 0.3, 0.5, 0.7 and 1% nanosilica and 5% lime. The clay specimens showed a tendency to decrease in strength as a result of freeze–thaw cycles. The maximum strength loss observed was around 41%. It was concluded that, it was not possible to achieve sufficient amount of improvement by using solely nanosilica in the clay specimens. The unconfined compressive strength of nanosilica and lime treated clay accelerated with curing time. Besides, the strength loss of specimens due to freeze–thaw cycles could be partially prevented with the addition of nanosilica and lime. Consequently, usage of nanosilica together with lime, resulted in a better improvement, even if the soil was subjected to freeze–thaw cycles.

Keywords Clay · Unconfined compressive strength · Freeze–Thaw cycles · Nanosilica · Quicklime

1 Introduction

The environmental conditions have an impact on the variation of the soil properties. Freezing of the ground is a seasonal phenomenon that can be encountered frequently in many parts of the world [1]. The freeze–thaw effects, especially on soils with expansive clay content, frequently cause great damage and costs to structures. It is an important issue to improve the properties of soils for freezing and thawing [2].

İ. Taş · T. Eskisar (✉)

Department of Civil Engineering, Ege University, Bornova, İzmir 35100, Turkey
e-mail: tugba.eskisar@ege.edu.tr

Bell [3] determined that the mineralogy of clay was a very important in the stabilization of the soils. The soil mineralogy and temperature criteria were efficient on the plasticity and strength gain rate of the soil, and the success of the stabilization. Bell [4], inspected the lime stabilization of clays with different mineralogies. When lime is added to the clay soils, calcium ions interact with clay minerals up to the lime fixation point. Lime is effective in terms of workability rather than strength up to the optimum lime content. Kaolin reacts to the lime later than montmorillonite, but montmorillonite would not have a higher late strength than kaolin [4]. Dash and Hussain [5] investigated the lime stabilization using quicklime in high and low plasticity soils. They pointed out that the presence of excess lime in silica-rich soils in which silica gel was formed, gave a rise to the reduction of the overall strength. The silica gel led to increased plasticity and swelling of the soils.

Zhang [6] presented that even a small amount of nanoparticles could be important on the behavior and mechanical properties of soils due to the high surface area of the nanoparticles affecting the physico-chemical behavior of the soils. Changizi and Haddad [7] assessed the effect of nanosilica particles to improve the mechanical properties of low and high liquid limit clay soils. The nanosilica Dash and Hussain ratios used in the study were determined as 0.5, 0.7, and 1.0%. The unconfined compressive strength increased by up to 56%. With the increase of nanosilica content, the deformations measured at the time of failure decreased and the elastic modulus values increased. The addition of nanosilica significantly improved the mechanical properties of the clay. Moayed et al. [8] investigated the interaction of kaolin clay and nanosilica in their study. The soils specimens treated with nanosilica contents ranging from 1 to 5% were examined. The remarkable increase in unconfined compressive strength was observed at 4% nanosilica content. Although nanosilica has been the point of focus, different nano-sized materials such as nano-copper, nano-clay and nano-magnesium nano-ZnO were also investigated in the literature [9, 10].

Kalhor et al. [11] subjected nanosilica treated fine-grained soils to nine freeze–thaw cycles, and recommended 2% nanosilica addition to the soils. Shahsavani et al. [12] reported that extension of curing time improved the unconfined compressive strength of the slag and nanosilica treated specimens against the freeze–thaw cycles.

Different types of additives have a possible use in the soil improvement, but the types of additives that can provide environmentally friendly solutions are limited. Nanosilica additive is in the “green binder” category and as a new additive, its full effect on soils have not been revealed yet [13]. Besides, the freeze–thaw behavior of the nanosilica added soils has been merely studied.

This study deals with the freeze–thaw cycle effects on characteristics of a clay soil stabilized with nanosilica and lime. Atterberg limits, compaction, unconfined compression and freeze–thaw tests are performed to observe the changes in the soil properties.

2 Materials and Testing Methods

2.1 Materials

The kaolin clay was derived in powder form from a local quarry and it was classified as a high plasticity silty soil MH according to ASTM D2487 [14]. ASTM D4318 [15] was followed in the determination of Atterberg limits, and ASTM D698 [16] was followed for the standard compaction test. The liquid limit of the soil was 52%, the plastic limit was 34%, and the plasticity index was 18%. The optimum water content of the soil was 32%.

Quicklime was preferred as a stabilizing agent. The lime was obtained from a quarry company. The chemical analysis of lime showed that 95.6% was CaO and 0.9% was MgO and the remaining was trace elements. The nanosilica particles were purchased from Molchem Industries Ltd.; they were 15 nm in size with a purity of 99.5%.

The lime content of the study was 5% by the dry weight of the soil. The nanosilica contents used in the study were 0.3, 0.5, 0.7 and 1%.

2.2 Testing Methods

The specimens of unconfined compressive tests and freeze–thaw tests were prepared in the following manner: First, the dry soil and lime were mixed. Then, nanosilica was mixed in the water for 5 min with a high speed (120 rpm) mixer and added to the dry mixture. The water contents of the specimens were adjusted to their optimum water contents. The specimens had a diameter 50 mm and a length of 100 mm. The specimens were covered with an airtight film to secure the water content and placed in a moisture room until the end of their curing time. The temperature of the moisture room was 23 ± 2 °C with a relative humidity of 90–95%.

The freeze–thaw tests were carried out on the specimens when the curing period was completed. In the freeze–thaw tests, the specimens were exposed to 5 or 10 freeze–thaw cycles. The freeze thaw tests were performed according to ASTM D560 [17]. The freezing temperature was in the range of -18 ± 2 °C and the thawing temperature was in the range of $+18 \pm 2$ °C. The time for each freezing or thawing action was 12 h; 1 cycle was completed in 24 h. The specimens were subjected to the unconfined compressive tests after their completion of the freeze–thaw cycles by following ASTM 2166 [18].

3 Results and Discussion

3.1 The Effect of Lime

The Atterberg limits of the 5% lime treated soil were determined. The liquid limit and the plastic limit of the treated soil was 75 and 44%, respectively. The rise in the Atterberg limits was due to the action of hydroxyl ions which modified the affinity of the surfaces of the clay particles for water. The plasticity properties obtained within the short-time of the test were governed by the rearrangement of clay particles induced by the addition of lime and not by bonding induced by the pozzolanic reactions [19].

The compaction tests of clay and lime treated clay were carried out separately (Fig. 1). With the addition of 5% lime to the soil, the maximum dry unit weight decreased and the optimum water content of the treated soil increased. The optimum water contents and the maximum dry densities of clay and lime treated clay soils were 32 and 38%, and 1.60 g/cm³ and 1.50 g/cm³, respectively.

The specimens were subjected to the unconfined compressive tests after the freeze–thaw cycles were completed. The clay soil had a strength of 205 kPa. After 5 and 10 cycles of freeze–thaw, the strength of the clay decreased to 192 and 160 kPa, respectively. The 5% lime treated specimen which was cured for a day and then subjected to 10 cycles of freeze–thaw resulted in a strength of 195 kPa. The strength of 5% lime treated clay was 312 kPa after 7 days and it increased to 408 kPa after 28 days.

In Fig. 2, it is seen that the behavior of clay has changed from ductile to brittle behavior with the action of freeze–thaw. The natural clay reached its peak strength at a strain of 6.09%, while the axial strain of clay after 10 cycles of freeze–thaw was 1.89%. Lime addition also contributed to the brittle behavior of the clay. The stress–strain curve of 28-day specimen of 5% lime treated clay is also given in Fig. 2.

Fig. 1 The optimum water content of clay and lime treated clay

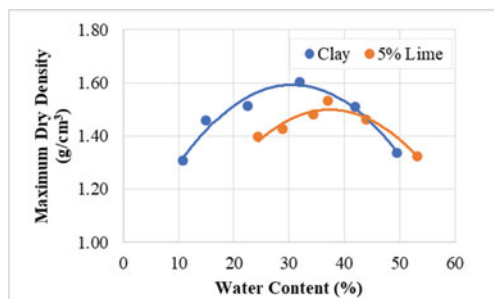
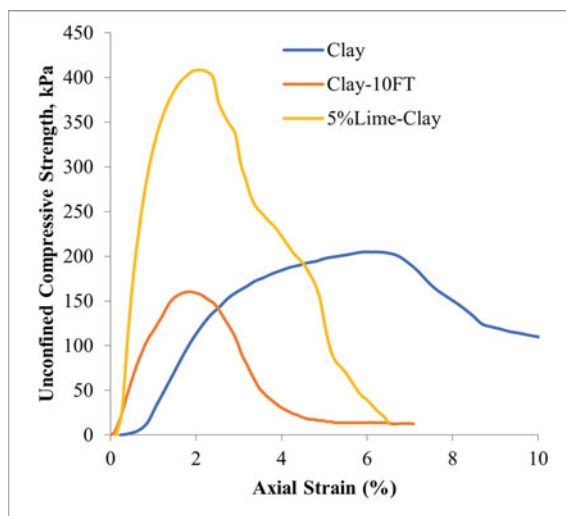


Fig. 2 Stress–strain curves of the specimens



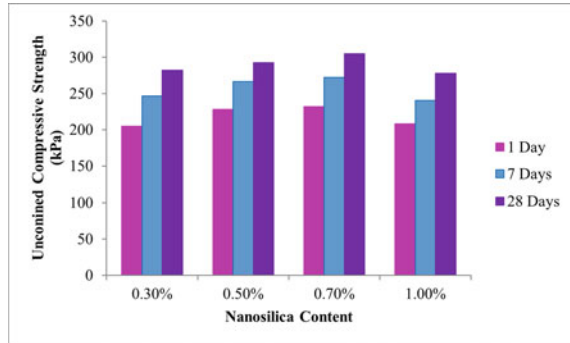
3.2 The Effect of Nanosilica

In order to examine the effect of the nanosilica on the strength, the specimens containing 0.3, 0.5, 0.7 and 1% nanosilica were prepared. The contribution of nanosilica was evident even in 1-day specimens (Fig. 3). The gradual increase of the strength was observed among 0.3, 0.5, and 0.7% nanosilica treated specimens. However, there was a decrement of strength in 1% nanosilica treated specimens. The excessive rate of nanosilica had a strength reducing effect rather than contributing to it. The addition of 0.7% nanosilica increased the strength to 305 kPa after 28 days and this strength was almost 1.5 times of the strength of the untreated clay soil. Therefore, the optimum nanosilica content was 0.7% in clay specimens. Changizi and Haddad [20] and Hu et al. [21] expressed that when water was added to the clay, the nanosilica particles produced a viscous gel across the diffuse double layer of the clay particles. Due to the viscous gel, the bonding force between the clay particles was much stronger than the absorbed water. The viscous gel reduced the distance between particles and increased the particle contact. The cohesion between the clay particles due to the viscous gel was stronger than the cohesion between the clay particles, due to the presence of absorbed water [7]. The viscous gel filled the macropores in the clays to some extent [21, 22].

When the 28-day specimens of 0.7% nanosilica treated and 5% lime treated specimens were compared, it was seen that lime treatment was still superior in terms of strength. For this reason, a better stabilization could be achieved with the simultaneous application of nanosilica and lime to the soils.

The effects of 5 and 10 freeze and thaw cycles were investigated on the nanosilica treated specimens. The cycles were consecutively repeated in this study until its effect on the soil strength became negligible, which was termed as an equilibrium [2,

Fig. 3 The strength of clay treated with different nanosilica contents



11]. The strength loss of 5 cycles of freeze–thaw was more pronounced compared to the strength loss of the specimens that were subjected to 10 cycles (Fig. 4). The soil strength reduction occurred in earlier cycles and after 5 to 10 cycles the strength reduction would reach to an equilibrium condition [23]. The strength decreased remarkably in 0.3 and 1% nanosilica treated specimens after 5 cycles of freeze–thaw. The strength of the specimen in 0 cycle was accepted as 100%, and the strength reduction calculated in percentage from this value was called “strength loss”. The strength loss of 0.7% nanosilica treated specimens was 16%, while the strength loss of 1% nanosilica treated specimens was 41%, indicating the deterioration level of the specimens after 10 cycles of freeze–thaw. Although trace amounts of nanosilica were used in this study, 0.5 and 0.7% nanosilica treated specimens kept the majority of their strength against the freeze–thaw cycles. In order to reinforce the binding effect of the soil particles, using nanosilica together with an additive such as lime would also help to prevent the deteriorations against freeze–thaw.

Fig. 4 The effect of freeze–thaw cycles on the nanosilica treated clay

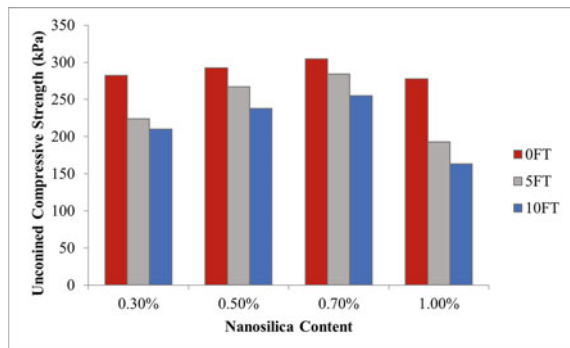
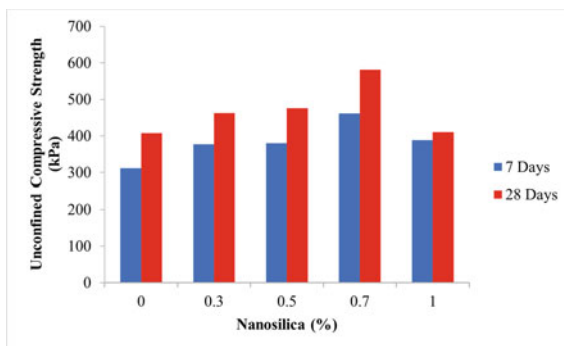


Fig. 5 The strength of the clay treated with nanosilica and lime



3.3 The Binary Effect of Nanosilica and Lime

According to the results of the unconfined compressive strength tests, the highest strength was achieved with 0.7% nanosilica-5% lime treated clay after 28 days (Fig. 5). The 28-day strength of the specimens treated with 0.7% nanosilica and 5% lime was 125% higher than their 7 day strengths. The 28-day strength of the same specimen was 581 kPa and it was the highest strength among the experimental groups.

An evaluation of the strength decrement of 7-days 0.7% nanosilica-5% lime treated specimens showed that, at the end of 5 freeze–thaw cycles, the strength of the specimens was 409 kPa. After 10 freeze–thaw cycles, the strength of the specimens decreased to 373 kPa. This result showed that the strength of the treated specimens had 1.82 folds more strength compared to that of untreated clay. Adding lime to the soil caused long-term pozzolanic reactions and nanosilica had an accelerating effect on the reactions in the soil medium. Besides, the formation of viscous gel increased the durability of the specimens when they were subjected to freeze–thaw cycles.

4 Conclusion

The effect of nanosilica and lime treatment on the unconfined compressive strength of a clay soil was assessed. The outcomes of the study are as follows:

- (1) As a result of lime treatment of the clay soil, the maximum dry unit weight decreased and the optimum moisture content of the soil increased.
- (2) The unconfined compressive strength decreased with freeze–thaw cycles in the clay and the lime treated clay. The strength of the clay was 205 kPa and the strength of 5% lime treated clay was 221 kPa. After 10 cycles of freeze–thaw, the strength of the clay and 5% lime treated clay decreased to 160 and 195 kPa, respectively.

- (3) The addition of nanosilica at different rates from 0.3 to 1% on clay soil showed some strength gain between 7 and 28 days. The highest strength was obtained with 0.7% nanosilica content. However, the strength of solely lime treated specimens were greater than the specimens that were treated with solely nanosilica.
- (4) The unconfined compressive strength of the specimens treated with the optimal amount of nanosilica and lime was 2.25 and 2.83 folds of the untreated clay after 7 and 28 days of curing, respectively. These results were the highest strength values obtained among the other experimental groups. The strength of 7-day specimens obtained after 10 freeze–thaw cycles was 373 kPa, being 1.82 times more than the strength of the untreated clay.

References

1. Lu Y, Liu S, Alonso E, Wang L, Xu L, Li Z (2019) Volume changes and mechanical degradation of a compacted expansive soil under freeze-thaw cycles. *Cold Reg Sci Technol* 157:206–214
2. Shahsavani S, Vakili AH, Mokhberi M (2021) Effects of freeze-thaw cycles on the characteristics of the expansive soils treated by nanosilica and electric arc furnace (EAF) slag. *Cold Reg Sci Technol* 182:103216
3. Bell FG (1995) Cement stabilization and clay soils, with examples. *Environ Eng Geosci* 1(2):139–151
4. Bell FG (1996) Lime stabilization of clay minerals and soils. *Eng Geol* 42(4):223–237
5. Dash SK, Hussain M (2012) Lime stabilization of soils: reappraisal. *J Mater Civ Eng* 24:707–714
6. Zhang G (2007) Soil nanoparticles and their influence on engineering properties of soils. In: *Advances in measurement and modeling of soil behavior*. Geo-Denver, pp 1–13
7. Changizi F, Haddad A (2017) Improving the geotechnical properties of soft clay with nano-silica particles. *Proc Instit Civil Eng-Ground Improve* 170(2):62–71
8. Moayed RZ, Rahmini H (2017) Effect of Nano-SiO₂ solution on the strength characteristics of kaolinite. *World Academy of Science, Engineering Technology. Int J Geotechnic Geolog Eng* 11(1)
9. Majeed ZH, Taha MR, Jawad IT (2014) Stabilization of soft soil using nanomaterials. *Res J Appl Sci Eng Technol* 8(4):503–509
10. Ghorbani A, Hasanzadehshooili H, Mohammadi M, Sianati F, Salimi M, Sadowski L, Szymanowski J (2019) Effect of selected nanospheres on the mechanical strength of lime-stabilized high-plasticity clay soils. *Adv Civil Eng*
11. Kalhor A, Ghazavi M, Roustaei M, Mirhosseini SM (2019) Influence of nano-SiO₂ on geotechnical properties of fine soils subjected to freeze-thaw cycles. *Cold Reg Sci Technol* 161:129–136. <https://doi.org/10.1016/j.coldregions.2019.03.011>
12. Shahsavani S, Vakili AH, Mokhberi M (2021) Effects of freeze-thaw cycles on the characteristics of the expansive soils treated by nanosilica and Electric Arc Furnace (EAF) slag. *Cold Reg Sci Technol* 182. <https://doi.org/10.1016/j.coldregions.2020.103216>
13. Aksu G, Eskisar T (2021) Mechanical behavior of cement-treated soils with nanosilica—a green binder. In: *Advances in sustainable construction and resource management. Lecture Notes in Civil Engineering*, vol 144. Springer, Singapore. pp 609–618
14. ASTM D2487. (2006). Standard practice for classification of soils for engineering purposes (Unified Soil Classification System). *Annual Book of ASTM Standards*
15. ASTM D4318. (2017). Standard test methods for liquid limit, plastic limit, and plasticity index of soils. *Annual Book of ASTM Standards*

16. ASTM D698. (2012). Standard test methods for laboratory compaction characteristics of soil using standard effort. Annual Book of ASTM Standards
17. ASTM D560. (2012). ASTM D560–96 standard test methods for freezing and thawing compacted soil-cement mixtures. ASTM Int. <https://doi.org/10.1520/D0560>
18. ASTM D2166. (2006). Standard test method for unconfined compressive strength of cohesive soil. Annual Book of ASTM Standards
19. Vitale E, Deneele D, Russo G (2020) Microstructural investigations on plasticity of lime-treated soils. *Minerals* 10(5):386. <https://doi.org/10.3390/min10050386>
20. Changizi F, Haddad A (2016) Effect of Nano-SiO₂ on the geotechnical properties of cohesive soil. *Geotech Geol Eng* 34:725–733. <https://doi.org/10.1007/s10706-015-9962-9>
21. Hu K, Chen X, Chen J, Ren X (2018) Laboratory investigation of the effect of nano-silica on unconfined compressive strength and frost heaving characteristics of silty clay. *Soil Mech Found Eng* 55:352–357. <https://doi.org/10.1007/s11204-018-9548-7>
22. Landman J, Paineau E, Davidson P, Bihannic I, Michot LJ, Philippe AM et al (2014) Effects of added silica nanoparticles on the nematic liquid crystal phase formation in beidellite suspensions. *J Phys Chem B* 118:4913–4919
23. Ghazavi M, Roustaie M (2010) The influence of freeze–thaw cycles on the unconfined compressive strength of fiber-reinforced clay. *Cold Reg Sci Technol* 61:125–131

Improvement of Shear Strength of Fine-Grained Soils by Waste Glass



Victor Ojotisa  and Ayse P. Balkis

Abstract Due to clay having little or no impressive engineering properties causes a need to develop its properties prior to construction taking place as foundation play a very essential and important role hence the need for soil stabilization techniques. This study focuses on the utilization of waste glass in stabilizing and improving the soil shear strength parameters. Waste glass passing 0.075 μm sieve and 0.300 μm sieve was sequentially added in soil with 0, 6, 8, 10 and 12%. According to unified soil classification system the soil is low plasticity clay, CL. Direct shear strength tests were performed on un-stabilized soil and waste glass added sample to see the effect of waste glass addition on cohesion and angle of internal friction. From the results obtained 10% was found to be optimum addition value for waste glass for this since it improves cohesion values from 4 to 12 kPa for 0.300 μm sieve passing added waste glass and 4–17 kPa for 0.075 μm sieve passing added waste glass while angle of internal friction showed a continual decrease for each waste glass added which may be attributed to the characteristics of the waste glass and chemical compositions. Results showed 8% to be the optimum value as internal angle of friction and cohesion values peaked but showed decrease as the percent increased afterwards. Waste glass increases the cohesion amongst the soil particles thereby changing the shear strength parameter for the soil. Waste glass is a suitable stabilizer for clay soil.

Keywords Cohesion · Direct shear test · Internal angle of friction · Soil stabilization · Waste glass

V. Ojotisa (✉) · A. P. Balkis
Cyprus International University, Via Mersin 10, Haspolat, North Cyprus, Turkey
e-mail: ojotisavictor@gmail.com

A. P. Balkis
e-mail: apekrioglu@ciu.edu.tr

© The Author(s), under exclusive license to Springer Nature Switzerland AG 2023
C. Atalar and F. Çinicioğlu (eds.), *5th International Conference on New Developments in Soil Mechanics and Geotechnical Engineering*, Lecture Notes in Civil Engineering 305, https://doi.org/10.1007/978-3-031-20172-1_48

493

1 Introduction

Soil since inception of time, has always been a crucial and essential building material. However some soils may have low mechanical properties which needs improvement. Such properties include shear strength, lateral earth pressure, consolidation, bearing capacity, slope stability and permeability & seepage amongst others. In which shear strength relates to the amount of shear a substance or material can endure or abide and not fracture. Shear strength knowledge is crucial as it's used in the design of foundations, embankments for dams, roads, pavement, excavations, levees etc. the analysis of the stability of slope is evaluated using shear strength and the bearing capacity of the soil. A method to overcome weakness of soil is called stabilization in which materials are injected or mixed with the soil to attain certain results which show a positive result on the properties and also an economical way to do so. Shear strength of soils depend on certain factors such as stress history, water content, soil structure, drainage conditions, rate of load, degree of saturation and soil composition amongst others. Waste is a big issue especially as the rate in which waste is generated, for example agriculture, private or commercial industries or hospitals etc. can't meet up with its rate of safe disposal without harming the area, environment etc. due to massive amount of waste. Emissions from waste sites or landfills are not of good benefit to the environment, humans or the ozone layer. A way to solve this dilemma is to recycle and reuse such materials by making them useful to certain needs and demands. Due to this dilemma, using waste glass a stabilizer was established. The aim of this study is to check the geotechnical properties of soil mainly shear strength which has been mixed and stabilized with waste glass at 0, 6, 8, 10 and 12% with tests conducted in a laboratory. This percentages were used in this study in relation with percentages used in previous studies, to have comparison values and also to see how it affects the clayey soil properties as well as to determine an optimum value. Ibrahim et al. [1] used waste glass on expansive soil [CH]. Tests such as Atterberg limits, unconfined compressive strength etc. was conducted with waste glass added in 6, 12, 18, 27, and 36% of the dry weight of soil. Results from the tests conducted showed a positive result and showed that the characteristics improved by adding glass. Olufowobi-Ogundoku et al. [2] used waste glass with clay soil. Tests such as moisture content, specific gravity, particle size distribution Atterberg limits, and direct shear tests were conducted. The soil was classified as a group 4–6 which was fair to poor. Waste glass was added in percent such as: 2,5,10 and 15%.Maximum values for cohesion and angle of friction were obtained at 10% waste glass although 15/5 cement was used as based throughout. Maximum cohesion and angle of internal friction values of 17.0 and 15.0 respectively were obtained at 10% glass powder content [3] used a clay soil sub grade with waste glass. They carried out tests such as compaction (optimum moisture content), CBR, and Atterberg limits. The soil was a 7–6 clay soil. Results showed that 10% waste glass was optimum percent to add by the dry unit weight of the soil to improve the subgrade. Sambo [4] used a black cotton soil which was obtained at about a depth of 7 m and mixed it with waste glass. Tests such as liquid limit, plastic limit, optimum moisture content, California bearing ratio

Table 1 Physical properties of soil

Properties	Values
Water content %	11.05
Plastic limit %	14
Liquid limit %	29
Plasticity index %	15
Specific gravity	2.55

Soil Type: CL, Lean clay

and maximum dry density were carried out. Waste glass was added in 0, 2, 4, 6, 8% replacement by weight. 8% showed the best results.

2 Research Significance

In this research waste glass (powdered) will be used in stabilizing soil. Shear strength test was conducted. Two major engineering properties will be namely cohesion [c] and angle of internal friction [ϕ] as they determined the shear strength of a soil. Comparison will be made between the cohesion and internal angle of friction values for raw soil sample and soil sample mixed with waste glass. A comparison will be made with previous studies to see if the optimum value obtained for them correspond.

3 Materials

3.1 Soil

The research was conducted by utilizing different materials such as soil, waste glass, and distilled water. The soil was oven dried and sieved to obtain fine soils [0.075 μm passing]. Only the fine part was used in this study which was 0.075 μm sieve passing. The grain size distribution of the soil was obtained in accordance with ASTM D421. The physical properties of the soil used are shown in Table 1 and sieved soil is shown in Fig. 1.

3.2 Waste Glass

The waste glass was obtained locally, cleaned, crushed using the Los Angeles abrasion machine then sieved to obtain 0.075 and 0.300 μm size passing. Sieved waste

Fig. 1 0.075 μm sieve passing soil



Fig. 2 0.075 μm sieve passing waste glass



glass of 0.075 μm passing and 0.300 μm passing is shown in Figs. 2 and 3, respectively. Figures 4 and 5 show the soil sample before and after mix. Waste glass was added to the soil sample by the dry unit weight of the soil.

Fig. 3 0.300 μm sieve passing waste glass



Fig. 4 Soil with waste glass before mix



Fig. 5 Soil with waste glass after thorough mix



4 Results and Discussions

4.1 Direct Shear Test

This test was conducted in drained conditions. As stated in the early part of this article the test was conducted with two different waste glass size sample namely $0.300\ \mu\text{m}$ sieve passing and $0.075\ \mu\text{m}$ sieve passing. Pace rate was kept constant throughout at $0.5\ \text{mm}/\text{min}$. Each test completion time until failure ranged from 10 to 13 min' with 13 min' been maximum and 10 min' minimum. For both 0.300 and $0.075\ \mu\text{m}$, cohesion showed a positive increase up till 10% addition. Figure 6 graph which indicates cohesion values against WG% addition for $0.3\ \mu\text{m}$ and show 10% WG peaking while Fig. 7 graph indicates angle of internal against WG% addition for $0.3\ \mu\text{m}$ and show the gradual decrease as WG increased. Figures 8 and 9 show a combined graph of cohesion and angle of internal friction values for $0.300\ \mu\text{m}$ while Figs. 10 and 11 show a bar graph of cohesion values and angle of internal friction. These figures show even at 6% addition of waste glass for 0.300 and $0.075\ \mu\text{m}$ respectively there is a continuous decrease as the percent goes up. These values corresponds with studies from AbdulZahra (2018), Benny et al. (2020) study which found 8% to be the optimum WG added to clay soil subgrade otherwise there will be a decline in value. Dadkhahs' et al. [5] pointed out the inverse increase and decrease can be antecedent towards the shape of the shear box and density as well. The variation in the results could also be attributed to soil types for example black cotton soil showed 8% to be optimum, likewise for high plasticity soil and the gradation or granular nature of the waste glass (Sambo 2019, Javed 2020). Jared (2020) shear strength parameter of soil showed the waste glass mixtures changed as there was increase cohesion but decrease in angle of friction among the soil particles mainly after 10%. It can be determined that the angle of internal friction and cohesion values for the soil would increase when Waste glass powder has been added to maximum value of 10% Al-neami et al. [6], Javed and Chakraborty [7]. Jareds' (2020) study showed 10% to be the optimum percent value to add waste glass (Tables 2 and 3).

Fig. 6 Cohesion against WG% 0.300 μm

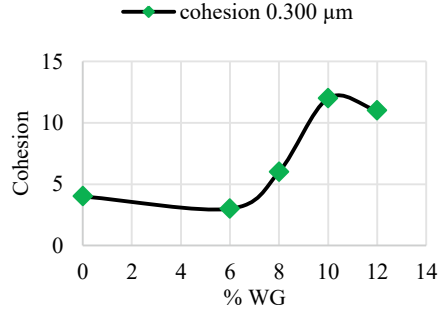


Fig. 7 Angle of internal friction against WG% 0.300 μm

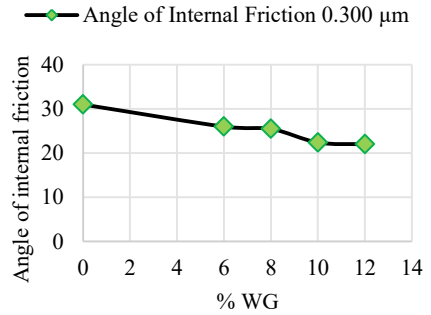
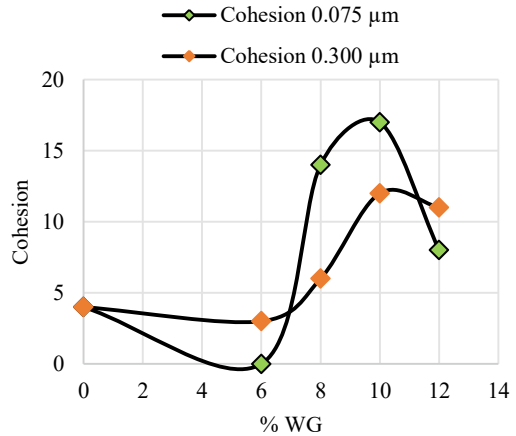


Fig. 8 A combined line graph of cohesion with WG%



4.2 Microstructural Analysis of WG in Fine Soil

Scanning electron microscopy (SEM) was conducted in each percent replaced but only was 0.075 μm at 8% and 0.300 μm at 8% is included in this paper. Circular prints on the images indicate waste glass. X-ray power diffraction (XRD) was conducted

Fig. 9 A combined line graph of angle of internal friction

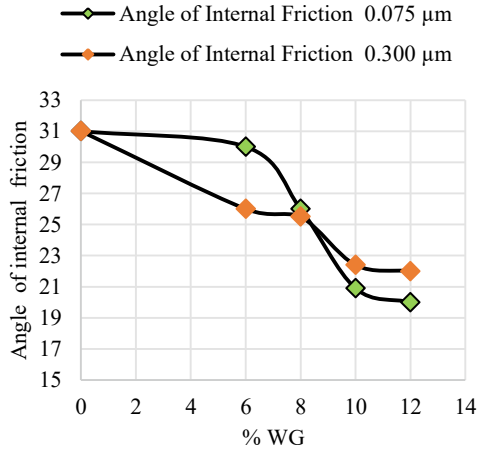


Fig. 10 A line graph of cohesion against WG% of 0.300 μm

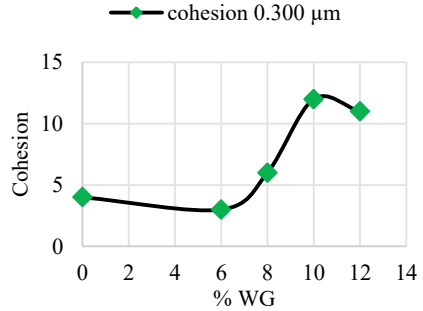
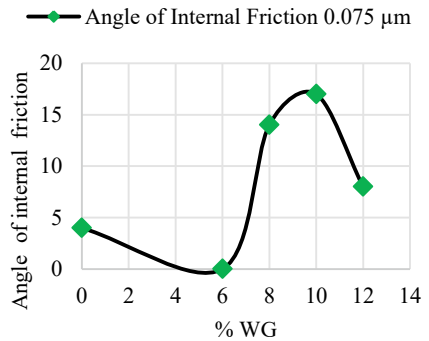


Fig. 11 A line graph of angle of internal friction against WG% of 0.075 μm



in the same fashion and 0.075 at 8% and 0.300 at 8% is included in this paper with 02si (quartz) been the highest mineral content which can be attributed to the waste glass and soil type. Other elements contained include CaCO₃, AlO₄, S-Ti₂, Mg-O etc. Some elements, on the other hand, have to be missing for good bonding with

Table 2 Shear strength parameter for 0.300 μm WG% added mixture

0.300 μm		
% of waste glass	Angle of internal friction[$^{\circ}$]	Cohesion [kPa]
0	31	4
6	26	3
8	25.5	6
10	22.4	12
12	22	11

Table 3 Shear strength parameter for 0.075 μm WG% added mixture

0.075 μm		
% of waste glass added	Angle of internal friction[$^{\circ}$]	Cohesion [kPa]
0	31	4
6	30	0
8	26	14
10	20.9	17
12	20	8

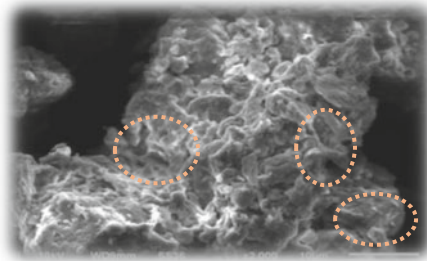


Fig. 12 SEM of 0.075 μm at 8% with 2000 magnification (author)

other elements to build a powerful compound that might maintain weak soil (Figs. 12 and 13).

5 Conclusion

For this study, multiple direct shear tests were carried out on low plasticity soil samples with various waste glasses been added at certain percent which have been sieved through 0.300 and 0.075 μm respectively with the intent to check how it impacts the shear strength.

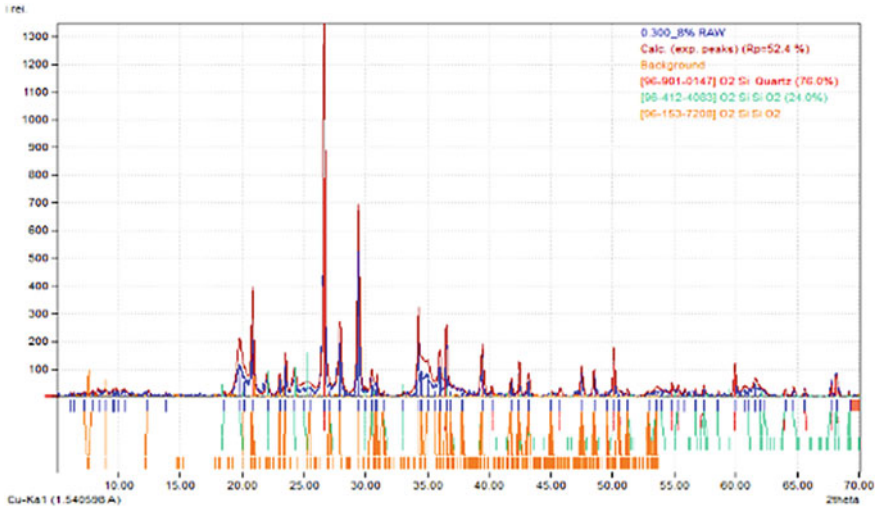


Fig. 13 Energy dispersive x-ray of 0.075 μm glass at 8% replacement (author)

For both 0.300 and 0.075 μm samples, cohesion showed a positive increase up till 10% waste glass addition. Angle of internal friction on the other hand showed a decrease as waste glass percent increased. There is increase in the frictional forces due to the movement of the soils particles which increase the shear strength for the granular materials. The test carried out for this test was bounded to direct shear test with drained conditions. The variation in the results could also be attributed to soil type for example black cotton soil showed 8% to be optimum, likewise for high plasticity soil and the gradation or granular nature of the waste glass according to literature. Shear strength parameter of soil showed the waste glass mixtures changed as there was an increase for cohesion but decrease in angle of friction among the soil particles mainly after 10%. According to the recent finding done, it can be said that the angle of friction and cohesion values for the soil would increase when Waste glass powder has been added to maximum value of 10%. Comprehensively it can be decided that utilization of waste glass for soil stabilization is a suitable, effective, cheap and environment friendly in terms of pollution.

Further studies should be considered with drainage factors for the shear tests and also using various soils types to compare the results. A focus could be in regards to how the chemical composition of waste glass affects soil properties and the values obtained in terms of cohesion and angle of internal friction. Tests can be conducted with various direct shear test box sizes, and the results obtained should be evaluated accordingly.

References

1. Ibrahim H, Mawlood Y, Alshkane Y (2019) Using waste glass powder for stabilizing high-plasticity clay in Erbil city-Iraq. *Int J Geotech Eng* 15:1–8. <https://doi.org/10.1080/19386362.2019.1647644>
2. Olufowobi J, Ogundaju A, Michael B, Aderinlewo O (2014) Clay Soil Stabilisation Using Powdered GlasS. *J Engi Sci Technol* 9:541–558
3. Lingwanda MI (2018) Use of waste glass in improving subgrade soil properties. *IJRETijreT*. <https://ijret.org/volumes/2018v07/i04/IJRET20180704005.pdf>
4. Sambo AHBOA, Sani JE (2019 May 5) Black cotton soil stabilization using glass powder. *Int J Innovative Res Sci Eng Technol*. https://www.researchgate.net/publication/333547655_Black_Cotton_Soil_Stabilization_using_Glass_Powder
5. Dadkhah R, Ghafoori M, Ajalloeian R, Lashkaripo G (2010) The effect of scale direct shear test on the strength parameters of clayey sand in Isfahan city, Iran. *J Appl Sci* 10(18):2027–2033. <https://doi.org/10.3923/jas.2010.2027.2033>
6. Al-Neami MA, Al-Soudany K, Dawod A (2015) Remediation Of cohesive soils using waste glass
7. Javed SA, Chakraborty S (2020) Effects of waste glass powder on subgrade soil improvement. 144, 30–42
8. Babatunde AO, Sani JE, Sambo H (2019) Black cotton soil stabilization using glass powder. 8, 5208–5214. <https://doi.org/10.15680/IJRSET.2019.0805053>
9. Salamatpoor S, Salamatpoor S (2017) Evaluation of adding crushed glass to different combinations of cement-stabilized sand. *Int J Geo-Eng* 8(1). <https://doi.org/10.1186/s40703-017-0044-0>
10. Siyab Khan M, Tufail M, Mateullah M (2018) Effects of waste glass powder on the geotechnical properties of loose subsoils. *Civil Eng J* 4(9):2044. <https://doi.org/10.28991/cej-03091137>
11. Lee T (2007) Recycled glass and dredged materials. 13. https://www.researchgate.net/publication/235023644_Recycled_Glass_and_Dredged_Materials